

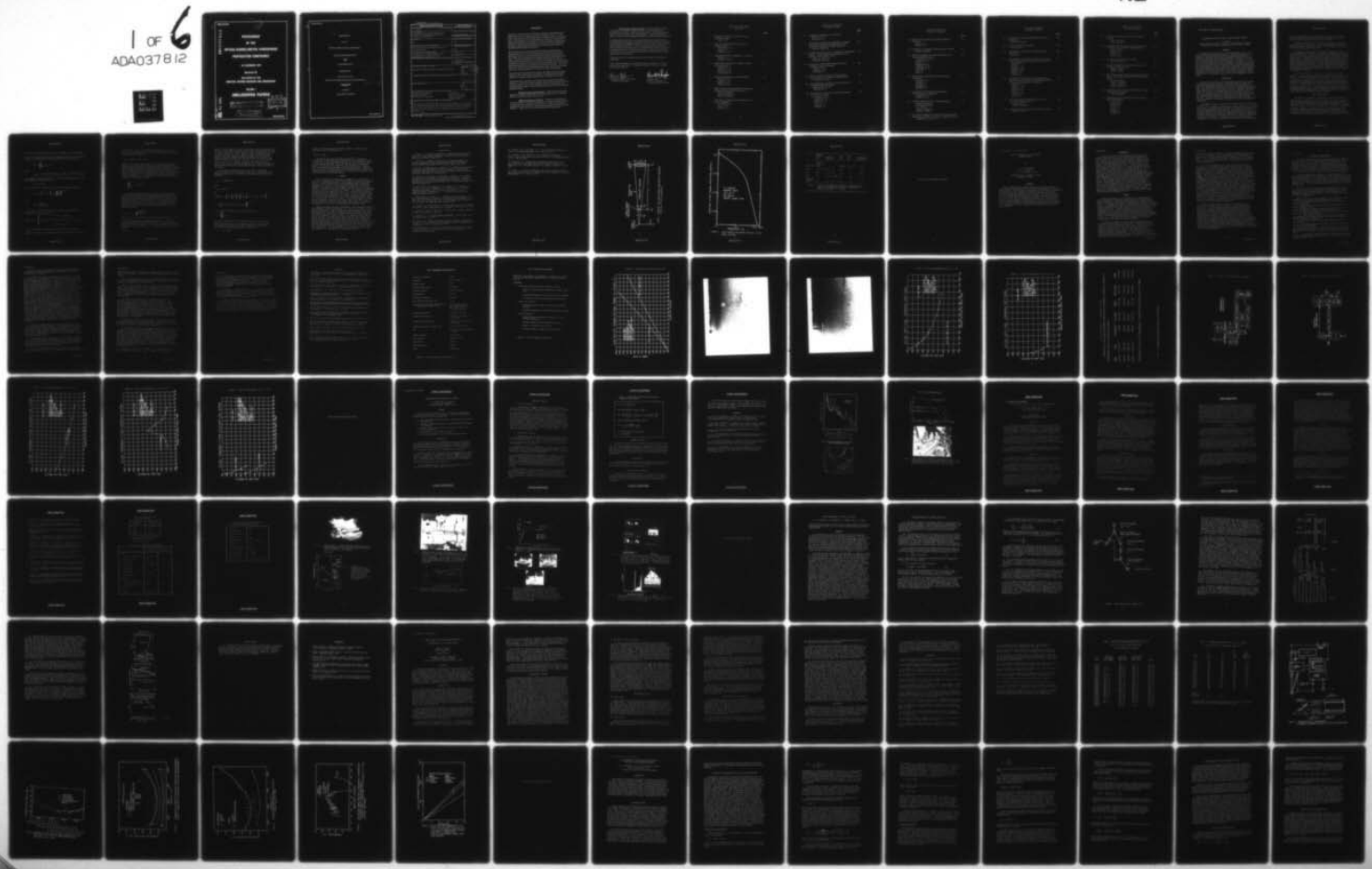
AD-A037 812

OFFICE OF THE DIRECTOR OF DEFENSE RESEARCH AND ENGINE--ETC F/G 20/14
PROCEEDINGS OF THE OPTICAL-SUBMILLIMETER ATMOSPHERIC PROPAGATIO--ETC(U)
DEC 76

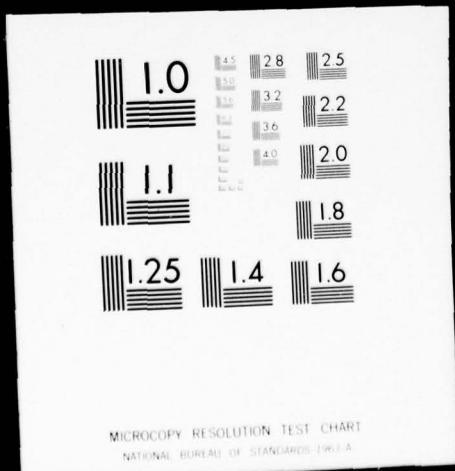
UNCLASSIFIED

1 OF 6
ADA037812

NL



I OF
ADA037812



UNCLASSIFIED

ADA037812

PROCEEDINGS
OF THE
OPTICAL-SUBMILLIMETER ATMOSPHERIC
PROPAGATION CONFERENCE

6-9 DECEMBER 1976

Sponsored By

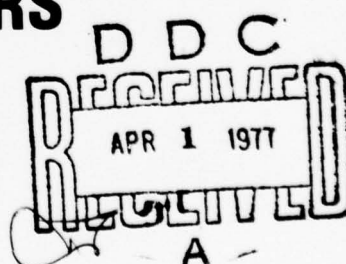
THE OFFICE OF THE
DIRECTOR, DEFENSE RESEARCH AND ENGINEERING

VOLUME 1

UNCLASSIFIED PAPERS

COPY AVAILABLE TO DDC DOES NOT
PERMIT FULLY LEGIBLE PRODUCTION

DISTRIBUTION STATEMENT A	
Approved for public release; Distribution Unlimited	



UNCLASSIFIED

12111
DDC FILE COPY

UNCLASSIFIED

⑥ PROCEEDINGS

OF THE

OPTICAL-SUBMILLIMETER ATMOSPHERIC

PROPAGATION CONFERENCE



6-9 DECEMBER 1976

Volume I. Un-
classified Papers.

SPONSORED BY

⑪ 9 Dec 76

THE OFFICE OF THE

DIRECTOR, DEFENSE RESEARCH AND ENGINEERING



⑫ 510p.

VOLUME 1

UNCLASSIFIED PAPERS

266 200

UNCLASSIFIED

Unclassified

SECURITY CLASSIFICATION OF THIS PAGE (When Data Entered)

REPORT DOCUMENTATION PAGE		READ INSTRUCTIONS BEFORE COMPLETING FORM									
1. REPORT NUMBER None	2. GOVT ACCESSION NO.	3. RECIPIENT'S CATALOG NUMBER									
4. TITLE (and Subtitle) Proceedings of the Optical-Submillimeter Atmospheric Propagation Conference (U), 6-9 December 1976, VOL 1		5. TYPE OF REPORT & PERIOD COVERED Conference Report									
7. AUTHOR(s) N/A		6. PERFORMING ORG. REPORT NUMBER									
9. PERFORMING ORGANIZATION NAME AND ADDRESS Office of the Director of Defense Research and Engineering		10. PROGRAM ELEMENT, PROJECT, TASK AREA & WORK UNIT NUMBERS									
11. CONTROLLING OFFICE NAME AND ADDRESS Deputy Director, Research and Advanced Technology, Rm 3E114, Pentagon Washington, D. C. 20301		12. REPORT DATE									
14. MONITORING AGENCY NAME & ADDRESS (if different from Controlling Office)		13. NUMBER OF PAGES									
		15. SECURITY CLASS. (of this report) Unclassified									
		15a. DECLASSIFICATION/DOWNGRADING SCHEDULE									
16. DISTRIBUTION STATEMENT (of this Report) Approved for Public Release, Distribution Unlimited											
17. DISTRIBUTION STATEMENT (of the abstract entered in Block 20, if different from Report)											
18. SUPPLEMENTARY NOTES											
19. KEY WORDS (Continue on reverse side if necessary and identify by block number) <table border="1" style="float: right; margin-right: 10px;"> <tr> <td>ACCESSION for</td> <td rowspan="4">NTIS DOC UNANNOUNCED JUSTIFICATION</td> <td>White Section</td> </tr> <tr> <td>BY</td> <td>Buff Section</td> </tr> <tr> <td colspan="2">DISTRIBUTION/AVAILABILITY</td> </tr> <tr> <td>DET. APPROV. BY</td> <td>ST</td> </tr> </table> Atmospheric Propagation Optical Propagation Submillimeter Propagation Meteorology Physical Meteorology Infrared Propagation Imaging Systems			ACCESSION for	NTIS DOC UNANNOUNCED JUSTIFICATION	White Section	BY	Buff Section	DISTRIBUTION/AVAILABILITY		DET. APPROV. BY	ST
ACCESSION for	NTIS DOC UNANNOUNCED JUSTIFICATION	White Section									
BY		Buff Section									
DISTRIBUTION/AVAILABILITY											
DET. APPROV. BY		ST									
20. ABSTRACT (Continue on reverse side if necessary and identify by block number)											
This report is one of a two volume set of papers submitted for presentation at the Optical-Submillimeter Atmospheric Propagation Conference held at the U. S. Air Force Academy on 6-9 December 1976. Volume 1 contains all unclassified papers and Volume 2 contains those papers which are classified.											

DD FORM 1 JAN 73 1473

EDITION OF 1 NOV 65 IS OBSOLETE

Unclassified

SECURITY CLASSIFICATION OF THIS PAGE (When Data Entered)

FOREWORD

The Office of the Director of Defense Research and Engineering, conducted a four-day symposium and workshop at the U. S. Air Force Academy in Colorado Springs, Colorado, from 6-9 December 1976. The purpose was to bring together members of the optical systems development, atmospheric sciences (optical propagation), and meteorological communities to review activities, summarize problems, and establish priorities for resolving deficiencies in atmospheric propagation research.

The overall goal of DoD sponsored propagation research and development is to provide the know-how for estimating and predicting the effects of the propagation environment (anywhere in the world) on DoD weapons and communications systems performance. One particular goal is to relate bulk parameters of the atmosphere measurable in the tactical environment to performance of defense systems to aid in assessing field employment opportunities and selecting optimum systems for particular missions. A second goal is to achieve an understanding of the effect of the environment on system design parameters to permit design optimization.

The conference emphasized low power and passive tactical applications in the visual and IR spectrum, but included some topics relating to strategic applications and the submillimeter region.

The symposium consisted of a formal session and two workshop sessions. During the formal session, invited and contributed papers were presented to provide a common frame of reference for the workshop discussions. Three topical areas were covered during the formal session:

Optical Systems Performance - What are critical propagation performance thresholds for EO imaging systems, guidance systems, and communications systems?

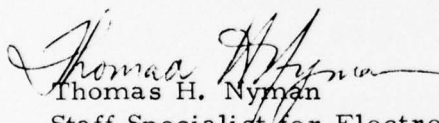
Optical Propagation Physics - What are capabilities of various models, simulation techniques, and measurement systems to represent the propagation environment? What meteorological parameters are required to support the propagation prediction capabilities? What are the current and planned investigations?

Meteorological Characteristics - What capabilities exist to measure or otherwise define the state of the atmosphere for propagation prediction? What data bases exist? How can these data bases be used to build/design climatologies? What are the future plans to improve environmental prediction for optical defense systems?

Following the formal session, the participants were split into four working groups according to scientific area to discuss major research and development technology needs across the systems, physics, and meteorology science areas. After the technology needs were presented for each scientific area, the working groups were reconstituted by application area to prioritize the needs by urgency and difficulty. The intent was to have each participant serve on one scientific and one applications working group.

A general review of conclusions and open discussion concluded the conference.

This volume presents the unclassified papers submitted for presentation at the conference. A companion volume (Volume 2) contains the classified papers.


Thomas H. Nyman
Staff Specialist for Electronics
Systems Technology


Kenneth W. Ruggles
Captain, USN
Military Assistant for
Environmental Sciences

TABLE OF CONTENTS
VOLUME 1

	<u>Page</u>
1. Atmospheric Effects on Army IR Laser Guidance Systems Lilly, J. Q.	1
2. Optical Communications in the Marine Boundary Layer Mooradian, G. C. Geller, M. Giannaris, R. J.	13
3. Submillimeter Wave Propagation - A Survey Gamble, W. L. Guenther, B. D.	35
4. Submillimeter System for Imaging Through Inclement Weather Hartman, R. L. Gamble, W. L. Guenther, B. D. Kruse, Paul W.	41
5. System Engineering in Limited Visibility Peterson, D. R. Blanton, V. D. Stamps, M. P. Fowler, B. W.	53
6. Water Vapor Line and Continuum Absorption Measurements in the Infrared Region White, Kenneth O. Watkins, Wendell R. Bruce, Charles W.	63
7. Atmospheric Transmission Modeling for DF Laser Propagation Meredith, R. E. Tuer, T. W. Woods, D. R.	79

TABLE OF CONTENTS
VOLUME 1 (Cont'd)

	<u>Page</u>
8. Propagation Modeling for E-O Sensors Fowler, B. W. Peterson, D. R.	95
9. Atmospheric Transmission Modeling: Proposed Aerosol Methodology With Application to the Grafenwohr Atmospheric Optics Data Base Roberts, Robert E.	103
10. Complex Refractive Index of Atmospheric Particulate Matter - Current State of Knowledge from E-O Systems Effects Point of View Lindberg, James D. Gillespie, James B.	135
11. Aerosol Size Distribution Measurements for Radiation Transfer Modeling Pinnick, R. G. Hoihjelle, D. L. Fernandez, G.	147
12. Effect of Relative Humidity on Aerosol Size Distribution and Visibility: Modelling Studies Fitzgerald, James W.	155
13. Fog Climatology in Central Europe and Inferred Propagation Characteristics Essenwanger, O. M. Stewart, D. A.	165
14. The Nature of Gun Smoke and Dust Obscuration Due to Cannon Firing Stuebing, E. W. Verderame, F. D. Doherty, R. W. Pinto, J. J. Lucia, E. A. Vinansky, G.	181

TABLE OF CONTENTS
VOLUME 1 (Cont'd)

	<u>Page</u>
15. Optical Aerosol Models and Light Scattering Programs Fenn, R. W. Shettle, E. P.	209
16. Atmospheric Turbulence Measurements at AMOS Hanson, Donald W.	245
17. Optical Propagation Through Turbulence in the Marine Boundary Layer Crittenden, E. C., Jr. Cooper, A. W. Milne, E. A. Rodeback, G. W. Kalmbach, S. H. Armstead, R. L. Land, D. Katz, B.	255
18. Description of Optically Relevant Turbulence Parameters Davidson, K. L. Fairall, C. Houlihan, T. Schacher, G. Hinsman, D.	273
19. A Program for EO Systems Performance Prediction in the Atmosphere Lutomirski, R. F. Shapiro, A. R.	289
20. Weather Support to Electro-Optical Systems Hodges, Donald B. Wachtmann, Ronald Try, Paul D. Johnson, William F. Dickson, Edwin B.	305
21. The Content and Some Limitations of Meteorological Data Bases Available for Optical Propagation Studies Mendenhall, Laurence D.	319

TABLE OF CONTENTS
VOLUME 1 (Cont'd)

	<u>Page</u>
22. Development of New Meteorological Services for EO Systems Ruhnke, Lothar H.	341
23. Seeing Through the Atmosphere Lund, Iver A.	347
24. Probability of Occurrence for Marine Optical Parameters Katz, B. S.	359
25. A Preliminary Comparison of High and Low Reso- lution Atmospheric Transmission Measurements Bergemann, R. Sola, M. Dowling, J. A. Haught, K. M. Horton, R. F. Walsh, J. L. Roberts, R.	375
26. Atmospheric Transmission Field Experiments Using IR Lasers, Fourier Transform Spectroscopy and Gas Filter Correlation Techniques Dowling, J. A. Haught, K. M. Horton, R. F. Hanley, S. T. Curcio, J. A. Garcia, D. H. Gott, C. O.	377
27. An Aerosol Measurement System for Laser/ Aerosol Interaction Studies Trusty, Gary L. Cosden, Thomas H.	403
28. Testing the Standard Marine Atmosphere Concept Gathman, Stuart	415

TABLE OF CONTENTS
VOLUME 1 (Cont'd)

	<u>Page</u>
29. A Facility for Characterization of Targeting Systems Pryce, James D. Kelly, Edward H.	427
30. Definition of the Propagation Environment With a Portable Long-Baseline Transmissometer Gerber, H. E. Stilling, R. K. Buser, R. G. Rohde, R. S.	433
31. The Advanced Optical Test Facility Spencer, James L.	443
32. Maritime Atmospheric Characterization at the San Nicolas Island Facility Wilkins, Lowell Shlanta, Alexis	455
33. Micro-Meteorological Measurements for Electro-Optical Propagation Tests at White Sands Missile Range Hoidale, Glenn B. Walters, Donald L. Norton, Colburn L. Pries, Thomas H.	465
34. Evaluation of the Propagation Environment Using Laser Radar Techniques Uthe, Edward E.	475
35. High Energy Laser Propagation Meteorological Sensitivity Analysis Cordray, D. Fitzgerald, J. Gathman, S. Hayes, J. Kenney, J. Mueller, G. Ruskin, R.	491

.... This paper is UNCLASSIFIED

ATMOSPHERIC EFFECTS ON ARMY IR LASER GUIDANCE SYSTEMS

J. Q. Lilly

US Army Missile Research, Development & Engineering Laboratory
US Army Missile Command, Redstone Arsenal, Alabama 35809

Abstract

This paper describes efforts to model atmospheric effects on IR laser terminal homing guidance systems. A theoretical model is described to rapidly calculate the time dependent beam wander due to atmospheric turbulence and results presented to illustrate the magnitude of expected spot sizes and movement about the target aim point for an IR laser designator tactical situation. The effects of attenuation of the atmosphere by molecular absorption and aerosol absorption and scattering are included in the model using a program developed for the Army Atmospheric Sciences Laboratory at New Mexico State University. The program developed at NMSU utilizes the McClatchey line parameters compilation and performs Mie theory calculations to estimate aerosol absorption and scattering effects. Results are presented to illustrate the magnitude of attenuation expected for typical atmospheric conditions.

INTRODUCTION

One of the major effects of the atmosphere which tend to degrade the performance of laser guidance systems is caused by random air temperature variations produced by air turbulence along the path of a laser beam transmitted through the atmosphere. The resulting refractive index variations cause phase distortions in the transmitted beam which change with time at a rate dependent on the wind velocity across the beam. The effects of the random variation in refractive index is to produce an enlarged spot at the target which moves about the aim point in a random fashion depending on the wind velocity and turbulence strength. The beam "jitter" or wander produced in this way adds to the jitter introduced by the guidance components to affect total system performance.

This paper describes a new analytical method recently developed by Fried (1), (2) for rapidly predicting spot movement and size as a function of transmitter characteristics, refractive index structure constant and the effective windspeed across the beam. The approach used is an alternate method to the Monte Carlo technique employed in several large computer codes wherein a series of random phase screens are introduced at several intervals along the path and used in a numerical solution to the scalar wave equation. The Monte Carlo method yields detailed information of the beam characteristics, but for many time realizations

UNCLASSIFIED

such as is required for laser designator tests, computation times become prohibitive since a separate laser-to-target calculation of several steps is required for each time of interest.

Following the description of the method used here, results are presented of calculations over a typical laser designator path for the assumed atmospheric conditions. Results of calculated spot size and beam deflections are also presented.

In addition to the effects of atmospheric turbulence, laser guidance systems are affected by the amount of attenuation occurring in the transmitted beam. Attenuation results in the achievement of lower intensity at the target thus reducing the signal received by a terminal homing device. Attenuation occurs from absorption and scattering of radiation by air molecules and particulate matter present in the atmosphere; however, molecular absorption and particulate scattering are the primary attenuating mechanisms. In cases where high concentrations of aerosol particles are present, scattering and absorption by particles may completely dominate the attenuation. Examples of cases where scattering becomes particularly important are in rain, fog, dust or high concentrations of smoke.

For the calculation of attenuation by molecules and aerosol particles, computer programs obtained from Miller⁽³⁾ and Gomez⁽⁴⁾ were utilized. The molecular absorption program uses the McClatchey et al⁽⁵⁾ line parameters compilation and computes high resolution molecular absorption, continuum molecular absorption, Rayleigh scattering by molecules, and incorporates the aerosol absorption and scattering model developed by Gomez⁽⁴⁾ at the Army Atmospheric Sciences Laboratory at White Sands Missile Range. Computed results of absorption and scattering transmissivities are presented for representative cases to illustrate their effects on Army IR laser guidance systems.

MODEL DESCRIPTION

For numerical evaluation of turbulence effects, the theoretical model developed by Fried⁽¹⁾ is used to calculate the power spectrum of angle-of-arrival fluctuations of a laser target designator beam. In this model, the illuminated spot at the target is treated as a receiver located a distance Z_s from a point which is a distance Z_d behind the designator (Figure 1). The point source is considered the origin ($Z = 0$) and its distance behind the designator is determined by the designator aperture diameter and beam divergence angle. The turbulent region exists only between the designator and target (distance Z_t) and

UNCLASSIFIED

this region is divided into N segments of length Δz_i for the computations. Following the method of Greenwood and Fried,⁽⁶⁾ the angle-of-arrival power spectrum is calculated according to the relation

$$F_\alpha(f) = \sum_{i=1}^N F_{\alpha,i}(f)$$

where

$$F_{\alpha,i}(f) = 1.32 \times 10^{-2} (\lambda/D_s)^2 (D_s/r_{o,i})^{5/3} f_{o,i}^{-1/3} f^{-2/3} G_\alpha(f/f_{o,i}).$$

f is temporal frequency in hertz, λ is the laser wavelength and D_s , the spot diameter, is calculated from

$$D_s = D_d + \theta_d Z_t$$

$r_{o,i}$ is Fried's⁽⁷⁾ coherence length for the i th segment defined by

$$r_{o,i} = \left\{ 16.7 c_{N,i}^2 \left(\frac{\Delta z_i}{\lambda^2} \right) \left(\frac{z_i}{z_s} \right) \right\}^{-3/5}$$

and

$$f_{o,i} = \frac{V_{eff,i}}{\pi D_s (z_i/z_s)}$$

$G_\alpha(f/f_{o,i})$ is a function evaluated by Greenwood and Fried⁽⁶⁾ and determined to fit the expression

$$G_\alpha(f/f_{o,i}) = \begin{cases} 1 & \text{, if } 0 \leq f \leq 0.332 f_{o,i} \\ 1.12 - 0.361 (f/f_{o,i}), & \text{if } 0.322 f_{o,i} < f \leq 3.1 f_{o,i} \\ 0 & \text{, if } 3.1 f_{o,i} < f \end{cases}$$

z_i is the distance from the virtual point source to the center of segment i , and $c_{N,i}^2$ is the refractive index structure constant of the

UNCLASSIFIED

i th segment. $v_{\text{eff},i}$ is the effective wind velocity of the i th segment and can include the effects of beam sluing by combining with the actual wind according to

$$v_{\text{eff},i} = v_{W,i} \pm \theta (z_i - z_d)$$

with the plus or minus sign chosen to account for the wind being opposed to or in the same direction as the angular sluing. An additional computation needed in the power spectrum calculation is to multiply each value by $(D_s/D_d)^2$ to correct the point source value for the finite aperture size of the laser designator. Using the method outlined, the power spectrum is computed for the range of frequencies from zero to the cutoff value at approximately three times the largest reference frequency, $f_{o,i}$. The variance of the power spectrum is the integral over frequency, or simply

$$\begin{aligned} f_i &= f_c \\ \sigma^2 &= \sum_{f_i} F_\alpha(f_i) \Delta f_i \\ f_i &= 0 \end{aligned}$$

To compute turbulence induced beam jitter, a random sequence of values is generated having the same approximate power spectrum and variance as was computed for the angle-of-arrival fluctuation. The random array is then Fourier transformed to obtain a time dependent array representing the angular beam jitter. To accomplish this, a random number routine⁽⁸⁾ is utilized to obtain a normally distributed sequence of values having unity variance and zero mean value and combine these numbers with the calculated power spectrum to get the following sequence

$$N_r(f_i) = N_{r,i} \sqrt{F_\alpha(f_i)/\Delta t}$$

Where $N_{r,i}$ is a value obtained from the random number routine, $F_\alpha(f_i)$ is one of the power spectra computed earlier and Δt is the time interval between values in the time sequence. A discrete Fourier transform (FFT) routine⁽⁸⁾ is used to perform the transformations from the frequency to the time sequence, so Δt must be chosen to satisfy the equation

$$M \Delta t \Delta f = 1$$

UNCLASSIFIED

where M is the number of values in the array. Another consequence of the DFT or FFT method is that the random array must be doubled in length to include values for an equal number of negative frequencies and this is done by folding the $N_r(f_i)$ array onto the second half of the doubled array thus creating a symmetric sequence of real values(9). This array when transformed into the time domain are a time ordered symmetric sequence of values in the range $-T \leq t \leq +T$ where $T = M\Delta t$.

The second half of the sequence represents one component of beam jitter at the target. A second independent set of values following the same procedure is necessary to determine the spot centroid movement at the target.

An additional computation made in the model of atmospheric turbulence effects is to determine the spot size increase due to turbulence and diffraction. The effective beam spread as determined by Fried(2) is

$$\theta_t = \theta_r \Phi(D_d/r_o)$$

where

$$\theta_r = 1.128 \frac{\lambda}{r_o}$$

and

$$\Phi(D_d/r_o) = \left\{ \frac{16}{\pi} \left(\frac{D_d}{r_o} \right)^2 \int_0^1 u du \left[\cos^{-1} u - (u)(1-u^2)^{1/2} \right] \right. \\ \left. \times \exp \left[-3.44 \left(\frac{D_d}{r_o} \right)^{5/3} u^{5/3} (1-u^{1/3}) \right] \right\}^{1/2}$$

r_o is defined in terms of the $r_{o,i}$ used earlier as

$$r_o = \sum_{i=1}^N r_{o,i}$$

The function $\Phi(D_d/r_o)$ ⁽¹⁰⁾ is evaluated numerically by a gaussian quadrature method using 100 increments across the interval (0,1). Total angular divergence of the spot determined by a quadrature combination with the designator optics divergence is

$$\theta_s = (\theta_t^2 + \theta_d^2)^{1/2}$$

UNCLASSIFIED

and the corrected spot size including turbulence, diffraction and designator optics contributions is

$$D_s' = D_d + \theta_s Z_t .$$

Included in the model developed by Fried⁽²⁾ is a method for calculating the power spectrum of angle-of-arrival fluctuations caused by turbulence in the propagation path from the laser designator spot to a sensor viewing the spot. The total beam jitter for the combined paths is then evaluated by adding the power spectrum for the sensor path to the laser spot power spectrum obtained previously. Computed power spectra for the sensor path are not included in the present investigation, however, results obtained for a typical laser designator path are presented in the following section.

RESULTS

A laser designator transmitting at $1.06\mu\text{m}$ over a 3 Km path was selected to illustrate the effects of atmospheric turbulence and attenuation on a terminal homing system. The transmitter aperture diameter selected was 5 cm with 0.15 mr angular beam divergence. Ground level atmospheric conditions of 2 m/s crosswind and C_N^2 of $10^{-12} \text{ m}^{-2/3}$ were assumed for the entire path. The computed angle-of-arrival power spectrum for these conditions is presented in Figure 2. The variance obtained by integrating the power spectrum curve is $1.0 \times 10^{-7} \text{ rad}^2$ which gives the standard deviation in beam jitter of 0.32 mr. Thus, the standard deviation in beam centroid movement at the target aim point is 0.96m, and for the calculated spot diameter of 0.51m results in random movement almost four times the spot size at the target. For reduced turbulence strength the spot movement is reduced by the square root of C_N^2 . Hence, for an order of magnitude reduction in C_N^2 , random spot movement is reduced to approximately 1/3m, which is still greater than the spot radius.

Computer programs obtained from New Mexico State University and the Army Atmospheric Science Laboratory^{(3), (4)} were used to compute absorption and scattering effects under atmospheric conditions important to laser designator operation. Molecular absorption and scattering coefficients were computed for clear air at standard sea-level conditions using the "built-in" atmospheric property values. For computing aerosol effects, single scattering calculations were made using the size distribution models available in the Mie theory program. Deirmendjian's Model C⁽¹¹⁾ distribution was used to represent the haze particle size distribution and size distributions for fog and smoke used the Khrgian and Mazin^{(12), (13)} modified Gamma distribution with the coefficients and particle densities given by Steinval⁽¹⁴⁾. The Junge Model⁽¹⁵⁾ was used to represent dust size distribution. Particle densities, index-of-refraction used, and the results of the calculations are presented in Table I.

UNCLASSIFIED

UNCLASSIFIED

References

1. Fried, D. L., "Computer Simulation of Turbulence-Induced Pointing Jitter for a Laser Target Designator," Optical Science Consultants, Placentia, CA, TR-203, March 1976.
2. Fried, D. L., "Method of Calculation of Turbulence Effects for Computer Simulation of Laser Sensor Pointing Jitter Performance", Optical Science Consultants, Placentia, CA, TR-214, June 1976.
3. Miller, A.; Armstrong, R. L.; Welch, C. W.; "Research in the Area of Atmospheric Modeling: High-Resolution Atmospheric IR Transmittance prediction (Part III)", Dept. of Physics, New Mexico State University, Las Cruces, NM, ECOM-75-5, December 1975.
4. Gomez, R. B.; Petracca, C.; Querfeld, C.; Hoidale, G. B.; "Atmospheric Effects for Ground Target Signature Modeling III - Discussion and Application of the ASL Scattering Model", Atmospheric Sciences Laboratory, US Army Electronics Command, White Sands Missile Range, NM, ECOM 5558, March 1975.
5. McClatchey, R. A.; Benedict, W. S.; Clough, S. A.; Burch, D. E.; Calfee, R. F.; Fox, K.; Rothman, L. S.; and Garing, J. S., "AFCRL Atmospheric Absorption Line Parameters Compilation", Air Force Cambridge Research Laboratories, L. G. Hanscom Field, Bedford, MA. AFCRL-TR-73-0096.26 Jan 1973.
6. Greenwood, D. P.; Fried, D. L., "Power Spectra Requirements for Wave-Front Compensative Systems", Jour. Optical Soc. of America, Vol.66, March 1976, pp. 193-206, also Rome Air Development Center, Griffiss Air Force Base, NY, RADC-TR-75-227, September 1975.
7. Fried, D. L., "Statistics of a Geometric Representation of Wavefront Distortion", Jour of the Optical Soc. of America, Vol.55, 1965, p.1427.
8. Sellers, W. R., Jr.; Gibbs, B. G., US Army Missile Command, Redstone Arsenal, AL, TR-WS-75-2, Jan 1975.
9. Brigham, E. O., The Fast Fourier Transform, Prentice-Hall, Inc., Englewood Cliffs, NJ, 1974.
10. Fried, D. L., "Optical Resolution Through a Randomly Inhomogeneous Medium For Very Long and Very Short Exposures", Jour of the Optical Soc. of America, Vol.56, Oct 1966, pp.1372-1379.
11. Deirmendjian, D., "Scattering and Polarization Properties of Water Clouds and Hazes in the Visible and Infrared", Applied Optics, Vol.3 February 1964, pp.187-196.

UNCLASSIFIED

12. Khrgian, A. Kh. and Mazin, I. P., "The Drop Size Distribution in Clouds", Tr. Tsent. Aero. Obs., Vol.7, 1952, pp.56-61.
13. Khrgian, A. Kh. and Mazin, I. R., "Analysis of Methods of Characterizing Cloud Droplet Distribution Spectra", Tr. Tsent. Aero. Obs., Vol.17, 1956, pp.36-46.
14. Steinval, O., "Computed Mie Scattering Properties for Laser Wavelengths in Various Atmospheric Media", Research Institute of Swedish Nat. Def., Stockholm, Sweden, FOA 2 Report C 2662-E1-E3, March 1974.
15. Junge, C., "The Size Distribution and Aging of Natural Aerosols as Determined From Electrical and Optical Data on the Atmosphere", Jour. of Meteorology, Vol.12, 1959, pp. 13-25.

UNCLASSIFIED

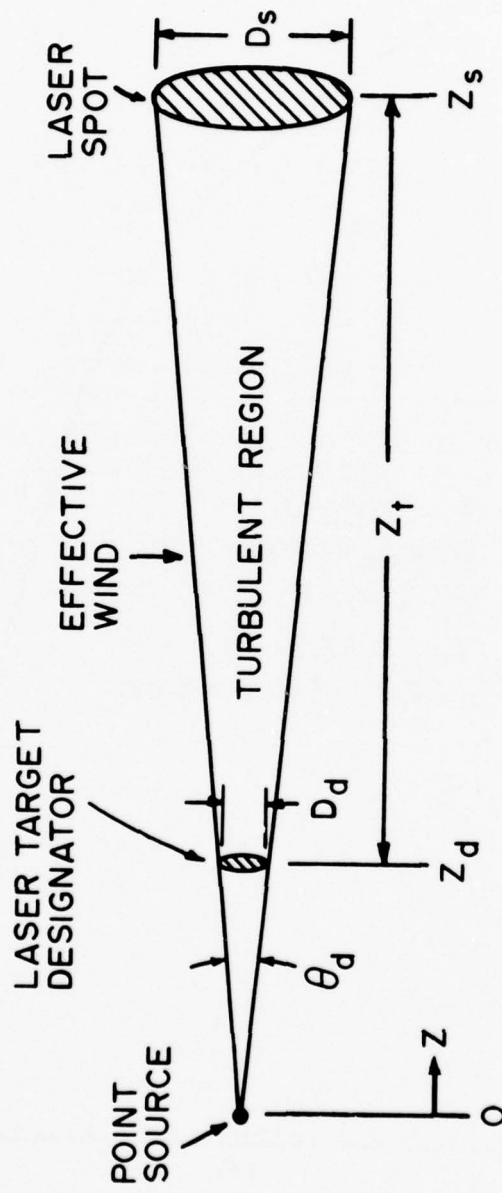


FIGURE 1. GEOMETRY FOR LASER TARGET DESIGNATOR TURBULENCE POINTING JITTER CALCULATION

UNCLASSIFIED

UNCLASSIFIED

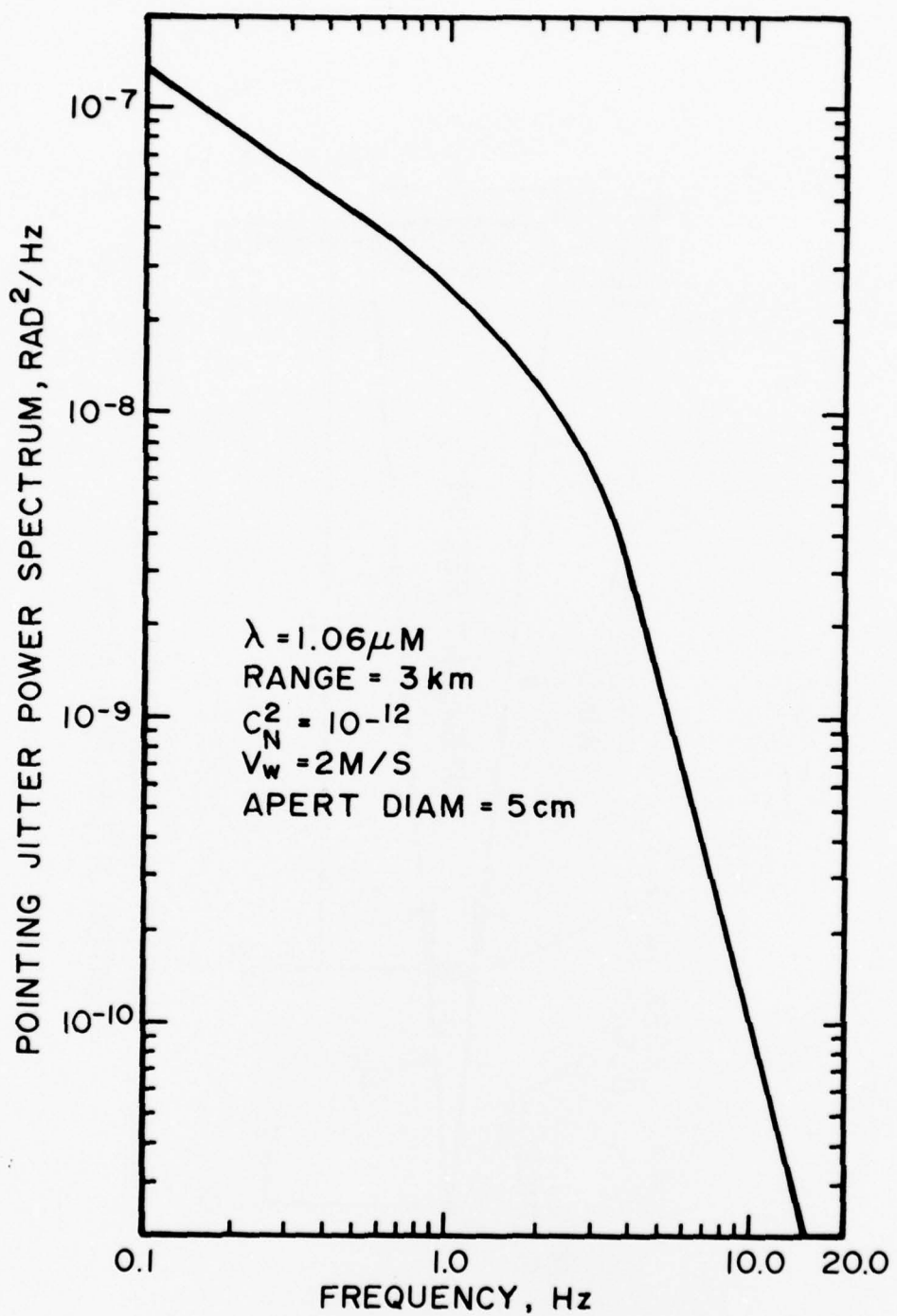


FIGURE 2. LASER TARGET DESIGNATOR POINTING JITTER POWER SPECTRUM

UNCLASSIFIED

	PARTICLE DENSITY, CM ⁻³	INDEX OF REFRACTION	K _{EXT} , KM ⁻¹	K _{ABS} , KM ⁻¹	TRANSMISSIVITY 3 KM PATH, %
	1962 U.S. STD., S.L.				
CLEAR AIR	COND.	--	0.0008	3.5×10^{-6}	99.8
HAZE	1.4×10^4	1.327 - 0i	0.22	0	51.7
FOG	100	1.327 - 0i	2.31	0	00.1
DUST	10^5	1.525 - 0.005i	8.2	0.4	~0
PETROLEUM SMOKE	10^5	1.65 - 0.7i	14.2	9.3	~0

TABLE I. CALCULATED ABSORPTION AND EXTINCTION COEFFICIENTS FOR
CLEAR AIR AND ATMOSPHERIC AEROSOLS. TRANSMISSIVITY
GIVEN FOR 3 KM PATH. $\lambda = 1.06 \mu\text{m}$.

(This page intentionally left blank.)

... This paper is UNCLASSIFIED

OPTICAL COMMUNICATIONS IN THE MARINE
BOUNDARY LAYER

by

Dr. G. C. Mooradian

Dr. M. Geller

Dr. R. J. Giannaris, LT USN

Naval Electronics Laboratory Center
San Diego, CA 92152

ABSTRACT

Optical communications systems operating in the marine boundary layer offer significant potential to increase the capabilities of Naval communications. These increased capabilities include reduced susceptibility to jamming, intercept, spoofing and direction finding; reduction in spectrum crowding; and potential high data rates. The true potential for E/O communications systems need to be better determined to evaluate its future use in Naval Telecommunications System into Task Group applications. Systems concept engineering as well as more extensive data on performance capabilities and limitations is needed. This is addressed for two candidate systems: OCCULT (Optical Covert Communications Using Laser Transceivers) and ELOS (Extended Line-of-Sight) Optical Communications system.

UNCLASSIFIED

INTRODUCTION

Current Navy operation communications systems suffer from a number of problems. There is no operational communication system which is not significantly susceptible to jamming, intercept, spoofing and direction-finding. Further, current communication systems significantly increase Fleet vulnerability to the threat of ARM (Antiradiation Missiles). Lastly, the existing systems suffer from limited data rates, spectrum crowding, high cost, large size weight power, etc. Several attempts at solving these problems in the RF spectrum are being carried out. In addition, it appears that optical communications systems have great promise in solving these problems for many applications.⁽¹⁾ This paper discusses two of the Naval optical communications systems being developed at the Naval Electronics Laboratory Center (NELC): OCCULT (Optical Covert Communications Using Laser Transceivers), and the ELOS (Extended Line of Sight) optical communications system. These systems address the requirement for exchange of tactical data between ships, both to the horizon and beyond. The effects of the atmosphere in the marine boundary layer represent the primary limitation to system performance and will be addressed here. Due to space restrictions, however, detailed technical analysis of the propagation results will be limited and the reader should consult the references.^{(2), (3)}

OCCULT

OCCULT is an optical 10.6μ heterodyne laser communications system, designed for nearly all-weather two-way voice, digital, and video transmission of information between ships to horizon limited ranges. It incorporates a number of technological advances, including the use of reciprocal pointing and tracking between terminals to achieve dramatic improvements in signal-to-noise ratio, link availability, and communication range. Although intended for tactical ship-to-ship communication in its current configuration, the same concepts and technology it has demonstrated can be employed for other terrestrial (including shore and airborne platforms) and ground-satellite communications. The performance characteristics of the OCCULT system are given in Fig. (1). It is clear that these performance levels compare very favorably with any RF or optical techniques.

The efforts in OCCULT have been divided between system considerations and propagation investigations. The systems considerations have focused on developing this optical communications technology to a level such that the system could be tested at sea between actual Navy ships. This test was conducted during amphibious exercise "Varsity Night," 6-19 August 1976. During this test the following was demonstrated: AJ, LPI ship/ship covert communications; full automatic tracking and acquisition in the full spectrum of ships motion; transmission of one video, four 20 kHz analog,

UNCLASSIFIED

UNCLASSIFIED

and one 20 kb/s digital channels both ways simultaneously; acquisition in 47 of 54 attempts on first scan revolution; and the capability of high precision station-keeping (relative bearing of $\pm 0.05^\circ$, range ± 2 yards). This successful test provided a demonstration that the OCCULT system is viable and has made feasible a whole new spectrum of Naval tactical communications.

In the period preceding the sea test, the OCCULT system has also proven to be a uniquely valuable experimental tool for optical propagation in the marine boundary layer. For a period of 4 months preceding the sea test, a program was conducted to measure the propagation of coherent 10.6μ radiation through turbulence and fog. Figure 2 gives the objective for these tests. While a detailed discussion of results here would prove too lengthy, the results can be summarized as follows: For the propagation path and location used (11 miles across San Diego Bay) the largest attenuation due to fog was 8 dB (for meteorological visibilities of less than 0.5 miles) when the high rate reciprocal tracking was engaged; large improvements in signal levels through fog were observed when trackers were engaged (typically, 10 dB or greater)(1),(2); as expected, large increases in average signal levels through turbulence were observed when trackers were engaged (up to 20 dB)(4),(5); the propagation of the coherent 10.6μ beam through fog can be characterized fully by only the "direct" beam attenuation (coherence is not perturbed because the scattered radiation contribution to the signal is negligible)(6),(7); the off-axis energy available for collection by a heterodyne interceptor is essentially the same in fog as it is in clear air. The effects of high rate reciprocal tracking seen in fog conditions could prove to be very significant but are not understood and require further investigation.

OCCULT has demonstrated the validity and practicality of several very important concepts from both the systems and propagation areas: (1) The large improvement in signal-to-noise ratio for coherent propagation through both turbulent and scattering media due to high rate reciprocal pointing and tracking; (2) the preservation of coherence in propagation through scattering media; (3) the ability to derive fine angle pointing information from a nutated received beam and track wavefront tilt to ≈ 200 hz; (4) the development of a computer controlled, closed loop high rate integrated coarse- and fine-angle pointing and tracking system; (5) the demonstration of the high degree of covertness attainable with infrared optical communications; (6) high accuracy frequency stabilization of tuned cavity lasers using Stark cells⁽⁸⁾; (7) the development of an acquisition scheme for narrow optical beam systems; (8) the feasibility of operation in a real Naval environment.

UNCLASSIFIED

ELOS OPTICAL COMMUNICATIONS

While OCCULT addresses the very critical requirement of wideband, nearly all-weather covert communications between ships, the range limitation of the horizon severely limits some applications. The following system, the ELOS optical communications system, addresses exchange of tactical information to beyond line-of-sight ranges for the control of task force units. While the ELOS system will most likely be limited to voice bandwidths, the application of this system as an AJ, LPI augmentation to HF techniques will prove extremely valuable.

A detailed, comprehensive analysis of extended line-of-sight optical communications has been completed. Links were studied utilizing both relay platforms and over-the-horizon forward scatter from aerosols (both haze and clouds). An in-depth review of the state-of-the-art and near-term future advances in system component performance was included, covering lasers, filters, photodetectors, pointing and tracking systems, and platforms.

One result of this analysis was an analytical model for over-the-horizon optical scatter propagation, based upon both the single and multiple scattering approximation. The model appears to be in reasonable agreement with previously available field data for over-the-horizon propagation.(9)

Based on the use of systems composed of state-of-the-art (1976) components, the following conclusions were drawn: (10,11)

1. The operating wavelength should be in the 1 to 3 micron range for both links.
2. Both relay and scatter over-the-horizon data links can use the same shipboard system.
3. Significant performance advantages can be achieved by exploiting propagation characteristics. These include:
 - a. Use of a vertical fan beam or optimally elevated beams in a scatter link at large ranges.
 - b. Positioning the relay platform at a high altitude to take advantage of the decrease in path loss caused by the vertical fall-off in aerosol concentration.
4. Models for the optical scattering channel must include the following:
 - a. Vertical exponential decrease in aerosol concentration and attenuation coefficient.
 - b. Vertical decrease in index of refraction. The simplest approximation is to replace the radius of the earth in the model by the "4/3 radius" (modeling of temperature inversions would be desirable).
 - c. Two modes of propagation: Single and multiple scattering. Contrary to intuition, the former dominates at longer ranges, and the latter at shorter ranges.

UNCLASSIFIED

Again, due to space restrictions, detailed technical depth is not possible and only the propagation mechanism utilizing clear air aerosols will be considered.

The primary factor which determines the percentage of time communication over a given distance at a given bit rate can be achieved is the meteorological visibility. Statistical studies of the occurrence of visibilities greater than a given value are available. When this is combined with performance characteristics of a typical system, both performance and link availability can be determined. Figure 3 shows the performance of a communication link using the results of the propagation model. For voice data rates, the transmitter is a pulsed Nd:YAG laser emitting 2.5 MW power at 1.06 microns with an average power of 10 watts. Note that for a marine atmosphere and visibilities as low as 5 miles, the communication range is approximately 30 miles. For visibilities of 10 miles, the range is increased to 55 miles. For 20-mile visibilities, the range increases to 110 miles. For teletype data rates and the same average power laser, the ranges become 35 miles, 76 miles, and 165 miles, respectively. On a worldwide basis, visibilities greater than 5 miles occur approximately 85% of the time, and 10 miles approximately 70%. This link availability for a given range is not substantially different from conventional HF techniques. The communications ranges are considerably greater at night, or if low clouds occur to provide a scattering layer. It is important to note that areas of operation with lower average visibility (e.g., the North Atlantic) also have a high occurrence of low cloud cover and that some areas of high operational interest, such as the Western Pacific and the Mediterranean, consistently permit greater ranges and higher availabilities. The interpretation of the visibility data on range, data rate, and availability is being continued.

To verify the propagation model, the characteristics of the scattering channel must be measured. The following describes experimental results from an over-the-horizon propagation link. The path loss (received power divided by transmitted power) was measured at 5145 Å with a 1-watt CW argon laser and at 1.06 microns and 5320 Å with a pulsed Nd:YAG laser. In the latter both wavelengths traversed identical propagation paths.

The scattering channel selected was a 39-mile path with almost all of it over the ocean. The transmitter was at NELC in Point Loma. The receiver was on the beach at the Marine Base at Camp Pendleton. The geometric horizon was 25 miles from the transmitter for the CW experiments, and was 12 miles for the pulsed.

Figure 4 is a photograph of the coastline from Camp Pendleton looking southward to the source. The transmitter is pointed directly at

UNCLASSIFIED

the geometric horizon. As there was a strong temperature inversion this night, the direct beam, ducted by this refractive index anomaly is clearly visible.

Figure 5 is the same view with the transmitter elevated 0.5° from the horizon. Superimposed on this photograph is an angular scale to obtain an estimate of the angular size of the source.

Figure 6 shows the path loss as a function of transmission elevation angle. The vertical axes is the path attenuation in db. The path loss for the ducted beam is -63 db. On the scale used, this data point would be outside the boundary of the graph. Part of this path loss, 41 db is due to the loss in beam spreading. The remainder, 21 db is from the loss of energy from the extinction coefficient integrated over this 63 kilometer path.

This enables a calculation of an integrated extinction coefficient of $.043 \text{ km}^{-1}$ to be made for this very long path. Note on the right hand side of the figure, the pertinent data is stated: PT is the transmitted power, THETA D is the beam divergence, D REC is the receiver diameter, FOV is the field of view of the receiver, R is the propagation path, VIS is the visibility as calculated from the extinction coefficient, BETA is the extinction coefficient, H TRANS is the height of the transmitter, H REV is the height of the receiver above sea level. This night was remarkably clear from a strong Santa Ana condition. Note that small value of ducting loss calculates into a visibility of 92 kilometers.

The data set of Figure 7 was taken about a month later under conditions more typical to the California coast. There was no temperature inversion, so the direct, non-scattered beam was not observed. For all the 4 points of data, the beam was not visually seen.

The comparison between the experimental values and the model are shown in Figure 8. The column labeled EXPERIMENT is the path loss with the transmitter pointed about one beam diameter above the horizon to insure that none of the energy is being ducted to the receiver. The next column SGL SCATT are the values from the single scattering model. The column next to this one, ERROR, gives the difference between the experiment and the single scattering theory. Note that there are large differences from 16 db to 30 db. The next column MULT SCATT are the results from the theory of multiple scattering. A comparison between this column and the experimental values indicate better agreement, with the differences clustered around 10 db.

The next set of experiments measured both the path loss and the pulse spreading in this type of scatter channel. The transmitter is

UNCLASSIFIED

a pulsed Nd(YAG) laser emitting both the fundamental at 1.06 microns and the first harmonic at .53 microns (Figure 9). Both wavelengths traverse the same propagation path to the receiver. The radiation was collected by a receiver (Figure 10). The two wavelengths are physically separated by a dichroic beamsplitter, detected, amplified, digitized and recorded. Real time display of the pulse shapes are available.

Figures 11 and 12 show the path loss as a function of transmitter elevation and azimuth scan angles at a wavelength of 5320 Å. Figure 13 shows the path loss at two wavelengths of 5320 Å and 1.06 microns through the identical atmosphere. In all these measurements there was no indication of pulse stretching or distortion.

In summary, we have made propagation measurements over the horizon by scattering from normal marine atmospheric aerosols. The measurements include propagation path losses and pulse distortion in the blue-green and at 1.06 microns. The model that has been developed is in substantial agreement with the data. Further scattering measurements will be made. The design and construction of a one-way communication link between NELC and San Clemente Island, (a distance of 128 kms) is in progress.

REFERENCES

1. "Atmospheric and Space Optical Communications for Naval Applications (U)," proceedings of 6th DOD Conference on Laser Technology, G. C. Mooradian, March, 1974.
2. NELC Technical Report 1994, "CO₂ Coherent Propagation (With Reciprocal Tracking) through the Marine Boundary Layer," R. J. Giannaris, G. C. Mooradian, and W. R. Stone, 28 June 1976.
3. NELC Technical Note 3232, "OCCULT, Optical Covert Communications Using Laser Transceivers," R. J. Giannaris, G. C. Mooradian, and W. R. Stone.
4. Applied Optics, v 10, p 1652, 1971, R. F. Lutomirski and H. T. Yura.
5. "Some Effects of Atmospheric Turbulence on Optical Heterodyne Communications," 1964 IEEE Convention Record, Part 6, p 337-342, 1964.
6. Pacific Sierra Research Corporation Report, Irradiance Due to Scattering at All Points in Space, by R. Lutomirski (in preparation).
7. Optical SATCOM: Joint NRL/NELC Optical-Satellite-Communication-Atmospheric Propagation Test Plan, NRL Problem N03-25, April 1975, Livingston, P.M. et al.
8. Applied Physics Letters, Vol. 25, p 615, 1974, "Stark Cell Stabilization of the CO₂ Laser," T. A. Nussmeier and R. L. Abrams.
9. Naval Research Laboratory Report 6152, Experimental Observations of Forward Scattering of Light in the Lower Atmosphere, by J. A. Curcio and L. F. Drummetter, Jr., 30 September 1964.
10. Extended Line of Sight Optical Communications Study, NELC TR 1988, June 1976
11. Over the Horizon Optical Communications Channel, proceedings, proceedings, Workshop on Remote Sensing of the Marine Boundary Layer, Vail, Colorado, August 1976, G. C. Mooradian, M. Geller, G. J. Barstow, K. E. Davies
12. Marine Weather of the World, June 1968, McDonnell Douglas Report F-063
13. Naval Weapons Center, China Lake, Technical Note 4056-16, Weather Effects on Infrared Systems for Point Defense, by F. E. Nicodemus May 1972.
14. Naval Electronics Laboratory Center Technical Note 2672, Voice Communication with a Flashlamp-Excited Blue-Green Dye Laser, by J. E. Celto, E. J. Schimitschek, and J. A. Trias, 23 April 1975.

OCCULT PERFORMANCE CHARACTERISTICS

Information Bandwidth	>5 MHz
Beamwidth	0.05° (1 mrad)
Radiated Power	0.5 W
Radiated Power Density	<100 mW/cm ²
Tracking Accuracy	0.005° (100 μrad)
Tracking Rate	360°/sec
Tracking Acceleration	3600°/sec ²
Full (Blind) Acquisition Time	~1 sec
Automatic Station-Keeping Capabilities (Accuracy at 32 km = 20 mi)	+15 m (+50 ft) range +0.1° relative velocity +0.51 m/sec (+1 kt) relative velocity
Sidelobe suppression	<-150 dB 1° off axis
Sidescatter (clear air)	-100 dB 90° off axis 1 m from beam
Sidescatter (marine haze)	-150 dB 10° off axis 1 km from beam
Signal-to-Noise Ratio (light fog)	~40 dB at 40 km (25 mi)
RFI	Emits none and is insensitive to RFI
Weight (antenna)	23 kg (50 lb)
Size (antenna)	0.056 m ³ (2 ft ³)
Prime Power	150 watts
Cost per Terminal	\$50,000
MTBF	>2,000 hours

Figure 1. OCCULT Performance Characteristics

OCCULT PROPAGATION EXPERIMENT

OBJECTIVE: Investigate the propagation of coherent 10.6μ radiation through the marine boundary layer, including turbulence and fog.

EXPERIMENT:

- ° Variation of CNR with optical thickness τ in fog
- ° Effects of particle size distribution, albedo, small τ , etc.
- ° Determine improvement in CNR with reciprocal tracking
- ° Correlation of CNR with meteorological visibility
- ° Clear air turbulence
 - ° Determine wavefront angle of arrival and amplitude behavior
 - ° Determine improvement in CNR with reciprocal tracking
- ° Off-Axis behavior
 - ° Determine angular brightness function vs τ (i.e., coherence diameter)
 - ° Possible Doppler spectrum spreading vs θ and τ
 - ° Effects of variable field of view
 - ° Off-axis radiance available for collection vs τ

Figure 2. OCCULT Propagation Experiment

Figure 3. Performance Characteristics of ELOS

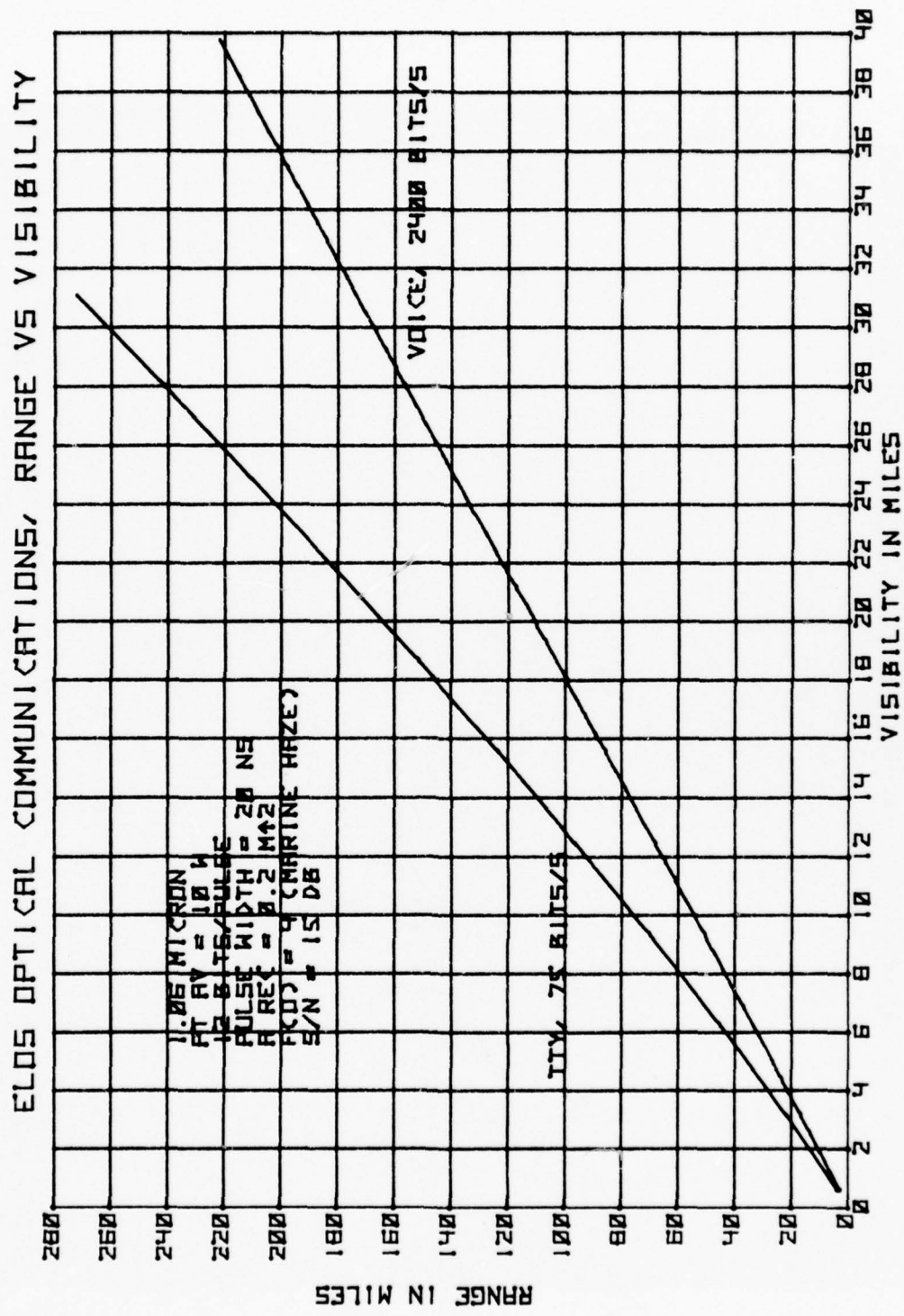




Figure 4. Ducted Beam

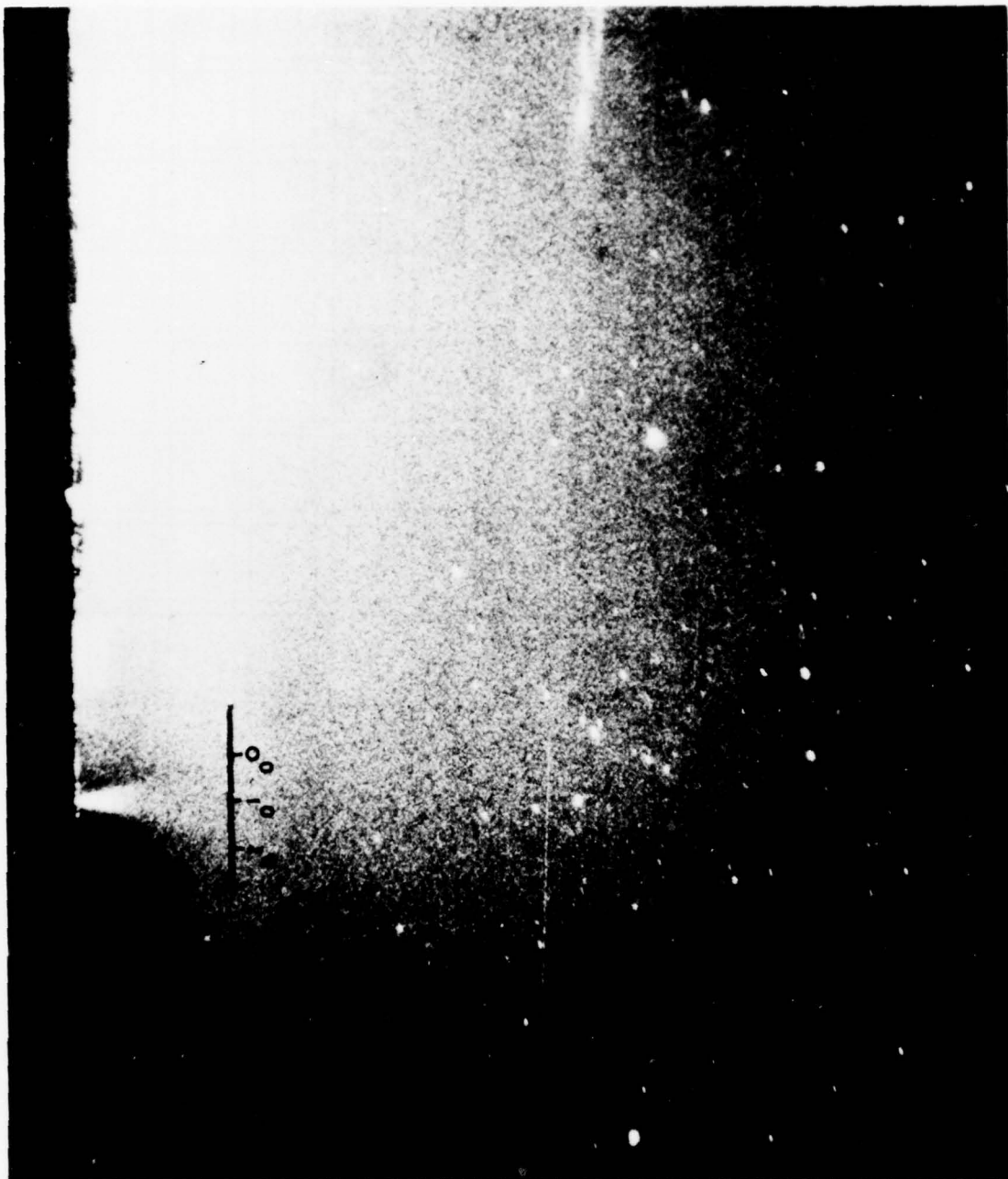


Figure 5. Transmitter Elevated 0.5°

Figure 6. Path Loss Measurements of Jan. 21, 1976

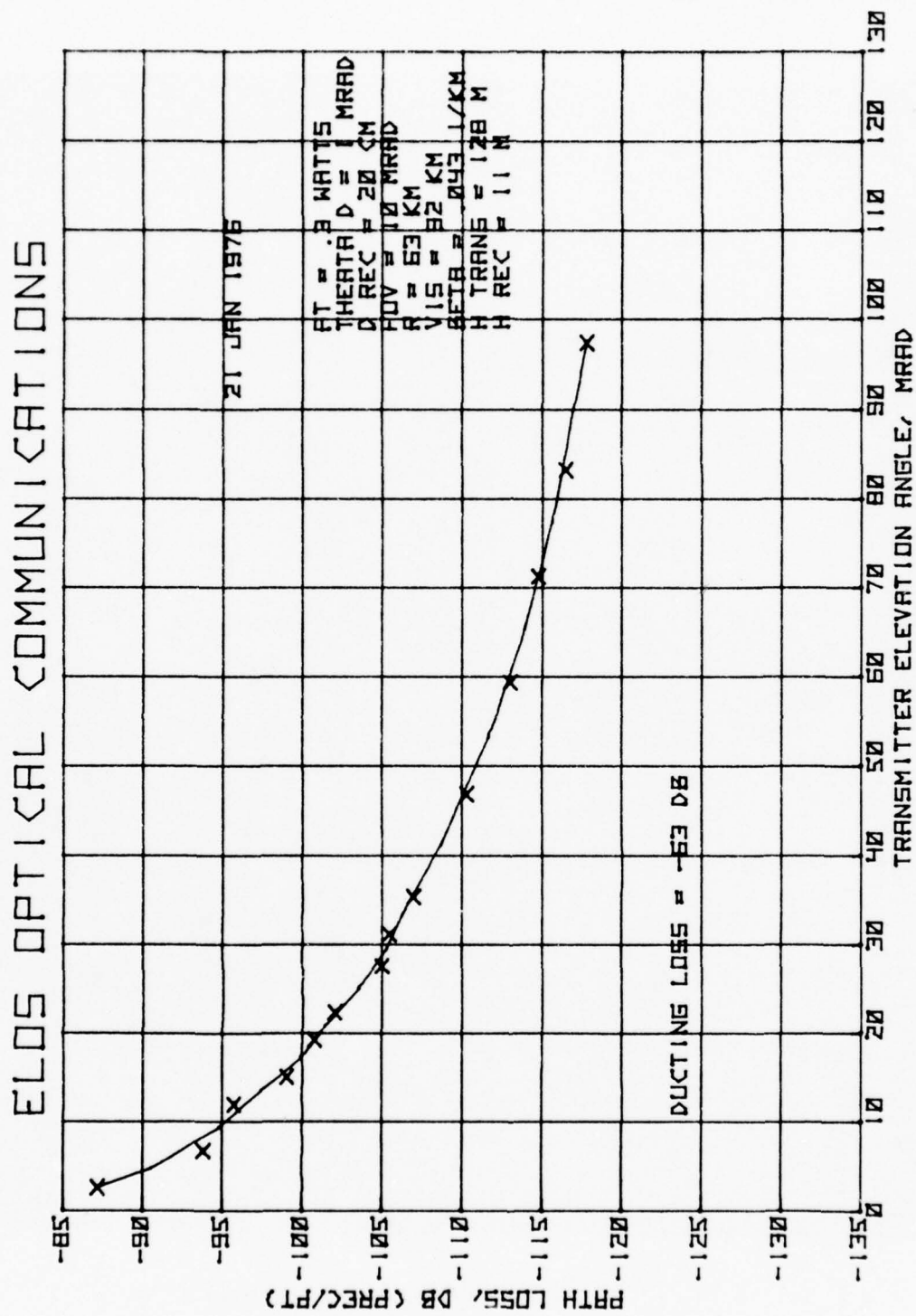
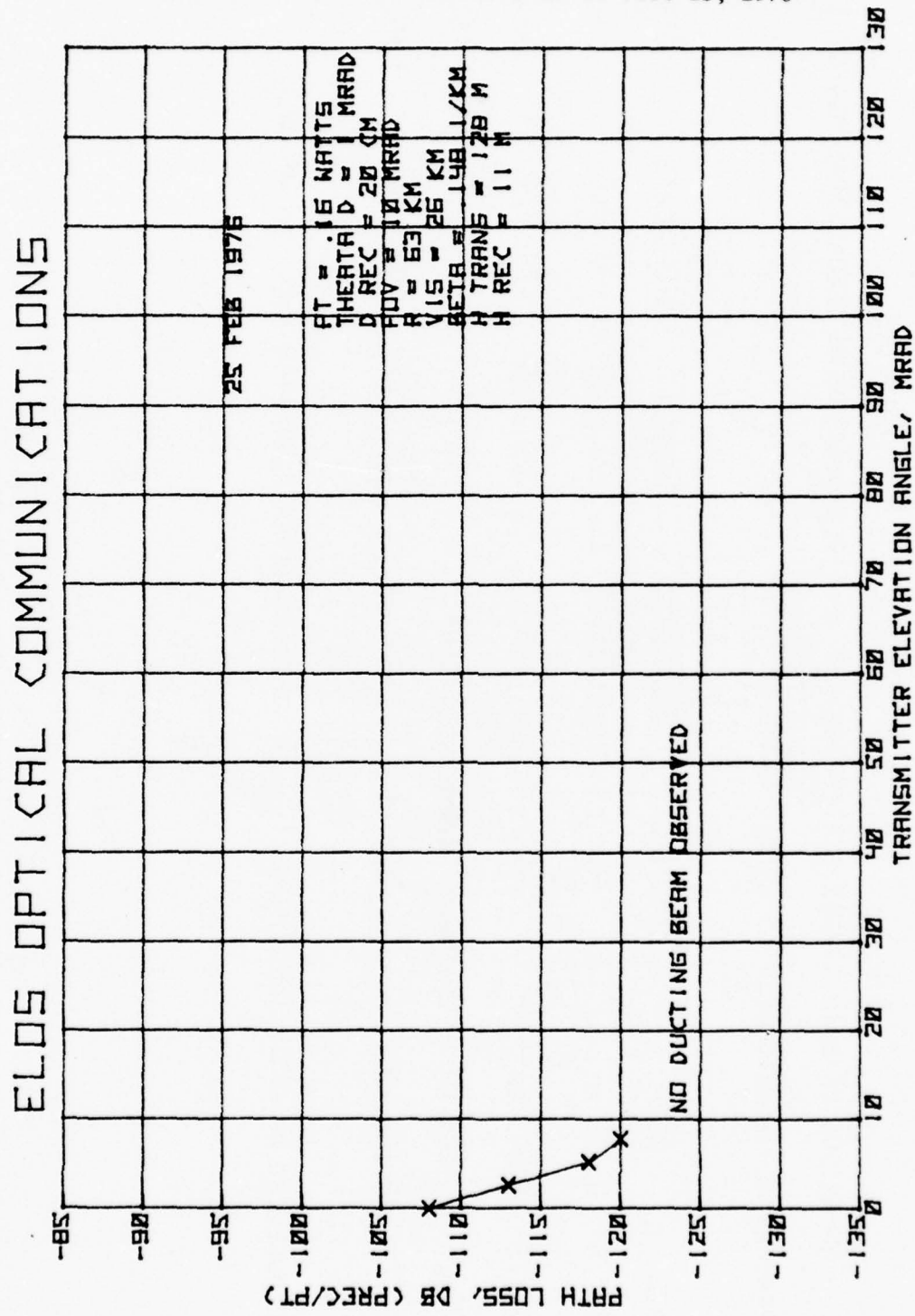


Figure 7. Path Loss Measurements of Feb. 25, 1976



ELLOS MODEL COMPARISON
 COMPARISON OF BOTH SINGLE SCATTERING AND MULTIPLE SCATTERING THEORETICAL MODELS TO
 EXPERIMENTAL RESULTS OVER 53-KM 0TH RANGE

DATE	BETA	EXPERIMENT*	SGL SCATT	ERROR	MULT SCATT	ERROR
1/15/76	0.115 km ⁻¹	-96 dB	-117.5 dB	-21.5 dB	-90.5 dB	+5.5 dB
1/21/76	0.043 km ⁻¹	-85 dB	-114.7 dB	-29.7 dB	-75.2 dB	+9.8 dB
1/28/76	0.126 km ⁻¹	-102 dB	-118 dB	-16 dB	-93.1 dB	+8.9 dB
2/25/76	0.148 km ⁻¹	-108 dB	-119.4 dB	-11.4 dB	-98.5 dB	+9.5 dB

*MEASUREMENT OF PATH LOSS (P_{RCVR}/P_{XMTR}) AT TRANSMITTER ELEVATION ANGLE OF ~ 3 MRAD

FIG 3. COMPARISON BETWEEN EXPERIMENT AND THEORIES

Figure 9. Schematic of Dual Wavelength Transmitter

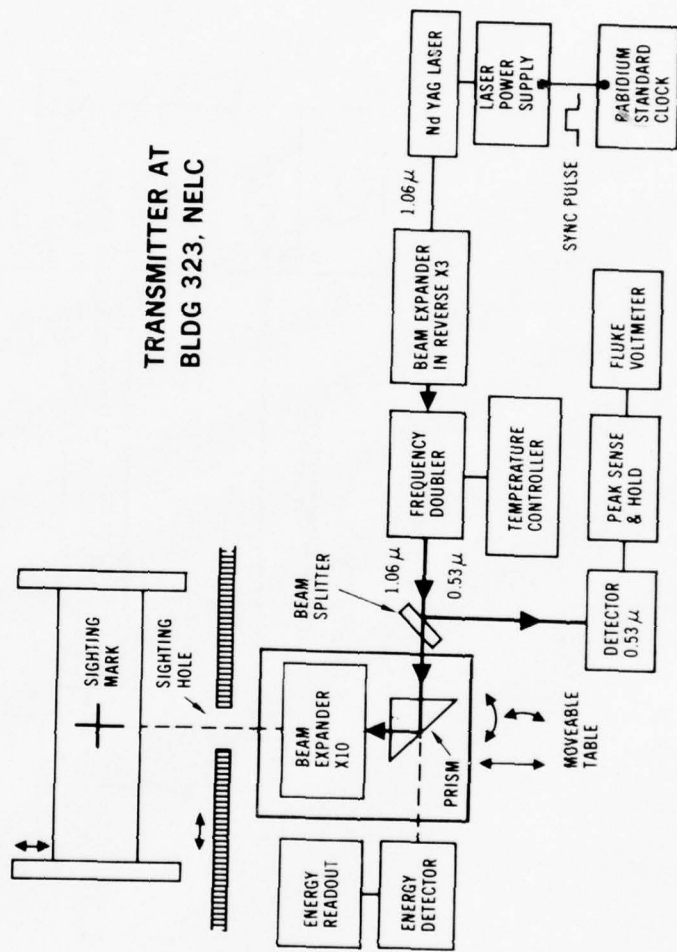


Figure 10. Schematic of Dual Wavelength Receiver

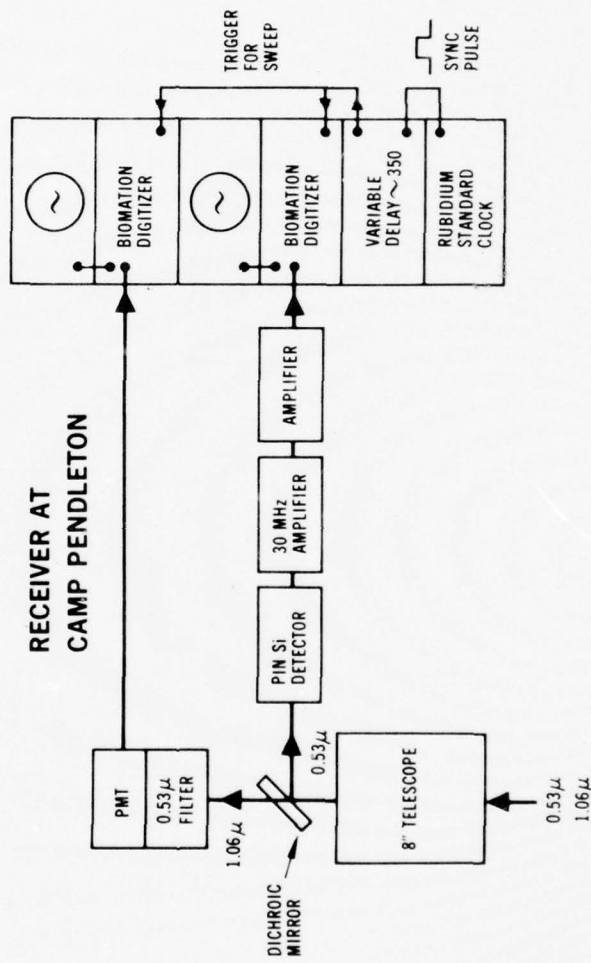


Figure 11. Path Loss Measurements of Sep. 30, 1976

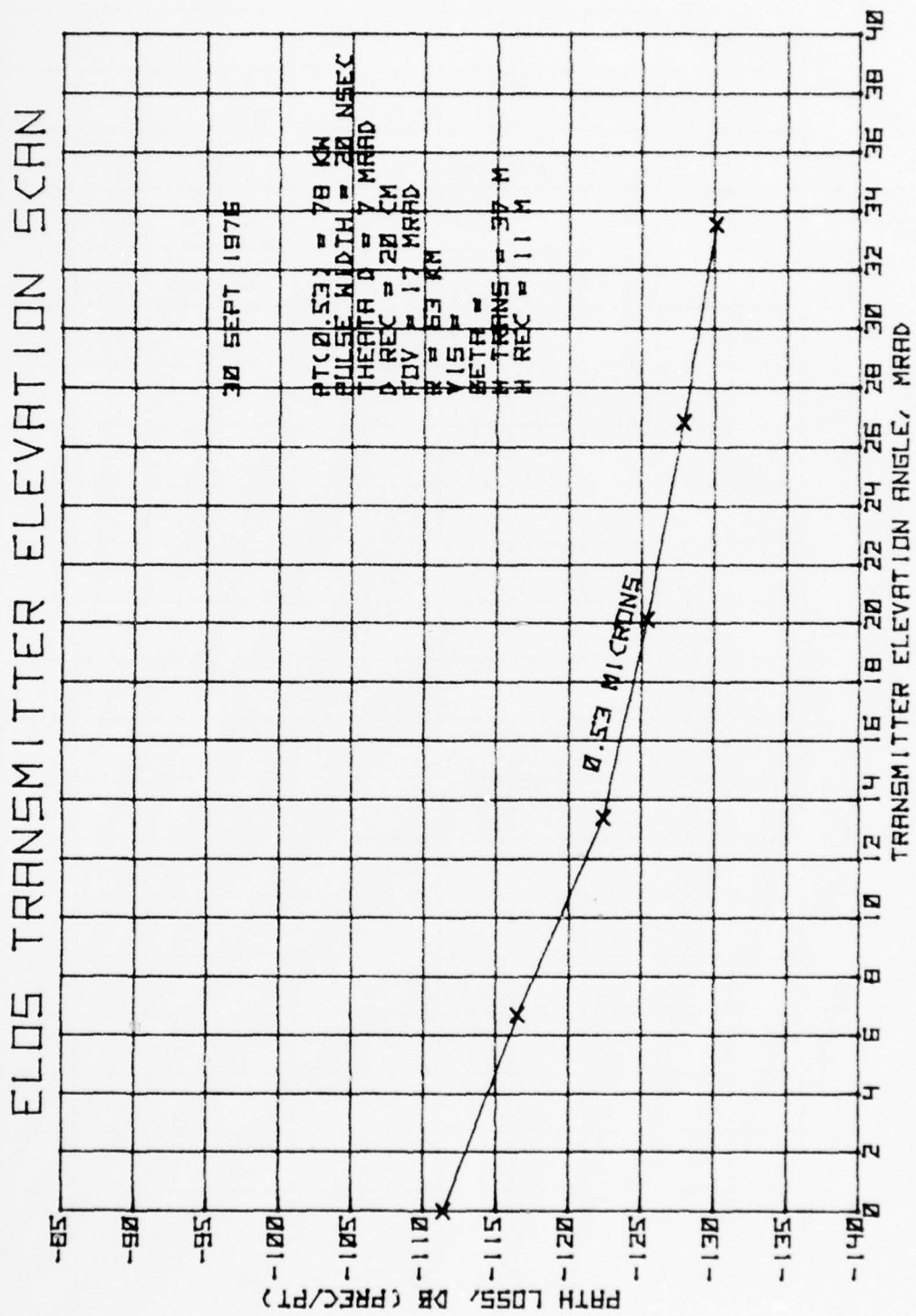


Figure 12. Path Loss Measurements of Sep. 30, 1976

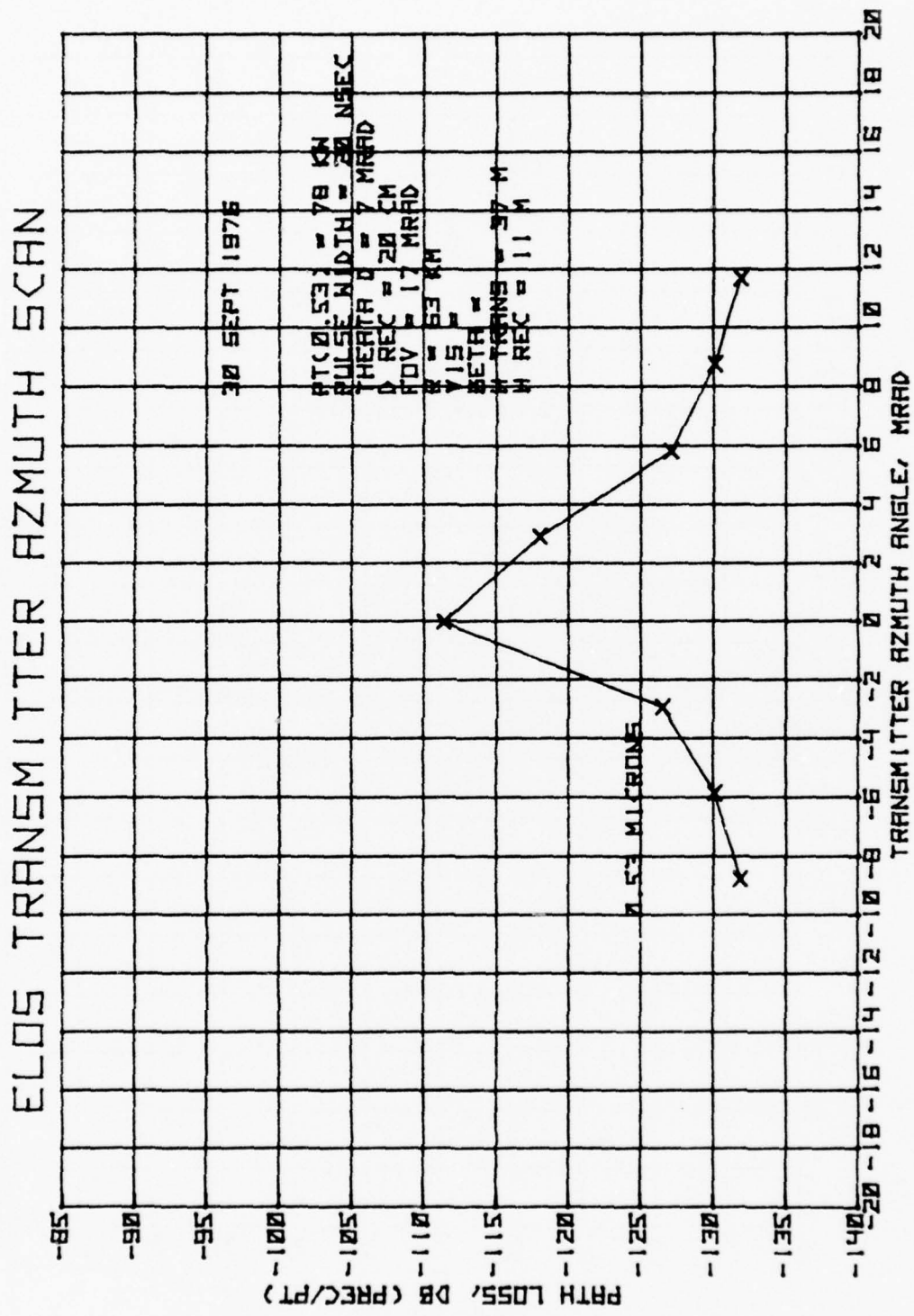
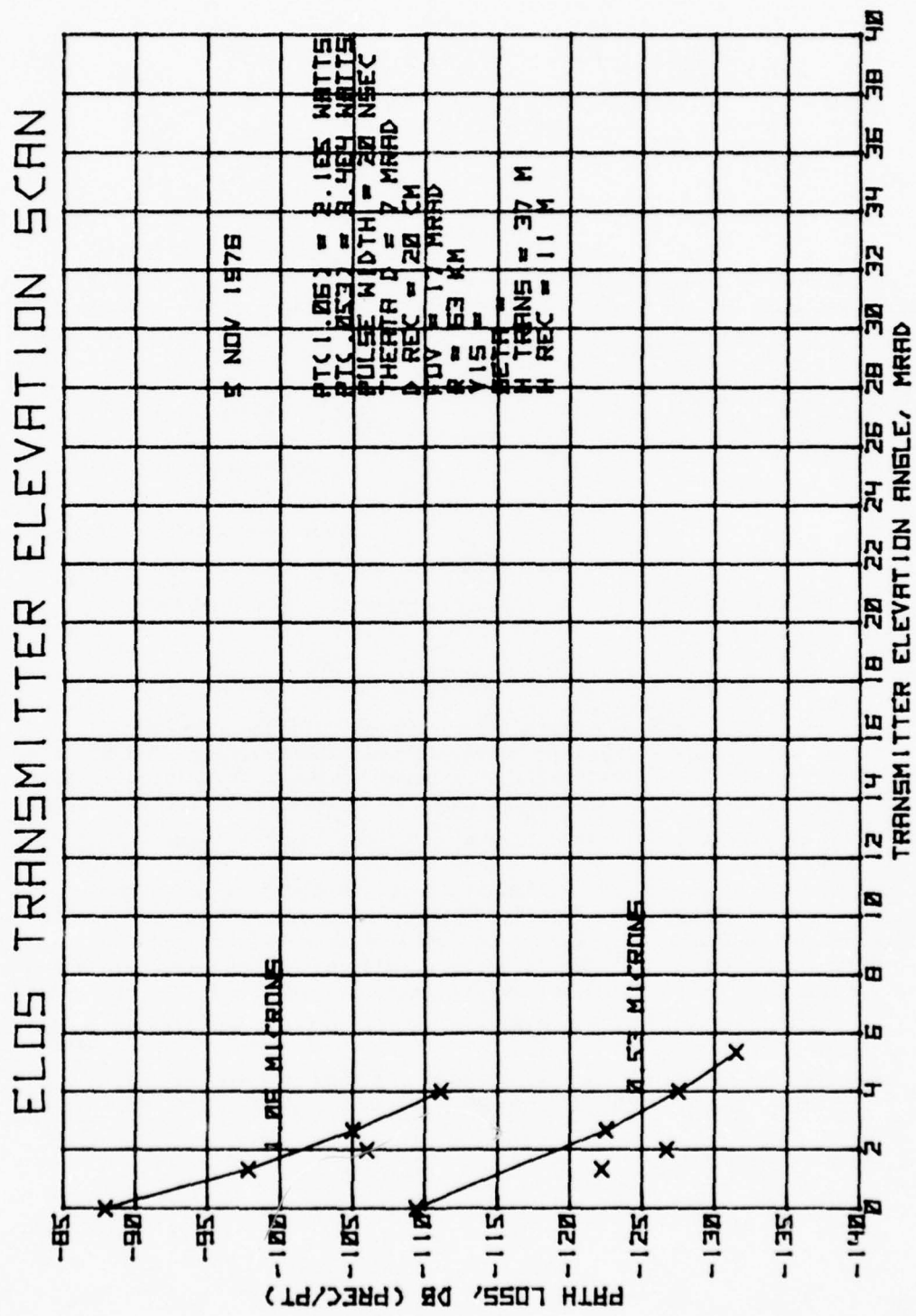


Figure 13. Path Loss Measurements of Nov. 5, 1976



(This page intentionally left blank.)

UNCLASSIFIED

SUBMILLIMETER WAVE PROPAGATION - A SURVEY

W. L. Gamble and B. D. Guenther
US Army Missile Command
Redstone Arsenal, Alabama 35809

ABSTRACT

A brief review of the current state of knowledge on submillimeter propagation in the atmosphere is presented. The critical data inadequacies are pointed out in the following list:

- 1) No experimental data on scattering to evaluate existing theoretical predictions.
- 2) Atmospheric absorption data do not include detailed meteorological measurement.
- 3) Present theories cannot predict the location or depth of the propagation windows.
- 4) Fluctuations are not adequately explained.
- 5) Extinction measurements in rain and fog are few in number.

INTRODUCTION

In the past, activity in the submillimeter region of the spectrum was limited to astronomers and spectroscopists. Recently, new sources such as relativistic e-beam devices, optical klystrons and optically pumped far infrared lasers have been introduced. It now appears possible to implement systems utilizing submillimeter wave radiation.¹

Before any system that is to operate in the atmosphere can be implemented, the propagation of submillimeter radiation (SMMW) must be characterized. The purpose of this paper is to briefly summarize the current state of knowledge and to point out the areas that require additional work. To aid the reader in obtaining an introduction to this field, an annotated bibliography has been prepared.²

It is recommended that the reader use this bibliography to obtain supporting material for comments made in this paper.

UNCLASSIFIED

UNCLASSIFIED

ABSORPTION SPECTRUM

A. Clear Air Absorption

The propagation of SMMW characterized by large absorption, which will limit the use of SMMW to relatively short ranges. A theoretical calculation of atmospheric absorption is shown in Figure 1, along with some experimental data.³ There are three possible contributors to the clear air absorption. Water vapor is the major absorber and the absorption is approximately proportional to the density of water vapor. To explain some experimental observations, a contribution (at the wavelengths near 1 mm) due to water vapor dimers has been suggested. However, the amount of absorption to associate with water vapor dimers has not been resolved. Ozone can contribute to absorption in SMMW region at high altitudes. All other gases do not contribute directly to the absorption for the following reasons: 1) The gas has a low frequency of occurrence. 2) There are no transitions in this wavelength region. 3) The absorption is small relative to H_2O .

B. Collisional Broadening

Oxygen and nitrogen do contribute to the absorption spectrum by collisional broadening of the absorption lines. The relative strength of the contribution of H_2O , N_2 , and O_2 to the collisional broadening is 5, 1, 0.6 respectively near line center, with the water vapor contribution increasing to 15 in the wings.

There are three generally used models to explain collisional broadening. They lead to line shape equations presented in TABLE I. Also presented in Table I are the names of investigators who have applied these line shapes to calculations in the SMMW region.

All of the line shapes give good agreement with experiment near the absorption line centers, but poor agreement in the wings as shown in Figure 1. A comparison between the three line shapes is shown in Figure 2. The continuum is an empirically derived addition made to obtain better agreement between experiment and the summation of known lines below 35 cm^{-1} . No one model has an advantage over the others at this time. The best choice of model depends on the spectral range of interest.

Another reason for the poor performance of theory in predicting the location and size of the windows is that lines 30 or more linewidths away from the windows are making major contributions to the shape and depth of the windows. None of the line shape functions is expected to perform adequately at distances more than about five linewidths from line center.

UNCLASSIFIED

UNCLASSIFIED

TABLE I. LINE SHAPES RESULTING FROM COLLISIONAL BROADENING MODEL LORENTZ

$g(K) = \frac{\Delta\nu}{(K - K_o)^2 + \Delta\nu^2}$
VAN VLECK-WEISKOPF (BASTIN; BURCH)
$g(K) = \left(\frac{K}{K_o}\right)^2 \left[\frac{\Delta\nu}{(K - K_o)^2 + \Delta\nu^2} + \frac{\Delta\nu}{(K + K_o)^2 + \Delta\nu^2} \right]$
KINETIC (ZHEVAKIN AND NAUMOV; EMERY)
$g(K) = \frac{4K^2 \Delta\nu}{(K_o^2 - K^2)^2 - 4K^2 \Delta\nu^2}$
K_o = LINE CENTER IN WAVE NUMBERS
$\Delta\nu$ = LINE WIDTH

AEROSOL SCATTERING

Theoretical calculations have been made of aerosol and rain scattering. An example is shown in Figure 3.⁴ Experimental confirmation does not exist. A measurement has been made in fog at 337 μm . There has been one measurement in snow that shows extinction varies linearly with snow-fall rates. Two measurements in rain do not agree but are approximately linear with rainfall rate and are less for a given rate than the attenuation in snow.

FLUCTUATIONS

One area not mentioned was that of fluctuations where there are only three or four investigators. The conclusion from these papers is that fluctuations decrease with increasing absorption.⁵

CRITICAL DATA INADEQUACIES

From the brief outline presented here, it is easy to see that information is lacking in almost every segment of propagation. If it were necessary to select one area that needs the most attention it would have to be the correlation of atmospheric propagation with meteorological parameters.

UNCLASSIFIED

UNCLASSIFIED

To fill this need, the US Army Missile Command has started a program to obtain this type data.⁶ Figure 4 shows the SMMW radar currently in use at the US Army Missile Command. It is hoped that over several years this system will provide a statistically meaningful data base for future modeling of SMMW system performance.

REFERENCES

1. R. L. Hartman, W. L. Gamble, B. D. Guenther, and P. W. Kruse, "Submillimeter Systems for Imaging Through Inclement Weather," Optical/Submillimeter Propagation Workshop (6-9 December 1976).
2. B. D. Guenther, J. S. Bennett, W. L. Gamble, and R. L. Hartman, "Submillimeter Research: A Propagation Bibliography," US Army Missile Command, Redstone Arsenal, Alabama, Technical Report (IN PRESS).
3. J. A. Bastin, "Extreme Infrared Atmospheric Absorption," Infrared Phys. 6, p. 209-221 (1966).
4. D. Deirmendjian, "Far Infrared and Submillimeter Scattering, II. Attenuation by Clouds and Rain," The Rand Corporation, R-1718-PR (February 1975).
5. A. V. Sukolev and E. V. Sukhovin, "Influence of the Atmosphere on the Propagation of Submillimeter Radio Waves," Proceedings of the Symposium on Submillimeter Waves, Polytechnic Press (1970).
6. W. L. Gamble and B. D. Guenther, "Submillimeter Laser Wave Propagation," Second International Conference and Winter School on Submillimeter Waves and Their Applications, San Juan, Puerto Rico (6-11 December 1976).

UNCLASSIFIED

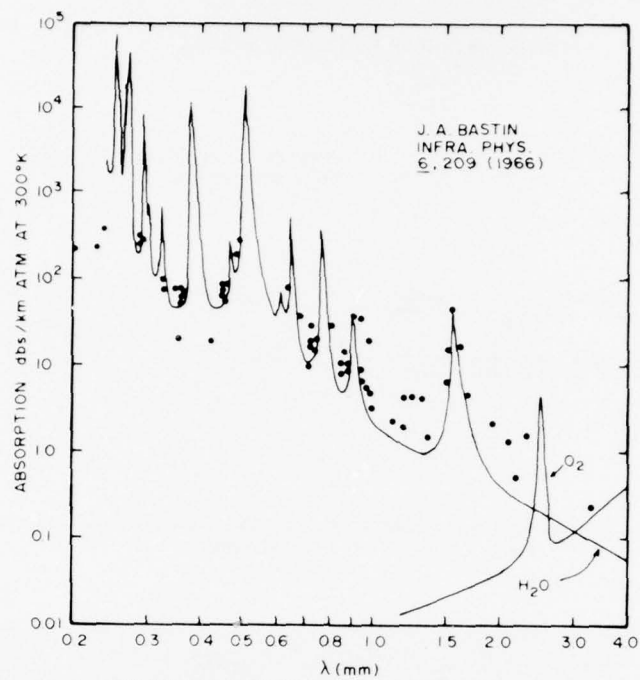


FIG. 1. COMPARISON OF THEORETICAL AND EXPERIMENTAL ATMOSPHERIC ABSORPTION BETWEEN 0.2 AND 4.0 MM. (AFTER J. A. BASTIN, INFRA. PHYS. 6, 209 (1966) WITH ADDITIONAL EXPERIMENTAL POINTS). THE SOLID CURVE LABELED H_2O IS THE THEORETICAL CURVE FOR WATER VAPOR. EXPERIMENTAL POINTS ARE INDICATED.

FIG. 2 CALCULATED ABSORPTION COEFFICIENT DUE TO INDIVIDUAL H_2O LINES

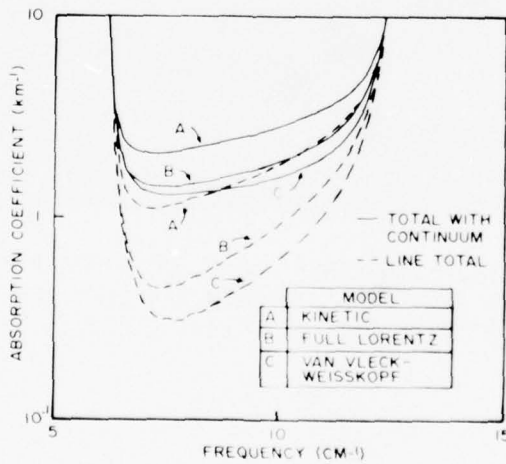


FIG. 3 CLOUD SCATTERING LOSSES

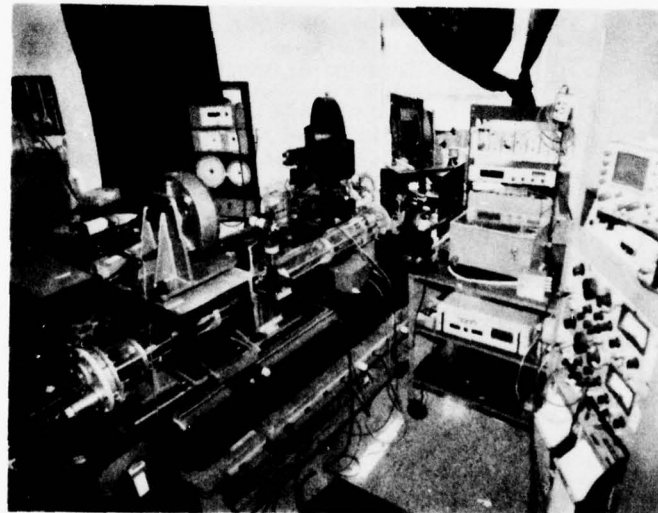
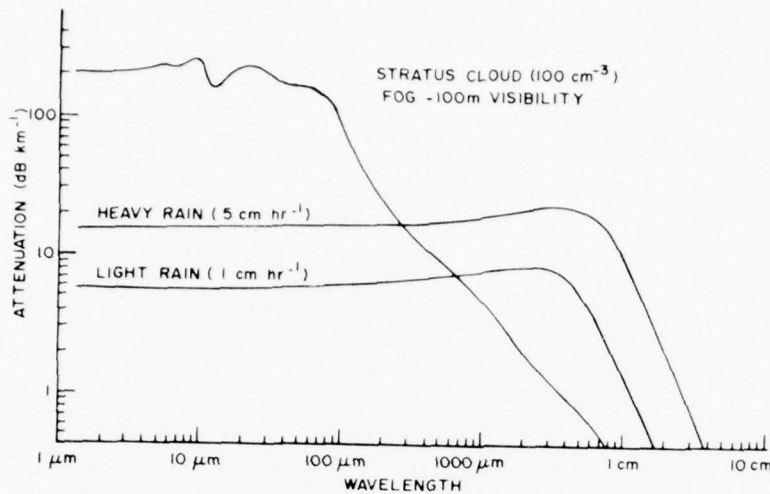


FIG. 4. SUBMILLIMETER LASER RADAR FOR PROPAGATION STUDIES. THIS SYSTEM PRODUCES A 12-INCH PARALLEL BEAM OF SMMW. IT HAS BEEN USED TO DATE AT 0.744, 0.890, 1.02 AND 1.2mm

UNCLASSIFIED

.... This paper is UNCLASSIFIED

SUBMILLIMETER SYSTEM FOR IMAGING THROUGH INCLEMENT WEATHER

R. L. Hartman, W. L. Gamble, and B. D. Guenther
US Army Missile Command
Redstone Arsenal, Alabama 35809

and

Paul W. Kruse
Honeywell Corporate Research Center
Bloomington, Minnesota 55420

ABSTRACT

If the US Army is to operate well during inclement weather, including fog, rain, snow, and low-lying clouds, it must have a transportable system which will provide a visual image at ranges of 1 to 5 km consistent with direct-fire weapons. The combined requirements of limited antenna aperture, small beam divergence, reasonable atmospheric absorption, and low scattering from aerosols direct us to the submillimeter portion of the spectrum.

We envisage a system employing a submillimeter source feeding an antenna (mirror) approximately 1 m in diameter. The illumination beam is scanned over the target area at TV frame rates. The receiver probably uses the same antenna, with the receiving element slightly displaced to compensate for the transit time during the dwell time on a resolution element. The return signal is used to paint a TV-like image on a CRT.

In 1974, Kruse performed an initial analysis of such a system. The predicted performance was good enough to arouse Army interest, and marginal enough to require a detailed experimental assessment. This paper describes the beginning of that assessment.

INTRODUCTION

During the fall and winter months, the visibility in West Germany is less than 1 km during one out of three mornings. On the average, these morning fogs last 5 to 6 hours, often not lifting until midday [1].

If the US Army is to operate well during inclement weather, including fog, rain, snow, and low-lying clouds, it must have a transportable system which will provide a visual image at ranges of 1 to 5 km consistent with direct-fire weapons. The combined requirements of limited antenna aperture, small beam divergence, reasonable atmospheric absorption, and low scattering from aerosols direct us to the submillimeter portion of the spectrum.

We envisage a system employing a submillimeter source feeding an antenna (mirror) approximately 1 m in diameter (Figure 1). The illumination beam is scanned over the target area at TV frame rates. The receiver probably uses the same antenna, with the receiving element slightly displaced to compensate for the transit time during the dwell time on a resolution element. The return signal is used to paint a TV-like image on a CRT. In addition to providing the imaging for target acquisition, the system could provide guidance for the delivery of a weapon system.

UNCLASSIFIED

UNCLASSIFIED

In 1974, Kruse performed an initial analysis [2,3] of such a system. The predicted performance was good enough to arouse Army interest, and marginal enough to require a detailed experimental assessment. This paper describes the beginning of that assessment.

There are two key issues: (1) does submillimeter radiation, in fact, penetrate the atmosphere as assumed, and (2) do tactical targets, in fact, provide sufficient return of a type useable to develop images?

PROPAGATION

A detailed look at the propagation question has been presented in another paper [4], and we refer the reader to that publication. From what is known about scattering, we quickly conclude that wavelengths longer than 100μ are required to penetrate inclement weather. Based on our knowledge of absorption, it is known that in the submillimeter region of the spectrum there are atmospheric attenuation windows. Several of these windows are presented in Table I. The attenuation values presented are for a relative humidity of approximately 43 percent. These attenuation values are not known accurately. To indicate the uncertainty, a range of experimentally-obtained attenuation values are presented in the table. The three longer wavelength windows have been selected for our initial study. For ease in recalling the window position, and because the position of the minimum in the windows are still uncertain, the windows are denoted as 1.3, 0.85, and 0.75 mm.

There are a large number of data inadequacies in the area of submillimeter propagation. There are no experimental data on scattering. Measurements of clear air absorption are inadequate due to their limited number and the lack of accompanying meteorological measurements. Present theories are inaccurate in the window regions, and fluctuations are not adequately explained. Even though there are a number of critical data inadequacies, there is sufficient information to obtain a preliminary evaluation of a system concept.

DETECTORS AND SOURCES

To answer the second question "can we form an image," we must first determine if adequate detectors and transmitters exist. Table II presents a brief list of available detectors. A detailed discussion on submillimeter detectors is presented by Putley and Martin [5]. For an operational system, a superheterodyne receiver will be required. InSb has operated as a superheterodyne detector at 1.5°K with an NEP of approximately $10^{-20} \text{ W/Hz}^{1/2}$. The best performance for a room temperature detector has been with a Schottky diode where an NEP of $10^{-16} \text{ W/Hz}^{1/2}$ was obtained [6]. This value is some four orders of magnitude worse than ideal. An NEP of $10^{-19} \text{ W/Hz}^{1/2}$ is expected in a 1- to 3-year timeframe by optimizing the detector for the submillimeter region.

Solid state and tube sources exhibit a rapid fall off in power output with increasing frequency as one approaches the submillimeter region

UNCLASSIFIED

UNCLASSIFIED

(Figure 2). There are carcinotrons available commercially* that will provide approximately 1 W of average power in the wavelength region of interest. The Russians have developed backward wave oscillators working in this wavelength region that are used for propagation measurements [8]. Optically-pumped submillimeter lasers offer the promise of providing 1 W of average power. Peak powers in the pulsed mode of megawatts have already been obtained. An up-to-date listing of over 500 lines already obtained in the submillimeter region is presented by Rosenbluh et al [8]**. Figure 3 shows one of the submillimeter lasers (a metal waveguide) being used at the US Army Missile Command. The CO₂ pump laser is shown (also a waveguide laser) in the foreground. In the far background is a dielectric waveguide submillimeter laser. We selected the laser for our submillimeter source because of cost.

SYSTEM PERFORMANCE

Using our knowledge about components and propagation, the performance of a submillimeter wavelength imaging system using the parameters presented in Table III was calculated. For standard conditions, it was found that the operational range is limited to approximately 1 km (Figure 4). It was also discovered that source powers in excess of 1 W are not required.

Fogs occur normally in the fall and winter months when the water vapor content of the atmosphere is much lower than the 7.5 g/m³ that was used to calculate Figure 4. Because submillimeter wave atmospheric attenuation is directly proportional to the water vapor density in the atmosphere, the fall and winter months should exhibit much lower absorption. This effect is shown in Figure 5 where the operating range of a submillimeter system is calculated when the meteorological visibility ranges from 0.1 to 1.0 km.

SPECKLE NOISE

Our calculations predict that a submillimeter wave system will be able to detect signals from targets at acceptable ranges during periods of low visibility; however, the calculations reveal nothing of the ability to image. There are three questions that need to be answered before we can determine if imaging is possible: (1) What are the effects of speckle noise on the system? (2) Can we handle the dynamic range required to produce images? (3) Was our assumed reflectivity of 10 percent (Table III) a realistic value to use in calculating system performance?

*The French CSF CO 10.1 o-type carcinotron. Also, Varian of Canada makes a kylstron operating at approximately 220 GHz.

**The reader should be informed that the listing was extracted from the literature without experimental review, and that there are errors in such areas as the CO₂ pump lines.

UNCLASSIFIED

Speckle noise arises because we have a coherent system. The effects of speckle on an imaging system have been evaluated [9,10]. It has been found that the effective resolution of a coherent system is reduced by a factor of five or more due to speckle noise [9]. This effect is shown in Figure 6. On the left is an image taken in incoherent light at fairly low resolution. On the right is the same image taken with coherent light with very drastic and high contrast speckle. The target is virtually unrecognizable and undetectable; however, the image information can be extracted from this "jumble of spaghetti" by appropriate averaging. If diverse images of the target are combined with no correlation between images, the speckle noise can be averaged to as close to zero as required. This can be done with different polarizations, different frequencies, and with the slight angular shifts. As you see, a diversity of 40 goes a very long way towards restoring the complete image. The actual required diversity varies with the contrast and the resolution of the system [10].

DYNAMIC RANGE

To determine the answers to the questions about dynamic range and reflectivity, it was decided to simulate the performance of a submillimeter imaging system by using an existing 3.2-mm imaging system [11]. Images, such as those shown in Figure 7, which simulate ranges of 0.7 and 2.5 km were obtained as well as high-resolution images [12]. A detailed index of images [13] as well as the digital images are available from the US Army Missile Command for qualified recipients. The presence of speckle is quite apparent in the images - no diversity was used during the recording of these images. The fact that the images were recorded is evidence that the dynamic range can be handled. To provide a measure of the average reflectance at 3.2 mm and to quantify the required dynamic range, all the data were calibrated against the reflectance from a 2-in. diameter gold sphere. A histogram of the data from one of the image files is shown in Figure 8. As can be seen from the histogram, a dynamic range of 40 dB is required to record the entire image. The file is displayed on the right of Figure 8 using eight grey tones spread over a dynamic range of approximately 25 dB.

CONCLUSIONS

The results of the experiments and calculations, to date, suggest that a submillimeter imaging radar could provide the Army an ability to operate in inclement weather, but it will require a comprehensive program of magnitude comparable to that which led to present FLIR technology or to laser range rangefinder/designator technology. It will take a decade to develop operational capability. If current studies prove that the Army needs can be satisfied with a submillimeter system, the system requirements will have a major impact on submillimeter technology during the next decade.

REFERENCES

1. US Army Field Manual No. 100-5, 1 July 1976.
2. Kruse, Paul W., A System Enabling the Army to See Through Inclement Weather, US Army Scientific Advisory Panel Report (June 1974).

UNCLASSIFIED

UNCLASSIFIED

3. Kruse, Paul W. and Garber, V., "Technology for Battlefield Target Recognition in Inclement Weather," Proceedings IRIS (23) (In Press).
4. Gamble, W. L. and Guenther, B. D., "Submillimeter Laser Wave Propagation," Optical/Submillimeter Atmospheric Propagation Workshop (6-10 December 1976).
5. Putley, E. H. and Martin, D. H., "Detectors," Chapter 4, Spectroscopic Techniques, Editor, Martin, D. H., North Holland Publishing Co., Amsterdam (1967).
6. Felterman, H. R., Clifton, B. J., Tannerwald, P. E., Parker, C. D., and Penfield, Hays, "Submillimeter Heterodyne Detection and Harmonic Mixing Using Schottky Diodes," IEEE Trans. MIT-22, pp. 1013-1015 (1974).
7. Babkin, Yu. S., Valitov, R. A., Dyubko, S. F., Kuz'michev, V. M., Makarenko, B. I., Sokolov, A. V., Svirch, V. A., Stroganov, L. I., and Schmidt, V. V., "Apparatus for Investigating the Propagation of Submillimeter Radio Waves," Instruments and Experimental Techniques, No. 1, pp. 243-244 (January-February 1968).
8. Rosenbluh, M., Temkin, R. J., and Button, K. J., "Submillimeter Laser Wavelength Tables," Applied Optics, 15, pp. 2635-2644 (1976).
9. Kozma, Adam and Christensen, Charles, R., "Effects of Speckle on Resolution," Journal of the Optical Society of America, 66, pp. 1257-1260 (1976).
10. George, Nicholas, Christensen, C. R., Bennett, J. S., and Guenther, B. D., "Speckle Noise in Displays," Journal of the Optical Society of America, 66, pp. 1282-1290 (1976).
11. Baird, J. M., Millimeter and Infrared Image Scans of Military Vehicles, Hughes Research Laboratory, Final Task Report on Contract F-30602-73-C-0191 (1976).
12. Guenther, B. D., Submillimeter Research: Preliminary Report on Millimeter and Infrared Images of Military Vehicles, US Army Missile Command, Redstone Arsenal, Alabama, Technical Report (In Press).
13. Guenther, B. D., Submillimeter Research: Index of 3.2 mm and 10.6 μ m Image Data Tapes, US Army Missile Command, Redstone Arsenal, Alabama, Technical Report (In Preparation).

UNCLASSIFIED

UNCLASSIFIED

TABLE I. ATMOSPHERIC WINDOWS
IN SUBMILLIMETER REGION

Wavelength (mm)	Attenuation (dB/km)
0.73	17 to 19
0.88	8 to 13
1.24 to 1.4	2.6 to 2.1
0.337	75

Note: Attenuation for standard
conditions (1 atms, 293°K,
7.5 g/m³ water vapor).

TABLE III. SUBMILLIMETER WAVE DETECTORS

	NEP (W/Hz ^{1/2}) at 500 μ m	Response Time (sec)
Thermal		
Ideal (Room Temperature)	5.5×10^{-11}	
Golay Cell (300°K)	10^{-10}	10^{-2}
Ideal (1.5°K)	9.8×10^{-17}	
Ge Bolometer	3×10^{-12}	10^{-3}
Photoconductor		
Ideal (1.5°K)	1.8×10^{-14}	
InSb (H Field)	10^{-11}	2×10^{-7}
Junction		
Schottky Diode (300°K)	10^{-16}	
Josephson Junction (1.4°K)	10^{-17}	10^{-8}
Superheterodyne		
Ideal	2×10^{-22}	
InSb	$\sim 10^{-20}$	

UNCLASSIFIED

UNCLASSIFIED

TABLE III. ASSUMPTIONS AND CHARACTERISTICS
OF INCLEMENT WEATHER IMAGING SYSTEM

Frequency	850 μ
Antenna Aperture	1 m
Quantum Efficiency	50%
Display S/N	50/1
Resolution/Frame	100 \times 100 Elements
Frame Rate	30/sec
Target Reflectivity	0.1
Clear Attenuation	10 dB/km
Rain Attenuation	15 dB/km
Fog Attenuation	2 dB/km
Visibility in Fog	270 m at 0.1 gm/m ³ H ₂ O

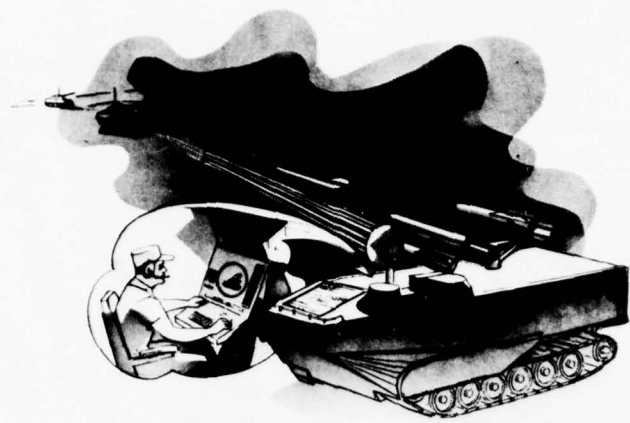


FIG. 1. SYSTEM CONCEPT. A SUBMILLIMETR WAVE IMAGING SYSTEM WITH A ONE-METER APERTURE TO LOCATE AND DIRECT FIRE AGAINST TARGETS CONCEALED BY FOG OR SMOKE.

LIMITS OF OUTPUT POWER

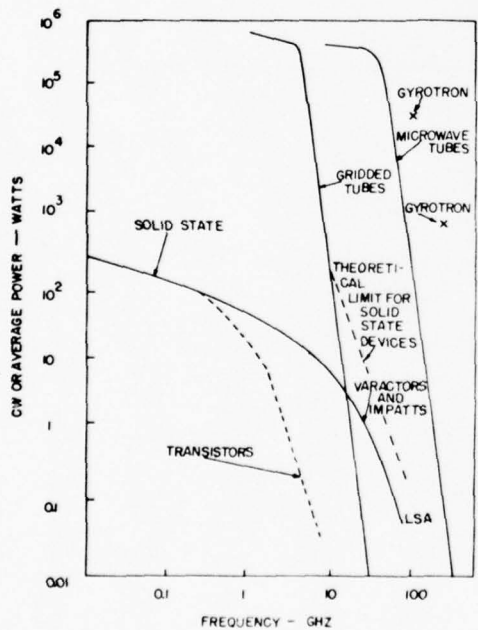


FIG. 2. MAXIMUM LIMITS OF AVERAGE OUTPUT POWER LIMITS ON OUTPUT POWER AS A FUNCTION OF FREQUENCY FOR TUBE AND SOLID STATE SOURCES FROM MICROWAVES p. 14, JULY 1976.

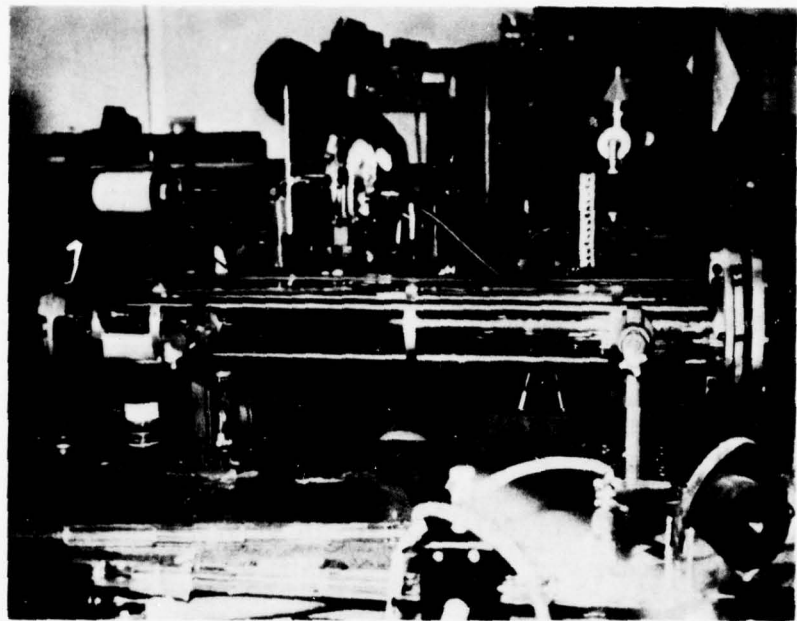


FIG. 3. OPTICALLY PUMPED, SUBMILLIMETER WAVEGUIDE LASER. THE WAVEGUIDE CO_2 LASER USED AS AN OPTICAL PUMP IS SHOWN IN THE FOREGROUND. THE GOLD TUBE IS THE METAL WAVE GUIDE OF THE SUBMILLIMETER LASER. A DIELECTRIC WAVE GUIDE SUBMILLIMETER LASER CAN BE SEEN IN THE FAR BACKGROUND.

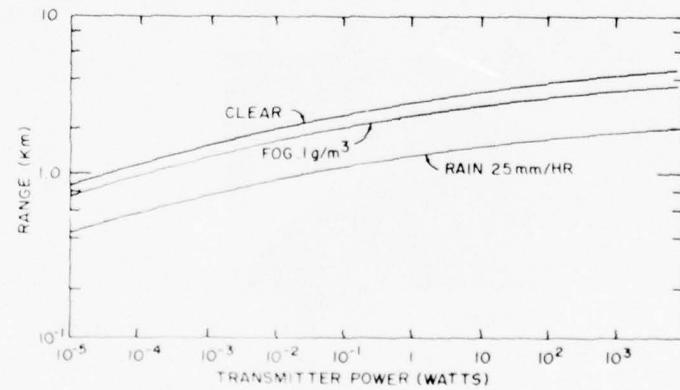


FIG. 4. RANGE OF AN INCLEMENT WEATHER 750 μm SYSTEM. PARAMETERS FROM TABLE III WERE USED TO CALCULATE THESE CURVES.

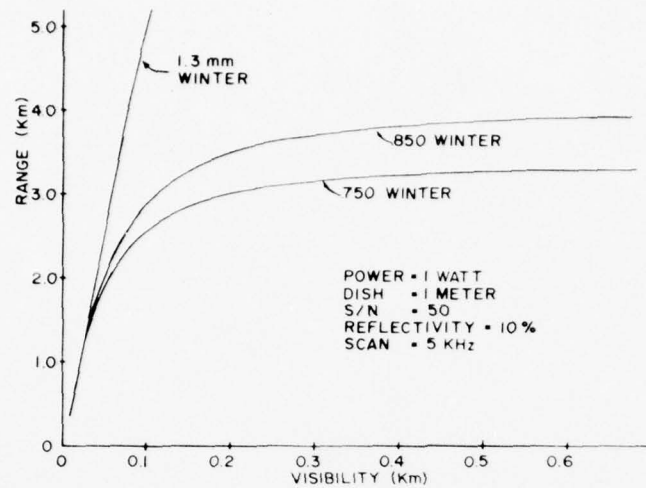


FIG. 5. SUBMILLIMETER OPERATING RANGE IN WINTER AS A FUNCTION OF VISIBILITY. A STANDARD METEOROLOGICAL DEFINITION OF VISIBILITY IS USED.

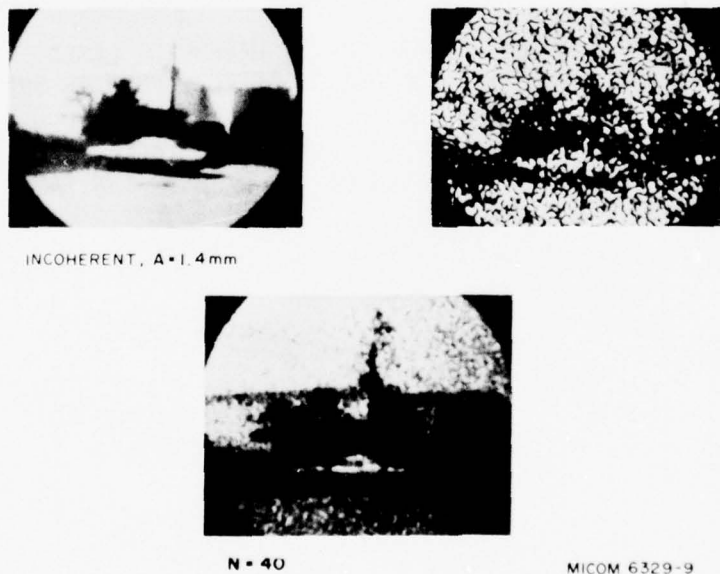


FIG. 6. EFFECTS OF SPECKLE NOISE ON RESOLUTION. ON THE UPPER LEFT IS AN INCOHERENT IMAGE PRODUCED BY AN IMAGING SYSTEM WITH A RESOLUTION MEETING THE IDENTIFICATION CRITERIA FOR THE CAR. ON THE UPPER RIGHT IS A COHERENT IMAGE USING THE SAME OPTICAL SYSTEM. SPECKLE NOISE CAN BE REDUCED BY ADDING IMAGES WITH STATISTICALLY INDEPENDENT SPECKLE NOISE AS IS SHOWN IN THE BOTTOM PICTURE WHERE 40 IMAGES HAVE BEEN ADDED.

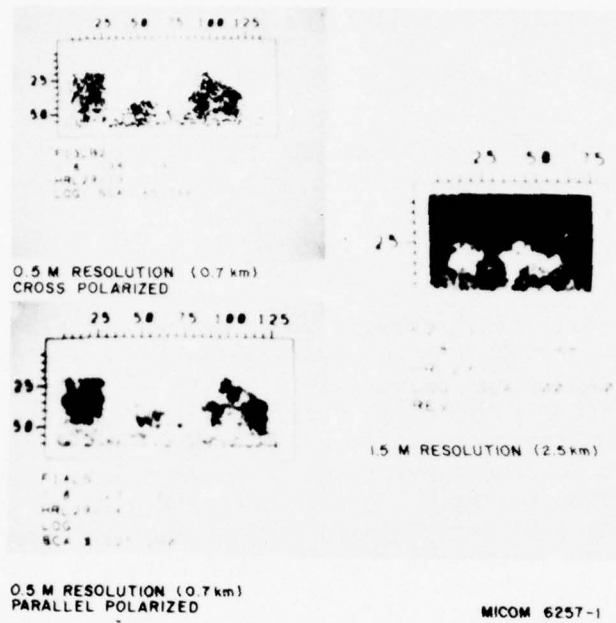


FIG. 7. 3.2mm IMAGES OF MILITARY VEHICLES. THE IMAGES ON THE LEFT SIMULATED A OPERATING RANGE FOR A 700 μ m SYSTEM OF 0.7 KM. THE IMAGES FROM LEFT TO RIGHT ARE A TRUCK, JEEP AND TANK. THE IMAGE ON THE RIGHT SIMULATES 2.5 KM RANGE AND CONTAINS A TRUCK, TANK AND OIL STORAGE TANK. THE SPECKLE NOISE IN THESE IMAGES IS APPARENT.

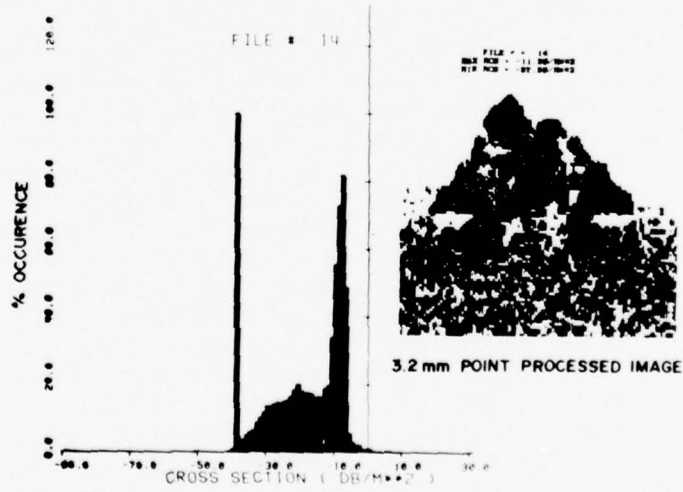


FIG. 8. DYNAMIC RANGE OF 3.2mm IMAGES: THE AXIS LABELED CROSS SECTION REFERENCES THE REFLECTIVITY MEASURED IN THE IMAGE TO THE REFLECTIVITY OF A 2-INCH GOLD SPHERE.

(This page intentionally left blank.)

SYSTEM ENGINEERING IN LIMITED VISIBILITY

D. R. PETERSON, V. D. BLANTON, M. P. STAMPS, and B. W. FOWLER

Advanced Systems Concepts Office, US Army Missile Research, Development and Engineering Laboratory, US Army Missile Command, Redstone Arsenal, Alabama 35809.

ABSTRACT

A considerable gap exists today between field data-atmospheric propagation models and synergistic systems engineering. This gap is characterized in the case of field data by an inadequate scope to allow complete description of the E-O system performance under meaningful battlefield conditions. Additionally, those propagation models that exist and are validated consume an excessive amount of computation time for specific condition evaluation of the E-O system performance even when the E-O system performance has been modeled in a compatible form. These difficulties increase geometrically when many E-O systems, both friend and foe, are played off in realistic condition simulations.

To bridge this gap, we propose the development of parametric models of limited visibility conditions as they spatially and temporally effect E-O system performances. In this paper, we outline the development of a simple haze/fog/smoke (HFS) model for use in a few-on-few simulation. The simulation is run using the Performance and Cost Analysis Model (PERCAM). In this outline, we show the limitations placed on the smoke model by the structure of the simulation. The design of the simulation necessitates the use of a statistical format for the smoke model. Accurate results depend on utilizing a sufficient number of Monte Carlo iterations. Hence, the detail of the statistical model increases the size and time requirement of the simulation. Further, the simulation structure is designed such that the user describes relevant functions by means of a set of particular catalogued components. A particular evaluation component is restricted to be a function of at most, four (4) independent variables. Within these limitations, we develop the smoke model from existing data/propagation models in terms of dynamic parametric inputs that yield systematic effects in a computational timeframe maintaining the usefulness of the overall simulation. As an ongoing check during model development, the smoke model is subjected to deficiency analyses and the final deficiency analysis, for the final, implemented model, is reviewed. Next, the results of overall simulation exercises are presented for typical scenarios and various limited visibility conditions including haze, fog, and large and small area smoke in conjunction with base-line terrain-only exercises. Typical scenarios include tank-tank and tank-antitank engagement. The apparent systems' deficiencies are discussed in terms of the deficiency analyses of the HFS model. Future needs for field data and propagation models to improve parametric models are described.

SYSTEM ENGINEERING IN LIMITED VISIBILITY

(U) The effect of Haze, Fog, and Smoke (HFS) on the prosecution of military operations is twofold: the physical and the psychological. The simulation of the psychological effect is difficult due to the lack of concise data and for the purpose of this analysis will be limited to a degradation of reaction time. Concentration will be placed on the physical effect.

(U) For imaging E-0 devices and the human eye, the physical effect of HFS is contrast degradation due to scattering rather than the extreme case of absorption. This physical effect and the typical inner intercept boundaries of systems such as TOW and DRAGON determined the limits of parametrization. The cases considered were those where the ATGM's Surveillance - Acquisition - Identification - Track (SAIT) was operative beyond this boundary and was the most crucial factor in system operation.²

(U) The effect of tank speed on detection was neglected except as it determined the instantaneous range between the tank and the ATGM, and the P_D was assumed to be distributed in range in Gaussian Form. Thus

$$P_D \text{ (TANK)} = \exp [-AR^2] \quad (1)$$

when R = range and A is a parameter incorporating contrast degradation, and the optics of the situation.

(U) For the ATGM, the P_D has the form,

$$P_D \text{ (ATGM)} = \exp [-ABR^2] \quad (2)$$

when B is the ratio of the characteristics area of the tank to the characteristic area of the ATGM launcher. A strict interpretation of this parameter removes all motional contribution to the P_D form.

(U) In this analysis, we assigned a P_D (TANK) of .14 at the visibility range (either $.3\text{-}9 \mu$ or $8\text{-}14 \mu$). This selection is arbitrary and the results were used only in a relative, comparative manner. (e.g. ATGM has a night sight, Tank does not) The SAIT mismatches between Tank and ATGM were incorporated in the B parameter. This is equivalent to assuming that the target dimension and spectral wavelength contributions to P_D are geometric and therefore separable.

(U) The extension of A to the IR from the visible is facilitated by the assumption that scattering only is important to first order. 3

$$\frac{A_{IR}}{A_{VIS}} = \frac{\sigma_{sc}(IR) I_0(IR)}{\sigma_{sc}(VIS) I_0(VIS)} \quad (3)$$

Where σ_{sc} is the scattering cross section of the media, and I_0 is a representative intensity without the media. It is further possible by judicious selection of the I_0 's to estimate equation (3) as

$$A_{IR} = A_{VIS} \frac{w_{IR}}{w_{VIS}} \quad (4)$$

(U) The total system simulation that was utilized for this study was PERCAM. PERCAM 4 is a performance and operational cost analysis model that was developed to integrate Army air defense requirements with advanced R&D technology, and modified to study land combat requirements. It can be used to determine the effectiveness of a system both technically and from a cost standpoint. The system being analyzed can be either offensive or defensive.

(U) N attackers versus M defenders and L targets can be simulated. The scenario is entirely flexible including the option of having groups of attackers in formation. The program size, detail, and turnaround time are flexible depending on the degree of detail of the data base the user desires.

(U) This flexibility is available because of a tool known as event logic trees or sometimes called element trees. The user can select from a library any components that he wishes to employ in constructing the element tree that will describe the attacker or defender tactics. The preprocessor develops the defender and attacker performance subroutines based on which components are utilized.

(U) A simple illustration of employing element trees is the functional description of a tiger stalking its prey. (1) Determine probability of a successful attack based on range and bearing of prey. (2) Decide either to attack or not to attack. (3) Continues along if there is no attack. (4) If attacking, action can be interpreted in terms of probability of kill. (5) Launching an attack consumes some time. (6) Attack results in either a kill or (7) no kill. This element tree is presented in figure 1.

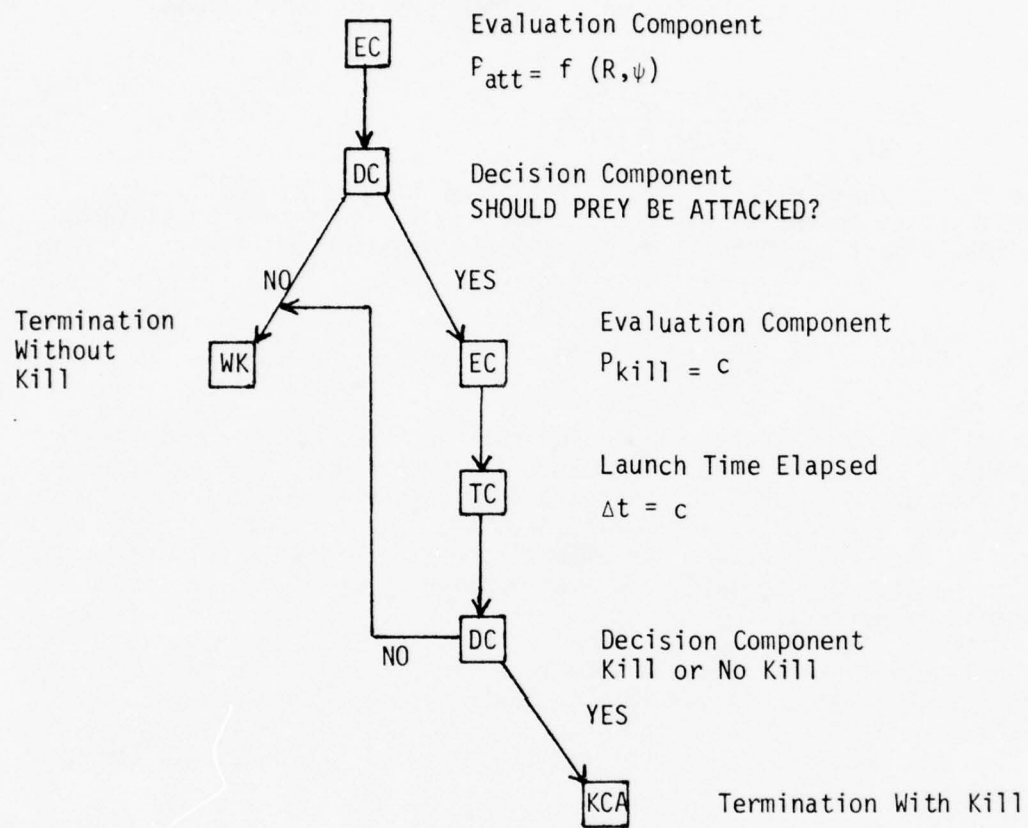


Figure 1. Tiger Stalking Prey Element Tree

This is a simple example utilizing only a few of the basic components available. It should be noted that the statistical data, e.g., P_D can be described as a function of up to four (4) independent variables. The decision component is determined by comparing a computed probability with a random number from 0 to 1. Not only does the utilization of element trees allow user flexibility, it also allows the influence of an individual component on total system effectiveness to be observed. A Monte Carlo iterative process is employed since the engagement outcome is a function of a number of probabilities. Normalized results are achieved by replaying the engagement as many times as the user specifies.

(U) There are certain restrictions placed on the Haze-Fog-Smoke model by integrating it into PERCAM. The HFS model must be statistical by nature to be implemented as an element in the event logic tree. For this reason the model is a calculation of P_D . It is limited to being a function of not more than four (4) independent variables. In this case P_D is a function of range, spectral wavelength, meteorology, the size of the tank, and the size of the ATGM launcher. This restriction motivated grouping the last four arguments into one parameter. The degree of accuracy of results that can be achieved using this model is dependent on the number of Monte Carlo iterations employed. However, as the number of iterations increases, the computer time and hence the simulation cost increases. This model was used to evaluate advanced concepts of air defense systems in the SHORADS category under adverse weather conditions. The scenario in figure 2 was utilized to demonstrate the effects of degraded meteorological visibilities on the performance of a SHORADS system against a fixed wing aircraft. This scenario consists of three (3) defenders located in position to defend the rear area. Four fixed wing aircraft are approaching at a speed of 250 m/sec at altitude of 60 meters. Masking and other critical parameters are accounted for in the model.

(U) Figure 3 shows the performance results of the SHORADS systems when meteorological visibilities are degraded from clear visibility of 23 km. down to poor visibility of 2 km. It can be seen that the probability of kill is highest at 23 km. visibility. At 10 km. visibility there is a noticeable degradation in kill probability. At 5 km. the kill probability is very poor, and by 2 km. the probability of kill has dropped to zero. The location of the attackers relative to the defenders in the scenario account for attackers 3 and 4 having lower kill probabilities.

(U) The effect of degraded meteorological visibility is illustrated in figure 3 where the SHORADS system relies on visual detection. However, in figure 4, when the visual detection is replaced by RF detection, preferably passive, the total system effectiveness is not greatly reduced by degraded meteorological visibility even though an IR sensor is used for acquisition.

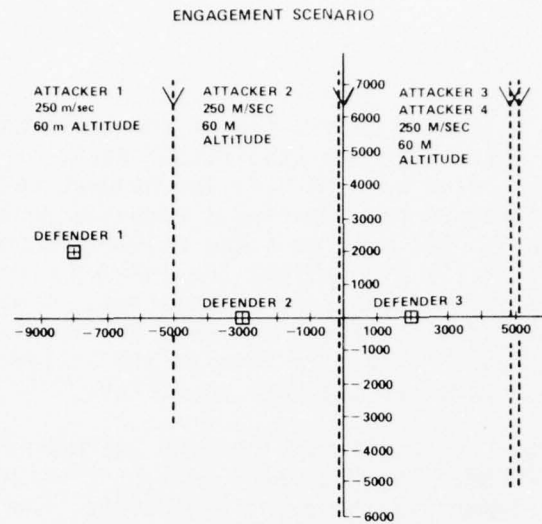


FIGURE 2

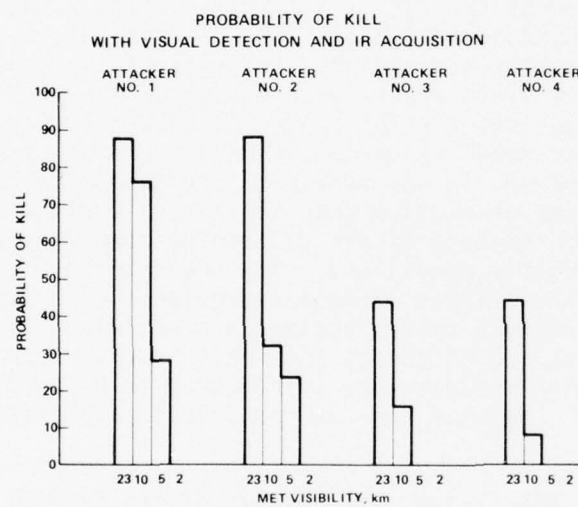


FIGURE 3

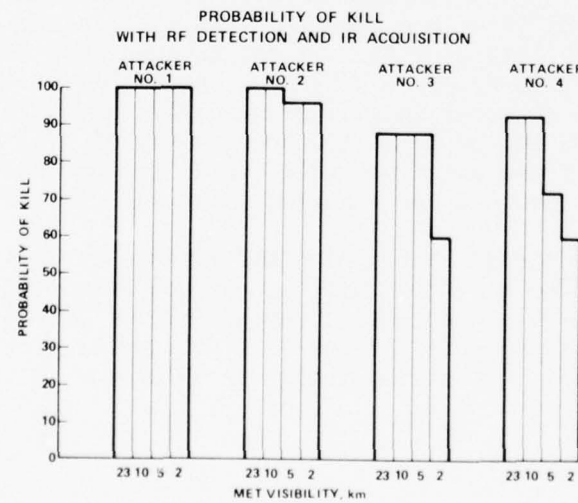


FIGURE 4

(U) Next the model was used to simulate a land combat engagement. The Tank - ATGM conflict was simulated in the following manner: the tank speed was taken to be between 8 and 12 m/sec, the tank gun shell's average speed was 500 m/sec and the reload time was 8 seconds. The tanks came to a complete halt when firing and were constrained to make no evasive maneuvers. No terrain or clutter masking was included. The tanks were uncorrelated to the extent that each tank was required to detect the ATGM site independently. The ATGM average speed was 350 m/sec. The reload time was varied from 0 to 90 seconds by 30 second increments. The ATGM site could completely exercise the SAIT function while an ATGM was in flight, but could not reload. P_k of the ATGM was taken to be .95 and its maximum range 3 km. The ATGM was assumed to have one second of level flight without guidance to incorporate post ATGM site destruction tank kills if they occurred.

(U) The plan of battle modeled the situation as a small representative part of a concerted real tank assault on a Blue FEBA. No retreat was allowed. Tanks detecting the ATGM site were diverted toward the site at maximum speed. P_k of the tank gun was modeled as 4 straight line approximations for the T-62 tank⁵ with small arms fire added at short range.

(U) Four visibility scenarios were chosen: an unaided eye, 1200 m nominal visibility day,⁶ the ATGM SAIT enhanced with a night sight that doubled the nominal visibility, the Tank SAIT similarly enhanced, and both Tank and ATGM SAIT enhanced. Three functions were measured in the simulation; the probability that the ATGM site would be destroyed in the engagement, the expected number of tanks destroyed per engagement, and the expected standoff range.

(U) The results of the simulation are shown in figure 5. Several conclusions may be drawn from this figure. As the reload time increases, the unaided eye, ATGM system will approach a one-for-one trade. Equipping tanks with night sights is performance effective to the tank whether the ATGM has a night sight or not because it offers an offset to ATGM's with night sights and excellent performance against ATGM's without night sights. Equipping ATGM sites with night sights improves performance markedly even if the tank has a night sight.

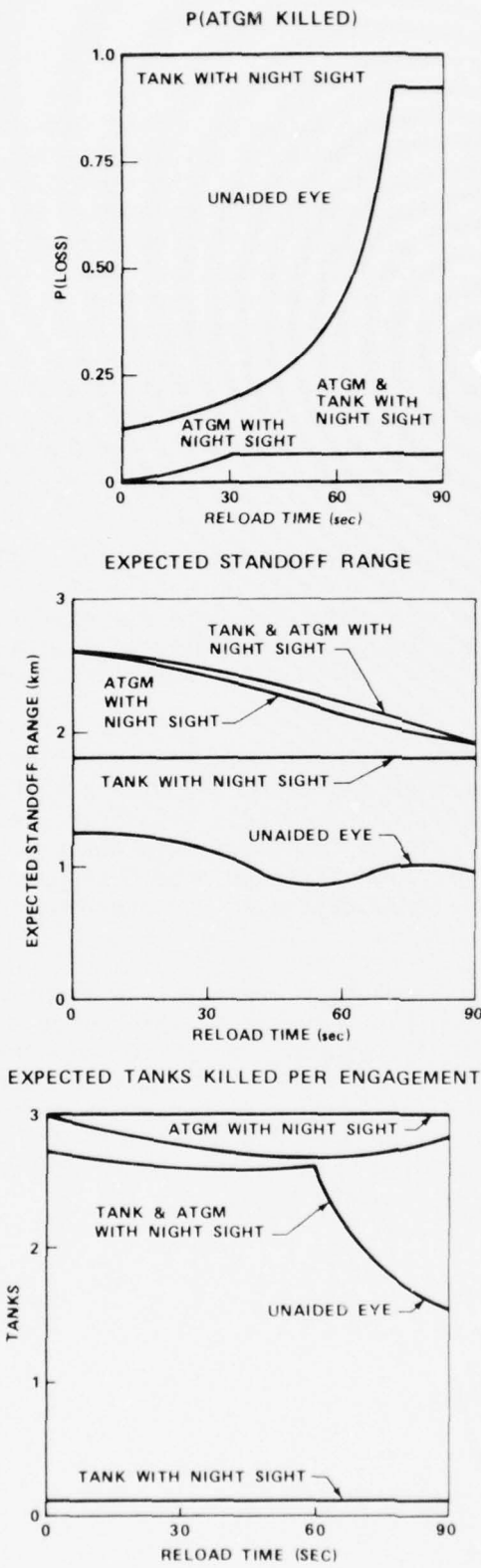


FIGURE 5

FUTURE EFFORTS

(U) Several future efforts are planned using this model as extensions of this investigation. The inclusion of terrain and clutter masking with maneuvering tanks incorporating masking doctrine is planned. Further, trade-offs between coherent and non-coherent IR images with conventional and fire-and-forget missiles will be conducted. Eventually, weapons mixes and larger scenarios will be investigated.

REFERENCES

1. Fowler, Bruce W., "Radiative Transfer for Imaging Purposes", Topical Meeting on Atmospheric Aerosols, 1976.
2. Pope, D. Brent and Fowler, Bruce W., "The Tank, The Missile, and Smoke", SAWG White Paper, 1976.
3. Fowler, Bruce W. and Peterson, Donald R., "Propagation Modeling For E-O Sensors", Optical/Submillimeter Atmospheric Propagation Workshop, 1976.
4. Air Defense System Performance and Operational Cost Analysis Model (PERCAM), DAAH01-75-C-0084, TRW Systems Group, Huntsville, Alabama, December, 1974.
5. TRADOC Bulletin #1, "Range and Lethality of US and Soviet Anti-Armor Weapons", 30 September, 1975.
6. The selection of 1200 M as a nominal visibility was based on results obtained by MICOM during participation in the Graffenwher, FRG field tests in 1975.

...This paper is unclassified

WATER VAPOR LINE AND CONTINUUM ABSORPTION MEASUREMENTS IN THE INFRARED REGION

Kenneth O. White
Wendell R. Watkins
and
Charles W. Bruce

Atmospheric Sciences Laboratory
US Army Electronics Command
White Sands Missile Range, New Mexico 88002

ABSTRACT

A comprehensive program to determine water vapor absorption as a function of pressure, temperature, and frequency in the 3-5 and 8-12 μm regions is underway at the Atmospheric Sciences Laboratory. Water vapor continuum measurements in the 3.5-4.1 μm region are presented in this paper. The measured continuum absorption under midlatitude summer (MLS) conditions is approximately a factor of two larger than predictions. The impact of these results on a recent investigation of thermal imaging systems is discussed. Absorption coefficients for the Navy/ARPA Chemical Laser (NACL) for MLS conditions are given.

INTRODUCTION

An accurate and detailed knowledge of atmospheric transmission is essential to the design, performance evaluation, and comparative testing of electro-optical systems. While many constituents contribute to the total atmospheric attenuation, the absorption due to water vapor is of greatest concern to system performance. Furthermore, the transmission in and at the edges of the two major transmission windows (3.0-5.0 μm and 8.0-12.0 μm) is most important since these are the bands in which infrared devices must operate. The generally low values of absorption in these spectral regions necessarily make them the most difficult to understand, and to model adequately.

Early measurements [1] of transmission did not include a measure of the water vapor continua and consequently, propagation predictions and design studies based on them often lead to erroneous absolute and relative performance predictions. As a case in point, in early years transmission at the carbon dioxide (CO_2) and deuterium fluoride (DF) laser frequencies was considerably overpredicted, since the magnitude of the continuum absorption was not generally known.

The general effect of these uncertainties is illustrated by the historical development of broadband FLIRs, which are generally designed to operate in either the 3-5 or 8-12 μm atmospheric windows. Early design

studies [2, 3, 4] were based on atmospheric transmission measurements by Yates and Taylor [1], which were reduced in such a way to omit the 10 μm water continuum. Thus, these design studies predicted optimistically high performance for FLIRs operating in the long wavelength window, relative to systems operating in the 3-5 μm window.

Later studies of relative performance of short and long wavelength FLIRs [5, 6, 7] were based on the Lowtran II atmospheric transmission model [8], which included a 10 μm continuum but did not include the 4 μm continuum. It now appears that this 10 μm continuum overestimates the absorption [9]. Thus, these studies tended to predict optimistically high performance for the short wavelength FLIRs relative to the long wavelength FLIRs. Effective design studies and systems analyses clearly require a better understanding of the water vapor continua.

In this work, water vapor continuum measurements in the DF (3.5-4.1 μm) region are presented. Using these results the power weighted absorption coefficient for a specific Navy/ARPA Chemical Laser (NACL) has been calculated. The impact of the new continuum data on a recently completed FLIR evaluation study [10] has been assessed.

EXPERIMENTAL APPROACH

The experimental equipment includes long-path absorption cells, spectrophones, line tunable pulsed and cw lasers, and continuously tunable diode lasers. The long-path cell experimental setup for the DF laser measurements is shown in Figure 1a. The DF laser sources used for both the absorption cell and spectrophone measurements are grating tunable pulsed Lumonics multigas lasers. They have an unstable resonator front reflector resulting in a doughnut-shaped, near-field TEM-00 output beam. The DF laser beam is made coincident with a visible He-Ne laser beam by using several mirrors M and one mirror M' with a central hole. Two precision adjustable lenses are inserted in the He-Ne beam to match the effective divergence of the two lasers. The DF output wavelength is checked by inserting a lens and spectrum analyzer into the DF laser beam. After the DF laser beam traverses the length of the laboratory, it is collected by mirror CM1. Mirror CM2 is used to match the f-number of the DF and He-Ne laser beams to the 21-m absorption cell optics. An optical flat B is used to split a portion of the beam to the cell input detector ID. The remaining portion of the beam passes through window W. A multi-path through the cell is obtained by using White-type reflective optics. The cell output beam is detected by the cell output detector OD. Teflon membrane filters F are placed in front of the detectors to diffuse the laser beam. Apertures A are placed in front of the detectors to prevent detector saturation. A more detailed account is given elsewhere [11]. Details of the signal analyzing system used for the absorption cell system is described in the literature [12]. A new technique, path differencing, is used in data acquisition to obtain nearly time independent results [13]. The technique uses rapid changes between two pathlengths to time average short-term and to eliminate long-term system drift normally encountered in long-path absorption cell measurements. Path differences

of from 1008 to 1512 m were used.

For the water vapor absorption measurements a measured amount of water was introduced into the 21-m cell under vacuum and allowed to evaporate. The equilibrium pressure was measured by a capacitance manometer. An 80%/20% mixture of N₂/O₂ was used to buffer the water vapor to 760 torr total pressure. The water vapor partial pressure was monitored by a dew-point hygrometer. Measurements were performed at two temperatures, 23°C and 65°C. The reference cell condition required for long-path cell measurements was a 760 torr 80%/20% mixture of N₂/O₂ with the corresponding amount of water vapor pressure replaced by O₂ since N₂ absorbs at several DF frequencies. Additional measurement technique details are given elsewhere [12, 13].

The pulsed source spectrophone used for these water vapor measurements consists basically of a cylindrical chamber with dominant longitudinal acoustically resonant mode near 1 kHz (Fig. 1b). This chamber is positioned within another cylindrical chamber made of stainless steel which is evacuable and bakeable. The spectrophone cell entrance and exit windows are located in the ends of this outer cylinder and are thus well removed from the entrance and exit apertures of the interior resonant chamber. This arrangement and acoustical dampers serve to avoid contributions to the spectrophone output signal due to the window absorption. An aluminum coated mylar diaphragm, forming a complete circular cylinder at the perimeter of the inner chamber, serves as a capacitance microphone sensor for the absorption signal. The time resolved signals from a number of laser pulses are summed on a point by point basis, displayed on an oscilloscope, and photographed for analysis. The set of relative absorption values is then referenced to a known absorption using methane as a trace gas in the same N₂/O₂ buffer gas. Additional details are given elsewhere [14].

EXPERIMENTAL RESULTS

65°C Water Vapor

Measurements of total water absorption were made with 72 torr of water vapor at 65°C. The measurements give a reasonable check on the water vapor theoretical modeling and allow a comparison with the water vapor continuum results of Burch [15] near his experimental conditions. The continuum values inferred from the present data were obtained by subtracting the calculated HDO and H₂O line contributions from the measured total water absorption values. The results are shown in Figure 2 along with the continuum predicted from Burch's measurement. The present results and the Burch results and prediction are in substantial agreement.

23°C Water Vapor

Natural water vapor absorption coefficients have been measured in both the White cell and in the spectrophone and deuterium depleted water vapor values have been measured in the White cell at 23°C with a water

vapor pressure of 14.3 torr. An analysis of the deuterium depleted water sample indicated 2% the natural HDO concentration [16]. Inferred continuum values at 23°C have been extracted from these absorption coefficients. These continuum values are given in Table I. An average of the three sets of data is shown as crosses in Figure 3 along with the continuum extrapolated from the Burch measurement and published measurements by the Ohio State University (OSU) group [17, 18]. The present results indicate a water continuum roughly twice as large as that of Burch near 3.8 μm , and about a factor of three greater near 3.5 μm . The inferred OSU continuum values indicate a continuum level slightly less than present values.

The Burch measurements of water vapor continuum did not include an analysis of how the expected error bounds on the self- and foreign-induced coefficients (C_s and C_f) influence the error in the total water continuum absorption coefficient k_c . We have used a Monte Carlo technique for evaluating the combination of the various errors including the effects of temperature extrapolation [19].

Briefly, the Monte Carlo technique employed selects statistically, from appropriate distribution functions, values for all the variables which have an associated uncertainty. The values for these variables are then combined, according to the governing equation, to evaluate a statistical sample for k_c . This procedure is repeated several hundred times (each time using new randomly generated numbers), until sufficient statistics are accumulated to evaluate accurately the total uncertainty in k_c .

Results of this analysis and a comparison with present results are shown in Figure 4. It is seen that the present values are well above the closest error bound. It is concluded that the high temperature measurements agree quite well with the Burch measurements, but that the 23°C extrapolation of Burch underestimates the continuum by at least a factor of two.

APPLICATIONS TO E-O SYSTEMS

An understanding of the water vapor continua in both the 3.0-5.0 μm and the 8.0-12.0 μm regions is important for predicting performance of high energy laser (HEL) devices, and for performance evaluations of broadband systems. We have applied the present results to predicting atmospheric molecular absorption of power extracted from the Navy/ARPA Chemical Laser (NACL). Although, absorption at a given NACL frequency is the sum of several water vapor and mixed gas components, the primary absorbers for the canonical midlatitude summer model atmosphere are HDO lines and the water vapor continuum.

Table II shows the fractional power output of the laser on the various laser lines [20]. The power weighted absorption coefficient is calculated in the table as 0.106 km^{-1} . The bottom row in the table shows

the individual contributions to the power weighted coefficients as 0.086 for H₂O and 0.020 for the other mixed gases.

The NACL effective absorption coefficient value of 0.106 km⁻¹ is about twice the value of 0.05 km⁻¹ that has commonly been quoted for the DF lasers. This discrepancy has three basic causes: (1) the increased continuum absorption level; (2) the large fractional power at P₁(11) where HDO absorption is very large; and (3) the large fractional power at P₂(10) where N₂O absorption is large. This case illustrates the importance of an accurate knowledge of the individual line absorption coefficients and the output power spectra of the specific laser device.

The significance of determining accurately the water vapor continuum absorption in the 3.0-5.0 μm region is indicated in analyses of performance of thermal imaging systems. Comparisons have been made of relative performance between FLIRs designed to operate in the 3.0-5.0 μm and 8.0-12.0 μm windows [10]. Transmission predictions, and therefore, FLIR performance, are impacted by the magnitude of the self and foreign broadening coefficients, their relative magnitude and their temperature dependence. The effect at the shorter wavelength window is shown in Figure 5 where the Burch continuum is inserted in the propagation model LOWTRAN III [21], which does not include a water vapor continuum. As shown, the continuum is varied between 0.5 and 2 times the nominal Burch model with significant effect. If the present value for the continuum was used the effect on transmission would be significantly greater, since at the short wavelength end of the measured values, the Burch values under predict by about a factor of three. In reference 10, calculations of the relative performance of short wavelength versus long wavelength FLIRs, using an expression similar to that of Barhydt, [3] were performed for several water vapor continua models (see Figure 6) [9, 22]. It is seen that the difference in relative performance predicted for extremes in these models is more than a factor of five at twenty kilometers range. Stated differently, the range difference for equivalent performance is about seven kilometers. Although, these calculations are for extremes in the models and for high humidity conditions, they are indicative of the importance of water vapor continuum on the performance of broadband infrared systems.

CONCLUSIONS

An understanding of the 3.0-5.0 μm and 8.0-12.0 μm water vapor continua are important for a broad range of E-O systems performance. Experimental and theoretical investigations should be pursued to attain a satisfactory understanding of the continua. Items of primary importance are: (1) absolute and/or relative magnitude of the self and foreign broadening parameters, (2) temperature and frequency dependence of the parameters.

At present, data in the short wavelength window exist only for the narrow band between 3.5 μm and 4.1 μm . Sufficient data to model water vapor absorption throughout the 3.0-5.0 μm region, including the small window between 4.5-5.0 μm should be obtained.

The Atmospheric Sciences Laboratory (ASL) water vapor absorption measurement program is now addressing and will continue to address over the next few years some of the above problems. The program is constrained by the current and projected level of resources within ASL. The present plans include efforts in HF/DF, CO and CO₂ laser spectral regions. These have already contributed to a fuller understanding of water vapor absorption.

REFERENCES

1. H. W. Yates and J. H. Taylor, 1960, "Infrared Transmission of the Atmosphere," NRL Rept. 5453, AD 240 188.
2. L. G. Mundie, 1967, "A Comparison of InSb and Ge: Hg Detectors for Air-to-Ground Reconnaissance," Rand Memorandum RM-5524-PR.
3. H. Barhydt, D. P. Brown and W. B. Dorr, 1970, "Comparison of Spectral Regions for Thermal Imaging Sensors," Proc. IRIS, 14, No. 2.
4. H. Barhydt, 1973, "Review of Spectral Region Choice," Proc. IRIS, 18, No. 1, pp. 313-314.
5. A. D. Schnitzler, 1973, "Image Detector Model and Parameters of the Human Visual System," J. Opt. Soc. Am., 63, 1357.
6. A. D. Schnitzler, 1974, "The Composite FLIR - Visual System I: Quantitative Relationships between Performance and Design Parameters," IRIS Specialty Group on Infrared Imagery, p. 85.
7. A. F. Milton, G. L. Harvey, J. C. Kershenstein and M. D. Mikolosko, 1975, "A Comparison of the 3-5 Micrometer and 8-12 Micrometer Regions for Advanced Thermal Imaging Systems Using the Lowtran II Atmospheric Transmission Model," NRL Memo Rept. 3098, EOTPO Rept. #22.
8. J. E. A. Selby and R. M. McClatchey, 1972, "Atmospheric Transmittance from 0.25 to 28.5 μm : Computer Code Lowtran 2," AFCRL-72-0745, AD 763-721.
9. R. E. Roberts, J. E. A. Selby and L. M. Biberman, 1976, "Infrared Continuum Absorption by Atmospheric Water Vapor in 8-12 μm Window," Appl. Opt., 15, 2085.
10. T. W. Tuer, 1976, "Thermal Imaging Systems' Relative Performance: 3-5 μm versus 8-12 μm ," Final Report SAI-76-005-AA, Science Applications, Inc., Ann Arbor, MI.
11. K. O. White and W. R. Watkins, 1975, "Absorption of DF Laser Radiation by Propane and Butane," ECOM-5563, AD A012169.
12. K. O. White, G. T. Wade, and S. A. Schleusener, 1973, "The Application of Minicomputers in Laser Atmospheric Experiments," Proc. IEEE, 61, 1596.

13. W. R. Watkins, 1976, "Path Differencing: An Improvement to Multipass Absorption Cell Measurements," Appl. Opt., 15, 16.
14. C. Bruce, 1976, "Development of Spectrophones for CW and Pulsed Radiation Sources," US Army Electronics Command Report No. ECOM-5802.
15. D. E. Burch, D. A. Gryvnak, and J. D. Pembrook, 1971, "Investigation of the Absorption of Infrared Radiation by Atmospheric Gases: Water, Nitrogen, Nitrous Oxide," Air Force Cambridge Research Laboratories, Hanscom AFB, MA, AFCRL-71-0124.
16. W. M. Thurston, Atomic Energy of Canada, General Chemistry Branch, Chalk River, Ontario, Canada, Private Communication, June 1976.
17. F. S. Mills, R. K. Long, and E. K. Damon, 1975, "Laser Absorption Studies," Ohio State University, TR-75-289.
18. F. S. Mills, 1975, "Absorption of Deuterium Fluoride Laser Radiation by the Atmosphere," PhD Dissertation, Ohio State University.
19. T. Tuer, SAI, Ann Arbor, MI, Private Communication, Nov 76.
20. P. Kafalas, MIT Lincoln Labs, MA, Private Communication, Jun 76.
21. J. E. A. Selby and R. M. McClatchey, 1975, "Atmospheric Transmittance from 0.25 to 28.5 μm : Computer Code Lowtran 3," AFCRL-TR-75-0255.
22. V. G. Kunde and W. G. Maguire, 1973, "Direct Integration Atmospheric Slant Path Transmittance Model for Interpretation of High Spectral Resolution Planetary Thermal Emission Spectra," NASA Goddard Report.

TABLE I. WATER VAPOR CONTINUUM ABSORPTION COEFFICIENT
 $(\text{km}^{-1}) \times 10^3$ FOR 14.3 TORR WATER VAPOR
 AT 23°C BUFFERED TO 760 TORR

Laser Line	Natural Water Vapor Spectrophone	Natural Water Vapor White Cell	HDO Depleted Water Vapor White Cell	Average
P ₁ (3)	-	92 + 4	117 + 2	105 + 18
P ₁ (4)	-	95 + 10	125 + 4	110 + 21
P ₁ (5)	96 + 5	60 + 7	90 + 15	82 + 19
P ₁ (6)	68 + 5	60 + 4	81 + 10	70 + 11
P ₂ (3)	-	43 + 10	76 + 7	60 + 23
P ₁ (7)	78 + 4	64 + 6	65 + 12	69 + 8
P ₂ (4)	62 + 6	45 + 5	89 + 6	65 + 22
P ₁ (8)	75 + 7	47 + 11	79 + 6	67 + 17
P ₂ (5)	57 + 3	54 + 7	70 + 5	60 + 9
P ₁ (9)	48 + 2	52 + 8	49 + 2	50 + 2
P ₂ (6)	49 + 3	50 + 8	52 + 9	50 + 2
P ₁ (10)	28 + 2	58 + 8	46 + 18	44 + 15
P ₂ (7)	48 + 5	51 + 6	52 + 7	50 + 21
P ₃ (4)	19 + 2	42 + 10	29 + 3	30 + 12
P ₂ (8)	38 + 4	36 + 7	28 + 10	34 + 5
P ₃ (5)	42 + 3	40 + 3	47 + 4	43 + 4
P ₂ (9)	37 + 4	35 + 9	34 + 6	35 + 2
P ₃ (6)	46 + 2	51 + 11	48 + 11	48 + 3
P ₂ (10)	39 + 4	39 + 20	25 + 13	34 + 8
P ₃ (7)	39 + 2	55 + 10	43 + 10	46 + 8
P ₂ (11)	-	51 + 8	42 + 7	47 + 6
P ₃ (8)	36 + 3	38 + 10	33 + 10	36 + 3
P ₃ (9)	40 + 3	41 + 7	43 + 11	41 + 2
P ₃ (10)	-	43 + 12	-	43 + 12
P ₃ (11)	-	34 + 15	70 + 6	52 + 25

TABLE II. ABSORPTION COEFFICIENTS (km^{-1}) $\times 10^3$ FOR NaCl
LASER LINES WITH 14.3 TORR WATER VAPOR AT 23°C

Laser Line	H_2O This Work	Total	Fractional Power	Power Weighted Line Abs. Coef.
P ₁ (8)	167	168	.01	1.7
P ₁ (9)	66	74	.02	1.5
P ₁ (10)	78	83	.08	6.6
P ₁ (11)	385 ^a	387	.10	38.7
P ₂ (8)	44	47	.03	1.4
P ₁ (12)	50 ^a	52	.03	1.6
P ₂ (9)	67	72	.08	5.8
P ₂ (10)	43	94	.18	16.9
P ₃ (7)	63	106	.01	1.1
P ₂ (11)	52	70	.14	9.8
P ₃ (8)	41	75	.02	1.5
P ₂ (12)	42 ^a	57	.01	.6
P ₃ (9)	41	57	.14	8.0
P ₃ (10)	44	71	.10	7.1
P ₃ (11)	38	87	.02	1.7
P ₄ (8)	42 ^a	93	.01	.9
P ₃ (12)	43 ^a	117	.01	1.2

Power
Weighted
Abs. Coef. 86 106.1

^aAt these laser lines, which were not measured in this work, interpolated continuum values were used with predicted line values.

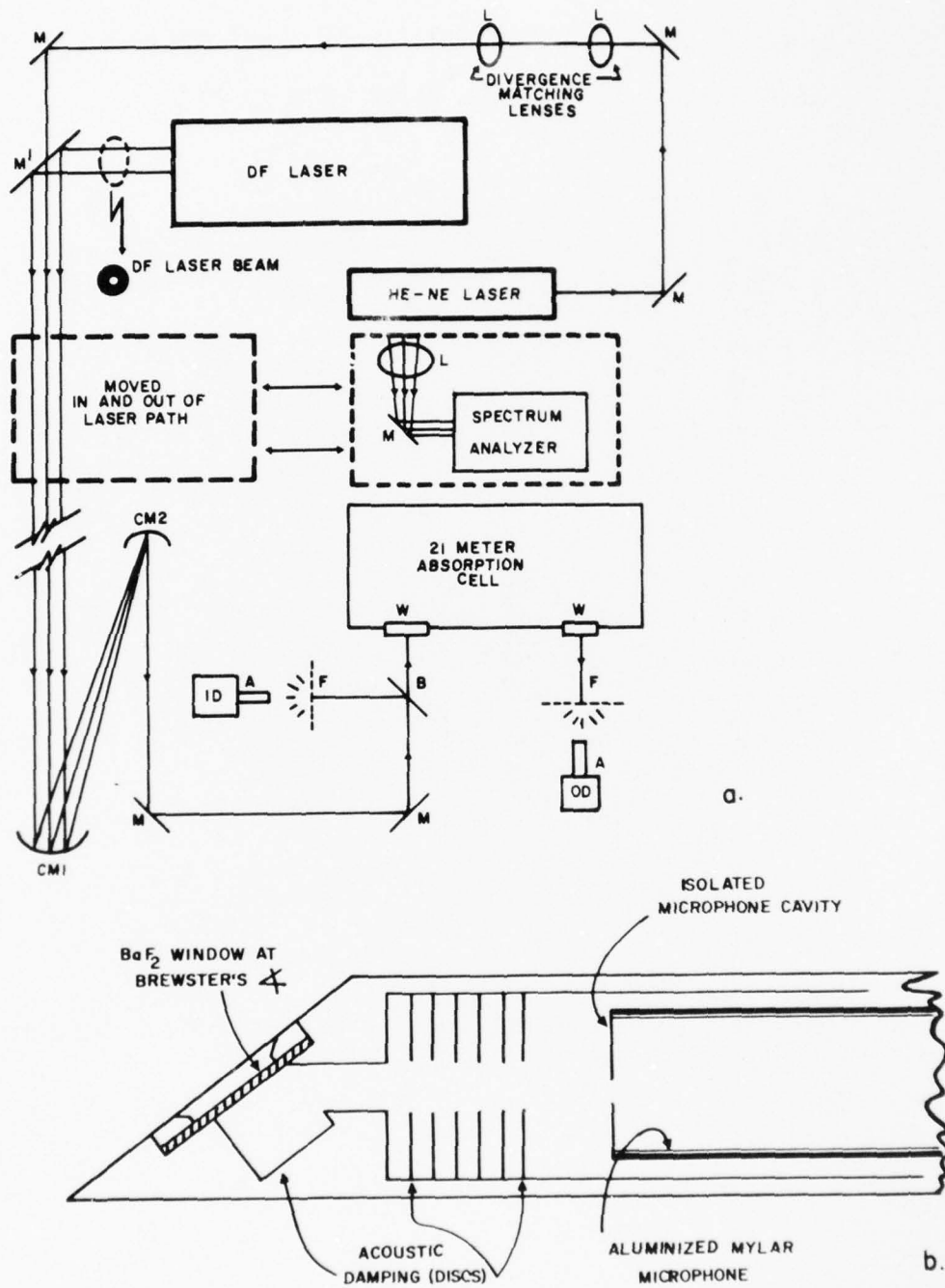


Figure 1 a. ABSORPTION CELL ARRANGEMENT
b. SCHEMATIC DRAWING OF PULSED SOURCE SPECTROPHONE

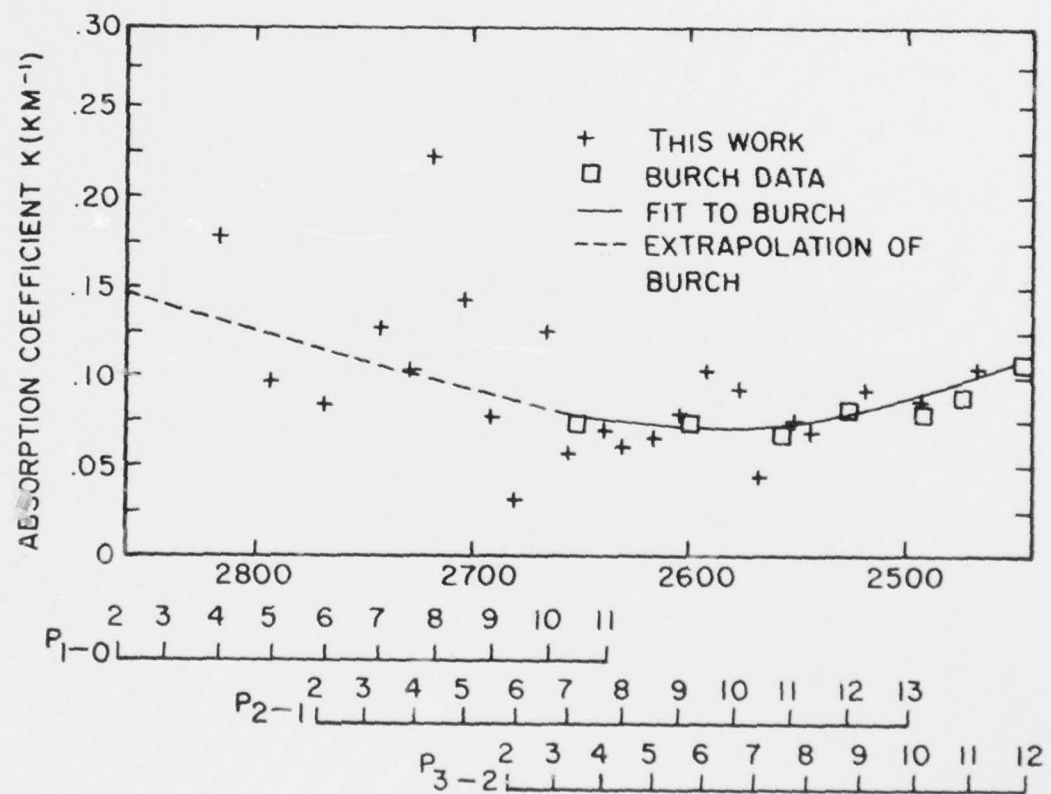


Figure 2. INFERRED CONTINUUM THIS WORK COMPARED TO BURCH RESULTS AT 65° C WITH 72 TORR WATER VAPOR BUFFERED TO 760 TORR

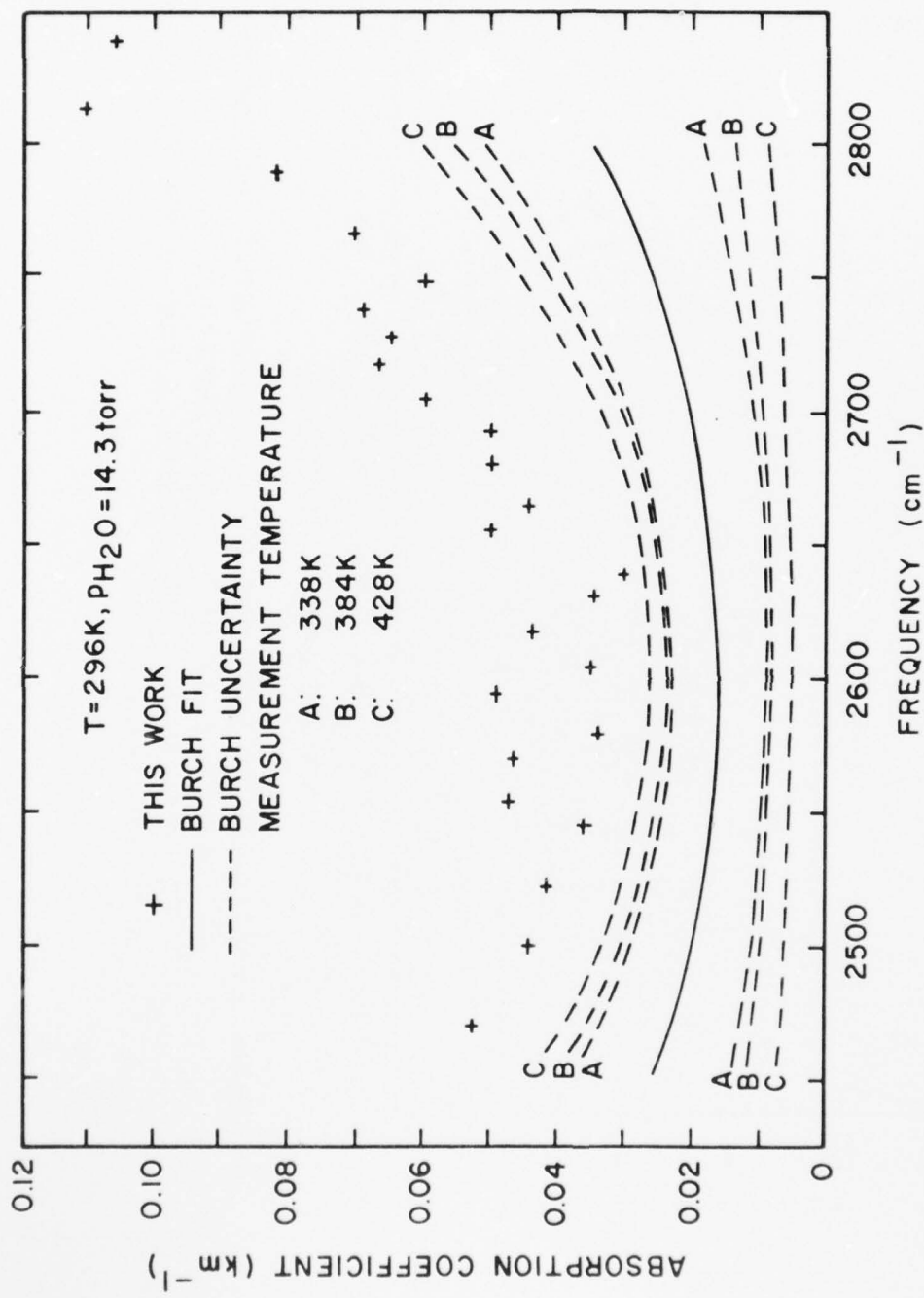


FIGURE 4. COMPARISON OF WATER CONTINUUM ABSORPTION MEASUREMENTS:
BURCH'S UNCERTAINTY BOUNDS AND THIS WORK MEASUREMENTS

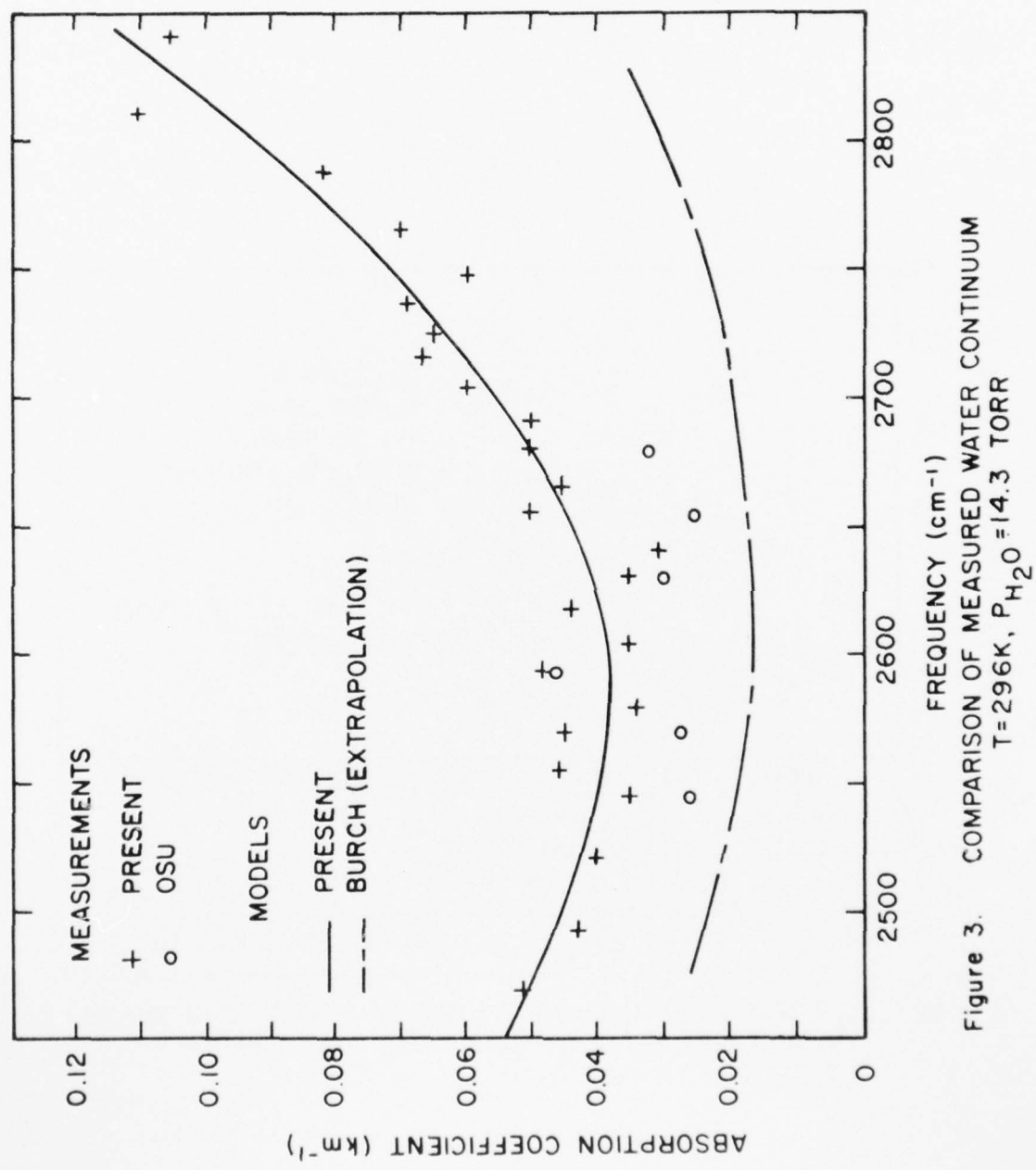


Figure 3. COMPARISON OF MEASURED WATER CONTINUUM
 $T = 296\text{K}$, $P_{\text{H}_2\text{O}} = 14.3$ TORR

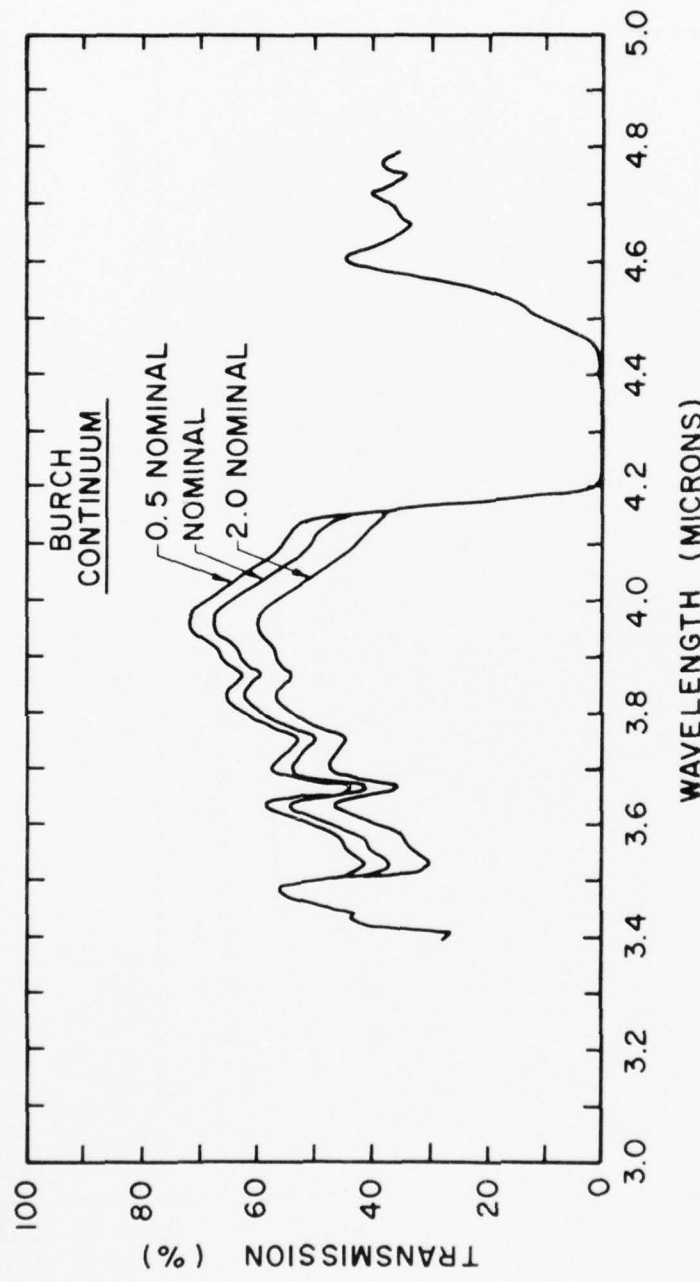


FIGURE 5. CALCULATED SWIR SPECTRAL ATMOSPHERIC TRANSMISSION FOR VARIOUS WATER CONTINUUM MODELS:
TROPICAL MODEL ATMOSPHERE, 8.5 km VISIBILITY, 0.75 km ALTITUDE, 5 km RANGE

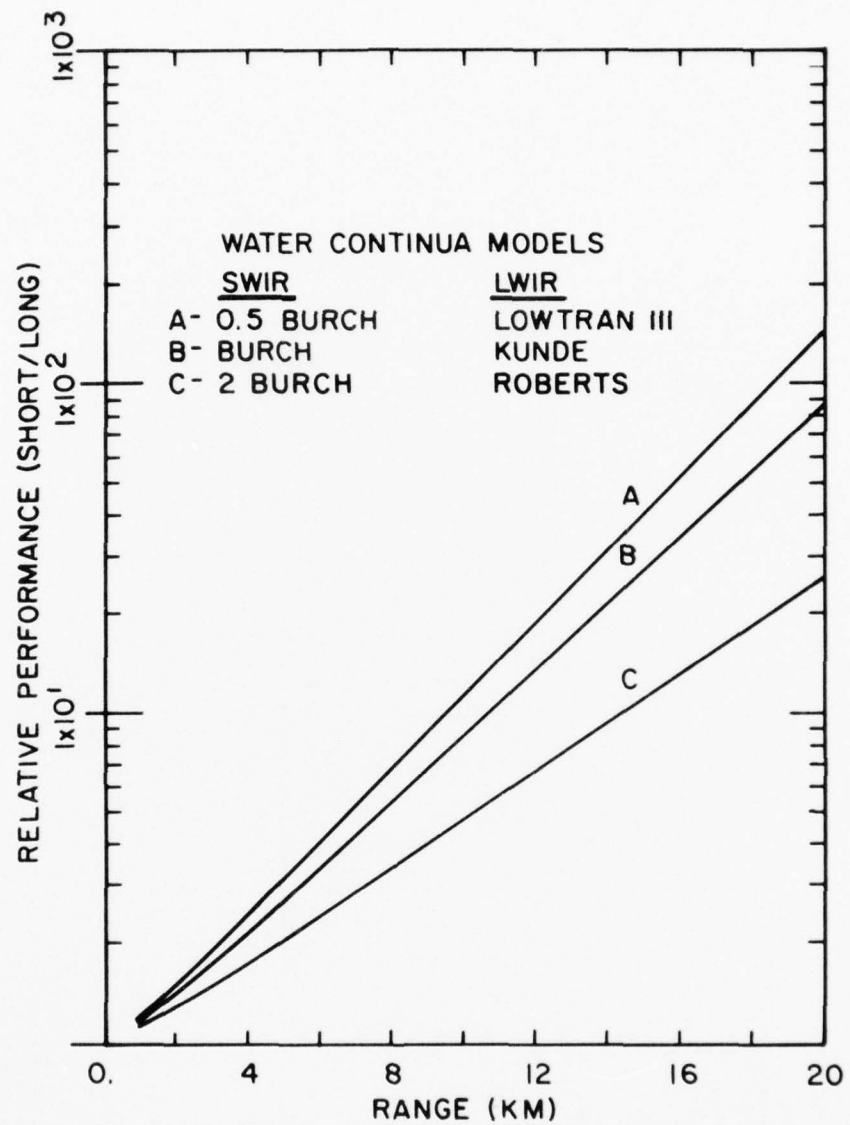


Figure 6. CALCULATED PERFORMANCE OF A 3.4-4.8 μ m FLIR RELATIVE TO AN 8.1-12.2 μ m FLIR FOR VARIOUS WATER CONTINUUM MODEL COMBINATIONS; TROPICAL ATMOSPHERE, OTHER CONDITIONS NOMINAL

(This page intentionally left blank.)

.... This paper is UNCLASSIFIED

ATMOSPHERIC TRANSMISSION MODELING FOR DF LASER PROPAGATION [†]

R. E. Meredith, T. W. Tuer and D. R. Woods
Science Applications, Inc.
15 Research Drive, Ann Arbor, Michigan

ABSTRACT

Algorithms for predicting atmospheric molecular absorption of DF laser radiation have been developed. The algorithms are based on infinite resolution calculations of molecular line absorption and molecular continuum absorption models. Comparisons between long path DF laser transmission data taken in the field and predictions based on the algorithms have been made, and excellent agreement with the wavelength sensitive component of the atmospheric absorption coefficient is found. The high energy laser and broadband applications are discussed, and suggestions for further investigations are made.

INTRODUCTION

Models capable of predicting the atmospheric molecular absorption at laser wavelengths are important for a wide variety of applications. There are many reasons why the development of such models for the broad range of military applications is complex. The primary source of this difficulty is the fact that the laser radiation is quite monochromatic, and the atmospheric molecular absorption depends strongly on wavelength, environmental conditions, and the details of the slant path between laser and receiver. A number of different molecules and absorption mechanisms contribute to extinction of a given laser line, and each absorption contribution obeys its own laws for scaling with altitude, temperature and geographic location [1, 2, 3].

For the last several years we have been engaged in programs directed toward developing algorithms for predicting atmospheric molecular absorption at DF laser frequencies. These programs have included a laboratory measurements of molecular absorption coefficients, development of models for temperature and water vapor dependence of "real world" absorption coefficients and comparisons of predicted molecular line absorption with DF laser measurements

performed in the field by the Optical Radiation Branch of the Naval Research Laboratory. In this paper, we present the results of these activities.

NATURE OF ABSORPTION AT DF WAVELENGTHS

Atmospheric molecular absorption at DF frequencies is a composite of separate contributions from many different molecular species and their isotopes. The atmospheric molecular absorption spectra may be very wavelength sensitive (the so-called line absorption spectra), or it may vary slowly with wavelength (the "continuum" absorption). Molecules which contribute significant line absorption in this wavelength region are: H_2O , HDO , CH_4 , N_2O and to a lesser extent, certain CO_2 lines. Also, continuum absorption from H_2O and N_2 is present. In general, line absorption at a given DF frequency comes from many lines, centered at or near the laser frequency. At sea level, each individual line is expected to have the same (Lorentz) functional frequency dependence near line center, but each line has a unique set of shape parameters. The large number of lines causes the absorption coefficient to have a complex dependence on wavelength. Thus, one might infer that a precise calculation of absorption coefficients for open air laser propagation may not be feasible. However, molecular physics and spectroscopy are very well developed subjects, and consequently one may expect to perform such calculations at some frequencies with a high degree of accuracy if an adequate data base is available, using simple molecular absorption models. The region of DF laser emission ($3.6 - 4.2 \mu m$) appears to be one where the absorption processes are well amenable to such modeling techniques. However, very precise data and proper treatment of continuum and wing absorption is necessary. In the remainder of this section, the nature of lines and continuum absorption will be discussed, and modeling procedures will be outlined.

Molecular Line Absorption

The transmittance $\tau(\nu)$ at a frequency ν near a line absorption center ν_0 is given by

$$\tau(\nu) = \exp [-\alpha_\ell(\nu) L]$$

where α_ℓ is the line absorption coefficient and L is the distance between (laser) source and receiver. At sea level, $\alpha_\ell(\nu)$ has a Lorentz shape:

$$\alpha_\ell(\nu) = \frac{S\gamma}{\pi[(\nu - \nu_0)^2 + \gamma^2]}$$

In the above, S is the absorption line strength, and γ is the pressure broadened half width at half maximum of the absorption coefficient. With the assumption of Lorentz shape, only the parameters S , γ , and ν_0 are required for predicting laser transmission through line absorbers. As will be commented on later, often $\delta\nu = |\nu_L - \nu_0|$, where ν_L is a laser frequency, is a more meaningful parameter for laser transmission.

The line center parameters ν_0 depend on the intramolecular forces of the molecule. They are therefore not variable for normal conditions of pressure and temperature. The S and γ parameters do vary in complex ways for each transition of each molecule, and for different temperature and pressure conditions.

The basic quantity upon which the strength S depends is the Einstein coefficient for induced absorption $B(f \leftarrow i)$.

$$S \propto B(f \leftarrow i)$$

$B(f \leftarrow i)$ is a function of only the molecular species and the initial and final states. It is independent of the temperature, pressure or concentration. Thus $B(f \leftarrow i)$ is the most fundamental quantity normally used to obtain line strengths. The temperature and concentration dependence of the line strength S enter through well understood processes. Thus, once the strength at single temperature and concentration (and thus the Einstein coefficient B) is known, the strength at all temperatures and concentrations can generally be determined with great confidence and accuracy. If T_1 and T_2 are two arbitrary temperatures, then S at T_2 may be obtained from S at T_1 as follows:

$$S(T_2) = S(T_1) \frac{Q_v(T_1) Q_r(T_1)}{Q_v(T_2) Q_r(T_2)} \exp \left| \frac{1.439 E (T_2 - T_1)}{T_1 T_2} \right|$$

where the Q are vibrational and rotational partition functions and E is the energy of the initial level.

The Lorentz width depends in a complicated way on the collision processes between the absorbing molecule and its collision partners [4]. Therefore, γ varies with collision partners (i. e., the

atmospheric gas constituents) and with temperature in a complicated way. It may vary rapidly with rotational state J , and to a lesser extent with the vibrational state, of the colliding molecules. Quantitatively, γ depends on the number of collisions the molecule experiences per unit time. Therefore, γ is the sum of the contributions of the various collision partners. If p_i is the partial pressure of the i^{th} molecular constituent in the atmosphere, then

$$\gamma = \gamma_s p_s + \sum_i \gamma_i p_i$$

where s and i refer to self and foreign collision partners respectively. Collectively,

$$\gamma = \gamma_s p_s + \gamma_f p_f$$

where f refers to foreign broadening. Often, γ_s is equal to γ_f or a few times greater, but in extreme cases, γ_s can be as much as ten times γ_f . Thus, if mixtures are such that $p_f \sim 10p_s$ or $100p_s$, the effects of self broadening in determining γ are usually slight. Therefore, laboratory measurements of line widths are feasible, since gas sample enrichments of about one part absorber to 100 parts broadener can be used.

The effect of temperature on γ depends on the gas mixture through the molecular collision mechanism. Kinetic theory predicts a \sqrt{T} dependence, but more realistic treatments of pressure broadening indicate a stronger effect for many cases. Temperature dependent half width data is not available, however, and in the present work, the \sqrt{T} dependence is assumed.

Continuum Absorption

The H_2O and N_2 continua arise from quite different mechanisms and consequently they have quite different wavelength and pressure dependencies. The H_2O continuum is thought to be the accumulation of far wing line absorption originating from lines in the strong vibration-rotation bands of H_2O located on both the long and short wavelength sides of $3.5 \mu\text{m}$. Since the distant wings vary slowly with wavelength, the H_2O continuum is not expected to have structure which varies rapidly with wavelength. In the distant wings of a Lorentz line, the absorption varies as follows

$$\alpha_{fw} \sim \frac{n_s S \gamma}{(\nu - \nu_0)^2}$$

where n_s is the number density per unit volume of H_2O or other absorber.

Since individual lines have a self and foreign broadened component, H_2O continuum is expected to have contributions from both, in this case. Thus, the H_2O continuum absorption coefficient is expressed as the sum of contributions from collisions with identical and foreign partners. Following Burch [5],

$$\alpha_c(H_2O) = n_s (C_s^0 p_s + C_f^0 p_f)$$

where C_s^0 and C_f^0 are empirical frequency dependent absorption coefficient parameters. In the DF region, Burch has deduced a value of C_s^0 for 296K, based on measurements of pure H_2O vapor maintained at high temperatures. He also suggested a value of $C_f^0/C_s^0 = 0.12$, in lieu of measurements of either C_s^0 or C_f^0 at the lower temperature. It is significant that the H_2O continuum has a mixed dependence on partial pressure of H_2O and foreign gases. Since n_s is proportional to p_s for ideal gases, the self broadening varies quadratically and the foreign broadening varies linearly with p_s .

In his measurements, Burch investigated the H_2O self broadened continuum at several temperatures. He found the data followed the empirical form

$$C_s^0 = c \exp(m/T).$$

We have used this form also, however we have used a slightly different fit of his data for m and c .

The N_2 continuum arises from the electric dipole forbidden fundamental N_2 vibration-rotation band centered at 2400 cm^{-1} . It absorbs via a transition moment induced by collisions with identical or foreign molecules. Since the N_2 absorbs only in the presence of a collision partner, the "rotational line widths" are expected to be very broad -- broader in fact than the approximately 4 cm^{-1} spacings between the transitions. Consequently, the N_2 self broadened continuum,

like the H_2O , is expected to show no spectral structure. However, it takes the shape of the R branch envelope of the forbidden vibration-rotation band.

The N_2 continuum absorption coefficient is also written as the sum of contributions from collisions with other N_2 molecules and with foreign species:

$$\alpha_c(\text{N}_2) = n_s (C_s^0 p_s + C_f^0 p_f)$$

where n_s is the number of N_2 molecules. Burch's measurements [5] show that $\text{N}_2\text{-O}_2$ collisions induce absorption almost as effectively as do $\text{N}_2\text{-N}_2$ collisions. Therefore, if O_2 is taken as the only foreign collision partner, $C_f^0 \approx C_s^0$. To this approximation,

$$\alpha_c(\text{N}_2) \approx C_s^0 n_s (p_s + p_f) \approx p_{\text{air}}^2$$

Therefore, since the $\text{N}_2\text{-O}_2$ mixing ratio is essentially constant the N_2 continuum varies approximately as the square of the total air pressure.

It is of interest to compare the pressure dependencies of the H_2O and N_2 continuum absorption coefficients in the DF region. The atmospheric N_2 continuum varies as the square of the partial pressure of N_2 , if the mixing ratio of N_2 and O_2 is constant,

$$\alpha_c(\text{N}_2) \approx C_s^0 n_s p_s \left(1 + \frac{p_f}{p_s}\right)$$

The H_2O continuum, on the other hand, varies more nearly linearly with H_2O partial pressure:

$$\alpha_c(\text{H}_2\text{O}) \approx C_f^0 n_s p_f \left(1 + 8.33 \frac{p_s}{p_f}\right)$$

where C_s^0 has been replaced by 8.33 C_f^0 , and where $n_s \propto p_s$. We have written $\alpha_c(\text{H}_2\text{O})$ in this form to emphasize the importance of C_f^0 relative to C_s^0 .

EXPERIMENTAL LINE PROFILE DATA

The accuracy of the absorption line strength, width, and center frequency information in the AFGL data tape [6] for lines important to DF laser transmission was investigated by performing high resolution spectroscopic survey measurements in the $3.6 - 4.0 \mu\text{m}$ wavelength region. The data were obtained with a three meter focal length, double passed, Ebert spectrometer at The University of Michigan Physics Department, having a resolution of 0.04 cm^{-1} . A 4.9888 ± 0.002 meter White cell was used to obtain gas sample path lengths of 20 to 400 meters. N_2O , CH_4 and HDO spectra were obtained.

A pulsed DF laser was constructed to allow measurements of the positions of atmospheric absorption lines relative to the DF laser lines. The DF laser line positions were simultaneously measured and recorded with the absorption line spectra on a two pen chart recorder. Further experimental details are given in reference 2.

Survey spectra confirmed that N_2O line parameters in the AFGL data tape were extremely precise. On the other hand, CH_4 data disagreed with values in the 1975 data tape by as much as an order of magnitude at some frequencies. Comparisons of new HDO data with the 1975 AFGL data tape indicated discrepancies ranging from ten or twenty percent at certain frequencies to factors of two to five in extreme cases. HDO is a primary absorber at DF frequencies at sea level; consequently precise measurements of HDO strength, width, and relative frequency $\delta\nu$ were made for HDO lines which impact DF propagation. Additional CH_4 data were not obtained since CH_4 is not a major absorber of DF radiation at sea level. An improved 1976 version of the data tape has been updated to reflect some of these measurements and the work of others. Quick comparisons indicate that the tape is substantially improved although an extensive detailed comparison has not yet been performed.

MODELING PROCEDURE

Molecular absorption coefficients at twenty-seven DF laser frequencies have been calculated from expressions given above for molecular line and continuum absorption. For a given frequency ν_L at which the i absorption lines contribute,

$$\alpha(\nu_L) = \sum_i [\alpha_t(\nu_L)]_i + \alpha_c(\text{H}_2\text{O}) + \alpha_c(\text{N}_2)$$

where the continuum absorption coefficients α_c are determined at the laser frequency ν_L .

A simple analytic function of atmospheric temperature and water vapor concentration has been fit to calculate absorption coefficients for twenty-seven DF laser lines. A least squares fitting code was used to determine the coefficients a_0, a_1, \dots, a_5 in the polynomial:

$$\alpha(\nu_L) = a_0 + a_1 T + a_2 p + a_3 Tp + a_4 p^2 + a_5 Tp^2$$

where $\alpha(\nu_L)$ is the molecular absorption coefficient (km^{-1}), T and p are the atmospheric air temperature ($^{\circ}\text{F}$) and water vapor partial pressure (torr), respectively.

SAI's standard line-by-line computer code was used to calculate the basis molecular absorption coefficients. These calculations are based on Heath and Rao's DF laser wavelengths, and an SAI modified version of the 1975 AFGL line parameter compilation. The AFGL compilation was modified to include recent SAI line parameter measurements discussed above for absorption lines near the $P_1(7)$, $P_1(8)$, $P_1(9)$, $P_2(7)$ and $P_2(9)$ DF laser lines. The temperature dependence of the continua absorption and the vibrational partition function were included. The water and nitrogen continua based on the Burch data [6] are included in the code.

RESULTS AND COMPARISONS

A representative plot of the temperature and humidity dependence of atmospheric molecular absorption coefficients is given in Figure 1 for the $P(10)$ line of the $v = 2 \rightarrow 1$ band of DF. This line has been chosen because it illustrates differences that occur because of the detailed features of the overlapped absorption spectrum. Absorption at $P(10)$ is dominated by N_2O absorption at low to moderate humidities, and it extrapolates essentially to a residual N_2O absorption coefficient at zero water vapor content. Lines dominated by water vapor absorption extrapolate essentially to zero absorption coefficient and in some cases with a much more sensitive dependence on temperature. Values calculated for the canonical Midlatitude Summer (MLS) model atmosphere are given in Table I.

The algorithms developed here have been used to provide calculations for comparison with long path ($\sim 5 \text{ km}$) DF laser field transmission measurements performed by the Naval Research Laboratory [7].

AD-A037 812

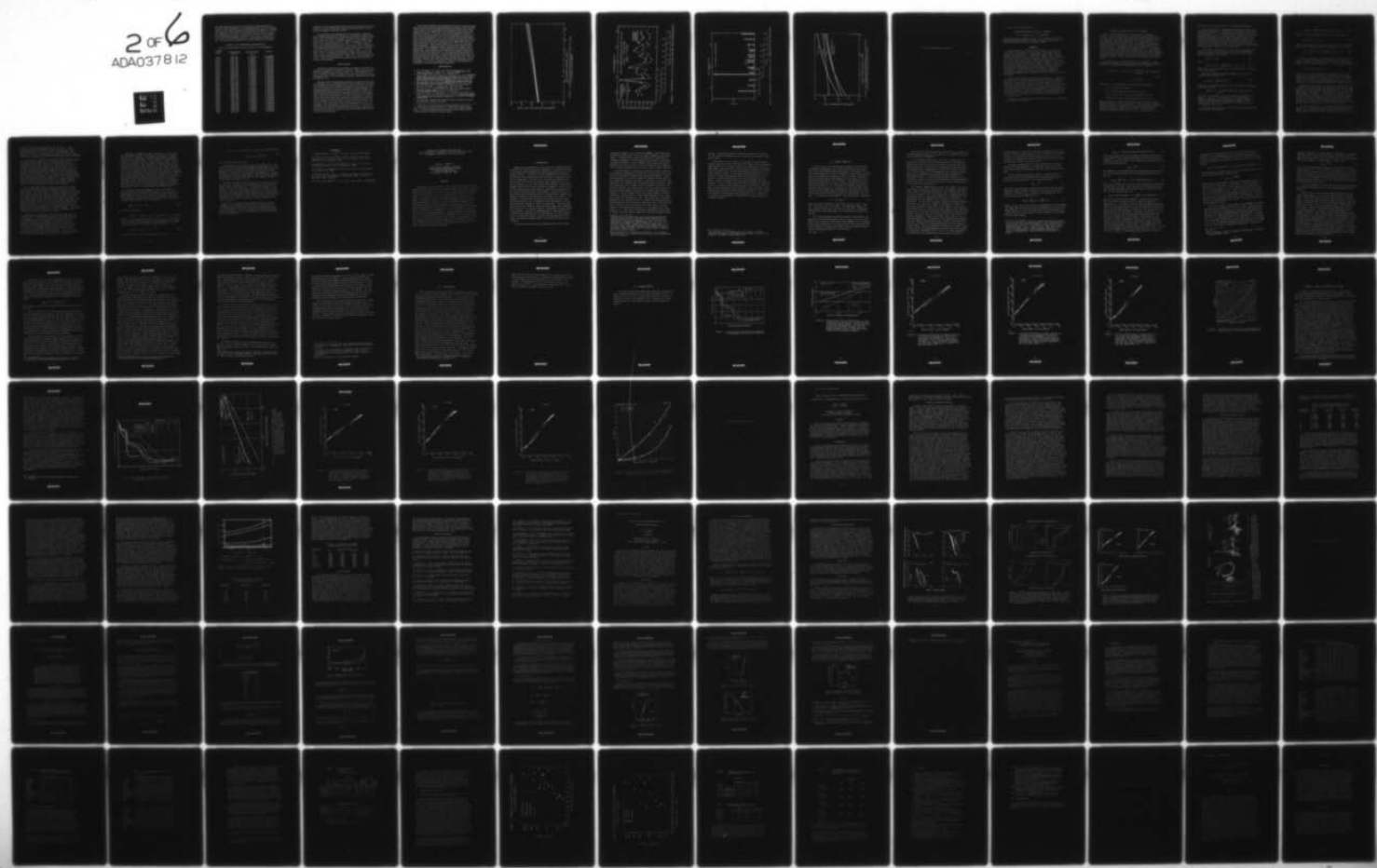
OFFICE OF THE DIRECTOR OF DEFENSE RESEARCH AND ENGINE--ETC F/G 20/14
PROCEEDINGS OF THE OPTICAL-SUBMILLIMETER ATMOSPHERIC PROPAGATIO--ETC(U)
DEC 76

UNCLASSIFIED

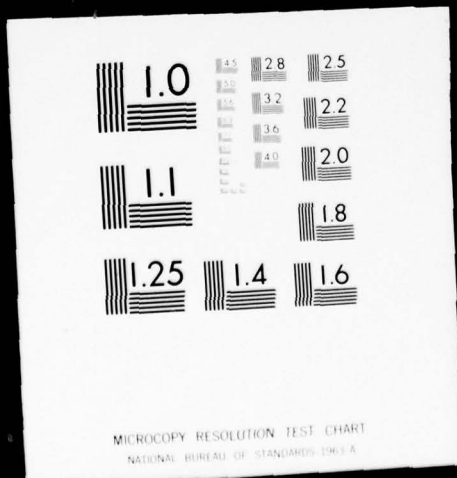
NL

2 of 6
ADA037812

EEC



2 OF 6
ADA037812



The NRL data were necessarily obtained for conditions unlike the canonical MLS atmosphere, so the algorithms were used to normalize the data to the model atmosphere for purposes of comparison. Absorption coefficient calculations are compared with NRL data in Figure 2. The calculations are shown to illustrate the good agreement obtained for the frequency dependent component of α_L using our recent data. If the early calculations were shown, the improvement would be striking. The reliability of absorption coefficient modeling for sea level

TABLE I. DF ABSORPTION COEFFICIENTS

Summer (MLS) Model at Sea Level (km^{-1}) for the Midlatitude

LASER LINES	FREQUENCY (cm^{-1})	WAVELENGTH (μm)	TOTAL
P ₃ (12)	2445. 354	4. 089387	0. 1016000
P ₃ (11)	2471. 243	4. 046547	0. 0788700
P ₃ (10)	2496. 720	4. 005255	0. 0498700
P ₂ (13)	2500. 427	3. 999317	0. 0468300
P ₃ (9)	2521. 769	3. 965470	0. 0356100
P ₂ (12)	2527. 389	3. 956652	0. 0351600
P ₃ (8)	2546. 373	3. 927154	0. 0533000
P ₂ (11)	2553. 951	3. 915502	0. 0364500
P ₃ (7)	2570. 522	3. 890260	0. 0674900
P ₂ (10)	2580. 095	3. 875826	0. 0717200
P ₃ (6)	2594. 197	3. 854757	0. 0361900
P ₂ (9)	2605. 806	3. 837584	0. 0529100
P ₃ (5)	2617. 386	3. 820606	0. 0242500
P ₂ (8)	2631. 066	3. 800741	0. 0314500
P ₁ (11)	2638. 390	3. 790190	0. 3698000
P ₃ (4)	2640. 075	3. 787771	0. 0578500
P ₂ (7)	2655. 863	3. 765254	0. 1004000
P ₁ (10)	2665. 218	3. 752038	0. 0454300
P ₂ (6)	2680. 178	3. 731095	0. 0653800
P ₁ (9)	2691. 608	3. 715251	0. 0453300
P ₂ (5)	2703. 998	3. 698228	0. 0307600
P ₁ (8)	2717. 538	3. 679801	0. 1458000
P ₂ (4)	2727. 308	3. 666619	0. 0503700
P ₁ (7)	2742. 997	3. 645647	0. 0343700
P ₂ (3)	2750. 093	3. 636241	0. 0508100
P ₁ (6)	2767. 968	3. 612759	0. 0858900
P ₁ (5)	2792. 434	3. 581105	0. 0687400
P ₁ (4)	2816. 380	3. 550657	0. 0841900
P ₁ (3)	2839. 791	3. 521386	0. 0897000

conditions is good enough that field data such as that shown may now be expected to yield valuable information on aerosol extinction, and on precise atmospheric molecular content.

The algorithms described here have been applied to calculating power weighted absorption coefficients for the Baseline Demonstration Laser (BDL) and for the Navy-ARPA Chemical Laser (NACL). The power spectrum of NACL is shifted primarily to wavelengths longer than $3.8 \mu\text{m}$, as shown in Figure 3. NACL propagation is severely impacted by HDO absorption at the $\text{P}(11) \nu = 1 \rightarrow 0$ line. Figure 4 shows four calculated power spectra. The NACL and BDL absorption is calculated from representative measured power spectra shown in which $\sim 35\%$ of the power is extracted from the $\text{P}(10) \nu = 2 \rightarrow 1$ line, which is known to be absorbed strongly by N_2O . The line selected NACL curve is obtained by shifting the measured NACL power spectrum to shorter wavelengths [$\text{P}(11) \rightarrow \text{P}(10)$, etc.] to avoid $\text{P}_2(10)$ and $\text{P}_1(11)$. This shows the potential propagation pay-off if such a line selection were possible.

CONCLUSIONS

Propagation algorithms for predicting atmospheric molecular absorption as a function of temperature and water vapor partial pressure have been developed for DF laser frequencies. The algorithms are based on infinite resolution calculations of absorption caused by molecular spectral lines, and on modeling continuum components using codes developed by SAI.

The algorithms developed show excellent agreement with the spectral dependence observed in long path DF laser transmission measurements performed in the field and with laboratory DF laser transmission measurements performed on simulated atmospheric paths. This is highly significant since early predictions based on HI-TRAN type modeling showed poor agreement, in general, thereby raising some doubt that such calculations are sufficiently precise for laser applications. It has been shown that for DF laser transmission, early disagreements with the spectrally sensitive line absorption components can be traced to inaccuracies in the DF line centers themselves and to the inadequacy of the data base available for the early AFGL compilations. Very importantly, these early disagreements are not attributable to the HI-TRAN/data tape approach itself. It is noted that the original motivations for developing the AFGL data compilation required much less precise values for the weak absorption lines than do current laser applications.

The success obtained in developing field verified DF transmission algorithms based on established principles of molecular theory and laboratory spectroscopy gives hope that propagation at all infrared laser frequencies can be modeled in the same straightforward manner with sufficient precision. At present, only sparse propagation measurements have been performed at CO laser frequencies, and these do not agree well with predictions. One can now expect that such discrepancies can be eliminated by using a more precise line parameter and continuum data base and proper treatment of line shapes and/or the continuum absorption. One may also expect that at DF, CO, and other laser frequencies, scaling algorithms also can be developed for high altitude and slant atmospheric paths so important for many military applications. The reliability of the algorithms gives hope that transmission measurements performed in the field can supply valuable information on aerosol extinction. In wavelength bands where total molecular absorption modeling is reliable, fixed frequency and high resolution spectral data can be used to extract aerosol extinction. This information, together with good meteorological characterization of the atmosphere, may lead to a quantitative, predictive understanding of atmospheric aerosol and particulate extinction.

REFERENCES

1. R. E. Meredith, T. W. Tuer, D. R. Woods, Investigation of DF Laser Propagation, ECOM-74-4, December 1974.
2. D. R. Woods, R. E. Meredith, F. G. Smith and T. W. Tuer, High Resolution Spectral Survey of Molecular Absorption in the DF Laser Region: Measurements and Calculations, RADC-TR-75-180, 1975.
3. D. R. Woods and R. E. Meredith, Application of High Resolution Spectroscopy to DF Laser Propagation, RADC-TR-76-71, 1976.
4. W. S. Benedict and L. D. Kaplan, "Calculation of Line Widths in H₂O-N₂ Collisions," J. Chem. Phys., 30, 388 (1959).
5. D. E. Burch, D. A. Gryvnak and J. D. Pembrook, Gases: Water, Nitrogen, Nitrous Oxide, AFCRL-71-0124, 1971.
6. R. A. McClatchey, W. S. Benedict, S. A. Clough, D. E. Burch, R. F. Calfee, K. Fox, L. S. Rothman and J. S. Garing, AFCRL Atmospheric Absorption Line Parameters Compilation, AFCRL-TR-73-0096, January 1973.
7. J. A. Dowling, Private Communication, Optical Radiation Branch, Naval Research Laboratory, 1975.

[†] This work was sponsored by the Naval Research Laboratory, The Atmospheric Sciences Laboratory, White Sands Missile Range, the U. S. Army High Energy Laser Systems Project Office and the Defense Advanced Research Projects Agency.

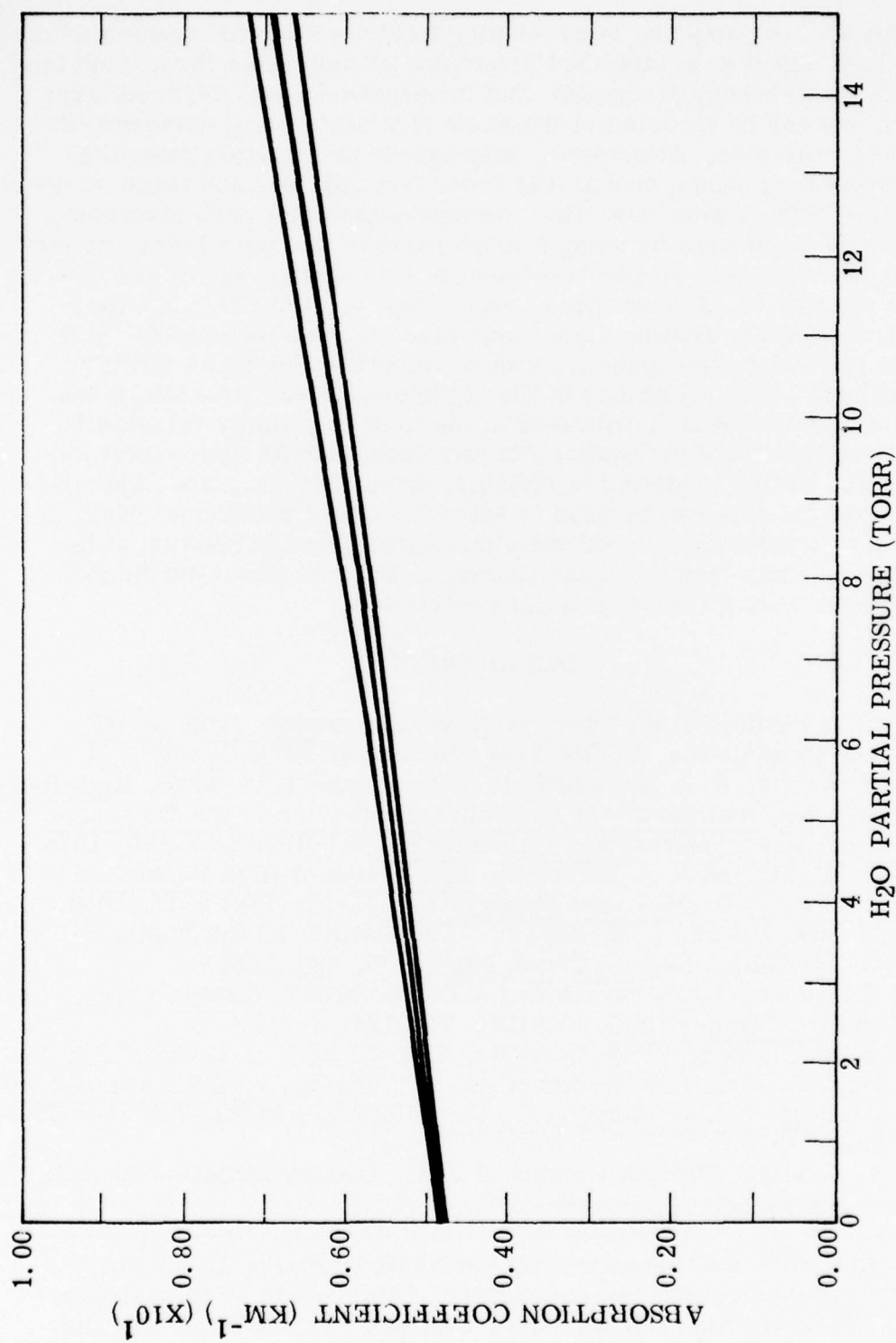


FIGURE 1. ABSORPTION COEFFICIENTS FOR THE $\text{P}_2(10)$ DF LINE
AT 2580.102 WAVENUMBERS

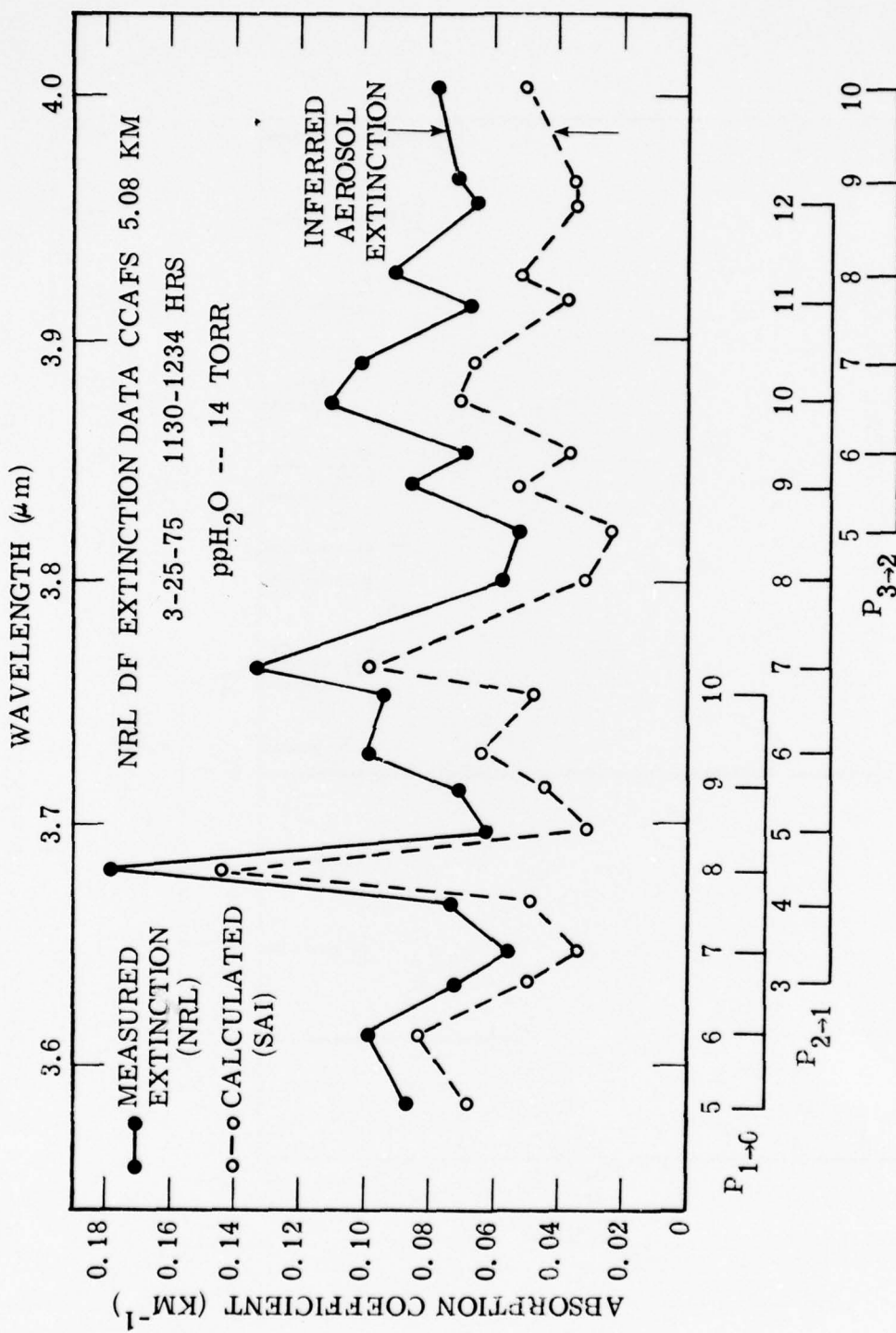


FIGURE 2. COMPARISON OF SAI CALCULATIONS WITH NRL FIELD MEASUREMENTS

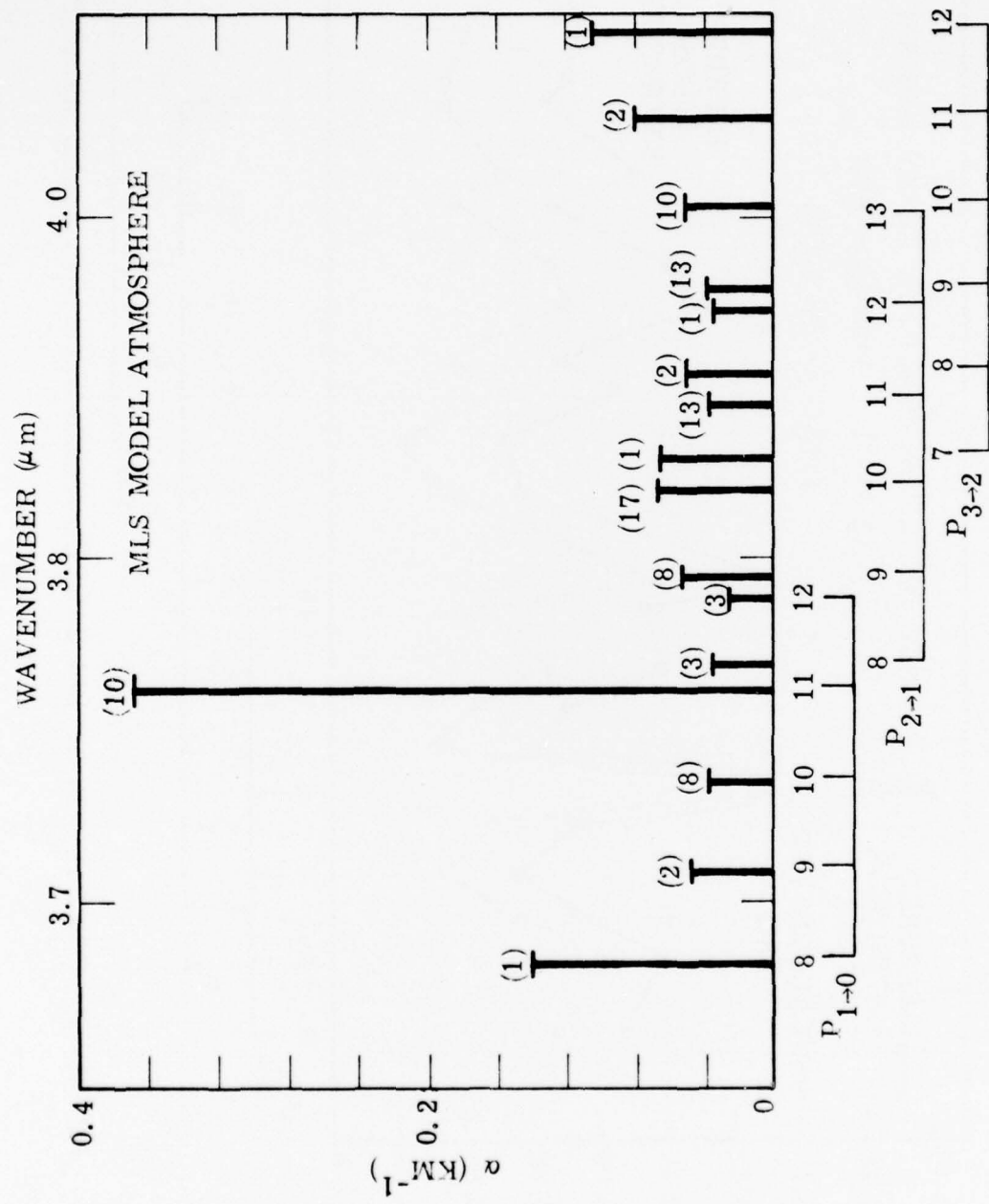


FIGURE 3. ABSORPTION COEFFICIENTS FOR NACL POWER SPECTRUM (MEASURED)

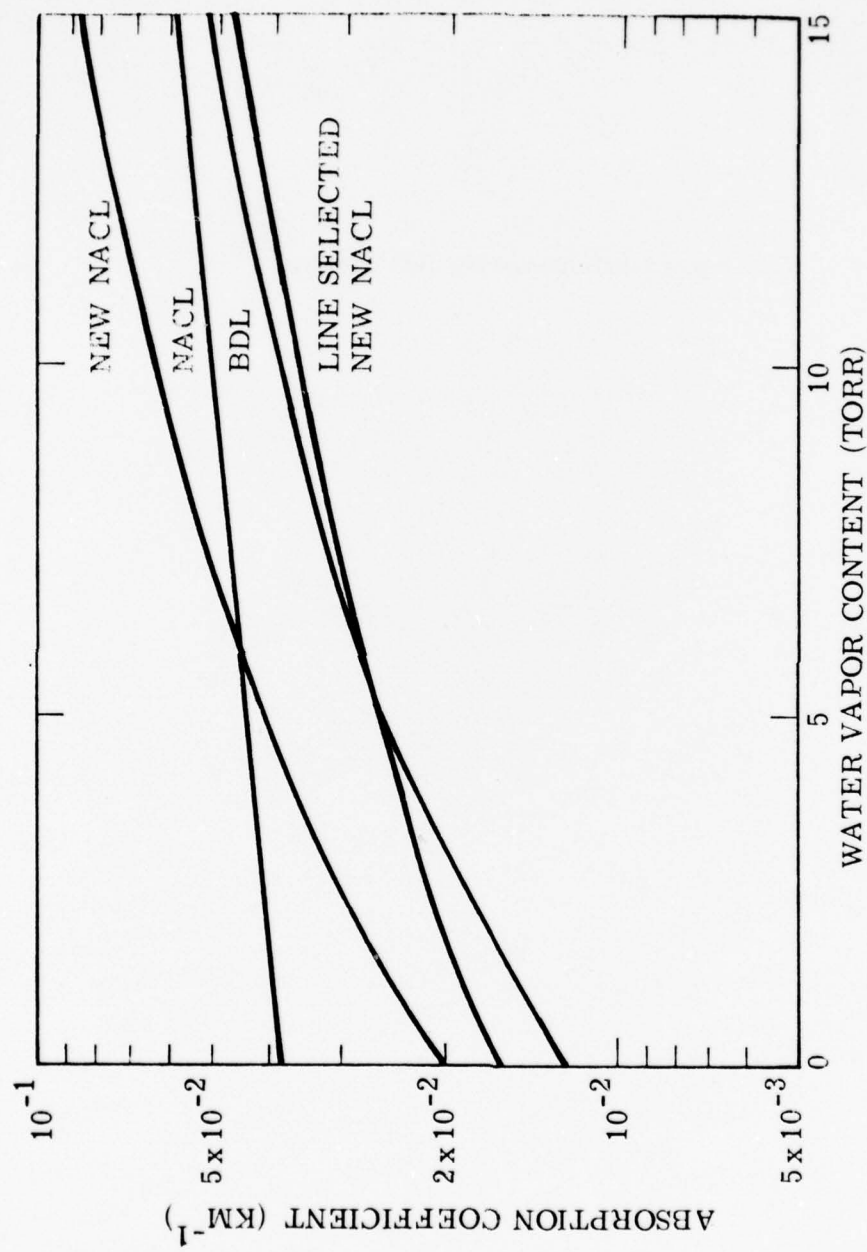


FIGURE 4. DF ABSORPTION COEFFICIENTS AS A FUNCTION OF
WATER VAPOR CONTENT FOR VARIOUS LASERS

(This page intentionally left blank.)

....This paper is UNCLASSIFIED

PROPAGATION MODELING FOR E-O SENSORS

B. W. FOWLER and D. R. PETERSON

Advanced Systems Concepts Office, US Army Missile Research,
Development and Engineering Laboratory, US Army Missile
Command, Redstone Arsenal, Alabama 35809.

ABSTRACT

Electro-Optical (E-O) sensor performance in limited visibility environments such as fog, haze, smoke and extinguishing gasses may be simulated if the media and the sensors are modeled in a compatible manner. This compatibility requisite dictates that both the intensity variations (for such things as missile seekers) and the contrast variations (for such things as TVs and FLIRs) in the field of view of the E-O sensor be accurately modeled. For aerosol and gas environments where the scattering contributions to the extinction process are appreciable, the Beer-Lambert Law does not adequately model the intensity/contrast variations. For sufficiently low density, independent scattering systems, the propagation modeling may be approached through either the particle or the wave formalisms of light.

The multiple scattering particle formalism is commonly developed from Chandrasekhar's Radiative Transfer Equation.¹ This equation has been traditionally solved for uniform boundary illumination, symmetric systems which do not correspond to those viewed by E-O sensors. We discuss techniques for solving the more general four dimensional radiative transfer equation for non-uniform boundary illumination, non-symmetric systems. These techniques, being both analytical and numerical in nature, are amenable to hybridization. We describe the implementation of a hybridized technique into a computer model.

Finally, we present some preliminary results, and discuss our planned future work.

PROPAGATION MODELING FOR E-O SENSORS

With the widespread use of E-O sensors in weapons systems, and the high cost of prototype construction and testing, it is of increasing importance that the performance of these sensors under conditions of limited visibility be predictable. This is especially true with regard to extinguishing media such as haze, fog, smoke, and obscurant gasses which may be naturally or artificially present on the battlefield, and which cannot be simulated in the laboratory easily. To perform this prediction, it is necessary that the rigor of the physical analysis of the light-media interaction provide sufficient information for sensor analysis. In most cases, E-O sensors view the world in terms of angular intensity and/or angular contrast distributions. Thus, the physical analysis must be sufficient to provide this information.

A theory exists for describing the transport of light particles through an extinguishing media, Radiative Transfer. The basic five-dimensional equation of this theory is

$$\mathbf{k} \cdot \nabla I(\mathbf{r}, \mathbf{k}) = -\alpha(\mathbf{r}) I(\mathbf{r}, \mathbf{k}) + \frac{\alpha(\mathbf{r}) \omega(\mathbf{r})}{4\pi} \int d^2 \mathbf{k}' p(\mathbf{r}, \mathbf{k}, \mathbf{k}') x I(\mathbf{r}, \mathbf{k}'), \quad (1)$$

where \mathbf{k}, \mathbf{k}' are propagation direction (unit) vectors,

\mathbf{r} is the position vector,

$\alpha(\mathbf{r})$ is the extinction coefficient at \mathbf{r} ,

$\omega(\mathbf{r})$ is the single scattering albedo at \mathbf{r} , and

$p(\mathbf{r}, \mathbf{k}, \mathbf{k}')$ is the scattering phase function at \mathbf{r} .

The $\mathbf{k} \cdot \nabla$ term is a directional derivative, the first Right-Hand-Side term is due to extinction along \mathbf{k} , and the second RHS term is due to scatter from all \mathbf{k}' (including \mathbf{k}) directions into direction \mathbf{k} . Traditionally, Equation (1) has been solved for uniform media ($\alpha, \omega, p \neq f(\mathbf{r})$) with uniform boundary conditions that reduce it to two dimensions, the

description of planar stellar or planetary atmospheres.

With the E-0 sensor problem, the formalism of the two dimensional solution is inadequate. While the restriction of uniform media is not excessively strong for many extinguishing media, it is for many smokes. Further, the uniform boundary conditions are definitely not applicable. This may be demonstrated by the simple example of the 8-14 μ intensity associated with a vehicle moving through a fog. In this case, even if the fog is entirely between the vehicle and the sensor, both sky and terrain are uniform in intensity, the vehicle itself causes a spacial nonuniformity in the boundary conditions at any instant.

To develop the solution for this case,² we expand the intensity I as a perturbation series in the albedo and separate Equation (1) in orders of scattering to yield a set of equations of the form,

$$\hat{k} \cdot \hat{\nabla} I_0 = -\alpha I_0, \quad (2)$$

and

$$\hat{k} \cdot \hat{\nabla} I_n = -\alpha I_n + \frac{\alpha}{4\pi} \int d^2 k' p I_{n-1}, \quad n > 0, \quad (3)$$

where the r , k , k' dependences are implied for the sake of notational brevity.

The phase function may be expanded in a series of Legendre polynomials (P_l),

$$p(\hat{k}, \hat{k}') = \sum_{l=0}^L a_l P_l(\hat{k} \cdot \hat{k}') \quad (4)$$

which may in turn be expanded using the spherical harmonic addition theorem,

$$p(\hat{k}, \hat{k}') = \sum_{l=0}^L \sum_{m=0}^l a_{lm} P_l^m(\mu) P_l^m(\mu') \cos(m\phi - m\phi') \quad (5)$$

where P_l^m is the m^{th} associated Legendre polynomial of order l , and μ, μ' are cosine of θ, θ' , respectively. Equation (4) differs from the phase function expansion used in planar atmosphere Radiative Transfer in the retention of the ϕ, ϕ' terms because of the asymmetry of the boundary conditions.

A source term similar to that used in planar Radiative Transfer may be defined as

$$J_n(r, k) = \frac{1}{4\pi} \int d^2 k' p(r, k, k') I_n(r, k'). \quad (6)$$

Equation (6) allows Equations (3) to be rewritten as

$$k \cdot \nabla I_n = -\alpha I_n + \alpha J_{n-1}, \quad (7)$$

and the combination of Equations (5) and (6) in principle parametrizes the source term to integrals of the form,

$$\int_{-1}^1 d\mu' \int_0^{2\pi} d\phi' P_1^m(\mu') \begin{pmatrix} \cos \\ \sin \end{pmatrix}(\phi') I_n(r, \mu', \phi'). \quad (8)$$

Further development of Equations (2) and (7) from this point is somewhat dependent on whether an analytic or numeric method will predominate. To date, we have been unable to find analytic expressions for the general integral

$$\int d\mu/\mu P_1^m(\mu) \exp(-\tau/\mu), \quad (9)$$

so the use of numeric methods is invoked at this point. While this selection develops a formalism that is more mathematically crude, and exceedingly costly of computer memory, the formalism is conceptually simple, and fairly responsive to varying boundary conditions as well as mirroring the finite element operation of imaging devices.

Because of the excessive computer memory required by a general five dimensional development (minimum 2M bytes) and the limitations placed by many operating systems (200-300K bytes), the formalism developed here is for the four dimensional, two spacial - two angular, case; the method of development, however is valid for the general case as well. While this two spacial dimension selection appears to impose a strong symmetry restriction on the boundary conditions (and thus the scenarios of interest), the restriction is really much weaker because of the integral approximation formula used in the ϕ' integration.

The extinction media is represented by an NxM array of points. For convention, the N side of the array will lie along the z direction, which is defined by the line of sight between the sensor and the object; the M side will lie

along the x direction perpendicular to the z. The y direction that is dropped from this derivation, would be perpendicular to x and z, and if implemented, add another dimension of points to the overall array. This addition is part of the reason for limiting the derivation, conserving computer memory while demonstrating the formalism.

If the first, second, and third nearest neighbor points for any interior point are considered, eight directions are determined. Selection of a Lobatto five point integration quadrature for the μ' integration⁵ fixes the distance ratio of the array to be $\Delta x = 1.155 \Delta z$, and a Simpson three point formula without derivative term for the ϕ' integration (envoking equal functional values at the end points) reduces the strength of the y direction symmetry restriction. Use of a three point Lobatto would give some further reduction and increase the accuracy one more degree of polynomial. Extension to the simplest three spacial dimension case (y direction included) could be simply achieved by use of either a five point Simpson, again without derivative term and equal functional end points, or two consecutive three point Lobattos.

This quadrature scheme for the source term is thus⁶ similar to the many flux calculations done previously, and reduces the calculation of Equation (8) to a sum of eight terms. At this point it becomes necessary to consider the relative merits of casting a point intensity formalism or a point source term formalism on the array. For this two spacial dimension case, the source term formalism is more efficient of computer memory for phase functions with less than eight terms. For the three spacial dimension case, the same is true for up to at least fourteen terms. Because the initial interest of this project was proof of principle and conservation of computer memory, the test phase functions selected with isotropic and Rayleigh, having one and four terms respectively. This development will therefore follow the source term route.

Selection of the source term formalism requires the calculation of the n^{th} order sources at the $N \times M$ points in the array. In the Rayleigh case, this means the use of $16 \times N \times M$ bytes for each order of scattering. It is obvious that J_0 may be developed directly from the boundary conditions and Equation (2) whose solution is the familiar Beer-Lambert Law. Higher order J 's appear to present more computational difficulty unless we introduce an integration scheme based on the interlace scan method used in TV video production. In this case we make use of the fact that only eight angular directions are needed to characterize each point in the array.

Therefore, rather than take each point in the array and calculate the n^{th} intensity at that point in each of the eight directions to compute the source integrals, the array is scanned by direction and direction defined line to cross all points. As an example, consider the direction along the line of sight to the sensor. At the first point in the array along the M side on the N side next to the object, the intensity is calculated from the previous order of scattering source term. This intensity is used to contribute one of the eight directional terms to the source term at that point for that order of scattering. This intensity is then used to calculate the intensity at the next point along the N line, but same M line with the previous order source at the new point. This intensity also contributes one of eight terms to the new source integrals. This proceeds until the N line is completed, and the next M line is taken and the process is repeated. Once all M and N lines are treated for this direction, the next direction is treated, with appropriate boundary adjustments, until all directions have been treated.

It remains now to demonstrate the calculation of the n^{th} intensity from the $n-1^{\text{th}}$ source. For this, we consider Equation (7) since Equation (2) is solved by the Beer-Lambert law with the boundary conditions. It has been noted that the $k \cdot \nabla$ term is a directional derivative. The selection of the eight directions used at each point allows Equation (7) to be rewritten as

$$\frac{d}{dl} I_n = -\alpha I_n + \alpha J_{n-1} , \quad (10)$$

which has solution,

$$I_n(l) = f \exp\{-\alpha(l-l_0)\} + J_{n-1}(1-\exp\{-\alpha(l-l_0)\}) \quad (11)$$

where $f = I_n(l_0)$, and the direction for J_{n-1} is specified. If the source about any point, in any direction is taken to be constant, then using the previous example, the n^{th} intensity at the first point in the line is

$$I(f.p.) = J(f.p.) (1-e^{-\alpha\Delta/2}) \quad (12)$$

and the intensity at the second point in line is

$$\begin{aligned}
 I(s.p.) = & I(f.p.)e^{-\alpha\Delta z} + J(f.p.)(1-e^{-\alpha\Delta z/2})e^{-\alpha\Delta z/2} \\
 & + J(s.p.)(1-e^{-\alpha\Delta z/2})
 \end{aligned} \tag{13}$$

and similarly down the line.

This completes the development of the formalism. The two dimensional case has been coded for constant α, ω , and p for a 51×31 array on the MICO M CDC 6600 macro computer. Results for the uniform illumination cases that may be compared with previous planar work have agreed to within the errors implicit in the numeric approximations. Results for tank and airplane type objects against the appropriate backgrounds are being analyzed now, but appear to agree within the experimental error.

Because of memory restrictions on this machine, there are no plans at this time to extend the existing code to either three dimensions or to non-uniform media until a larger machine is available. It has been brought to our attention that with the recent advances in virtual memory systems, there are now several 1B byte 16 bit word minis on the market that would handle the full five dimensional formalism. Additionally, one manufacturer of such machines has shown such interest in the stressing nature of this formalism as to offer a quadruple precision compiler to insure accuracy.

While it is evident that hardware exists to fully implement this formalism, there is still a problem of validation due to the lack of contrast degradation data in the mid ($3-5\mu$) and far ($8-14\mu$) IR for even naturally occurring media. It is not therefore stressing that the five dimensional case be treated until further validation data is available.

FOOTNOTES

1. Chandrasekhar, S., *Bull. Am. Math. Soc.*, 53, p 641(1947).
2. Fowler, B. W., *Proceedings of the Topical Meeting on Atmospheric Aerosols, Their Optical Properties and Effects*, NASA CP series, December 1976.
3. Busbridge, I. W., *The Mathematics of Radiative Transfer*, Cambridge University Press, Cambridge, 1960.
4. Arfken, G., *Mathematical Methods For Physicists*, Academic Press, New York, 1970.
5. Abramowitz, M., and I. A. Stegun, *Handbook of Mathematical Functions*, National Bureau of Standards, 1964, and Dover, New York, 1965. (edited)
6. Larkin, and Churchill, *J. Am. Inst. Chem. Engrs.*, 5, 467(1959).

ATMOSPHERIC TRANSMISSION MODELING:
PROPOSED AEROSOL METHODOLOGY WITH APPLICATION TO THE
GRAFENWÖHR ATMOSPHERIC OPTICS DATA BASE

Robert E. Roberts

Institute for Defense Analyses
Science and Technology Division
400 Army Navy Drive
Arlington, Virginia 22202

ABSTRACT

Using Mie calculations for a wide variety of measured and assumed particle size distributions we have established a strong relationship between the total volume content of the particulate along the transmission path and the aerosol extinction coefficient. We have also used field measurements, such as those taken at Grafenwöhr, FGR, to further establish the validity of this relationship. Both theory and experiment suggest that a phenomenological scaling of photopic transmission (related to normal meteorological visibility) to the IR windows is possible which furthermore is independent of the structure or shape of the particle size distribution. A second important implication is that a simple possibly remote measurement of a quantity related to the volume or mass of the aerosol could provide a direct measure of the IR transmission (an IR visibility meter). Such a routine meteorological measurement would clearly be of use to sensor performance modeling.

UNCLASSIFIED

I. INTRODUCTION

Making valid predictions of the effects of changing weather conditions on sensor performance remains an outstanding problem in the design and development of improved electro-optical (E/O) imaging systems. In order to better understand the weather-performance relationship there are two kinds of questions which must be addressed. For the first case, one is primarily concerned with the statistical analyses that eventually leads to the procurement of one system rather than another. A pertinent example which falls in this category is whether a FLIR or active TV will operate most effectively in a particular scenario such as a Central European winter environment. The second class of questions, which represents more of a deterministic approach to sensor performance, influences the deployment of a system. For example, if the weather conditions at a given time and place are either known or can be predicted with confidence, one must determine which system or option is preferable. Another apparently subtle yet important question along these lines addresses the selection of an optimal spectral band within a single atmospheric window. The key to answering any of these questions in a rational way depends upon the availability of a valid atmospheric transmission model to provide the quantitative link between our extensive meteorological data base and actual performance.

By far the most practical and widely used of the current

UNCLASSIFIED

UNCLASSIFIED

atmospheric models is the so-called LOWTRAN 3 code¹ developed by Selby and McClatchey of the Air Force Geophysics Laboratory (AFGL). Although this routine is adequate for defining the broadband atmospheric window regions and provides a reasonably accurate description of the uniformly mixed gas molecular absorption², it does not fare so well in describing the degradation of image propagation by the major culprit, namely aerosols.

There are several points well worth noting with respect to the two major atmospheric constituents (namely water vapor and aerosols) and their influence upon sensor performance. First, they represent the two most important radiation attenuators in the atmospheric windows and second, they tend to fluctuate both temporally and spatially with varying weather conditions. Since the attenuation due to water vapor is primarily a function of absolute humidity and temperature it does not effect sensors to any appreciable degree in dry winter or desert type climates. However, it can be a major factor for humid summer or tropical conditions, particularly for long working ranges such as those which might be encountered at sea. The effect due to aerosols depends not only upon the amount of aerosol as monitored by the meteorological visibility at the mesoscale level or the particle size distribution at the microlevel but also upon the composition of the particulate matter (i.e., sea spray, fog, dust, smoke, etc.). The aerosol contribution dominates in dry winter or desert operation and is significant during the summer months

¹LOWTRAN is the generic name of an evolutionary atmospheric model developed at AFGL. The most recent publication describing this code is represented by J.E.A. Selby and R.A. McClatchey, "Atmospheric Transmittance from 0.2 to 28.5 μm : Computer Code LOWTRAN 3," AFCRL-TR-75-0253, May 1975. It should be noted that LOWTRAN 3 has been further updated into two newer codes designated LOWTRAN 3a and LOWTRAN 3b which include an improved water vapor continuum as well as several additional aerosol models.

²The H_2O vapor is not strictly considered to be a uniformly mixed gas since its concentration or mixing ratio changes with absolute humidity.

UNCLASSIFIED

as well. For most problems of interest the aerosol component is more complex to model and a more significant influence than water vapor.

The purpose of this paper is to propose a simple phenomenological aerosol model and review some recent field transmission measurements such as those conducted at Grafenwöhr, FRG by the Army Night Vision Laboratory (NVL) during the period of November 1975 to January 1976. Since the measurements represent a temperate winter climate our discussion and subsequent conclusions apropos to sensor performance will be directed primarily at aerosol effects representative of Central European fogs and hazes. There is a common confusion about relative and absolute humidity. In the German winter the absolute humidity tends to be quite low while the relative humidity tends to be quite high. High relative humidity favors formation of mist and haze, while high absolute humidity absorbs infrared radiation. The subject of broadband infrared water vapor absorption as it relates to the humidity and atmospheric temperature has been discussed in a separate paper³.

³R.E. Roberts, L.M. Biberman, and J.E.A. Selby, "Infrared Continuum Absorption by Atmospheric Water Vapor in the 8-12 μm Window," IDA Paper P-1184, April 1976.

UNCLASSIFIED

II. AEROSOL MODELING

To be of use in the operational planning of E/O missions our weather measurements and forecasting must have the capability of predicting IR image propagation. This means that we must either make better use of our present data collection techniques with updated transmission models or we must determine which new meterological measurements are necessary for an improved understanding of the IR windows. Two separate and distinct mechanisms are involved in the attenuation of infrared and optical signals, i.e., the amount of radiant energy transferred by the atmosphere is determined by two principal types of constituents namely gaseous molecules and aerosols or particulates with their respective attenuation coefficients β_{mol} and β_{aer} . At a particular wavelength λ the transmission is given by

$$T_{\lambda} = \exp(-\beta_{\text{tot}} L) \quad (1)$$

where the total attenuation coefficient is $\beta_{\text{tot}} = \beta_{\text{mol}} + \beta_{\text{aer}}$ and L represents the path length. The magnitude of β_{mol} or β_{aer} clearly depends upon the optical properties, atmospheric concentration, and temperature of the molecular or particulate species.

In a previous paper by Roberts, Biberman, and Selby³, the problems of determining proper values of β_{mol} for the 8-12 μm region were covered in some detail with emphasis on the dominant water vapor attenuation. The conclusion of that paper was that in the absence of significant aerosol effects a more realistic sensor performance analysis is now possible.

³op. cit.

UNCLASSIFIED

The problem of predicting better values of β_{aer} remains an outstanding problem and is the subject of a current study under the sponsorship of DDR&E/RAT.

It is possible, under well controlled circumstances, to measure the composition and size distribution of atmospheric particulates and then use this information through a Mie scattering calculation to predict the transmission characteristics. Unfortunately such a measurement is far from routine and even if it were it might still be inadequate due to spatial inhomogeneities and temporal fluctuations along the atmospheric transmission path. It would therefore seem advisable if not necessary to adopt a so-called thermodynamic or phenomenological methodology which does not depend upon the direct measurement of the particle distribution.

The current LOWTRAN aerosol model, for example, uses measured optical properties (representative of average continental, rural, urban, or maritime conditions) with a prototypical distribution to predict via a Mie computation a scaling model for the extrapolation of the visual range to IR transmission. The scaling law used in LOWTRAN is not intended to hold for fog conditions. It also will not apply correctly for high humidity conditions but holds for a range of intermediate conditions within the accuracy to which the visual range is usually known. Even though this is a step in the right direction the underlying assumption is that for a particular environment, such as a continental haze, the shape or functional form of the distribution remains unchanged. In many if not most cases this is not a valid representation. For example in an evolving fog formation the water droplet distribution tends to grow in the sense that there are relatively more larger particles as the visibility becomes lower. This is illustrated dramatically in Fig. 1 where we have plotted some representative particle size distributions as measured in Grafenwöhr, FGR. It is, of course, impossible to accommodate such an effect with any single distribution.

UNCLASSIFIED

In the remainder of this section we will reexamine some of the aspects of Mie scattering theory⁴ with the intent of motivating a simple and more general scaling model that does take into account such changes but does not depend explicitly upon either a measured or assumed size distribution.

Although our application in this paper will be to water droplet or fog measurements, the arguments used to postulate the scaling model are generally valid for other particulates as well.

For a specified wavelength λ which is large compared to the particle size r the Mie extinction cross section σ_{ext} behaves in the following way for an absorptive medium

$$\sigma_{\text{ext}} \sim r^3 \quad (2)$$

where the proportionality constant depends upon the wavelength dependent complex index of refraction. The total aerosol extinction coefficient β_{aer} is given by the average over the particle size distribution $n(r)$ via

$$\beta_{\text{aer}} = \int \sigma_{\text{ext}} \, dn \sim \int r^3 \, dn \quad . \quad (3)$$

Hence, in this limit which should be appropriate for IR radiation and light fogs or hazes the aerosol attenuation at a given wavelength depends only upon the 3rd moment of the distribution or specifically the total volume V of particulates, in a straightforward linear fashion

⁴It is not our intent to provide a detailed outline or derivation of the Mie scattering equations. The interested reader is referred to any one of a number of useful texts on this subject, such as (a) H.C. Van de Hulst, "Light Scattering by Small Particles," John C. Wiley and Sons, New York, 1957; or (b) D. Deirmendjian, "Electromagnetic Scattering on Spherical Dispersions," American Elsevier Publishing Co., 1969.

UNCLASSIFIED

$$\beta_{aer} \sim V \text{ (long wavelength absorptive limit)} \quad (4)$$

If we next examine the other extreme, sometimes referred to as the geometric limit, where the particles are typically large compared to the wavelength of the radiation, then large particle scattering dominates and

$$\sigma_{ext} = 2\pi r^2. \quad (5)$$

Once again a size averaging yields the desired result related now to the effective area A for the given distribution as in Eq. (2)

$$\beta_{aer} \sim \int r^2 dn \sim A \text{ (short wavelength limit)} . \quad (6)$$

This result should hold well for visible radiation transmission through fogs and rain. Assuming real world distributions are well behaved one might on the basis of Eqs. (4) and (6) postulate the following scaling law

$$\beta_{aer} \text{ (long wavelength)} = C_\lambda \beta_{aer}^{3/2} \text{ (short wavelength)} \quad (7)$$

where the proportionality constant C_λ depends only upon the spectral bands of interest and the particle composition.

Equations (2) - (4) refer to the so-called Rayleigh scattering region for absorbing particles (such as small water droplets in the 10 μm wavelength region) and Eqs. (5) and (6) refer to the geometrical scattering region. Equation (7) attempts to simplistically relate the Rayleigh and geometrical scattering regimes. Although this limit might be appropriate for the scaling of visible transmission data to the 10 μm infrared window, it is not our intent to formulate a general and practical scattering model on this basis. For example with distributions containing a large number of particles with $r > 10 \mu m$ the long wavelength limit is not reached and Eq. (7) will not be valid. However, it would appear that for most fog-like

UNCLASSIFIED

UNCLASSIFIED

conditions the assumption for Eq. (7) are more nearly true. A validation of this assumption will be made in the following sections. Equation (7) differs from the current LOWTRAN aerosol model¹ which essentially provides a linear scaling for all wavelengths

$$\beta_{aer} \text{ (long wavelength)} = C_\lambda \beta_{aer} \text{ (short wavelength)} \quad (8)$$

The application of weather data to these results is usually provided by the Koschmieder⁵ relationship

$$\beta_{aer \text{ vis}} = \frac{3.91}{v} \quad (9)$$

derived using a 2% contrast transmission requirement where v is the reported visual range. For moderately clear conditions (meteorological range of 10 km or greater) the assumptions for Eq. (8) are more nearly true. Unfortunately these are not the kinds of conditions which are normally critical in determining the limits of sensor performance/weather capability. It is the severe limited visibility environment which is usually responsible for incapacitating an E/O system. For these cases Eq. (8) is not generally valid.

It is not our goal in this paper to necessarily determine the validity requirements for Eq. (7) or (8). Rather we would like to provide the motivation for adopting a more general and flexible model that incorporates both extremes and is not restricted to a single assumed particle distribution. Although Eq. (7) is interesting in that it is insensitive to the details of the particle distribution for the cases where it could apply (i.e., 10.6 μm radiation and medium fog conditions) it is probably too restrictive for general applications. However, the

¹op. cit.

⁵W.E.K. Middleton, "Vision Through the Atmosphere," University of Toronto Press, 1968.

UNCLASSIFIED

arguments leading to it are relevant to that goal. In particular since there is such a small change in the functional dependence of β_{aer} upon r (i.e., from V to $V^{2/3}$ for the extremes) then it is probably not presumtuous to assume that

$$\beta_{aer} = F(V) \quad (10)$$

for any selected wavelength independent of possible realistic shape changes, etc., in the particle distribution. The critical conclusion and assumption to be tested is that *for a particular aerosol and spectral region the attenuation or extinction is most critically dependent upon the volume of particulate in the atmospheric path and not so much upon the detailed description of the distribution function.*

If this statement is a valid one (as we hope to demonstrate below) then the ramifications to the modeling community are manifold.

First of all for most weather conditions other than extremely dense fogs Eq. (10) is most appropriate for IR radiation. This results from the fact that the typical particle sizes in hazes and fogs are usually smaller than the long wavelength of IR radiation. For this particularly simple case the aerosol extinction is directly proportional to the volume of particulate. This will be validated experimentally in the following discussion. Therefore a simple measurement of a quantity related to the volume of particulate along the transmission path (i.e., g/m^3) could provide a direct measure of the IR transmission characteristics. Thus one could make a routine, possibly remote measurements of the IR "visual range" since it is proportional to the liquid particulate content. This kind of meteorological measurement which does not require a tedious point-to-point IR transmission measurement could in turn be used directly in the weather-sensor performance analysis. One possible measure would be the integrated backscatter from a LIDAR system as discussed in the next section.

UNCLASSIFIED

UNCLASSIFIED

Secondly, in lieu of such a measurement, Eq. (10) can be exploited in order to provide an improved scaling of the normal photopic visual range to the IR, which is not dependent upon possible shape changes, etc., in the particle size distribution. For example, if the aerosol attenuation has a strong functional dependance only upon the volume content V (as suggested by Eq. (10)) then a unique relationship exists (independent of V) between the extinction coefficients for two different spectral bands:

$$\beta_{\text{aer}}(\text{IR}) = G(\beta_{\text{aer}}(\text{vis})) \quad (11)$$

where again the link to the weather data base is provided by Eq. (9).

We are using the IR and visible portion of the spectrum only as representative examples. The above statements clearly hold for other wavelength regions as well. Equation (7) as well as the LOWTRAN example of Eq. (8) are just special cases of the more general formulation given by Eq. (11). The applicability of Eq. (11) ultimately depends upon the validity of Eq. (10). In the following paragraphs we hope to provide such a verification using the published results of Deirmendjian^{4b} as well as an extensive set of Mie calculations for measured particle distributions from the Grafenwöhr field experiments.

The Deirmendjian calculations^{4b} of the aerosol extinction coefficients for six different water droplet distributions including three haze models and three cloud models are shown in Fig. 2 for 0.7 μm and 10 μm radiation. As one proceeds from the various haze models to the cloud models the particle distributions become broader and contain a greater number of large particles as indicated by the volume of liquid water. As suggested by the earlier arguments, there is indeed a strong smooth

^{4b}D. Deirmendjian, "Electromagnetic Scattering on Spherical Dispersions," American Elsevier Publishing Co., 1969.

UNCLASSIFIED

relationship between the extinction coefficient, at each wavelength, and the particulate volume. The data for other wavelengths also show this behavior. Furthermore, a regression analysis on β_{aer} (10 μm) versus β_{aer} (0.7 μm) yields β_{aer} (10 μm) $\sim \beta_{aer}^{1.47}$ (0.7 μm) with a coefficient of determination $r^2 = 0.99$. This supports the limiting form of Eq. (7) which suggests β_{aer} (10 μm) $\sim \beta_{aer}^{1.50}$ (0.7 μm).

Several hundred particle distribution measurements, including balloon experiments to study the verticle lapse rate, were made using the Knollenberg PMS counter during the Grafenwöhr test. Using these measured distributions (several representative ones are shown in Fig. 1). R. Pinnick⁶ of the ECOM Atmospheric Science Laboratories performed an extensive set of Mie scattering calculations. Although the distributions inherently contain a certain degree of experimental error, the calculations employing them nonetheless provide a valid data base upon which to test our central thesis represented by Eq. (10). Figures 3-5 show the results of those calculations plotted versus liquid water content for each distribution at wavelengths of 1, 4, and 10 μm , respectively. The water content is computed from the measured distributions assuming the aerosols were predominantly water. This does not pose a real restriction since the Mie calculations were based upon these distributions using pure liquid water optical properties. The relatively small amount of spread shown in these figures is in fact primarily due to the range of particle size restrictions imposed by the PMS counter. For example depending upon the fogs density, different particle size ranges were used (indicated by \square and \times in Figs. 3-5). A measurement made using a given particle setting on the equipment therefore necessarily excludes some particles otherwise measured using a different range setting. In general the points clustered most tightly on a given line in Figs. 3-5 represent a single range

⁶A more extensive account of this work will be published in a forthcoming paper by R. Pinnick and this author.

UNCLASSIFIED

setting for the instrument. However, even neglecting the instrumental artifacts, the match between β_{aer} and V is still quite good - again supporting the contention of Eq. (10). Finally one finds for this 311 point data base that $\beta_{aer}(10 \mu m) \sim \beta_{aer}^{1.49}(1 \mu m)$ and $\beta_{aer}(4 \mu m) \sim \beta_{aer}^{1.42}(1 \mu m)$ again supporting Eq. (7). It should be noted that each of the above sets of calculations were performed for liquid water complex indices of refraction. In both cases the real and imaginary index is a strong function of the wavelength. The appropriate references for the Deirmendjian computations are cited in his text^{4b} whereas the Pinnick calculations are representative of the Hale and Querry⁷ measurements for liquid water.

The main point which we wish to emphasize here is that the above results are indicative of a large number of distributions. For the case of the Grafenwöhr PMS measurements the particle size distributions vary drastically in shape from case to case (much more than is indicated in Fig. 1). Although the PMS counter excluded particles with radii greater than 8 μm we have found that this artifact of the distribution measurement does not affect the results shown in Figs. 3-5 to any significant degree. This is most likely due to the rapid exponential falloff of $n(r)$ versus r as illustrated in Fig. 1. Furthermore the Deirmendjian calculations have no such restrictions and still show a smooth functional relationship between aerosol extinction and liquid water content. This is also the case for the broad large particle distributions representing the three cloud models (cf. Fig. 2).

As further support for the contention that aerosol extinction is most strongly dependent upon liquid content rather than the explicit functional form of the distribution, Katz⁸ has

^{4b} op. cit.

⁷ G.M. Hale and M.R. Querry, "Optical Constants of Water in the 200 nm to 200 μm Wavelength Region," App Optics 12, 555 (1973).

⁸ B. Katz, private communication (1976).

UNCLASSIFIED

performed an analysis analogous to the one in this paper for the maritime aerosol environment. Using a maritime aerosol distribution⁹ whose form depends upon meteorological factors such as wind velocity and relative humidity, Katz was able to show an even closer relationship than is indicated in Figs. 3-5 for extinction versus liquid content and for wavelengths from the visible to long wavelength IR region of the spectrum. In fact this relationship was found even though his particle index of refraction was dependent upon the met parameters through a varying mix ratio between pure liquid water and sea salt.

The conclusion of the above discussion is that for a large number of different measured and assumed distributions the volume of particulate is in fact the most critical parameter in determining the aerosol extinction and thus scaling laws and subsequent analysis based upon Eq. (10) and (11) should be valid¹⁰. Work by Hänel and his collaborators together with our own current efforts¹¹ indicates that a similar dependence exists for solid particulates as well.

⁹ W.C. Wells, G. Gal, and M.W. Munn, "Aerosol Distributions in Maritime Air," Lockheed Palo Alto Research Laboratory Report (1976).

¹⁰ G. Hänel, "The Properties of Atmospheric Aerosol Particles as Functions of the Relative Humidity at Thermodynamic Equilibrium with the Surround Mois Air," *Adv. Geophysics* 19 (1976).

¹¹ Work in progress by R. Pinnick and R. Roberts.

UNCLASSIFIED

III. CONCLUSIONS

Most current aerosol models suffer considerably (especially for fog conditions) from reliance upon a single or finite number of scaled particle size distributions. It is clear from the Grafenwöhr measurements and the analysis presented here that this methodology is not valid. The outcome of using any prescribed particle distribution is a linearized model as given in Eq. (8). A major part of the motivation for this work was to demonstrate that such a restrictive assumption is unnecessary and contradictory to modeling the real atmospheric aerosol environment, particularly for limited visibility conditions. Our extinction versus volume content analysis shows that for a wide variety of cases (such as the Grafenwöhr measurements) the volume content of particulate along the transmission path is the most important parameter in determining the aerosol extinction. Thus a more general and valid aerosol scaling model can be derived (as given by Eq. (11)) which is independent of the intricate behavior of the particle distribution. Implicit support for this contention is also provided by the Grafenwöhr transmission measurements shown in the Appendix. This paper also suggests that a relatively simple measurement of the liquid content along a given transmission path could provide a direct indication of the IR propagation along that path. One very enticing possibility for a real time and remote measurement would be to use a visible LIDAR technique. The measured backscatter profile represents a sensitive measure of the liquid water content along the prescribed LIDAR path¹³. Thus one is

¹³E.E. Utley and R.J. Allen, "A Digital Real-Time LIDAR Data Recording, Processing, and Display System," *J. Optical and Quantum Electronics* 7, 121 (1975).

UNCLASSIFIED

UNCLASSIFIED

presented with the exciting possibility of rapidly and remotely monitoring the IR atmospheric propagation characteristics using a laser ranging device operating in the visible part of the spectrum. An experimental test of this hypothesis will be carried out as part of the Army Night Vision Laboratory atmospheric propagation program in February 1977.

UNCLASSIFIED

UNCLASSIFIED

IV. ACKNOWLEDGEMENTS

The author gratefully acknowledges the many contributions and stimulating discussions with Lucien Biberman of IDA. In addition he would like to thank Ronald Pinnick of the ECOM Atmospheric Science Laboratory for his collaborative efforts and Barry Katz for providing the author with his maritime results.

UNCLASSIFIED

UNCLASSIFIED

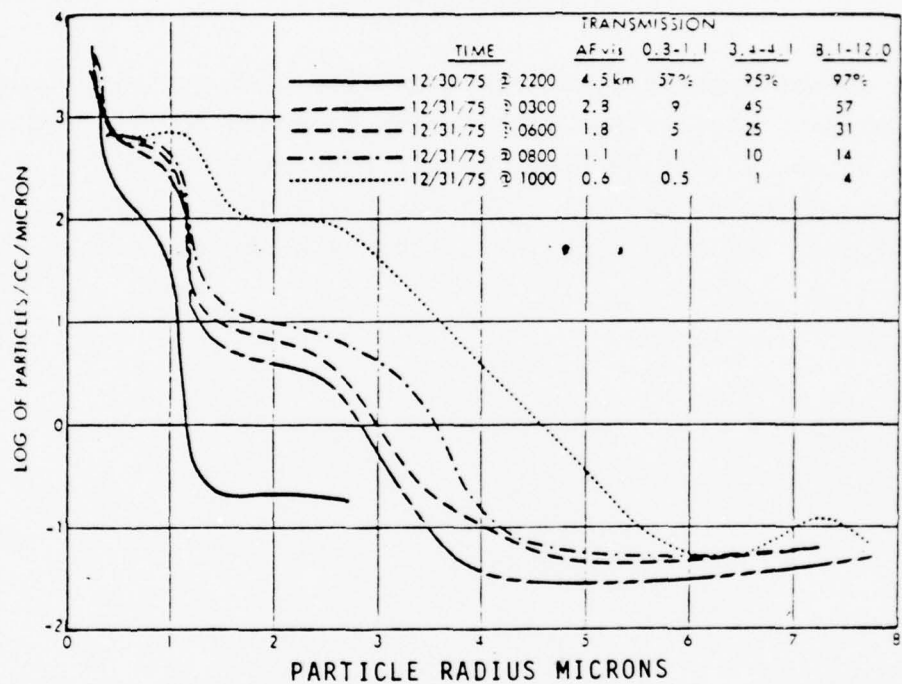
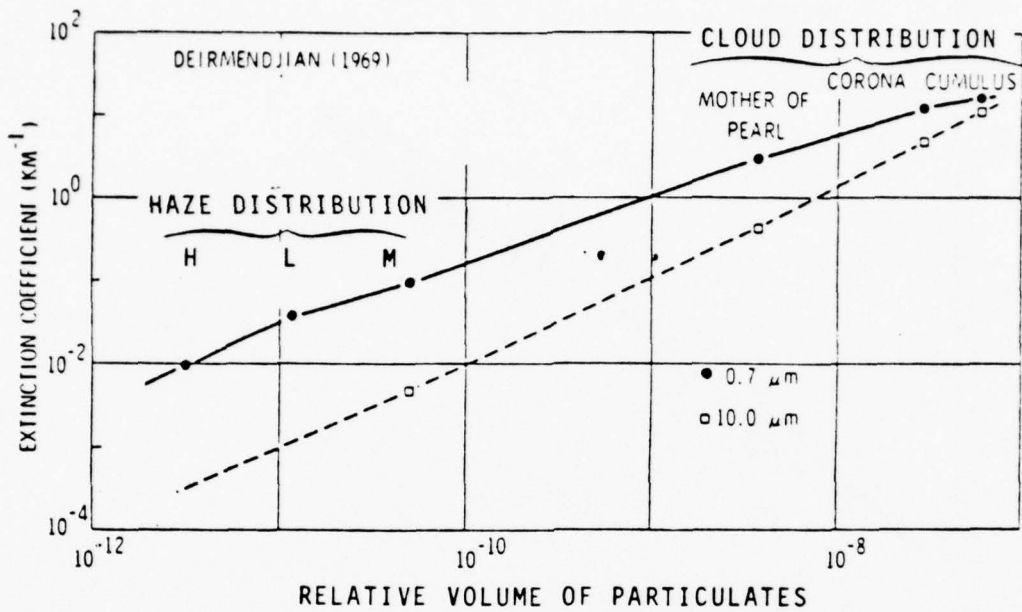


FIGURE 1. Particle Size Distributions as Measured in Grafenwöhr, FGR during Fog Formation.

UNCLASSIFIED

UNCLASSIFIED

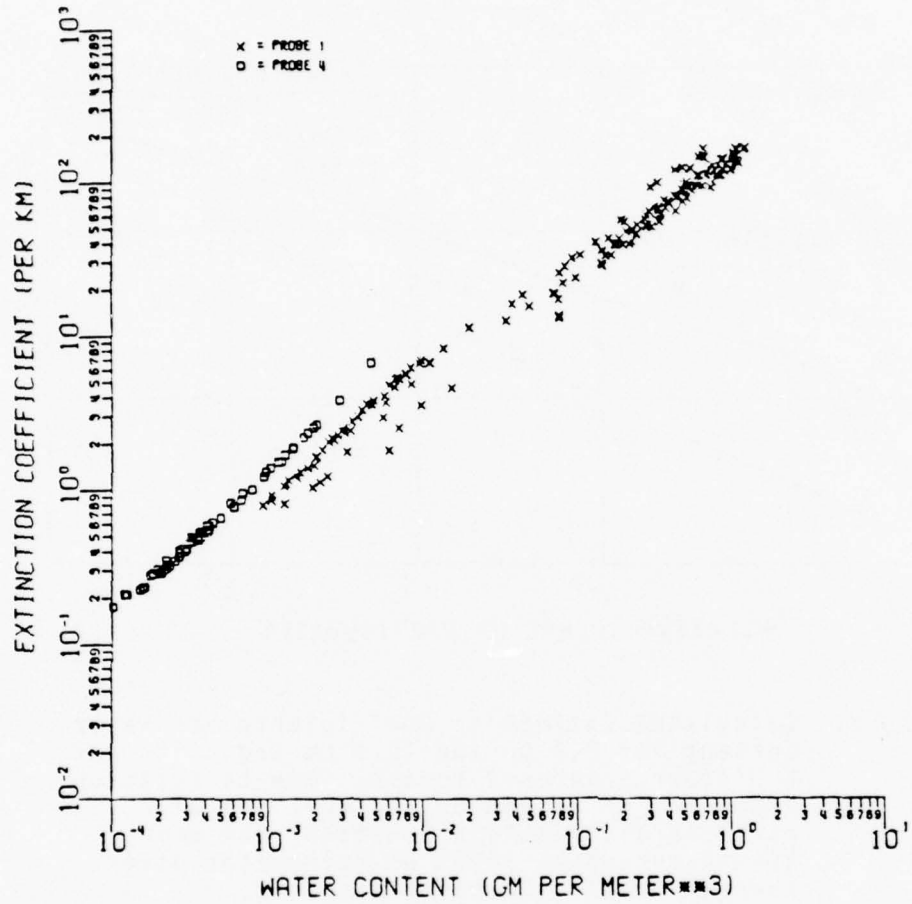


4-1-76-4

FIGURE 2. Calculated Extinction Coefficients vs. Water Content for 0.7 μm and 10.0 μm Radiation and 6 Different Aerosol Models. Mie calculations according to Deirmendjian (Ref. 4b) with particle distribution functions and wavelength dependent index of refraction given therein for liquid water droplets.

UNCLASSIFIED

$\lambda = 1.0 \mu\text{m}$



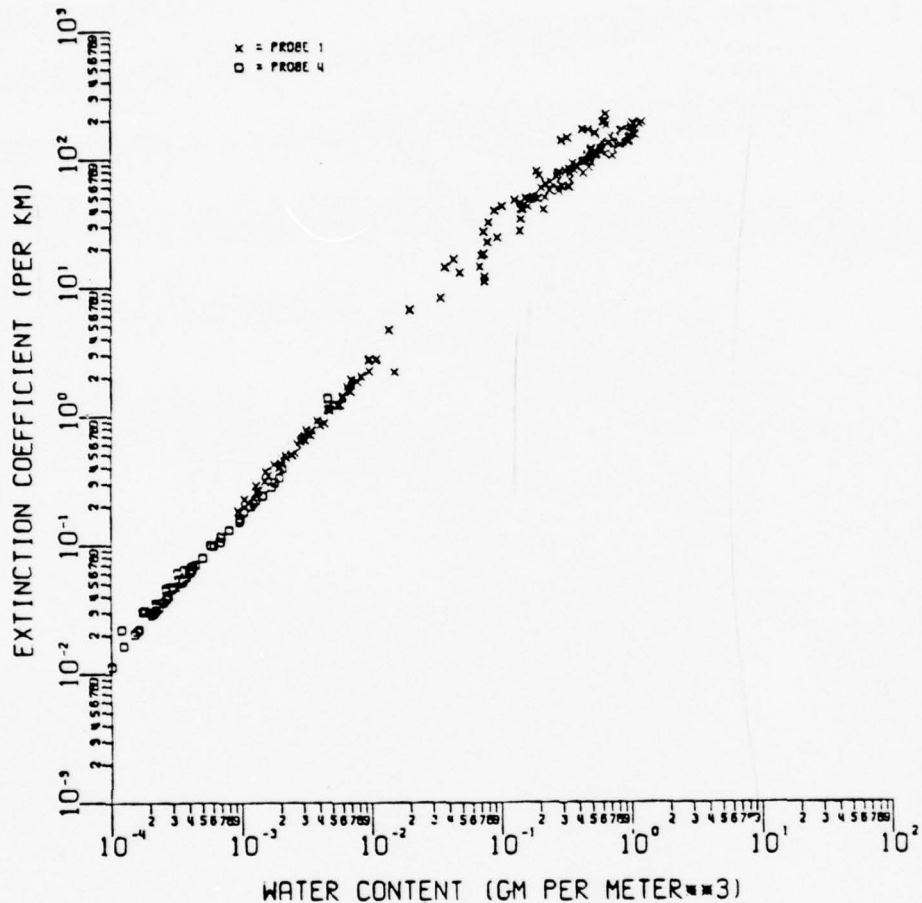
7-29-76-21

FIGURE 3. Extinction Coefficient vs. Water Content for 4 μm Radiation and Measured Particle Distributions from Grafenwöhr. Each point represents a distinctly different measured distribution. Mie calculations performed with the liquid water optical properties of Hale and Querry (Ref. 7).

UNCLASSIFIED

UNCLASSIFIED

$\lambda = 4.0 \mu\text{m}$

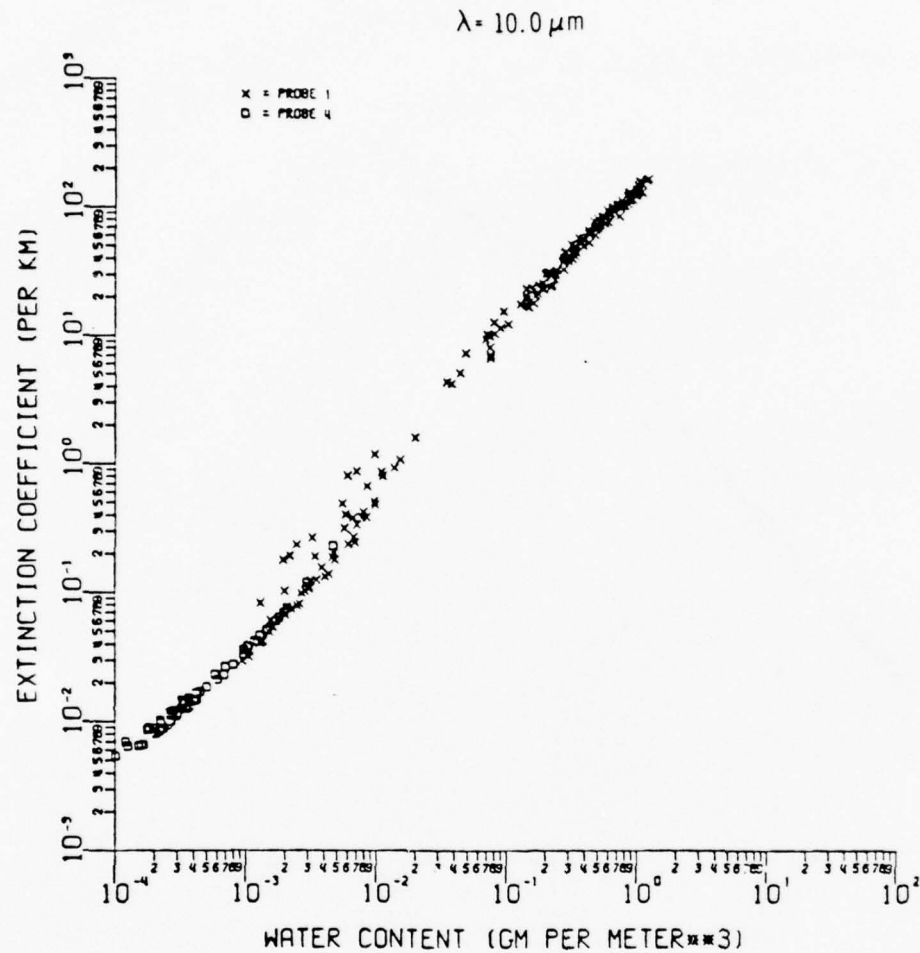


7-29-76-20

FIGURE 4. Extinction Coefficient vs. Water Content for 1 μm Radiation and Measured Particle Distributions from Grafenwöhr. Each point represents a distinctly different measured distribution. Mie calculations performed with the liquid water optical properties of Hale and Querry (Ref. 7).

UNCLASSIFIED

UNCLASSIFIED



7-29-76-22

FIGURE 5. Extinction Coefficient vs. Water Content for $10 \mu\text{m}$ Radiation and Measured Particle Distributions from Grafenwöhr. Each point represents a distinctly different measured distribution. Mie calculations performed with the liquid water optical properties of Hale and Querry (Ref. 7).

UNCLASSIFIED

UNCLASSIFIED

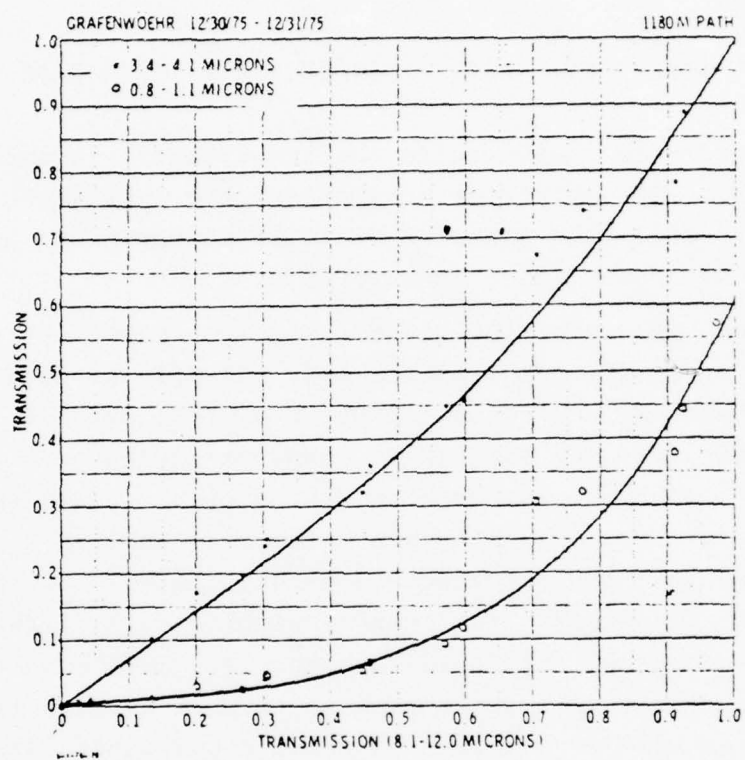


FIGURE 6. Transmission in the 3.4-4.1 μ m and 0.8-1.1 μ m band vs. the 8.1-12.0 μ m band for Grafenwöhr.

UNCLASSIFIED

UNCLASSIFIED

APPENDIX: SCOPE OF EXPERIMENTAL DATA BASE

In order to characterize the atmospheric transmission for a quantified German winter environment the Army Night Vision Laboratory conducted a series of field measurements at Grafenwöhr, FGR from November 1975 - January 1976.

Since the Grafenwöhr field tests were performed during the winter, for most conditions the most significant contribution to the atmospheric attenuation was from fine particle aerosols such as haze and fog as well as large particles such as rain and snow. In the previous sections we presented arguments which suggested a strong relationship between aerosol extinction coefficients in different spectral bands. Clearly the same relationship then exists for transmission as well. Towards the end of December 30 and during December 31, 1975 a particularly clean set of measurements were made on what appears to be a textbook example of stable ground fog conditions. In Fig. 6 we have plotted the transmission for the 0.8-1.1 μm and 3.4-4.1 μm band as a function of the 8.1-12.0 μm transmission. The agreement with the analysis presented in the aerosol modeling section is excellent. The molecular absorption component has not been normalized out of these curves. It is however constant to within a few percent for the conditions cited in Fig. 6. It also shows that there is perhaps a slight favoring of the 8.1-12.0 μm region over the competitive 3.4-4.1 μm IR band. The transmission in the IR regions is significantly greater than the .8-1.1 μm band. The particle distribution and composition measurements for this time period bear this out as well.

The measured particle distributions together with the measured transmission and AF visibility estimates for representative

UNCLASSIFIED

points during 30-31 December are shown in Fig. 1. The trend is quite clear. The left curve represents the best of the visibility and transmission which are growing progressively poorer with time and with the successive shifting of the curves to the right. There is a drastic change in the shape of the distributions with the larger particles having a greater representation as the visibility drops. This again underlines the necessity of having aerosol models which are not explicitly dependent upon a single representative size distribution as is the case for LOWTRAN. LOWTRAN 3b will include additional aerosol models, although none of these are representative of fog conditions, such as those occurring at Grafenwöhr. The more general aerosol scaling models discussed in the earlier portion of this paper can accommodate this flexibility.

In this Appendix we have made no attempt to present a comprehensive review of the Grafenwöhr trials. That will form the subject matter of a more comprehensive report sponsored jointly with the Army Night Vision Laboratory and Atmospheric Science Laboratory. Instead we have tried to highlight some of the most important elements of the field measurements as they relates to atmospheric modeling and sensor performance in particular.

A study is currently in progress at IDA which shows that similar relationships exist between transmission bands for other different environments such as English maritime, and Camp A.P. Hill, Virginia. This study lends further experimental documentation to the proposed aerosol model. We are also carrying out a more detailed comparison of aerosol models (derived from computations such as those presented in this paper) with a more extensive limited visibility data base from Grafenwöhr¹².

¹²R. Bergemann, R. Pinnick, R. Roberts, and M. Sola, work in progress.

UNCLASSIFIED

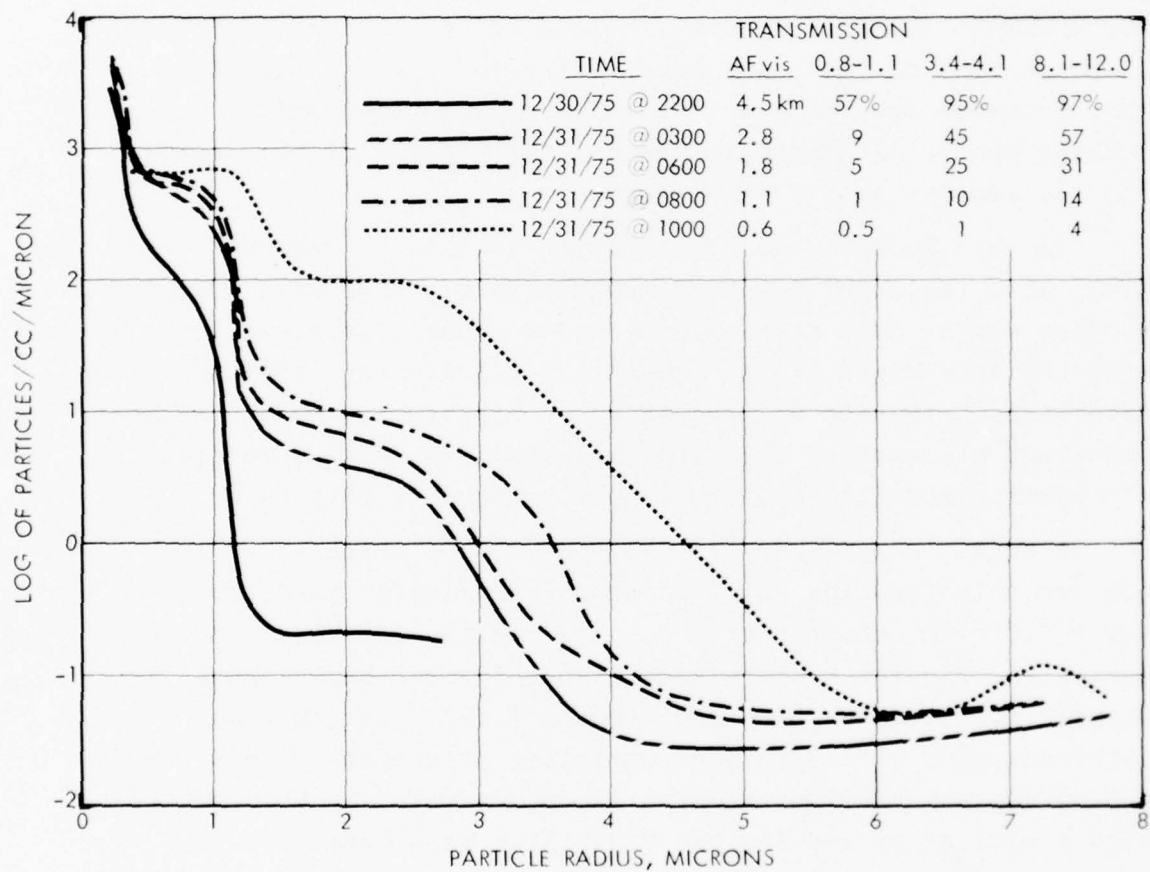


FIGURE 1. Particle Size Distributions as Measured in Grafenwöhr, FGR during Fog Formation.

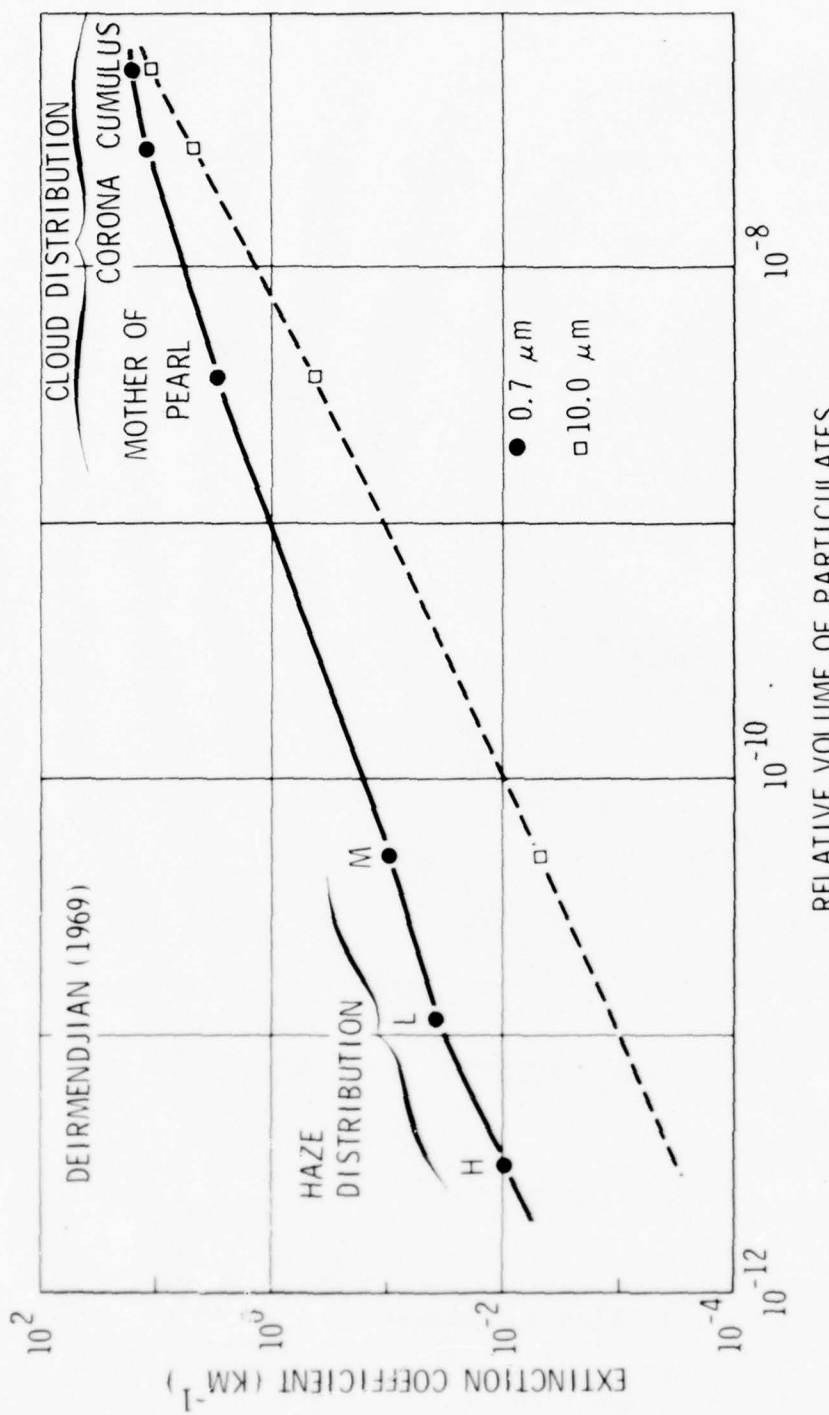
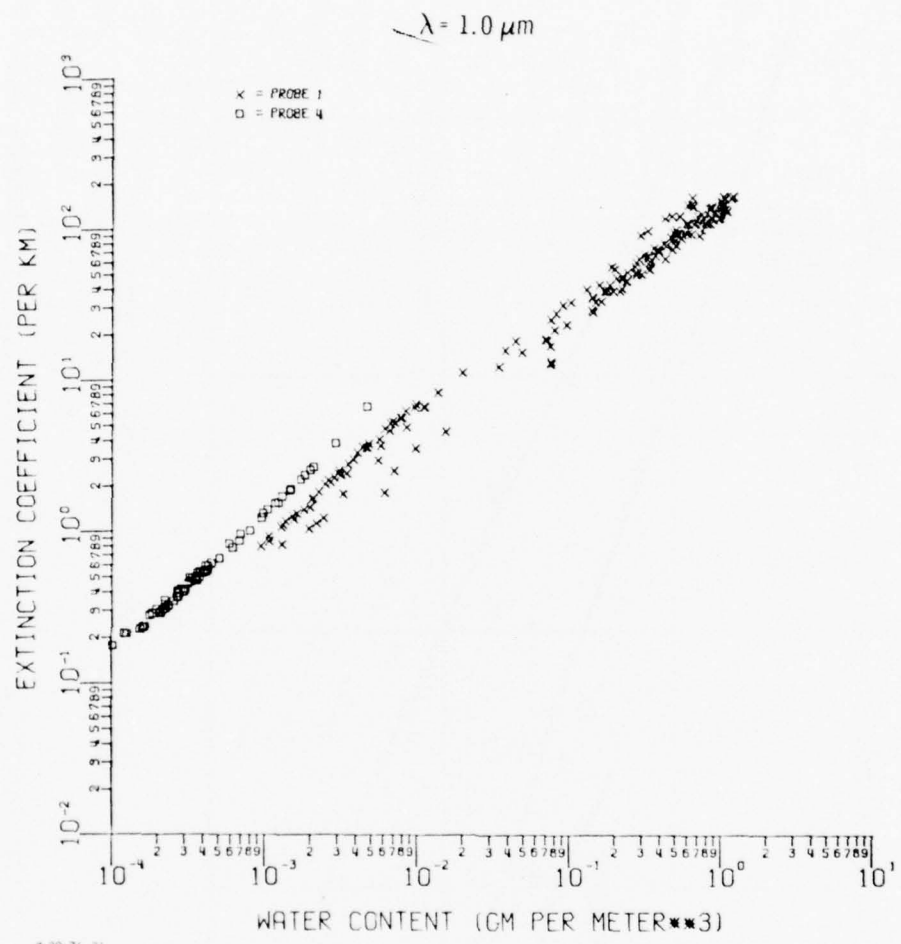


FIGURE 2. Calculated Extinction Coefficients vs. Water Content for 0.7 μm and 10.0 μm Radiation and 6 Different Aerosol Models. Mie calculations according to Deirmendjian (Ref. 4b) with particle distribution functions and wavelength dependent index of refraction given therein for liquid water droplets.

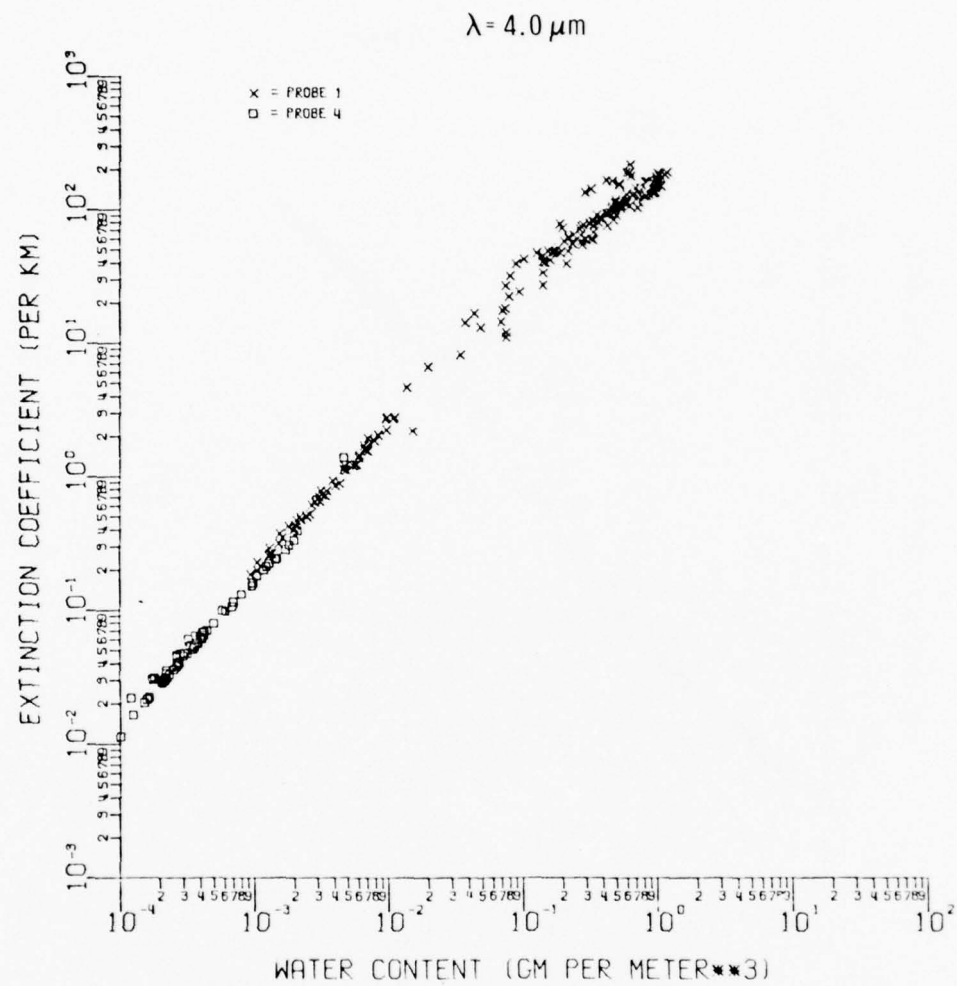
4-12-76-8

UNCLASSIFIED



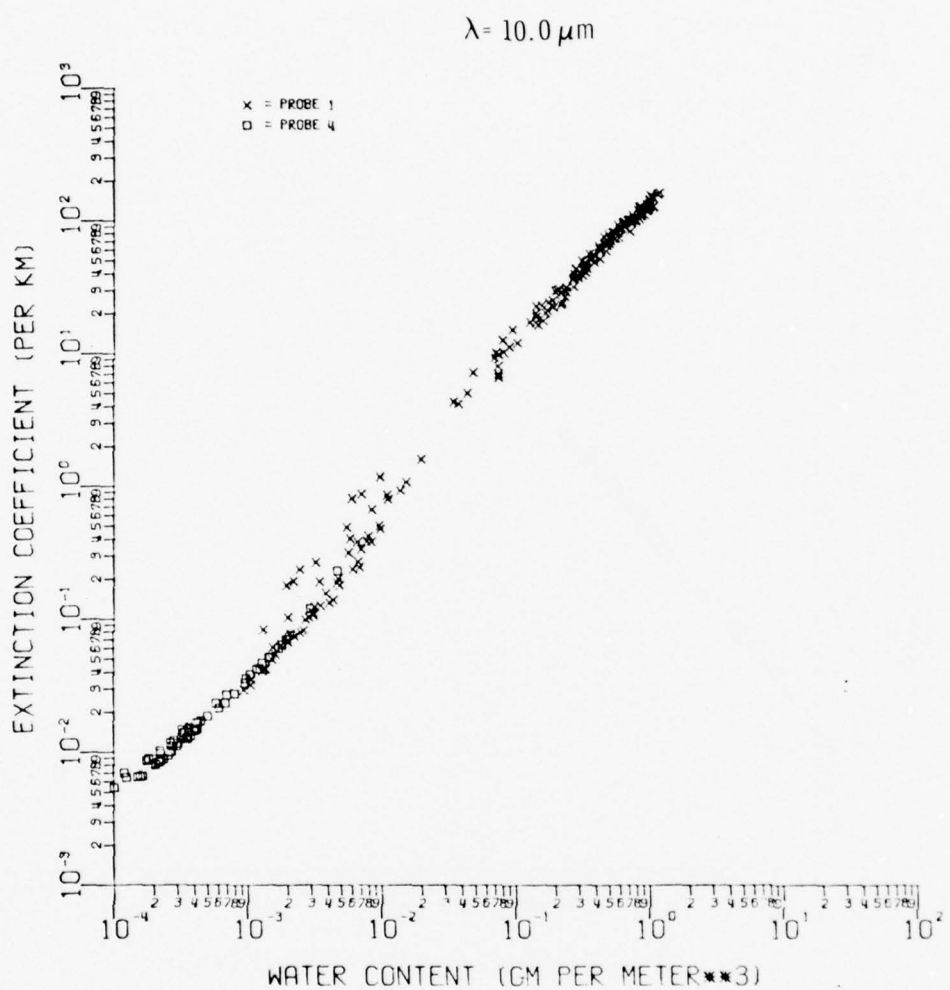
7-29-76-21

FIGURE 3. Extinction Coefficient vs. Water Content for 4 μm Radiation and Measured Particle Distributions from Grafenwöhr. Each point represents a distinctly different measured distribution. Mie calculations performed with the liquid water optical properties of Hale and Querry (Ref. 7).



7-29-76-20

FIGURE 4. Extinction Coefficient vs. Water Content for 1 μm Radiation and Measured Particle Distributions from Grafenwohr. Each point represents a distinctly different measured distribution. Mie calculations performed with the liquid water optical properties of Hale and Querry (Ref. 7).



7-29-76-22

FIGURE 5. Extinction Coefficient vs. Water Content for 10 μm Radiation and Measured Particle Distributions from Grafenwohr. Each point represents a distinctly different measured distribution. Mie calculations performed with the liquid water optical properties of Hale and Querry (Ref. 7).

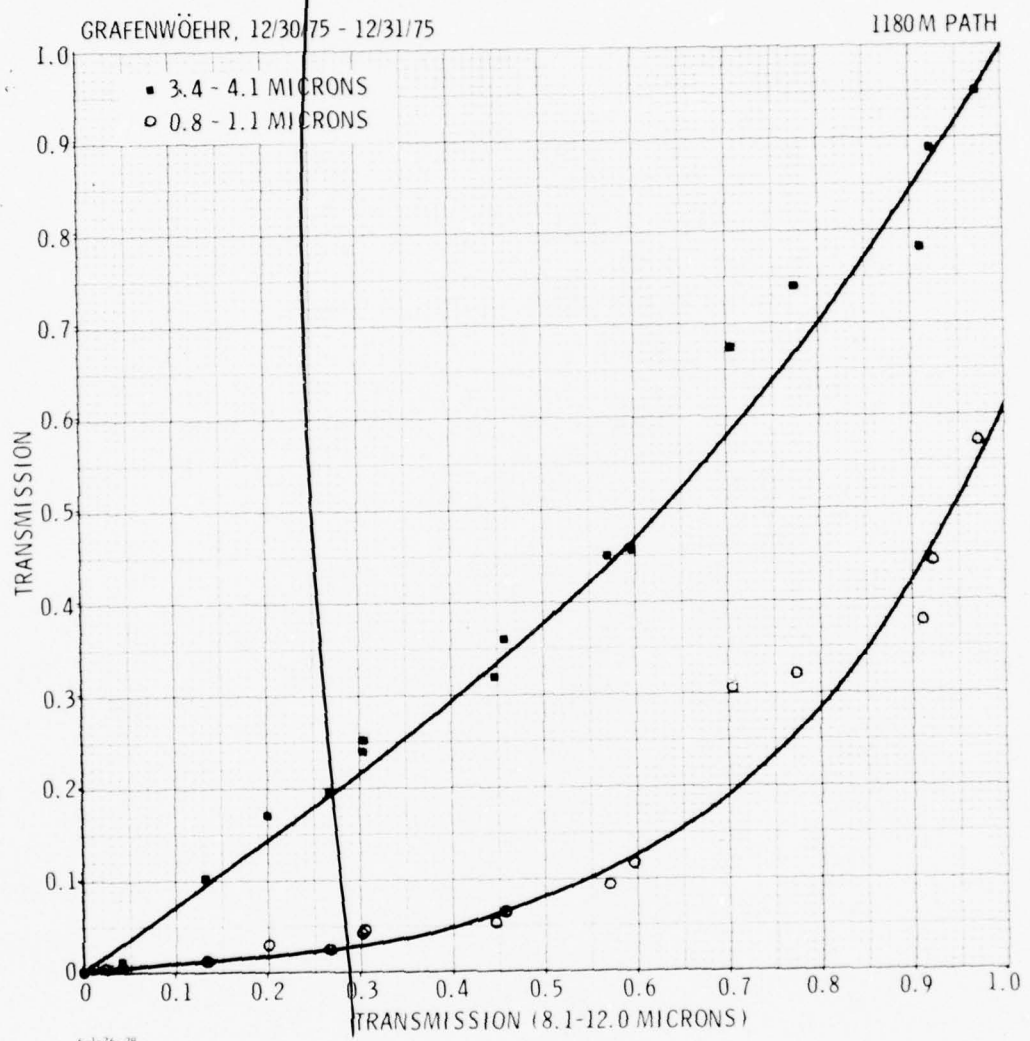


FIGURE 6. Transmission in the 3.4-4.1 μm and 0.8-1.1 μm band vs. the 8.1-12.0 μm band for Grafenwöehr.

(This page intentionally left blank.)

.... This paper is UNCLASSIFIED

COMPLEX REFRACTIVE INDEX OF ATMOSPHERIC PARTICULATE MATTER -
CURRENT STATE OF KNOWLEDGE FROM E-O SYSTEMS EFFECTS POINT OF VIEW

James D. Lindberg
James B. Gillespie

Atmospheric Sciences Laboratory
US Army Electronics Command
White Sands Missile Range, New Mexico 88002

ABSTRACT

This paper discusses the complex refractive index of atmospheric particulate matter and the current status of methods of measurement of both the real and imaginary parts. Current deficiencies in knowledge of this index, and measurement methods are pointed out. An effort is made to show why we need to measure this quantity, and where future effort should be directed in order to provide the kind of data needed to properly model the effects of atmospheric particulates on E-O system performance. Specific work being done to alleviate some of the difficulties is also described.

INTRODUCTION

In order to quantitatively describe the interaction of visible or infrared radiation with any aerosol such as fog, haze, dust or smoke, the Mie theory is still the most useful computational tool we have available. Being strictly valid only for aerosols composed of spherical particles, it does not solve all of our problems. But nevertheless, it is good enough in most cases and practical enough in application so that it constitutes the heart of most modern computer codes that try to model important aerosol optics problems.

In order to use the Mie theory to predict the optical properties of an aerosol, two general kinds of information about the particles or droplets in the aerosol are required. The first kind is the spectral number density of the particles - how many there are per unit volume, and what their sizes are. The second kind of information is knowledge of the optical characteristics of the materials of which the particles are composed, and this means the complex refractive index. Unlike the spectral number density, which is a physical property of an aerosol, the complex refractive index is wavelength dependant, and if the particles are not homogeneous in composition - as is the case in natural dust - may vary radically from particle to particle in the aerosol. It is this

second kind of information, the complex refractive index - how well we can determine it, how well we need to determine it, and what we already know about it - that is the subject of this paper.

REVIEW OF MEASUREMENT METHODS

In general the refractive index of any material¹ is a complex number, it has a real part which tends to describe how the material refracts or reflects light, and an imaginary part which describes the sample's ability to absorb light. When we talk of methods of measuring these two numbers, the real and imaginary parts, for a particular substance, it is necessary to group materials into two categories. The first is optically homogeneous materials that don't significantly scatter light at the wavelength of interest. This includes most liquids, many optically clear solids like glass, and high quality single crystals such as some specimens of quartz or calcite. The second group of materials is those available only in solid powdered form, those which can only be obtained as samples which scatter as well as absorb light. Most atmospheric dust materials, particularly in arid regions, fall into this category, as do fly ash and smoke particles from industrial pollution sources.

For the first kind of materials, which can be obtained with an optically flat surface that reflects but does not significantly scatter light, the problem is not difficult in principle. For a collimated plane polarized beam of light incident on an optically flat surface, the well known Fresnel equations completely describe the reflectance as a function of the angle of incidence and angle of polarization of the radiation, and the complex refractive index of the materials involved. One can measure such a specular reflectance for several angles of incidence or polarization angles, and solve the Fresnel equations simultaneously for the real and imaginary parts of the refractive index. In practice the error budget and other experimental difficulties lead to complications that quickly add to the difficulty of the problem, but nevertheless a closed solution does exist. Basically what is called for are careful measurement technique and sophisticated data reduction methods. The complex index of liquid water, the most important single aerosol component, can and has been obtained by such methods². Measurements on sulfuric acid solutions have been made in this way³. Querry⁴ is currently using such techniques to measure the optical constants of phosphoric acid and other liquids of importance in the optics of artificial (countermeasures) aerosols. Some of the soil derived minerals that are commonly found in atmospheric dust are mineral species that can be obtained in large clear monocrystals. From specular reflectance measurements made on polished sections of such high quality crystals the Fresnel equations approach can yield good results. Quartz, calcite and gypsum are such minerals, and for at least one of these, quartz, good results have been published by Peterson and Weinman⁵. In general we can say that for the group of materials that don't scatter light, adequate methods exist for obtaining the complex refractive index, in

the visible and infrared spectral regions, or for whatever wavelengths adequate radiation sources and detectors are available.

For the second group of atmospheric particulate materials the problem is much more difficult, and as we shall point out, not yet completely solved. Many of the soil minerals and other materials found in the earth's aerosol do not exist in anything other than powdered form or in solid masses of fine particles. Clay minerals, which show strong highly wavelength selective absorption in the infrared, are examples of such materials. One cannot find a clear single crystal of illite clay for example that is large enough to permit specular reflection measurements to be made, so the Fresnel equations approach is not directly useable here. Typically, silicate clay minerals are composed of crystals only a few microns in size. Thus in making optical measurements on such materials one must use a sample that is basically a powder in nature. Such a sample both scatters and absorbs light, and that is the heart of the problem of determining the complex refractive index of such materials. In any measurement one must separately account for attenuation due to scattering and absorption.

Up until a few years ago, no methods existed for determining the complex index of a powder of unknown composition or particle size such as atmospheric dust. Because of the clear need for such data, Volz⁶, in a pioneering effort in the field, attempted to apply a form of the Fresnel equation approach. He pressed atmospheric particulate samples in a steel die with polished surfaces, and obtained pellets upon which pseudospecular reflectance measurements could be made. He obtained valuable information about the infrared complex index of samples. Fischer⁷ then developed a diffuse reflectance/transmittance method for measuring the imaginary index only. Other workers^{8,9} suggested methods for measuring the imaginary index of samples collected on a membrane filter, without removing the sample from the filter. Diffuse reflectance methods^{10,11} are now available which satisfactorily measure the imaginary index of dry particulates in the visible and near infrared spectral region. Such methods are not useful in the infrared yet, because diffuse reflectance spectroscopic technology is not well developed for wavelengths much beyond about 2 μ m. Fischer¹² has extended his methodology to the middle infrared and has published some good data. Unfortunately, Fischer's work, which was done as part of a dissertation in West Germany, is not being continued at the moment. However, Schleusener et al.¹³ have used spectrophone technology to solve this problem, and measurements of the imaginary refractive index at all important visible and infrared laser wavelengths can now be made. Schleusener and Lindberg¹⁴ have recently measured the imaginary index of atmospheric particulate samples representing extremes of composition in the visible and near infrared using a helium neon laser, and in both infrared atmospheric window regions using tunable deuterium fluoride and carbon dioxide lasers.

All of the methods described previously provide values of the imaginary refractive index of dry atmospheric particulate matter. In general, it is safe to say that reasonably satisfactory methods do exist now for obtaining the imaginary index of dry solid particles in the 0.4 to 11 μ m spectral region. By "reasonably satisfactory", we mean that while resulting data do have significantly large error bars in general, the accuracy appears to be good enough for the majority of military E-0 systems effects modeling applications. We will comment further on this below.

Evaluation of the effect of humidity on the complex refractive index of particulate matter is in need of further work. Many atmospheric particulates materials are water soluble or hygroscopic in nature, and go through a complicated transition from dry irregularly shaped grains at low humidities to droplets of liquid solutions at High relative humidity. The complex index of the particles is of course severely altered by such a transition. Hanel¹⁵ has done some excellent work on this problem in the visible spectrum, and has shown how the complex index varies from that of a dry grain at low humidity to that of liquid water at high humidity, in a continuous, but surprisingly complicated manner. Extension of his approach into the infrared region would provide useful information about this problem.

The most hopeful solution to the general problem of measuring the imaginary index as a function of relative humidity would probably be to take advantage of recent work by Bruce¹⁶. He is developing spectrophone technology to the point where it can separately measure the particulate and gaseous absorption components of absorption of laser energy in an aerosol. The important point is that this is an in situ spectrophone approach, and will deal with the particulates in their suspended state in the air, rather than with a sample collected (and therefore modified) by some mechanical process. If such a device, coupled with more conventional imaginary index measurement methods were applied to the problem, the state of knowledge of the imaginary index of refraction for atmospheric particulate materials could be brought to a satisfactory state as far as E 0 systems performance modeling is concerned.

There is one area where available methodology and knowledge is not satisfactory. This is the problem of measuring the real part of the complex refractive index for dust particles such as we have been discussing. Hanel has developed a method for measurement of the real index of atmospheric dust samples in connection with his variation with humidity work mentioned above.¹⁷ However, this method is confined in applicability to the visible spectrum, although extension to the infrared is conceivable. The older attempt by Volz to apply Fresnel equations methods to the problem of measuring the complex index does offer some small promise as a solution, but could never provide the

humidity variation information that is needed. Another possibility is to use dispersion analysis and Kramers- Kronig techniques to estimate the real refractive index from knowledge of the wavelength dependence of the imaginary index. This can in principle be done because the real and imaginary parts of the complex refractive index are not independent. However, such techniques call for much more accurate measurements of the imaginary part than are currently available. Therefore we can say that right now no satisfactory methods are available for measurement of the infrared real refractive index of many of the common atmospheric particulate materials. We will comment on the impact of this deficiency in the next section.

REQUIRED MEASUREMENT ACCURACY

So far we have given a brief discussion of the current capability of determining the optical constants - the complex refractive index - of the liquid and solid particles in the atmospheric aerosol. Now we address the question of how satisfactory the current knowledge of this complex index is, and how adequate are the existing measurement methods. The really relevant question is, how well we need to know the complex index, from an E-0 systems optics point of view. We can make a modest beginning at answering this question by examining some typical Mie calculations of the sort that go into E-0 systems performance models. Suppose we take as an example a log normal size distribution of atmospheric particulate matter such as might be found in a rural area on a day without fog, high winds, or unusual meteorological conditions such as snow or rain. We will then normalize the size distribution to represent $100 \mu\text{gm}/\text{m}^3$ of particulate matter, a not uncommon value. Using Mie theory, and choosing several complex indices, we can then calculate the corresponding absorption, scattering, and extinction coefficients for such an atmospheric aerosol. An example of such calculations for two different wavelengths is shown in Table I. The refractive indices were chosen to illustrate how variations in their magnitudes can affect the computational result. We will now examine this table, and show that it suggests some interesting things about our need for complex refractive index information data.

Consider first the results calculated for a wavelength of one micrometer. We see that for this case, significant variations in complex refractive index cause only trivial changes in the extinction coefficient for the aerosol. So from a strict attenuation point of view, the complex refractive index is not so important. The particle size distribution is really the important factor. This is because for short wavelengths many atmospheric dust particles are large compared to the wavelength, and to a good approximation extinction coefficient is proportional to the total geometric shadow area of the particles, regardless of composition or complex index. Looking at the calculations for a $10 \mu\text{m}$ wavelength, however, we see that this is not the case. Smaller variations in the imaginary index cause more significant changes in

extinction. This is because for $10 \mu\text{m}$ radiation the wavelength is no longer small compared to the important particles in the size distribution.

TABLE I. MIE CALCULATIONS SHOWING THE EFFECT OF VARIATIONS IN THE COMPLEX REFRACTIVE INDEX

Wavelength Micrometers	Complex Index	Extinction Per km	Scattering Per km	Absorption Per km
1	1.5-.005i	.0249	.0211	.0038
1	1.5-.050i	.0249	.0134	.0115
1	1.8-.005i	.0251	.0212	.0039
1	1.8-.050i	.0250	.0140	.0110
10	1.5-.100i	.0184	.0119	.0065
10	1.5-.500i	.0228	.0085	.0143
10	2.5-.100i	.0343	.0240	.0103
10	2.5-.500i	.0321	.0159	.0162

We know from available data (examples of which are shown later) that in the visible and near infrared region the imaginary index can vary about as shown in the upper part of Table I, and we can measure this quantity with an accuracy of about a factor of two in error. It is known that the real index does not vary greatly in this region, and again the variability is probably not unlike that shown in the upper part of Table I. Therefore, from an extinction point of view, current measurement techniques are probably adequate, in the visible and near infrared region.

Note however, that for applications where more than just an estimate of attenuation is needed, the complex index is somewhat more important. If, for example, one is concerned about using laser radiation for secure communications purposes or as a target designator perhaps the scattering coefficient is the more important quantity. It can be seen from the upper part of Figure I that changes in complex index do have a fairly direct effect on the scattering and absorption coefficients. A change in imaginary index produces opposing effects in the scattering and absorption coefficients, and these effects tend to cancel out in the sum, which of course is the extinction coefficient. Nevertheless, current technology can produce the optical constant data needed for the visible and neodymium laser wavelength ($1.06 \mu\text{m}$) region.

At longer wavelengths however, the current situation is not so nice. In the spectral region around $10 \mu\text{m}$, the imaginary refractive indices of natural aerosol materials are highly wavelength dependent, and can vary over much wider limits than implied by the numbers used

in the lower part of Table I. As shown in the work of Peterson and Weinman⁵, both the real and imaginary refractive indices for quartz can vary from values as low as 0.3 to as high as 7.0, in a rather narrow spectral interval. This is very much different from the situation in the visible spectrum. If we look at the bottom part of Table I we see that such variability would have a profound effect on extinction as well as scattering and absorption calculations. Fortunately, not all dust particles are quartz, and much averaging occurs because natural aerosols contain a mixture of materials. Nevertheless, a large part of natural mineral dust consists of complex silicate materials, which have chemical bonds not unlike those of quartz, and very little is currently known about the complex indices of such materials. Work is in progress in our laboratory on measuring the imaginary index of atmospheric particulate materials at laser wavelengths (DF and CO₂) in both infrared window regions, as will be discussed in the next section. But, as pointed out in the last section of this paper, no methods are available for directly measuring the real part of the complex index in the infrared for such materials. Table I makes it clear that the real index is as important as the imaginary in some cases. We believe that this is a serious deficiency in the current state of knowledge and measurement capability as far as the complex refractive index of atmospheric particulate matter is concerned.

The kind of parametric variation study shown in Table I is intended here only as an example of the kind of thing that needs to be done to really know where to put our efforts as far as determining the complex index of aerosol components is concerned. What is shown here is only to illustrate one or two current deficiencies that we consider to be important, it is in no way comprehensive. In any particular case - for each E-O system application - one must make similar calculations for different atmospheric conditions, and compare the resulting uncertainties to other systems problems. The purpose here was only to give our view of current status of the technology available for providing the input data needed to prepare atmospheric propagation models that are actually useful to the E-O systems community.

AEROSOL OPTICS RELATIONSHIP TO ROUTINE METEOROLOGICAL DATA

All by itself information about the optical constants of aerosols is not of much value to the E-O systems community. What the individual responsible for design, development or testing of some E-O system really wants to know is, "what are fog, haze, dust, smoke, etc. going to do to my equipment, what limitations are they going to impose on its real performance"? For input information about all he can really have to work with is knowledge of where in the world the system will be required to operate, and some idea of the prevailing meteorological conditions, based on rather straightforward routine met data. Its not possible to go out and measure transmission, scattering, or the optical constants of aerosols for all the locations and circumstances which

are now or may be of importance to U. S. military operations. We have to make generalizations, and construct workable models, so that it is possible to look at current meteorological data, and make a reasonable assessment of the optical nature of the atmosphere, for any particular location and season of year. The most important input information about the complex refractive index of atmospheric aerosol materials needed in order to construct such models is two fold. We need to know the mean or typical values, along with extreme values to establish limits of variability, for different classes of geographical localities. Then we need to determine, at least empirically, how the complex index varies with prevailing meteorological circumstance. We will now briefly describe efforts that we are making to do this; and show some preliminary samples of resulting data.

We have initiated a program which examines collected atmospheric particulate samples from a variety of locations in North America, Panama, Europe¹⁸, and Israel. We are currently measuring the imaginary index of such samples continuously throughout the 0.4 to 1.7 μm spectral region, as well as in the 3-5 and 9-11 μm spectral windows, using discreet laser sources. We also determine composition and the imaginary index of these component materials. In addition, for reasons discussed earlier, we are trying to develop methods of measuring the real refractive index of these materials. With each sample collected, we are obtaining records of meteorological data relevant to that sample. The objective of all this is to develop the data base, and formulate the relationships (either theoretical or empirical) needed to adequately relate aerosol optics to meteorological observations.

In Figure 1 and Table II there are samples of preliminary results which have been presented elsewhere^{14, 19}. Notice that in the visible and near infrared the imaginary index can vary more than an order of magnitude in different parts of the world. An important feature of the data presented in Table II is the fact that the imaginary index in the 9 to 11 μm region shows a strong wavelength dependence, whereas in the 3-5 window region it shows a more monotonic, somewhat weaker wavelength dependence. Note too that in the 9-11 μm region the wavelength of peak absorption is different for the two samples shown. This is because of the distinctly different composition of the samples from different localities. These comments are general features of particulate samples, and illustrate some of the details that must be taken into account in constructing propagation effects models.

Another feature related to the above work is the fact that all aerosol particles do not always have the same complex refractive index. Different particle size regimes are composed of radically differing materials, and this means that for atmospheric dust, both natural and battlefield induced, the complex index varies significantly with particle size. Preliminary work on this point is being done both in West Germany²⁰, and in or laboratory²¹. Table III shows some measurements of imaginary index made on a particulate sample which has been broken down into eight

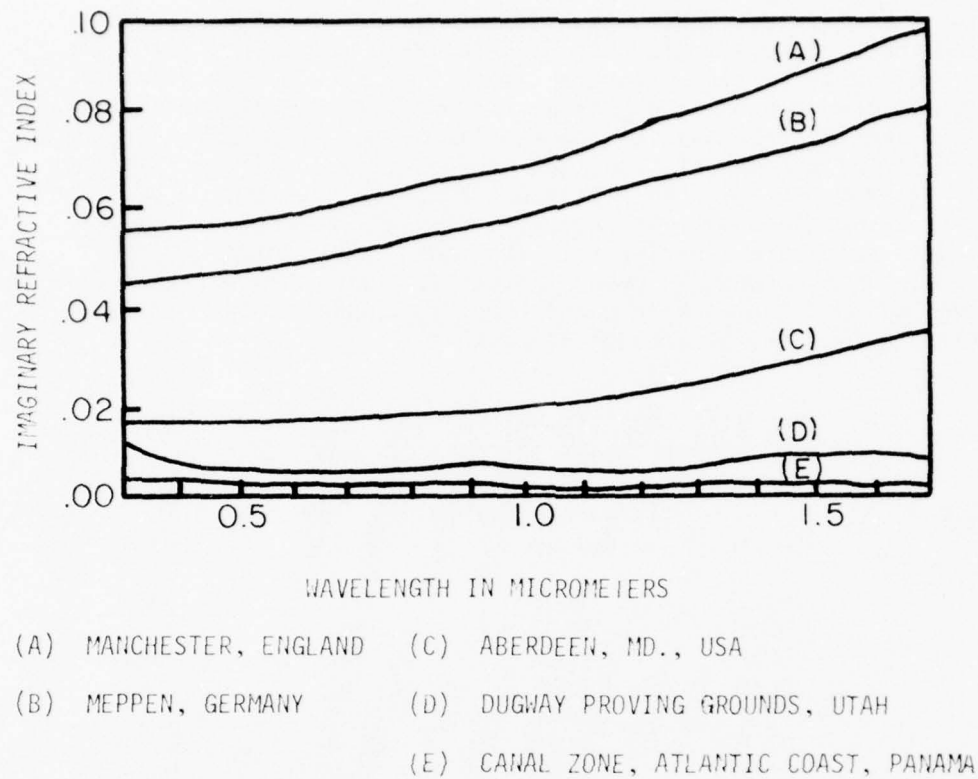


FIGURE 1. Selected examples of visible near infrared imaginary refractive indices of atmospheric particulate samples.

TABLE II. SPECTROPHONE MEASUREMENTS
 OF IMAGINARY REFRACTIVE INDEX

Wavelength Micrometers	White Sands, New Mexico	Grafenwöhr West Germany
1.06	.006	.040
3.61	.010	.056
3.80	.009	.054
4.01	.010	.056
9.220	.430	.406
9.695	.626	.221
10.661	.158	.115

particle size categories, using an Andersen 2000, Inc. cascade impactor. In the data presented here the size categories are as stated by the instrument manufacturer, we have not yet completed our work on confirming them. However, the data do illustrate the point clearly. The fact that small particles have a tendency to show a much greater index than do larger ones is a general tendency in most atmospheric particulate samples. Because of the non-linear nature of Mie calculations, the use of a constant "average" or "effective" value of imaginary index for all the particles in a size distribution does not produce the same result as obtained when the actual individual values are used. This has been pointed out earlier²². The significance of this effect must be taken into account in producing workable aerosol computational models, and part of the work in our laboratory on world wide particulate samples is aimed at accomplishing this.

TABLE III. RELATIONSHIP OF IMAGINARY
REFRACTIVE INDEX TO PARTICLE SIZE

Size Range in μm	Imaginary Refractive Index			
	0.3 μm	0.7 μm	1.06 μm	1.50 μm
>11	.0027	<.0005	<.0005	<.0005
7-11	.0055	<.0005	<.0005	<.0005
4.7-7	.0068	<.0005	<.0005	<.0005
3.3-4.7	.0068	<.0005	<.0005	<.0005
2.1-3.3	.0082	<.0005	<.0005	<.0005
1.1-2.1	.0118	.0020	.0020	.0027
0.65-1.10	.0080	.0068	.0068	.0068
0.43-0.65	.0053	.0060	.0075	.0100

CLOSING REMARKS

We have briefly mentioned some of the available methods of measuring the complex refractive index of atmospheric particulate samples themselves, and of the individual materials of which they are composed. It appears that adequate methods exist for measuring the imaginary index in the 0.4 to 11 μm region, and while the currently available data are not sufficient, active work is in progress to correct the situation. The real index, which can be quite important in the infrared, is another story. Currently it can be measured well only for liquids (fortunately, one of the most important aerosols components is liquid water) and solid materials that can be obtained in large, clear non-scattering samples. But for an important class of particles found in atmospheric aerosols no methods exist for measuring the real refractive index. We have indicated that this is a deficiency in current technology, and have shown that there is a resulting gap in the data base needed to adequately model infrared propagation effects in aerosols. In addition we have mentioned some of our efforts that are intended to

remove these data base deficiencies, and provide an understanding of the relationships between practical meteorological observations and the limitations the corresponding aerosols will impose on various electro optical systems. This latter point is in our view the most important part of the work, because we feel that the real value research in aerosol optics is to provide the capability of inferring the performance of a particular optical system in any geographically significant location, from routine meteorological data.

NOTES AND REFERENCES

1. To be completely general we should point out that in optically anisotropic crystals- including most of the mineral matter found in atmospheric dust - three complex refractive indices, one for light vibrating with its electric field vector parallel to each of three orthogonal axis are required to describe the material at any given wavelength. This is not currently an important problem as far as the optics of atmospheric aerosols is concerned.
2. Hale, G. M. and M. R. Querry, "Optical Constants of Water in the 200 nm to 200 μ m Wavelength Region", Appl. Opt. 12, 555-563 (1973).
3. Palmer, K. F. and D. Williams, "Optical Constants of Sulfuric Acid: Application to the Clouds of Venus?", Appl. Opt., 14, 208-219 (1975).
4. Querry, M. R., "Basic Electromagnetic Properties of Selected Condensed Materials in the Infrared"; work being done under Army Research Office Grant No. DAAG 29 76 G8185.
5. Peterson, J. T. and J. A. Weinman, "Optical Properties of Quartz Dust Particles at Infrared Wavelengths", J. Geo. Res. 74, 6947 (1969).
6. Volz, F. E., "Infrared Refractive Index of Aerosol Substances", Appl. Opt. 11, 755 (1972).
7. Fischer, K., "Bestimmung der Absorption von Sichtbarer Strahlung durch Aerosol Partikeln", Beitr. Phys. Atmos. 43, 244 (1970).
8. Lindberg, J. D. and D. G. Snyder, "Determination of the Optical Absorption Coefficient of Powdered Materials whose Particle Size Distribution and Refractive Indices are not Known", Appl. Opt. 59, 274-9 (1974).
9. Bhardwaja, P. S., J. Herbert, and R. J. Charlson, "Refractive Index of Atmospheric Particulate Matter: An in Situ Method for Determination", Appl. Opt. 13, 731-734 (1974).
10. Lindberg, J. D. and L. S. Laude, "A Measurement of the Absorption Coefficient of Atmospheric Dust", Appl. Opt. 13, 1923-7 (1974).

11. Lindberg, J. D, "Absorption Coefficient of Atmospheric Dust and other Strongly Absorbing Powders: An Improvement on the Method of Measurement", *Appl. Opt.* 14, 2813-2815 (1975).
12. Fischer, K., "Mass Absorption Indices of Various Types of Natural Aerosol Particles in the Infrared", *Appl. Opt.* 14, 2851-2856 (1975).
13. Schleusener, S. A., J. D. Lindberg, K. O. White, and R. L. Johnson, "Spectrophone Measurements of Infrared Laser Energy Absorption by Atmospheric Dust", *Appl. Opt.* 15, 2546-2550 (1976).
14. Schleusener, S. A. and J. D. Lindberg, "The Imaginary Refractive Index of Atmospheric Dust: Measurements Using DF and CO₂ Laser Spectrophones", in preparation.
15. Hänel, G., "The Realpart of the Mean Complex Refractive Index and the Mean Density of Samples of Atmospheric Aerosol Particles", *Tellus* 20, 371 (1968).
16. Bruce, C. B., "Development of Spectrophones for CW and Pulsed Radiation Sources", ECOM-5802, Atmospheric Sciences Laboratory, White Sands Missile Range, New Mexico.
17. Hänel, G., "Computation of the Extinction of Visible Radiation by Atmospheric Aerosol Particles as a Function of the Relative Humidity, Based Upon Measured Properties", *Aerosol Sci.* 3, 377 (1972).
18. Some of this sampling work is being done through our participation in NATO project OPAQUE.
19. Lindberg, J. D. and J. B. Gillespie, "Measurements of Imaginary Refractive Indices of Atmospheric Particulate Matter from a Variety of Geographic Locations", presented at the Symposium on Radiation in the Atmosphere, in Garmisch-Partenkirchen, W. Germany, 19-28 Aug 76.
20. The Meteorological Institute of the Univ. of Mainz, Germany under the leadership of Prof. K. Bullrich, is addressing this problem.
21. Lindberg, J. D. and, J. B. Gillespie, and B. D. Hinds, "Variation of Imaginary Refractive Index with Particle Size in Atmospheric Dust", in preparation.
22. Lindberg. J. D., "Review: The Composition and Optical Absorption Coefficient of Atmospheric Particulate Matter", *Optical and Quantum Electronics*, 7, 131-139 (1975).

...This paper is unclassified

AEROSOL SIZE DISTRIBUTION MEASUREMENTS FOR RADIATION TRANSFER MODELING

R. G. Pinnick
D. L. Hohjelle
and
G. Fernandez

Atmospheric Sciences Laboratory
US Army Electronics Command
White Sands Missile Range, New Mexico 88002

ABSTRACT

Particulate size distributions measurements made during fog and haze in wintertime in West Germany have been used in calculations of the particulate extinction at visible and IR wavelengths. The results show an approximate $1/\lambda$ dependence on wavelength for light haze (10 kilometer visibility) conditions, but nearly neutral (wavelength independent) extinction for heavy fog (300 meter visibility) conditions. Significant increases in extinction with altitude for fog are evident. These results also show there exists rather simple relationships between particulate extinction and liquid water content, and furthermore, that particulate extinction in the IR is related to particulate extinction in the visible, for a variety of fog and haze conditions. However, these results are based on a relatively small data base, and more measurements under different meteorological conditions and at different locations are needed. Finally, preliminary results of similar measurements on desert aerosols at White Sands in New Mexico are presented. The results suggest a correlation of particle turbidity with relative humidity.

INTRODUCTION

To assess the effects of natural and artificial aerosols on the operation and performance of electro-optical systems, measurements of the size distribution is needed. Use of light-scattering instruments for such measurements has real advantage: namely the measurement is done in-situ and in real time, and the particles are not disturbed appreciably during measurement. We have made size distribution measurements of fog and haze particulates in Grafenwöhr, West Germany, and desert dust in New Mexico with a commercial (Knollenberg) light-scattering particle counter. Particular attention has been given to the calibration of the instrument; the calibration advertised by the manufacturer has not been used.¹ Typical results for a wide range of atmospheric visibility conditions are given here, and to a first approximation it is suggested that particulate extinction for visible through middle-IR wavelengths is related to the total aerosol mass, at least for continental fog and haze.

FOG AND HAZE MEASUREMENTS

Measurements of fog and haze particle size distributions made with a balloon-borne particle counter showing typical vertical variability observed over the first 150 meters altitude is shown in Figure 1. These measurements are for conditions with visibilities ranging from about 10 km for the profile marked "light haze" to approximately 300 meters for the profile marked "heavy fog". The corresponding particulate extinction cross sections at 0.55, 4, and 10 micrometer wavelengths, predicted using the size distributions shown in Figure 1 and under the assumption the particles are spherical water droplets, are shown in Figure 2. The inferred liquid water content is also shown. Aside from the obvious large increases in extinction and liquid water content with altitude for the more turbid conditions, the following observations are made: (1) For relatively clear conditions the extinction dependence on wavelength is roughly $1/\lambda$, but for low visibility fog conditions there is nearly neutral (wavelength independent) extinction. (2) There is a definite correlation of extinction and liquid water content for a broad range of particle size distributions. To pursue the implications of this correlation we have replotted the data in Figure 2 along with most of the remaining Grafenwöhr data in Figure 3. The result is that the extinction at visible wavelengths (the results at 1 micrometer are about the same as the results at 0.55 micrometer) is approximately proportional to the integrated particulate cross-sectional area, a result expected from geometrical optics for particles large compared to the wavelength. At 4 and 10 micrometers wavelength, the extinction is very nearly proportional to the integrated particulate volume.

We have fitted the data in Figure 3 with straight lines and have come up with the following empirical relationships between extinction and particulate water content:

$$\sigma(1) \approx 190 w^{.76}, \sigma(4) \approx 380 w^{1.08}, \sigma(10) \approx 130 w^{1.13} \quad (1)$$

Where $\sigma(1)$, $\sigma(4)$, and $\sigma(10)$ refer to the particulate extinction cross sections at 1, 4, and 10 microns in km^{-1} , and w refers to particle water content in gm/m^3 .² As a final remark, we note that empirical expressions relating particulate extinction at 1, 4, and 10 microns can be derived from our results. For example, from (1) above we get

$$\sigma(10) \approx 0.053[\sigma(1)]^{1.49}, \sigma(4) \approx 0.22[\sigma(1)]^{1.42} \quad (2)$$

We suggest these rather simple relationships can be used to predict IR atmospheric particulate extinction based on visible atmospheric extinction (approximated here by 1 micron wavelength results) for continental haze and fog. This remark should be qualified by noting that our results are based on a relatively small data base. More measurements at different

locations and under different meteorological conditions to enlarge this data base are clearly warranted.

DESERT AEROSOL MEASUREMENTS

We have also made measurements of desert aerosols at White Sands in New Mexico with the light-scattering particle counter. In this case, since the particles are known to be irregular and of mixed composition, interpretation of the data, as well as prediction of extinction, is less straightforward and contains more uncertainties. Some results of our measurements are shown in Figure 4. Plotted are the temporal variations of aerosol concentration (for particles with radii > 0.2 micrometer), an aerosol concentration ratio (number of particles with radii ≥ 0.2 micrometer/number of particles with radii > 0.3 micrometer), which is a measure of the size distribution of the aerosol, and the relative humidity, for a 3-day period in June, 1976. The particle concentration tracks the relative humidity, suggesting particle growth by accretion of water for conditions when relative humidity is greater than 60%. Such a growth mechanism would, of course, change the aerosol optical properties and further complicate the problem of predicting the radiation transfer effects of these particles. More definitive measurements and modeling of desert aerosols, addressing the problem of irregular particles and the effects of particles of mixed composition are needed.

CONCLUSIONS

An adequate data base of aerosol size distribution measurements for the purpose of modeling their effects on radiation transfer does not yet exist. More attention needs to be given to instrument calibration and to more definitive measurements. Relative humidity and visibility are two bulk parameters of the atmosphere that appear to be related to aerosol extinction from visible wavelengths through the middle-IR.

REFERENCES

1. R. G. Pinnick and E. B. Stenmark, 1976, "Response Calculations for a Commercial Light-Scattering Aerosol Counter," ECOM-5597, Atmospheric Sciences Laboratory, US Army Electronics Command, White Sands Missile Range, New Mexico.
2. Similar correlations of liquid water content and extinction have been made: Kumai, Motoi, 1973: "Artic Fog Droplet Size Distribution and Its Effect on Light Attenuation," *J. Atmos. Sci.* 30, 635-643; Barteneva, O.D. and E. A. Polyakova, 1965: "A Study of Attenuation and Scattering of Light in a Natural Fog Due to Its Microphysical Properties," *Izv., Atmos. and Oceanic Phys.* 1, 193-207; Eldridge, R. G., 1966: "Haze and Fog Aerosol Distributions," *J. Atmos. Sci.*, 23, 605-613.

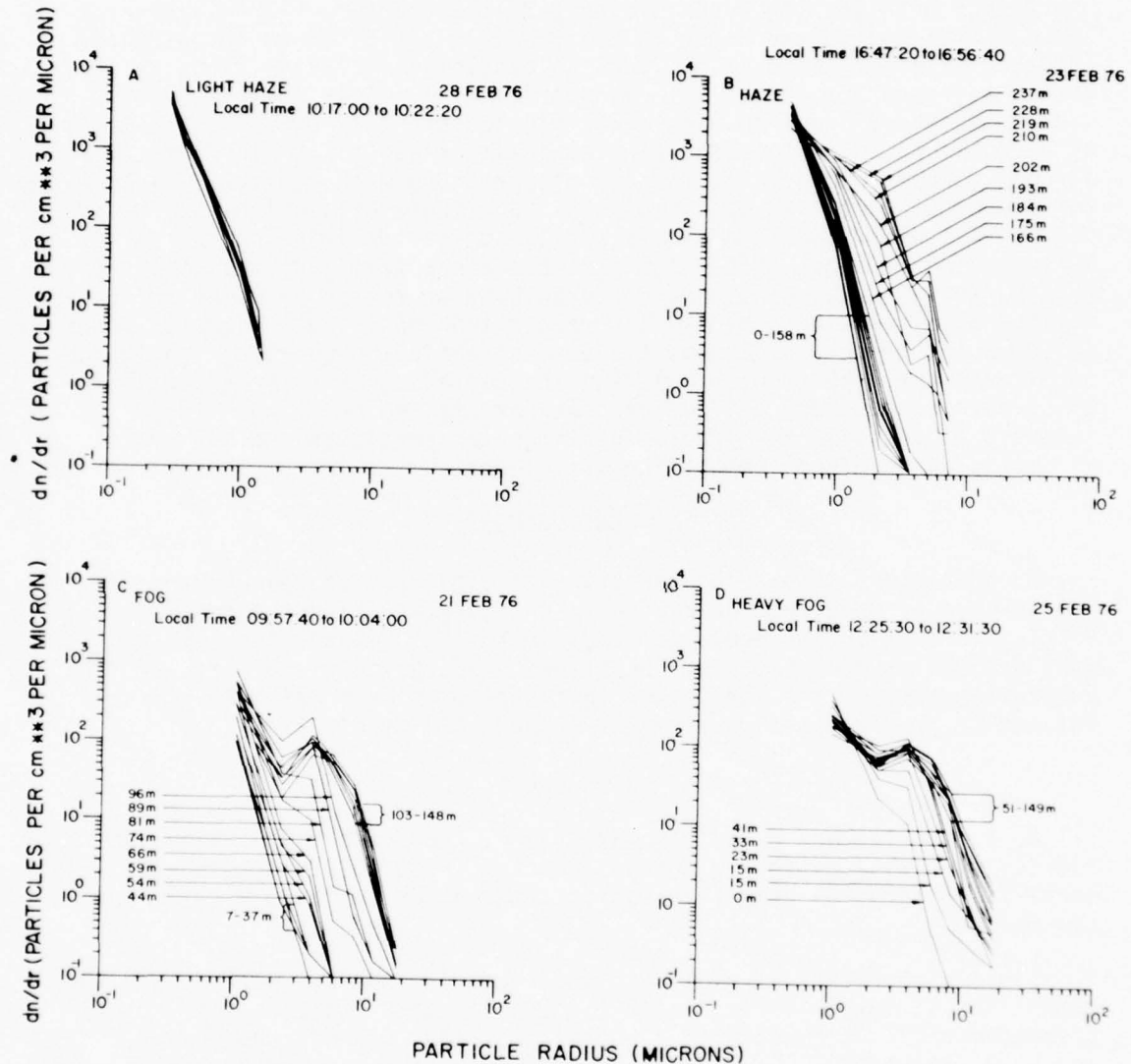


Figure 1. Particulate size distribution measurements made with a tethered balloon-borne aerosol counter for several haze and fog conditions. Each size distribution is for a particular altitude in the corresponding profile in Fig. 2, and the altitude range or ranges are indicated.

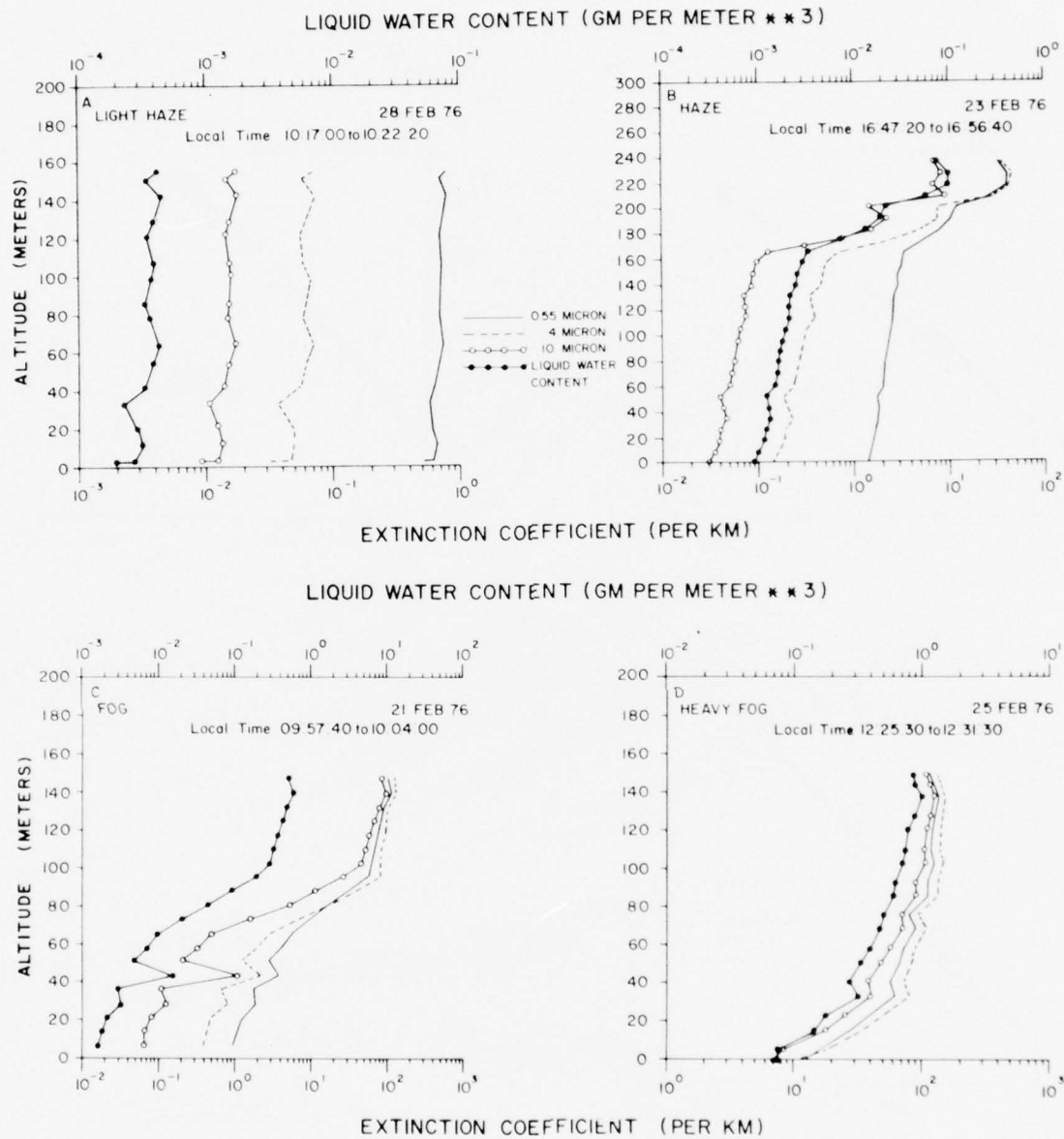


Figure 2. Profiles of particulate extinction and water content inferred from particle size distribution and concentration measurements (shown in Fig. 1) made with a balloon-borne aerosol counter. The solid "w" curve indicates the liquid water content and the solid, dashed, and dotted curves indicate the inferred extinction at 0.55, 4, and 10 microns. The date, local time (hours, minutes, seconds), and time frame interval for the measurements are given.

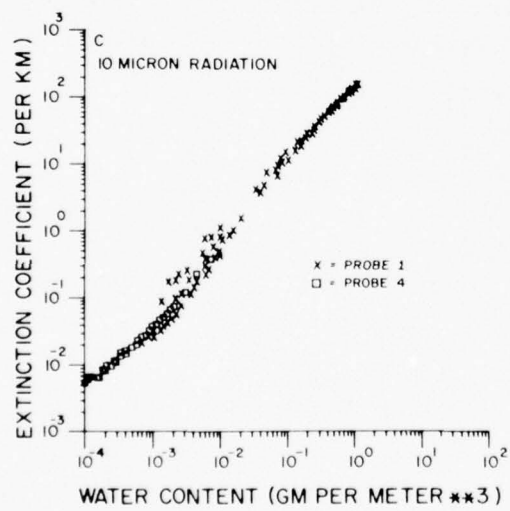
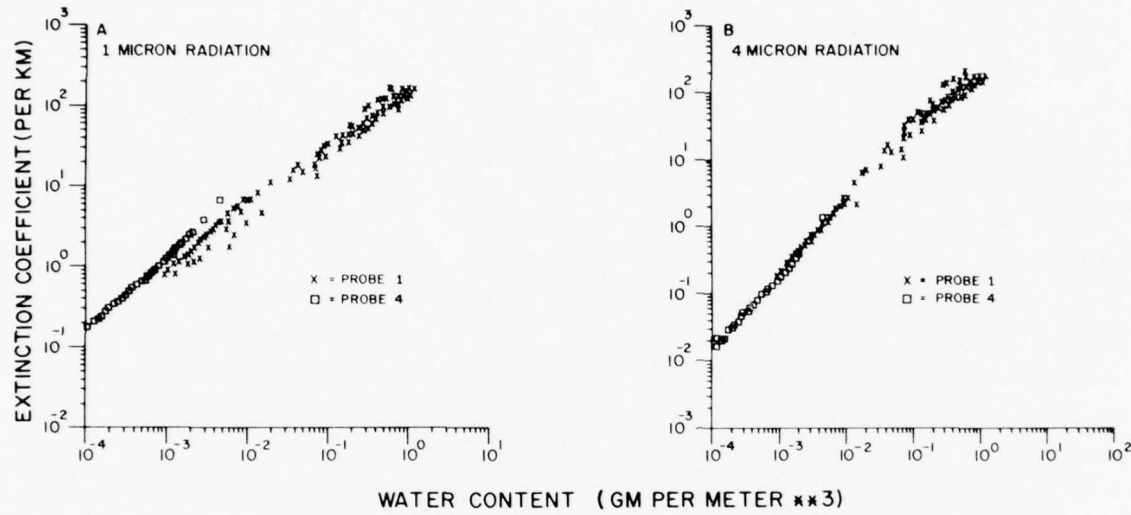


Figure 3. Values of the Mie theory calculated particulate extinction at 1-, 4-, and 10-micron wavelengths vs particulate liquid water content for a variety of particle size distributions of atmospheric fog and haze (212 in all). The probe range setting 1 or 4 indicates the aerosol counter used to make the size distribution measurements on which this data is based was set on two different ranges of sensitivity.

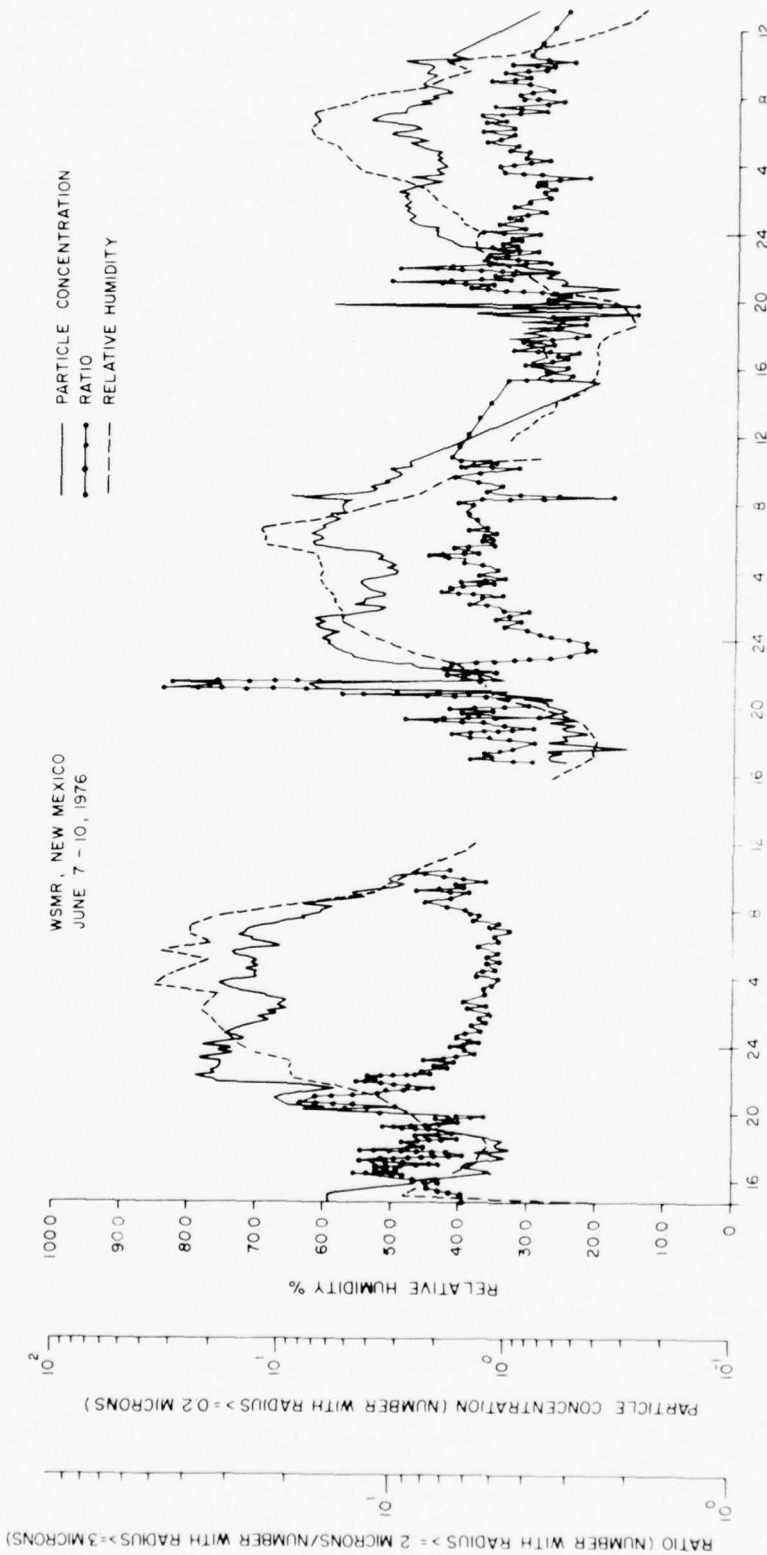


Figure 4. Measurements of aerosol concentration and relative humidity for a 3-day period at White Sands in New Mexico. Plotted are values of the relative humidity (dashed curve), particle concentration (number of particles per cc with radius > 0.2 micrometer-solid curve), and particle concentration ratio (number of particles with radii > 0.2 micrometer/number of particles with radii ≤ 0.3 micrometer-solid curve with dots).

(This page intentionally left blank.)

UNCLASSIFIED

....This paper is UNCLASSIFIED

EFFECT OF RELATIVE HUMIDITY ON AEROSOL SIZE DISTRIBUTION AND VISIBILITY: MODELLING STUDIES

James W. Fitzgerald
Naval Research Laboratory
Washington, D. C. 20375

ABSTRACT

Aerosol particles can be assumed to be in equilibrium with their environment when the ambient relative humidity is less than 100%. Approximation formulas expressing the equilibrium size of soluble and partly soluble particles as a function of relative humidity are derived. These formulas are combined with a dry aerosol size distribution model to compute the effect of relative humidity on visibility and particle size distribution. Above 100% relative humidity (i. e., fog) water vapor condenses preferentially on those aerosol particles which can exceed their critical size at the prevailing supersaturation. A numerical model which predicts the evolution of the droplet size distribution and visibility in maritime advection fogs is described. Data collected in fogs during a cruise of the USNS Hayes were used to test the predictive ability of the model. Good agreement was found between the observed and predicted fog microphysical properties.

1. INTRODUCTION

Optical propagation in the atmosphere is affected by the aerosol load. Aerosol particles absorb and scatter light in an amount which is proportional to their number and size (cross-sectional area). The marine aerosol size distribution is primarily a function of relative humidity, wind speed, atmospheric stability and air mass history. In order to assess quantitatively and realistically the effect of the propagation environment on the performance of electrooptical systems, the dependence of the aerosol size distribution on the above-mentioned parameters must be known. This paper describes some recent work on modelling the effect of relative humidity on aerosol size distribution and visibility.

2. AEROSOL SIZE AS A FUNCTION OF RELATIVE HUMIDITY

A solid aerosol particle which is composed totally, or in part, of a water-soluble material will undergo a transition to a saturated (or, in the case of very small particles, supersaturated) solution droplet when some critical value of relative humidity, less than 100%, is reached. The relative humidity at which this transition occurs depends on the chemical composition and, to a lesser extent, on the size of the particle. Below the transition point, particles acquire small amounts of water by adsorption and show little change in size with relative humidity. At relative humidities above the transition point, a particle (or more correctly, an aqueous solution droplet) grows by the absorption of water vapor. Above the transition point, the size of an aerosol particle is quite sensitive to the ambient relative humidity.

2.1. THEORY

Junge (1952) introduced the concept of a mixed nucleus to help explain the observed response of atmospheric aerosol particles to increases in relative humidity. Let us consider the simplest model of a mixed nucleus. In this model an aero-

UNCLASSIFIED

sol particle consists of an insoluble core surrounded by a shell of a soluble component in the form of a pure salt. The relationship relative humidity and the equilibrium size of such a particle, at relative humidities above the phase transition point, may be expressed (Fitzgerald, 1975)

$$S = \exp \left[\frac{2\sigma'}{r\rho' R_v T} \right] \left[1 + \frac{i\epsilon\rho_d M_w r_d^3}{M_s \{ \rho' [r^3 - r_d^3(1-\epsilon)] - \epsilon\rho_d r_d^3 \}} \right]^{-1}, \quad (1)$$

where S is the equilibrium saturation ratio (percent relative humidity divided by 100); r is the equilibrium radius of the particle (solution droplet); r_d and ρ_d are the radius and density of the dry particle; M_w is the molecular weight of water; M_s is the molecular weight of the soluble component; i is the van't Hoff factor; R_v is the specific gas constant of water vapor; ϵ is the mass fraction of soluble material in the dry particle and σ' and ρ' are the surface tension and density of the aqueous solution of the salt.

Junge (loc. cit.) found good agreement the observed growth with increasing humidity of artificially produced mixed nuclei consisting of a pure salt as the soluble component and the theoretical growth curves for the same particles. Measurements by Winkler (1973) have shown, however, aerosol particles in continental air masses exhibit more limited growth with increasing humidity than predicted by Eq. (1) for the fraction of soluble material contained in the particles. This deviation in behavior from Eq. (1) is explained by the fact that the soluble component of continental aerosol particles is actually a mixture of different salts. Ionic interactions in a mixed solution increase the solubility of the various ions and result in a reduction of water vapor lowering.

Measurements by Mészáros and Vissny (1974) and Jaenicke et al. (1971) of the size distribution and chemical composition of the marine aerosol indicate that sea-salt nuclei predominate above $1.0 \mu\text{m}$ radius (the so-called giant particles). Sea-salt nuclei were also found to comprise a sizeable, though variable, fraction of the large (0.1 to $1.0 \mu\text{m}$ radius) particles. The growth curves (size vs. relative humidity) of sea-salt nuclei are very nearly the same as those of pure sodium chloride particles. The behavior of sodium chloride particles is described by Eq. (1).

Eq. (1) is not a convenient form of the relationship between particle size and relative humidity for use in modelling the effect of relative humidity on aerosol size distribution, since particle size is not given as an explicit function of relative humidity. An accurate approximation to Eq. (1), in which the equilibrium radius of an aerosol particle is given as an explicit function of the variables r_d , S and ϵ , is presented in the following section.

2.2. APPROXIMATION FORMULAS

Eq. (1) was used to compute S as a function of r , r_d and ϵ for particles composed of some common salts. A plot of r as a function of r_d showed that, in the optically important size range of $0.05 \leq r_d \leq 5.0 \mu\text{m}$, a nearly linear relationship exists between $\log r$ and $\log r_d$ for $S \leq 0.995$. This suggested an approximation formula of the form

$$r = \alpha r_d^\beta, \quad (2)$$

where the parameters α and β are functions of S and ϵ .

The dependence of α on S and ϵ (for $\epsilon \geq 0.3$) may be expressed to within 5% accuracy, by

$$\alpha = \xi \{ 1 - k_1(1-\epsilon) - k_2(1-\epsilon^2) \} \exp \left(\frac{0.066S}{\Phi - S} \right), \quad (3)$$

UNCLASSIFIED

UNCLASSIFIED

where

$$\Phi = \begin{cases} 1.058, & 0.81 \leq S \leq 0.97 \\ 1.058 - \frac{0.0155(S-0.97)}{1.02-S^{1.4}}, & 0.97 < S \leq 0.995 \end{cases}$$

and

$$\left. \begin{array}{l} k_1 = 10.2 - 23.7S + 14.5S^2 \\ k_2 = -6.7 + 15.5S - 9.2S^2 \end{array} \right\}$$

The value of ζ depends only on the chemical composition of the soluble component of the particle. Table I lists the value of ζ for nine common electrolytes. Of these, $(\text{NH}_4)_2\text{SO}_4$ and NaCl are important constituents of atmospheric aerosols.

TABLE I.
VALUE OF THE PARAMETER ζ
FOR VARIOUS ELECTROLYTES

ELECTROLYTE	ζ
$(\text{NH}_4)_2\text{SO}_4$	1.20
NH_4NO_3	1.27
NaNO_3	1.40
NH_4Cl	1.48
CaCl_2	1.55
NaBr	1.58
NaCl	1.62
MgCl_2	1.69
LiCl	1.85

Fig. 1 shows α as a function of S for a particle composed entirely of ammonium sulfate ($\epsilon = 1.0$) and for a partly soluble particle composed of 30% by mass ($\epsilon = 0.3$) of ammonium sulfate.

The value of β is quite insensitive to both the chemical composition and mass fraction of soluble material in a particle. The functional dependence of β on S can be described, to within 3% accuracy (provided $\epsilon \geq 0.3$), by

$$\beta = \exp\left(\frac{0.00077S}{1.009 - S}\right), \quad S \leq 0.995. \quad (4)$$

For the moment, let us focus our attention on sodium chloride particles which, as we have pointed out, describe the behavior of sea-salt nuclei quite closely. Measurements have shown that with increasing humidity a sodium chloride crystal becomes a saturated solution droplet at a relative humidity between 70-75%. With decreasing humidity, however, a sodium chloride solution droplet becomes supersatura-

UNCLASSIFIED

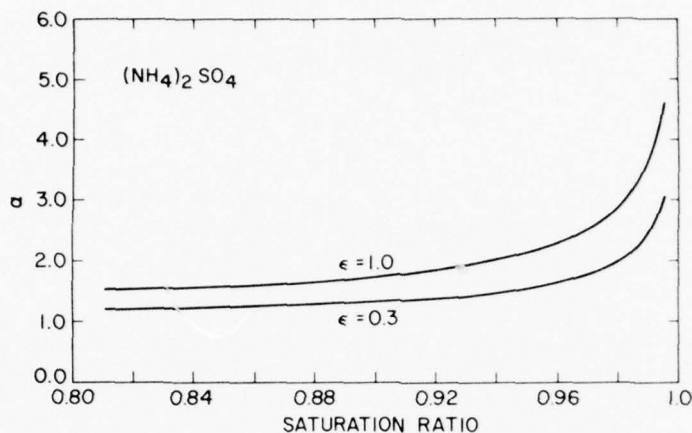


FIGURE 1. Parameter α as a function of saturation ratio for particles composed of two different percentages of ammonium sulfate.

ted and recrystallizes at a relative humidity between 35-45%. For the specific case of NaCl, an expression for α , valid for the entire range of relative humidity between 40 and 99.5%, is obtained by multiplying the right side of Eq. (3) by the factor A which is given by

$$A = \begin{cases} 1.0, & S \geq 0.8 \\ 1.16 - 0.2 S, & 0.4 \leq S \leq 0.80. \end{cases}$$

Since the relative humidity in the boundary layer over the ocean goes below 40% very infrequently, sea salt droplets will have little opportunity to crystallize. Therefore, sea-salt nuclei can be assumed to exist as solution droplets between 40 and 75% relative humidity.

2.3. EFFECT OF RELATIVE HUMIDITY ON AEROSOL SIZE DISTRIBUTION AND VISIBILITY

The formulas derived above can be applied to investigate the effect of relative humidity on the size distribution of a chemically homogeneous aerosol. It is well established that in the range $0.1 \leq r_d \leq 5.0 \mu\text{m}$, the size distribution of natural aerosols can be represented by a power law of the form (Junge, 1963)

$$\frac{dN}{d \log r_d} = Cr_d^{-\nu} \quad , \quad (5)$$

where N is the number of particles per unit volume which have a radius $\leq r_d$. The value of ν typically is between 2.5 and 3.5.

For a chemically homogeneous aerosol, a one-to-one correspondence exists between r and r_d . This means that $N(r) = N(r_d)$, r and r_d being related by Eq. (2). From Eqs. (2) and (5) we obtain

$$\frac{dN}{dr} = \frac{C}{2.36} \alpha^{\nu/2} r^{-(\nu/2 + 1)} \quad . \quad (6)$$

UNCLASSIFIED

Eq. (6), in conjunction with Eqs. (3) and (4), describes, in an approximate manner, the effect of relative humidity on the size distribution of an aerosol of uniform composition. Eq. (6) shows that the slope of the size distribution will decrease from ν to 0.94ν , as the relative humidity increases from 80 to 99%.

To illustrate the use of Eq. (6) to compute the effect of relative humidity on visibility, we consider an aerosol composed of solution droplets of sodium chloride (which describes the behavior of a sea-salt aerosol). Measurements have shown that the refractive index, m , of sodium chloride solution droplets for visible light is essentially the same as that of water. Accordingly, for the refractive index of NaCl solution droplets we took the value $m = 1.33 - 0.0i$. Since there is no absorption, the extinction coefficient of the aerosol population is equal to the scattering coefficient, k_s . Visibility, therefore, is equal to $3.91/k_s$. For an aerosol having a size distribution given by Eq. (6), k_s may be written

$$k_s = \frac{\pi C}{2.3\beta} \alpha^{\nu/\beta} \int_{r_1}^{r_2} r^2 r^{-(\nu/\beta+1)} Q dr , \quad (7)$$

where Q is the scattering efficiency factor and is computed from Mie scattering theory.

Eq. (7) was used to compute visibility as a function of relative humidity for an aerosol composed of NaCl solution droplets. The parameter C was taken to be 0.5. For ν we assumed a value of 3. We considered only the contribution to k_s of droplets which had a dry radius in the range 0.05 to $2.5 \mu\text{m}$. Results of the computations are shown in Fig. 2.

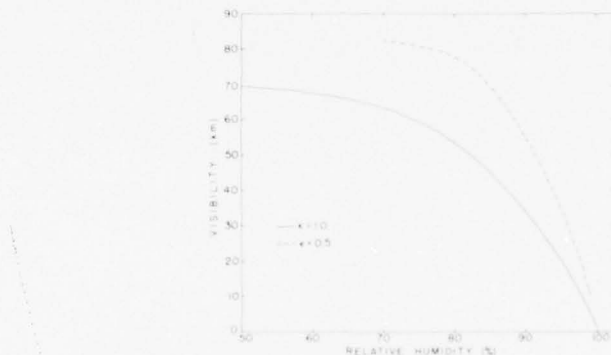


FIGURE 2. Visibility as a function of relative humidity, assuming an aerosol of sodium chloride solution droplets.

Fig. 2 shows that in the case of totally soluble NaCl particles ($e = 1.0$), the visibility can be expected to decrease by a factor of about 50 as the relative humidity increases from 50% to 100%. The dashed curve, for the case of particles composed of 50% sodium chloride and 50% of an insoluble component, was included to show the effect of reduced particle growth with humidity due to the presence of insoluble material. In this case, the crude assumption was made that the index of refraction of solution droplets containing an insoluble core, was the same as that of totally liquid salt solution droplets.

UNCLASSIFIED

UNCLASSIFIED

3. MARINE FOG VISIBILITY MODEL

When the relative humidity in the atmosphere exceeds 100%, water vapor condenses preferentially on certain aerosol particles, referred to as cloud condensation nuclei (CCN). These are particles which, by virtue of their composition, size and other properties, have a critical saturation ratio less than the saturation ratio attained in fogs and clouds. The critical saturation ratio of a particle is the maximum value of the equilibrium saturation ratio exhibited by the Kohler curve [a plot of Eq. (1) giving equilibrium saturation ratio vs. size] of the particle. Particles whose critical saturation ratio is exceeded by atmospheric conditions can experience unlimited growth and are no longer in stable equilibrium with the ambient humidity. These particles are said to be activated.

Visibility in fog will depend on: 1) the supersaturation spectrum of CCN (i. e., the number of particles per unit volume which have critical saturation ratios less than or equal to a given value) characterizing an air mass, 2) the rate at which moisture is made available for condensation and 3) the length of time droplet growth has proceeded.

A one-dimensional, numerical model of the evolution of droplet size distribution and visibility during the early stage of formation of maritime advection fogs has been developed. This model computes the growth, by condensation, of a population of cloud condensation nuclei contained in a parcel which is advected with the wind. The driving force for fog formation is a prescribed time rate of increase in the saturation ratio of the parcel in the absence of condensation. This humidity increase is viewed as resulting from infrared radiative cooling and from turbulent exchange of heat and moisture with the sea surface.

3.1. MODEL FORMULATION

The model is formulated by equations describing the time rate of change of saturation ratio and temperature of the parcel, by an equation for the time rate of change in water vapor mixing ratio due to condensation and by a droplet growth equation for each size class of condensation nucleus. These are:

$$\frac{dS}{dt} = \dot{S} + \frac{P}{\xi e_s} \left(\frac{dx}{dt} \right)' + \frac{L^2 M_w}{R^* T^2 (c_{pd} + x c_{pv} + w c_w)} \left(\frac{dx}{dt} \right)', \quad (8)$$

$$\frac{dT}{dt} = - \frac{R^* T^2}{L M_w} \dot{S} - \frac{L (dx/dt)'}{c_{pd} + x c_{pv} + w c_w}, \quad (9)$$

$$\left(\frac{dx}{dt} \right)' = - \frac{4}{3} \pi \frac{d}{dt} \int_0^{\infty} \rho' r^3 n(r) dr, \quad (10)$$

$$r \frac{dr}{dt} = \frac{\frac{D' e_s}{\rho_L R_v T} \left(S - B \exp \left[\frac{a}{r} \right] \right)}{1 + \frac{D' e_s L^2}{K' R_v^2 T^3} B \exp \left[\frac{a}{r} \right]}. \quad (11)$$

In these equations S is the saturation ratio of the ambient air; t is time; P is atmospheric pressure; ξ is the ratio of the specific gas constant of dry air to that of water vapor; e_s is the saturation vapor pressure over a plane surface of

UNCLASSIFIED

pure water; L is the latent heat of condensation; $(dx/dt)'$ is the time rate of change of water vapor mixing ratio due to condensation; w is liquid water mixing ratio; R^* is the ideal gas constant; c_{pd} , c_w and c_l are the specific heats at constant pressure of dry air, water vapor and liquid water, respectively; ρ_l is the density of water and $n(r)$ is the droplet size distribution function (droplets per gram of air per unit size interval).

In Eq. (11), $B_{exp}(a/r)$ is given by the right-hand side of Eq. (1) and D' and K' are so-called modified vapor diffusion and heat conduction coefficients, respectively. These coefficients allow for the transition from a kinetic theory growth regime valid for droplets which are small compared to the mean free path of water molecules in air to a purely diffusional growth regime valid for larger droplets. Defining equations for D' and K' are given by Fitzgerald (1974).

The first term, δ , on the right in Eq. (8) is the driving force for fog formation and is the rate at which the saturation ratio of the advecting parcel increases due to external influences such as infrared radiative cooling and diffusive cooling to the sea surface. The second term on the right in (8) represents the contribution to dS/dt due to the depletion of water vapor by the growing droplets. The third term in Eq. (8) expresses the effect of the release of latent heat. In Eq. (9), the first term on the right is the rate at which the temperature would have to decrease to produce a value of dS/dt equal to δ ; the second term is the rate of warming due to latent heat release.

The set of differential equations consisting of Eqs. (8), (9) and (10) the integral in (10) being replaced by a summation over a discrete droplet population and a droplet growth equation for each size class of nucleus (droplet) is integrated numerically using the standard fourth-order Runge-Kutta scheme. The principal inputs to the model are a prescribed value of δ and the supersaturation spectrum of cloud condensation nuclei of the air mass in which fog forms.

3.2. MODEL VERIFICATION

Observations made inside and outside several advection fogs during a cruise of the USNS Hayes off the coast of Nova Scotia in August 1975, were used to test the predictive ability of the model. The model was used to predict the evolution of visibility and droplet size distribution, at an altitude of 20 m, in the first 30 km downwind of the forming edge of these fogs. The values of δ used in these computa-

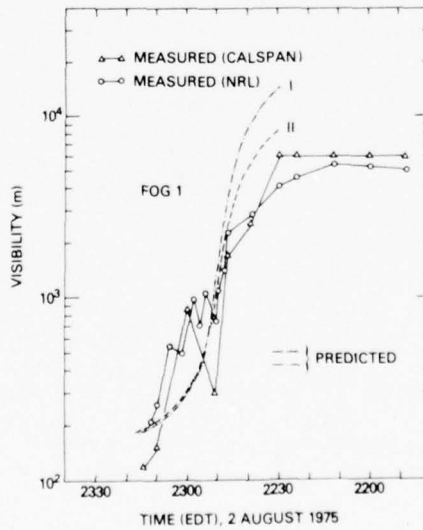


FIGURE 3. Comparison of observed and model-predicted visibilities for fog of 2 August 1975.

UNCLASSIFIED

tions were the measured rates of increase in the relative humidity of the advecting air mass as the fog boundary was approached.

Figures 3 and 4 show comparisons of measured and model-predicted visibilities for two fogs. Visibility was measured with an EG&G Forward Scatter Meter (used by Calspan Corp.) and with an MRI Fog Visiometer (used by the Naval Research Laboratory). Visibility predictions I and II were obtained using two different estimates of the supersaturation spectrum of CCN of the air at the time of fog formation. It is seen that the model predicted the visibility in these fogs with success. Both the predicted magnitude and time scale of the decrease in visibility as fog is en-

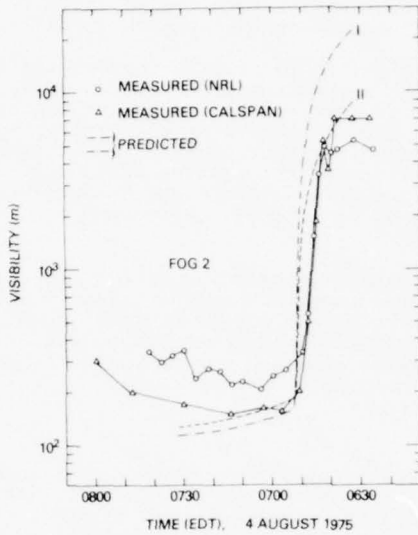


FIGURE 4. Comparison of observed and model-predicted visibilities for fog of 4 August 1975.

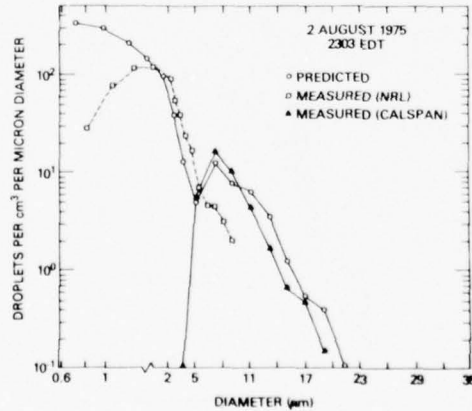


FIGURE 5. Comparison of observed and predicted droplet size distributions at a point 10 km downwind of the forming edge of the fog of 2 August 1975.

UNCLASSIFIED

UNCLASSIFIED

countered are in good agreement with observations. Measured and predicted visibilities agree to within a factor of two in fog.

Figures 5 and 6 are a comparison of measured and predicted droplet size distributions in the two fogs. Plotted is the droplet number density per micron diameter as a function of droplet size. The droplet measurements of the Naval Research Laboratory (NRL) were obtained with an Axially Scattering Spectrometer Probe, manufactured by Particle Measuring Systems, Inc. Calspan Corporation employed an impactor. This particular instrument is quite reliable for droplets larger than $4 \mu\text{m}$ diameter.

The model-predicted size distributions are bimodal. The bimodality results from the activation of only a portion of the nucleus population. Figures 5 and 6 show that the predicted distribution of activated droplets is in good agreement with the impactor data. It is also seen that the model was able to predict the high number density of small ($< 3.0 \mu\text{m}$ diameter) droplets detected with the scattering probe. The small droplets were "invisible" to the impactor.

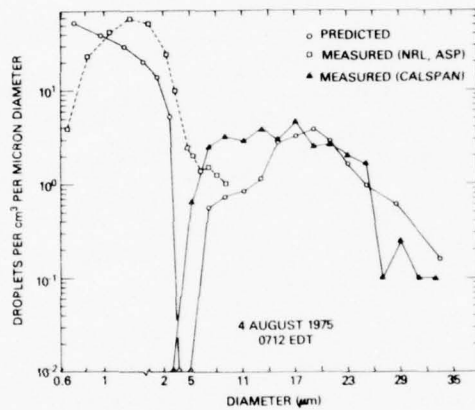


FIGURE 6. Comparison of observed and predicted droplet size distributions at a point 25 km downwind of the forming edge of the fog of 4 August 1975.

REFERENCES

Fitzgerald, J. W., 1974: Effect of aerosol composition on cloud droplet size distribution: A numerical study. *J. Atmos. Sci.*, 31, 1358-1367.

Fitzgerald, J. W., 1975: Approximation formulas for the equilibrium size of an aerosol particle as a function of its dry size and composition and the ambient relative humidity. *J. Appl. Meteor.*, 14, 1044-1049.

Jaenicke, R., C. Junge, and H. J. Kanter, 1972: Messungen der Aerosolgrossenverteilung über den Atlantik. *Meteor Forschungsergebnisse, Reihe b*, Nr. 7, Verlag Bornträger, Berlin, pp. 1-54.

Junge, C., 1952: Die Konstitution des atmosphärischen Aerosols. *Ann. Meteor.*, 5, 1-55.

Junge, C., 1963: *Air Chemistry and Radioactivity*. Academic Press, 383 pp.

Mészáros, A., and K. Vissy, 1974: Concentration, size distribution and chemical nature of atmospheric aerosol particles in remote oceanic areas. *Aerosol Sci.*, 5, 101-109.

UNCLASSIFIED

Winkler, P., 1973: The growth of atmospheric aerosol particles as a function of relative humidity. II. An improved concept of mixed nuclei. Aerosol Sci., 4, 373-387.

....This paper is UNCLASSIFIED

FOG CLIMATOLOGY IN CENTRAL EUROPE AND
INFERRRED PROPAGATION CHARACTERISTICS

by

Dr. O. M. Essenwanger and Dr. D. A. Stewart
US Army Missile Research, Development and
Engineering Laboratory
US Army Missile Command
Redstone Arsenal, Alabama 35809

ABSTRACT

Fog is one of the major obstacles to infrared and submillimeter wave propagation. Unfortunately, observational programs relating electro-optical propagation characteristics and atmospheric observations have not been made systematically, especially from the viewpoint of climatology.

Visibility is routinely observed for synoptic purposes, but classification of fog into various categories is seldom made. The present investigation will attempt such classification. As background material, some factors of general climatological information on visibility in Central Europe are presented (i.e. seasonal and diurnal variability and duration of fog). Fog is broken down into categories on the basis of objective criteria suitable for computer analysis of large data collectives.

This climatological study, although a first step, is insufficient to describe propagation characteristics in the infrared and submillimeter wavelength regions because propagation depends largely upon liquid water content and drop-size distributions which are not available in standard meteorological data. The data are limited even when the presently available measurements in various parts of the world are considered. Therefore, it is necessary to take each existing set of measurements and classify it according to the type of fog which is probably represented. This classification will be used to determine propagation characteristics for the different types of fog. Then we will refer back to the climatological data to determine temperature, pressure, and water vapor content usually associated with it. These parameters are needed to determine the clear air contribution to attenuation of the electromagnetic energy.

Finally, expected climatological variations of attenuation characteristics of infrared and submillimeter energy will be discussed.

I INTRODUCTION.

It is generally agreed upon that the electro-optical propagation characteristics are affected by the moisture content of the atmosphere and aerosols. Although impedance by non-aqueous aerosols is an important contribution, it is not the special topic of this discussion. Consequently, only the atmospheric moisture and its classification for visibility $\leq 1 \text{ km}$ will be examined for the Central European area.

It is common knowledge that visibility, if determined by an observer, is not a very precise meteorological characteristic. The visual range depends not only on the obscuration by water vapor, haze, or dust, but also on luminance and contrast of an object. Thus, the visibility as reported in the synoptic code, unless measured by instrumentation, must be considered as an atmospheric element of limited precision. Nonetheless, even coarse measurements have statistical properties, and deficiencies of the individual observations can be at least partially overcome by statistical analysis.

The importance of low visibility for electro-optical propagation cannot be overemphasized. These conditions are predictable (see e.g. Biberman, 1976, Essenwanger, 1973a), a fact which could be exploited in tactical situations to the disadvantage of electro-optical systems. Consequently, the evaluation of the electro-optical systems with reference to atmospheric effects must include proper consideration of these atmospheric conditions.

The customary tabulations of climatic elements include frequency of occurrence of visibility, and it should not be too difficult to obtain this information on visibility. Lesser known is the duration of events below a certain threshold, e.g. visibility $\leq 1 \text{ km}$ which is customarily called fog in meteorological terminology. Although the classes of fog are known from a theoretical point of view (e.g. radiation, advection, frontal, etc.), statistical information is scarcely available in the literature, and one can find statements like: "Fog in Central Europe is mostly of the radiative type" without statistical proof.

The authors have attempted to shed some light on this problem and assess the impact of their findings on electro-optical systems.

II. FREQUENCY AND DURATION OF LOW VISIBILITY IN CENTRAL EUROPE.

Although the frequency of occurrence of visibility is documented in various published and unpublished tabulations (e.g. Essenwanger, 1973a, b or Guss, 1959, etc.) it may be worthwhile to emphasize a few facts. Table I is included to stress the diurnal, seasonal, and orographic variability of events with visibility ≤ 1 km. As expected, frequencies are higher in winter and much lower in summer. Furthermore, fog peaks at sunrise, which is illustrated by the shift of the maximum to later hours (09 GMT) from summer to winter for most of the stations. The variability among stations displays the important role of the local orography. Thus, averaging as is customary in many climatological studies does no justice to proper evaluation of electro-optical systems. This fact has been stressed by Biberman (1976) too. The stations and period of record are the same as utilized by Essenwanger in an earlier study (1973b).

Although the contrast between fog occurrence in summer and winter is well known, the high rate of occurrence during the fall season at many stations in Central Europe is often overlooked (see Table II). Fluctuations of fog frequency from year to year are common, and a short record of one year must therefore be examined very carefully as to its typical standing within a longer series of data.

The climatological background may be completed with a survey of maximum duration in hours and days (Table III). It is relatively easy to establish the consecutive number of hours for the duration of fog. The problem of counting the consecutive days is rendered more difficult because of the question whether fog originating in the evening and lasting until the next morning should be counted as two days with fog. Under such a system a fog of 26 hours duration generated at 11 p.m. could emerge as 3 days with fog if the counting system were not changed. One solution would be the definition of a day from 6 p.m. to 6 p.m. the next day because fog origination is at its lowest point at 6 p.m. (see Essenwanger, 1973a). This division resolves the problem of the given example but will lead to others. A simple alternative has been employed here.

The fog was classified by its initial hour. The subsequent day was counted into the fog category when fog was observed at the same hour the next day. Thus, Table IIIb displays the maximum number of days where fog occurred on consecutive days for the same hour of the day. Although this formulation may not satisfy all problems, it permits evaluation of the predictability and implies limitations of electro-optical systems.

TABLE I. FREQUENCY OF VISIBILITY ≤ 1 km

a) DECEMBER THROUGH FEBRUARY.

	00	03	06	09	12	15	18	21 GMT	ALL
HANNOVER	6.0	6.5	6.5	7.4	4.0	3.0	3.6	4.6	5.2%
HOF	10.1	8.7	11.2	11.3	5.2	6.4	7.4	8.2	8.5
WEIDEN	6.2	(6.0)	5.6	6.8	3.0	2.6	3.9	4.4	4.8
STUTTGART	5.4	7.2	7.9	7.6	3.5	2.8	2.9	3.9	5.1
HEIDELBERG	7.5	7.9	8.5	11.0	7.8	6.3	6.8	6.2	7.7
BITBURG	9.6	11.4	12.5	13.2	9.1	7.3	7.0	7.9	9.8
HAHN	16.2	18.1	18.1	19.7	15.8	14.6	14.0	13.5	16.2
SEMBACH	6.7	7.7	8.5	11.3	7.1	5.2	5.6	5.7	7.2
FUERSTENFELDBRUCK	16.0	16.8	16.3	13.0	7.2	7.2	11.3	14.4	12.8
GRAFENWOEHR	6.3	6.9	8.6	11.2	5.2	3.0	4.4	5.9	6.5
FRANKFURT/MAIN	6.2	6.8	7.7	9.9	6.5	6.2	4.8	5.3	6.7
FULDA	3.5	3.9	7.5	9.7	6.5	3.6	3.7	2.2	5.9
BERLIN	3.5	4.2	4.9	7.2	4.3	2.9	2.4	2.8	4.0

b) JUNE THROUGH AUGUST.

	00	03	06	09	12	15	18	21 GMT	ALL
HANNOVER	0.8	4.4	2.2	0.2	-	-	-	0.0	0.9%
HOF	2.2	7.7	4.7	0.6	0.6	0.5	0.6	0.6	1.6
WEIDEN	1.5	(2.2)	2.9	-	-	-	-	-	0.8
STUTTGART	0.4	1.7	2.2	0.2	-	-	-	0.0	0.6
HEIDELBERG	0.2	1.0	1.7	0.2	0.0	0.0	0.0	0.0	0.4
BITBURG	0.8	3.3	5.5	0.5	0.0	0.1	0.0	0.2	1.3
HAHN	2.3	5.6	6.5	1.6	0.5	0.3	0.7	1.0	2.3
SEMBACH	0.9	3.3	5.3	0.7	-	-	0.0	0.2	1.3
FUERSTENFELDBRUCK	0.9	3.2	3.4	0.3	-	0.0	0.1	0.1	1.0
GRAFENWOEHR	1.7	6.0	10.6	1.3	0.0	-	-	0.2	2.4
FRANKFURT/MAIN	0.2	1.5	2.1	0.2	-	0.0	0.0	0.0	0.5
FULDA	1.3	6.8	11.3	2.8	0.1	-	-	-	2.9
BERLIN	0.1	0.4	0.4	0.1	0.0	-	0.0	0.0	0.1

TABLE II. FREQUENCY OF VISIBILITY ≤ 1 KM IN CENTRAL EUROPE (WINTER 09, OTHER SEASONS 06)

	DEC-FEB	MAR-MAY	JUN-AUG	SEP-NOV
STUTTGART	7.4%	4.1	2.5	15.3%
HEIDELBERG	11.3	2.7	1.7	13.9
BITBURG	15.1	5.4	5.7	15.4
HAIN	20.2	8.0	5.9	20.2
SEMBACH	12.4	3.4	5.6	15.7
FUERSTENFELDBRUCK	12.7	5.7	3.6	19.4
GRAFENWOEHR	10.9	11.3	12.2	23.3
FRANKFURT/MAIN	10.0	2.6	2.5	13.0
FULDA	9.9	8.8	12.1	26.3
BERLIN	7.8	2.2	0.3	6.2

III. RADIATION AND NON-RADIATION FOG.

It is usually assumed that radiation fog has a lower liquid water content and smaller droplets than other types of fog. Consequently, radiation fog generates less impedance on electro-optical systems than other types of fog. Because information on this type of fog is not given in the synoptic code, no simple statistical analysis can be performed. Thus, conclusions about the types of fog are customarily made on the basis of general meteorological background. E.g., it is assumed that fog in coastal areas comprises primarily advection fogs and mixture of air masses while fog in continental areas is predominantly of the radiation type. For the evaluation of electro-optical systems the impact of these conclusions is significant. The authors have attempted therefore to elucidate some facts and examine the question whether statistical information and classification of fog can be obtained by computerized methods.

In the time available for this study more sophisticated systems could not be designed. Consequently, it was decided to split the group with low clouds, where the temperature decreases between 0 and 5°F, equally between the two groups. The frequency within the five original groups is exhibited, however, for the reader's own judgment and conclusions.

TABLE III. MAXIMUM DURATION OF VISIBILITY \leq 1 KM.

a) HOURS.

	JAN	FEB	MAR	APR	MAY	JUN	JUL	AUG	SEP	OCT	NOV	DEC
STUTTGART	45	15	13	11	8	6	8	7	13	18	56	33
HEIDELBERG	72	66	16	10	6	6	7	9	10	45	65	45
BITBURG	52	48	19	9	7	7	6	9	14	28	61	53
HAHN	71	52	34	23	12	18	13	13	16	87	99	96
SEMBACH	33	56	14	8	12	11	11	10	14	41	28	53
FUERSTENFELDBRUCK	92	44	15	6	6	5	6	8	21	31	81	123
GRAFENWOEHR	19	19	15	11	11	11	10	9	19	18	28	33
FRANKFURT/MAIN	61	71	29	10	7	5	6	8	11	39	61	46
FULDA	17	13	7	9	9	7	9	7	13	17	36	17
BERLIN	31	31	22	6	9	3	6	12	10	21	20	35

b) DAYS.

STUTTGART	5	5	3	3	2	2	3	2	6	7	6	4
HEIDELBERG	7	8	2	2	2	1	3	1	4	9	6	5
BITBURG	6	5	3	2	3	3	5	3	3	10	5	8
HAHN	9	7	4	4	4	5	4	3	4	9	10	8
SEMBACH	4	5	2	3	3	5	2	5	8	7	4	5
FUERSTENFELDBRUCK	11	4	4	2	2	2	2	2	8	6	6	13
GRAFENWOEHR	3	7	4	4	5	3	2	5	6	7	4	4
FRANKFURT/MAIN	3	6	2	2	1	1	2	2	5	8	12	6
FULDA	4	6	3	3	2	4	2	6	7	20	4	3
BERLIN	3	4	7	2	1	1	1	1	3	4	4	5

The authors' inference of the two groups is found in the last two columns of Table IV. Although the percentages for the two stations diverge somewhat in 3 seasons, surprisingly the winter provides about the same percentages split. If these tentative results hold up in a subsequent and more thorough and sophisticated analysis, fog in wintertime in Central Europe may not be mostly of the radiative type. Even a considerable reduction of the non-radiative group would leave a sizable fraction of the non-radiative type. The consequences for electro-optical systems, if these tentative conclusions can be confirmed are obvious.

IV. Mie Calculations.

We at Physical Sciences Directorate (Micom) are primarily interested in atmospheric propagation of infrared and submillimeter waves through fog in Europe, but there is a severe shortage of the needed measurements. Our special goal is to relate infrared and submillimeter propagation characteristics to standard meteorological measurements, but the systematic atmospheric measurements to develop such relationships are unavailable at the present. Therefore, it was decided to make theoretical computations and use these for estimating the atmospheric attenuation.

Space limitations for this report do not permit discussion of the Mie theory which was used for the computations. The theory is discussed extensively by Kerker (1969) in Chapter 3, and additional useful information on Bessel functions is found in Weeks (1964) on pages 533-538. The accuracy of our computational procedure was checked by making test calculations for comparison with tables of normalized efficiency factors published by the U. S. Bureau of Standards (1949) and Irvine and Pollack (1968).

The necessary amount of computation depends upon the ratio of particle radius to wavelength of electromagnetic radiation, and computation time is much longer for visible wavelengths than for longer wavelengths. Therefore, it was assumed that scattering is the only source of attenuation at visible wavelength and that the index of refraction of water is 1.33. These assumptions permitted the use of normalized scattering efficiency factors given in Appendix J of McCartney (1976) taken from Penndorf (1957).

The complex index of refraction of liquid water at 10.5 μm in the infrared was taken to be $1.185 - 0.0662i$ after Hale and Querry (1973).

The complex index of refraction at 1250 μm was taken to be $2.63 - 1.1407i$ after Davies et al. (1970). This was in reasonable agreement with values which could be interpolated from tables in Rozenberg (1974).

TABLE IV. FOG CLASSIFICATION.

a) FRANKFURT (1946-1970).

No Fog	With Precip	FOG				FOG		
		f_c	With Clouds f_{c_0} 0 to -5°	f_{c_5} $< -5^{\circ}$	Pure radiation f_r	Other	Predomi- nately radiation	
DEC-FEB	91.7%	1.4	1.7	4.1	0.8	0.3%	62	38%
MAR-MAY	96.6	0.6	0.4	1.2	0.4	0.8	47	53
JUN-AUG	97.5	0.1	0.3	1.6	0.1	0.4	47	53
SEP-NOV	85.8	1.4	2.9	5.9	1.5	2.5	51	49

b) GRAFENWOEHR (1959-1970).

DEC-FEB	90.4	4.3	1.0	1.7	0.6	2.0	63	37%
MAR-MAY	87.4	4.0	0.4	2.4	2.6	3.2	44	56
JUN-AUG	86.9	3.0	0.0	2.2	2.8	5.1	31	69
SEP-NOV	75.2	5.7	1.0	5.2	3.9	9.0	37	63

$$\Delta t = t_{06} - t_{00} \text{ (in } {}^{\circ}\text{F)}$$

$$\text{Predominately radiation} = f_r + f_{c_5} + 0.5 f_{c_0}$$

Fog drop-size distributions were obtained from Garland (1971), Eldridge (1966), and Pederson and Todsen (1960), and results of the computations of attenuation are shown in Figs. 1 and 2. One sees immediately that there is a great deal of scatter in the data. This result is consistent with measurements made by Bisyarin et al. (1971) at 10.6 μm in real fogs. Richer (1970) found appreciable changes of propagation at 140 GHz (2143 μm) within one fog during a time when no apparent visibility changes occurred. One should not assume that the attenuations in Fig. 2 for 1250 μm are the total attenuations in a real fog. Attenuation by water vapor is significant at this wavelength and would have to be added.

V. INFERENCES ABOUT EUROPEAN FOGS.

Using the above computations and climatological data, one can infer attenuation characteristics of fogs in Europe.

From the data in Figs. 1 and 2 we estimated attenuation in radiation and non-radiation fogs. Attenuation in non-radiation fogs was calculated from the four fogs labeled advection in the figures. The unknown fogs had drop-size distributions which would be expected in radiation fogs, and all were included in the estimation of attenuation in radiation fogs. The mean 10.5 μm attenuation was 37 per cent of visible attenuation in radiation fogs, and 78 per cent of visible attenuation in non-radiation fogs. This is not inconsistent with Bisyarin et al. (1971) who found that the mean ratio of attenuation at 10.6 μm to attenuation at 0.63 μm was 0.38 for several real fogs and 0.43 for laboratory fogs. They indicated that about fifteen per cent of their ratios were less than 0.20 and about fifteen per cent were greater than 0.60 in the real fogs. Our estimate that 10.5 μm attenuation is expected to be 78 per cent of the visible attenuation in advection fogs is much higher than any estimates by Johnston and Burch (1967), but their work was mainly concerned with laboratory fogs. At 1250 μm the attenuation by fog droplets is 2.00 per cent of the visible attenuation in non-radiation fogs and 0.78 per cent of visible attenuation in radiation fogs. Table V shows the expected mean attenuations at three different visibilities. Past experience with German fogs indicates that a visibility less than 400 meters occurs about 40 per cent of the time, and a visibility less than 200 meters occurs in about 20 per cent of the fog cases.

At 1250 μm one must also consider attenuation by water vapor, and we used the model developed by Webster (1973). Table VI shows the mean seasonal attenuation of each type of fog by water vapor. The third column contains the weighted mean water vapor attenuations based on the mean of the per cent durations obtained for Frankfurt and Grafenwoehr in the last two columns of Table IV.

FIGURE 1. ATTENUATION OF FOG DROPLETS AT 10.5 MICROMETERS AS A FUNCTION OF VISIBILITY.

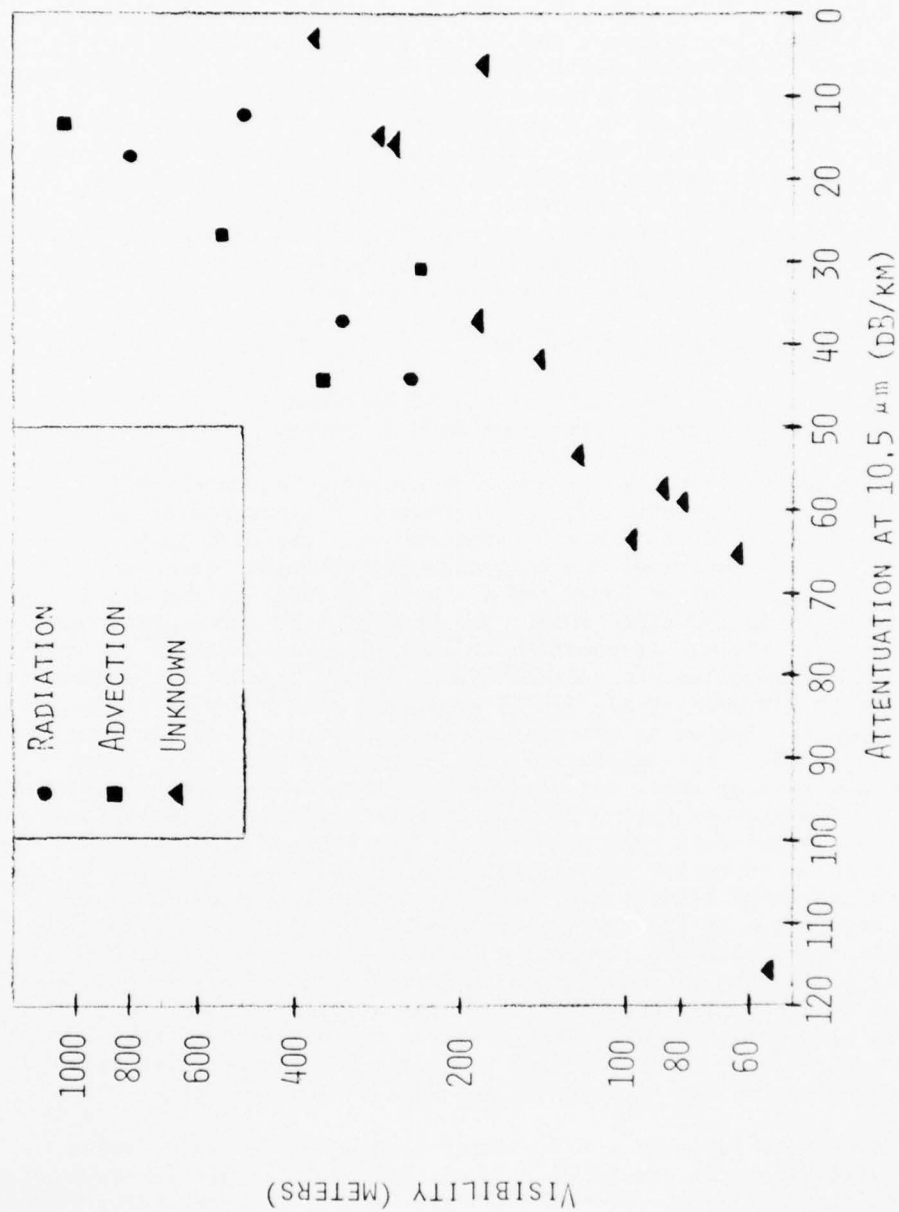


FIGURE 2. ATTENUATION OF FOG DROPLETS AT 1250 MICRÔMETERS
AS A FUNCTION OF VISIBILITY.

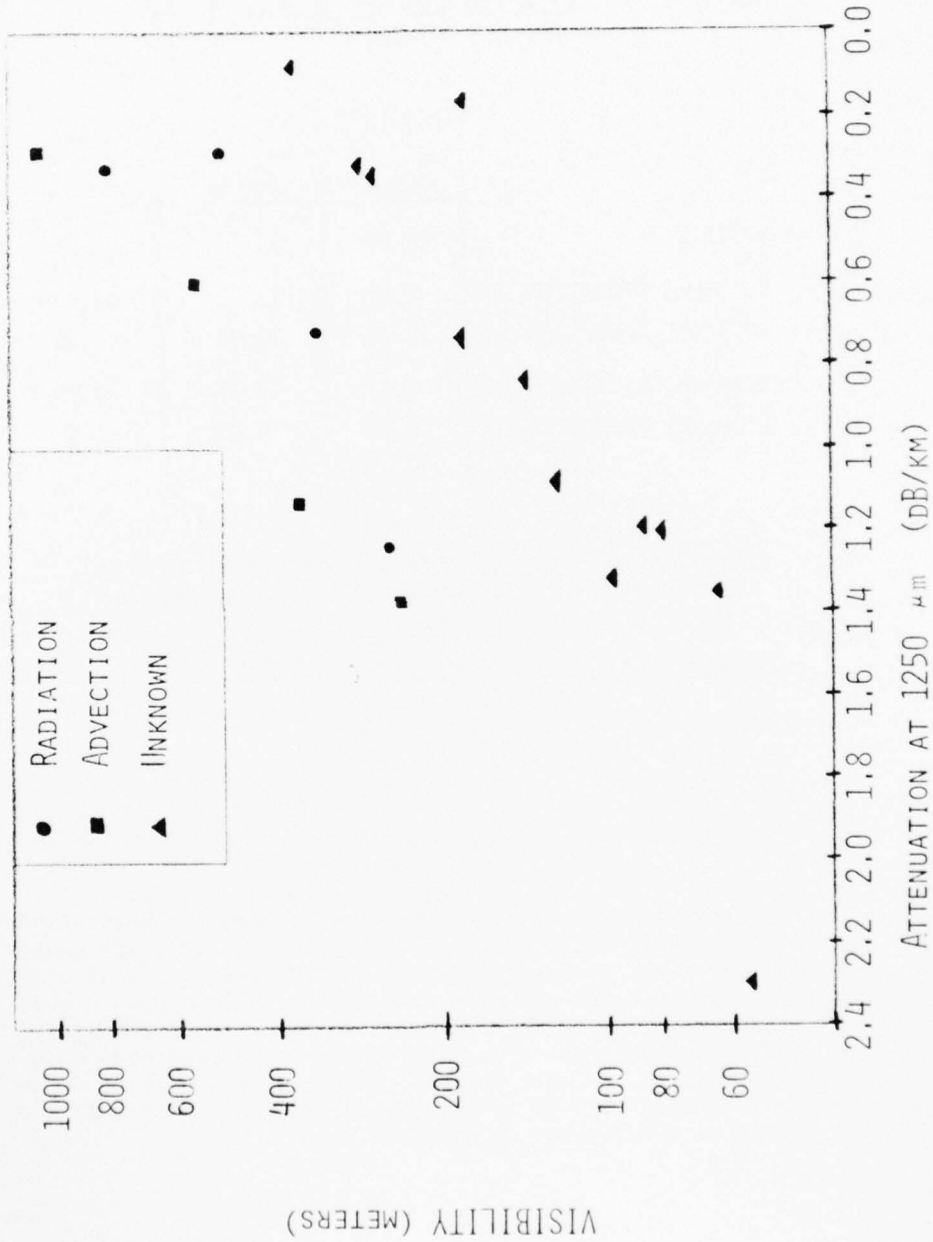


TABLE V. EXPECTED MEAN ATTENUATION BY FOG DROPLETS (dB/km).

VISIBILITY

	1000 m	400 m	200 m
VISIBLE	16.99	42.77	84.95
10.5 μm , RADIATION FOG	6.29	15.82	31.43
10.5 μm , ADVECTION FOG	13.25	33.36	66.26
1250 μm , RADIATION FOG	0.13	0.33	0.66
1250 μm , ADVECTION FOG	0.34	0.86	1.70

TABLE VI. MEAN SEASONAL ATTENUATION OF 1250 μm BY WATER VAPOR IN FOGS (dB/km).

SEASON	NON-RADIATION	RADIATION	WEIGHTED MEAN
DEC-FEB	2.19	1.79	2.04
MAR-MAY	2.54	2.42	2.47
JUN-AUG	3.94	3.72	3.83
SEP-NOV	3.23	2.98	3.09

Finally, Table VII gives the overall mean attenuations expected in fogs in Europe based on data from Frankfurt and Grafenwoehr. No attempt was made to consider variations of water vapor as a function of visibility because the data have not yet been analyzed this way. All results must be considered tentative because of the limited data. We plan to analyze data from more stations and from more drop-size distributions in the near future. However, we feel that it is safe to conclude that 10.5 μm attenuation will normally be much greater than 1250 μm attenuation in European fogs.

TABLE VII. ESTIMATED MEAN ATTENUATION IN FOG (dB/km) AS A FUNCTION OF VISIBILITY.

VISIBILITY			
	1000m	400m	200m
DEC-FEB			
10.5 μm	10.64	26.78	53.20
1250 μm	2.30	2.70	3.35
MAR-MAY			
10.5 μm	9.46	23.80	47.28
1250 μm	2.70	3.04	3.60
JUN-AUG			
10.5 μm	9.00	22.66	45.01
1250 μm	4.04	4.37	4.90
SEP-NOV			
10.5 μm	9.35	23.54	46.76
1250 μm	3.31	3.65	4.21

VI CONCLUSIONS.

Our tentative classification of fog has shown that probably more non-radiation type of fog exists in Central Europe than commonly anticipated. We shall attempt to follow up our study with a more thorough and sophisticated analysis.

Attenuations and scattering efficiencies were calculated for 10.5 μm and 1250 μm for radiation and non-radiation type of fog. Although our results are tentative, they show that attenuation would be much higher at 10.5 μm than at 1250 μm in Central European fogs. We shall expand our studies, however, by including additional data for Central European fogs after the more sophisticated analysis of fogs in Central Europe has been completed.

VII REFERENCES.

Biberman, L. M., 1976: Effect of weather at Hannover, Federal Republic of Germany, on performance of electro-optical imaging systems. IDA, Paper P-1123, pp 273.

Bisyarin, V. P., I. P. Bisyarina, and A. V. Sokolov, 1971: Attenuation of 10.6 μm laser radiation in artificial and real fog. Radio Eng. Elect. Phys., 16, 1589-1594.

Davies, M., G. W. F. Pardoe, J. Chamberlain, and H. A. Gebbie, 1970: Submillimetre- and millimetre-wave absorptions of some polar and non-polar liquids measured by Fourier transform spectroscopy. Trans. Faraday Soc., 66, Part 2, 273-292.

Eldridge, R. G., 1966: Haze and fog aerosol distributions. J. Atmos. Sci., 23, 605-613.

Essenwanger, O. M., 1973a: On the duration of widespread fog and low ceiling in Central Europe and some aspects of predictability. US Army Missile Command Technical Report RR-73-9, pp 55.

Essenwanger, O. M., 1973b: On spatial distribution of visibility and clouds in Central Europe. US Army Missile Command Technical Report RR-73-10, pp 60.

Garland, J. A., 1971: Some fog droplet size distributions obtained by an impaction method. Quart. J. Roy. Meteor. Soc., 97, 483-494.

Guss, H., 1959: Sichtweite und Bewoelkung an deutschen Verkehrsflughaeften. Ber. Dt. Wetterdienst, Nr. 52, pp 57.

Hale, G. M. and M. R. Querry, 1973: Optical constants of water in the 200-nm to 200 μm wavelength region. Appl. Optics, 12, 555-563.

Irvine, W. M. and J. B. Pollack, 1968: Infrared optical properties of water and ice spheres. Icarus, 8, 324-360.

Johnston, D. R. and D. E. Burch, 1967: Attenuation by artificial fogs in the visible, near infrared, and far infrared. Appl. Optics, 6, 1497-1501.

Kerker, M., 1969: The Scattering of Light and Other Electromagnetic Radiation, Academic Press, see pp. 27-75.

McCartney, E. J., 1976: Optics of the Atmosphere. New York, John Wiley and Sons, 408 pp.

Pedersen, K. and M. Todsen, 1960: Some measurements of the micro-structure of fog and stratus clouds in the Oslo area. Geofysiske Publikasjoner, 21, No. 7, 1-16.

Penndorf, R., 1957: New tables of total Mie scattering coefficients for spherical particles of real refractive index. J. Opt. Soc. Am., 47, 1010-1015.

Richer, K. A., 1970: Environmental effects on radar and radio-metric systems at millimeter wavelengths. Proc. Symposium on Submillimeter Waves, Polytechnic Institute of Brooklyn, Mar 31 - Apr 2, 1970, pp. 533-543.

Rozenberg, V. I., 1974: Scattering and Attenuation of Electromagnetic Radiation by Atmospheric Particles. NASA Technical Translation F-771 of a Russian Hydrometeorological Press publication in Leningrad in 1972.

U. S. National Bureau of Standards Computation Laboratory, 1949: Tables of Scattering Functions for Spherical Particles. Washington, D. C., U. S. Government Printing Office. (Printed in 1948 and issued 25 January 1949.)

Webster, D. W., 1973: Military Potential of the Extreme Infrared: Technology and Applications. Naval Weapons Center Report TP 5565. Catalogued under AD915347. (Distribution is limited to U. S. Government agencies.)

Weeks, W. L., 1964: Electromagnetic Theory for Engineering Applications. New York, John Wiley and Sons, 744 pp.

VIII ACKNOWLEDGEMENT:

The authors wish to express their appreciation for the assistance by Mrs. H. Boyd and Mr. D. McLain in establishing computer programs for the classification of fog. Mrs. C. Brooks deserves our thanks for her patience in typing the manuscript during the short allotted time.

(This page intentionally left blank.)

.... This paper is UNCLASSIFIED

THE NATURE OF GUN SMOKE AND DUST OBSCURATION
DUE TO CANNON FIRING

E. W. Stuebing, F. D. Verderame, R. W. Doherty,
J. J. Pinto, E. A. Lucia, and SP4 G. Vinansky

Pitman-Dunn Laboratory
Frankford Arsenal
Philadelphia, PA 19137

ABSTRACT

Fire control systems must contend with maintaining target visibility during firing. In addition, sophisticated future fire control systems have been proposed which provide an optical guidance link to the projectile, or track a fired projectile along its trajectory and sense the miss distance at the target for automatic correction. To be successful, these systems must be able to optically track the projectile during the first few seconds after firing, during which time the transparency of the atmosphere near the muzzle is very seriously degraded by gun gases, gun smoke, and dust clouds created from the ground by muzzle blast. This paper presents an analysis of optical transmission data in three wavelength regions (visible, near IR, and far IR) collected for single shot firing of a Rarden 30 mm cannon. Spectroscopic and light scattering techniques are used to identify muzzle gas and aerosol components, and a quantitative model is constructed using Mie scattering calculations to identify equivalent monodisperse aerosols for the smoke and dust. Concentrations of ammonia gas from the muzzle emission which produce significant extinction in the $10.6\mu\text{m}$ spectral region are identified and their dissipation with time is followed. Aerosol obscuration effects are found to be due to two separate aerosols arising in different time regimes after firing. Obscuration is initially attributed to a water-based gun smoke aerosol of $1.0\text{-}1.5\mu\text{m}$ particles followed in 3 to 6 seconds by a clay-based dust aerosol of $4\text{-}5\mu\text{m}$ particles rising from the ground. The evolution of each aerosol in terms of changing particle sizes and number densities is followed, and the interplay of absorption effects and scattering effects at various wavelengths is discussed.

UNCLASSIFIED

INTRODUCTION

Sophisticated future fire control systems have been proposed which track a fired projectile along its trajectory and sense the miss distance at the target for automatic correction. To be successful, the system must be able to optically track the projectile during the first few seconds after firing, during which time the transparency of the atmosphere near the muzzle is very seriously degraded by gun gases, gun smoke, and dust clouds created from the ground by muzzle blast. We here present an analysis of optical transmission data in three wavelength regions (visible, near IR, and far IR) collected for single shot firing of a Rarden 30 mm cannon, which results in a quantitative model for the gun smoke aerosol and for the dust aerosol responsible for the obscuration. The purpose of this study is to contribute data on obscuration effects which is required as part of an assessment of the relative potential of lasers operating at wavelengths of $0.53\mu\text{m}$, $1.06\mu\text{m}$, and $10.6\mu\text{m}$ for providing an active projectile tracking system. This study was sponsored by the Photoelectric Laboratory and by the Automatic Cannon Technology Fire Control Office of the Fire Control Development and Engineering Directorate, Frankford Arsenal.

DATA RESOURCES

The optical transmission data on which this study is based was taken from a series of experiments conducted by Heater, Pontelandolfo, and McKeough¹ at Aberdeen Proving Ground during the summer of 1974. Each shot of the Rarden 30 mm cannon was filmed and optical transmission data was recorded for a path 93 feet long, parallel to the gun-target axis and passing alongside the muzzle. These radiometric measurements were made in two optical bands of 200 \AA width centered about wavelengths of $0.53\mu\text{m}$ and $1.06\mu\text{m}$, and in a third optical band of $0.22\mu\text{m}$ width centered about $10.6\mu\text{m}$. The films of each shot were reviewed to select for analysis one with wind conditions as quiet as possible in order to avoid confounding intrinsic aerosol effects with transmission changes due to wind moving the aerosol cloud around in the optical path; in this way shot #3 was selected for detailed analysis. The data are shown in Figure 1.

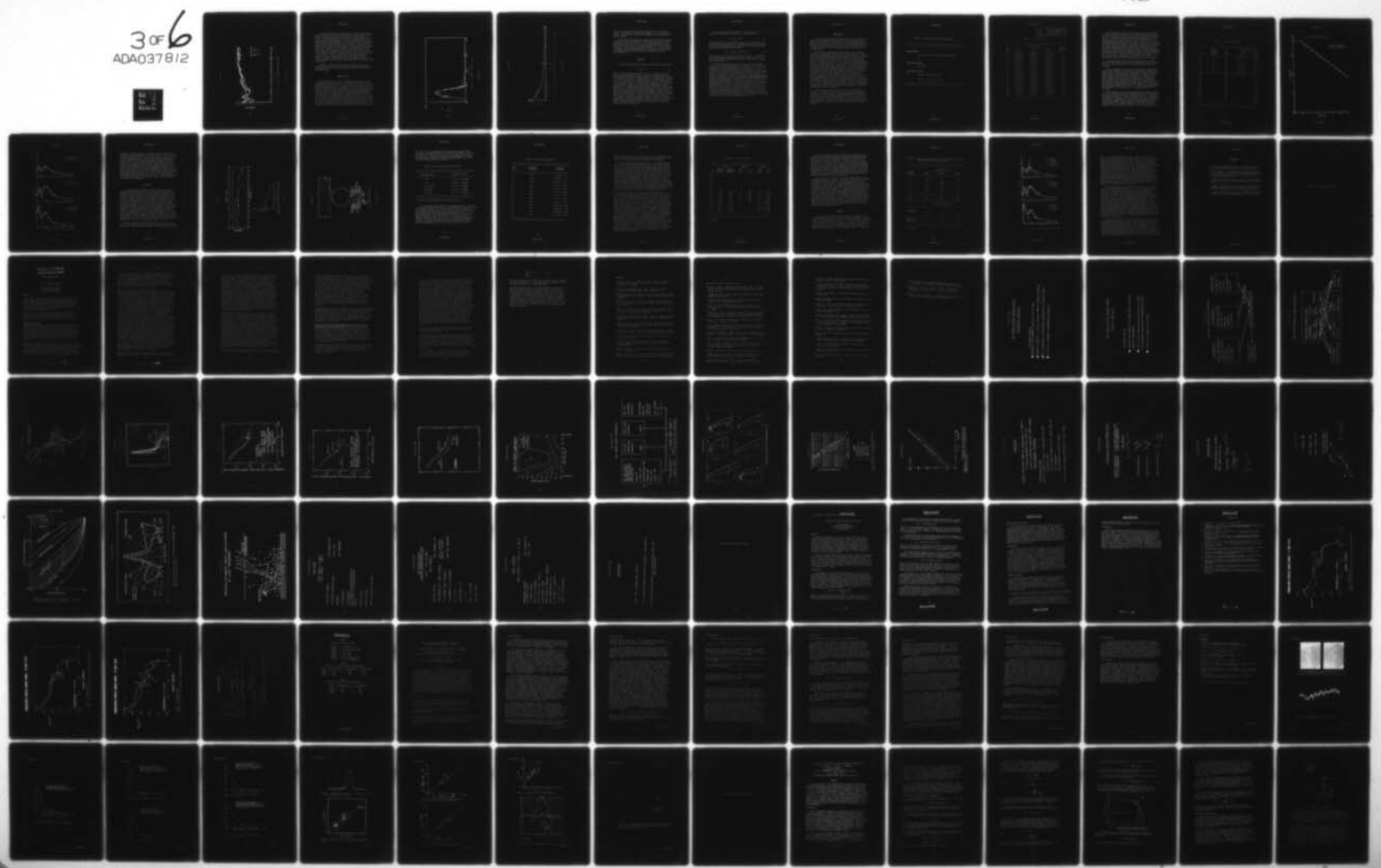
AD-A037 812

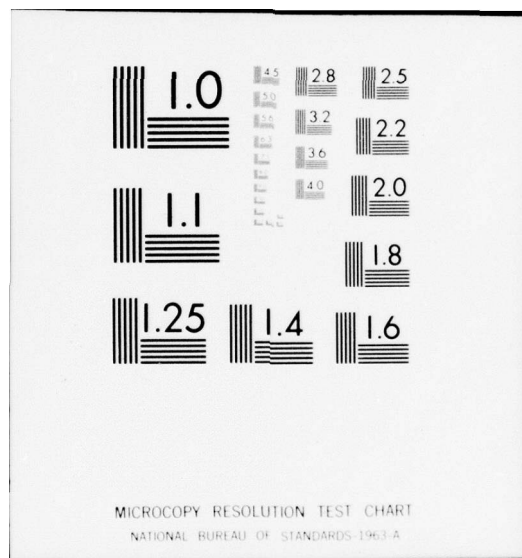
OFFICE OF THE DIRECTOR OF DEFENSE RESEARCH AND ENGINE--ETC F/G 20/14
PROCEEDINGS OF THE OPTICAL-SUBMILLIMETER ATMOSPHERIC PROPAGATIO--ETC(U)
DEC 76

UNCLASSIFIED

NL

3 of 6
ADA037812





UNCLASSIFIED

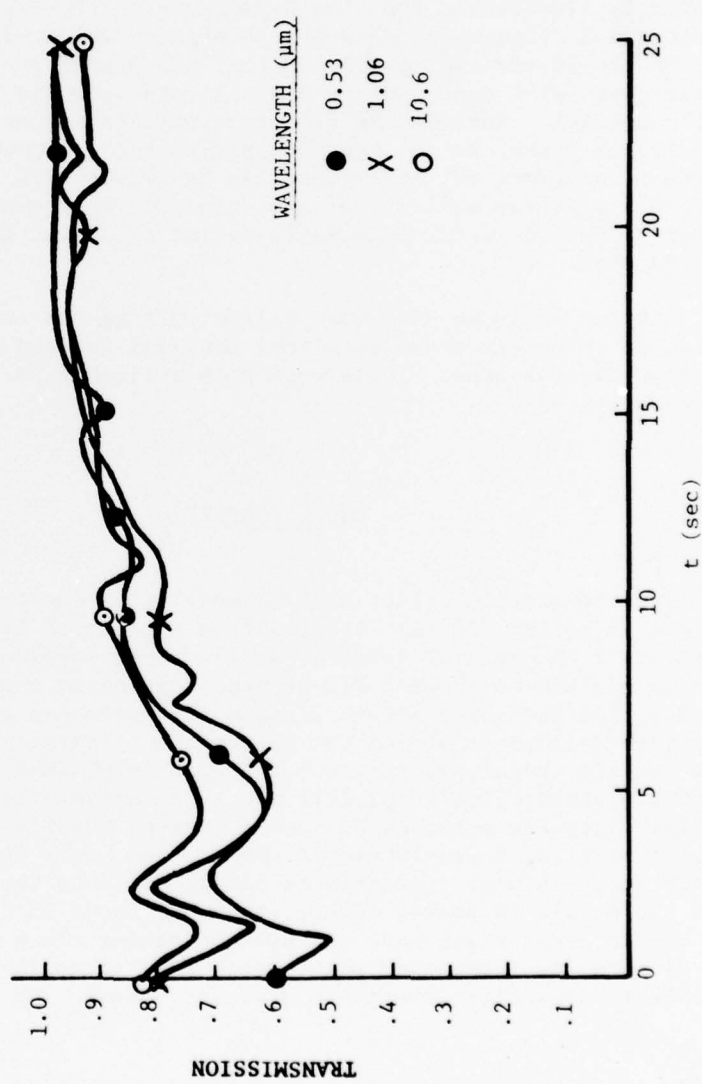


Fig. 1. Transmission vs. Time (secs.) for Shot 3.

UNCLASSIFIED

The infrared transmission spectrum over a similar optical path was available for one of the other shots (#4). This data, as reduced from the Fourier transform spectrometer recording, is shown in Figure 2. The basic envelope of the peak in the 800-1450 cm^{-1} region is the emission of the glowing coil source. The jagged absorption bands along the high wavenumber side of the envelope are due to water, the strong absorption doublet in the 900-1000 cm^{-1} region and nearby weaker bands are due to ammonia (NH_3). Following the decay of this doublet in time showed the time dependence of the NH_3 absorption which is plotted in Figure 3. This NH_3 absorption falls within the band pass of the 10.6 μm radiometer, so that the presence of NH_3 in the muzzle gases will confound the optical data we would like to attribute to the aerosol. Because the spectrometer data was not available for shot #3, it cannot be related directly to the radiometer data of Figure 1; however, NH_3 absorption can be expected to interfere seriously with the validity of any inference on the aerosol based on 10.6 μm radiometer data, especially during the first 2-3 seconds following the shot.

Samples of loose dirt were collected from the surface of the ground at three different locations near and forward of the muzzle by the experimental crew. These were made available to the authors for laboratory study.

MODEL CONCEPT

The obscuration effect will be modeled as due to two aerosols: (1) gun smoke and (2) dust created from the ground by muzzle blast. In Figure 1 the general features at all three wavelengths show a transmission minimum at about 1 1/2 seconds, rising to a maximum at 2 1/2 seconds, followed by a second minimum at 4 seconds, and then gradually rising to well above 90% as the obscuration clears. Examination of the data for all shots¹ reveals that this double minimum (min-max-min) structure within 5 seconds, followed by relatively smooth restoration of visibility, is a common feature. Viewing the films of the shots shows that first a greyish-white smoke cloud forms in the air in front of the muzzle almost instantly on firing (it does not appear to issue from the muzzle as smoke, rather the smoke forms in the air), and second, the muzzle blast shock wave can be seen racing along the ground sweeping along a low-lying dust skirt which then rises in a swirling, turbulent cloud after the shock wave has passed. By timing the visible

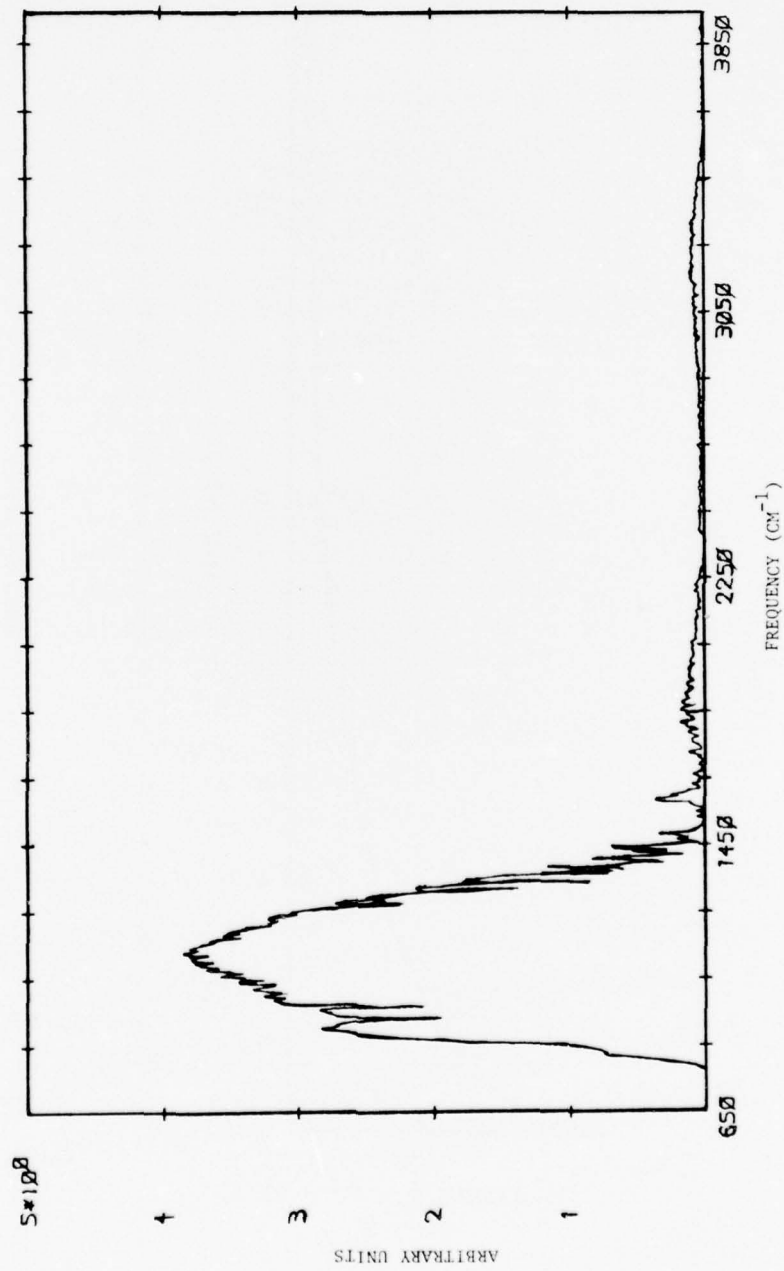


Figure 2. Infrared Spectrum of Gun Smoke and Gases.

UNCLASSIFIED

UNCLASSIFIED

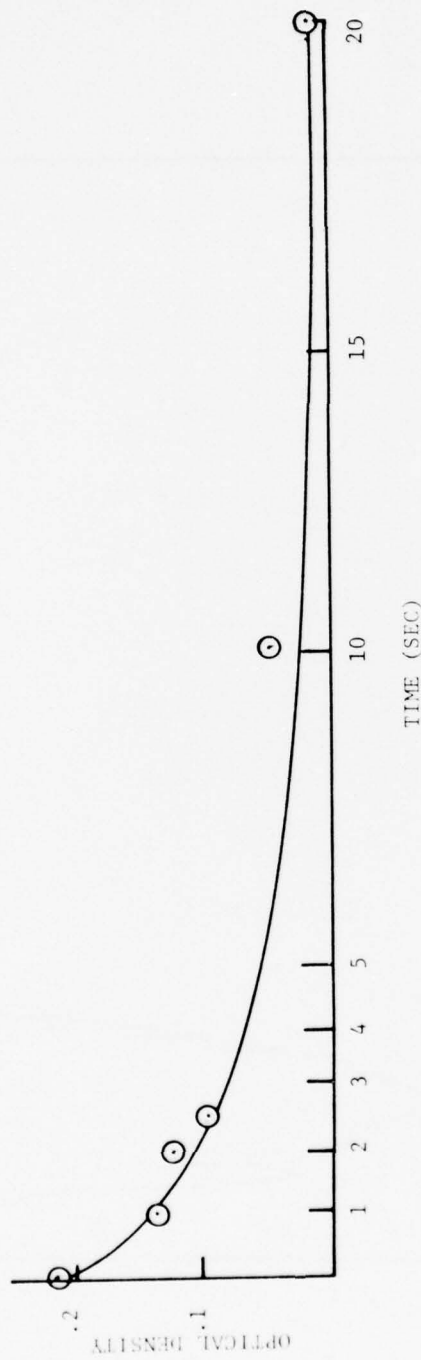


Figure 3. Optical Density Due to Ammonia as a Function of Time (Shot 4), $\nu = 930 \text{ cm}^{-1}$.

UNCLASSIFIED

UNCLASSIFIED

effect on the screen, this dust cloud appears to reach the optical path of the radiometers (about shoulder high) in 3 to 5 seconds after firing. This agrees in time with the appearance of the second transmission minimum.

We propose then the following concept model. The initial obscuration is due to gun smoke which for reasons identified below increases in opacity for the first second or so and then dissipates. As the smoke cloud dissipates, the dust cloud rising from the ground enters the optical path resulting in increasing opacity for a while and then dissipates. The min-max-min transmission behavior is then attributed to smoke-dissipation-dust-dissipation. The following sections explore the detailed nature of these two aerosols based on the data for Shot #3 (Fig. 1).

APPROACH

In an extinguishing medium a light beam is attenuated according to

$$I = I_0 e^{-\epsilon C l} \quad (1)$$

where I is the transmitted intensity, I_0 is the incident intensity, ϵ is an extinction coefficient, and C and l are the concentration and path length in the medium in units appropriate to those used to specify ϵ . In aerosol studies C is commonly given as a number density in units of particles per cm^3 and l is given in meters. The extinction coefficient ϵ is then in units of cm^3/m which is an area (i.e., 10^{-2}cm^2), and has a particular value for any given particle depending on its composition (refractive index), size, shape, and the wavelength of light incident on it. Assuming spherical particles, then from the wavelength, particle size, and refractive index the extinction cross-section (C_{ext}) may be calculated using the well known Mie theory.² In general the particle may be composed of a material which absorbs light at the wavelength of interest so that the observed extinction will be due to absorption as well as scattering. In this case the refractive index will be a complex number with an imaginary component related to the degree of absorption. Therefore performing such calculations with accuracy will require knowing the real and imaginary components of the refractive index, at the wavelengths of interest, for the material of which the aerosol particles are composed.

UNCLASSIFIED

The transmission (T) as reported in Fig. 1 is the ratio of transmitted to incident light intensity. Then from Eq. (1)

$$T = I/I_o = e^{-\epsilon Cl} \quad (2)$$

The transmission is not conveniently related to the parameters ϵ and C which are directly related to the aerosols we wish to characterize. Therefore the transmission data is digitized at 0.5 second intervals and converted to optical densities (OD)

$$OD = -\log T = (1/2.303) \epsilon Cl \quad (3)$$

which provide a more convenient linear relationship. The experiment is then analyzed by seeking model aerosols for which values of ϵ , C , and l can be derived which will lead to OD vs. time curves in agreement with the data.

The approach may be summarized as follows. First a candidate material for the aerosol particles is chosen and real and imaginary components for its refractive index are selected at each of the three wavelengths for which experimental data was collected. Second a series of Mie scattering calculations are performed at each wavelength for spherical particles of this material at a variety of particle diameters. Third an effective particle diameter in the cloud must be selected at each point in time. This is done by comparing the observed ratios of extinction at the various wavelengths [$OD(0.53\mu\text{m})/OD(1.06\mu\text{m})$ and $OD(0.53\mu\text{m})/OD(10.6\mu\text{m})$] to the ratios predicted from the Mie calculation for the various sized particles. Because the amount of extinction depends strongly on the ratio of particle size to wavelength, this measure can be used as a sensitive indicator of particle size. Unfortunately it is not always unique to a single particle size, as we shall see. Finally, with ϵ fixed by the choice of refractive index and the choice of particle size selected from the ratios of OD's at different wavelengths, the product Cl can be determined to agree with the magnitude of the observed extinction. For convenience in reporting we shall take the cloud to be uniform over the 93 foot path length and report C as an effective number density (units = cm^{-3}).

UNCLASSIFIED

SMOKE MODEL

The early obscuration phenomena including the first transmission minimum to the maximum at 2.5 seconds is to be attributed to gun smoke. As pointed out previously, the presence of significant amounts of NH_3 in the vicinity of the muzzle is to be expected during this time and confound the extinction data in the $10.6\mu\text{m}$ region. We shall therefore rely on the data at $0.53\mu\text{m}$ and $1.06\mu\text{m}$ in constructing the gun smoke model.

The presence of significant amounts of NH_3 is to be expected following the combustion of nitrocellulose base propellants. The products of nitrocellulose combustion are shown in Table I. The water gas reaction follows an equilibrium appropriate to the high temperature, high pressure conditions inside the bore as the projectile travels down the barrel. When the projectile exits from the muzzle there is a sudden, catastrophic loss of temperature and pressure which freezes the concentrations at essentially those typical of the in-bore high temperature, high-pressure environment. Under these conditions there is an equilibrium established between the H_2 in the water gas reaction, the N_2 , and NH_3 which results in the observed significant concentrations of NH_3 . Note that gaseous water will also be released and suddenly cooled as the projectile exits the muzzle. Also a variety of hygroscopic metals and metal oxides are present from propellant additives or primer mixes. These can be expected to form active condensation nuclei for the suddenly cooled water resulting from propellant combustion, and for atmospheric water in the vicinity of the muzzle. Water droplets are therefore selected as a model material for the gun smoke aerosol. This water is certainly contaminated with a variety of materials, however without further data on chemical composition, it seems a reasonable first approximation to model the gun smoke as a pure water aerosol.

The results of Mie calculations on water drops are given in Table II. The complex indices of refraction at the wavelengths of interest are shown in the box. From the magnitude of the imaginary components it is clear that pure water has effectively no absorption at 0.53 and $1.06\mu\text{m}$, and moderate absorption at $10.6\mu\text{m}$. For various particle diameters, the optical density per particle/ cm^3 per meter path length [cf., ϵ in Eq. (3)] is given for each wavelength along with the ratio of these extinctions at the two wavelengths of principal interest.

UNCLASSIFIED

Table I. Products of Nitrocellulose Combustion.

Major Products

CO, CO₂, H₂, H₂O (Water Gas Equilibrium)

N₂

Major Minor Products

CH₄, NH₃

Minor Minor Products

C, K₂O, SnO₂, Na₂O, BaO

(Pb, Sb, Si, Zr, Ca, Al)

UNCLASSIFIED

0.53	1.335 (1-0.000000001 ζ)
1.06	1.325 (1-0.000000808 ζ)
10.6	1.182 (1-0.06091 ζ)

Table II. H_2O Calculation.

Diam. (μm)	OD/Part/Meter			$\frac{OD}{OD} \frac{0.53}{1.06}$
	0.53	1.06	10.6	
0.1	0.464(-10)	0.282(-11)	0.179(-10)	16.5
0.5	0.150(-6)	0.258(-7)	0.225(-8)	5.81
0.9	0.104(-5)	0.367(-6)	0.133(-7)	2.83
1.0	0.134(-5)	0.565(-6)	0.183(-7)	2.37
1.1	0.164(-5)	0.824(-6)	0.245(-7)	1.99
1.2	0.182(-5)	0.112(-5)	0.320(-7)	1.62
1.3	0.195(-5)	0.150(-5)	0.409(-7)	1.30
1.4	0.210(-5)	0.193(-5)	0.517(-7)	1.09
1.5	0.210(-5)	0.238(-5)	0.637(-7)	0.88
1.6	0.195(-5)	0.295(-5)	0.778(-7)	0.66
1.7	0.201(-5)	0.351(-5)	0.941(-7)	0.57
1.8	0.215(-5)	0.405(-5)	0.113(-6)	0.53
1.9	0.207(-5)	0.475(-5)	0.134(-6)	0.44
2.0	0.233(-5)	0.530(-5)	0.157(-6)	0.44
5.0	0.176(-4)	0.220(-4)	0.326(-5)	0.80
10.0	0.678(-4)	0.692(-4)	0.332(-4)	0.98
20.0	0.292(-3)	0.278(-3)	0.278(-3)	1.05

UNCLASSIFIED

The development of the water aerosol model is shown in Table III. At each of the 0.5 second intervals, the observed ratio of extinction at the two wavelengths is shown. Referring to the theoretical results in Table II allows the identification of an effective particle diameter. Of course the actual aerosol will be polydisperse (i.e., have a distribution of particle sizes); we model it here in terms of an equivalent monodisperse aerosol. For example, at time zero the measurements show an OD at the $0.53\mu\text{m}$ wavelength 2.4 times greater than the OD at $1.06\mu\text{m}$. Referring to Table II shows that for drops of pure water this ratio would be expected from drops $1.0\mu\text{m}$ in diameter. Then considering the absolute OD's actually observed at $0.53\mu\text{m}$ and $1.06\mu\text{m}$ and the cross sections ϵ of a $1.0\mu\text{m}$ water drop at these two wavelengths, one finds from Eq. (3) the required number density in the two cases to be 5.3×10^3 and 5.8×10^3 , which are assigned as the range of uncertainty, and for the model a value of 5.6×10^3 is chosen. This process is repeated at each half second interval up to 2.5 seconds.

Note that during the first 1 1/2 seconds the particle number density remains rather constant while the drops grow in size from 1.0 to $1.4\mu\text{m}$. After this the drop size remains stable while the cloud dissipates.

After 2.5 seconds the effect of the rising dust aerosol dominates the observed extinction. Nevertheless, there remains a significant amount of water whose effect must be subtracted from the observed OD data in order to characterize the dust aerosol. A plot of H_2O drop number density vs. time, Figure 4, shows that once droplet growth stops and the water cloud begins to dissipate, the reduction in $\log(N)$ appears to be quite linear as shown by the circled points. This trend was simply extrapolated, number density values read at successive 1/2 second intervals [triangles in Fig. (4)], and the droplets assumed to remain stabilized at $1.4\mu\text{m}$ diameter. The results are shown below the dotted line in Table III. Table II data then allows the calculation of remaining OD due to dissipating water at each wavelength.

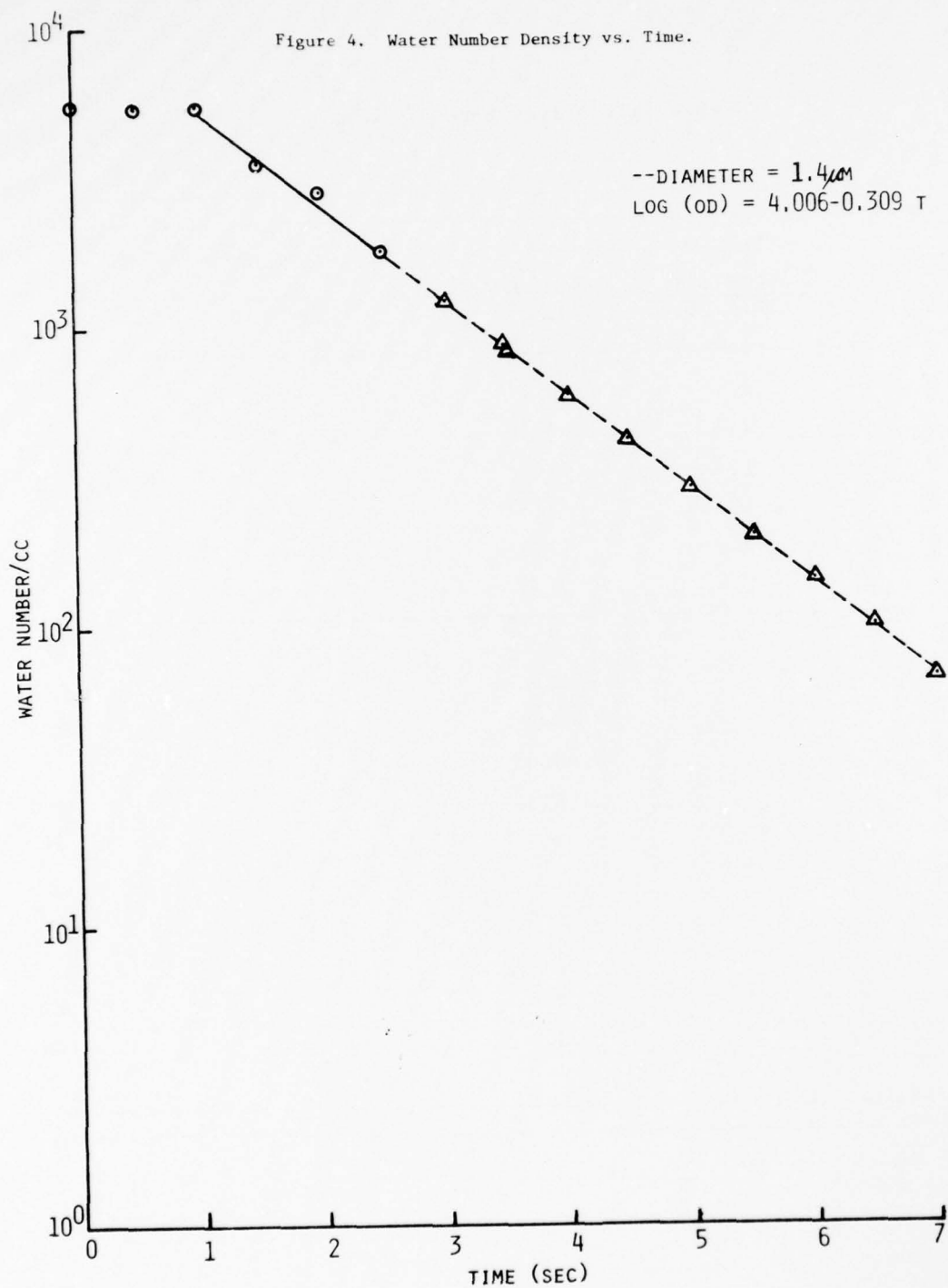
The OD effects due to the final water model are shown in Figure 5, where the circled points show the experimental data, and crosses plot the effect contributed by the water model of Table III. The behavior at $0.53\mu\text{m}$ and $1.06\mu\text{m}$ is very well reproduced, with the exception of the point at 2.5 seconds. This is the cross-over point at the transition between a smoke-dominated cloud and a dust-dominated cloud; it would be reasonable to expect significant contributions from both aerosols here. As the model attempts to account for the effect entirely in terms of the smoke aerosol, it is not surprising that the

UNCLASSIFIED

Table III. Water Aerosol Model.

Time	Observed OD(0.53) OD(1.06)	Diam. (μ m)	N_{H_2O} (Units = 10^3)	
			Range	Model
0.0	2.4	1.0	5.3 - 5.8	5.6
0.5	2.1	1.1	5.3 - 5.4	5.4
1.0	1.7	1.2	5.4 - 5.6	5.5
1.5	1.1	1.4	3.4 - 3.6	3.5
2.0	1.2	1.35	2.8 - 2.9	2.8
2.5	1.1	1.4	1.4 - 2.3	1.8
3.0		1.4		1.2
3.5		1.4		.85
4.0		1.4		.60
4.5		1.4		.42
5.0		1.4		.29
6.0		1.4		.20
7.0		1.4		.07
8.0		1.4		.034
9.0		1.4		.017
10.0		1.4		.008
15.0		1.4		.002

UNCLASSIFIED



194

UNCLASSIFIED

UNCLASSIFIED

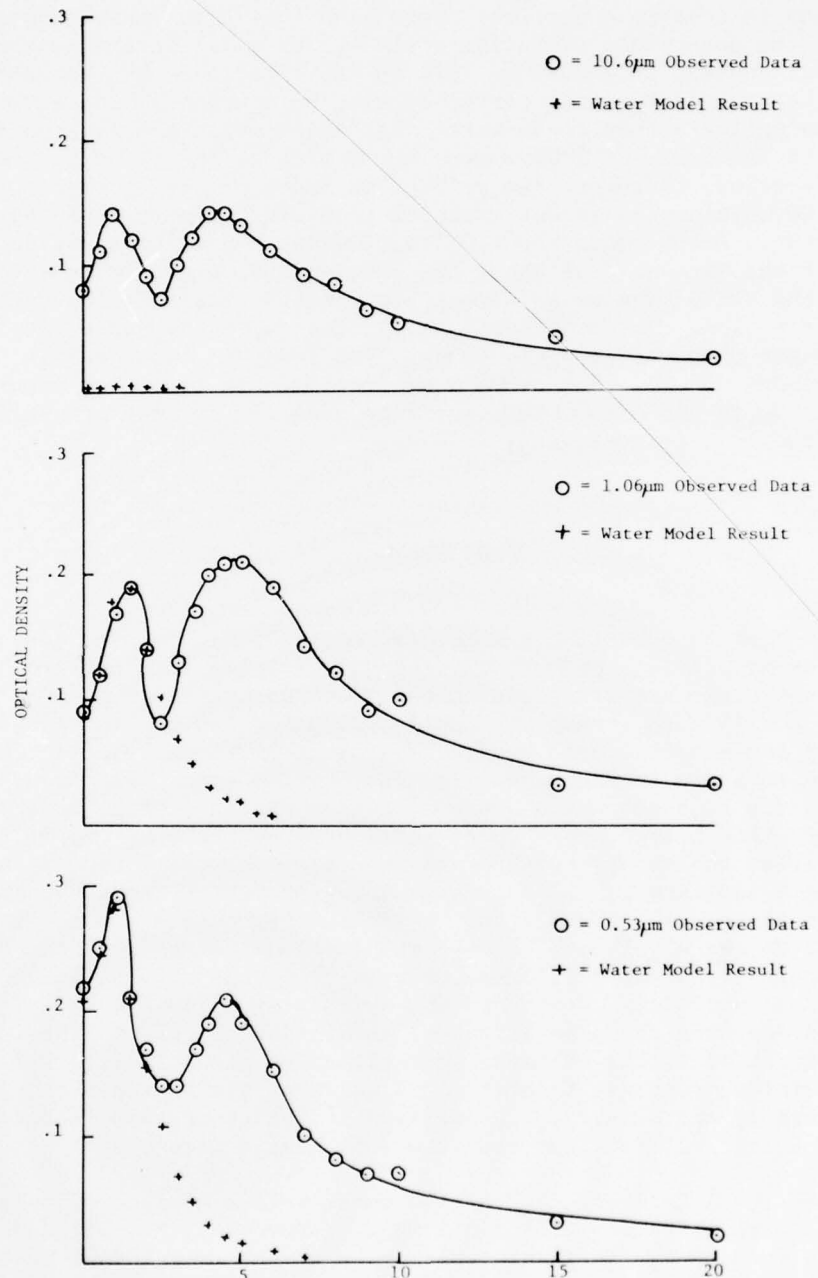


Figure 5. Optical Density Due to Gun Smoke Model.

UNCLASSIFIED

UNCLASSIFIED

agreement is less than perfect. Note also that this model cannot explain the observed obscuration at $10.6\mu\text{m}$ at all. In the context of our model concept this must be left to the effects of NH_3 gas absorption or contaminants which certainly must be present in the water. It seems unlikely that these water impurities would absorb significantly at the 0.53 and $1.06\mu\text{m}$ wavelengths because the cloud has no apparent color, therefore the refractive index of the particles at these two wavelengths is not expected to differ greatly from that of pure water. Furthermore the $1.0\text{--}1.4\mu\text{m}$ diameter particles are on the order of the same size as these two wavelengths, a condition which causes the extinction to be strongly dominated by scattering rather than absorption. On the other hand, $10.6\mu\text{m}$ radiation has a wavelength much longer than the particle size. This leads to considerably enhanced absorption in the overall extinction. If absorbing impurities are present in the water, they would be expected to most strongly affect the $10.6\mu\text{m}$ wavelength.

DUST MODEL

In order to establish a model refractive index for the dust particles comprising the aerosol, the dirt samples returned from the experiment site were examined. After sieving, the fines passing through a #320 mesh screen were mulled with KBr and pressed to form a pellet for spectroscopic study. The spectrum in the visible and infrared is shown in Figure 6. The KBr host is transparent in the visible; its IR spectrum is shown with that of the dust in order to sort out which features are to be attributed to the dust sample. In the visible, the smooth featureless increase in transmission with wavelength indicates: (1) only scattering processes are attenuating light in the sample, and (2) the particles responsible are not small compared to the wavelength because the increase is not sufficiently rapid (for very small particles compared to wavelength, Rayleigh scattering conditions obtain and the extinction follows λ^{-4}). The infrared spectrum shows a variety of absorption features. The infrared spectrum of a clay of known composition is shown in Figure 7 with the absorption features identified in terms of their origin on various components of the clay.³ By comparison of the absorption features of Figures 6 and 7 it is clear that the dust sample is a clay.

From the literature, refractive index values typical of rural aerosols were taken for 0.53 and $1.06\mu\text{m}$.⁴ However, absorptions are expected to strongly influence extinction at the long $10.6\mu\text{m}$ wavelength,

UNCLASSIFIED

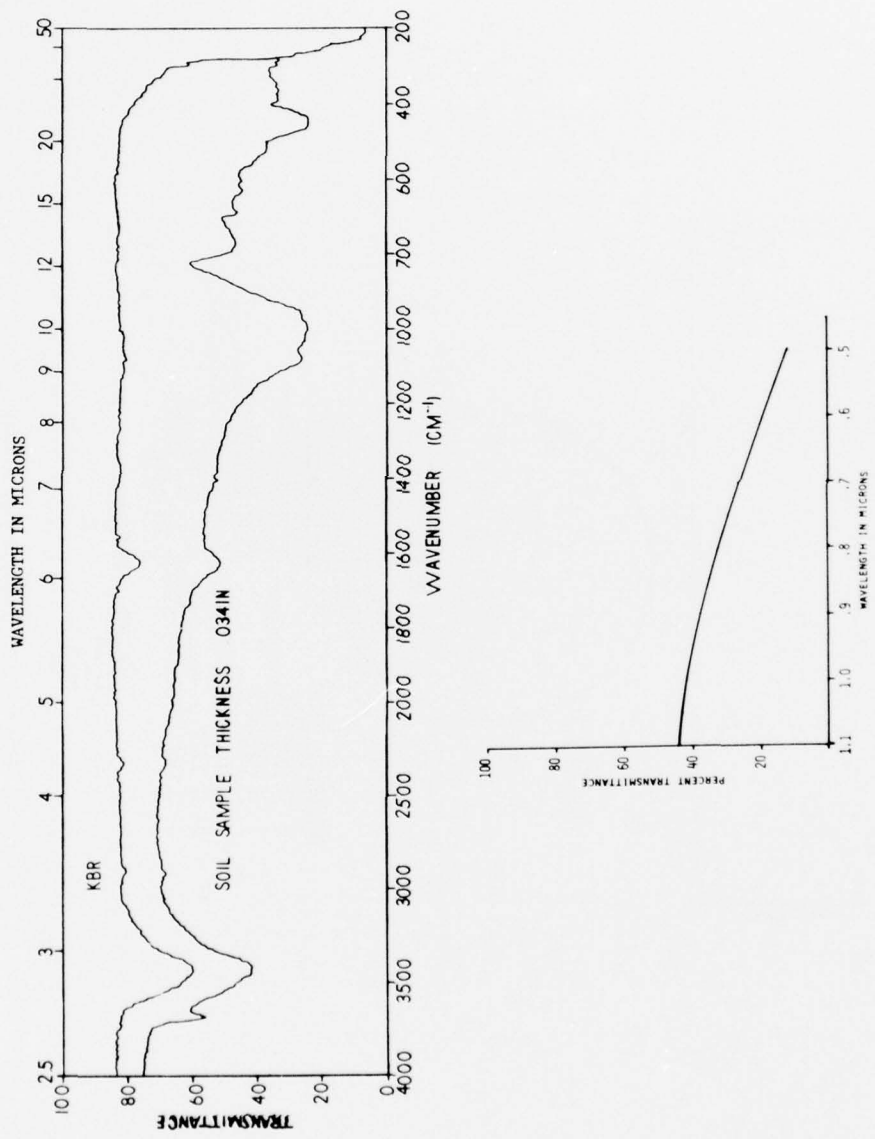


Figure 6. Visible and Infrared Spectrum of Dust Sample.

UNCLASSIFIED

UNCLASSIFIED

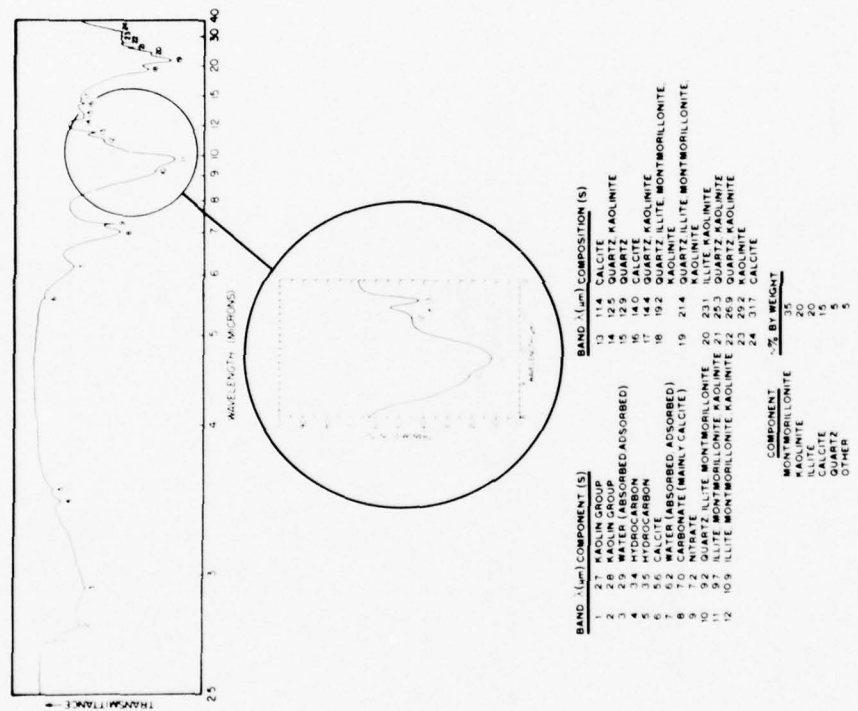


Figure 7. Infrared Spectrum of Clay.

UNCLASSIFIED

UNCLASSIFIED

and clays of various compositions show absorptions at $10.6\mu\text{m}$ which vary over a wide range (greater than an order of magnitude). Therefore, in addition to a typical refractive index at $10.6\mu\text{m}$ ³, calculations were conducted for imaginary refractive index components at the lower and upper bounds expected for commonly occurring clays³. All of the refractive indices are given in Table IV.

Table IV. Model Refractive Indices for Dust

Wavelength (μm)	Refractive Index ^{a.}
0.53	1.51 (1.0 - 0.0093 ϵ)
1.06	1.49 (1.0 - 0.01342 ϵ)
10.6 (typical)	1.67 (1.0 - 0.0808 ϵ)
10.6 (min)	1.67 (1.0 - 0.0599 ϵ)
10.6 (max)	1.67 (1.0 - 1.1078 ϵ)

a. See text for identification of literature sources.

Mie calculations were performed at a variety of particle diameters and the ratios $\text{OD}(0.53)/\text{OD}(1.06)$ and $\text{OD}(0.53)/\text{OD}(10.6)$ constructed. These are tabulated in Table V. The listed values at $10.6\mu\text{m}$ are those for the typical refractive index, with the range of results for the minimum and maximum $10.6\mu\text{m}$ absorptions shown in parenthesis. The ratio $\text{OD}(0.53)/\text{OD}(1.06)$ is an oscillating function of particle size, hence unique assignment of particle size based on this ratio alone is not possible. The ratio $\text{OD}(0.53)/\text{OD}(10.6)$ is a monotonically decreasing function of particle size for fixed refractive index; furthermore, the range of values about the "typical" value is quite small for large particles (absorption has little effect as particles approach the

UNCLASSIFIED

Table V. Dust in Air Calculation.

Diam. (μm)	$\frac{\text{OD (0.53)}}{\text{OD (1.06)}}$	$\frac{\text{OD (0.53)}}{\text{OD (10.6)}}$
1.1	0.69	27.3 (36.2 - 3.2)
1.5	0.59	17.6 (22.7 - 2.0)
2.0	0.87	11.0 (14.0 - 1.3)
2.5	1.03	6.1 (7.4 - 0.82)
3.0	1.08	4.4 (5.1 - 0.76)
3.5	0.80	2.7 (3.1 - 0.66)
4.0	0.89	2.1 (2.4 - 0.72)
4.5	0.96	1.5 (1.6 - 0.67)
5.0	1.07	1.25 (1.3 - 0.72)
5.5	0.91	0.96 (0.98 - 0.66)
6.0	0.92	0.90 (0.90 - 0.69)
6.5	0.94	0.80 (0.79 - 0.67)
7.0	1.04	0.77 (0.77 - 0.70)

UNCLASSIFIED

wavelength in size) and grows to reflect the order of magnitude variation in imaginary refractive index component as absorption dominates extinction with particles small compared to the wavelength.

The experimental optical density data for 3.0 seconds and later were adjusted by subtracting the effect of the water model shown in Fig. 5. The residual OD at each wavelength is then to be attributed to the dust aerosol. Ratios for this adjusted experimental data are shown in Table VI along with size and number density values characterizing two possible dust aerosol models to fit this data. At 3.0 seconds the ratio $OD(0.53)/OD(1.06)$ from Table VI could be satisfied by particles of diameter $3.0\mu\text{m}$ or $5.0\mu\text{m}$ (of Table V). By 3.5 seconds this ratio has dropped somewhat. Table V shows that this change in behavior could be accommodated at either 3 or $5\mu\text{m}$ particles and at both sizes this decrease in ratio could be accounted for by particles either growing or shrinking! Referring to the second ratio in Table VI [$OD(0.53)/OD(10.6)$] shows a consistent increase in this value between 3.0 and 5.0 seconds. Recalling the Table V monotonic theoretical trend in this ratio for fixed refractive index (whatever the refractive index is for the particular Aberdeen dust, it is fixed in value), it is apparent that particle sizes are decreasing during this time.

Two possible models then explain the experimental data. One has dust particles of about $5\mu\text{m}$ diameter present at 3.0 seconds after firing with size diminishing thereafter; the second starts at particles of about $3\mu\text{m}$ and again reduces in size with time. This reduction in size with time is reasonable as the heavy particles will be the first to settle out of the dust cloud. Extensive Mie calculations to fill in data between the diameters shown in Table V lead to the assignment of particles sizes shown in Table VI. As with the water aerosol model, number densities are then calculated to provide the magnitude of obscuration observed. At 6.0 seconds and beyond, the obscuration curves at the various wavelengths come close together so that small variations (within experimental noise) cause them to cross and result in rather wild variations in the critical ratios. A reliable analysis of this data is not possible. For the $5\mu\text{m}$ model the $OD(0.53)/OD(1.06)$ ratio cannot be matched; for the $3\mu\text{m}$ model this first ratio can be approximately satisfied by the $1.8\mu\text{m}$ diameter particles shown in Table VI, but these particles cannot match the $OD(0.53)/OD(10.6)$ ratio even within the widest limits of reasonable $10.6\mu\text{m}$ absorption behavior (hence the dotted line flagging this data in Table VI is used to indicate unreliability). In general, the observed $10.6\mu\text{m}$ obscuration behavior falls closer to the middle of the range of expected refractive indices for the model using $5\mu\text{m}$ diameter particles than for the $3\mu\text{m}$ particle model which would require a clay composition of extremely strong absorption properties.

UNCLASSIFIED

Table VI. Clay Aerosol Model.

Time	Data		Model 1		Model 2	
	OD(0.53) OD(1.06)	OD(0.53) OD(10.6)	Diam. (μm)	N_3 (cm^{-3})	Diam. (μm)	N_3 (cm^{-3})
0.0						
0.5						
1.0						
1.5						
2.0						
2.5						
3.0	1.09	0.76	4.8	140	2.55	500
3.5	1.02	1.00	4.6	280	2.4	1075
4.0	0.95	1.17	4.5	380	2.35	1425
4.5	0.94	1.33	4.4	450	2.35	1640
5.0	0.89	1.35	4.1	480	2.1	1770
6.0	0.75	1.20			1.8	1600
7.0	0.74	1.09			1.8	1170
8.0	0.63	1.00			1.8	1000
9.0	0.78	1.19			1.8	815

a. See text.

UNCLASSIFIED

The three sieved dust samples returned to the laboratory were used to produce aerosols by shocking a container in which they rested and drawing the resulting dust cloud through a five-stage Battelle impactor for particle size analysis. The results for each of the three samples are shown in Table VII. The mean particle sizes agree with Model 1. As a check on the validity of the theoretical approach used in this study, each of these polydisperse aerosols from Table VII was used as the basis of a Mie calculation, the results of which were used to construct the ratios $OD(0.53)/OD(1.06)$ for the separate polydispersions. Using each of these ratios to enter Table V, the predicted particle size for an equivalent monodisperse aerosol was found. These are shown in the last row of Table VII. The agreement with the actual mean particle sizes is remarkably good!

The final results of the clay dust model combined with the water smoke model are shown in Figure 8. At times of 3.0 seconds and greater the optical density due to water (crosses) and that due to clay (triangles) will add together to closely reproduce the experimental results at 0.53 and $1.06\mu\text{m}$. At $10.6\mu\text{m}$ the range of results for the two clay models is indicated. The observed effects would be expected from a rather ordinary clay in Model 1; for Model 2 to be correct the clay would have to have been composed of an unusually strongly absorbing species. Because scattering strongly dominates the extinction at 0.53 and $1.06\mu\text{m}$, and because the real components of the refractive indices of clays do not vary greatly, the observed extinction at these short wavelengths would be expected to be reasonably transferable to other geographical locations (types of clays). The indicated range of obscuration at $10.6\mu\text{m}$ can be read as suggesting the range of effects that might be found at other sites and hence suggests that "worst-case" conditions could result in twice the $10.6\mu\text{m}$ optical density observed during Aberdeen Proving Ground tests.

SUMMARY

The obscuration due to single shot firing of the Rarden 30 mm cannon is modeled as resulting from two different monodisperse aerosols arising sequentially in time. The first aerosol, gun smoke, is composed of water drops condensed upon expansion of the water vapor product of propellant combustion and of atmospheric water vapor precipitated on condensation nuclei formed from propellant and primer combustion. This smoke cloud forms in front of the muzzle within a small fraction of a second after the projectile exits. Initially particles are spherical

UNCLASSIFIED

Table VII. Particle Size Composition (%) for Aerosols Produced from Aberdeen Proving Ground Clay Samples.

Particle Diameter	Sample Location		
	Muzzle	Royco	Lamp
8	15.7	20.7	9.0
4	79.1	69.0	83.4
2	4.6	8.8	5.4
1	0.5	1.3	1.4
0.5	0.1	0.2	0.8
Total	100	100	100
Particle Size (μm)			
Mean Particle Size	4.5	4.6	4.2
Equivalent Monodisperse ^a	4.3	4.4	4.2

a. See text.

UNCLASSIFIED

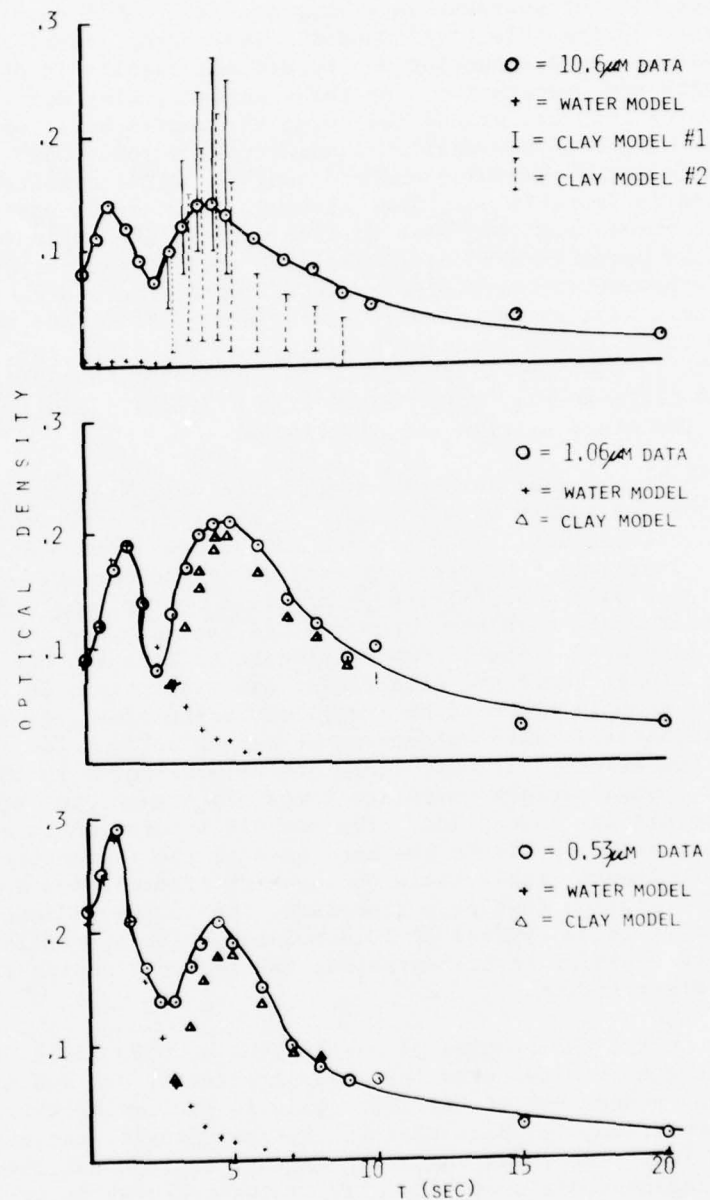


Figure 8. Optical Density Due to Gun Smoke and Dust Model.

UNCLASSIFIED

drops of about $1.0\mu\text{m}$ diameter which grow during the first second of time to $1.4\mu\text{m}$ without decrease in number density. As a result obscuration increases during this first second. Thereafter, particle size remains constant and dissipation of the aerosol results in decreased number density and obscuration. By three seconds, clay dust, which has been rising from the ground following the muzzle blast wave, begins to reach the height of the muzzle in quantities which produce more obscuration than the remaining smoke cloud. Particle diameter at three seconds is probably near $5\mu\text{m}$, although it would be possible for particles of about half this size to also satisfy the optical data. In either case particle size decreases with time thereafter due to settling of the heavier particles. The rising dust cloud causes continuously increasing number density at the muzzle level during the period from three to six seconds; however, the effect of the concomitant decrease in particle size results in increasing obscuration only up until the fifth second, after which time visibility continuously improves as the cloud settles and dissipates.

These smoke and dust aerosol models agree well with the optical data at $0.53\mu\text{m}$ and $1.06\mu\text{m}$ wavelengths. In these cases the obscuration is due to scattering which is a process not strongly dependent on wavelength. Therefore, the data gathered using radiometers with relatively large band pass filters should also be representative of the effect that would have been observed had lasers operating at these wavelengths been used. The $10.6\mu\text{m}$ wavelength effects are not due to the aerosols alone; there are significant gas absorptions in this region due to ammonia produced by propellant combustion. In addition, the gun smoke aerosol based on pure water cannot account for the observed $10.6\mu\text{m}$ effect. It must therefore be attributed to absorptions due to contaminations which are certainly present in the water or to the ammonia gas absorption. The ammonia absorption is a doublet falling almost entirely within the band pass of the radiometer; however, the $10.6\mu\text{m}$ wavelength itself falls on the high transmission spike between the absorption doublet. Therefore, the $10.6\mu\text{m}$ radiometer results are not expected to be typical of $10.6\mu\text{m}$ laser effects, the laser being expected to be superior in transmission, particularly during the first two seconds after firing.

Finally unlike the results at wavelengths of 0.53 and $1.06\mu\text{m}$, the $10.6\mu\text{m}$ wavelength results, even for aerosol effects, are due principally to absorption rather than scattering. This is particularly true of the dust obscuration, in which case the optical density can be expected to vary by a factor of three depending on the geographical location (i.e., chemical composition of the clay). The obscuration at 0.53 and $1.06\mu\text{m}$ wavelengths is due to scattering and is relatively insensitive to clay species or water impurities. Therefore, the $0.53\mu\text{m}$ and $1.06\mu\text{m}$ data is more likely transferable from location to location, with some dependence in the gun smoke expected on local conditions of relative humidity.

UNCLASSIFIED

REFERENCES

1. J. Heater, C. Pontelandolfo, and J. M. McKeough, "Rarden 30 mm Obscuration Measurements", Frankford Arsenal Report (1975).
2. E. W. Stuebing, J. J. Pinto (FA), and R. B. Gomez (Atmos. Sci. Lab.), "PGAUSS-LT: A Program for Computing Optical Properties of Single Scattering Aerosol Clouds of Homogeneous Particles", Frankford Arsenal Report (1975).
3. G. Hoidale, Atmospheric Sciences Laboratory, US Army Electronics Command, White Sands Missile Range, New Mexico, Private Communication.
4. G. Hanel, "Computation of the Extinction of Visible Radiation by Atmospheric Aerosol Particles as a Function of the Relative Humidity, Based upon Measured Properties", Aerosol Sci. (1972).
5. K. Fischer, "Bestimmung der Absorption von sichtbarer Strahlung durch Aerosolpartikeln", Beitr. Phys. Atm. 43, p. 244 (1971).

UNCLASSIFIED

(This page intentionally left blank.)

UNCLASSIFIED

OPTICAL AEROSOL MODELS

AND

LIGHT SCATTERING PROGRAMS

R. W. Fenn and E. P. Shettle
AF Geophysics Laboratory
Hanscom AFB, MA 01731

ABSTRACT

In this paper two separate, but related subjects are being discussed: First, a summary of present AFGL aerosol optical models is given. The rational and the approach for the development of these models is presented. Some of the characteristics of these models, of particular interest to tactical applications, are illustrated on two examples. A discussion on the limitations of present models follows, and some aspects of future improvements are reviewed.

The second part is a concentrated review of scattering codes and algorithms for contrast transmittance calculations. The discussion is limited to a few methods which are widely used in military applications. The advantages and limitations of these methods are being discussed.

Optical Aerosol Models.

Earlier versions of the AFGL LOWTRAN Transmission Code (Selby, McClatchey, 1972) included two aerosol models for surface visibilities of 23 and 5 kilometers to describe the effects of aerosol attenuation. Approximately two years ago, we decided that sufficient new experimental data had been accumulated by the scientific community to justify the development of a number of more specific aerosol models which would describe different environments and seasonal dependence. The objectives which we set ourselves for these aerosol models are summarized in Vugraphs 1 and 2.

The approach, which was used for developing these models was to compile the available information on the aerosol concentration, size distribution, and refractive index and to generate through MIE calculations the optical effects of aerosols and to obtain by matching these derived quantities against results from direct optical measurements the final 1976 optical aerosol models (Shettle, Fenn, 1975) (Vugraph 3). These optical aerosol models describe the coefficients for scattering and absorption, angular

scattering, and polarization as a function of wavelength, height, and type of environment (Vugraph 4). These four parameters are sufficient to derive any atmospheric optical quantity such as transmission (for instance for LOWTRAN, HITRAN), scattering out of a light beam as in laser propagation, contrast transmission, or background radiance. Whereas transmission calculations only require the knowledge of the scattering and absorption coefficients, all other quantities require the input of all four aerosol optical properties.

These optical models describe the various optical parameters, for instance the attenuation coefficient at a certain wavelength, as a function of altitude (Vugraph 5). For the lower boundary layer models have been defined for a maritime, rural and urban aerosol which can be scaled for various surface visibilities. For the upper troposphere, models for the fall-winter and spring-summer season were developed and in the stratosphere models for various levels of volcanic dust injection have been defined. These models have been described in more detail by Shettle and Fenn, 1975 (an AFGL report in preparation). In the following a few examples of the characteristic features of these models will be discussed. Vugraph 6 shows examples of aircraft measurements of atmospheric extinction coefficients as a function of altitude (Duntley et. al., 1972). Six profiles are shown from flights conducted on different days over a period of a few weeks in southern Germany. One will notice that in all cases a very distinct low level haze layer of approximately 1.5 kilometers thickness was present. A series of flights conducted in the area of St. Louis, Missouri showed a similar average vertical haze profile. On the other hand, the vertical profiles obtained from flights in New Mexico showed a much more constant decrease of haze concentration with altitude. Based on these results and other data we decided that the low level aerosol profiles, especially in urban and industrial environments, would be more realistically described by a low level haze layer rather than by an exponentially decreasing haze concentration. Vugraph 6 also shows another important feature. Although the measured surface visibilities only varied by 20-30%, the extinction coefficient varied by a factor of 5 at an altitude of only 150-200 meters above the ground. This indicates that considerable discrepancies in slant path transmission calculations can occur if they are only based on a surface visibility and a simple vertical aerosol profile. There is strong indication that such variations in aerosol properties with altitude are closely related to the temperature profile. Such dependences, however, must be studied in more detail before modeling attempts of these features can be made.

Vugraph 7 shows the wavelength dependence of the different types of surface layer aerosol models. Also all models, as shown in Vugraph 7,

are normalized at $.55\mu\text{m}$ wavelength, one can notice an order of magnitude difference in the extinction coefficient for some of the models for longer wavelengths. This is primarily due to different types of size distribution. On the other hand one can also see that there is only a small difference in the extinction coefficients for the rural and urban models. If one compares, however, in Vugraphs 8A and B the absorption and scattering coefficient contribution to the total extinction coefficient in these two models separately, one can see a large difference in the absorption coefficient which is of significance in multiple scattering effects. As an example, Vugraph 9 shows the ratio of calculated contrast transmission for the urban versus rural models. In this example it is assumed that a detector located at 20 km altitude is looking at the ground terrain under various polar view angles and for different solar zenith angles of the illuminating sun; for high sun angles the contrast transmittance for the urban model will be 30% greater than for the rural model; for very low sun angles, the contrast transmittance for the urban model will be only 70% of that for the rural model. In other words there can be a factor of almost 2 difference in this ratio depending on the type of aerosol model, although the surface visibilities are identical in both cases.

Although these 1976 optical aerosol models can describe many natural aerosol situations quite adequately, several improvements are necessary to make them more suitable for specific military problems (Vugraph 10). For applications of these models to the high relative humidity haze and foggy environments of Central Europe, it is very important to incorporate a direct dependence of the aerosol optical effects on the relative humidity, especially for relative humidities above 90%. Also models for fogs, optically thin clouds, and precipitation are needed. Much work on these dependencies has been done already and some examples are referenced in Vugraph 10. A deficiency of the existing models which is of particular concern to Navy applications is the absence of a model describing the low level marine aerosol. This aerosol has a large sea spray component in the lower few tenths of meters above the sea surface, and is therefore strongly dependent on wind speed. The specific aerosol of a battlefield environment is another model which needs to be developed. The existing optical aerosol models have no statistical significance. It is, therefore, necessary to develop an atmospheric optical climatology. Several experimental efforts are in progress which may provide a statistical data base at least for a limited number of environments.

The deficiency which is most easily accessible for a short term solution is the effective relative humidity. There exists considerable experimental

and theoretical data which shows the dependence of visibility on relative humidity. Vugraph 11 shows results of model calculations of aerosol size distributions due to changes in relative humidity for various types of aerosols (Hanel, 1972). These models 1-6 represent an average aerosol during summer in Central Germany, sea spray, Atlantic Ocean aerosol, Atlantic Ocean aerosol with Sahara dust, urban Central Germany aerosol in winter, and mountain aerosol, in that order. One can see that in all cases the aerosol particles begin to grow as the relative humidity reaches values of 75% or more. The growth rate for an aerosol particle is more or less independent of its size for relative humidities up to 95%. Only for relative humidities larger than 95% the size distribution begins to change. This implies that scaling of these aerosol models for different wavelengths by the visibility (or better the extinction coefficient) is equivalent to scaling according to relative humidity as long as the humidity is below 95%. Different scaling laws have to be developed for very high relative humidity.

Several studies have also been developed in the past on the relationship between horizontal visibility and liquid water content in fogs (Vugraph 12) (aufm Kampe, Weickmann, 1957). Such a dependence might be useful for modeling optical properties of fogs. Similar relationships for dry continental aerosols do not appear to be unique enough to be very useful (see Vugraph 13 from Horvath & Charlson, 1969). Vugraph 14 summarizes the conclusions concerning present aerosol model status and necessary improvements in aerosol models.

Multiple scattering radiation background and contrast transmittance calculations for military applications. Many military applications require a capability not only for forecasting the beam transmittance but also the various effects of angular scattering, the most important one being atmospheric contrast transmittance. Vugraph 15 shows the relationships which describe atmospheric contrast transmittance. One can see that atmospheric contrast transmittance τ_c is a function of path radiance P , reflected ground radiance N_{Bo} , and beam transmittance T . Of these three independent variables, P is the most difficult one to obtain experimentally or theoretically.

The formulation of contrast transmittance for a horizontal path, viewing a black object against the horizon sky, goes back to Koschmieder, 1924. His simple relationship, however, is based on some very important assumptions: Horizontal homogeneity of atmospheric optical properties, cloudless sky and others.

An extension of Koschmieder's theory for horizontal visibility to downward looking slant paths was found by Duntley in 1948 (see Vugraph 17). Assuming that the path radiance is primarily due to single scattering along the path from a ground target to an airborne detector, it is possible to find a direction looking at the horizon sky which forms the same angle α with the direction of the sun as the angle α between sun and viewing direction. One can, therefore, substitute for the path radiance in Vugraph 15 the sky radiance in a given direction and, therefore, Duntley's method is called the sky to ground ratio method. Duntley in his 1948 paper as well as Middleton, 1952, and Bailey and Mundie, 1969, gives various values for this sky to ground ratio K for different types of environmental conditions. Vugraph 18, from Duff, 1972, shows the dependence of contrast transmittance on beam transmittance and K factor. Indicated in this vugraph are also the identifiers given by Duntley and others for some of the K factor values. One may notice that the contrast transmittance depends very strongly on the K factor. For vegetation type backgrounds (forest) K factor values range from about 5 for a clear sky to 25 for an overcast sky. A comparison of these values with experimental data (Vugraph 19, from Duff, 1972) shows that the K factor values for these conditions are too high by a factor of approximately 4-5. It follows from the basic concept of substituting a measurement of the horizon brightness for the path radiance, that the sky to ground ratio method loses its physical basis under overcast cloudy sky conditions and that, therefore, the K factor no longer describes the path radiance under cloudy skies.

The first rigorous solution to the atmospheric contrast transmission problem was found by Coulson and others, 1960, for a pure molecular Rayleigh scattering atmosphere.

Of much more value for practical applications was the adoption of Monte Carlo techniques to multiple light scattering by Wells and Collins, 1965, and Plass and Kattawar, 1968. The Monte Carlo method treats light energy as photons incident on top of the atmosphere (Vugraph 20). One traces each photon along a random path through the atmosphere with the different processes of scattering by air molecules and aerosols. The characteristic capabilities of the Monte Carlo method are summarized in Vugraph 21.

A different method for contrast transmittance calculations based on two scattering processes only was developed by the Vidya Corp. and later on improved by the AWS (Breitling & Pilipowskyj, 1970). Some of the features of this technique are summarized in Vugraph 22.

Other Methods

More recently a technique which has many of the advantages of the Monte Carlo code but promises to be much more efficient in computer time was developed by Whitney et. al., 1973 (Vugraph 23).

The methods mentioned above on contrast transmittance calculations are those most commonly applied to military problems. The Monte Carlo method definitely is the most general one and allows to describe the largest variety of atmospheric conditions and geometries. Its main disadvantage is the extremely long computer time required. The DART program promises to offer an optimum tradeoff between efficiency and applicability in the near future. The sky to ground ratio method requires improvement in the definition of the K factor based on experimental data. With such improvements, however, it may still be a very simple and useful tool for making quick estimates of contrast transmittance (Vugraph 24).

REFERENCES

Arnulf, A., Bricard, J., Cure, E., Veret, C. (1957): Transmission by Haze and Fog in the Spectral Region 0.35 to 10 Microns. *JOSA*, Vol. 47, No. 6, 491-498.

aufm Kampe, H.J., Weickmann, H.K. (1957): "Physics of Clouds" in Meteorological Monographs, Vol. 3, No. 12-20, Am. Met. Soc.

Bailey, H.H., Mundie, L.G. (1969): The Effects of Atmospheric Scattering and Absorption on the Performance of Optical Sensors. Rand Memorandum RM5938-PR.

Barnhardt, E.A., Street, J.L. (1970): A Method for Predicting Atmospheric Aerosol Scattering Coefficients in the Infrared. *Appl. Opt.*, Vol. 9, No. 6, 1337-1344.

Blifford, I.H., DeLuisi, J.J., Takamine, J.A. (1972): Models of Tropospheric Aerosol Size Distribution Derived from Measurements at Three Locations. *J. Geoph. Res.* 77, 4529-4538.

Breitling, P.J., Pilipowskyj, S. (1970): "Computer Simulation of Optical Contrast Reduction caused by Atmospheric Aerosols." AIAA Paper No. 70-194.

Coulson, K.L., Dave, J.V., Sekera, Z. (1960): Tables Related to Radiation Emerging from a Planetary Atmosphere with Rayleigh Scattering. Univ. of Calif. Press, Los Angeles.

Deirmendjian, D. (1964): Scattering and Polarization Properties of Water Clouds and Hazes in the Visible and Infrared. *Appl. Opt.*, 3, 187-196.

- (1969): Electromagnetic Scattering on Spherical Polydispersions, American Elsevier, N.Y.

Duff, E.A. (1972): Atmospheric Contrast Transmission: Application to the Visual Detection and Electro-Optical Lock-On Problem. Thesis, AFIT, GEP/PH/72-4.

Duntley, S.Q. (1948): The Reduction of Apparent Contrast by the Atmosphere. *JOSA* 38, 179-191.

Duntley, S.Q., Johnson, R.W., Gordon, J.I. (1972): Airborne Measurements of Optical Atmospheric Properties, Summary and Review, AFCRL-72-0593.

Duntley, S.Q. (1976): Unpublished data

Elterman, L. (1964): Atmospheric Attenuation Model, 1964, in the Ultra-violet, Visible, and Infrared Regions for Altitudes to 50 Km. AFCRL-64-740, Sept. 1974.

- (1968): UV, Visible, and IR Attenuation for Altitudes to 50 Km, 1968. AFCRL-68-0153, April 1968.
- (1970): Vertical Attenuation Model with Eight Surface Meteorological Ranges 2-13 Km. AFCRL-70-0200, March 1970.

Fischer, K. (1973): Mass Absorption Coefficient of Natural Aerosol Particles in the 0.4 to $2.4\mu\text{m}$ Wavelength Interval. Beitr. Phys. Atm. 46, 89-100.

Fitzgerald, J.W. (1975): Approximation Formulas for the Equilibrium Size of an Aerosol Particle as a Function of its Dry Size and Composition and the Ambient Relative Humidity. J. Appl. Met., Vol. 14, 1044-1049.

Grams, G. et. al. (1974): Complex Index of Refraction of Airborne Soil Particles. J. Appl. Met. 13, 459-471.

Hanel, G. (1972): The Ratio of the Extinction Coefficient to the Mass of Atmospheric Aerosol Particles as a Function of the Relative Humidity. Aerosol Science 1972, Vol. 3, 455-460.

Horvath, H., Charlson, R.J. (1969): The Direct Optical Measurement of Atmospheric Air Pollution. American Ind. Hyg. Ass. J., Vol. 30, 500-509.

Ivlev, L.S. (1967): Aerosol Model of the Atmosphere, Prob. Fiz. Atmos. No. 7, Leningrad, 125-160, Translation AD 760-393.

Ivlev, L.S. (1969): Atmospheric Aerosol, in Radiation Characteristics of the Atmosphere and the Earth's Surface, ed. K. Ya. Kontratev. Translation TT-71-58003.

Junge, Chr. (1963): Air Chemistry and Radioactivity, Academic Press, N.Y.

- (1972): Our Knowledge of the Physico-Chemistry of Aerosols in the Undisturbed Marine Environment. J. Geoph. Res. 77, 5183-5200.

Kattawar, G.W., Plass, G.N. (1968): Radiance and Polarization for Multiple Scattered Light from Haze and Clouds. Appl. Opt., 7, 1519.

Koschmieder, H. (1924): Theorie der Horizontalen Sichtweite, Beitr. Phys. freien Atm. 12: 33-53; 171-181.

Lindberg, J.D., Snyder, D.G. (1973): Determination of the Optical Absorption Coefficient of Powdered Materials whose Particle Size Distribution and Refractive Index are Unknown. Appl. Opt., Vol. 12, 573-578.

Middleton, K.W.E. (1952): "Vision through the Atmosphere," Univ. of Toronto Press.

Mossop, S.C. (1964): Volcanic Dust Collected at an Altitude of 20 Km. Nature 203, 824-827.

Penndorf, R. (1954): The Vertical Distribution of MIE Particles in the Troposphere. Geoph. Res. Paper No. 25, AFCRL, March 1954.

Schickel, K.P. (1975): Sampling of Droplet Distributions from Water Clouds. DFVLR Report 75-25.

Selby, J.E.A., McClatchey, R.M. (1972): Atmospheric Transmittance from 0.25 to 28.5 μ m: Computer Code LOWTRAN 2. AFCRL-72-0745, Dec. 1972.

Shettle, E.P., Fenn, R.W. (1975): Models of the Atmospheric Aerosols and their Optical Properties. AGARD Conference Proceedings No. 183, Optical Propagation in the Atmosphere.

Twitty, J.T., Weinman, J.A. (1971): Radiative Properties of Carbonaceous Aerosols. J. Appl. Met. 10, 725-731.

Volz, F. (1960): Optik d. Dunstes, Hdb. d. Geophys. Bornträger, Berlin, 822-897.

- (1970): On Dust in the Tropical and Midlatitude Stratosphere from Recent Twilight Measurements. J. Geoph. Res. 75, 1641-1646.

- (1972): Infrared Absorption by Atmospheric Aerosol Substances. J. Geoph. Res., 77, 1017-1031.

- (1972): Infrared Refractive Index of Atmospheric Aerosol Substances. Appl. Opt. 11, 755-759.

Volz, F. and Shettle, E.P. (1975): Optical Constants of Meteoric Dust. In print.

Wells, M.B., Collins, D.G. (1965): Monte Carlo Codes for Study of Light Transport in the Atmosphere. Report ECOM-00240-F, Aug. 1965.

Whitby, K.T., Husar, R.B., Liu, B.Y.H. (1972): The Aerosol Size Distribution of Los Angeles Smog. *J. Colloid. and Interface Sc.*, 39, 177-204.

Whitney, C.K., Var, R.E., Gray, C.R. (1973): Research into Radiative Transfer Modeling and Applications. AFCRL-TR-73-0420.

AFGL (AFCRL) OPTICAL AEROSOL MODELS,

APPLICABILITY OBJECTIVES

The Models must be:

- Applicable to any optical/IR system from 0.2 to $40 \mu\text{m}$.
- Describe vertical variations from surface to 100 Km altitude continuously.
- Be representative for characteristic geographical and seasonal regimes.
- Must have a statistical (Climatological) significance.

AFGL (AFCRL) OPTICAL AEROSOL MODELS,

SCIENTIFIC OBJECTIVES.

The Models must be:

- Comprehensive Models for all optical effects (extinction, scattering, polarization);
- Based on the existing experimental data and consistent with atmospheric physical and meteorological concepts;
- Therefore, internally self-consistent.

AFGL OPTICAL AEROSOL MODEL DEVELOPMENT

CONCENTRATION

Elterman 1964, 1968, 1970
 Duntley et al. 1972, 1976
 Fenndorf 1954
 Blifford et al. 1974
 Ley 1967 1969

Deirmendjian 1964, 1969
Junge 1963, 1972
Whitby 1972
Mossop 1964
Volz 1970, 1975

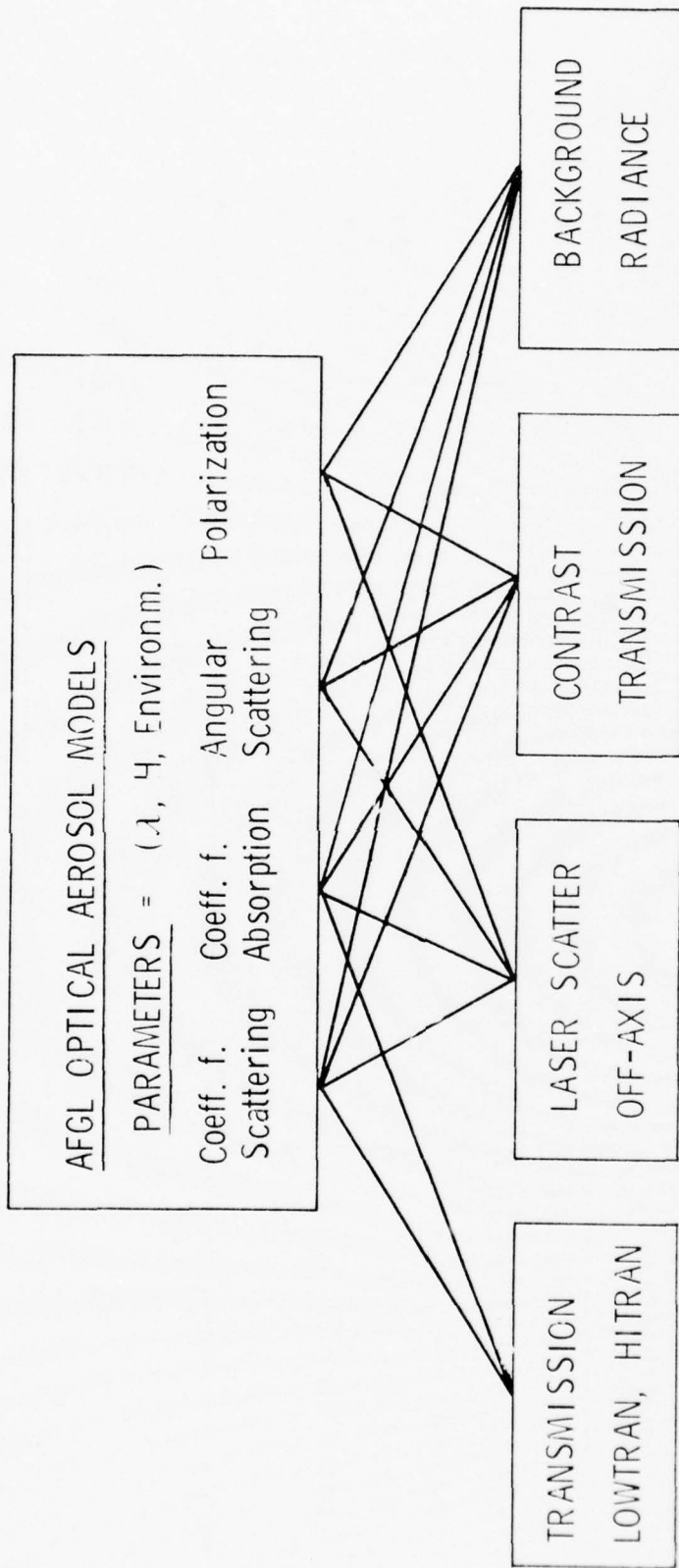
Volz 1960, 1972
Grams 1974
Fischer 1973
Twitty-Weinmann 1971
Lindberg 1973

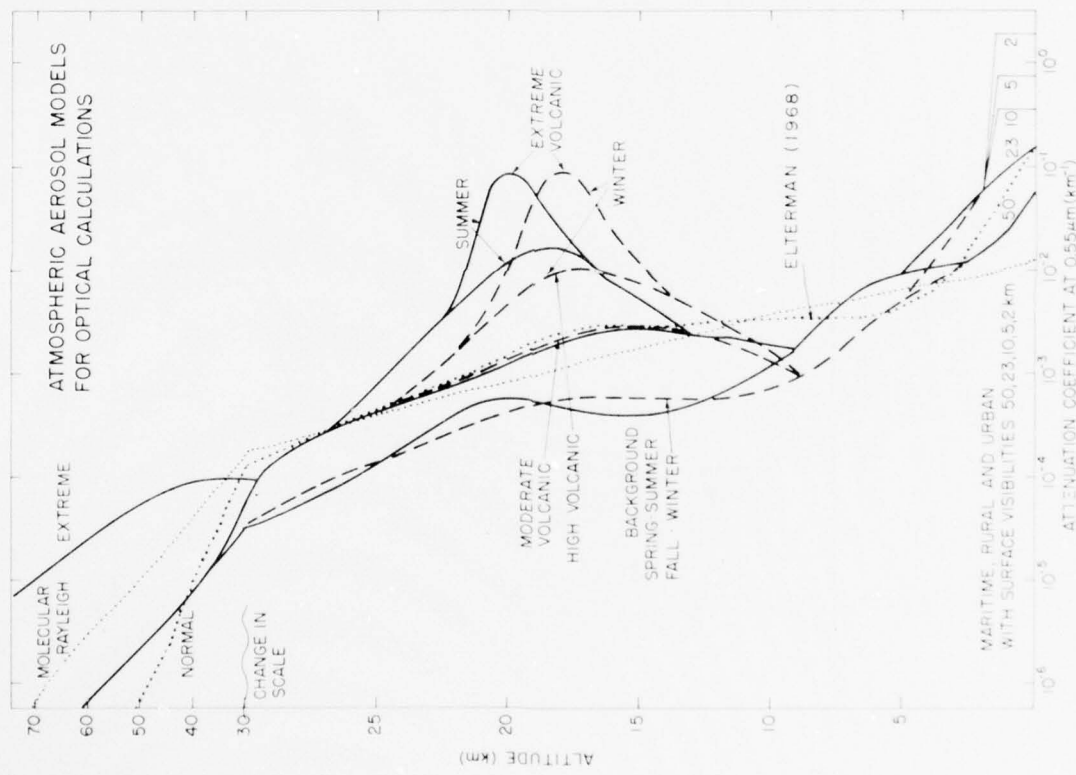
MIE - CALCULATIONS

AFGL OPTICAL AEROSOL MODELS, 1976

**DIRECT ATM. OPT.
MEASUREMENTS
FOR VERIFICATION**

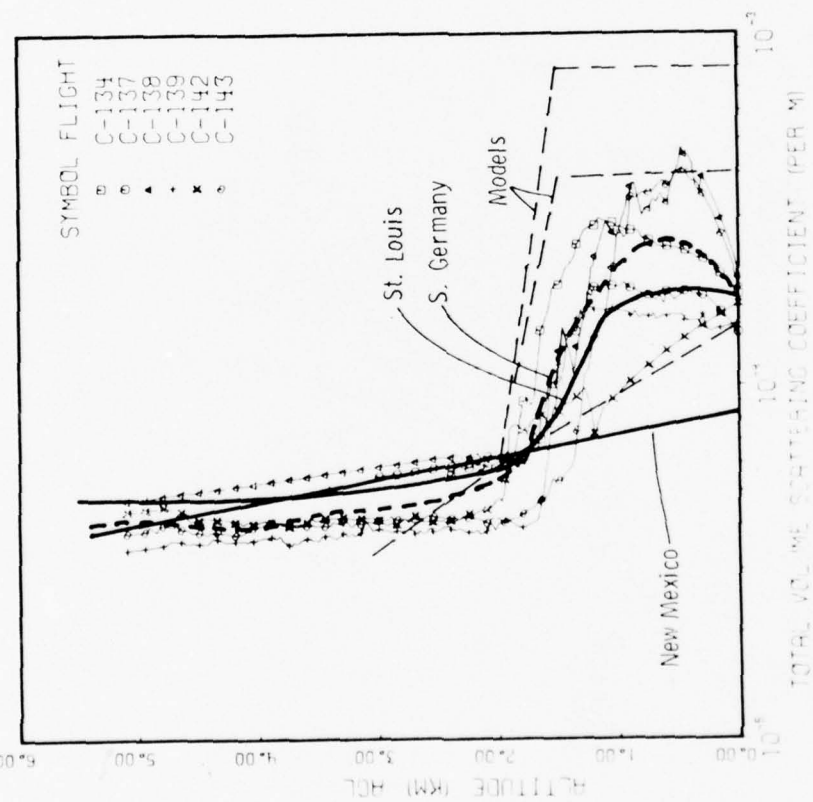
AFGL OPTICAL AEROSOL MODEL APPLICATION





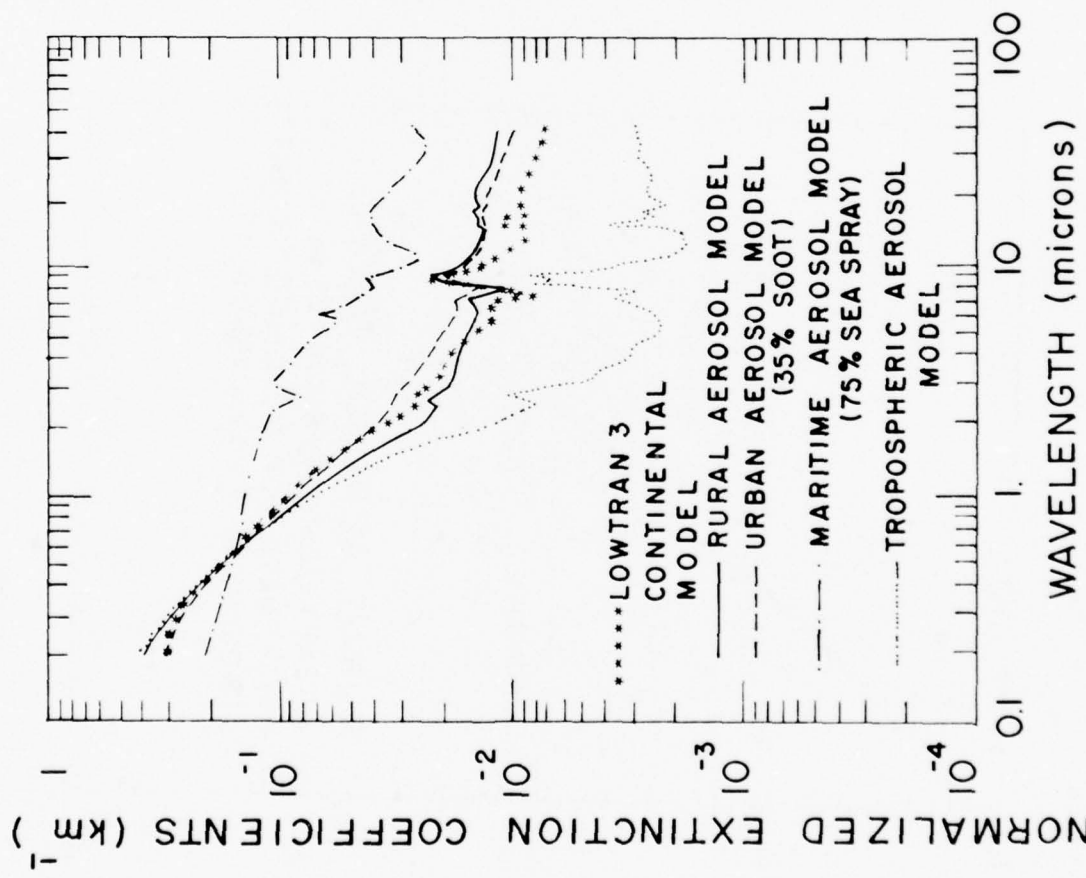
VUGRAPH #6

SCATTERING FOR HAVENVIEW FLIGHTS
FILTER 5 PSEUDO-PHOTOPIC
MEMMINGEN TRACK

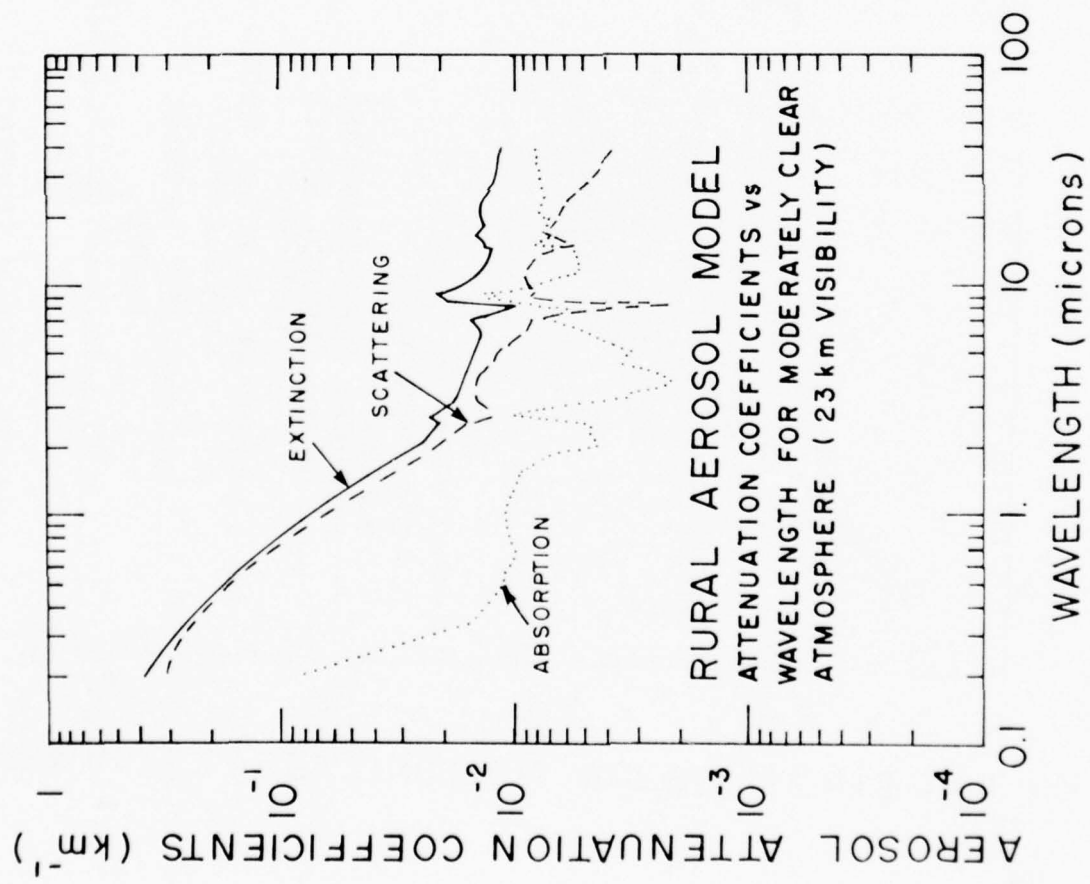


Total Volume Scattering Coefficient for Filter 5 (Pseudo-photopic)
for the six HAVENVIEW flights

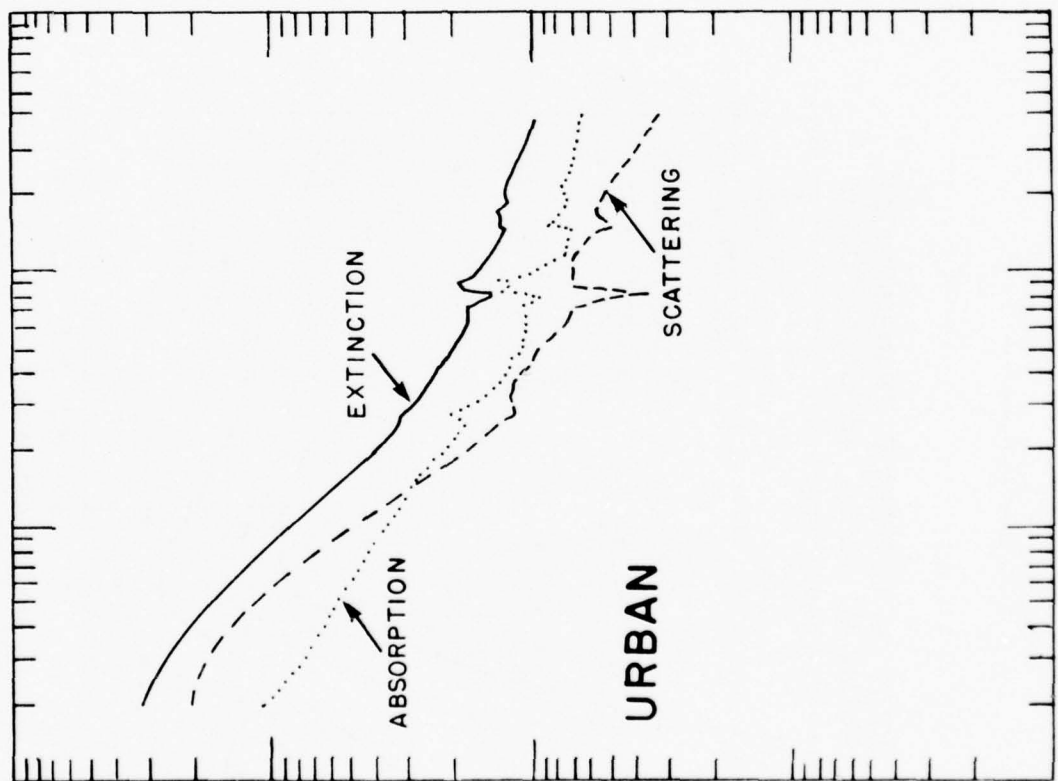
V U G R A P H 7

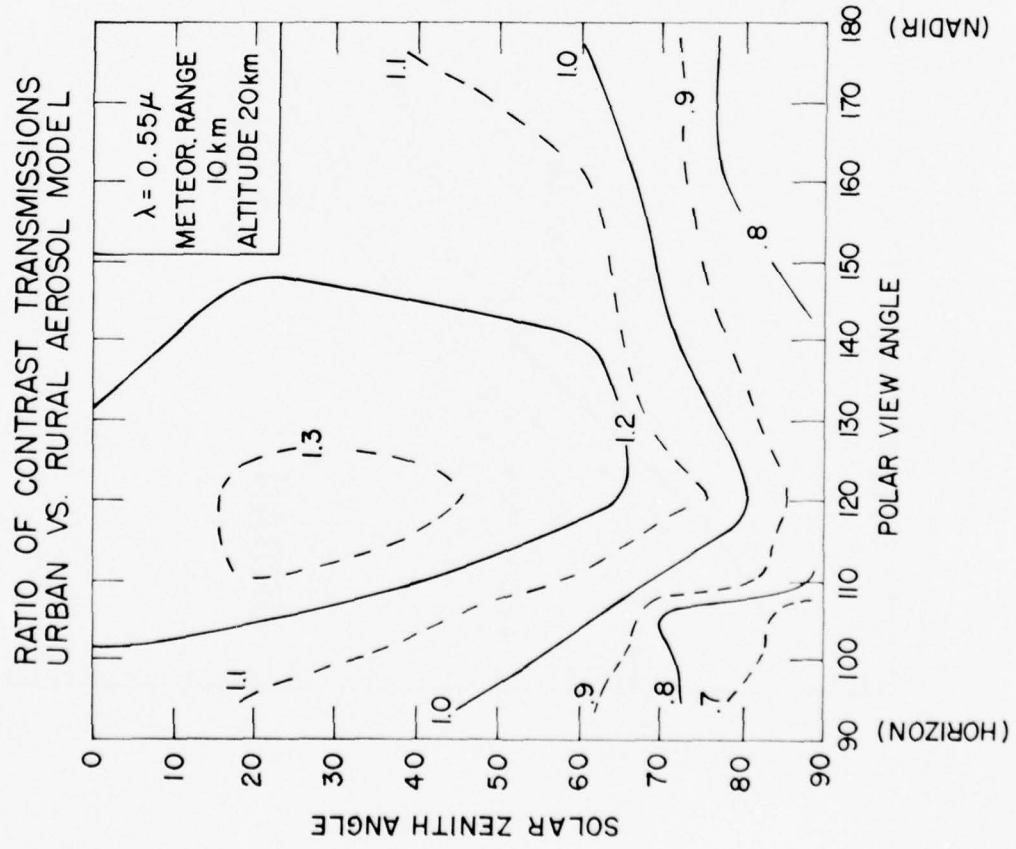


VUGRAPH 198A



V U G R A P H #8B





AFGL AEROSOL MODELS IMPROVEMENTS

REL. HUM. EFFECTS,
DEVELOPING FOGS,
FOGS, THIN CLOUDS,
PRECIPITATION

AFGL, 1977
U. Mainz, 1976
Barnhardt-Street, 1970
Fitzgerald 1975
Arnulf, 1957
Schickel, 1975
et. al

LOW LEVEL
MARINE ENV.
SEASPRAY

(NAVY)

BATTLE FIELD
ENVIRONM.

(ARMY)

ATM. OPT.
CLIMATOLOGY,
STATISTICS

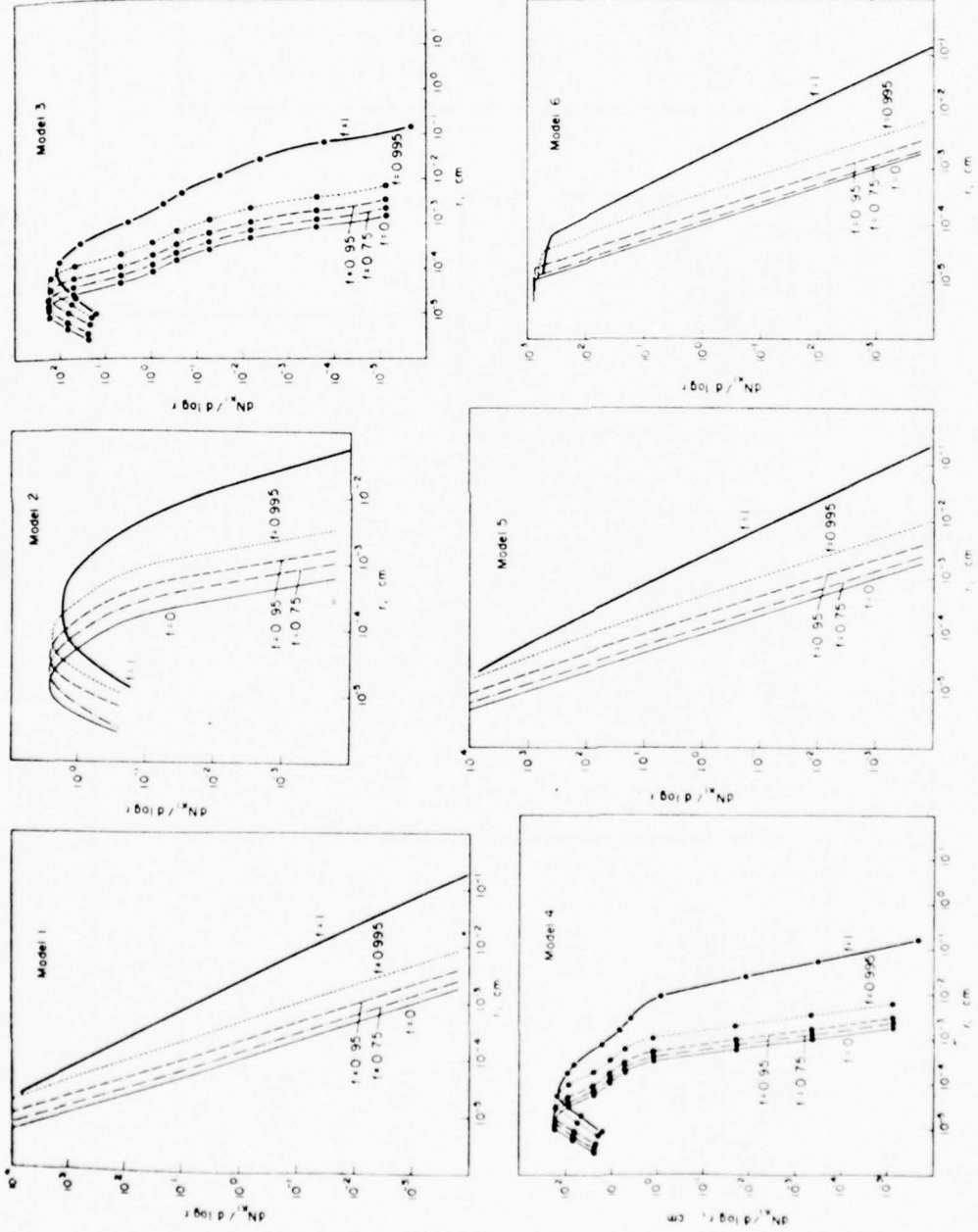
NATO OPAQUE
Navy OSP

Korean Atm.
Opt. Progr.

NAT. Programs:
e.g. UK

AFGL 1976 OPTICAL
AEROSOL MODELS

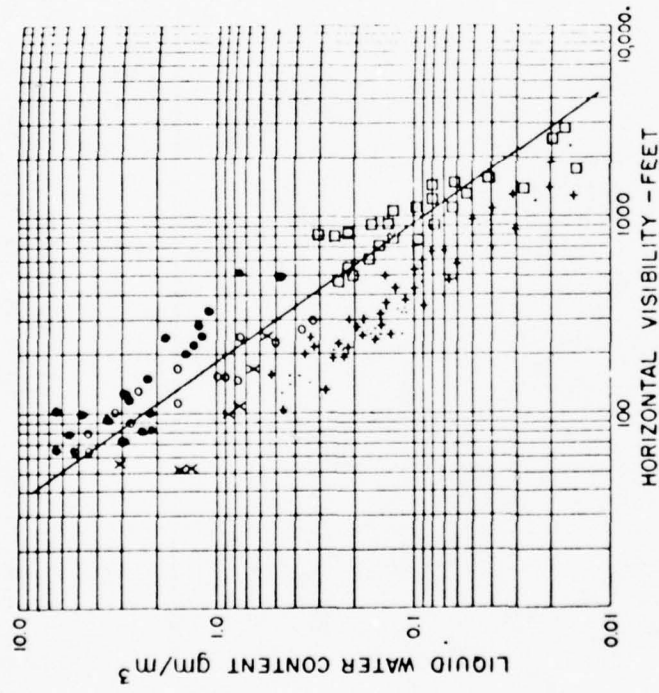
AEROSOL STANDT. MODELS
FOR OPT. /IR ATM. PROPERTIES



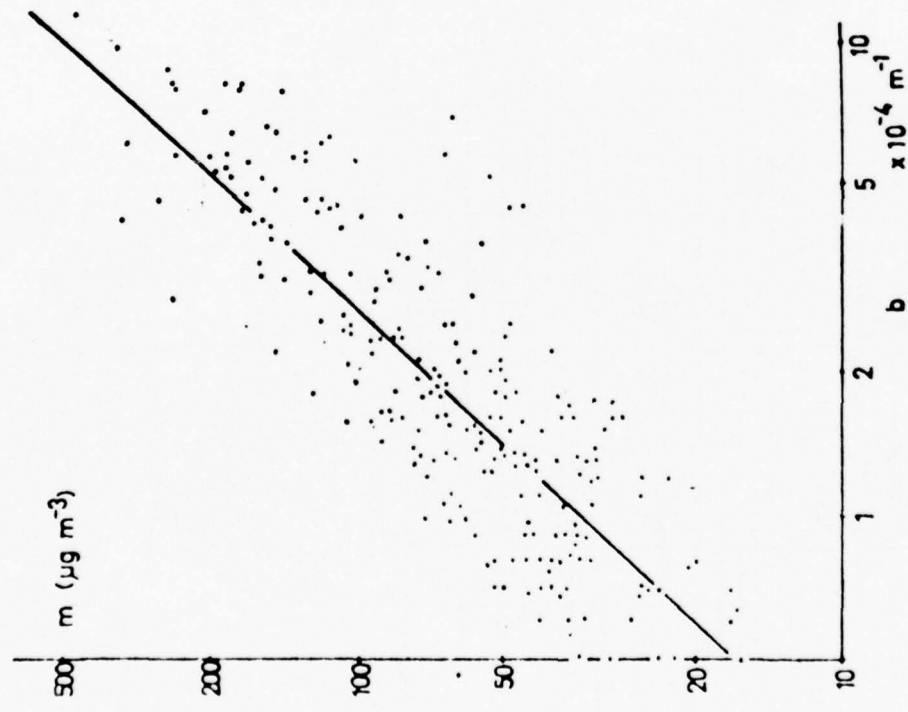
Aerosol size distributions, $dN/d \log r$, for each of the 6 models, versus relative humidity f .
 Np is the particle number per cm^3 . The curves are valid for increasing relative humidity.

(4.5 / F 45)

V U G R A P H #12



Relationship between visibility and water content in different kinds of clouds. The solid line represents the average of sea and high mountain fogs according to Radford.



Measured mass concentration and light-scattering coefficient for atmospheric aerosols at different locations.

CONCLUSIONS

PRESENT: Representative Models for Surface Layer ($2 < V < 200$ Km)
for average continental rural, urban and
maritime environment (except lower 10-20 m seaspray)
Upper Troposphere, Stratosphere

IMPROVEMENT THRUSTS:

Near-Term: Explicit high relat. humidity effects ($RH > 95\%$),
transition to fogs;
define additional models for fog(s), clouds (water and
ice), precipitation;

define battlefield environment model(s);

Far-Term: Develop statistical significance for these models

ATMOSPHERIC CONTRAST TRANSMITTANCE

$$\frac{\text{Apparent radiance from target (or background)}}{\text{target (or background)}} = \left\{ \frac{\text{Transmitted radiance from target (or background)}}{\text{target (or background)}} \right\}$$

$$+ \left\{ \frac{\text{Path radiance}}{\text{Path radiance}} \right\}$$

$$N_{T,B} = N_0 \cdot R_{T,B} \cdot T + P$$

$$\text{Inherent Contrast } C_0 = \frac{N_{T_0} - N_{B_0}}{N_{B_0}}$$

$$\text{Apparent Contrast } C_r = \frac{N_{T_r} - N_{B_r}}{N_{B_r}}$$

$$\text{Contrast Transmittance } \tau_c = \frac{C_r}{C_0} = \frac{1}{1 + \frac{P}{N_{B_0} \cdot T}}$$

KOSCHMIEDER, 1924

Contrast Attenuation for horizontal paths against horizon sky:

$$B_{\text{black object}} = B_{\text{horizon}} \cdot \left(1 - e^{-\sigma r} \right)$$

$$C = \frac{B_{\text{bl. obj.}} - B_h}{B_h}$$

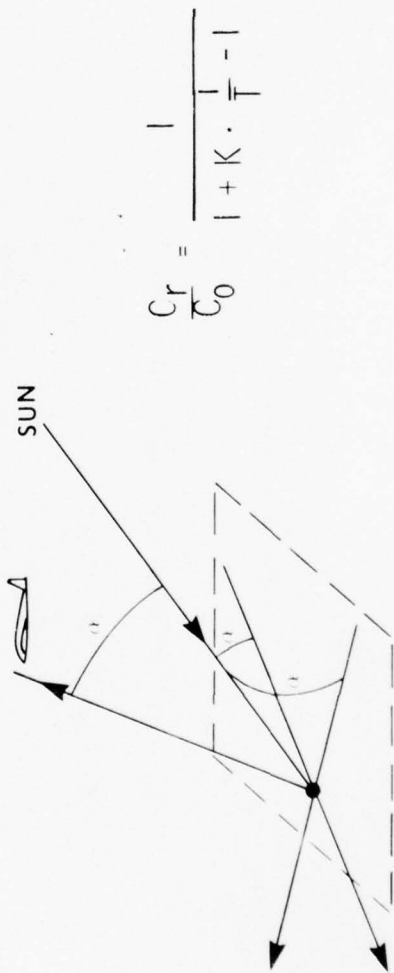
$$\frac{C_r}{C_0} = \tau_c = e^{-\sigma r}$$

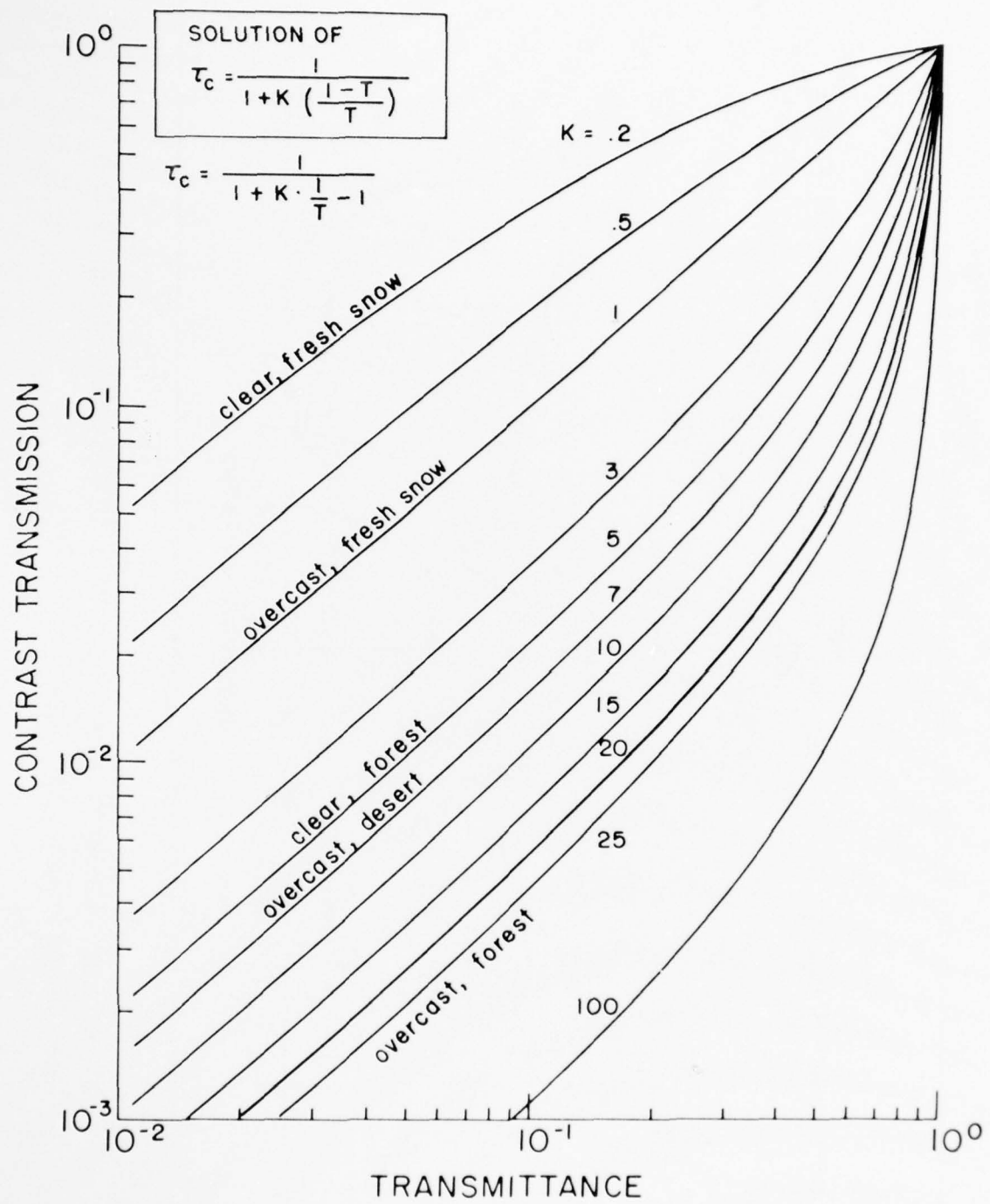
DUNTLEY, 1948

Also Middleton, 1952

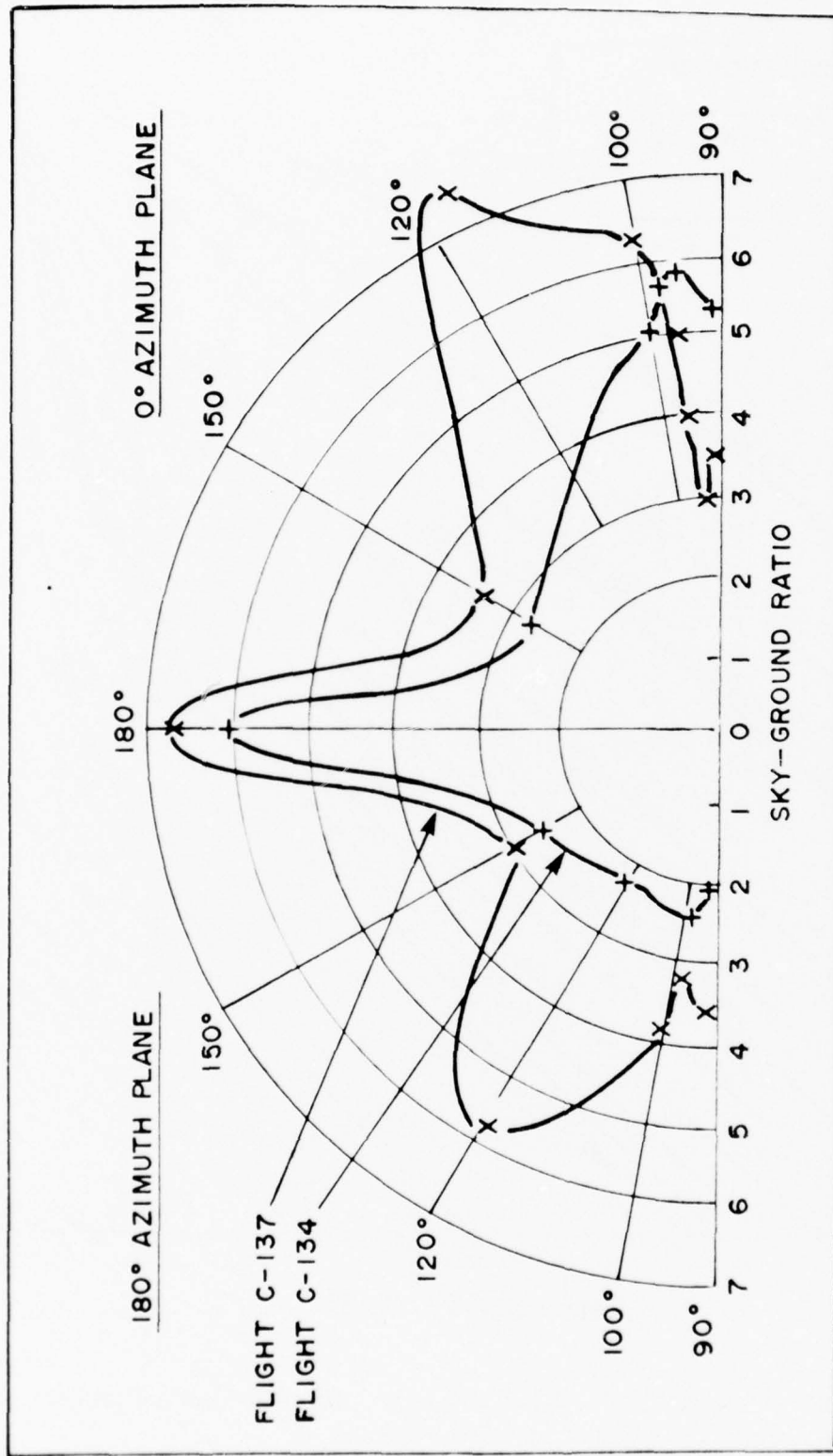
Bailey & Mundie, 1968

SKY - GROUND RATIO K
for downward vision.





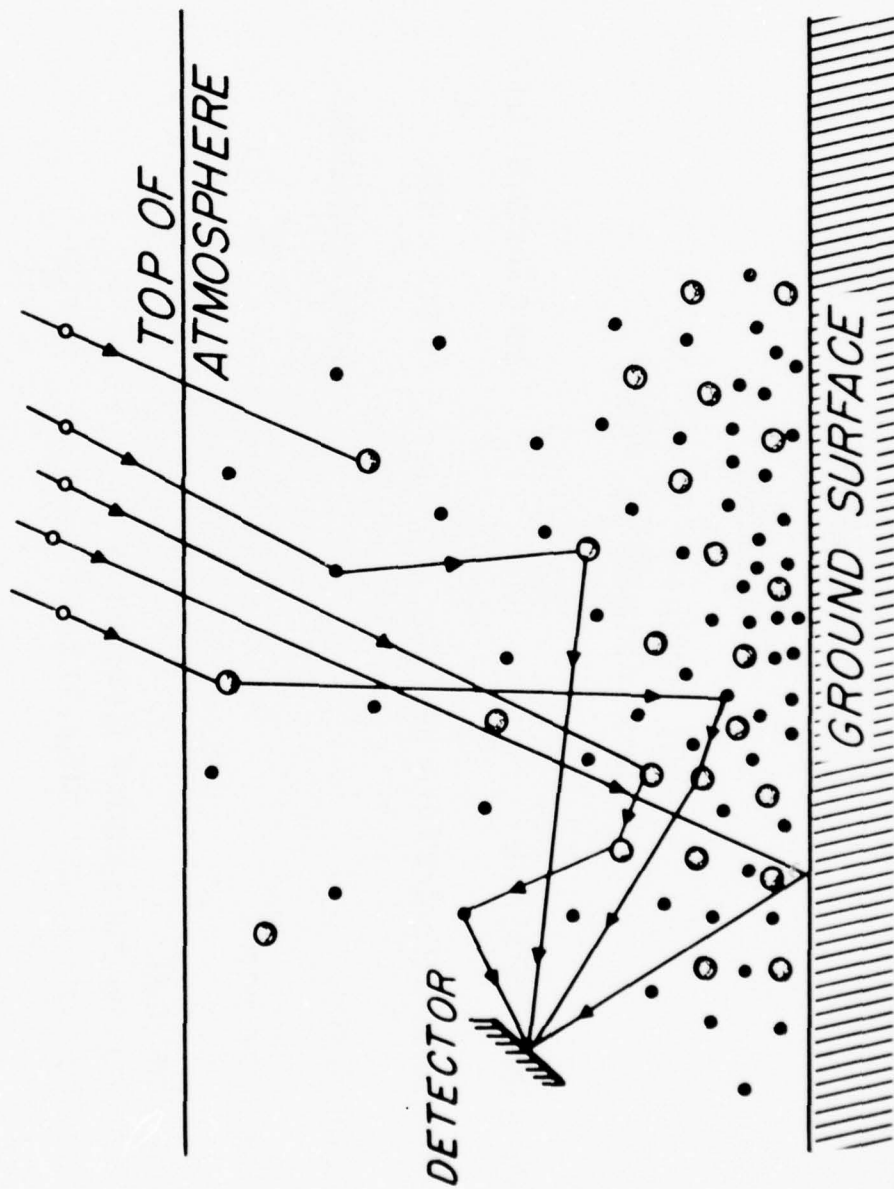
Dependence of Contrast Transmission Upon Air-Transmittance
for Differing Values of Sky-Ground Ratio, K



Sky-ground ratio versus receiver zenith angle in the solar plane. Data taken during Project Haven View.

V U G R A P H #20

PRINCIPLE OF MONTE CARLO CALCULATIONS
OF LIGHT TRANSPORT



MONTE CARLO

Wells, Collins et. al 1965 ff
Flass, Kattawar 1968 ff

Sky & Terrain Radiance

Path Radiance (Contrast Transm.)

Polarization

Time Dependence

Any Wavelength
Plane Parallel and Spherical Atmospheres
Plane Parallel, Point Isotropic or Laser
Sources.

Arbitrary Albedo

Arbitrary Geometry

Arbitrary Vertical Atm. Structure

Long Computer Time

Errors $< 10\%$

Many Applications

AIR WEATHER SERVICE
CONTRAST TRANSMITTANCE MODEL

VIDYA - AWS, late 1960's

Double Scattering

Downward Viewing

Short Computer Time

Plane Parallel Atm., Horiz. Stratified

Errors \leq 15% within
Specified Parameters

O₃ Absorption Above Atmosphere

Photo-recon Applications

No Absorption in the Atmosphere

$0.4 < \lambda < 0.7 \text{ m}$

Ground Albedo - 0.25

$V \geq 2 \text{ Km}$

Zenith Angles 0-60°

Solar Illumination

DART - PROGRAM

Draper Laboratory (C. Whitney et. al. 1972 ff)

Dodecahedron Approach
to Radiative Transfer

17 Radiation Streams

Sky & Terrain Radiance

Path Radiance (Contr. Transm.)

Single Scattering, Exact

Plane Parallel or Spherical Atmosphere

Plane Parallel Source (Sun)

In Principal Any Wavelength

Arbitrary Geometry

Arbitrary Vertical Structure

Short Computer Time

Errors $\leq 10\%$?

CONCLUSIONS

MONTE CARLO METHOD: MOST GENERAL

DART: POSSIBLY OPTIMUM TRADE-OFF EFFICIENCY - APPLICABILITY

SKY/GROUND RATIO-METHOD: WITH IMPROVEMENTS USEFUL FOR
ROUGH ESTIMATES

(This page intentionally left blank.)

UNCLASSIFIED

ATMOSPHERIC TURBULENCE MEASUREMENTS AT AMOS

Donald W. Hanson
Rome Air Development Center
Griffiss AFB, New York 13441
(315) 330-3144

Abstract

Atmospheric turbulence is created by random, small scale, high frequency, temperature fluctuations in air. Theory has been developed which relates the propagation of light through the atmosphere to the temperature turbulence in the atmosphere. Thus in order to design and predict the performance of optical systems which transmit through the atmosphere some estimate of the temperature turbulence must be available. The Compensated Imaging (CI) prototype will be delivered to the ARPA Maui Optical Station (AMOS) for field testing. Therefore, an extensive measurements program is being conducted at AMOS to determine the characteristics of the turbulence above AMOS.

Several instruments have been deployed to AMOS to gather the atmospheric data. These instruments include microthermal probes to measure turbulence at ground level, an acoustic sounder to obtain a turbulence profile up to 100m, a profilometer to obtain a turbulence profile from 1km to 25km, and a Seeing Monitor which provides a measure of the integrated turbulence from ground level up through the atmosphere. Data from the various instruments is compared. A comparison of the measured profiles with profiles predicted from rawinsonde data is given.

Introduction

The propagation of light through the atmosphere is a function of the existing temperature turbulence. Temperature turbulence is small changes over short distances in the temperature of air which induce apparent path length changes in the propagation path. Extensive theory has been developed which relates optical propagation parameters to temperature turbulence parameters. The theory shows that optical propagation is a function of both the total strength of the turbulence and of the distribution of the turbulence. A parameter, r_o , has been defined which is a measure of total turbulence strength.¹ The following equation can be used to calculate r_o if the temperature turbulence profile is known:

$$r_o = \left[0.42 \left(\frac{2\pi}{\lambda} \right)^2 \int_{\text{path}} C_n^2(h) dh \right]^{-\frac{1}{3}}$$

where λ is the wavelength of light and $C_n^2(h)$ is the value of the optical structure constant at the distance h from the receiver. Notice that r_o is not a function of where the turbulence is, only of the integrated value.

UNCLASSIFIED

UNCLASSIFIED

The parameter r_o can be used to calculate residual errors in optical systems which use deformable mirrors, as shown by the following equation:²

$$\sigma_\phi^2 = .141 \left(\frac{d}{r_o}\right)^{5/3} \text{ rad}^2$$

where σ^2 is the mean square optical phase error over the telescope aperture due to the discrete distance, d , between actuators on the deformable mirror. Notice that as r_o increases, ie. turbulence decreases, the residual error decreases.

The apparent motion of an object when viewed through the atmosphere or the ability to point a laser through the atmosphere is also only dependent on r_o and is given by the following equation:³

$$\sigma_\alpha^2 = .184 \left(\frac{D}{r_o}\right)^{5/3} \left(\frac{\lambda}{D}\right)^2 \text{ rad}^2$$

where σ^2 is the variance in the angle of arrival of an object (or the variance in the pointing angle of a laser), D is the aperture of the receiving or transmitting system, and λ is the wavelength of light.

The above parameters depend only on r_o , or the integrated turbulence strength. Some other propagation parameters depend on the distribution of turbulence. For example, the variance in the log-amplitude of light propagating through the atmosphere is given by the following equation:

$$\sigma_\ell^2 = .56 \left(2\pi/\lambda\right)^2 \int h^{5/6} C_n^2(h) dh$$

where σ_ℓ^2 is the variance in the log-amplitude of the light and h is the distance from the point receiver to the turbulence. Notice that for the same value for the integrated strength of turbulence various values of σ_ℓ^2 could be obtained depending on what the distribution of turbulence was between the receiver and the optical source.

The above are just a small number of examples which show the correlation between turbulence and optical propagation parameters. It is apparent that the performance of optical systems which propagate through the atmosphere will depend on the turbulence existing during the time at which the system is operating. Also the design of systems which attempt to correct for aberrations induced by the atmosphere will be a function of the turbulence conditions in which the systems will operate.

A Compensated Imaging prototype is currently being fabricated for deployment to the ARPA Maui Optical Station (AMOS). To support the design of that system instrumentation was developed to measure turbulence at AMOS and numerous experiments have been conducted using the instrumentation. A description of the sensors, experiments conducted, experimental data, and comparison with models is given below.

UNCLASSIFIED

UNCLASSIFIED

Measurement Instrumentation

Instruments have been deployed to AMOS which measure a turbulence profile from ground level up through the atmosphere as well as the integrated strength of turbulence r_o .⁴ Microthermal probes measure the turbulence at the height of the telescope aperture (15m) an acoustic sounder measures the turbulence from 15m to 100m, and a variable spatial frequency scintillometer measures the turbulence from 100m up through the rest of the atmosphere. A seeing monitor uses a variable spatial frequency chopper to measure r_o . For the profiles of 17, 18, and 21 Nov presented below the acoustic sounder was not operational. Microthermal probes mounted on a light aircraft were used to measure turbulence from 3000m down to 37m above the site.⁵

Measured Data

Profile measurements were made in November of 1975.⁵ The profiles are plotted in figures 1, 2, and 3. A summary of r_o measurements taken to date is given in table I.⁴⁻⁸ A cross check on the data was made by calculating a value of r_o from the turbulence profiles shown in figures 1 to 3. The values calculated from the profiles, along with values of r_o measured by the seeing monitor, are shown in table II. The data in table II show that for the three days when data was obtained the profile r_o is larger than the seeing monitor r_o . Since the values measured by the seeing monitor are in the range of previous measurements it appears as if some turbulence was missed when measuring the profile. This is very possible since the aircraft which made the measurements was not directly over the peak of the mountain when the lowest altitude measurements were made. If a layer between 20 and 80 meters thick at a C_n^2 value $10^{-14} \text{ m}^{-\frac{3}{5}}$ were added to the profile, the profile and seeing monitor r_o values would compare quite closely.

Turbulence Models

Yura has compared the measured profiles to profiles predicted by models of the atmosphere.⁹ The equations used to model the atmosphere are shown in figure 4. The last equation is a model developed by Hufnagel, it relates an average wind velocity to turbulence.¹⁰ The rest of the equations are derived from empirical data of Koprov and Tsvang¹¹ and Bufton.¹² The profiles that Yura obtained are shown in figures 1, 2, and 3 as dashed lines. The values of r_o obtained by Yura from the models are shown in table II.

Values of σ^2 , for a point receiver, calculated from the model atmosphere and values of σ^2 calculated from the measured profiles are given in table III.

In general the shape of the model profiles, and the values of r_o obtained from the model profiles are in reasonable agreement with measured values. The values of log-amplitude variance calculated from the model atmosphere are significantly higher than those calculated from the measured profiles for 18 and 21 Nov. This agrees with the data shown in figures 2 and 3.

UNCLASSIFIED

where the model atmosphere is seen to have higher values of C_n^2 at high altitudes than the measured profile.

Future Plans

The acoustic sounder is expected to be operational at AMOS in mid December. Starting in January of 1977 profile measurements will be made on a routine basis. The seeing monitor will be used to measure r_o while the profile measurements are made. The value of r_o obtained from the profile will be compared with the value measured with the seeing monitor. Also another instrument is scheduled for deployment to AMOS which will measure r_o . A combination of these three independent measures of r_o should provide a good estimate of r_o . Model profiles will be developed from rawinsonde wind data and compared with measured profiles. Modifications to the models, if necessary and possible, will be proposed. A similar measurement program is also scheduled to be conducted at the RADC Advanced Optical Test Facility, located near Rome, N.Y.¹³

UNCLASSIFIED

UNCLASSIFIED

References

1. Fried, D.L., J. Opt. Soc. Am. 56, 1372 (1966).
2. Greenwood, D.P. and Fried, D.L., Power Spectra Requirements for Wavefront-Compensative Systems, RADC-TR-75-227, equation 68 page 35.
3. Reference 2, equation 70 page 36.
4. Miller, M.G., Zieske, P.L., and Dryden, G., Turbulence Characterization and Control, RADC-TR-76-189.
5. Miller, M. Zieske, P., and Hanson, D., Characterization of Atmospheric Turbulence, SPI Symposium on Imaging Through the Atmosphere, Reston, Virginia (1976).
6. Greenwood, D.P., et.al., AMOS Seeing Quality Measurements, RADC-TR-75-295.
7. Miller, M.G., and Kellen, P.F., Topical Meeting on Imaging in Astronomy, Cambridge, MA. (1975).
8. Schneiderman, A.M., and Karo, D., OSA Topical Meeting on Speckle Phenomena in Optics, Microwaves and Acoustics, Pacific Grove, CA (1976).
9. Yura, H., Optical Phase and Scintillation at AMOS, Interim Report for ARPA ORDER 2843, SAMS0 TR to be published.
10. Hufnagel, R.E., Variations of Atmospheric Turbulence, OSA Topical Meeting on Optical Propagation Through Turbulence, Boulder, CO (1974).
11. Koproff, V.R. and Tsvang, L.R., Characteristics of Very Small Scale Turbulence in a Stratified Boundary Layer, Atmos. and Oceanic Phys. 22, 1142 (1966).
12. Bufton, J.L., Comparison of Vertical Turbulence Structure with Stellar Observations, Appl. Opt. 12, 1785 (1973).
13. Spencer, J.L., The Advanced Optical Test Facility, ODDR&E Workshop on Optical/Submillimeter Workshop, U.S. Air Force Academy, Colorado Springs, CO (Dec 1976).

UNCLASSIFIED

TURBULENCE PROFILE ABOVE AMOS - 17 NOV 1975

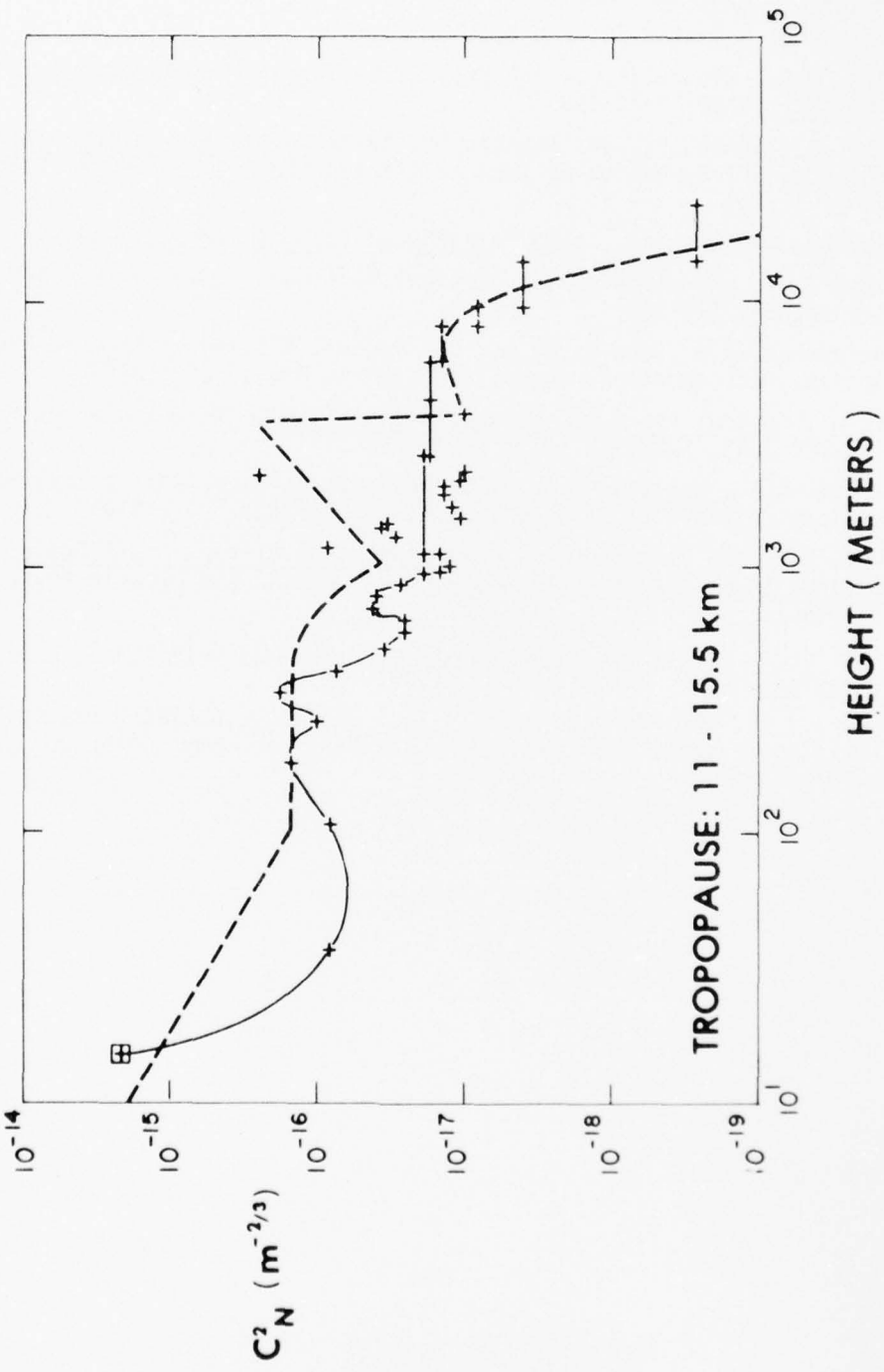


FIGURE 1. TURBULENCE PROFILES
Measured (solid line) and model (dashed line) temperature turbulence profile

TURBULENCE PROFILE ABOVE AMOS - 18 NOV 1975

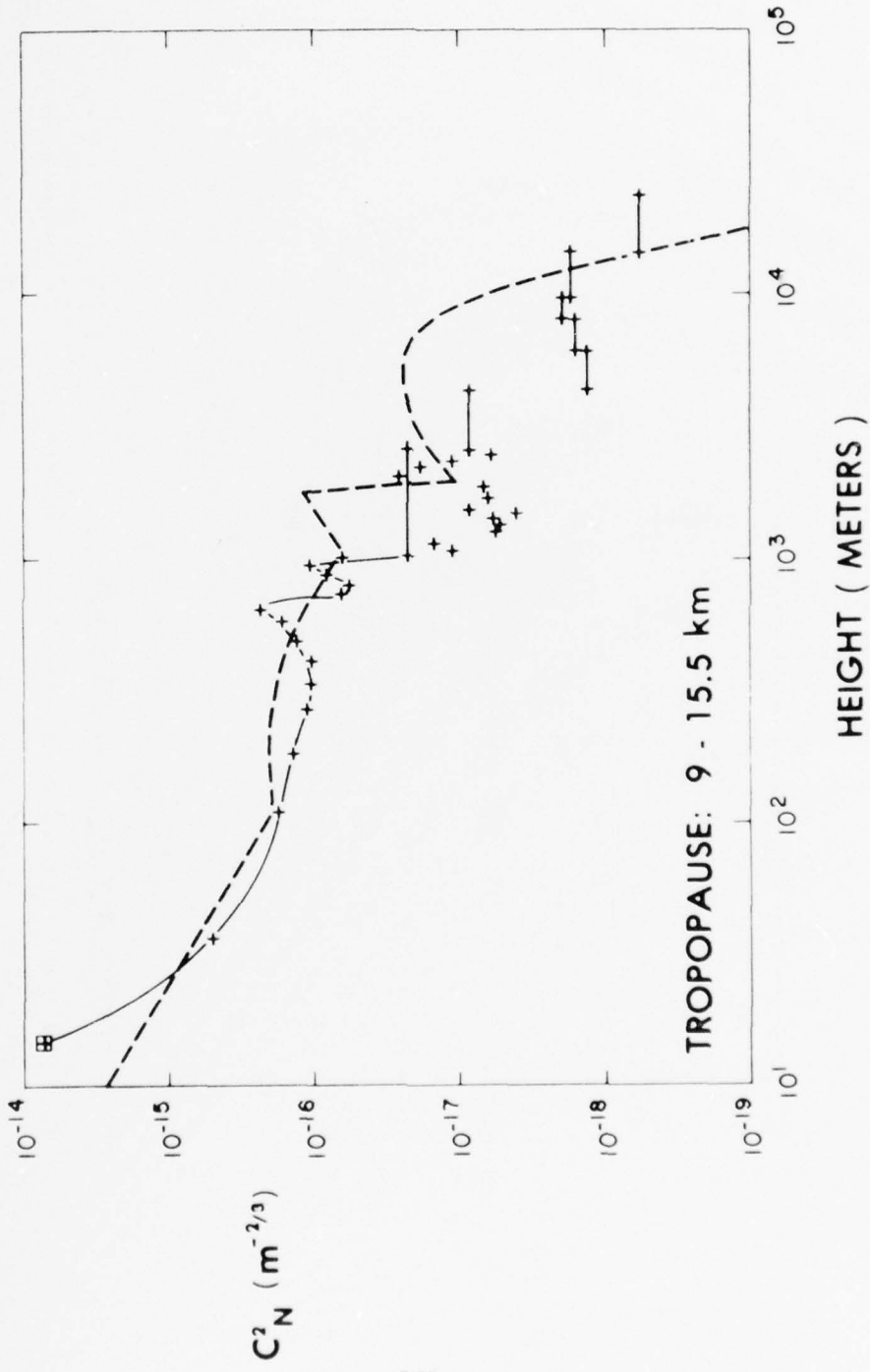


FIGURE 2. TURBULENCE PROFILES
Measured (solid line) and model (dashed line) temperature turbulence profile

TURBULENCE PROFILE ABOVE AMOS - 21 NOV 1975

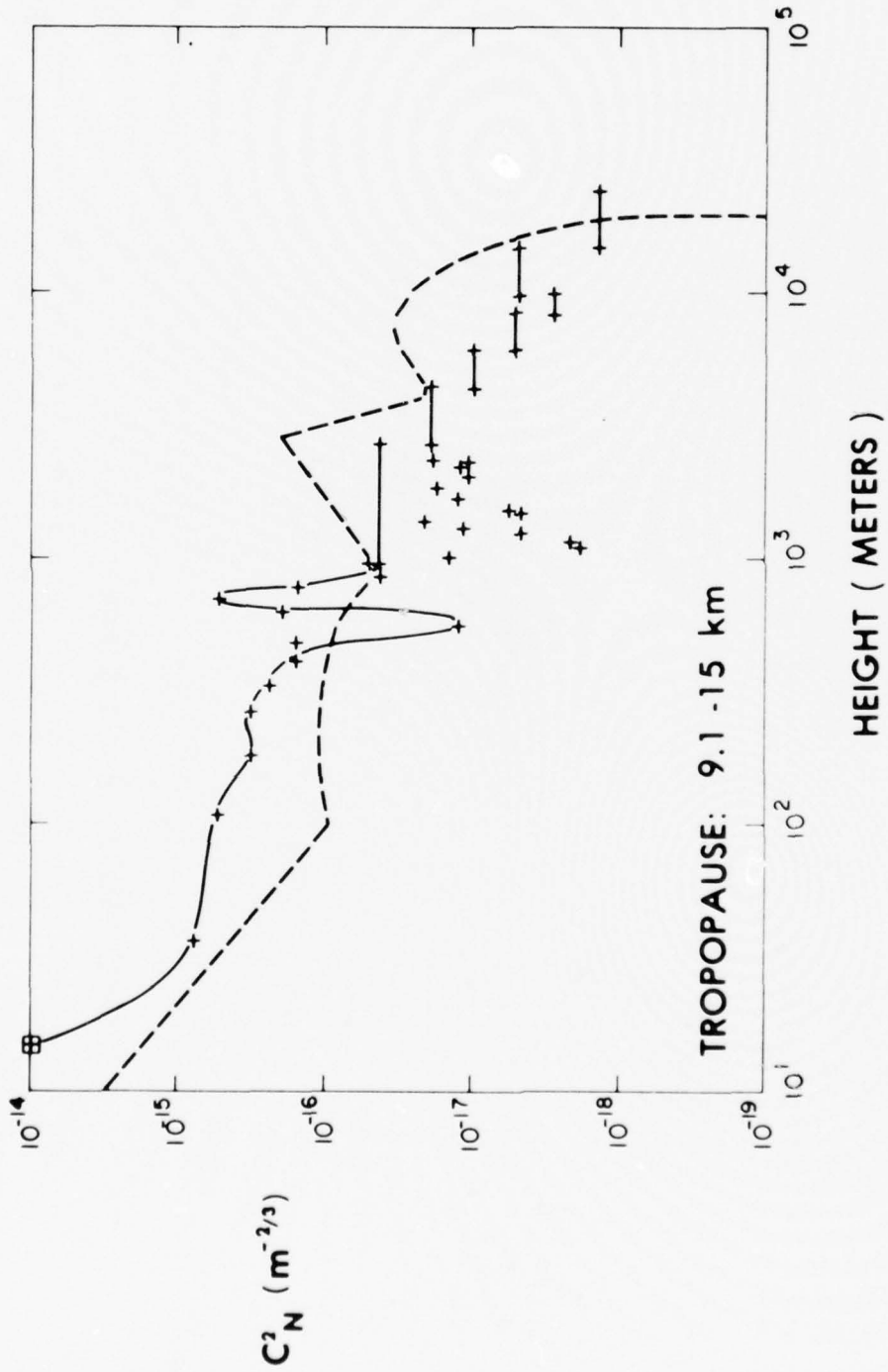


FIGURE 3. TURBULENCE PROFILES
Measured (solid line) and model (dashed line) temperature turbulence profile.

EMPIRICAL MODEL

$$C_n^2 = \begin{cases} 7.0 \times 10^{-14} h^{-4/3} & , 10m < h < 100m \\ 1.5 \times 10^{-16} & , 100m < h < 500m \\ 1.5 \times 10^{-16} - 1.125 \times 10^{-16} \left(\frac{h-500}{500} \right) & , 500m < h < 1000m \\ 3.75 \times 10^{-17} + 7.95 \times 10^{-17} \left(\frac{h-1000}{1000} \right) & , 1000m < h < 2000m \\ 1.17 \times 10^{-16} - 5.85 \times 10^{-17} \left(\frac{h-2000}{2000} \right) & , 2000m < h < 3000m \end{cases} \quad (6)$$

INFRA-RED

$$C_n^2 (h, V) = 5.99 \times 10^{-23} (V/27)^2 h^{10} e^{-h} + 2.72 \times 10^{-16} e^{-h/1.5} \quad h > 3000m$$

FIGURE 4. MODEL EQUATIONS

Equations used to model the temperature turbulence above MCS.

UNCLASSIFIED

TABLE I

Measured values of r_0 at AMOS

Date	Range of r_0 - cm
Aug 74	2.9 - 18.3 (mean 10.2)
Jun 75	4.1 - 6.4
Aug 75	5.1 - 10.3
Nov 75	8.8 - 24.7
May 76	7.4 - 13.9
Jun 76	5.4 - 13.3 (mean 8.9)
Jul 76	6.2 - 14.4 (mean 9.3)

TABLE II

Values of r_0 , in cm, obtained by various methods

Date	Measured Profile	Seeing Monitor	Yura Modelling
17 Nov	25.7	10.4	17.1
18 Nov	24.9	15.4	17.4
21 Nov	16.6	11.6	14.4

TABLE III

Calculated values of log-amplitude variance- σ_L^2

Date	Measured Profile	Model Profile
17 Nov	.018	.028
18 Nov	.008	.026
21 Nov	.019	.056

UNCLASSIFIED

OPTICAL PROPAGATION THROUGH TURBULENCE
IN THE MARINE BOUNDARY LAYER*

E. C. Crittenden, Jr., A. W. Cooper, E. A. Milne,
G. W. Rodeback, S. H. Kalmbach, and R. L. Armstead

Environmental Physics Group
Naval Postgraduate School, Monterey, CA., 93940

D. Land and B. Katz
Naval Surface Weapons Center, White Oak,
Silver Spring, MD. 29010

ABSTRACT

Measurements of image resolution through the atmosphere, as expressed by the optical transfer function (OTF), have been made over the ocean with laser sources at wavelengths .4880, 0.6328, 1.06, and 10.6 μm for ranges from 0.3 to 19 km. Measurements are made with a slit scanning telescope with Fourier deconvolution of the instrument function. OTF curve shapes are in good agreement with the Fried theory and good internal agreement exists between long term OTF, short term OTF, and image wander. Predicted behavior, based on C_n from point C_T and from scintillation, is in reasonable agreement with observed behavior in view of the differences in relative weighting as a function of path position. Considerable scatter in the results still exists, indicating intermittency in the boundary layer flow.

INTRODUCTION

The work to be reported here is part of a joint interdisciplinary project, including measurement of both the optical and the meteorological parameters connected with optical propagation in the marine boundary layer.

This paper will report some optical results, and the following paper by K. L. Davidson will report related meteorological work.

The general objective has been to determine the optical effects of turbulence in the marine boundary layer and to relate these effects to the micrometeorology, with the intention of providing a basis for verification of theoretical models and prediction of the optical effects from large scale meteorology.

UNCLASSIFIED

Experimental data have been taken on optical ranges of 4 to 19 km, from land to land across Monterey Bay and ranges of 0.2 to 5 km from the NPS Research Vessel Acania to land. The locale of the ranges is shown in Figure 3 of the paper by K. L. Davidson et. al. following this paper.

The optical property of primary interest has been the optical transfer function (OTF) of the atmosphere. In general the OTF is a two dimensional property. However, for an isotropic medium the one dimensional transfer function is adequate. It is expressed in terms of spatial (angular) frequency, in lines per radian, or for convenience, in lines per milliradian. The spatial angular frequency is equal to $F \cdot f$ where F is the focal length and f is the spatial frequency in lines per unit length. The OTF of the atmosphere describes the ability of an optical system to resolve images through the atmosphere. By reciprocity, it describes equally well the image spread, or "blur" for an imaging system, or the beam spread at a distant "focus" for a beam-forming projecting system.

The OTF is obtained here by scanning a slit across the image of a distant point object. The signal, thus obtained, is the line spread function. The spatial frequency spectrum of a point object is constant with frequency, so the spatial frequency spectrum of the image is the OTF, except for the effects of diffraction, finite slit, and aberrations of the telescope, or imaging system. Under the assumption of linearity, the image is the convolution of the spread function of the telescope and that of the atmosphere. The telescope spread function is measured in the laboratory and unfolded from the observed image line spread function by Fourier transform deconvolution. The resulting spatial frequency spectrum is thus that of the atmosphere alone, as if observed with a perfect diffractionless telescope (within the limitations of system noise).

Two sets of representative slit scanned image line spread functions are shown in Figure 1. The turbulence level, as indicated by C_n , the turbulence structure constant for optical index, is $3 \times 10^{-8} \text{ m}^{-1/3}$ for the left-hand diagram and $5.5 \times 10^{-8} \text{ m}^{-1/3}$ for the right-hand diagram, or C_n^2 of 9×10^{-16} and $30 \times 10^{-16} \text{ m}^{-2/3}$. The successive scans were made at a repetition rate of 50 Hz - displaced vertically as a function of time in Figure 1 for display. The range was 4 km and the wavelength .6328 μm laser light.

Although there is considerable random structure, the average of many images is smooth and symmetrical. This symmetry permits the modulation transfer function (MTF) for the

UNCLASSIFIED

UNCLASSIFIED

averaged image function to be synonymous with the OTF. The complex OTF then has only a real part and no imaginary part, and the modulus is the same as the function.

The mutual coherence function (MCF) is also the same function as the MTF. As a result, the behavior of the atmosphere for image resolution also yields information of value relative to coherence length, pertinent also to communications problems. Although the same quantity as MTF, the MCF is usually expressed in terms of another variable ρ , where $\rho = \lambda Ff$.

Two types of line spread function averages are useful. First, the long exposure, or long term, average is the average shape, irrespective of displacement of the image. Second, if the center of area (or in some cases the centroid) is calculated and centered before averaging, another average curve is obtained. This will be called the "short exposure" or "short term" averaged line spread function. This line spread function is narrower than the long term line spread function. It has the general width of an actual short exposure, but the random structure has been averaged out. After Fourier deconvolution to remove the instrument broadening, the Fourier transforms of the long term and short term line spread functions are the curves of long term and short term MTF (or OTF) of the atmosphere. Representative curves appear in later figures. The shifts, required to center each individual line spread function to obtain the short term average, are stored in the computer. They vary with time as shown in Figure 2. This behavior is the "image wander" or "beam wander". The particular trace shown is too short to give a good average value for sigma of the wander excursion (the probable deviation). This segment was chosen for Figure 2 because the motion is suggestive of influence of the ocean waves over which the light was propagating. The value of sigma calculated by the computer includes the complete sequence of line spread functions utilized. The value of sigma from the image wander serves as a measure of C_n . According to the theory of Fried¹ and others the variance $\langle \alpha^2 \rangle$ of the image wander is given, for $D > \lambda L$, by:

$$\langle \alpha^2 \rangle = (2.91) \cdot (3/8) (1.026) L D^{-1/3} C_n^2$$

where L = range, D = diameter, λ = wavelength. It is interesting to note that image wander is independent of the wavelength of the light employed.

UNCLASSIFIED

UNCLASSIFIED

The shape of the MTF curves, as given by Fried², is:

$$M(f, z) = e^{-\frac{2.91}{2} \beta 4\pi^2 C_n^2 z \lambda^{-1/3} (Ff)^{5/3} [1-\alpha(Ff\lambda/D)]^{1/3}}$$

where F = focal length, D = aperture diameter, f = spatial frequency, Ff = angular frequency, $\alpha = 0$ in long-term or $1/2$ in far-field short-term, or 1 in near-field short-term, $\beta = 1$ in plane wave or $3/8$ in spherical wave.

Other models³ exist for the shape of the MTF curves, but the Fried model has been utilized as it includes short and long term MTF.

For the long-term case, for which $\alpha = 0$, the above expression has the form:

$$M = e^{-x^{5/3}}$$

For this function, there is a useful relationship between the spatial angular frequency, $(Ff)_{1/2}$, at which the MTF = $1/2$, and the full width at half maximum, $(\Delta\theta)_{1/2}$, of the line spread function. This is:

$$(Ff)_{1/2} \cdot (\Delta\theta)_{1/2} = 0.40$$

The constant 0.40 is dimensionless, resulting from the product of lines per radian by radians. This is useful for cases of large atmospheric broadening of the image, where the necessity for deconvolving the instrument function becomes relatively small. None of the data reported in this paper were reduced in this manner, but the relationship is useful for a quick qualitative estimate in the field.

A plot of the observed short term MTF for 0.4880 μm is shown in Figure 3. The points are experimental points and the solid curve is a best fit theoretical curve for the Fried model, with C_n and the zero frequency point as adjustable parameters. The measured zero frequency point is undependable because it represents the area under the line spread function and thus is sensitive to zero adjustment. The line spread curves are zeroed in the wings before calculation but still the zero frequency points are undependable. Incidentally, this zeroing drops out essentially all of any aerosol scatter broadening that might be present, since such scattering is expected to produce several orders

UNCLASSIFIED

UNCLASSIFIED

of magnitude wider spread, with a gaussian shape.

Observed long term MTF values for four wavelengths, .4880, .6328, 1.06, and 10.6 μm taken at essentially the same time as for Figure 3, are shown in Figures 4 through 7. The best fit curves are the solid lines, using the Fried long term model. The values of C_n required for fit are quoted in the inserts in each figure. The short term C_n of Figure 3 and the long term C_n values of Figures 4-7 are all very close in value. Values of C_n derived from image wander are also quoted in the inserts and are also very close in value. The shapes of the curves are all well fitted by the Fried model.

During the measurement of C_n from MTF, values of C_n are also obtained from three other independent sources, for comparison. C_n is also obtained from C_T , the turbulence structure constant for temperature fluctuation, by measurements on board the Acania, located near the optical path. C_n is also obtained from C_T measurements at the receiver end of the optical path. C_n is related to C_T by means of the relationship⁴:

$$C_n^2 = \left(\frac{79P}{T^2} \cdot 10^{-6} \right)^2 C_T^2$$

C_n is obtained from scintillation of the intensity for a laser beam transmitted along the optical path, by measuring the probability of occurrence of a given intensity as a function of the logarithm of the intensity. Such a probability density curve is shown in Figure 8.

The data points are on-line processed as plotted, to give the sigma of the Gaussian curve as a least squares best fit: The solid line is the calculated Gaussian curve. C_n is obtained from sigma for the curve by use of the relationship⁵:

$$\sigma^2 = 0.52 k^{7/6} C_n^2 z^{11/6}$$

Use of this method to determine C_n requires some caution, as the value of sigma will saturate and not exceed unity. For very large C_n , (long path, or short wavelength), sigma can become supersaturated and gradually decrease below unity. However, operation at several wavelengths permits use of scintillation without danger of error due to saturation. If sigma is well below unity for the long wavelengths, no correction is needed. Sigma also depends on the aperture size. Care must be exercised to utilize a small enough

UNCLASSIFIED

UNCLASSIFIED

aperture to avoid aperture averaging effects, or a correction may be utilized to allow for the effects of finite aperture. Friehe⁶ has pointed out that there can be a contribution to C_n from humidity fluctuation. Although this is often about 10-20% of the C_n from thermal fluctuation it apparently can be larger. This contribution was omitted here.

C_n depends on height above the water for turbulent flow in the marine boundary layer. For unstable conditions (temperature decreasing with height more rapidly than the adiabatic equilibrium rate) C_n varies as $h^{-4/3}$. This variation has been verified optically⁷. Because of this, care must be exercised to maintain constant height above the water. For long paths, correction is needed, as the height varies due to the earth's curvature and index gradient bending of the light path.

A comparison of C_{nT} , obtained from C_T measured at the ship located midway in the optical path, with the path integrated C_{n0} obtained optically from scintillation, is shown in Figure 9. In this case the wind was a steady northwest prevailing wind with conditions essentially uniform along the path. The agreement is satisfactory, considering that it is a comparison of a point observation at the center of the path with a path integrated value. Agreement is often not this good, presumably because the wind velocity is not uniform along the path.

A comparison of values of C_n from short term MTF, taken with the slit scanning telescope, with values of MTF measured with a shearing interferometer is shown in Figure 10. The two types of measurements were made simultaneously over very nearly the same path, with the shearing interferometer measurements made by a group from Lincoln Laboratory⁸. The points are grouped about a line of unity slope, indicating essential agreement between the two types of measurement. The shearing interferometer measures a quantity slightly different from that usually obtained with the slit scanning telescope. The shearing interferometer measures the average of MTF (modulus) for each scan. The slit scanning data can be processed to obtain that same information, but is usually processed so as to obtain the average of the OTF (or equivalently the MTF of the average line spread function). The difference between the two methods is in practice very minor.

A comparison of C_n obtained from short term MTF with that obtained from long term MTF is shown in Figure 11.

UNCLASSIFIED

UNCLASSIFIED

The points again cluster about a line of unity slope, indicating the two techniques are in essential agreement.

A comparison of C_n from MTF with that from scintillation is shown in Figure 12 for a 4.04 km range. On this path some shore influence was present on the telescope end. As we will see shortly the disagreement of about a factor of two, with C_n from MTF higher than from scintillation, would be consistent with an increase in C_n near the telescope due to shore influence.

A plot of the results from a recent run, 29 July 1976, is shown in Figure 13. The Acania was stationed at midpath on a range of 18.8 km, measuring C_n by means of C_T for thermal fluctuation. Similar thermal measurements were made at the telescope end of the path at the mobile lab on Point Pinos. The results clearly show the diurnal variation. It was a clear day with a well developed northwest wind from noon to dusk at 2000. At the mobile laboratory end the air flowed over a small hillock and a road, apparently contributing a high local C_n . This situation has been corrected in subsequent runs (in progress at the time of this meeting). Values of C_n from MTF measured for various wavelengths are also plotted, in Figure 13. Two points are also plotted for C_n from scintillation, using a 10.6 μm laser, a long enough wavelength to avoid saturation even at this long range.

The behavior shown in Figure 13 is understandable in terms of the weighting factors that apply when C_n is a function of position along the path. For scintillation with a spherical wave, the integrated value of C_n^2 is given by:

$$\int_0^z (z-z')^{5/6} \left(\frac{z'}{z}\right)^{5/6} C_n^2(z') dz'$$

This weights the contribution more heavily in the center of the path, as shown in Figure 14. For MTF, for a spherical wave,

$$M(f) = \exp \left\{ -1.46 k^2 D^{5/3} \int_0^z C_n^2(z') \left(\frac{z'}{z}\right)^{5/3} dz' \right\}$$

This weights the contribution to MTF strongly at the receiver end of the optical path, as shown in Figure 14.

UNCLASSIFIED

UNCLASSIFIED

In view of the weightings as indicated in Figure 14 the C_n obtained from MTF would be expected to lie between the telescope shore-end point values from C_T , and the ship point value, as observed, at least up till dusk at 2000. The scintillation values also would be expected to lie between the values from thermal measurements, but below the MTF C_n values, as is observed. After dusk the airflow was irregular and reversed direction in some regions along the path, so that it is not surprising that the MTF value goes above the thermal point values on the ship and shore.

CONCLUSIONS

The results indicate excellent agreement between the Fried model and the MTF curve shape for both short term and long term MTF. The behavior as a function of wavelength also follows the Fried model. C_n values obtained from short term MTF, long term MTF, and wander show internal agreement. C_n values obtained from MTF and wander are in essential agreement with C_n values from scintillation and point thermal measurements, bearing in mind the relative weightings that apply as a function of path position for each of the measurements. Relatively large fluctuation in observed C_n indicate the existence of intermittency in the airflow in the marine boundary layer.

UNCLASSIFIED

REFERENCES

1. Fried, D. L., J.O.S.A., 55, 11, 1427 (1955)
Collins, S.A. and Damon, E. K., RADC TR-71-124 (1971)
2. Fried, D. L., J.O.S.A., 56, 10, 1372 (1966)
3. Yura, H. T., J.O.S.A., 63, 567 (1973)
4. Ochs, G. R., Bergmann, R. R., and Snyder, J. R.,
J.O.S.A., 59, 2, 231 (1969)
5. Fried, D. L., J.O.S.A., 57, 2, 175 (1967)
6. Friehe, C. A., La Rue, J. C., Champagne, F. H., Gibson, C. H., and
Dreyer, G. F., J.O.S.A., 65, 12, 1502 (1975)
7. Cooper, A. W., Crittenden, E. C., and Schroeder, A. F., paper WB4,
digest of technical papers, Opt. Soc. topical meeting, 9-11 July,
Boulder, Colo.
8. We are indebted to D. Kelsall, E. S. Cotton, L. C. Marquet, and
W. Stiehl of Lincoln Laboratory for this data.

* This work was supported by Naval Sea Systems Command (PMS405)

UNCLASSIFIED

UNCLASSIFIED

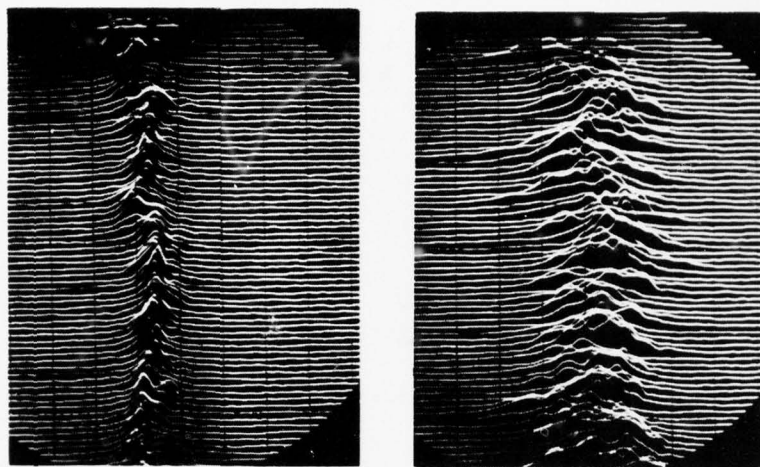


FIGURE 1. LINE SPREAD FUNCTIONS FOR TWO LEVELS OF TURBULENCE. Left: $C_n^2 = 9 \times 10^{-16}$. Right: $C_n^2 = 30 \times 10^{-16} \text{ m}^{-2/3}$

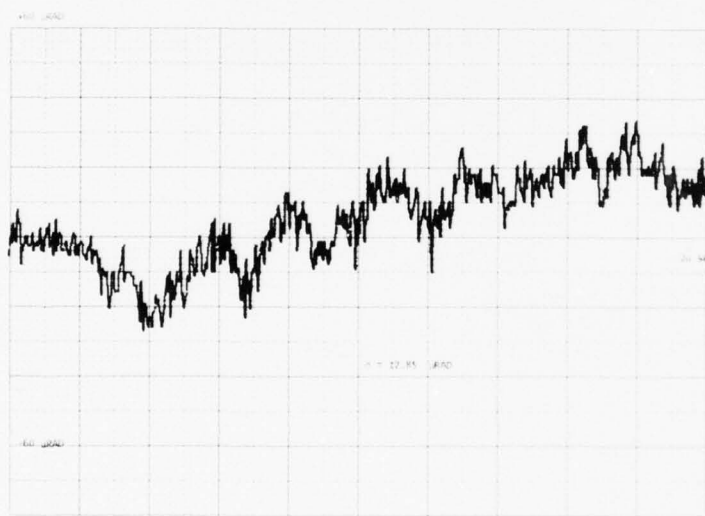


FIGURE 2. IMAGE WANDER AS A FUNCTION OF TIME.

UNCLASSIFIED

UNCLASSIFIED

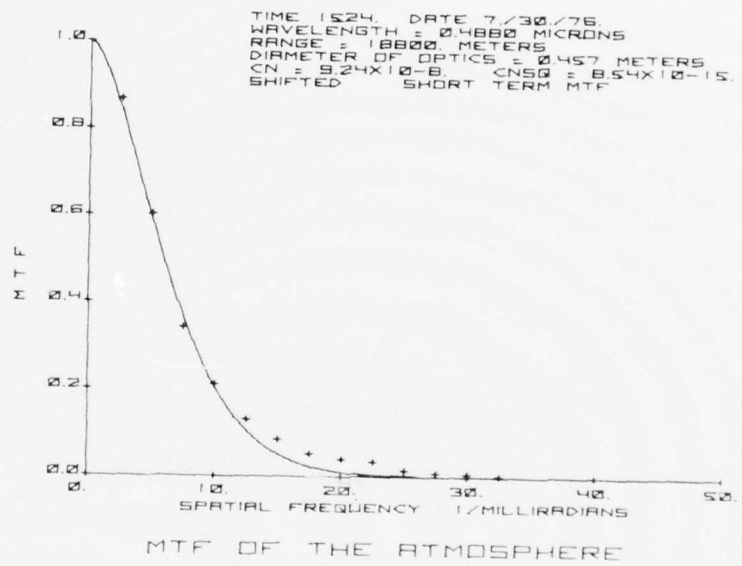


FIGURE 3. SHORT-TERM MTF OF THE ATMOSPHERE.

UNCLASSIFIED

UNCLASSIFIED

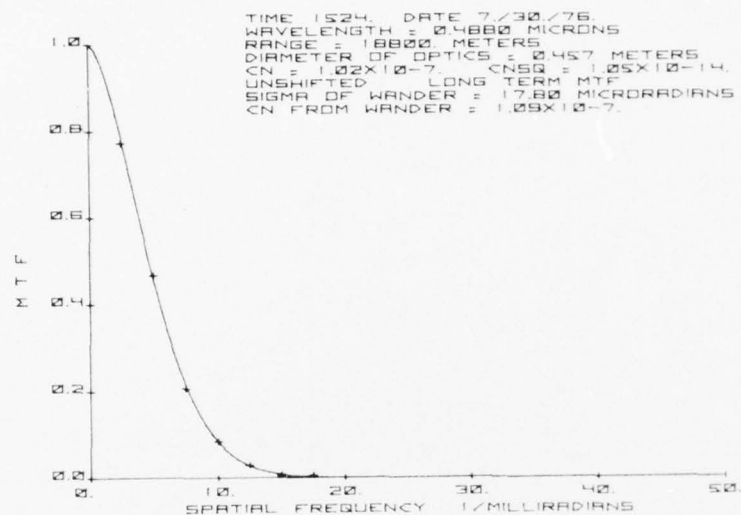


FIGURE 4. LONG-TERM MTF, 0.4880 micrometers

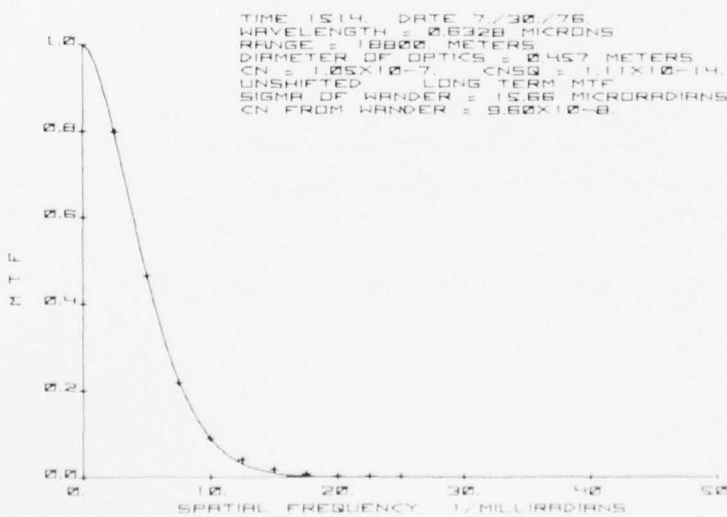


FIGURE 5. LONG-TERM MTF, 0.6328 micrometers

UNCLASSIFIED

UNCLASSIFIED

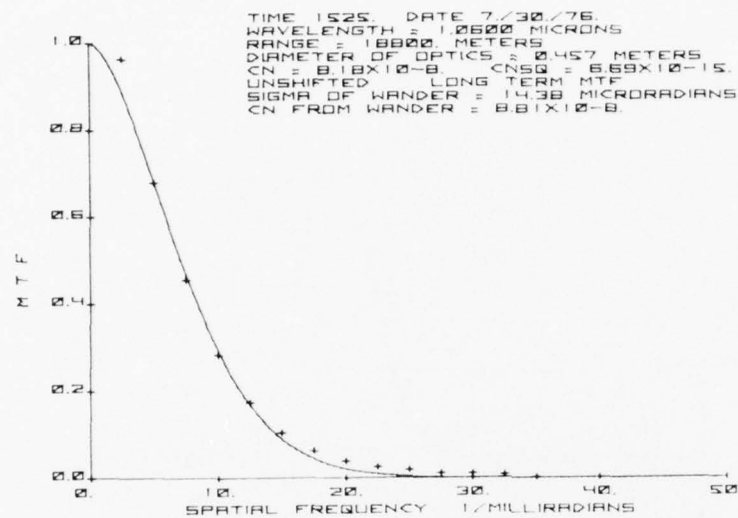


FIGURE 6. LONG-TERM MTF, 1.06 micrometers

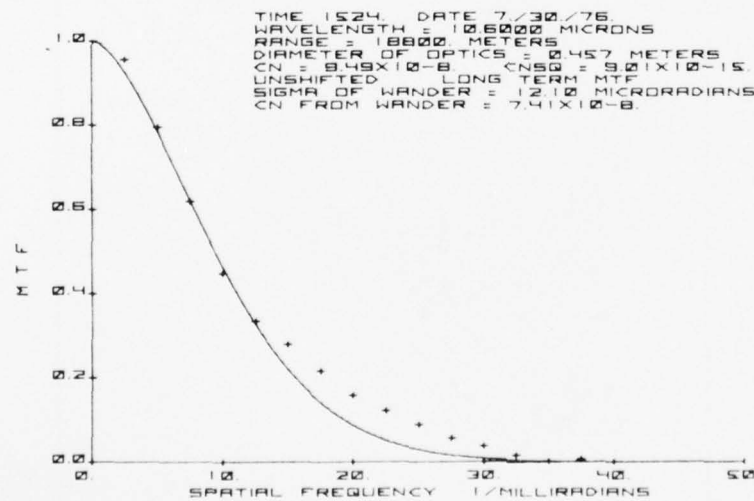


FIGURE 7. LONG-TERM MTF, 10.6 micrometers

UNCLASSIFIED

UNCLASSIFIED

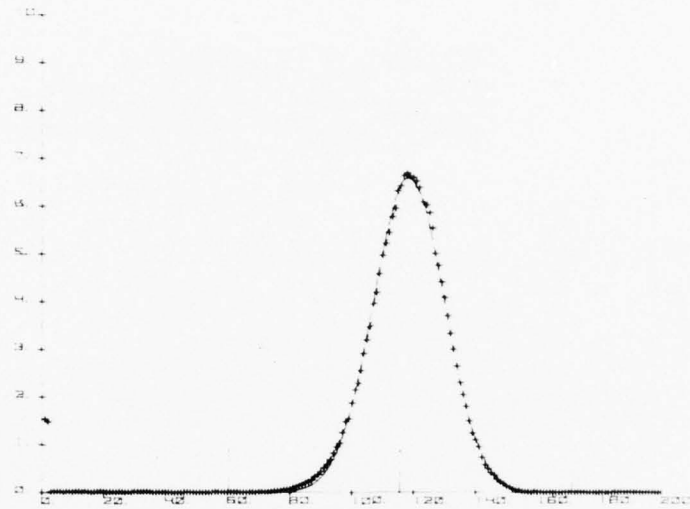


FIGURE 8. SCINTILLATION. Frequency of occurrence as a function of the logarithm of the intensity.

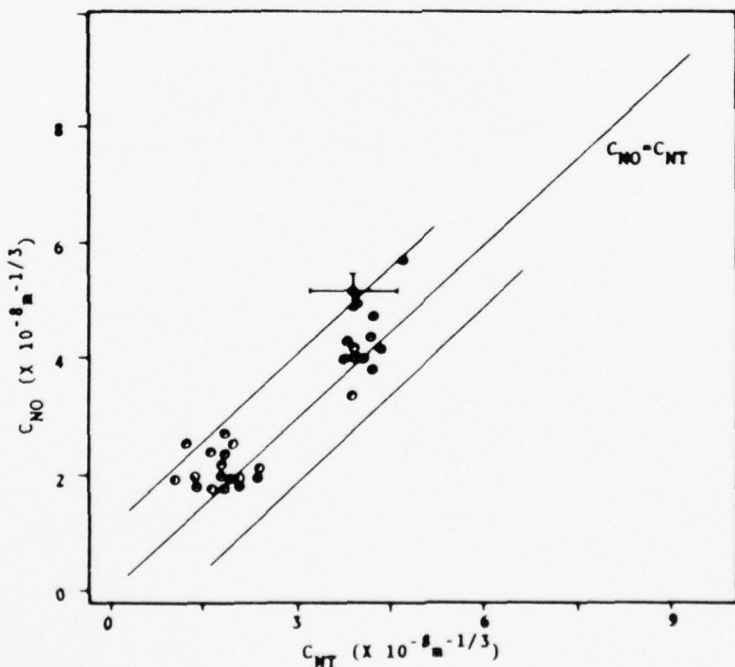


FIGURE 9. COMPARISON OF C_N VALUES. C_{NO} , optically measured along a 4 km path, vs. C_{NT} , thermally measured at the path center.

UNCLASSIFIED

UNCLASSIFIED

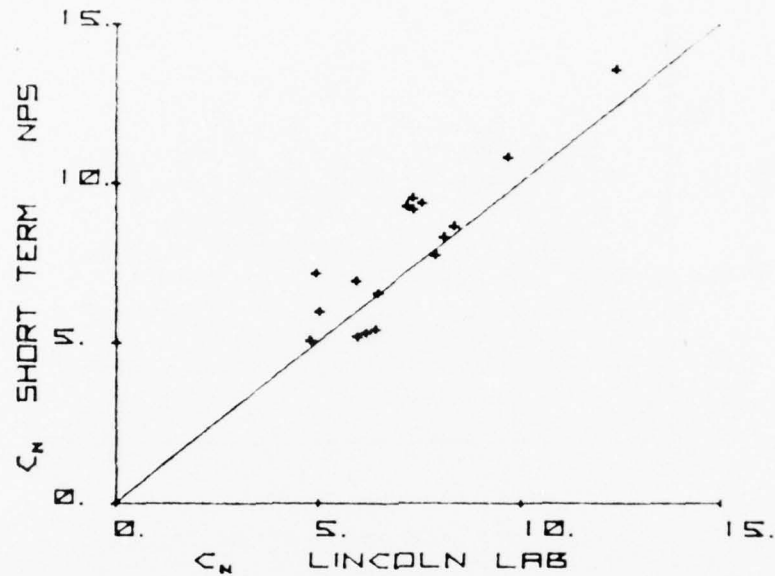


FIGURE 10. C_n FROM SHORT-TERM LINE SPREAD MTF VS. C_n FROM LINCOLN LAB. SHEARING INTERFEROMETER.

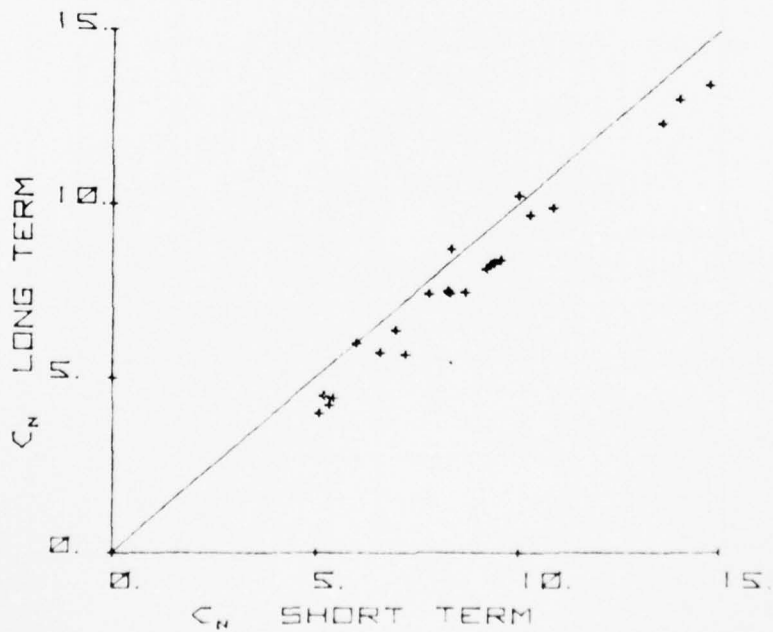
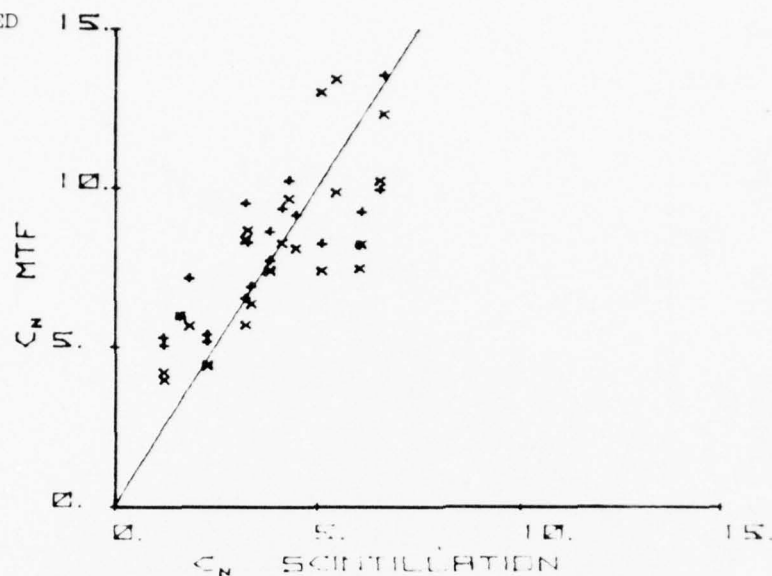
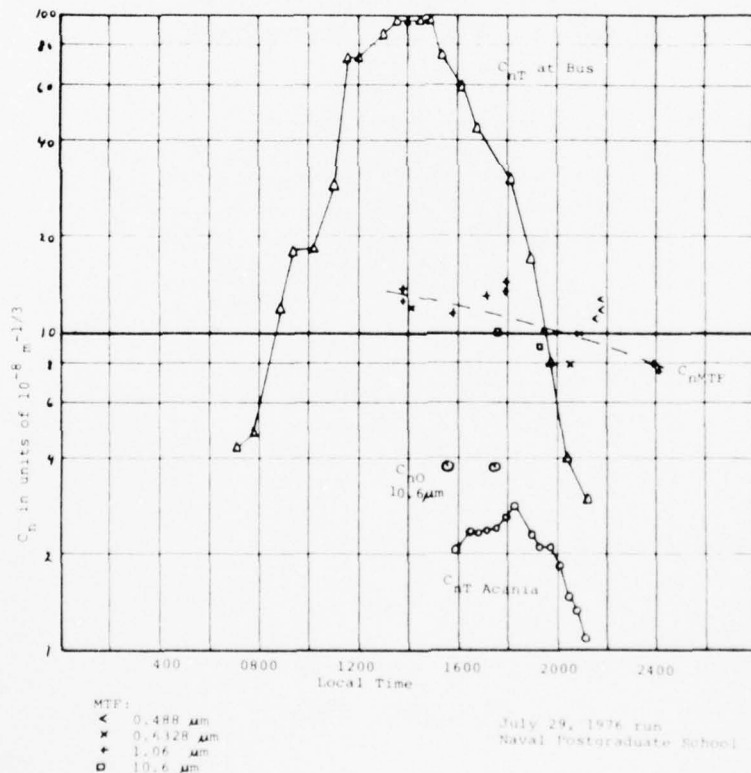


FIGURE 11. LONG-TERM VS. SHORT-TERM MTF VALUES OF C_n .

UNCLASSIFIED

UNCLASSIFIED

FIGURE 12. C_n FROM MTF VS. C_n FROM SCINTILLATIONFIGURE 13. C_n BY FOUR INDEPENDENT METHODS VS. TIME OF DAY
UNCLASSIFIED

UNCLASSIFIED

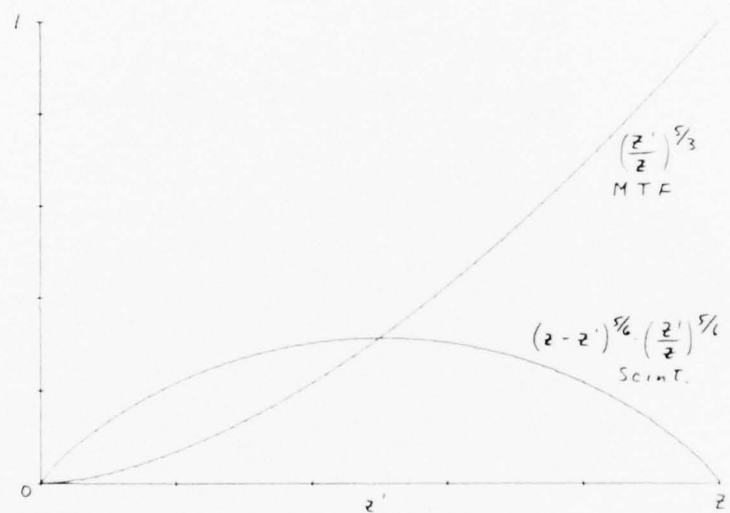


FIGURE 14. RELATIVE WEIGHTING OF C_n AS A FUNCTION OF POSITION ALONG THE PATH, FOR MTF AND FOR SCINTILLATION. The telescope end of the path is at the right.

UNCLASSIFIED

(This page intentionally left blank.)

DESCRIPTION OF OPTICALLY RELEVANT TURBULENCE PARAMETERS*

K. L. Davidson, C. Fairall, T. Houlihan
and G. Schacher

Environmental Physics Group
Naval Postgraduate School, Monterey, CA 93940

LT D. Hinsman, USN
Fleet Numerical Weather Central, Monterey, CA 93940

ABSTRACT

Existing approaches for relating small scale optically relevant turbulence parameters to bulk parameters are examined. Recent formulations for the temperature structure function parameter, C_T^2 , based on overland observations, are compared with overwater (shipboard) results. Considerable disagreement occurs between the overland predictions and the overwater results when stability conditions depart from the neutral case. Overwater results exhibiting intermittency in turbulence intensities, which is a possible factor for the disagreement, are examined. C^2 estimates computed from C_T^2 measurements are also compared with C_n^2 estimates computed from Fleet Numerical Weather Central (FNWC) surface analyses and the FNWC diagnostic boundary model. Again, little agreement is observed due to the high air temperature values in the FNWC analyses.

INTRODUCTION

Optical propagation through the atmosphere is influenced by the turbulent fluctuation of velocity and scalar quantities, as well as turbulent transports of aerosols. Utilization of present and designated future EO systems is ultimately related to the capability of describing several characteristics of the turbulence regime from readily predicted or measured parameters, i.e., bulk parameters. Unfortunately, turbulence parameters previously examined in most detail often turn out, at specific times, to be viewed as not being the most necessary with regard to existing EO systems and tactical requirements. However, successful formulations relating turbulent characteristics to bulk parameters are significant since analogous techniques can be applied to describe other boundary layer characteristics.

In this study, one turbulent parameter associated with propagation effects is examined with regard to its relationship to bulk parameters. It is the temperature structure function parameter, C_T^2 . C_T^2 is optically relevant because it is the primary contributor to the refractive index structure function parameter, C_n^2 , for optical wave lengths, viz.,

$$C_n^2 = (79 \times 10^{-6} F/T^2)^2 C_T^2 \quad (1)$$

where P is the barometric pressure and T is the ambient temperature. C_n^2 is significant because it is the only parameter necessary to describe the intensity of refractive index fluctuations over those scales which contribute to spatial and temporal degradation of light coherence due to phase and amplitude distortion in propagating wave fronts. Equation (1) is an approximation because it excludes humidity-temperature covariance fluctuation contributions to C_n^2 which have recently been shown to have possible significance for optical wave lengths. (Friene, et al. 1975).

The marine boundary layer is the regime considered in this examination. Bulk parameters evaluated for estimating C_T^2 are measured wind, temperature and humidity profiles. Also evaluated are C_T^2 values estimated from stability fields obtained from Fleet Numerical Weather Central (FNWC) objective analyses. Finally, some considerations regarding this FNWC marine boundary-layer diagnostic model are presented.

Theoretical considerations for estimating C_T^2

The temperature structure function parameter, C_T^2 , is defined by the following expression

$$C_T^2 = \overline{[T'(x) - T'(x + r)]^2} / r^{2/3} \quad (2)$$

where $T'(x)$ and $T'(x + r)$ are temperature fluctuations at two points separated by the distance r . r is greater than the inner scale, ℓ_o , but less than the outer scale, L_o .

An alternate expression for C_T^2 , which involves the rates of dissipation of turbulent kinetic energy (ϵ) and temperature variance (χ) is

$$C_T^2 = \beta \chi \epsilon^{-1/3} \quad (3)$$

where β is an empirical constant with a value of 3.20. This last form is the one which enables indirect estimates of C_T^2 to be made from mean conditions, since ϵ and χ can be related to boundary layer transports via balance expressions.

Equation (3) enters one of the two forms for the one-dimensional variance spectral expression for temperature fluctuations, $S_T(k)$. In the inertial subrange:

$$S_T(k) = .25 C_T^2 k^{-5/3} \quad (4)$$

$$S_T(k) = .80 \chi \epsilon^{-1/3} \epsilon^{-5/3} \quad (5)$$

where k is the one-dimensional streamwise wave number

The ability to estimate C_T^2 from bulk meteorological descriptions depends on our understanding of production and dissipation of the small-scale turbulent fluctuations within mean wind, temperature and humidity distributions. Existing scaling laws, validated for equilibrium and horizontally homogeneous conditions, yield the following empirical expressions for χ and ε , which define C_T^2 on the basis of Eq. (3), in terms of turbulent transports (U_*^2 , $\bar{V}_3\theta$ and \bar{V}_3q),

$$\varepsilon Z/U_*^3 = f_1(Z/L) \quad (6)$$

$$\chi Z/T_*^2 U_* = f_2(Z/L) \quad (7)$$

where

$$T_* = \bar{V}_3\theta/U_*$$

and

$$L = - \frac{T U_*^3}{g K (\bar{V}_3\theta + \bar{V}_3q)}$$

T_* is the scaling temperature, L is the Monin Obukhov stability scaling length and Z/L is the stability parameter. Both L and T_* are independent of height in the near surface constant flux layer, $\sim 20-30$ meters.

An empirical expression relating C_T^2 to boundary fluxes is obtained by direct substitution of Eqs. (6) and (7) into Eq. (3), viz.,

$$C_T^2 = T_*^2 Z^{-2/3} f_3(Z/L) \quad (8)$$

To relate C_T^2 to more readily available bulk parameters, the boundary fluxes ($-\bar{V}_1\bar{V}_3$, $\bar{V}_3\theta$ and \bar{V}_3q) need to be related to mean wind, temperature and humidity gradients. This approach is based on an assumed maintenance of the mean profiles by turbulent transports, an approach which neglects radiative heating and cooling. In this regard, Z/L has been experimentally related to the Richardson number, Ri ,

$$Z/L = f_4(Ri) \quad (9)$$

where

$$Ri = \frac{q(\bar{\theta}_V/\partial Z)}{T(\bar{\theta}_U/\partial Z)^2}$$

$f_4(Ri)$ is an empirical function which has been well documented for the constant flux layer both over land (Businger, et al., 1971).

T_*^2 has been empirically related to the temperature gradient, height and Richardson number as

$$T_*^2 = Z^{4/3} \left(\frac{\partial \bar{\theta}}{\partial Z} \right)^2 f_5(Ri) \quad (10)$$

where $f_5(Ri)$ is an empirical function which likewise has been well documented for the constant flux layer over land.

Combining Eqs. (8), (9) and (10) yields the following expression for C_T^2 , in terms of gradient measurements

$$C_T^2 = Z^{4/3} \left(\frac{\partial \bar{\theta}}{\partial Z} \right)^2 f_6(Ri) \quad (11)$$

where $f_6(Ri)$ is a function formed by combining $f_4(Ri)$ and $f_5(Ri)$ in Eqs. (8) and (9), respectively. $f_6(Ri)$ has been determined for the overland constant flux layer and represents the curve in Fig. 1 shown in conjunction with overland results. (Wyngaard, et al., 1971).

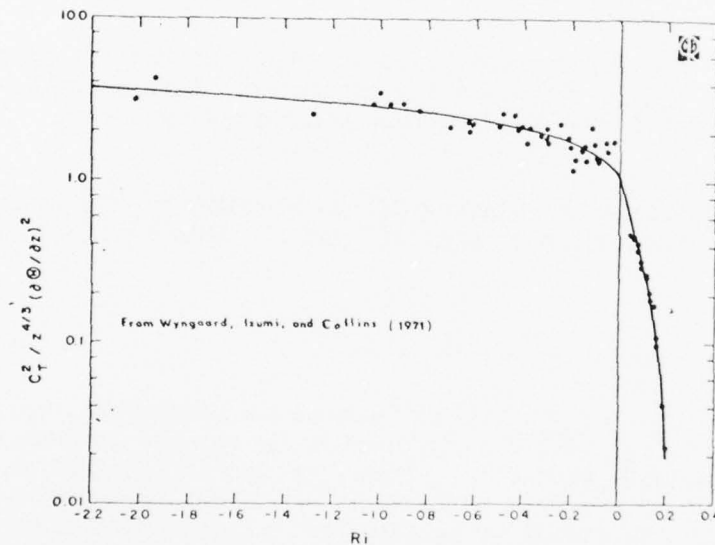


Fig. 1. The Dimensionless Temperature-Structure Parameter versus Richardson Number.

Direct (Eqs. 2 and 4) and profile (Eq. 11) C_T^2 determinations in this study were examined by plotting the dimensionless temperature function,

$$C_T^2 / [Z^{4/3} (\partial \bar{\theta} / \partial Z)^2]$$

versus Ri distribution. This defined the $f_6(Ri)$ function.

The general relation for C_T^2 , Eq. (8), has been further simplified so that input requirements are only single level values of wind, temperature and humidity in the air along with surface temperature values and humidity. (Friehe, 1976). Such formulations require bulk exchange coefficients for momentum, heat and humidity. Friehe selected recent coefficients based on an examination of numerous overwater results. (Friehe and Schmitt, 1976). Satisfactory agreement was reported with the overland formulation on the bases of three sets of overwater results.

Frisch and Ochs (1975) modified Eq. (7) to examine C_T^2 measurements above the marine inversion by adding the height of the marine inversion as another scaling parameter. They were able to obtain a reasonable description of observed height variation for C_T^2 to levels up to 8/10 the distance to the marine inversion base. For most cases, the latter level is above what is considered to be the constant flux layer.

An expression parallel to Eq. (11) exists for the specific humidity structure function parameter. C_q^2 , since temperature and specific humidity are both passive scalar quantities in the turbulent flow. In such an expression, $\partial\bar{q}/\partial Z$, would simply replace $\partial\bar{\theta}/\partial Z$ in Eq. (11), which would have the form

$$C_q^2 = Z^{4/3} \left(\frac{\partial \bar{q}}{\partial Z} \right)^2 f_7(Ri) \quad (12)$$

$f_7(Ri)$ should be similar to $f_6(Ri)$, differing only by a constant. Overwater measurements of specific humidity and mean profile data are examined in this study.

Experiments and Analysis

Shipboard observational experiments to describe the small scale properties of atmospheric turbulence were performed aboard the Naval Postgraduate School research vessel, ACANIA, anchored off Pt. Pinos in Monterey Bay and in the vicinity of the Channel Islands, California. Simultaneous shoreline measurements were also made in conjunction with the Monterey Bay shipboard measurements. The open ocean data were compared with FNWC results.

The shipboard sensor arrangement used in all experiments appears in Fig. 2. The Monterey Bay overwater measurement locations and the shoreline measurement locations appear in Fig. 3. The open-ocean measurement region and locations of FNWC grid points appear in Fig. 4. For comparison purposes, FNWC could estimate C_n^2 only at the indicated grid points, since surface values of wind, temperature and humidity are interpolated to these grid points from reports in their vicinity. Unfortunately, some of these grid point values were influenced by reports from overland locations.

LEGEND

\bar{U}	Cup Anemometer
$\bar{\theta}$	Quartz Thermometer
Q	Humidiometer
u	Hot Wire
T'	Platinum Wire
q	Lyman - α

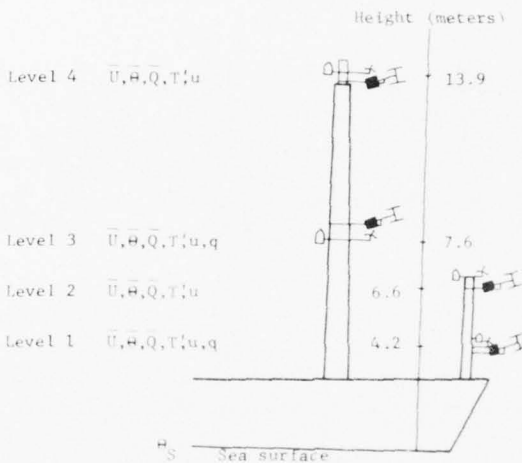


Fig. 2. Shipboard Sensor Arrangement

Mean wind measurements were made with a cup anemometer wind profile register system. The set has a characteristic low starting speed with a small amount of internal friction which aids in checking inertial overshoot. Quartz crystal probes were used to measure mean temperatures at each level. The resolution for each probe was 0.005°C . Lithium chloride sensors were used to measure relative humidity values. Both mean temperature and humidity sensors were housed in aspirated shelters at each measurement level.

Data logging for the mean system was accomplished using an NPS developed micro-processor based data acquisition system. This MIDAS (Microprocessing, Integrated Data Acquisition System) utilizes a central processing unit to control the sampling, averaging and recording of mean meteorological data. The operator is interfaced with the system via a teletype unit for full duplex input/output communication and program control. Once initiated, the system is fully automated in sampling the tailored list of sensors every thirty seconds and periodically printing output values averaged over the selected interval of from one minute to one hour. Output values are printed on the teletype in columnized format with the time of print as the leader. The teletype features a paper tape punch to produce a data copy concurrent with the printout.

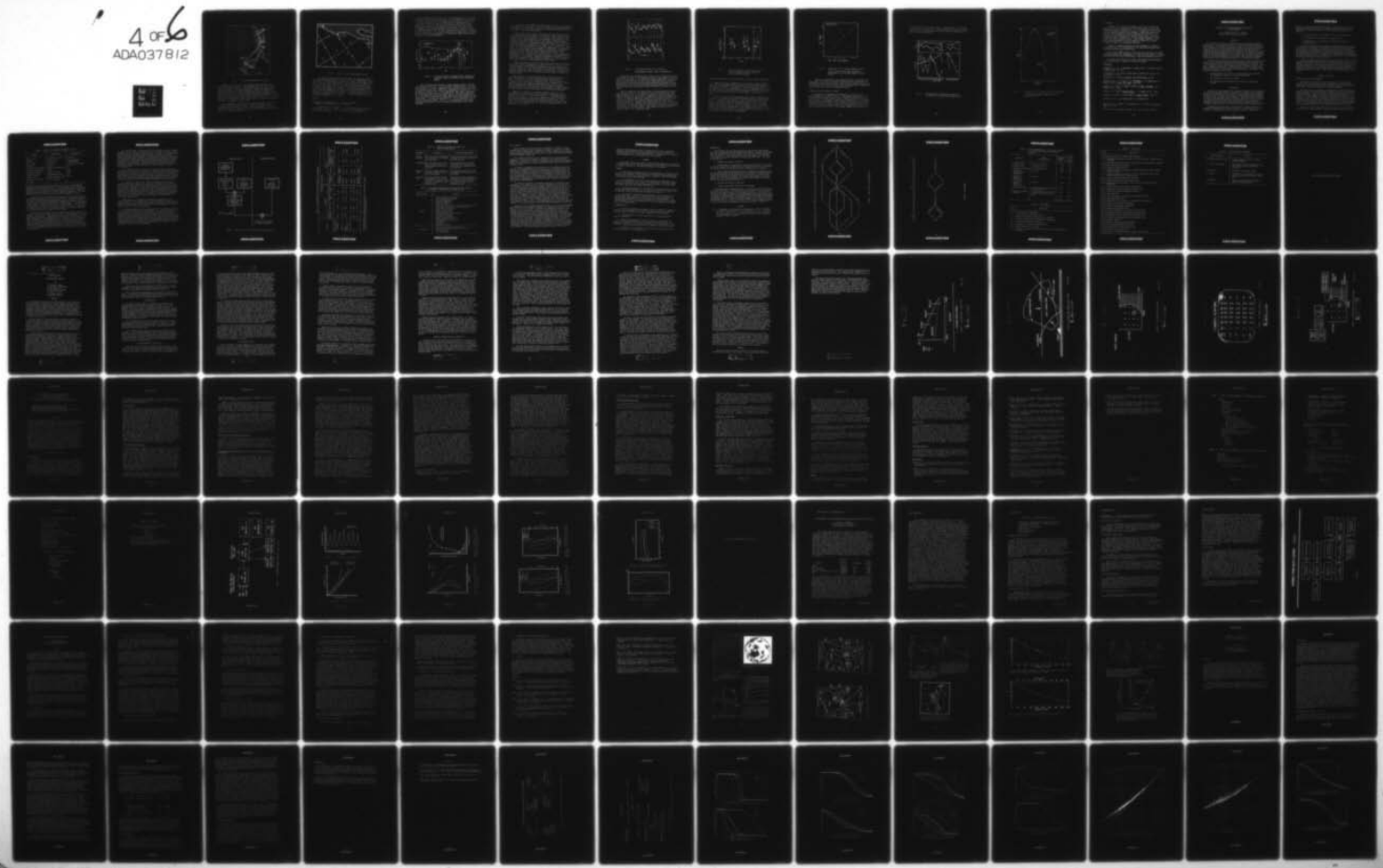
AD-A037 812

OFFICE OF THE DIRECTOR OF DEFENSE RESEARCH AND ENGINE--ETC F/G 20/14
PROCEEDINGS OF THE OPTICAL-SUBMILLIMETER ATMOSPHERIC PROPAGATIO--ETC(U)
DEC 76

UNCLASSIFIED

NL

4 of 6
ADA037812



4 OF ∞

ADA037812



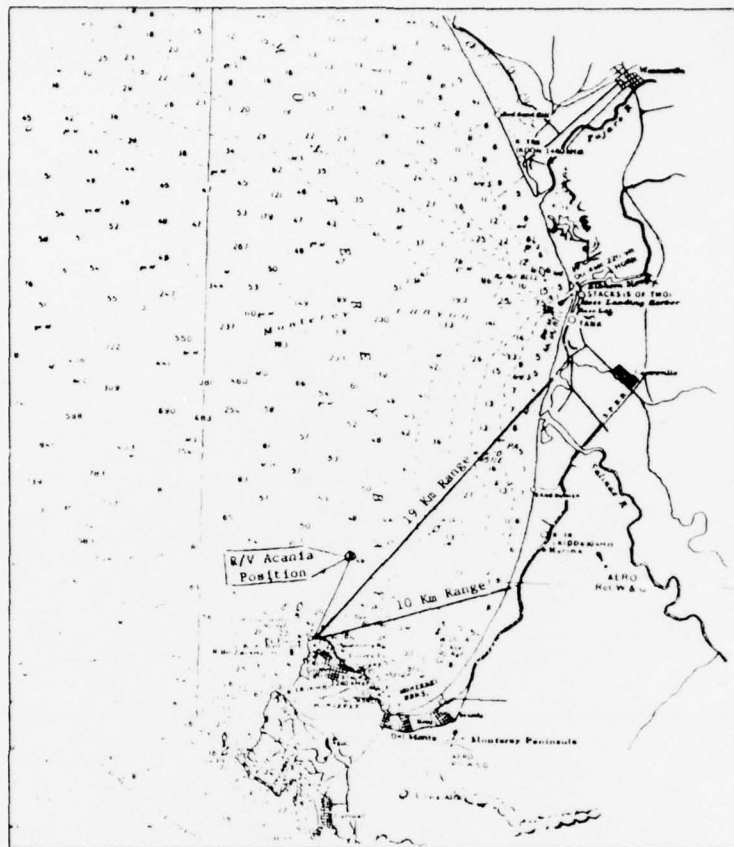


Fig. 3. Shoreline Measurement Locations

Temperature fluctuations were measured using resistance wire bridges with platinum wires. The baseband portion of this system is a balanced bridge excited by a 3KHz signal with a synchronous detector on the output. The system featured a response to temperature variations as small as 0.004°C in magnitude and up to 1KHz in frequency. Humidity fluctuations were measured using Lyman-Alpha sensors. These devices consist of an ultra-violet source tube and detector separated by an absorbing air gap. Specific humidities were measured on the basis of the absorption of ultra-violet light by the 1215A Lyman-Alpha transition of hydrogen in water vapor.

Both temperature and humidity fluctuation data were recorded on a 14-channel FM analog tape recorder. Real time readout on an 8-channel chart recorder was used to check the quality of the signals from the instruments. The charts were also used to select the periods analyzed for the investigation.

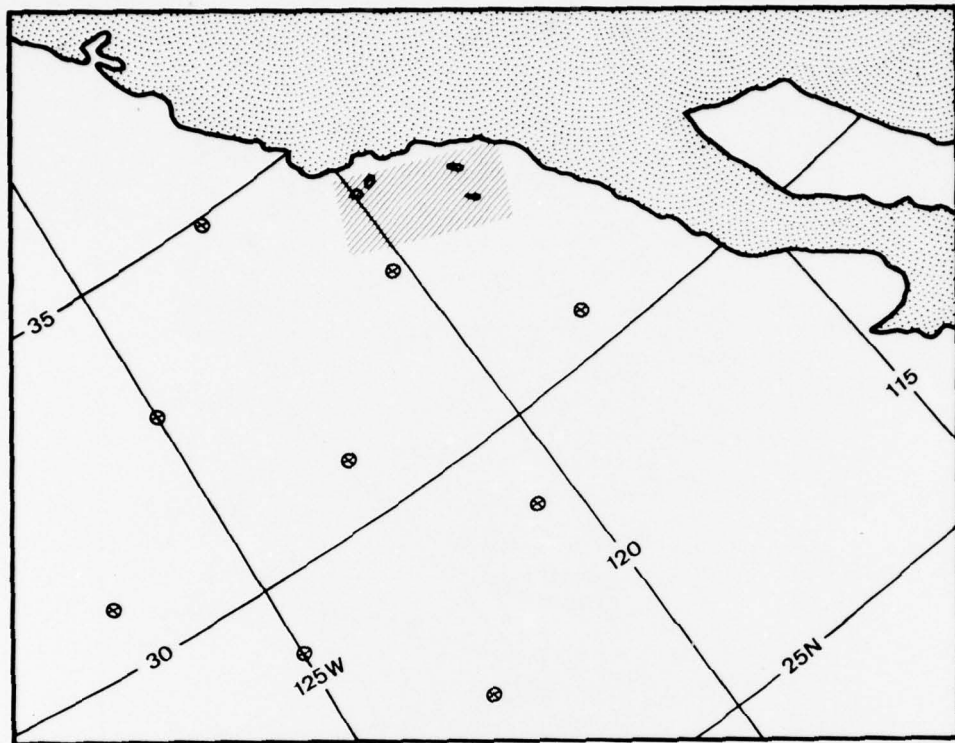


Fig. 4. FNUC Grid (with Measurement Region)

For analysis, individual mean wind (\bar{U}), mean temperature ($\bar{\theta}$) and mean specific humidity (\bar{q}) values were plotted on a logarithmic scale. Then, best fit lines drawn through the data points and gradient values were computed to define independent variables in Eq. (11); $\partial\bar{\theta}/\partial Z$ and $\partial\bar{U}/\partial Z$. C_T^2 value were computed from both variance spectral analyses of single temperature sensor signals, based on Eq. (4), and variance analyses of the temperature difference between paired sensors, Eq. (2). Friehe (personal communication) suggests that results from the latter analyses are least influenced by signal contamination due to salt accumulation on the wire. The nature of the latter influences has been described by Schmitt, et al. (1976).

RESULTS

Dimensionless Structure Function Parameters (DSFP) - temperature and specific humidity results:

A comparison of 114 overwater C_T^2 results with overland predictions appears in Fig. 5. These C_T^2 results were calculated using variance (Eq. 2) spectral (Eq. 4) and profile (Eq. 11) data.

overland determination of $f_0(Ri)$, Eq. (11), by Wyngaard, et al. (1971). Individual overwater results appear as dots and averages of these results over Ri intervals of 0.25 appear as dots within a larger circle. A possible distribution for mean DSFP values is delineated by the dashed line. The error bars are standard deviations from the mean within each interval and the number at the top of each error bar is the number of observations defining the mean value. Scatter or bias of individual points from the mean values were not related to the method used to estimate C_T^2 , i.e., spectral analysis of single sensor signal fluctuations, variance analyses of the difference signal between paired sensors, or profile measurements.

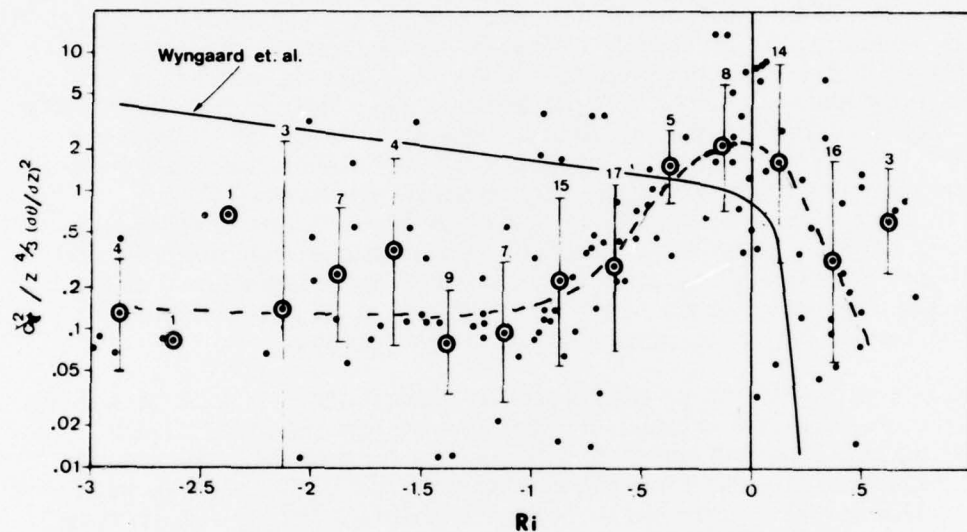


Fig. 5 Overwater Results for Dimensionless Temperature Structure Function Parameter versus Richardson Number.

The two significant features of the overwater results, relative to overland results, are: (1) for unstable conditions, $Ri < -5$, mean DSFP values are an order of magnitude less than the overland values and (2) mean DSFP values are, essentially, independent of Ri for $Ri < -1.0$. As neutral conditions ($Ri = 0$) are approached, mean DSFP values agree satisfactorily with the overland predictions. For stable conditions ($Ri > 0$), mean DSFP values are higher than the overland prediction but do decrease with increasing Ri , neglecting a mean value defined by only three points. It should be noted that $Ri = .21$ is considered to be a critical Richardson number. For $Ri > .21$, Archimedes' work retards turbulent fluctuations to such an extent that the flow is not fully turbulent.

In general, mean temperature DSFP results in Fig. 6 are of sufficient quantity and represent a sufficient number of separate experiments to attribute the trends to properties of the turbulent regime in the near surface marine boundary layer.

Two reasons for the obvious differences in mean DSFP magnitudes and trends could be the influence of the wave induced motion and the aerodynamically smooth property of the surface. With regard to the latter, several investigations of the momentum drag coefficient have yielded results which imply that the sea surface, although having roughness elements, is an aerodynamically smooth surface to the overlying airflow for wind speeds up to 5 msec⁻¹. This is plausible because the roughness elements move at phase speeds attributed to gravity waves. Such a condition would diminish the importance of mechanical production (wind shear) on the intensity of turbulence and lead to a regime influenced primarily by the temperature gradient. This appears to be the case since DSFP values for $Ri < -1$ are essentially independent of Ri . However, as neutral conditions are approached and the influence of mechanical production becomes more important, mean DSFP results approach values observed overland, i.e., in a turbulent regime influenced by an aerodynamically rough surface.

Higher mean DSFP values under stable conditions are most probably due to wave induced undulations in temperature and velocity fields. The wave-induced fluctuations are expected to be more significant for a stable regime since the fluctuations associated with the mean wind shear are damped out. Wave influence on the intensity of temperature fluctuations was identified in overwater data for stable conditions by Davidson (1974).

The existence of secondary circulations and the presence of the waves are suspected to have contributed to the scatter in the DSFP, along with errors in determining $\partial\theta/\partial Z$. Platform or sensor influence is not considered a significant factor because θ is a scalar and also because the temperature measurements are very accurate. Longer averaging times would perhaps have decreased the degree of scatter but were not used because of the uncertainty of mean estimates for twenty minute averages was viewed to be tactically significant.

Figure 6 is included to illustrate temporal variation in C_n (determined from paired sensor C_n estimates). Coincident C_n and u_* traces in Fig. 6 are from strip chart records of analog RMS outputs 30 sec/time constants. Inputs to the RMS device were differences between paired temperature and between paired velocity wires. The former is directly proportional to C_n^2 and the latter is proportional to u_*^2 , since the velocity structure function is proportional to $\epsilon^{2/3}$ and hence, to u_*^2 (Eq. 6).

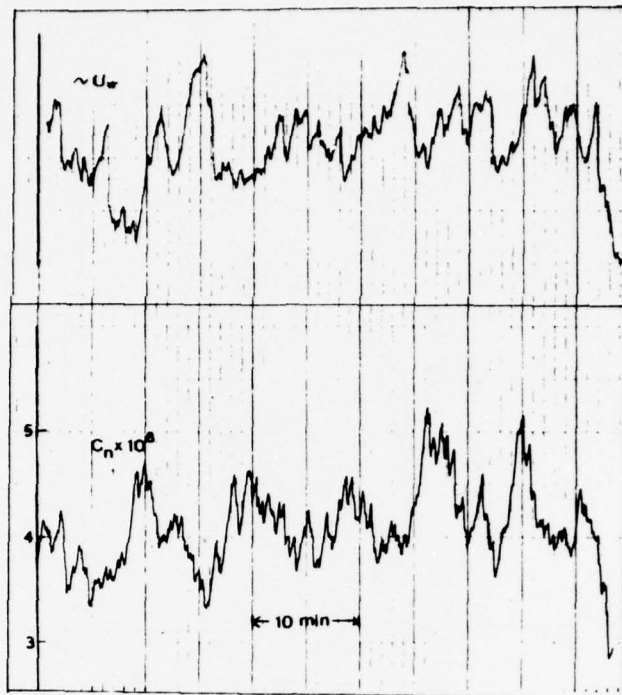


Fig. 6. Strip Chart Records of C_n (from C_T Measurements) and U_s (from ϵ Measurements).

Significant C_n variations with a time scale of 8-10 minutes appear in the trace in Fig. 6. The variations in C_n do not appear to be associated with variations in U_s which also exhibit significant variability. During the observations, the 8-10 minute variations were associated with secondary circulations which were manifested by surface windrows. Although not quantified, the equilibrium status between the waves and overlying shear was considered to have influenced the observed variations.

Specific humidity DSFP results from a limited number of measurements appear in Fig. 7. A significant result is that specific mean humidity DSFP values are an order of magnitude less than temperature DSFP values (Fig. 5), which was not expected for these two scalar quantities. A different empirical constant in the universal spectral expression for the specific humidity would account for some of the observed difference. However, the present uncertainty in the value of this constant is not large enough to account for the order of magnitude difference. The limited number of data points restricts interpretations on the trends of the mean values. The scatter is observed to be as large as that for the temperature DSFP

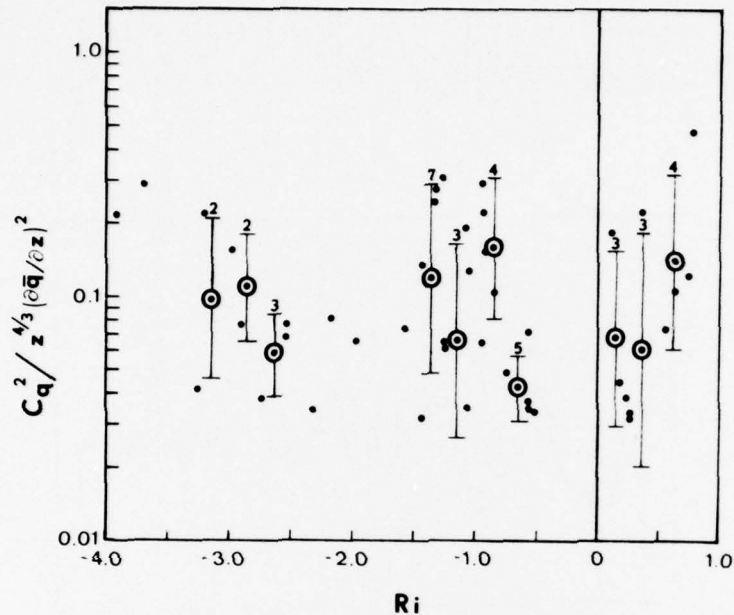


Fig. 7. Overwater Results for the Dimensionless Specific Humidity Structure Function versus Richardson Number.

Comparison of Measured C_n^2 Results and C_n^2 values obtained from FNWC:

Figure 8 presents a comparison of C_n^2 results computed from C_n^2 values obtained by FNWC surface analyses and by direct measurements aboard the R/V ACANIA for the region and grid points shown in Fig. 2. The comparison is for an experimental cruise in September-October 1976. The FNWC diagnostic boundary layer code computes stability on the basis of a stability parameter which is transformed to an equivalent Z/L value.

Figure 8 indicates little agreement since order of magnitude differences occur without any consistency between estimates and measurements. A comparison with regard to time of day (00Z and 12Z), shown in Fig. 9, indicates that the disagreement is not associated with night or day analyzed fields. In the top panel of Fig. 9, the FNWC analyzed air temperatures are shown to be always larger (up to 5°C) than the observed air temperature. This difference was enough to cause an error in the analyzed versus observed stability regime and could be the primary cause for the C_n^2 disagreement.

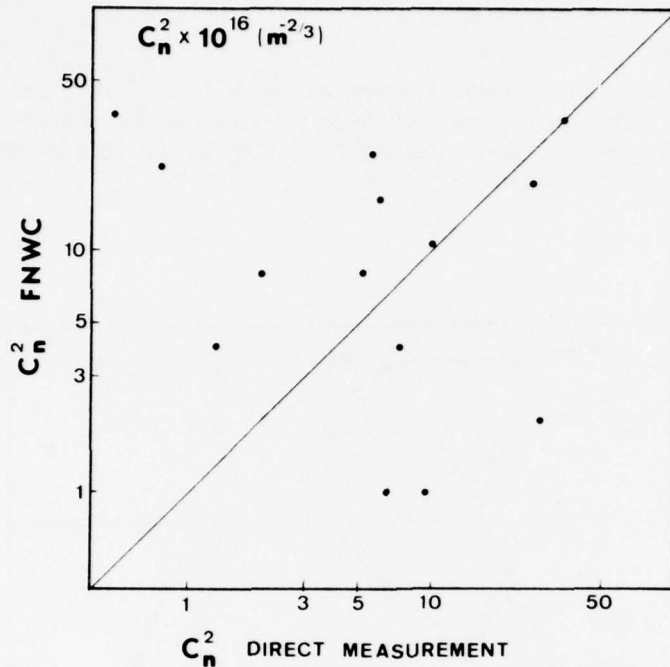


Fig. 8. Comparisons of C_n^2 Values computed from C_T^2 Values Obtained from Direct Shipboard Measurements and from FNWC Analyzed Surface Fields.

Higher air temperatures most likely occurred in the FNWC analyzed surface field because overland observations were interpolated to neighboring overwater grid points in the objective analysis procedures. This affected the overwater values during both night time (1200Z) and daytime (00Z) hours over the comparison periods.

Overwater versus shoreline results:

A comparison of shipboard and shoreline C_n^2 estimates from C_T^2 measurements is shown in Fig. 10. The relative positions of the coincident measurements appear in Fig. 2 where the shoreline site is on Pt. Pinos. The purpose of showing this comparison is to illustrate that shoreline measurements are not sufficient to define the overwater regime which has been shown in the previous discussion to differ significantly from the overland regime. The overwater-shoreline differences are manifested by the 10^3 difference between the coincident C_n^2

values as well as the diurnal ranges at each location. Crittenden, (1976) discuss the importance of these results with regard to interpreting optical propagation results from overwater ranges where the optics are shoreline based.

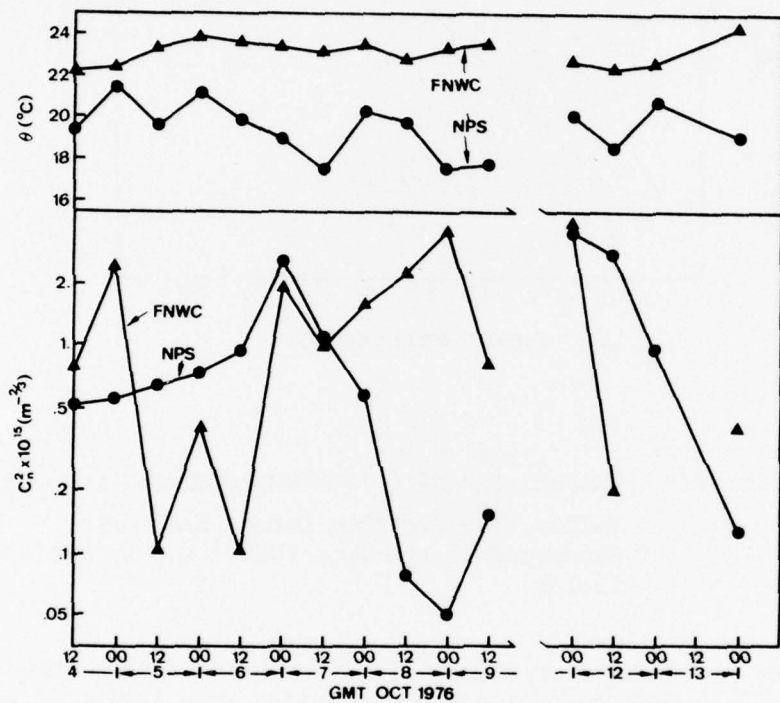


Fig. 9. Observed (NPS) and FNWC Air Temperature (10 meters) C_n^2 Values versus Time of Day

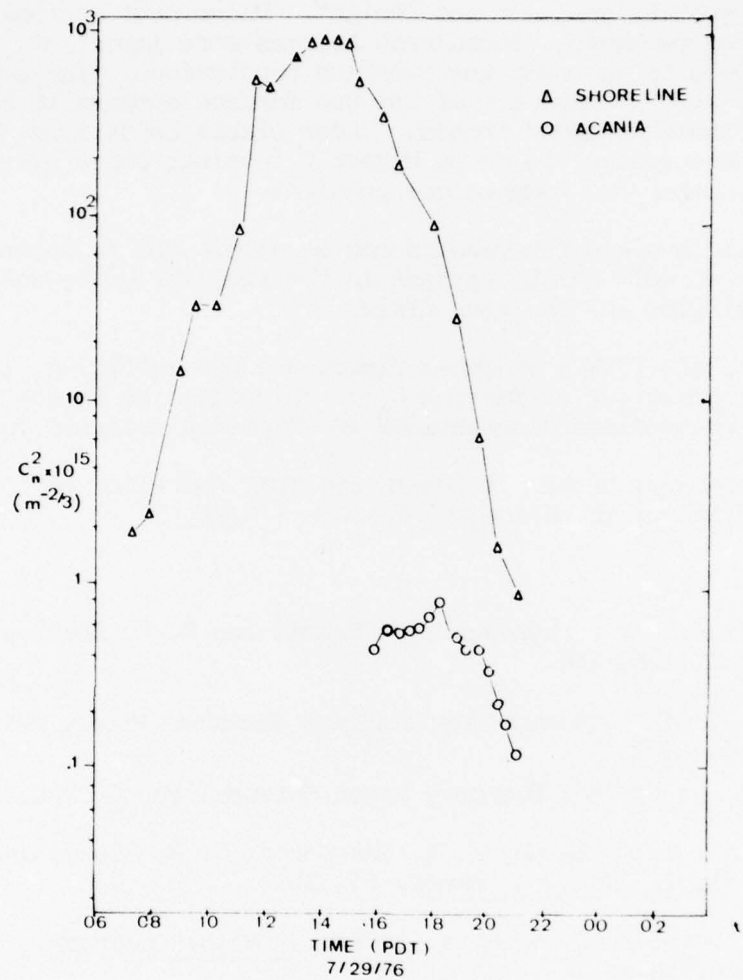


Fig. 10. Comparison of C_n^2 Results from C_T^2 Measurements on Overwater ship (R/V ACANIA) and on the Shore (see Fig. 2).

CONCLUSIONS

Overwater C_T^2 results, if scaled on the basis of stability parameters, do not coincide with the overland predictions. Under extremely unstable conditions, $R_i < -1$, C_T^2 appears to depend only on the temperature gradient and height. Under near neutral conditions, when mechanical turbulence becomes more important, the overwater results approach the overland predictions. The aerodynamically smooth character of the sea surface appears to be the reason for these observed trends. Under stable conditions, the wave influence appears to cause higher C_T^2 values for a given Richardson number and temperature gradient.

Scatter in overwater results can be attributed to secondary circulation as well as disruptions in the equilibrium between the overlying airflow and the wave field.

Large scale (FNWC) analyzed fields are not sufficient to define stability regimes for estimating C_T^2 . This could be unique to regions influenced by overland observations in objective analysis procedures.

One final conclusion, it is evident that shoreline measurements are not sufficient to define the overwater regime.

REFERENCES

Businger, J. A., J. C. Wyngaard, Y. Szumi, and E. F. Bradley (1975), J. Atmos. Sci., 28, 184.

Crittenden, E. C., Optical Submillimeter Workshop Procs, Air Force Academy, Nov. 1976.

Davidson, K. L. (1974), Boundary Layer Meteorology, 6, 305.

Friehe, C. A., J. C. LaRue, F. H. Champagne, C. H. Gibson and G. F. Dreyer (1975), J. Opt. Soc. Amer., 65, 1502.

Friehe, C. A. and K. F. Schmitt (1976), J. Phys. Oceanogr., 6, to appear in Nov. issue.

Friehe, C. A. (1976), Applied Optics, to appear in Dec. issue.

Frisch, A. S. and G. R. Ochs (1975), J. Appl. Meteor., 14, 415

Schmitt, K. F., C. H. Gibson and C. A. Friehe (1976).

Wyngaard, J. C., Izumi, Y., and Collins, S. A. (1971), J. Opt. Soc. Amer., 61, 1646.

* This work was supported by Naval Sea Systems Command (PMS405)

UNCLASSIFIED

A PROGRAM FOR EO SYSTEMS PERFORMANCE PREDICTION IN THE ATMOSPHERE

R. F. Lutomirski and A. R. Shapiro
Pacific-Sierra Research Corporation

ABSTRACT

In this paper, we outline a possible approach to obtaining an improved capability for predicting the performance of electro-optical (EO) systems in the atmosphere. The program is driven by the needs of the two potential users of this capability: 1) the systems analyst--who requires aggregate synoptic conditions for many different operational conditions, and 2) the field commander--who requires short-term, local forecasts. The degree of uncertainty in the atmospheric propagation path is a function of the temporal and spatial extent of the mission parameters, and the significance of these uncertainties depends on the design parameters of the system. This observation separates the stochastic from the engineering aspects of the EO prediction problem.

The authors have shown that an atmospheric mutual coherence function (MCF) exists not only for the refractive-index fluctuations due to turbulence, but also for concentrations of molecules and for distributions of aerosols. These can be combined to yield a total atmospheric MCF. The study on which this paper is based has identified an overall atmospheric MCF as the single, most applicable quantity for predicting EO systems performance. Therefore, in this paper, we have focused on the issues:

1. The applicability of the MCF as a uniform measure for describing the atmospheric interface of EO systems performance.
2. The feasibility of predicting the MCF.
3. The measurements and instrumentation required for determining the MCF.

INTRODUCTION

The number of weapon systems whose performance depends on the propagation of visible and infrared radiation is increasing. The system analyst requires means for evaluating alternative solutions for performance in the atmospheric environment, and the combat officer needs to choose among available weapons and battle plans in advance of the engagement. The study on which this paper is based [1] addressed the problem of providing both of them with a quantitative prediction of the probable limitations imposed by the anticipated atmospheric conditions on the combat performance of communication and surveillance systems operating in the visible to submillimeter wavelength region.

Performance prediction would be facilitated by a general measure of propagation degradation that could be applied in a uniform manner to all EO systems. An atmospheric MCF which contains the effects of turbulence,

UNCLASSIFIED

UNCLASSIFIED

molecules, and aerosols, and which was used in a previous analysis of the OPSATCOM, has been identified as the single, most applicable quantity for predicting EO systems performance. The study therefore focused on three questions:

1. The applicability of the atmospheric MCF as a uniform measure.
2. The feasibility of predicting the atmospheric MCF.
3. The measurement and instrumentation required to predict the atmospheric MCF.

The Technical Discussion of this paper (abstracted from Ref. 1) presents an overview of the effects of the atmosphere on EO systems performance and the importance of performance prediction as required by both the systems analyst and the field commander. The concept of temporal and spatial parameter prediction, as driven by the requirements of the mission, is developed, and characteristic values of the parameters are presented for several missions. The section concludes with a discussion of the applicability of the atmospheric MCF for predicting this parameter variation.

A survey of existing meteorological facilities and data banks and optical propagation measurement programs was also conducted during the study [1]. The findings of this survey and of the analytic studies were used to arrive at a tentative assessment of the utility and limitations of these resources for EO performance prediction. In the third section of this paper, we present a summary of the results of this assessment, including recommendations, a five-year program plan, a PERT chart, a task summary, and required support categories.

TECHNICAL DISCUSSION

ELECTRO-OPTICAL SYSTEM PERFORMANCE

The parameters that determine the performance of EO systems may be classified in three categories: design, operational, and environmental. To first order, the combat performance is determined by the set of parameters identified in Table I and classified in the manner suggested.

The system analyst is concerned with predictions of the aggregated performance envelope over some statistical ensemble of operational and environmental conditions. Within this context, tradeoffs must be made between cost, mission flexibility, theatre specificity, and probable availability. In contrast, the field commander is primarily concerned with short-term battle planning. In this context, the operational parameters are known and usually contained within a narrow range. The main uncertainty is due to the sensitivity of EO performance to normal fluctuations in the environmental parameters. Thus, the commander's battle plans and his choice of weapon systems will be strongly influenced by the predicted meteorological conditions.

The point of view of the system analyst is seen to be very different from that of the field commander. The system analyst requires only a gross

UNCLASSIFIED

UNCLASSIFIED

TABLE I. PRIMARY EO PERFORMANCE PARAMETERS BY TYPE

Design	Operational	Environmental
Field of view	Geographic location	Turbulence
Aperture	Time of year	Variable gaseous constituents
Focal length	Time of day	Suspended particulates
Resolution	Altitude	Haze
Radiometric sensitivity	Target and background	Fog
Noise equivalent power	Range	Cloud
Wavelength response	Closing velocity	Rain
Temporal response	Engagement duration	Snow
Radiated power	Mission planning time	
Transmitter beam width	Time to respond	
Scan rate		

description of the probability distribution of each of the environmental parameters averaged over many years. On the other hand, such probability distributions may be required for many different combinations of operational parameters; e.g., location, time of year, time of day, altitude. Thus, the apparent simplicity evaporates. The field commander requires only a single probability function for his location and planned engagement scenario.

Perhaps an even more significant difference between these two users of EO performance prediction is the action to be taken. The system analyst will consider variations in the design parameters so as to increase or decrease the range of operational and environmental parameters that may be serviced by a single system. The field commander, on the other hand, has at his disposal a small number of systems, each of which is fixed in design. The predicted performance may force him to reconfigure his battle plans (e.g., time of day) to accommodate one or more of these weapon systems or to plan an engagement to be conducted without the benefit of any of them.

Many different EO systems have been invented and many more remain to be invented. Given a well defined propagation path, the performance of any such system can be predicted. The principal problem is the variability and consequent uncertainty in the propagation path. The effect and significance of these variations in the propagation path is a function of the design parameter. But the degree of uncertainty in the propagation path is clearly a function of the operational parameters and is in no way determined by the design parameters. This observation permits a convenient and succinct treatment of the propagation prediction requirements for all possible EO systems in terms of the operational characteristics of the missions in which they are to be employed.

UNCLASSIFIED

This approach (Fig. 1) separates the truly stochastic from the engineering aspect of the problem of the prediction of EO combat performance. Implementation requires that the relevant stochastic properties of the propagation path be reduced to a minimum and be defined as a function of routinely measurable meteorological variables. An additional requirement is that these meteorologically derived variables which describe the propagation properties be convenient for engineering calculations of performance given the design parameters of the EO system. Then these variables must be chosen so as to provide a practical bridge between the stochastic and engineering aspects of the problem. The MCF of the atmosphere is a good candidate for such a bridging parameter.

Since the meteorological forecast must interface with the operational parameters (see Fig. 1), it is necessary to specify the quantities of interest and to explore the range of values that must be considered. The dimensions of meteorological variability are time and space, and their effect on EO system performance involves an integration over some limited domain in both time and space. Thus, the relevant mission operational parameters are those listed in the middle column of Table I which define the temporal and spatial domain.

EO systems may be employed in a large and disparate set of military missions. However, a review of the temporal and spatial characteristics of these missions suggests that they may be treated by means of a fairly small set of classes. The result of such an investigation is presented in Table II. Table II is not intended as a final solution; it is simply an example of the simplification afforded by this approach. The spatial parameters are self-explanatory, but the designations for the temporal parameters need amplification. This is provided in Table III, together with a brief description of the manner in which they are to be used to specify the requirements for meteorological prediction.

A description of the pertinent meteorological variables that are routinely observed by the weather services of the military services is provided in Table IV. During this study, we did not establish a requirement for additional observations. This question should be investigated, and is recommended as part of the multi-year program.

The engineering aspect of the problem (see Fig. 1) requires the application of well known techniques and relationships. But the large number of design parameters (Table I) that are available for manipulation precludes any general solution. The various tradeoffs in the presence of an adverse propagation medium between field of view, f/number, and spectral and temporal response can be explored in great detail once the domain of operational parameters is specified. The simple example of the improved contrast provided by range-gating an active EO system in a scattering medium suffices to illustrate the benefits that may be realized by improvements in the prediction of the propagation properties of the atmosphere.

UNCLASSIFIED

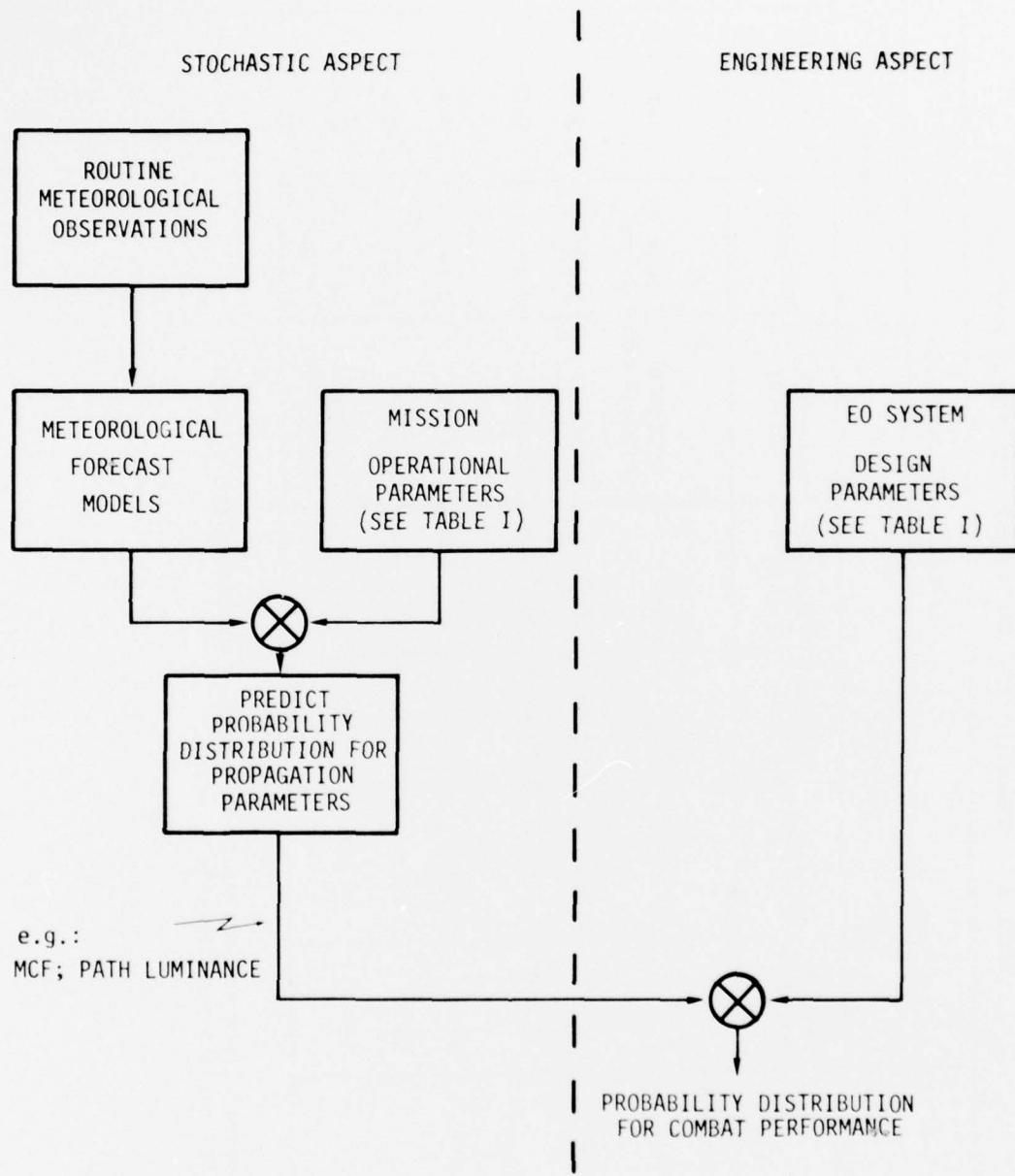


FIGURE 1. SCHEMATIC OF EO SYSTEM COMBAT PERFORMANCE PREDICTION

UNCLASSIFIED

UNCLASSIFIED

TABLE II. CHARACTERISTIC VALUES FOR OPERATIONAL PARAMETERS

Mission	Operational Parameter							
	Temporal			Spatial				
	Mission Duration	Timeliness	Planning Time	Averaging Time	Geographical Coverage	Altitude	Atmospheric Propagation Path (km)	Sea Water Path (m)
Reconnaissance								
Strategic	Cont.	15 min	Yrs	Secs	Northern Hemisphere	Space to Ground	7-21	0
Tactical	30 min	Hrs	12 hr	10^{-4} sec	Europe	0-10	1-20	0-100
Target Acquisition	30 min	Secs	12 hr	10^{-3} sec	Europe	0-10	1-20	0-100
Fire Control*	Mins	Secs	12 hr	10^{-3} sec	Europe	0-10	0-2	?
IFF	Mins	Secs	12 hr	10^{-3} sec	Europe	0-10	0-2	0-100
C ³	Cont.	15 min	12 hr	Secs, .	Northern Hemisphere	Space to Ground	0.1-10	0-100

* High-energy laser weapons would have similar characteristics except possibly for shorter "Mission Duration."

UNCLASSIFIED

UNCLASSIFIED

TABLE III. TEMPORAL OPERATIONAL PARAMETERS AND PREDICTION REQUIREMENTS

Parameter	Definition	Prediction Requirements
Mission Duration	The total period during which the system must be available for operation.	Prediction must be in terms of an average and variance for periods of this duration.
Timeliness	The time window after a command is given within which the system must perform its function.	The probability of an outage whose duration is greater than the specified "timeliness" must be predicted.
Planning Time	The time interval between a decision to employ the system and its employment.	The prediction must span a forecast ahead from the decision to employment.
Averaging Time	The time over which the system integrates the incident radiation to provide a single reading or indication to the ultimate user.	The prediction must describe the magnitude of those components of the temporal fluctuation whose periods are greater than the "averaging time."

TABLE IV. PERTINENT METEOROLOGICAL VARIABLES ROUTINELY OBSERVED AND RECORDED AT WEATHER-SERVICE OBSERVING SITES

Time Interval	Variable
Hourly	Station atmospheric pressure Air temperature (dry bulb) Dew-point temperature Wet-bulb temperature Relative humidity Total sky cover (fraction of sky covered by clouds) Cloud amount (fraction of each cloud layer) Cloud type and direction Height of cloud base Total opaque sky cover Sunshine duration (few stations) Precipitation amount Visibility (horizontal) Weather phenomena (type) Obstructions to vision (type) Wind direction Wind speed Maximum wind speed
3- or 6-hourly	State of ground (wet, frozen, etc.) Wind-waves and swell height and direction Water temperature Soil temperature

UNCLASSIFIED

UNCLASSIFIED

USE OF THE MCF

There are many EO systems which can be degraded in performance by the atmospherically induced loss of transverse coherence of radiation. Examples include coherent (heterodyned) communication systems, imaging systems, and all those systems which depend on the spot size of a laser beam that has propagated along an atmospheric slant path.

This transverse coherence loss is quantified by the cross-correlation function of the fields in a direction transverse to the direction of the propagation, which defines the MCF. By analyzing these systems, the degrading effect of the atmosphere can then be expressed in many cases in terms of the atmospheric MCF.

It should be recognized that the MCF is, by its definition, an optical quantity, and is measurable by optical means (e.g., by interferometry). By modeling the atmosphere, the MCF can be approximately expressed in terms of the turbulence, molecules, and aerosols in the medium, and these models can then be used to predict the effects of the atmosphere on these systems. However, the dependence of the performance of the systems on the MCF is valid independent of the accuracy of the atmospheric models used for estimating the MCF; as such, measurements of the MCF can be used to directly specify the performance of these systems.

For prediction purposes, the possible approaches for estimating system degradation are to either directly correlate measurements of the MCF with meteorological variables such as wind speed, humidity, cloud cover, etc., or to use the approximate mathematical expressions for the MCF in terms of the turbulent temperature fluctuations, the molecular concentration, and the aerosol sizes, concentrations and refractive indices, and to attempt to predict the dependence of the latter quantities on the gross meteorological variables. An example of the first approach is the attempt to predict visibility under different atmospheric conditions, and an example of the second is the prediction of turbulence strengths or particle-size distributions in different environments. Both of these approaches are of value; while the first approach is more direct for EO systems applications, the second has been studied to a far greater extent by meteorologists and atmospheric scientists.

The thrust of the technical discussion of Ref. 1 (Vol. II) was to provide a description of the atmosphere sufficient for modeling and determining the MCF, and to indicate the use of the MCF in EO performance prediction. The summary of Ref. 1 presented a description of the refractive index of the atmosphere sufficient to develop the main characteristics of propagation through turbulence and aerosols, and examined the assumptions and limitations in calculating the MCF for the atmospheric models developed. Specific applications included an analysis of those EO systems that depend on the propagation of a finite laser beam. The relation between the laser irradiance distribution and the MCF was presented, and examples were given for an atmosphere containing molecules, turbulence, and aerosols. The problem of single large-angle scattering was also discussed, and the effects of the atmospheric turbulence, molecules, and aerosols on the resolution of EO imaging systems was considered. The overall modulation transfer function (MTF) of the

UNCLASSIFIED

UNCLASSIFIED

combined atmosphere-imaging system, the generation of path or background luminance, and resultant reduction in apparent contrast were shown to be directly related to the overall atmospheric MCF. A discussion of the results and recommendations for measurements were also presented.

SUMMARY

This summary presents an outline of the executive summary of our study [1]. The approach taken was to identify deficiencies and develop a multi-year program to improve predictions of the combat performance of EO systems.

FINDINGS

1. There are two potential users for this capability: the system analyst and the field commander. The system analyst requires aggregate synoptic predictions, but for many different operational conditions. The field commander requires short-term, local forecasts.

2. The atmospheric MCF is the optical quantity most applicable to predicting the performance of EO systems. The deficiencies of existing formulations are in evaluating multiple large-angle scattering, the variance under stationary conditions, and temporal fluctuations.

3. The data requirements for MCF prediction are determined by the characteristic operational parameters for the missions in which the EO system is to be employed. These were tentatively identified in Table II.

4. With regard to meteorological measurements, the most efficient set for MCF prediction is not known. Furthermore, the accuracy required in meteorological measurements for this purpose has not been determined. The existing meteorological data bases do not appear to contain all the information necessary to predict EO performance for the field commander, and perhaps not for the system analyst.

RECOMMENDATIONS

1. A five-year program with a budget of about \$11 million is required to develop, test, and evaluate an EO combat performance prediction capability that will serve the needs of both field commander and system analyst.

2. The deficiencies in current formulations of the atmospheric MCF should be remedied.

3. Numerical experimentation should be employed to investigate the utility of alternate meteorological measurements and the sensitivity of EO performance prediction to the accuracy of meteorological measurements or predictions. Existing meteorological data bases should be used where possible.

4. Investigate the development of a portable field instrument for the direct measurement of the atmospheric MCF.

UNCLASSIFIED

UNCLASSIFIED

PROGRAM PLAN

The atmospheric MCF has been identified as the optical quantity most applicable to predicting the performance of EO systems. However, deficiencies have been identified in the model and the data base, and the application of such a predictor to operational regimes of interest remains to be verified. A five-year plan has been developed to provide the needed input. The steps in the plan are:

1. Complete and validate the model.

2. Perform numerical experiments to analyze the sensitivity of the MCF to the uncertainties in the aerosol sizes, concentrations, etc., to determine the accuracy with which the meteorological parameters must be measured.

3. Develop model atmospheres that have the temporal and spatial resolution necessary to predict the performance of EO systems for various missions. The model atmospheres can be generated by the collection of suitable atmospheric data, by model development, and by direct measurements of the atmospheric MCF. For several missions, the characteristic temporal and spatial scales of interest are given in Table II.

4. Analyze and improve the data base.

5. Develop a performance predictor for EO systems.

The program plan is presented in Fig. 2 in the form of a PERT chart, and is described in Table V. The allocation of the fraction of the total effort among the major subobjectives is also provided in Table V. The division of resources is roughly 25 percent for acquiring specialized meteorological data 25 percent for completing and validating the model and defining the atmospheric sensitivities, and 50 percent for development, test, and evaluation of the EO performance predictor. Table VI provides a summary of the tasks which appear on the PERT chart, and the function of each of five types of support activity that will be required to implement this program is defined in Table VII.

REFERENCE

1. R. F. Lutomirski, A. R. Shapiro, and R. Greenwell, *A Program to Predict the Combat Performance of Electro-Optical Systems: Vol. I--Executive Summary and Program Plan; Vol. II--Technical Discussion*, PSR Report 606, Final Report on Contract N00123-75-C-0818 for Naval Electronics Laboratory Center, May 1976.

UNCLASSIFIED

UNCLASSIFIED

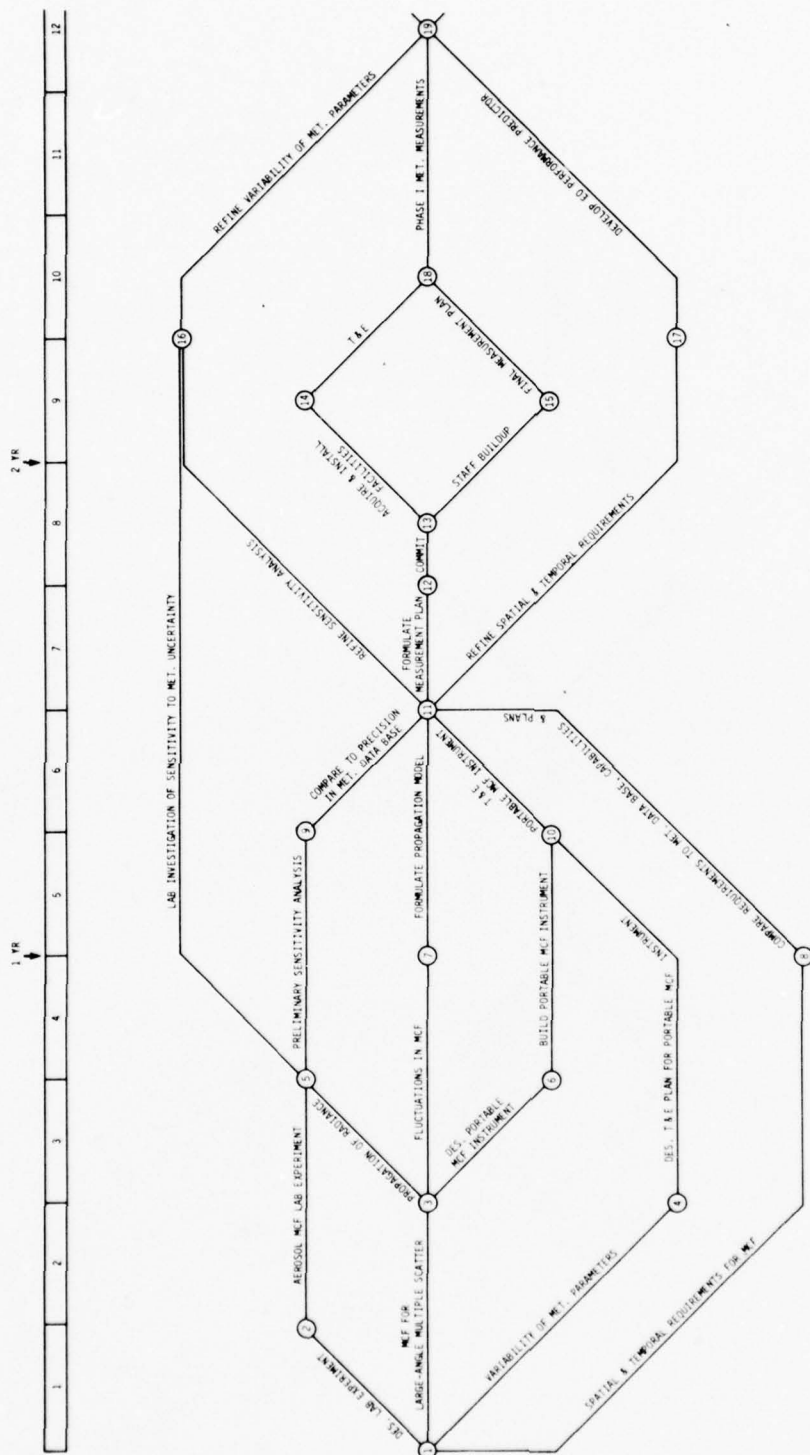


FIGURE 2. PERT CHART OF THE PROGRAM PLAN

UNCLASSIFIED

UNCLASSIFIED

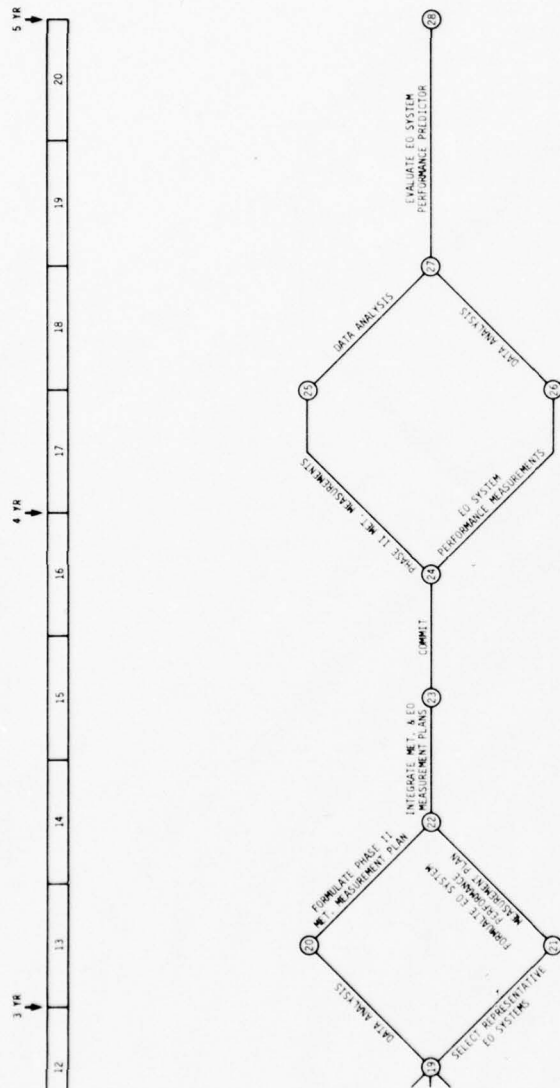


FIGURE 2. (Continued)

UNCLASSIFIED

UNCLASSIFIED

TABLE V. FIVE-YEAR PROGRAM PLAN. The overall objective of this plan is improved EO performance prediction.

Subobjective	Tasks (see PERT chart)	Required Resources (\$K)	Fraction of Program
1. Complete Model	1-2,1-3,2-5,3-5,7-11	485	.05
2. Validate Model	3-6,4-10,6-10,10-11	485	.05
3. Sensitivity Analysis	3-7,5-9,5-16,11-16	500	.05
4. Variance of Meteorological Parameters	1-4,16-19	265	.02
5. Spatial and Temporal Requirements	1-8,11-17	375	.04
6. Spatial and Temporal Deficiencies	8-11,9-11	190	.02
7. Improve Data Base	11-12,12-13,13-14,13-15,14-18,15-18,18-19,19-20	2,950	.27
8. Develop Performance Predictor	17-19,19-21,20-22,21-22,22-23,23-24,24-25,24-26,25-27,26-27,27-28	5,465	.50
		10,715	1.0

TABLE VI. TASK SUMMARY

Task	Description
1-2	Design laboratory experiment
1-3	Develop MCF for large-angle scatter
1-4	Analyze variability of meteorological parameters
1-8	Define EO system spatial and temporal requirements
2-5	Aerosol MCF laboratory experiment
3-5	Propagation of radiance, numerical model
3-6	Design portable MCF instrument
3-7	Analysis of temporal structure of MCF for "fixed" meteorological conditions

UNCLASSIFIED

UNCLASSIFIED

TABLE VI. (Continued)

Task	Description
4-10	Design T&E plan for portable MCF instrument
5-9	Preliminary sensitivity analysis of MCF to variations in meteorological conditions
5-16	Laboratory investigation of MCF sensitivity to meteorological parameters
6-10	Build portable MCF instrument
7-11	Formulate propagation model
8-11	Compare EO system requirements to meteorological data base, capabilities, and plans
9-11	Compare required MCF precision to that in meteorological data base, initial identification of deficiencies
10-11	Test and evaluate portable MCF instrument
11-12	Formulate meteorological measurement plan
11-16	Refine sensitivity analysis: MCF as function of meteorological parameters
11-17	Refine EO spatial and temporal requirements
12-13	Commitment to meteorological measurement plan
13-14	Acquire and install measurement facility
13-15	Staff build-up
14-18	Test and evaluate meteorological measurement facility
15-18	Final measurement plan
16-19	Refine model of variability of meteorological parameters
17-19	Develop EO performance prediction
18-19	Phase-I meteorological measurements
19-20	Analyze meteorological data
19-21	Select representative EO system for field testing
20-22	Formulate Phase-II meteorological measurement plan
21-22	Formulate EO system performance measurement plan
22-23	Integrate meteorological and EO measurement plans
23-24	Commit to Phase II
24-25	Phase-II meteorological measurements
24-26	EO system performance measurements
25-27	Analyze Phase II meteorological data
26-27	Analyze EO performance data
27-28	Evaluate EO system performance prediction capability

UNCLASSIFIED

UNCLASSIFIED

TABLE VII. REQUIRED SUPPORT CATEGORIES

Support Category	Function
1. Meteorological data base	Provide parameter values for EO performance predictor
2. EO field measurements	Experimental basis for development, test, and evaluation of EO performance prediction
3. Facilities	Support for propagation program
4. Analysis	Development of EO performance predictor and specification of data input requirements
5. Laboratory	Support for analysis and propagation program field measurements

(This page intentionally left blank.)

UNCLASSIFIED

.... This paper is UNCLASSIFIED
WEATHER SUPPORT
TO
ELECTRO-OPTICAL SYSTEMS

by

Maj Donald B Hodges
Lt Col Ronald F Wachtmann
Lt Col Paul D Try
Lt Col William F Johnson
Mr Edwin B Dickson
Air Weather Service
Scott AFB, Illinois

ABSTRACT

Environmental sensitivities of Electro-Optical (E-O) systems are briefly discussed. Differences in lock-on ranges for television and infrared acquisition devices under various weather conditions, the ability of infrared systems to acquire targets at night, the ability of microwave systems to acquire targets at night and in adverse weather conditions, and the decided loss of target resolution of microwave compared to television systems are considered. It is concluded that no one type of Precision Guided Munition (PGM) will be optimum for all situations, and a mix of different types of PGMs is required to maximize the potential for success.

Present methods of operational support consist of forecasts of ceiling and visibility. The Air Weather Service (AWS) objective is to provide one weather parameter for each target, type of weapon, and time of day. This will be accomplished through use of a matrix which specifies the probability of a clear line-of-sight (CLOS) as a function of altitude and range for each target and weapon system. These data can then be used in target and weapon selection, and the determination of optimum delivery tactics.

The probability of obtaining a CLOS may be determined from a combination of the probability of obtaining a cloud-free line-of-sight (CFLOS) and the atmospheric seeability, a complex function of the weather conditions, target contrast, illumination and detection threshold of the weapon. Air Force activities which are pointed toward attainment of this capability are discussed. AWS's Environmental Technical Applications Center (ETAC) at Scott AFB can now provide CFLOS probabilities using synoptic cloud observations for stations around the world. The use of the 3D Neph automated cloud analysis in a statistical model for predicting the probability of a CFLOS between two moving vehicles is presently under study. In the near future, AWS will publish the E-O Handbook to allow field forecasters to use and assess state-of-the-art- rapid manual methods to produce CLOS probabilities. ETAC is adapting radiative transfer models for automated prediction of target

UNCLASSIFIED

UNCLASSIFIED
UNCLASSIFIED

lock-on ranges as part of the weather support plan (WSP) for the TV Maverick. Although operational computer-produced CLOS forecasts for the Maverick are still at least two years in the future, it is anticipated that experience gained in this program may be readily applied to the support of other PGMs. The status of the E-0 tower and its use in providing a data base for future verification of CFLOS and CLOS forecasts are discussed. Plans for data collection in denied areas are considered.

Future plans call for development of a generalized WSP for PGMs. This plan is directed toward an AWS capability to support all types of TV guided, laser guided, and imaging infrared guided weapons.

AWS has initiated the development of an operational dynamic CFLOS model. This model will be designed to satisfy many operational requirements for CFLOS forecasts and will operate from real-time meteorological data available at the Air Force Global Weather Central.

INTRODUCTION

The purpose of this paper is to present our capabilities for weather support to electro-optical weapons systems. We will also describe where we are going in developing our capabilities in this support. In order to provide a background for this discussion, we will briefly describe the weather sensitivities of electro-optical systems. From this description, we can develop specific weather parameters which the decisionmaker needs in order to improve the effectiveness of E-0 systems employment. Following a brief description of current methods of weather support, we will describe those efforts which are directed toward future support concepts.

The Air Weather Service has been involved in support to several different types of electro-optical systems for several years. Much of the development effort in Air Weather Service is currently directed toward two particular types of E-0 systems: high energy lasers and precision guided munitions (PGMs).

We are supporting the development of high energy lasers at two locations. Our staff meteorologists at the Air Force Weapons Lab are performing weather studies in direct support to the laser development in being there. Also, the Environmental Technical Applications Center is currently modeling the effects of clouds on laser weapons employment. However, the body of this paper will be primarily concerned with our present and planned support for PGMs.

PGM ENVIRONMENTAL SENSITIVITIES

There are three basic types of guidance systems employed on PGMs. These three are the TV, the forward looking infrared, and the microwave systems. Once a target is acquired, either visually or through use of an acquisition sensor, successful lock-on using any system depends not

UNCLASSIFIED
UNCLASSIFIED

only on the inherent contrast in the target-background scene, but also on transmission of the contrast from target to sensor through the intervening atmosphere. Neither the TV or the IR systems can see through clouds. In addition, the contrast transmission through the atmosphere is degraded by haze and dust for the TV system. For the infrared system the degradation results from water vapor and wet aerosols. While the microwave systems can see through most clouds, they are limited by heavy clouds and precipitation. The differing characteristics of these systems lead to some significant employment decisions. The infrared systems can acquire targets at night and microwave systems can acquire them at night and in adverse weather situations. However, the decided loss of resolution of microwave systems can make them unsuitable for identification of certain types of targets, particularly in the close air support role. Consequently, the TV guided systems will continue to play a significant role where target discrimination requires a high resolution in the image.

It is generally known that the probability of kill of the guided weapons has proven to be significantly greater than that of the unguided systems. However, the values obtained in combat and other operational experience have been substantially lower than those obtained in a controlled test environment. Results have shown that the success rate drops significantly in the poor weather environment. However, it has also been shown that the wider variability of weather conditions in the poor weather regimes has widened the range in the probability of kill in poor weather areas as depicted by error bars in Figure 1. It is precisely this variability which indicates that the employment success rate can be markedly enhanced by using forecast changes in weather in employment decisions. The current thrust in our development efforts, then, is to attain a capability to provide forecasts of those weather sensitive parameters which will assist in optimizing employment of these weapon systems.

Because of the differing environmental sensitivities of the various weapon systems, there are significant differences in the limiting factors for different types of systems. For example, the lock-on ranges have been found to be greater for the TV systems than for the IR systems in summer and in rural areas, while that of the IR systems is greater in winter and in urban areas. These differences in lock-on range, combined with differences in resolution, indicate that no one type of PGM will be optimum for all situations. A mix of different types of PGMs is required to maximize our potential for success.

OPERATIONAL SUPPORT

Given a variety of available weapons, selection decisions on weapons systems must be made at several command levels. Regional and seasonal variations in weather will affect stockpiling decisions, while daily variations will influence the decisions on weapons upload, target selection, and delivery tactics. These weather factors and other decision affecting parameters combine in a complex fashion to determine the probability of a given operation. For example, various phenomena combine to

100-100000-
100-100000

limit the employment of a TV guided weapon system (Figure 2). The launch envelope for the weapon is determined by aerodynamic capabilities of the weapon, its delivery platform, and the range required for warhead arming. Given what we know about the target and its defenses, we can determine the minimum safe launch range. Finally, the base of clouds and the visibility determine the maximum range for target acquisition and lock-on.

Present methods of operational support consist of forecasts of ceiling and visibility which are provided by staff weather officers supporting the operational commander. Although this type of information has proven useful to our customer, we recognize that it has inherent limitations. We believe that a more useful tool would be a parameter which relates the effects of clouds and visibility restrictions directly to the probability of acquiring and locking onto a target.

Our objective is to provide one weather parameter for each target, type of weapon and time of day. One method which can be used is to convert the cloud forecast into a probability of a cloud-free line-of-sight to the target for any altitude. However, the seeability or clear-air lock-on range is a complex function of not only the weather conditions, but also of target contrast, illumination and the detection threshold of the weapon. We, therefore, plan to combine these parameters and the cloud-free line-of-sight probability into a single parameter which specifies the probability of a clear line-of-sight to the target.

The weather data needed for decisions may be presented in the form of a matrix which specifies the probability of a clear line-of-sight as a function of altitude and range for each target and weapon system (Figure 3). These data can be used in target and weapon selection, and the determination of optimum delivery tactics. For the TV system, the times of day during which the illumination exceeds the required threshold value can also be given.

Objective and subjective probability methods and procedures are available, have proven themselves operationally, and combined with decision theory, significantly improve weather support. Proper verification theory and procedures are also available and have been shown to be useful. AWS will actively pursue the systematic integration of probability forecasts, mission success indicators, and decision theory into all aspects of weather support from wing/base level up through sophisticated command and control systems. The preferred method of presenting weather information to decisionmakers is by mission success indicators (MSI).

A weather MSI (WMSI) is the probability that all stages of a mission will have favorable weather. A probability forecast is not a WMSI unless the event is tailored to a specific decision. Favorable weather is defined by operational requirements. A probability forecast of 80% for weather better than 200 and 1/2 is not an MSI for the mission that needs 500 and 1/2. WMSIs fall into two categories. The first is operational or forecast MSIs which are dependent on current weather, the most recent

set of forecasts, and climatology. These would be for an imminent date and time, usually within the next three or four days. Planning or climatological WMSIs are the average prospect of favorable weather at a given time of year and time of day. These are required for optimal planning.

WMSIs link the weather to the mission. The importance of our SWOs in interacting with the operator to determine and define the mission weather sensitivities is fundamental to the implementation of a useful product which will provide the decisionmaker with the weather information he needs. If an operation is weather sensitive, then that sensitivity can be quantified. By combining the weather information into a single number, we reduce comm and display requirements. The decisionmaker has only one number to consider instead of trying to assess what a synoptic map presentation and the sky cover/visibility/weather description means.

There are more things we should know about MSIs. First, they are intrinsically a tailored product, a product that is fitted to the constraints of a given mission or plan. Next, we must consider the fact that weather events are related in both time and space. This interdependency of weather events must be factored into the weather MSI. AFGL is working on this problem for us through research contracts at St Louis University and National Weather Service's Techniques Development Lab. Finally, MSIs may be used for simple single go/no-go criteria or to predict the probability of success of any one or all of the events of a continuous multiple event scenario (e.g., takeoff, aerial refuel, strike a target, and recovery).

Weapons selection planning can be assisted by MSIs. In Figure 4, MSIs are presented for specific targets, altitudes (tactics) options, and types of weapons. This information is all based upon operator determined threshold information. Based upon such thresholds, the MSI array shows the meteorological probability of success for each weapon type and tactic. Any significant weather is indicated under a "problem" column. The operator can consider the different risks associated with different delivery tactics and the store of each weapon type available (iron bomb, TV, IR, or RADAR guidance, or laser designator) and compare each MSI to the critical probability to make weapon and tactics selection for each target.

EFFORTS TO OBTAIN REQUIRED CAPABILITY

The acquisition of the capability for probabilistic real-time forecasts involves a very significant development effort. Our efforts are being conducted on two levels. The first level involves climatological studies to provide data for planning. The second area of our development effort involves the improvement of our operational support capabilities to precision guided munitions. Both levels of effort are of course directed toward supporting not only PGMs but all types of electro-optical weapons systems.

UNCLASSIFIED
UNCLASSIFIED

Much of our development effort is being conducted at the Environmental Technical Applications Center, commonly known as ETAC, at Scott Air Force Base. The three-dimensional nephanalysis serves as a basis for this effort.

The 3D-neph is an automated cloud analysis which uses all available data including surface weather reports, aircraft reports, and meteorological satellite data. The use of satellite data means that we are no longer dependent solely on surface weather reports in developing cloud climatology. The program logic estimates total cloud cover, cloud types, and cloud tops from the satellite data. The 3D-neph is a high resolution cloud analysis performed on a 25-nautical mile grid spacing worldwide. This grid spacing is consistent with the length scale of most tactical decisionmaking. The analysis is performed every three hours for the northern hemisphere and every six hours for the southern hemisphere. The analysis divides the atmosphere into 15 layers from the surface to 40,000 feet. The analysis fields are used to initialize our automated cloud forecasts, which can also be produced on a 25-nautical mile grid for selected regions. The 3D-neph data are forwarded to ETAC for use in compiling a cloud climatology applicable to their studies for planning.

ETAC is currently conducting a study to use the 3D-neph data fields in a statistical model for predicting the probability of a cloud-free line-of-sight between two moving vehicles; e.g., an intruder aircraft and an interceptor missile. This study has particular applicability to the SAC mission.

At present, ETAC provides cloud-free line-of-sight probabilities through use of a program based on synoptic cloud observations stored in the ETAC data base for stations around the world. The model used in this program is a static model as opposed to the dynamic model proposed for the 3D-neph. However, it is a capability in being.

The Air Force Geophysics Lab at Hanscom Field is also involved in the development effort for our E-0 systems support. Iver Lund's extensive studies of a three-year period of all-sky cloud photographs taken at Columbia MO has provided objective probability curves for predicting cloud-free line-of-sight as a function of cloud-type and cloud-amount for use in static models. These results have served as a basis for the ETAC cloud-free line-of-sight programs. AFGL has also performed an exhaustive study of a set of 1/4 million observations of clear line-of-sight taken by MAC, SAC, and commercial airline pilots during a five-year period in the 1960s and is publishing a series of atlases of world-wide climatological cloud-free line-of-sight probabilities.

The staff meteorologists at the Air Force Weapons Lab are working on the cloud-free line-of-sight problem for moving observers and are also performing detailed studies of the aerosol and optical turbulence effects of high-energy laser applications.

UNCLASSIFIED

Much of our current effort at Headquarters Air Weather Service is directed toward development of a generalized WSP for PGMs with a first draft due by the spring of 1977. The outline for the first draft includes not only a section applicable to all types of PGMs, but also sections applicable specifically to TV, laser guided and imaging IR systems. Annexes are anticipated for the TV infrared Maverick, GBU-15 (SAC employment), GBU-15 (TAC employment), PAVE SPIKE, PAVE TACK, laser guided bombs and E-0 guided bombs. We have prepared a draft AWS E-0 Handbook for use by our weather detachments supporting operational wings. This handbook is designed as a primer on atmospheric effects on PGMs and will contain both rapid and more detailed manual methods of predicting clear line-of-sight probabilities. The rapid methods will become available to our operational units with the publication of Volume I of the handbook early next year.

Our operational model development at ETAC is the first phase of a two-stage effort to develop a capability at the Air Force Global Weather Central (AFGWC) for real-time forecast support to the TV Maverick. As previously mentioned, AFGWC has recently initiated the development of a cloud-free line-of-sight model which will use the cloud analysis and forecast products at the AFGWC (e.g., the 3D-neph). They will also adapt current radiative transfer models for prediction of target lock-on ranges. The final phase of the effort will be an evaluation of the additional skill obtained by use of these models. This development is a multiyear effort. Depending on the results of the evaluation and the availability of computer resources, our long-range objective is the operational implementation of these models at the AFGWC.

In Figure 5, we show how the concept for semiautomated operational support is tied together. The support cycle will be initiated when operational wings submit a list of weapons and target locations to the AFGWC. The operational cloud-free line-of-sight and clear line-of-sight models will predict cloud-free line-of-sight and clear line-of-sight parameters for each target location using AFGWC data fields. These parameters will be transmitted to the staff weather officer who will combine them with data on target contrast and the resolution of the acquisition sensor. The product provided to the operational decision-maker is the probability matrix for CLOS and lock-on for each target.

An important link in development of our capabilities in E-0 support is the relationship between standard meteorological observables (ceiling, visibility, wind, temp, humidity, etc) and the operational decision parameters (cloud-free line-of-sight and clear line-of-sight). To meet this need, we plan to exploit data available from the electro-optical tower facility at Wright-Patterson AFB. The E-0 tower facility is an avionics lab project designed for a real-world evaluation of bread-board models of electro-optical systems. The wide variability in weather conditions at Wright-Patterson AFB offers an opportunity to test these systems in a wide-ranging and realistic environment. The facility will be fully instrumented with a capability to measure a full spectrum of both meteorological and optical properties of the atmosphere.

UNCLASSIFIED

There is a dedicated staff meteorologist assigned to this facility for meteorological support. We are optimistic about the valuable understanding we will obtain from this facility about the impact of weather on E-0 systems.

Looking to the future, we are attempting to obtain the equipment to obtain information to support E-0 systems in what would normally be data denied areas. We will briefly discuss the Battlefield Targeting Support System (BATSS), Pre-Strike Surveillance Recon System (PRESSURS) and Required Operational Capabilities (ROCs) which will be submitted by Air Weather Service to our higher headquarters. The draft ROC for BATSS states the requirement for an unmanned, automatic, surface-based sensor system to obtain essential weather data from battlefield/target or semi-permissive areas. This ROC is intended for AWS support of Army and Air Force operations. The draft ROC for PRESSURS states the requirement for an airborne sensor system to obtain measurements of the most critical weather parameters over tactical target areas and semipermissive environments.

The minimum essential performance characteristics of the ROC for BATSS call for a hand-emplaced remote weather station capable of being deployed by one man, and an air-droppable, ground-emplanted sensor system. The minimum acceptable weather parameters are: cloud height/ceiling, weapon-to-target visibility/seeability, cloud cover, winds, precipitation, pressure, temperature, and humidity. The remote weather stations should be capable of interrogation, directly or through a relay, by a master control station. There is a need to communicate, process, and display these data to Army and Air Force weather personnel for input to the operational decisionmaking process. Interoperability of the remote stations with the REMBASS and/or Air Force tactical ground sensor systems, to include use of communication links, is required. The optimum performance characteristics for the hand-emplaced remote weather station include the minimum essential parameters plus the detection of thunderstorms/lightning, state of the ground, low-level winds to 300 meters AGL, and illumination. An air-droppable ground-emplanted remote weather station should also be developed with the same measurement capabilities as the hand-emplaced station.

The minimum essential performance characteristics of the ROC for PRESSURS call for the capability to obtain cloud height/ceiling, weapon-to-target visibility and cloud cover measurements. The target acquisition device may be a TV camera operating in the visible or near infrared (IR) spectrum, or it may be an imaging IR system operating in the 8-12 micrometer region. Seeability measurements are needed to the nearest 1 nautical mile over a range from 1 to 8 nautical mile. Data collection will be accomplished through use of remotely piloted vehicles.

SUMMARY

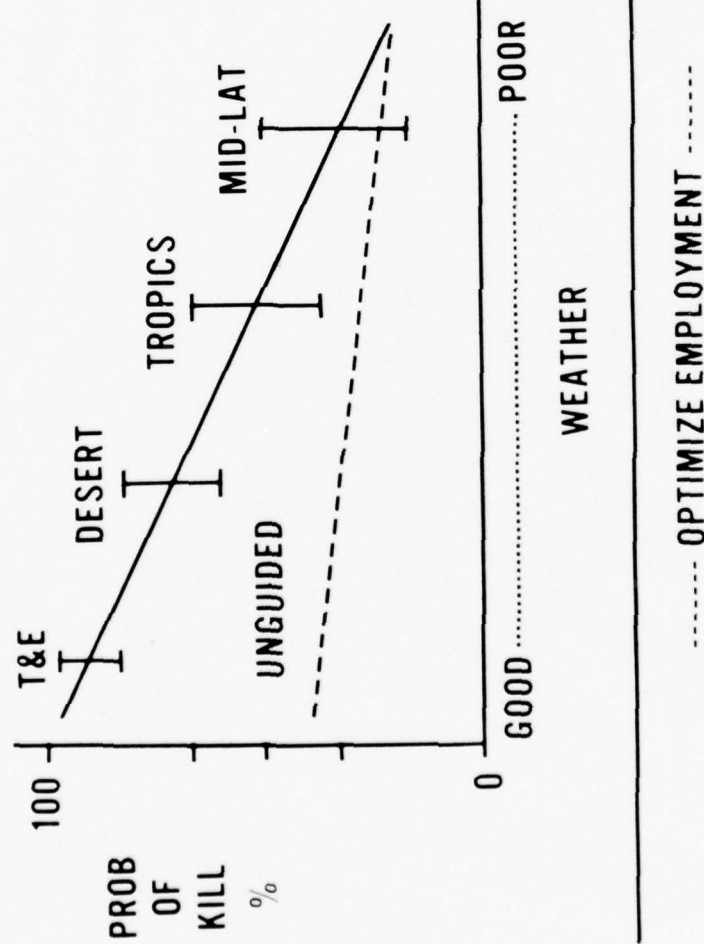
We have outlined the present capabilities for weather support to electro-optical systems. This support includes ceiling and visibility

UNCLASSIFIED

REF ID: A65100
[REDACTED]
forecasts and climatological cloud-free line-of-sight probabilities upon request for selected locations. The Electro-Optical Handbook will be distributed to our field units soon to improve their capabilities in E-O support.

The future holds bright prospects for providing meaningful and tailored forecast products for E-O support. The development of dynamic models for clear line-of-sight probabilities will result in a better assessment of weather impacts on these systems. The data obtained in the various observational programs will enable us to relate the clear line-of-sight directly to standard meteorological observations. These programs, along with the model development at ETAC, are directed toward an operational capability for tailored support from the AFGWC. The time schedule for achieving our objectives will depend on availability of resources in today's fiscal climate.

UNCLASSIFIED



----- OPTIMIZE EMPLOYMENT -----

FIGURE 1. PGM EMPLOYMENT SUCCESS RATE

AW6 167 DN

UNCLASSIFIED

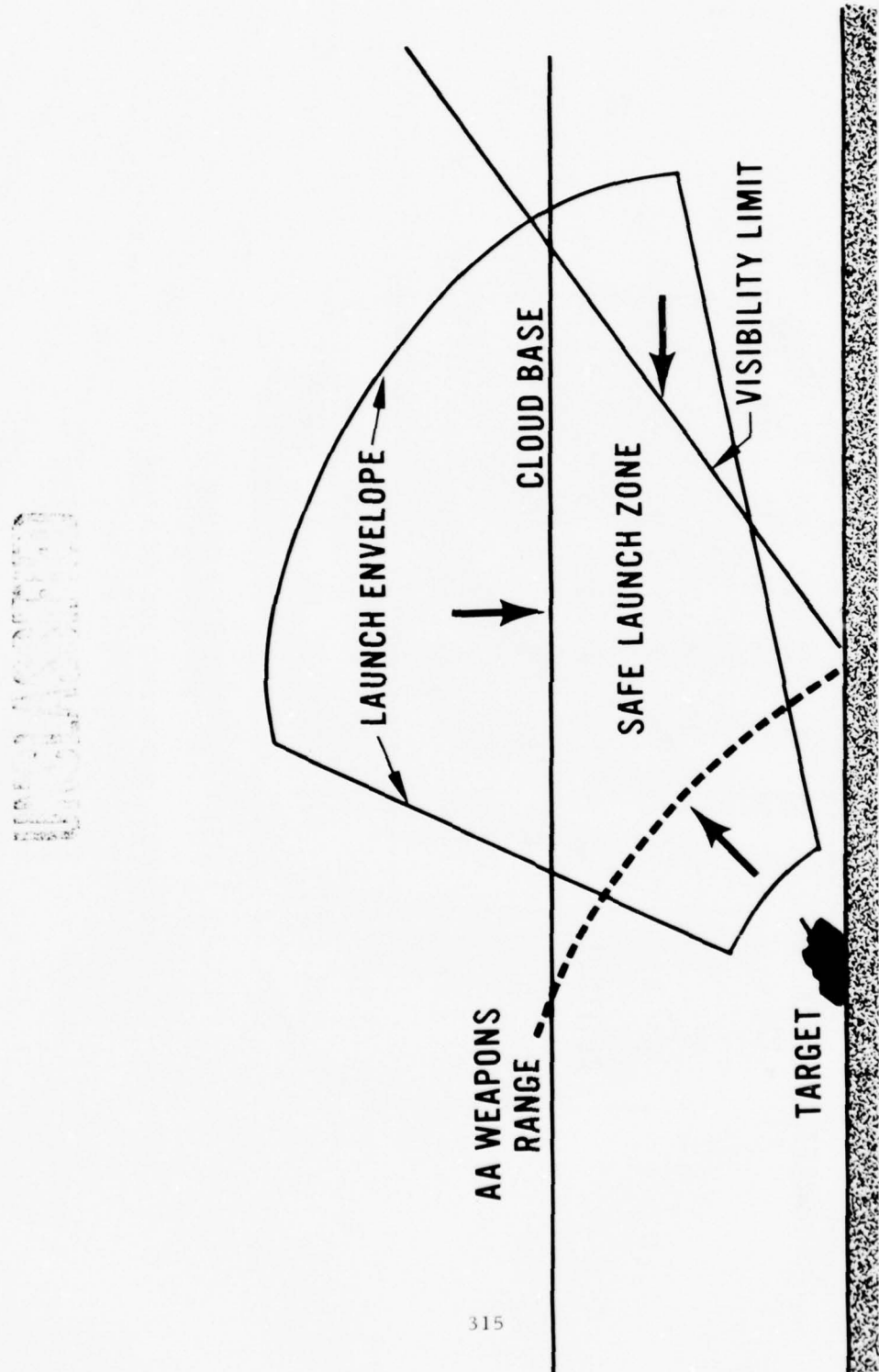


FIGURE 2. OPERATIONAL EFFECT ON TV SYSTEM
AW 6-172 DN

-- TARGET/WEAPON

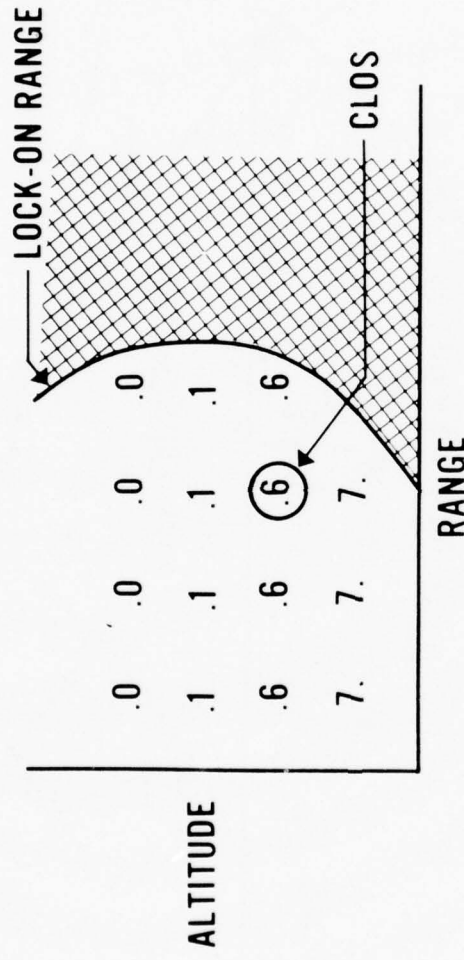


FIGURE 3. DATA NEEDED FOR DECISIONS

AW 6 173 DN

5 TARGETS-20 OPTIONS

TGT	ALT	VIS	TV	IR	RA	LA	PRNT
E-22	H	30	25	30	85	20	FG
	L	45	40	50	85	35	
E-24	H	40	35	80	85	30	HZ
	L	75	70	75	85	75	
J-14	H	30	30	30	45	25	CL
	L	80	75	80	85	85	
K-7	H	35	30	25	40	25	RA
	L	50	45	40	55	40	
K-27	H	10	10	05	15	05	SN
	L	25	20	25	35	20	

FIGURE 4. MSI WEAPONS SELECTION

AW 6 1095 DO

UNCLASSIFIED

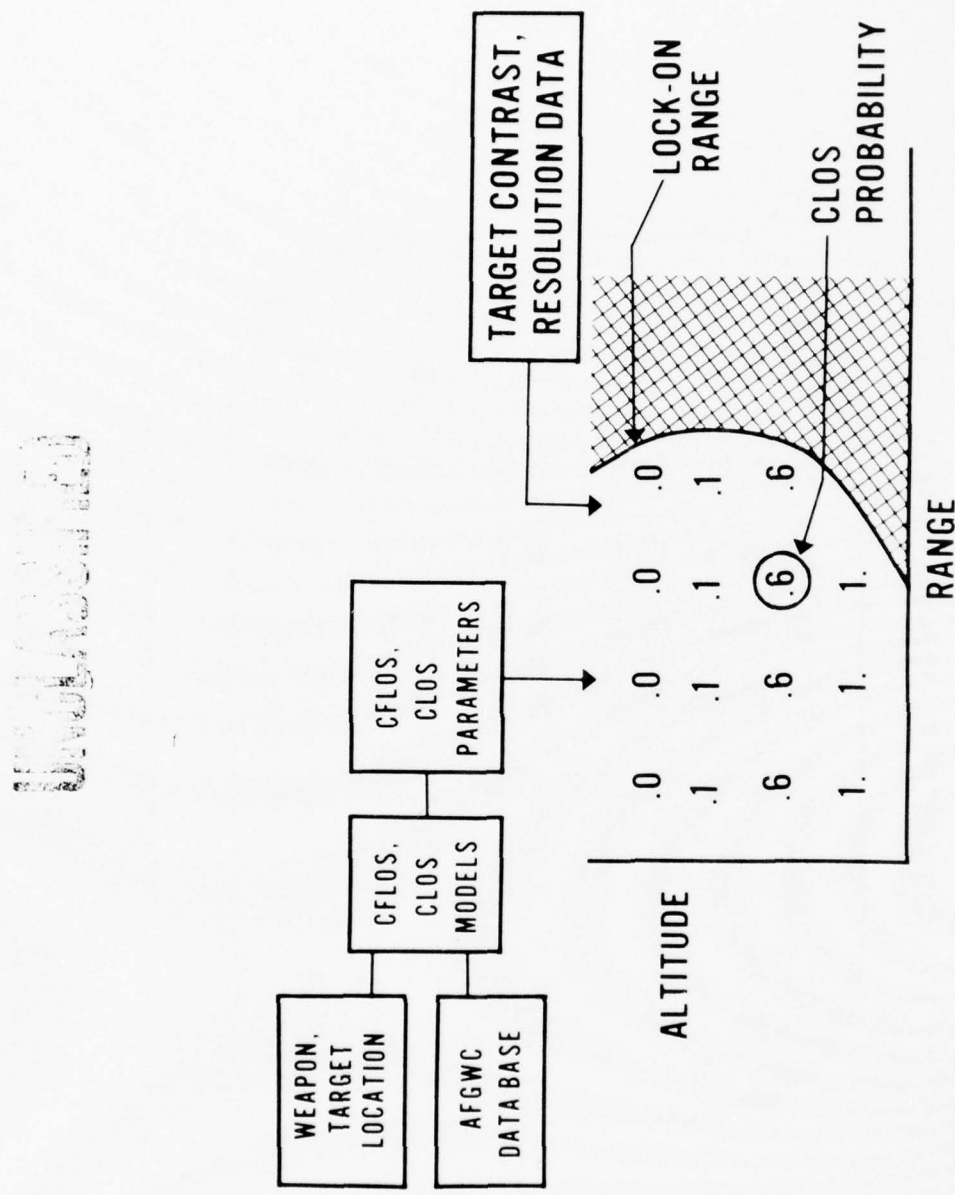


FIGURE 5. SEMIAUTOMATED OPS SUPPORT CONCEPT

AW 6 178 DN

UNCLASSIFIED

UNCLASSIFIED

THE CONTENT AND SOME LIMITATIONS OF
METEOROLOGICAL DATA BASES
AVAILABLE FOR OPTICAL PROPAGATION STUDIES (U)

by

Laurence D. Mendenhall, Captain, USAF
Electromagnetic Propagation Section
USAF Environmental Technical Applications Center
Scott Air Force Base, Illinois 62225

Abstract

This presentation is intended to provide a very brief overview of the kind of meteorological data that are available to the DoD community to support studies and analyses of environmental effects on electro-optical systems. The prime objective of this paper is to stimulate discussion in the workshops to follow rather than to stand as a definitive paper on the subject. The quantity and the quality of this data base will be discussed. The paper contains examples of errors inherent in some of these data, as well as limitations in our ability to measure meteorological quantities, and the impact such errors and limitations can have on performance evaluation. The emphasis in this paper is on the USAF Environmental Technical Applications Center (ETAC) data base, but inherent errors and limitations apply to meteorological data bases in general. Finally, we identify some needs which, if fulfilled, would enhance the ability of the DoD community to predict the performance of electro-optical systems.

Introduction

This paper has as its prime objective the stimulation of discussion on how available meteorological data can be used in studies and analyses of the performance of electro-optical systems. Thus, it does not purport to serve as a comprehensive source document on the subject. Discussed below are some of the problems encountered by the author and other analysts at USAFETAC during the course of studies and analyses of atmospheric effects on electro-optical systems. The material suggests that more attention must be paid to inherent errors in the data base before drawing

UNCLASSIFIED

UNCLASSIFIED

conclusions about the performance of a particular system. Information in this paper on the content of data bases emphasizes the USAFETAC data base.

Data Sources

The meteorological data acquired by USAFETAC includes surface and upper-air observations taken worldwide and collected continuously by the Air Weather Service (AWS) Automated Weather Network (AWN) at Carswell AFB, TX. The AWN receives these observations through connections into national and international circuits (Figure 1). Most overseas observations are transmitted by the various countries under data exchange agreements arranged through the World Meteorological Organization (WMO). Two UNIVAC 1108 computers at Carswell decode, audit, and distribute the observations. All observations are transmitted computer-to-computer to the Air Force Global Weather Central (AFGWC) at Offutt AFB, NE. Here, they are validated, error checked, and reformatteed for use at AFGWC in order to provide real-time operational support. Once each day all observations received at AFGWC are transmitted via the Advanced Research Projects Agency (ARPA) computer link to USAFETAC at Scott AFB, IL. The 3-D Nephanalysis data, which are derived from the Defense Meteorological Satellite Program (DMSP) and other data sources, are mailed from AFGWC to USAFETAC's Operating Location A at Asheville, NC for processing and archival.

Data Coverage Worldwide

The following statistics are for October 1976, but they provide meaningful numbers which are typical for all months of the year. The AWS Master Station Catalog contains a total of 13,889 stations worldwide. However, 4325 of these stations did not transmit any observations during October 1976. In the Northern Hemisphere, 11,349 stations normally report and 2408 normally report in the Southern Hemisphere. Of the 9500-plus stations reporting surface observations, 6566 report only at synoptic observation times (00Z, 03Z, 06Z, etc.). About 1600 stations report every hour, while only 1300 stations report more than one type of observation. For these reasons and because some stations operate only during daylight hours, the total observation count varies considerably from hour to hour.

Figure 2 shows this observation count at each Greenwich (GMT) hour during October 1976. The number of observations received during any one-hour period ranged from a high of 7323 to a low of 1695. These numbers do not include roving

UNCLASSIFIED

UNCLASSIFIED

ship observations. On the average, USAFETAC received about 3800 ship observations per day.

There are 2800 upper-air stations worldwide, which 2204 of these in the Northern Hemisphere. Of the 2800 stations only 1700 were active in that they reported at least once during October. The most reporting at any one time was 772. Most upper-air stations report only at 00Z and 12Z, and a few report at the intermediate hours of 06Z and 18Z.

Much of the data available to USAFETAC, especially prior to 1965, actually belongs to the National Climatic Center (NCC) at Asheville, NC. The period of record of these data varies considerably from country to country and with the type of data, but generally goes back to the 1940's. Scandinavian data goes back to 1900, while Russian and Chinese observations commence in 1932. Efforts are underway at NCC to acquire ship observations going back to 1860. Additional detail on the various data sets and their periods of record appear in the publication "Data Sets for Meteorological Research," published in 1975 by the National Center for Atmospheric Research (Jenne, 1975).

Meteorological Variables Measured

Table 1 lists the atmospheric elements measured at most stations. Not all stations report all of these elements, however. For example, many stations do not report the amount of cloud in each layer, but they only report the total cloud amount and the amount of low or middle cloud. Table 2 lists the variables measured by an upper-air station using a radiosonde.

Some Limitations and Inherent Errors in Meteorological Observations

None of the meteorological variables which are routinely measured include propagation elements, and some variables are not measured objectively. From Table 1 we see in the surface observations that two variables of fundamental importance to most electromagnetic propagation problems, cloud amount and visibility, are measured subjectively. Runway visibilities are normally measured objectively, i.e., with a transmissometer, but are generally only reported for values below about 2 km. Moreover, runway visibilities are not generally available in the computerized data base prior to 1973, and many events are available only for some of the stations reporting hourly. However, since the runway visibility reported depends upon the runway light

UNCLASSIFIED

UNCLASSIFIED

setting used at the time of the observation and this light setting is not recorded anywhere, these data appear to have little or no practical use.

Table 3 lists some of the variables that affect an observer's report of the prevailing visibility. In recent years, manpower cuts at Air Force stations may have further reduced the validity of such observations since an observer no longer mans the representative observation site at many stations. The weather station observer does not have an unobstructed view of the horizon in all directions and his observations may suffer. In addition, the METAR code, used mostly in Europe by about 400 stations, does not allow the reporting of visibilities above 12 km. Some recent work (Hering, 1971; Reiss, et al., 1976) show that with proper station surveys and statistical methods that it is possible to adjust the reported prevailing visibilities to eliminate or reduce some of the biases resulting from the variations in the type of markers available, etc.

Another problem arises with reporting visibilities at night. Observers must use lights to estimate the visibility, but the source intensity and size of the light strongly affect the visibility so measured. Figure 3 illustrates this fact by comparing the nighttime visibility with an equivalent daytime visibility for various source intensities. Shown also are some actual observations made by Bennett at the Royal Aircraft Establishment and the Kew Observatory in the 1930's. The calculations were made using the Bouguer-Lambert and Allard's laws, using a threshold intensity for the eye of one lumen/km². These curves indicate two things: 1) that one should not mix nighttime and daytime visibilities together when making statistical summaries; and 2) when making transmission calculations that require surface visibilities to define the surface extinction coefficient, as in LOWTRAN, one must correct a nighttime visibility to an equivalent daytime value prior to employing the model.

Upper-air observations are, in many ways, more problem-prone than surface observations. First, most radiosondes cannot report each element continuously since the transmitter must alternate between measuring humidity or temperature. As a result, fine-scale variations may be missed. Second, to derive winds the radiosonde transmitter is tracked by ground radar or radio direction-finding, but the accuracies in tracking permit computation of only average wind values over layers 300-500 meters thick or more. This averaging removes the turbulent fluctuations and shear zones that may be important to optical propagation calcula-

UNCLASSIFIED

UNCLASSIFIED

tions. Third, the temperature and humidity elements have contributed to the data reliability problem over the years. Nearly every country that makes radiosonde observations uses a different instrument design. For example, Table 4 shows some of the humidity elements used currently and in the last 20 years (Mendenhall, 1974). The United States used a lithium-chloride element until about 1961 when it changed over to a carbon hygristor. Naval radiosonde stations made the conversion several years later. With the change in the element came changes in response time, accuracy, and precision. Then, as a result of large errors discovered in intercomparison tests during Project BOMEK in the late 1960's (Teweles, 1970), the National Weather Service (NWS) began using a modified humidity duct. The old duct permitted indirect solar radiation to impinge on the hygristor resulting in errors of up to 50% in the relative humidity measurements at high sun angles (Morrissey and Brousaides, 1970). Such errors can have an adverse impact on the computed performance of some infrared sensors. For example, Figure 4 shows the effect of up to a 37%* error in humidity on the computed transmission in the 2.95-micron band of a Defense Support Program sensor as a function of zenith angle.

In general, humidity sensors become unreliable at colder temperatures and lower pressures. Consequently, most countries do not report humidities at heights above the -40°C temperature level. However, both China and Russia report humidities to the top of the sounding. For many years these data were used by people who were unaware of its gross error. Figure 5 (Mendenhall and Boesiger, 1976) provides some insight into just how bad these values are. The mixing ratios of two Russian stations are compared with the high-quality frost-point hygrometer observations obtained by Mastenbrook (1968) at the Naval Research Laboratory (NRL). While the comparison is meaningless below the tropopause, the differences in the stratosphere are significant. The Russian data show consistently high values (generally exceeding 100 ppm) while there exists no evidence from other measurements that stratospheric moisture values average above about 3 ppm. Estimates of humidities above the -40°C temperature level are possible using some recently developed models (Mendenhall, et al., 1975; Mendenhall, 1976).

* Humidity errors ranged from 2.8% at 3 km to a maximum of 37% at 8 km, then decreasing to zero at 9 km.

UNCLASSIFIED

UNCLASSIFIED

A more serious problem with the Russian radiosonde humidity data are the apparently large errors that may occur in the troposphere. We can ignore those data above the tropopause because we know pretty well what the humidity is in the stratosphere. After performing some research into the characteristics of the Russian radiosonde we hypothesized that perhaps ascents through supercooled clouds or precipitation could cause either the linkage or the humidity element to freeze in place. To check this hypothesis we ran a comparison of soundings taken simultaneously at a US station (Nome, Alaska) and at a Russian station about 200 km across the Bering Strait (Mendenhall and Boesiger, 1976). First, we ran the comparison without regard to the weather conditions at the time of the sounding. The results, shown in Figure 6, reveal that the relative humidities reported by the Russian radiosonde are on the average as much as 20% higher than those reported by the US instrument. [We believe that the US instrument in use then (1973) is the more reliable of the two.] For these same soundings the temperatures, in the mean, differed by less than 0.4°C.

For further comparison we introduced the constraint that the Russian station must have precipitation occurring at the time of the sounding, with the US station reporting overcast or precipitation. The results of this comparison appear in Figure 7 and show even larger differences in the relative humidities. At 400 mb, for example, the Russian sounding gives an average relative humidity 40% higher than that given by the US sounding. Also, the standard deviation of the Russian observations was considerably less than that observed for the US measurements, suggesting a much more sluggish response for the former. The freezing level was at or near the surface for all cases used here. A total of 18 sounding pairs were used to produce the data at all levels, except only five pairs were used for the 400-mb level. Finally, Figure 8 shows the results obtained when conditions were clear at both stations. Under clear conditions the two instruments produce similar results.

The significance of what we have just shown is as follows: First, regardless of which instrument was correct (and probably neither was), significant differences existed which are not real. These differences could erroneously lead one to predict that a certain system might perform differently at the two locations. Second, these observational differences appear to be a function of the meteorological conditions themselves, further complicating the problem. As a footnote, we are continuing to investigate this particular problem at USAFETAC with the objective of further quantifying the errors and determining how they vary with weather

UNCLASSIFIED

UNCLASSIFIED

conditions. Preliminary evidence shows that Japanese soundings may possess similar problems.

Problems with Data Sets

We have already described some of the limitations and inherent errors in meteorological observations. Table 5 lists the general problems inherent in data sets of the kind possessed at USAFETAC.

A large number of the problems affecting the quality of the USAFETAC data base have been brought about by the need to automate. From the early 1940's to about 1965 data were hand-punched at Asheville from hard-copy records. Considerable effort expended in quality control resulted in a consistent and good quality data base. With the advent of the AWN in the mid 60's data were taken from the circuits on paper tapes, decoded at USAFETAC, and placed on magnetic tape. By 1973 data were decoded and then placed on magnetic tape directly at AFGWC. Problems encountered in the conversion to automation, especially from 1970 to 1973, resulted in a lot of holes and erroneous data in the archive. This situation deteriorated further because of the elimination of most of the quality control efforts as a result of manpower reductions.

A few examples will serve to illustrate the kinds of problems encountered with computer processing of observations. Coding practices vary from country to country and even within countries. For example, in Asian Russia the 7-group of the synoptic code contains 12-hour precipitation amounts at 0000Z and 1200Z, while in European Russia this same group contains 6-hour precipitation amounts. But the 0600Z and 1800Z observations contain 12-hour precipitation amounts. Sometimes there are errors in reporting or in decoding which lead to gross errors, e.g., 300 mm of precipitation at a station with no history of clouds during the preceding 12 hours. If a station omits a code group, then all subsequent groups in that report will be decoded wrong, e.g., clouds decoded as dew point, precipitation decoded as pressure change, etc.

We are attempting at USAFETAC to improve the quality of our data base through identification of problems in the daily processing of incoming data. Earlier this year we implemented the Problem Identification Program (PIP) which detects class errors, for instance, errors produced by coding changes. This program has already been deemed a great success. For example, the METAR reports contained missing

UNCLASSIFIED

UNCLASSIFIED

dew points which the decoders interpreted as a dew point of 4.8°C . The PIP detected this and this has already been corrected in the decoder software. The PIP also identified that Canadian precipitation amounts were not being decoded at all. Investigation revealed this problem existed since 1974. The PIP identified a total of 15 such problems in the few months of its existence.

Not mentioned previously are analysis and forecast fields produced on a grid. Upper-air analysis fields are also archived at USAFETAC, and some forecast fields may be in the near future. Changes in analysis routines and models will produce problems in using these data bases.

Satellite Data Base

We now turn our attention to unconventional data bases, of which the satellite data base is the principal one. The 3DNEPH (Table 6) data base is produced from processed visible and infrared satellite data, surface observations, pilot reports, and radiosonde data (Coburn, 1971). The data processors merge all of these sources to produce the best estimate of the vertical and horizontal cloud structure. Originally using only DMSP data, AFGWC began including NOAA satellite data in the 3DNEPH during the past year. The USAFETAC archive contains 3DNEPH since 1970, with Southern Hemisphere available only since 1974.

As with conventional data there are limitations in these data also. The satellite processors (software) must make decisions as to what brightness or radiance level constitutes clouds rather than background, for instance. Sea-surface and ground-surface temperatures provide a reference level to the infrared processor in this regard. Snow cover may be mistaken for clouds by the video processor. To improve quality here a separate snow cover data base, determined largely from conventional sources, is queried and visible satellite data are not used in areas reporting snow cover. The most reliable data in 3DNEPH is total cloud cover. In data-dense areas the amount of cloud in each layer is also probably quite good, but over data-sparse areas such as oceans, quality for elements other than total cloud cover is probably quite low.

Special Data Sets

Table 7 lists a few of the special data sets available through the National Climatic Center, Asheville, NC. These data sets include some electro-optical measurements, e.g., solar radiation and turbidity. The solar radiation data

UNCLASSIFIED

UNCLASSIFIED

base consists of hourly and daily solar radiation amounts for stations in the US, Canada, Pacific Islands, and Iceland, and go back as far as 1952. The US network now consists of 121 stations. However, these data also contain serious errors, though, and a half-million dollar effort is underway at NCC to clean up the solar radiation data. Figure 9 (Jessup, 1974) shows a comparison of the response of three different pyranometers with the traveling standard.

Turbidity data from 1971 to the present are available for about 60 global stations. In 1973, this network consisted of 80 stations, 50 of them in the US. These data may also contain serious errors due to calibration problems and the lack of properly trained and motivated personnel to take the observations.

Hourly precipitation data are available for North America, several Central American countries, and for some of the islands beginning in July 1948.

Weather radar data are available only for the US and consist mostly of PPI photos taken at several elevation angles several times each hour. Since about 1974, quantitative digitized data are available for four National Weather Service stations.

Ozone data consist of measurements taken in balloon ascents made at 13 North American stations in the AFCRL (now AFGL) Ozonesonde network for the period January 1963 to May 1969. Also, the Naval Research Laboratory has made monthly soundings at Washington, DC since 1964. Additional sounding data are available from several satellites.

An extremely large volume of various kinds of data are available from the various satellites. A 1973 publication of the National Space Science Data Center (NSSDC) gives a compilation of the satellite and instrument programs of the United States, Russia, United Kingdom, and France.

A more comprehensive listing of meteorological data sets appears in a recent document published by the National Center for Atmospheric Research entitled, "Data Sets for Meteorological Research" (Jenne, 1975). A similar WMO publication lists data suitable for computer processing for various countries (WMO, 1972).

Needs

This brief review of data bases and some of the inherent limitations thereof serves to identify some basic needs

UNCLASSIFIED

UNCLASSIFIED

(Table 8). A principal obstacle in the way of providing quantitative estimates on errors in data is the lack of information on the instrumentation used by the various countries. Aperiodically, the WMO (WMO, 1973) conducts surveys but these surveys need to be done routinely. More effort must be expended on quality control of the data base, with additional sophistication of programs like PIP. Also needed are intercomparisons between instruments as was done in BOMEX and GARP. To permit better assessment of electro-optical systems performance, more use should be made of special electro-optical measurements. An inventory of these should be made to permit ready access in modeling work. Finally, better meteorological measurements need to be made during field tests of electro-optical systems.

Conclusions

A considerable amount of data are available for use in studies and analyses of weapons systems performance. The quality of these data is another matter. We have seen that serious errors may exist. Researchers and analysts must pay more attention to the errors inherent in the meteorological data and the impact these errors have on the results of studies on the performance of electro-optical systems. Also, much work remains to relate the meteorological data to optical and other propagation quantities pertinent to electro-optical systems performance. Special measurements, such as those being made in OPAQUE, should help in this regard.

Acknowledgements

The author gratefully acknowledges the assistance of Capt Charles Quigley, SMSgt Dave Bailey, SMSgt Dale Marks, and MSgt Victor Smith of the Data Base Management Section, Data Automation Branch, USAFETAC for providing statistics on observations received at USAFETAC.

References

Bennett, M. G. (1935): "Further Conclusions Concerning Visibility by Day and Night." Quart. J. Roy. Meteorol. Soc., 61:179-188.

Bilton, T., E. C. Flowers, R. A. McCormick, and K. R. Kurfis (1974): "Atmospheric Turbidity with the Dual Wavelength Sun Photometer." In: Solar Energy Data Workshop, November 29-30, 1973, NSF-RA-N-74-062, September 1974, pp. 61-67.

UNCLASSIFIED

UNCLASSIFIED

Coburn, Allen R., Maj, USAF (1971): "Improved Three Dimensional Nephanalysis Model." AFGWC Technical Memorandum 71-2, June 1971.

Hering, W. S., H. S. Muench, and H. A. Brown (1971): "Field Tests of a Forward Scatter Visibility Meter." AFCRL-70-0315.

Jenne, Ray L. (1975): "Data Sets for Meteorological Research." NCAR-TN/1A-111; July 1975, National Center for Atmospheric Research.

Jessup, Edward (1974): "A Brief History of the Solar Radiation Program." In: Solar Energy Data Workshop, November 29-30, 1973, NSF-RA-N-74-062, September 1974, pp. 13-18.

Mastenbrook, H. J. (1968): "Water Vapor Distribution in the Stratosphere and High Troposphere." J. Atmospheric Sci., 25:2, pp. 299-311.

Mendenhall, L. D. (1974): "Accuracy of Radiosonde Humidity Observations." USAFETAC Project 7400 (Unpublished).

Mendenhall, L. D. (1976): "An Evaluation of Several Models for Describing the Atmospheric Water-Vapor Profile Above the -40°C Temperature Level." USAFETAC Report 8035.

Mendenhall, L. D. and D. Boesiger (1976): "Preliminary Results in Error Assessment of USSR Radiosonde Data." USAFETAC Project 7161 (Unpublished notes).

Mendenhall, L. D. and C. Naegelin (1976): "Conversion of Nighttime Visibilities to Equivalent Daytime Values." USAFETAC (Unpublished notes).

Mendenhall, L. D., T. E. Stanton, and H. W. Henderson (1975): "A Model for Describing the Atmospheric Water Vapor Profile Above the -40°C Temperature Level." USAFETAC Report 7584.

Morrissey, J. F. and F. J. Brousaides (1970): "Temperature-Induced Errors in the ML-476 Humidity Data." J. Appl. Meteorol., 9:805-808.

Reiss, N. M., R. A. Eversole, and J. J. Mangano (1976): "Use of Prevailing Visibility Data for Aerosol Studies." Paper to be presented at Topical Meeting on Atmospheric Aerosols, Their Optical Properties and Effects, Williamsburg, VA., 13-15 December 1976.

UNCLASSIFIED

UNCLASSIFIED

Teweles, S. (1970): "A Spurious Diurnal Variation in Radiosonde Humidity Records." Bull. Amer. Meteorol. Soc., 51:9, pp. 836-840.

World Meteorological Organization (WMO) (1973): "Radiosonde and Radiowind Data Accuracies and Anticipated Program Changes." (Draft prepared by NOAA.)

World Meteorological Organization (WMO) (1975): "Catalogue of Meteorological Data for Research - Part III: Meteorological Data Recorded on Media Usable by Automatic Data-Processing Machines." WMO-No 174, TP 86.

UNCLASSIFIED

UNCLASSIFIED

TABLE I. TYPE OF DATA REPORTED IN A SURFACE OBSERVATION.

Surface

- Temperature
- Dew Point
- Pressure
- Wind Direction, Speed
- Visibility
- Clouds
 - Total Cover
 - Total Low or Middle
 - Height of Low or Middle
 - Type of Low, Middle, High
 - Ceiling Height (not all stations)
- Present Weather
- Precipitation Amount (6 hourly)
- Depth of Snow on Ground
- Waves
 - Period
 - Height
 - Direction

TABLE II. TYPE OF DATA REPORTED IN AN UPPER-AIR OBSERVATION.

- Pressure
- Temperature
- Relative Humidity (dew point)
- Wind Direction and Speed

Vertical Coverage: Surface to \sim 30 Km

UNCLASSIFIED

UNCLASSIFIED

TABLE III. VARIABLES THAT ENTER INTO A PREVAILING VISIBILITY OBSERVATION.

Availability of Markers at Various Ranges
Type of Objects Used as Markers (trees,
poles, towers, hills, etc.)
Size of Object
Observers Eye Characteristics (contrast
threshold, sensitivity, etc.)
Illumination Level
Light Intensity
Sun Angle

TABLE IV. SOME HUMIDITY SENSORS USED RECENTLY IN RADIOSONDES.

Lithium Chloride	(U.S.)
Carbon Hygristor	(U.S.)
Human Hair	(Europe)
Rolled	
Straight	
Goldbeater Skin	(USSR, Europe)
Capacitance (hemicap)	(Finland)

TABLE V. PROBLEMS WITH DATA SETS.

Raw Observations

Different Instrumentation Country To Country

Continuous Changes in Instrumentation — Accuracy
Changes With Time

Code Variations Country To Country and Intra-
Country

Code Changes

Missing Observations or Elements

Processed Data (analysis and forecast fields)

Changes in Models

UNCLASSIFIED

UNCLASSIFIED

TABLE VI. SATELLITE DATA BASE (3DNEPH).

Northern Hemisphere
Southern Hemisphere
Every 3 Hours
Grid \sim 48 Km (at 45°N)
15 Layers (surface to 17 km)
Type of Low, Middle, and High Clouds
Present Weather
Maximum Cloud Top
Minimum Cloud Base
Total Cloud Cover
Amount of Clouds in Each Layer

TABLE VII. SPECIAL DATA SETS.

Solar Radiation
Turbidity
Hourly Precipitation
Weather Radar
Photos
Digitized
Ozone
Satellite
Infrared
ERTS
Soil Temperature

UNCLASSIFIED

UNCLASSIFIED

TABLE VIII. NEEDS.

Inventory of Instrumentation Accuracies
(Continuously Updated)

Surface

Upper Air

Satellite

Additional Quality Control

Inventory of Electro-Optical Measurements

Better Meteorological Measurements During
Electro-Optical Field Tests

UNCLASSIFIED

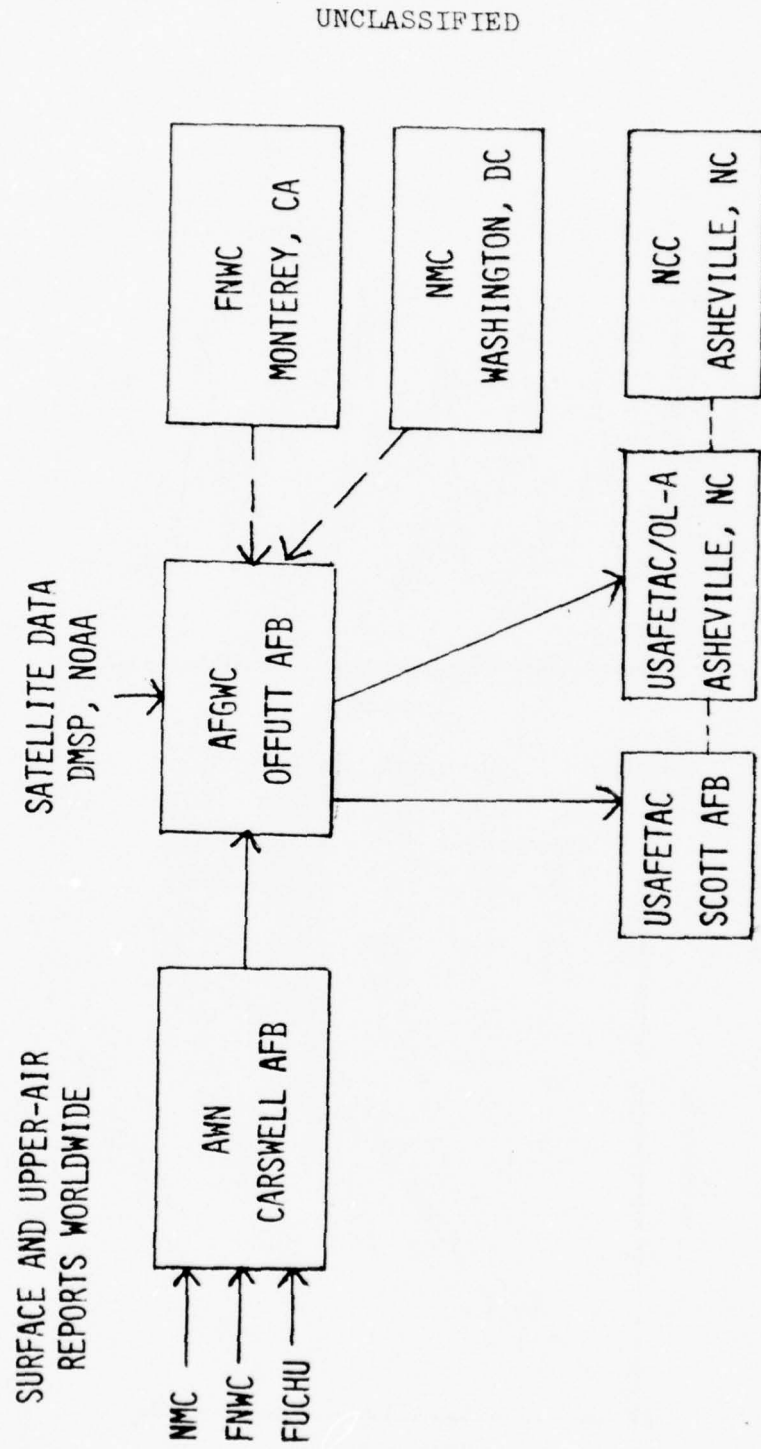


Figure 1. USAFETAC Meteorological Data Sources.

UNCLASSIFIED

UNCLASSIFIED

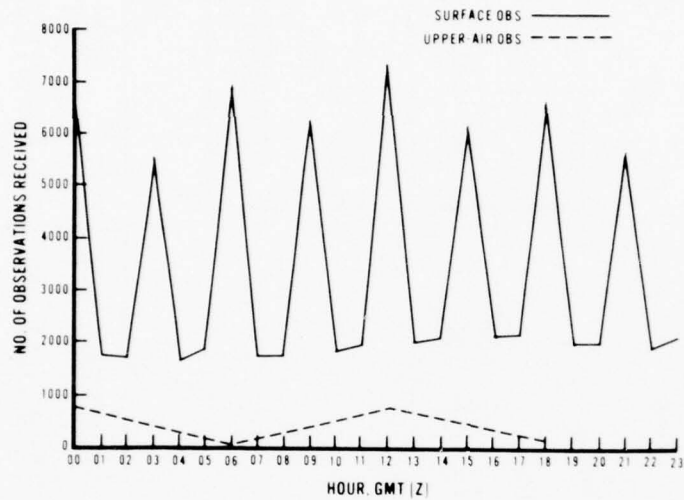


Figure 2. Observation Frequencies.

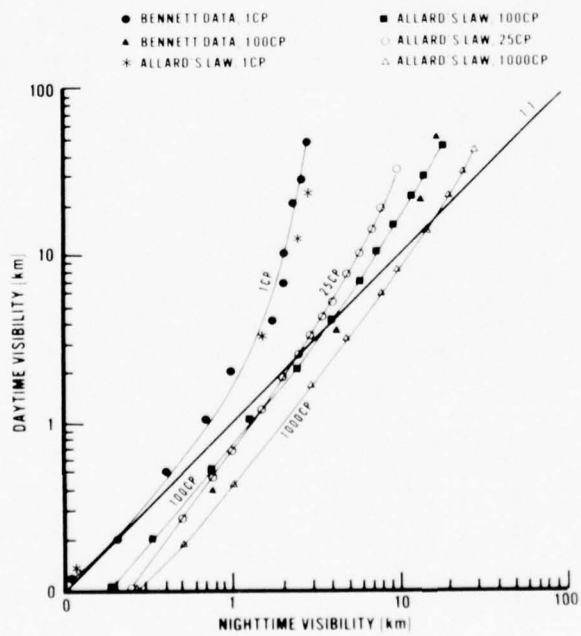
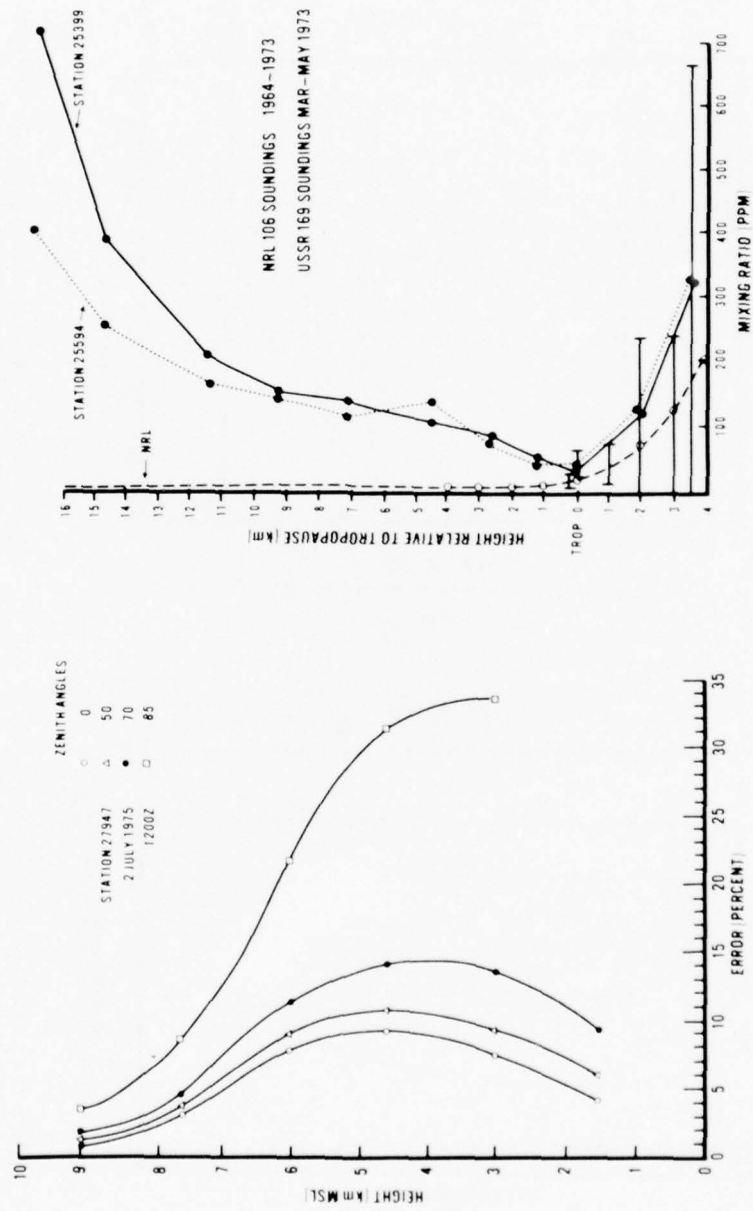


Figure 3. Nighttime vs Daytime Visibilities.

UNCLASSIFIED

UNCLASSIFIED



UNCLASSIFIED

Figure 4. Error in Transmission in 2.95-Micron Band Due to Errors Up to 37% in Humidity.

Figure 5. Comparison of Two Russian Stations and the Naval Research Laboratory Mean.

UNCLASSIFIED

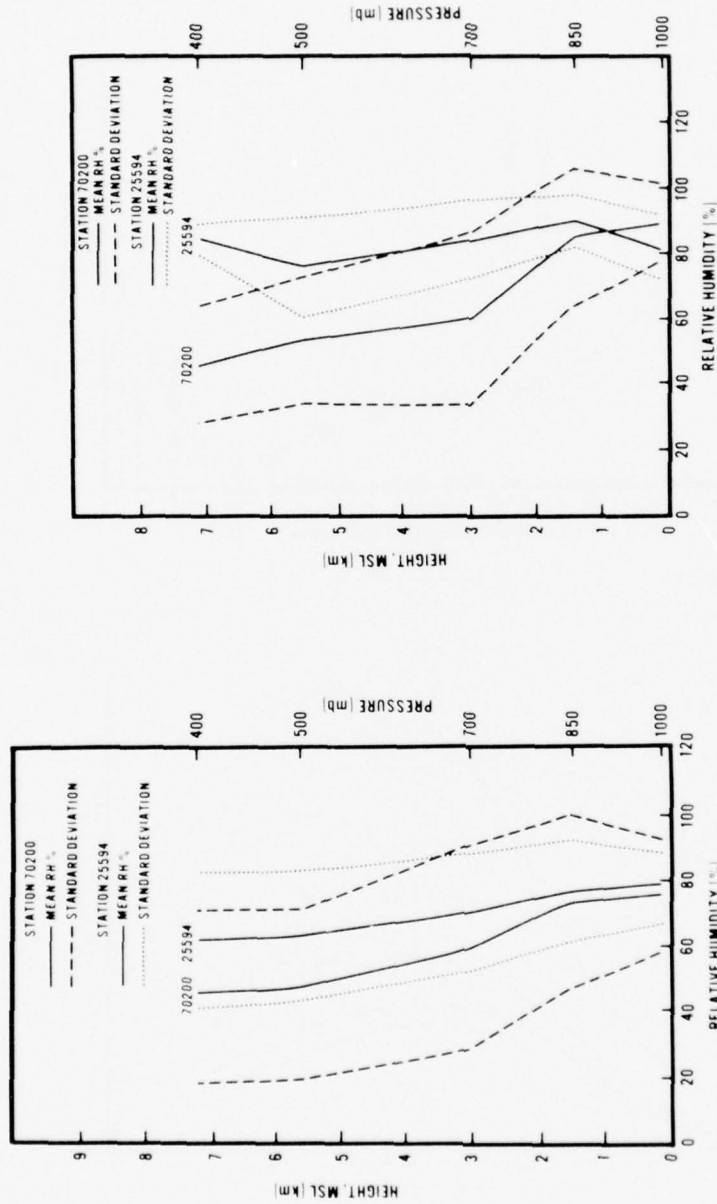


Figure 6. All Observations for Stations 25594 and 70200, March through May 1973.

Figure 7. Precipitation at 25594 and Cloudy at 70200, March through May 1973.

UNCLASSIFIED

UNCLASSIFIED

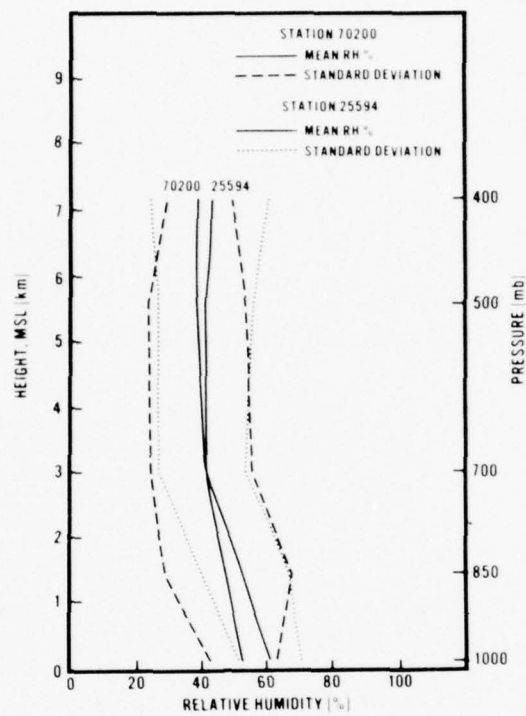


Figure 8. Clear at Both Stations 25594 and 70200, March through May 1973.

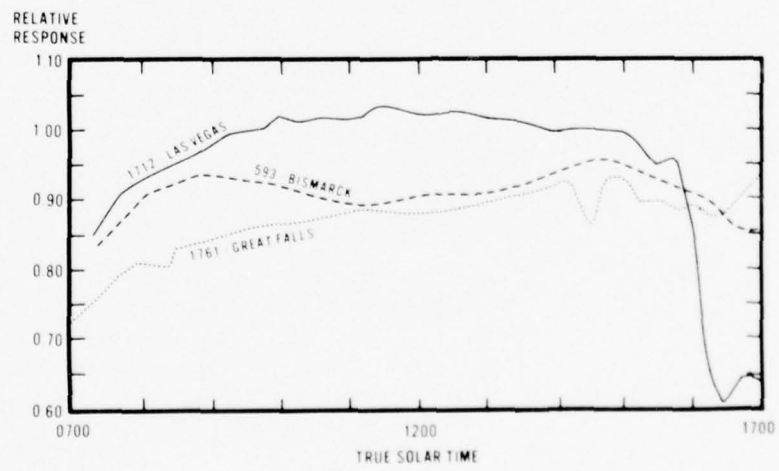


Figure 9. Interdiurnal Variation of Response of Three Pyranometers.

UNCLASSIFIED

(This page intentionally left blank.)

....This paper is UNCLASSIFIED

DEVELOPMENT OF NEW METEOROLOGICAL SERVICES FOR EO SYSTEMS

Lothar H. Ruhnke
Naval Research Laboratory
Washington, DC 20375

Two years ago the Navy, through the Electrooptics Council recognized the need to survey its research and development efforts in regard to meteorological services for supporting Navy EO systems. As a result service needs were defined, existing relevant R&D projects identified and through a Navy wide effort a plan evolved to develop a new service capability in meteorology. On October 28 of this year the Navy Material Command established the Electrooptics Meteorology (EOMET) Project within its Exploratory Development Program. Simultaneously the Office of Naval Research, as well as relevant program offices were asked to complement the EOMET Program with appropriate basic research and advanced development projects. An overview of existing Navy projects with their EOMET relevant budgets is shown in Table I.

Table I

<u>Project</u>	<u>Sponsor</u>	<u>Category</u>	<u>FY77 Funding</u>
EOMET	NAVMAT	6.2	500K
Marine Fog	AIR370	6.1	500K
Atm. Sciences	ONR400	6.1	100K
Optical Signature Program	NAVMAT	6.2	400K
HEL	PMS405	6.3	1000K

In the objectives of the EOMET Program three types of users are identified which need services on the propagation environment. These are EO equipment and systems developers, deployment planners and fleet users. Because electrooptics and atmospheric sciences must interact strongly within the EOMET Program, because competence in this area of research is spread over several Navy laboratories and because of a rather complex management infrastructure below the level of Assistant Secretary of the Navy for R&D, the management plan for EOMET is also rather complex. It involves NAVAIR as executive agent, an advisory group of Navy managers which have responsibilities for related projects, and a planning panel of laboratory scientists.

UNCLASSIFIED

The problems we are facing at present can be best categorized through the project logic (Fig. 1). Basic research on propagation both through modeling and experimentation will be the building block for performance assessments of all EO systems. Together with good descriptions of system characteristics performance models will describe limitations imposed by the environment. Such performance models together with statistical data on the atmospheric state can be used to derive R&D requirements for the meteorological community. Not only is it important to single out these atmospheric parameters which need special attention like water vapor, turbulence and aerosol, but it is extremely important to specify needed accuracy, range, sensitivity, and resolution. Although e.g. aerosol concentration is very influential to the performance of EO systems, it is not yet determined what resolution in the size spectrum is needed. For research purposes we use an instrument with 32 size classes, but for establishing a climatology for operational use such instruments are prohibitive if economy and technical complexity have to be considered. These sensitivity analyses will not only guide developers of new meteorological instrumentation but also will set requirements on field experimentation, which often, when assuming a Navy environment, leads to costly operations at sea. Most of the data needed in support of EO systems is not now readily available from direct measurements and in the near future will be available only with great difficulties. A prediction based on conventional meteorological data and computer models for some of the meteorological processes will likely be the alternative. At present the establishment of a statistical data base for ocean users is only feasible by modeling. Aerosol extinction coefficients, optical turbulence parameters, heat and vapor fluxes or inversion heights are feasible parameters to be derived from synoptic scale variables like wind, pressure, sea surface temperature and relative humidity.

The EOMET Project content (Table II) can easily be used to discuss some of the pertinent problems this project faces at present.

UNCLASSIFIED

U. CLASSIFIED

Table II. EOMET Project Content

Propagation Modeling and Experimentation
Performance Modeling and Experimentation
Sensitivity Analysis
Instrument Development
Climatology
Real-time Support
Forecasting

Propagation Research

At present basic propagation physics is studied under support by the High Energy Laser Program Office. Because of the applied aspect of this program only selected research topics can be investigated. A Scanning Michelson Interferometer is used to verify by experiment with 0.1 wavenumber resolution a number of calculated absorption lines in wave bands of importance to high energy laser applications. What is needed is a comprehensive study of propagation physics to establish a research base for assessing performance of all possible Navy EO systems with support from basic research funds.

Numerical propagation modeling has been advanced substantially by AFGL. Improvements are needed, however, for Navy environments. In the Mediterranean Sea in the path from the ship's bridge to a ship at the horizon one has to penetrate 60 cm of precipitable water leading to a 1% transmission case in the 10 to 12 micron IR band in the absence of aerosol. Considering further a highly variable aerosol and median visible ranges of 10 km near the sea surface, one has also to consider that aerosol is of very high importance as a limiting parameter to photopic and IR systems. Propagation algorithms, which take aerosols into account need to be flexible enough to accept either aerosol data as inputs or suitable secondary parameters like visibility, wind, or relative humidity as the availability of data demands. Some standardization seems appropriate to treat input parameters.

Performance Modeling

Propagation codes by themselves are not sufficient to predict performance of specific EO systems. Propagation codes as building blocks together with systems characteristics and target signatures must be used to develop numerical performance models. A necessity is a good definition of

UNCLASSIFIED

UNCLASSIFIED

performance. For operational use a standardization of meteorological input parameters would be helpful.

Sensitivity Analysis

To set requirements on the meteorological communities it is needed to study performance of most EO systems under development. Problems arise because almost no performance definitions exist nor a good sample description of the environment over the ocean surface.

Instrument Development

Requirements for sensing remotely the atmospheric boundary layer exist for water vapor, aerosol, temperature inversions and optical turbulence. At a recent Navy Workshop (9 August 1976 in Vail, Colorado) remote sensing needs and possible techniques were discussed in detail. It seems that there are ample options open with more solutions than problems. Technology transfer from research to applications, however, seems fairly costly and delays are therefore standard practices.

Problems on shipboard in-situ instrumentation are mainly concerned with IR transmissometry, aerosol spectrometry and visibility instrumentation.

Some satellite based measurements seem feasible and need exploration. There are measurements of aerosol loading by albedo measurements over cloud-free water areas, microwave and IR radiative surface temperature measurements and microwave sensors of white caps as a measure of aerosol sources.

Field Measurements

High cost in return for a sparse data flux are the main problems with field investigations. Some field work, however, is unavoidable and will be carried out at fixed stations, representative of ocean climate, on research expeditions for verification experiments of theories and prediction modeling, and through ships of opportunities to collect climatology data.

Meteorological Processes

The main problem in this area is the prediction of aerosol size spectrums and extinction coefficients from

UNCLASSIFIED

UNCLASSIFIED

data on relative humidity, visibility, wind and other available meteorological variables. For dry and calm conditions visibility informations and an assumption of a model size distribution are probably sufficient. At high winds ($>7\text{m/sec}$) aerosol production by white caps needs to be considered. At relative humidity above 80% aerosol growth is an added factor. At saturation, rate of change of relative humidity has to be incorporated in prediction codes for proper estimates of size distributions in haze, fog and stratus conditions. Rate of change of relative humidity can be modeled by considering heat and vapor fluxes. A connection of these exists to the mean wind flow, the surface temperature and inversion height, all parameters which are available from synoptic scale data. So the problem of predicting microscale and optical properties from conventional weather data seems solvable. Optical turbulence can similarly be predicted from mean winds, temperature stability and surface conditions.

Climatology

In time statistical data on a few important parameters like aerosol and optical turbulence need to be collected for design and deployment decisions on EO systems. It is important to agree early on what specific data should be stored. At present it seems that the extinction coefficient in the visible e.g. the visible range is a sufficient parameter to describe the aerosol condition climatologically. Should it become necessary to store statistically extinction versus wavelength or concentration versus size, then an agreement should be reached on data resolution. A further problem at present is the fact that actual data from ocean areas is very sparse and will be so for some time. The problem of using a sparse data set with statistical significance needs to be considered. Extrapolations from measurements made e.g. at San Nicolas Island or Monterey to other areas in the Pacific Ocean probably can be made using some caution.

The theme of this workshop implies a discussion on future plans. As far as the EOMET Project is concerned we plan to solve the above problems.

EOMET PROJECT LOGIC

NRL

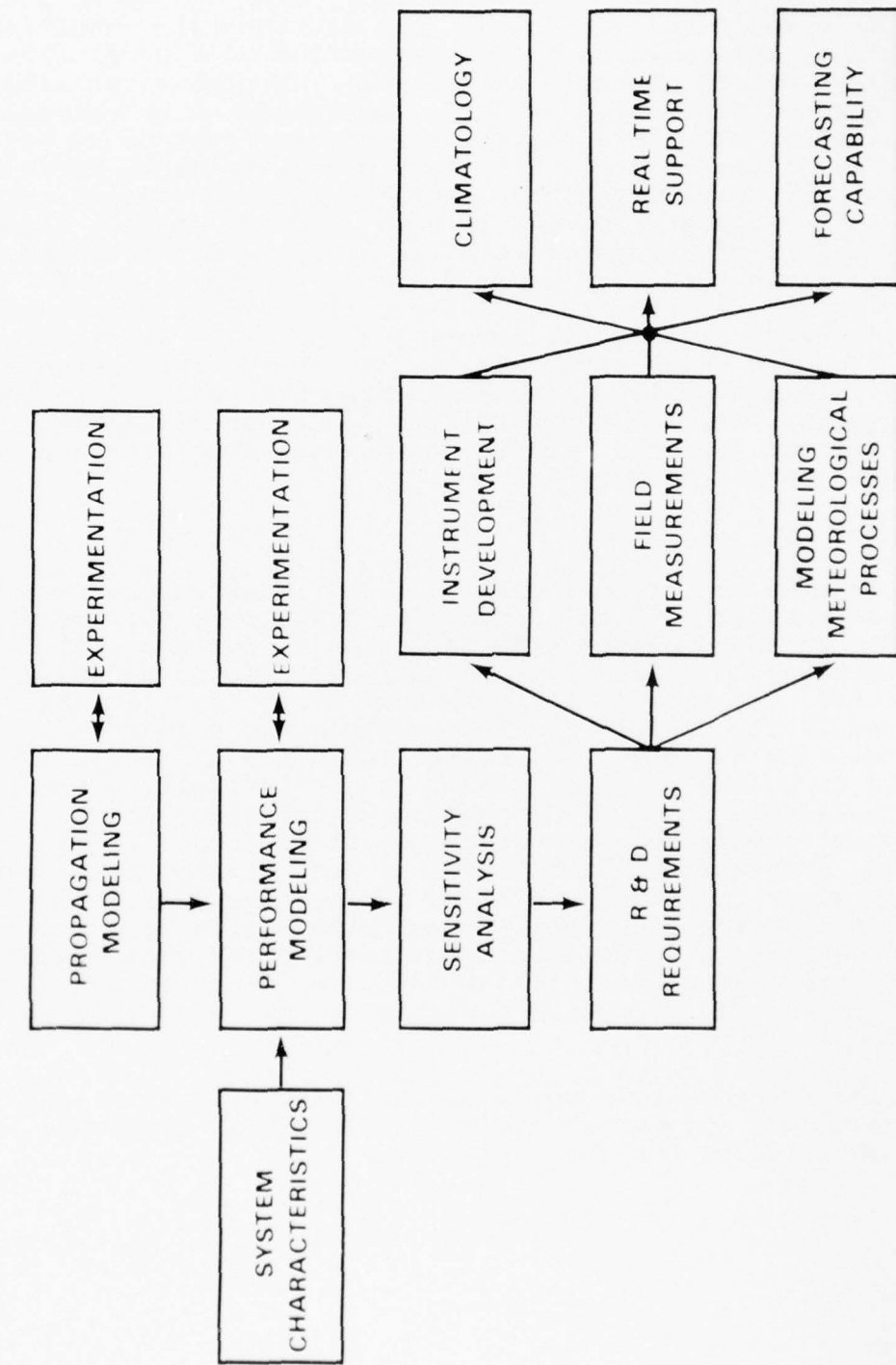


FIGURE 1

SEEING THROUGH THE ATMOSPHERE

Iver A. Lund
Air Force Geophysics Laboratory
Hanscom AFB, MA. 01731

Abstract

In most source-to-receiver chains the atmosphere can be regarded as the transmission link. A knowledge of the properties of this link is often essential for estimating the utility of transmitting or receiving equipment. Some of these properties are measured directly, whereas others must be inferred by indirect methods.

The National Weather Services throughout the world collect observations of weather conditions on a routine basis, usually each hour of the day. Some of these observations, such as temperature, are accurately measured, while others, such as cloud-cover, are subjectively estimated. By far the largest number of observations are taken from the surface of the earth.

The increased use of optical, infrared and microwave observing and transmitting devices has resulted in a greater demand for information on humidity, haze, clouds and precipitation. For a number of years, the Design Climatology Branch of the Air Force Geophysics Laboratory has been taking special observations and conducting special studies to obtain better information to provide to designers and operators. A few of these efforts will be described. They will include the use of sunshine observations, whole-sky photographs, special radar observations, hourly weather observations and special observations taken by aircrews, to obtain climatic probabilities of haze, clouds and precipitation along lines-of-sight.

This paper will describe statistical models for estimating persistence, recurrence and joint probabilities of some of the weather events that may limit the utility of electro/optical systems. These models can be used to estimate the number of targets that may be simultaneously "weather protected" or to estimate the length of time adverse weather will hinder operations.

1. Introduction

More than twelve years ago the Design Climatology Branch of the Air Force Cambridge Research Laboratories started to look seriously at the problem of seeing through the atmosphere. We have had a small effort devoted to studying this problem ever since. I will briefly review some of our work.

2. Probabilities from Sky Cover and Sunshine Observations

In 1963 we conceived of the idea of using sunshine observations to estimate the probability of clear lines-of-sight through the atmosphere (Lund 1965, 1966). More than 100 stations have kept continuous sunshine records for over 50 years. However, most stations have changed instrumentation several times. For a good review of this instrumentation see Foster and Foskett (1953).

In general, all of the instruments are designed to record sunshine when the sun's disk is visible and to record cloudy when it is not. This design goal has been only approximately achieved. The Maring-Marvin thermometric sunshine duration recorder, used for many years by the U.S. Weather Bureau, now the National Weather Service, did not provide a very accurate record of the duration of visibility of the sun's disk. The photoelectric sunshine recorder used at many stations over the past 20 years is a much better instrument. I stated in my article (Lund 1966):

"A clear line-of-sight is defined as one which permits sufficient bright sunshine (radiation) to pass through the atmosphere to activate the sunshine recorder. Presumably such a condition would also permit sensing a signal through the atmosphere with an optical or infrared detector. The path length is the distance from the top of the atmosphere to the surface of the earth.

"Since the sunshine recorder does not detect thin clouds, the probability of a clear line-of-sight, as defined in this paper, exceeds the probability of a cloud-free line-of-sight by an amount equal to the probability of "thin" clouds, roughly 6 to 20 percent at the stations under study."

Most of the sunshine recorders are mounted on the top of buildings near weather stations where sky cover observations are taken. For every hour of the day, we know the sun's angular elevation above the horizon, the percent of the sky covered with clouds, and whether or not sunshine was recorded. From this information relationships between the variables were obtained. The most frequently used relationship was developed by McCabe (1965) of the Environmental Technical Application Center. It is shown in Fig. 1. It shows the percent of sunshine as a function of mean cloud cover and sun angle. The mean cloud cover for every hour of the day and every month of the year is known for hundreds of places. Therefore, if your detector, or transmitter, can operate under the conditions when the recorder indicates sunshine, this graph gives a good estimate of the percent of time favorable conditions exist. We have learned, however, that many devices require much more nearly cloud-free conditions than that detected by the sunshine recorder.

3. Probabilities from Whole-Sky Photographs

In order to more accurately estimate the probability of truly cloud-free conditions, we let a contract with the University of Missouri

(Shanklin and Landwehr, 1971) to take photographs of the whole sky from the National Weather Service observing site at the airport in Columbia, Missouri. A Nikon F camera with a 180 degree (fisheye) lens and 35 mm infrared film was used to take high contrast photographs of the whole sky every daylight hour, synoptic with the National Weather Service's observations, for a period of more than three years.

A typical whole-sky photograph is shown in Figure 2. Usually there is good contrast between the cloudy and cloud-free areas. There are times, however, when it is difficult to distinguish clouds near the sun-shield and to distinguish between clouds and haze overhead.

Figure 3 depicts the template that was used to determine azimuth and elevation angles. The template was placed over each photograph. Two students independently examined the center of each of the 33 circles for the presence of clouds. These 33 lines-of-sight were recorded as either cloudy or cloud-free. (Most of the haze conditions were included among the cloud-free cases since the infrared wave lengths penetrate most haze.)

3.1 Single Site Probabilities

Methods for estimating single site cloud-free lines-of-sight (CFLOS) probabilities were published by Lund and Shanklin (1972, 1973). Figure 4 depicts relative frequencies of CFLOS as a function of elevation angle and total sky cover, as determined from the photographs. The curves are shown without any smoothing. The relative frequencies consistently increase with decreasing cloudiness. With but few exceptions, probabilities of CFLOS increase as the zenith angle is approached. Failure to increase consistently is likely due to minor sampling instabilities.

The lines in Figure 4 were subjectively smoothed and used as estimates of probabilities of CFLOS as a function of elevation angle and sky cover. The publications cited above describe how these curves can be used to estimate CFLOS probabilities for any location with a long record of sky cover observations.

3.2 CFLOS Probabilities over Germany

The models were applied to long records of sky cover observations taken over Germany at the four mid-season months, four times per day at four elevation angles. Figure 5 shows the highest probability of seeing the ground through the entire atmosphere at a 30° angle during the most favorable season of the year and the most favorable time of the day. This is usually near midnight in summer. Figure 6 shows the lowest probability. There are several small "bull's eyes" of less than 20%. Almost all places in Germany have times when the climatic probability of a CFLOS at 30° is less than 30%. The "bull's eyes" are indicative of strong local variations.

3.3 Persistence and Recurrence Probabilities

A total of 13,215 high-contrast, whole-sky photographs were studied to derive estimates of cloud-free and cloudy line-of-sight persistence and recurrence probabilities (see Lund 1973b).

Hourly persistence is defined as an uninterrupted sequence of cloud-free or cloudy lines-of-sight spaced 1 hr. apart. Five-minute persistence is defined likewise but the photographs are spaced 5 min. apart. The condition between photographs is unknown.

Only the persistence results will be discussed. The recurrence results are available in the paper Lund (1973b).

The persistence study clearly shows that persistence at Columbia, Missouri varies with seasons and time of day. The most persistent cloud-free conditions are always observed in the fall and the least persistent conditions are always observed in the summer. The relative frequencies are shown in Figure 7. Cloud-free persistence is shown by the solid lines and cloudy persistence by the dashed lines. The solid line marked average shows that if a line-of-sight is cloud-free at the initial time, it was also cloud-free 1 hr. later 82% of the time, again cloud-free 2 hr. later 71% of the time, ..., and was cloud-free for six consecutive hourly observations 46% of the time. The five-minute persistence probabilities are shown by the full-length solid line. When this line is extended to the hourly periods it runs well below the other lines. This clearly illustrates that closely spaced observations are required to obtain the true duration probabilities. It is assumed that duration lines would be at least several percent lower than the 5-min persistence lines.

The 5-min interval persistence relative frequencies were derived from 231,660 observations, 33 observations per photograph. Figure 8 shows persistence relative frequencies as a function of the sky cover reported by the weather observer. The uppermost solid line shows that when the observer says there are zero-tenths of the sky covered by clouds and a line-of-sight was cloud-free, it was also cloud-free 5 min. later 99.8% of the time, ..., and it was cloud-free for eleven consecutive 5-min. periods 98.4% of the time. There were 26,399 cloud-free lines-of-sight on the photographs when the weather observer reported zero-tenths sky cover. Most of the lines are consistent with expectations. That is, the probability of lines-of-sight remaining cloud-free decreases with increasing cloudiness.

We have not had any opportunity to test how well they apply elsewhere. There is a good chance that these probability estimates apply quite well in most mid-latitude locations.

3.4 Multiple Site Probabilities

We are developing models for estimating joint probabilities of

weather events. Targets may be weather protected by fog, wind, precipitation, or other weather elements, depending upon the type of munitions used. The question is often asked: What is the probability that all targets, in a given area, will be jointly weather protected. A model (Lund 1973b) was developed for estimating this probability. New models requiring only unconditional sky cover probabilities are being developed. I will only take time to point out a few facts about the new models. Figure 9 shows nine observing sites along the east coast of the U.S. Every station has an almost perfectly complete record of more than 13 years of hourly observations of many weather elements. Figure 10 shows the correlation of active precipitation between the stations. Figure 11 shows the temporal correlation where the scale is adjusted so that one hour equals 22 miles. There is good agreement between spatial and temporal correlation.

With this kind of information, we believe that we can successfully estimate joint probabilities of weather events.

Space does not permit me to describe models that we have developed for estimating the areal coverage of weather events (Gringorten 1976).

4. Probabilities from In-Flight Observations

Standard surface cloud observations are not sufficient for obtaining CFLOS probabilities between the ground and a point in the atmosphere below the top of all clouds. For this reason an in-flight observation program has been conducted by the Air Force. Aircrew members have taken about 275,000 observations under this program, to date. They consider haze as well as clouds along lines-of-sight. Space does not permit me to completely describe this program. It is briefly described in Lund (1972).

Figure 12 shows estimates of the probability of a CFLOS to the earth's surface from 20,000 feet, in summer, at an angle of 60° below the horizon. The large figures are relative frequencies and the small figures, in parenthesis, give the number of observations. Figure 13 is an analysis of Figure 12. These figures indicate the type of information that will soon be available in published form from the inflight line-of-sight program. One of the deficiencies of this program is that most of the observations were taken from above 10,000 ft. U.S. Army helicopter squadrons in Germany are making low-altitude observations for us. It is too early in the program to know whether these observations will satisfy our needs for better low-altitude probabilities.

Figure 14 shows profiles of CFLOS probabilities as a function of altitude. The observations were taken between 0° and 10° E. Long. and 40° and 50° , and 50° and 60° N. Lat. The northern area is largely over the North Sea. The southern area is mostly over France. Clearly most of the clouds are below 5,000 ft where we have the fewest observations.

5. Probabilities from Radar Observations

Virtually no quantitative information exists on how often attenuation due to precipitation occurrences along microwave ray paths, will affect microwave transmission at various elevation angles. Therefore, AFCRL, with the cooperation of the National Weather Service, conducted a 3-year program of photographing the scope of WSR 57, 10-cm radar every three hours with the antenna in each of four elevation angles, 0, 15, 30, and 45 degrees. Again space does not permit me to describe this program, but we want you to know of its existence, and the fact that 3 years of data are available for 17 United States locations.

6. Remarks

Most of the efforts to obtain CFLOS probabilities from whole-sky photographs and sky-cover observations have been published, except for new models being developed for obtaining joint probabilities and a CFLOS probability atlas that is being jointly prepared with the Environmental Technical Application Center. Results from the in-flight and radar observation programs are incomplete as these programs are still underway. The Design Climatology Branch of AFGL is, however, responding to requests for information from these programs with provisional probability estimates.

References

Foster, N. B., and L. W. Foskett, 1953: A photoelectric sunshine recorder. *Bulletin American Meteorological Society*, 34, 212-215.

Gringorten, I. I., 1976: Areal coverage estimates by stochastic modelling. *Environmental Research Papers*, No. 573. AFGL, Hanscom AFB, MA.

Lund, I. A., and M. D. Shanklin, 1972: Photogrammetrically determined cloud-free lines-of-sight through the atmosphere. *J. Appl. Meteor.*, 11, 773-782.

Lund, I. A., and M. D. Shanklin, 1973: Universal methods for estimating probabilities of cloud-free lines-of-sight through the atmosphere. *J. Appl. Meteor.*, 12, 28-35.

Lund, I. A., 1972: Haze-free and cloud-free lines-of-sight through the atmosphere. *Environmental Research Papers*, No. 413. AFCRL, Hanscom AFB, MA.

Lund, I. A., 1973a: A model for estimating joint probabilities of cloud-free lines-of-sight through the atmosphere. *J. Appl. Meteor.*, 12, 1040-1043.

Lund, I. A., 1965: Estimating the probability of clear lines-of-sight from sunshine and cloud cover observations. *J. Appl. Meteor.*, 4, 714-722.

Lund, I. A., 1966: Methods for estimating the probability of clear lines-of-sight, or sunshine, through the atmosphere. *J. Appl. Meteor.*, 5, 625-630.

Lund, I. A., 1973b: Persistence and recurrence probabilities of cloud-free and cloudy lines-of-sight through the atmosphere. *J. Appl. Meteor.*, 12, 1222-1228.

McCabe, J. T., 1965: Estimating mean cloud and climatological probability of cloud-free lines-of-sight. Technical Report 186, Environmental Technical Applications Center, USAF, Bldg. 159, Navy Yard Annex, Washington, D.C., 26 pp.

Shanklin, M. D. and J. B. Landwehr, 1971: Photogrammetrically determined cloud-free lines-of-sight at Columbia, Missouri. Final Report under Contract No. F19628-68-C-0140, Air Force Cambridge Research Laboratories, Bedford, Mass. 185 pp.

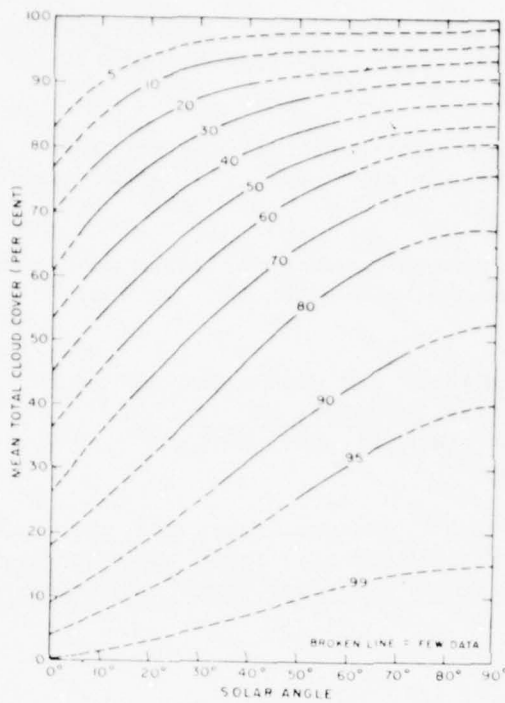


Fig. 1 Approximate per cent of mean sunshine as function of cloud cover and sun angle (after McCabe).

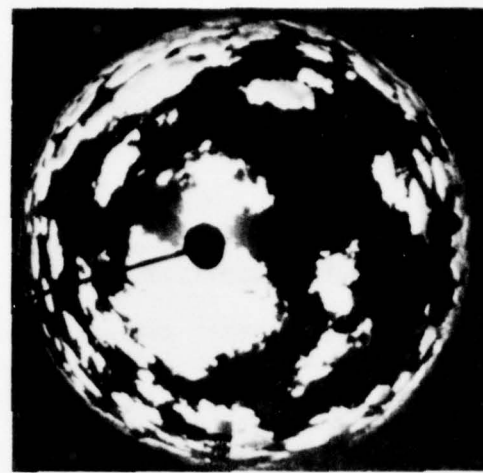


Fig. 2 An example of whole-sky photograph.

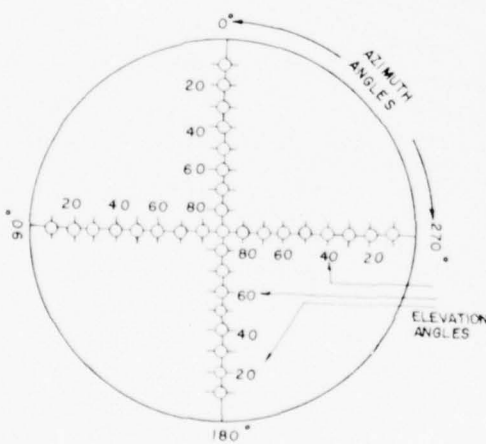


Fig. 3 Template used to determine azimuth and elevation angles.

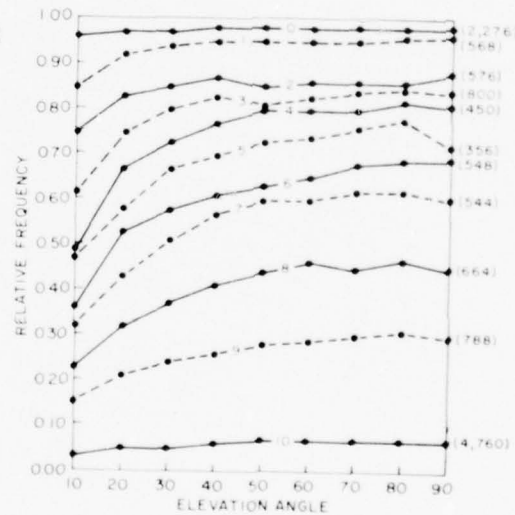


Fig. 4 Relative frequencies of cloud-free lines-of-sight (CFLOS) as a function of elevation angle and observed total sky cover, in tenths. Each point is based on the number of observations shown at the end of the line.

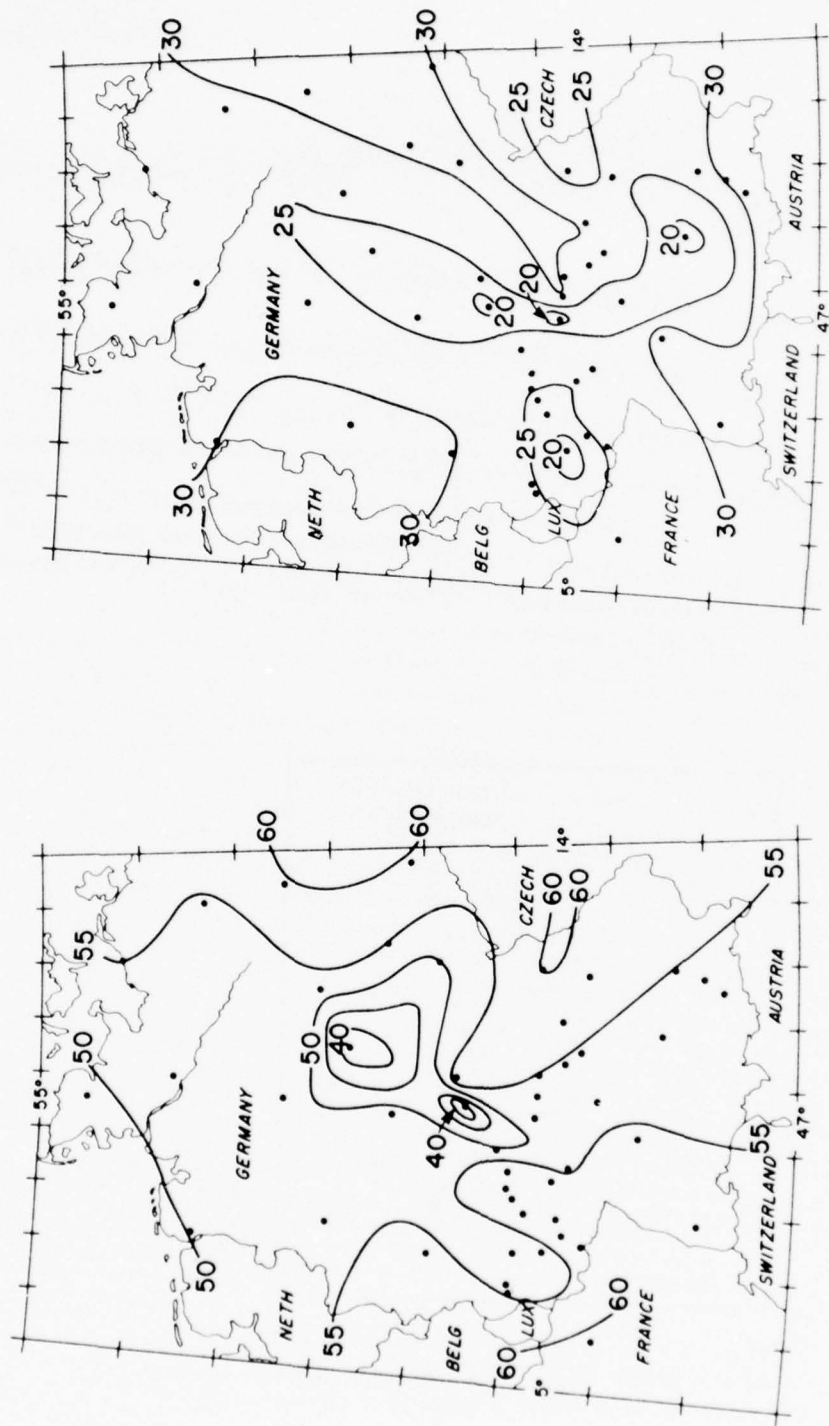


Fig. 5 The highest probability of a CLOS for any season or hour of the day.

Fig. 6 The lowest probability of a CLOS for any season or hour of the day.

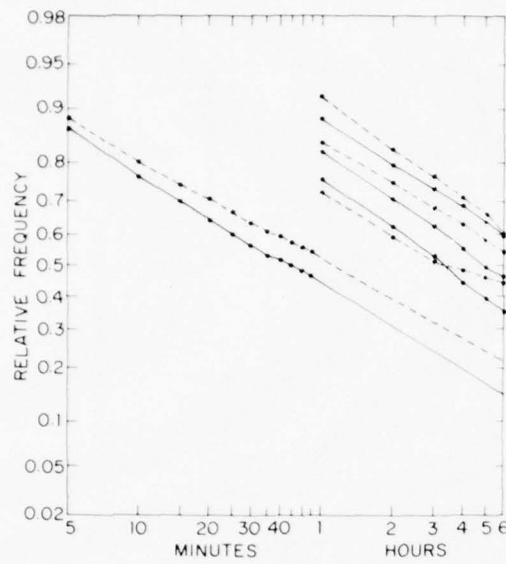


Fig. 7 Cloud-free (solid lines) and cloudy (dashed lines) persistence relative frequencies obtained from whole-sky photographs taken at Columbia, Mo. (see text).

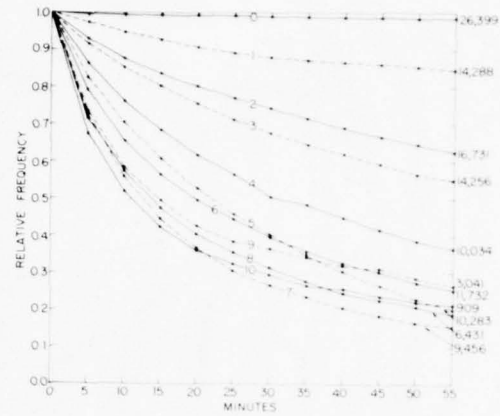


Fig. 8 Cloud-free line-of-sight persistence relative frequencies as a function of sky cover (tenths), and 5-min intervals of time. The numbers at the end of the lines are the number of observations of CFLOS at time zero.

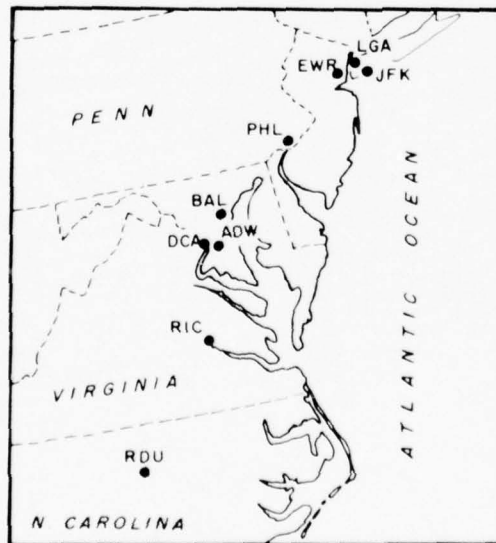


Fig. 9 Location of the nine stations whose winter and summer hourly observations were studied.

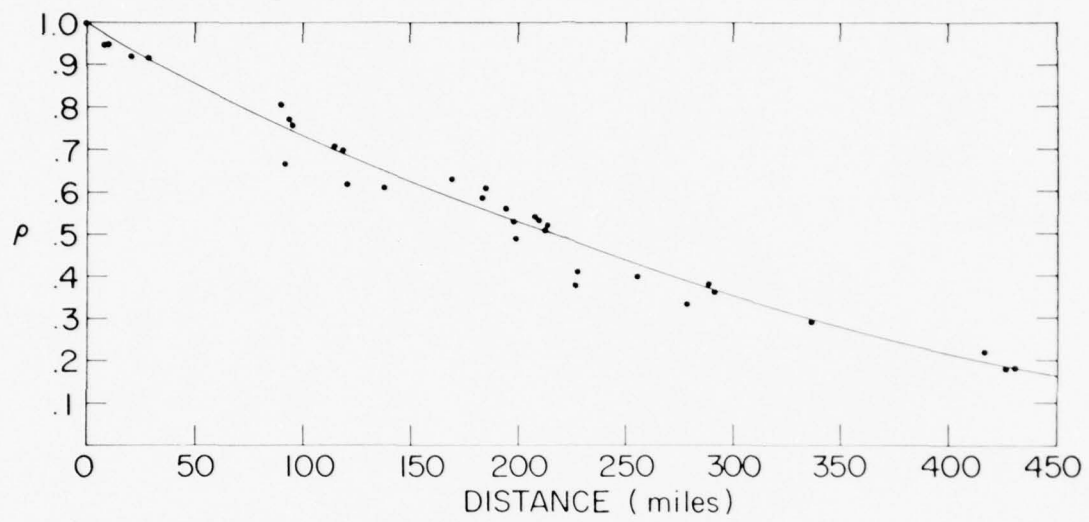


Fig. 10 Correlation coefficients of active precipitation plotted as a function of distance between sites, in summer.

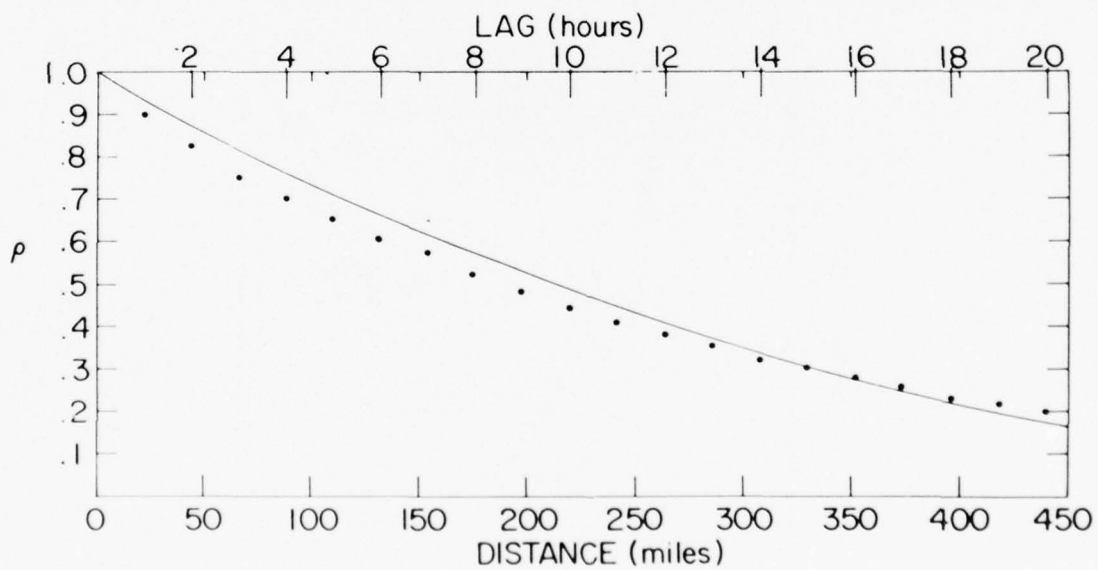


Fig. 11 Correlation coefficients of active precipitation plotted as a function of time lag between observations, in summer.



Fig. 13 An analysis of Fig. 12.

Fig. 12 Estimates of the probability of a CFLOS to the earth's surface at 60° below the horizon from 20,000 ft, in summer.
(Estimates are based on the number of observations shown in parenthesis).

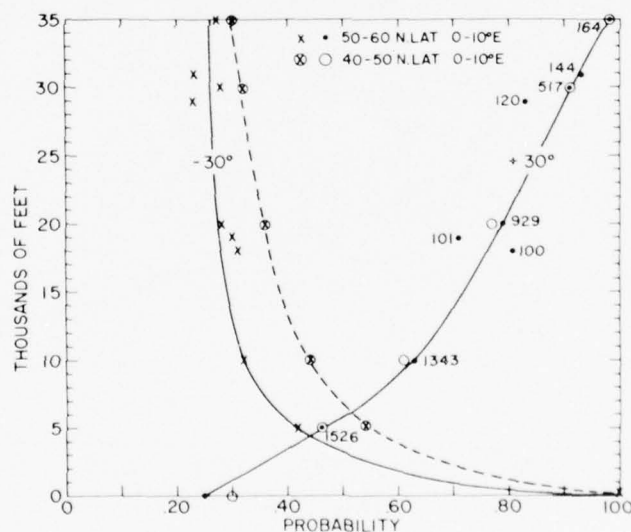


Fig. 14 The probability of a CFLOS as a function of altitude. The $+30^{\circ}$ curve gives the probability of seeing blue sky above the aircraft. The -30° curve gives the probability of seeing the earth's surface below the aircraft.

UNCLASSIFIED

PROBABILITY OF OCCURRENCE FOR
MARINE OPTICAL PARAMETERS

B. S. Katz

Naval Surface Weapons Center
White Oak Laboratory
Silver Spring, Maryland 20910

ABSTRACT

In order to support electro-optics system planners, designers and users with probability of occurrence information on surface marine propagation conditions techniques have been developed to convert large quantities of previously stored weather products to statistics of specific propagation parameters. The meteorology to propagation parameter models include Lowtran 3 which converts temperature and absolute humidity to absorption coefficients, Naval Postgraduate School semi-empirical models that convert air-sea temperature difference and surface winds to the refractive index turbulence structure function C_N^2 , and an aerosol model that uses wind and relative humidity to produce both aerosol size and number distributions, and a complex index of refraction.

Calculations have recently been completed converting a full years data from two North Atlantic weather ships into extinction coefficients at .55, 1.06, .5-1.1, 3.8 and 8-12 microns. These calculations will be presented for each ship as a function of season as well as a comparison between individual wavelengths or bands.

UNCLASSIFIED

Introduction

A number of electro-optical systems are in various stages of development and will hopefully be released for Fleet use beginning in a few years. These include applications in connection with surveillance, intelligence gathering, ASMD search and track and weapons control. Due to the degrading influence that the marine atmospheric conditions have on visible and IR wavelenghts associated with these systems, it is important that early in the design stages these systems are optimized for use in such environments. This optimization procedure includes a proper mix of optical bands to keep effectiveness constantly high and prevention of expensive over design that cannot be used a large percentage of time. The systems analyst plays an important role in this procedure and should have available statistical information on atmospheric conditions and their influence on system components for all locations in which these systems must operate.

A first step in determining quantitatively the atmospheric limitations on system use is to specify the optical parameters that describe the magnitude of the interaction of optical waves with specific environmental conditions. This listing would include the atmospheric turbulence structure function C_N^2 , aerosol extinction values for various wavelengths or bands and molecular absorption when applicable. Since average values of meteorological parameters are readily available from marine atlases, the development, improvement or collection from the E/O community at large of propagation codes relating optical parameters to atmospheric conditions allows one to determine nominal operating conditions for areas of interest. Unfortunately this procedure, while providing a set of inputs for system codes, does not allow for determination of statistical effectiveness for different system configurations. When considering the cost for new systems, it is not an unjust question for the operational community to ask, "Just how often can I expect to effectively use this system and what is its maximum range?" In order to help answer these questions a program was originally initiated by the Navy's High Energy Laser program and now continued by Seafire to do a statistical evaluation of propagation conditions in marine environments. Since Seafire is being developed as a stand-alone fire control to be used primarily with guided projectiles, emphasis has been placed on TV, 1.06 designator and FLIR (8-12 micron) optical bands. The basic premise as shown in block diagram form in Figure 1 was to acquire large quantities of stored meteorological raw products from ship reports and convert each observation individually into a set of propagation parameters using propagation codes obtained from the E/O community. These multiple sets of propagation parameters can now be either developed into a probability of occurrence format or randomly selected to yield a small subset for driving system codes. The codes used and the procedure for using this large matrix of data will be described in subsequent sections of this report.

Propagation Codes and Sources of Data

The majority of the meteorological ship data was obtained from the Navy Weather Service Detachment in Asville, North Carolina. It consisted of a full year (1965) set of surface observation (every three hours) for two North Atlantic ships (J&M). These ships main mission were to take both surface and

UNCLASSIFIED

upper air meteorological data in well defined locations. Ship J was located at 52.5° latitude and 20.0° longitude while Ship M was further north at 65° latitude and -2° longitude. A smaller amount of observations for the Eastern Mediterranean was received from Dick Ameigh at GE, Utica, New York.

The most important set of parameters from each observation included air, sea and dew point temperatures, wind speed, barometric pressure, visibility and present weather condition (rain type). The surface observations also include cloud height and coverage which will be used in future guided projectile effectiveness studies and ship signature studies respectively.

The computer code that was developed to convert the weather data to optical parameters can be broken down into the following: (1) molecular absorption coefficients as a function of air temperature and absolute humidity derived from Lowtran 3 calculations; (2) semi-empirical turbulence model relating the refractive index structure constant C_N^2 to air-sea temperature difference, surface winds gradient, and absolute humidity; (3) aerosol model that uses relative humidity and wind speed to produce an aerosol size/number distribution, a complex index of refraction and finally aerosol extinction values.

The Lowtran 3 code developed at AFGL provided transmission calculations for evenly spaced wavelengths in the 8-12 micron band at various values of temperature, water vapor (GM/m^3) and range. For a given absolute humidity, and temperature and range each transmission value was weighted by the thermal derivative of Planck's radiation equation ($300^{\circ}K$ source). These values were then averaged over wavelength to provide an effective transmission for the 8-12 band. This effective transmission value for a specified atmospheric condition was converted into an effective molecular absorption coefficient ($/Km$) by assuming an exponential decrease with range. These effective extinction coefficients were used to derive a scaling law for temperature and water vapor content (see Figure 2). This scaling law was necessary since tens of thousands of calculations are needed. This effective extinction technique was also used in the aerosol extinction code with a silicon sensor responsivity curve used as a weighting factor for TV wavelength calculations.

The basic aerosol model came from Dr. Mike Dunn, Lockheed, Palo Alto, California. This model was developed by fitting data that was taken over water and published in the open literature. It uses relative humidity and wind speed to calculate an aerosol size and number distribution. Constants associated with the wind velocity were varied to improve comparisons with scattering data taken by Optical Science division of the Naval Research Laboratory. Mie scattering calculations were done with a four region closed form approximation scheme developed by Van De Hulst. Comparisons with full Mie codes indicate a maximum 5% error. The complex index is varied from that of a high concentration salt water mixture to pure water as aerosols grow with increasing relative humidity.

The turbulence code was provided by Dr. Davidson of the Naval Postgraduate School. In the code small scale atmospheric fluctuations are related to mean wind speed and air water temperature and humidity differences by Monin-Obukhov profile relationships. The empirical stability terms in the profile relationships

UNCLASSIFIED

are those proposed by J. Wynnguard after evaluating many years of land experiments. These relationships have been modified by Dr. Davidson to account for variations found during his over water measurements program.

CALCULATIONS AND STATISTICS

The meteorological data was broken into twelve groups corresponding to four seasons for each North Atlantic weather ship (NAJ or NAM) and the Eastern Mediterranean data (MED). Each seasonal calculation was coded with the above identifiers coming first followed by the first two letters from the season. In the Mediterranean data "SD" corresponds to summer day since the data was taken either at noon time or midnight. Each seasonal set of data was converted to a set of optical parameters an observation at a time using the models previously mentioned. For each seasonal set of propagation parameters, the parameters individually were formated into probability density functions, integrated into probability of occurrence values and plotted on either linear or semi-log scales. The following parameters were calculated:

- 1) TV - aerosol extinction coefficient .5-1.1 microns
- 2) Designator - aerosol ext. coeff. 1.06 microns
- 3) FLIR
 - a) Aerosol extinction 8.-12. microns
 - b) Molecular absorption 8.-12. microns
 - c) Total extinction (a+b)
- 4) Visibility - aerosol extinction .55 microns
- 5) Turbulence - C_n^2

Figures 3A and 3B show examples of the absolute humidity for all three stations in a probability of occurrence format. These curves provide information on the probability that a parameter will have a value greater than a specific amount. For example in Figure 3A, the N.A. ship J winter months (NAJWI) represented by the x curve has an absolute humidity greater than 7.5 torr forty percent of the time. Since torr is almost equal to gm/m³ at these temperatures and pressures, Figure 3B indicates that the Eastern Mediterranean summer (MEDSD) has more water vapor with greater than 20. torr forty percent of the time.

OPTICAL PARAMETERS

The probability of occurrence information for optical parameters from different locations can be combined to indicate differences in propagation conditions from one location to another. This is shown for ships M and J in Figures 4A, 4B, and 6 with parameters 1.06 and 8-12 micron aerosol extinction coefficients (/KM) and C_n^2 respectively. They can be recombined as in Figure 5 to indicate the change in aerosol extinction with wavelength for a single location (NAJWI). In the 8-12 micron region where molecular absorption

UNCLASSIFIED

is an important part of the total extinction coefficient, the relative importance of both aerosols and water vapor can be delineated by plotting these parameters on the same graph. Figures 7A and 7B show this difference for NAJWI and MEDSD locations. Low water vapor and high winds tend to equalize the importance of the two affects in the N.A., while low winds and higher water vapor in the Eastern Mediterranean causes molecular absorption processes to dominate. This high water content (Figure 3B) is related primarily to the high summer temperatures.

The comparison between aerosol extinction coefficients particularly .55 micron to other wavelengths is important because at sea visibility measurements are considered a standard procedure. If the relationship between wavelengths were fixed, the determination IR system effectiveness in real time would be simplified and directly relatable to visibility. Unfortunately experiments have generally indicated a smaller relative difference at low visibilities than at high visibilities. The aerosol distribution model used in this study increases the number of particles beyond one micron with increasing wind speed and relative humidity. Calculations yield a continuous variation of relative difference as conditions go from low to high visibility. Figures 8A and 8B have 650 sets of aerosol extinction coefficients from NAJWI calculations comparing 1.06 to 3.8 microns and .55 to 8-12 microns. The large circles in Figure 8A come from simultaneous measurements of the two wavelengths taken by the Optical Radiation Branch at the Naval Research Laboratory during tests in Florida. The calculated data compares favorably with the measurements but a great deal more data over an extended visibility range is needed to verify these relationships. This is particularly true for the wavelengths in Figure 8B where the differences can be an order of magnitude.

A further check on the validity of the aerosol model to statistically represent aerosol conditions was carried out using the ship reported subjectively measured visibilities. Figure 9 shows both the measured (VISD) and calculated (VISC) values for visibility. The calculated visibility was derived by dividing the .55 extinction coefficient into 3.91 (2% transmission definition of visibility). The data in this figure was from ship J in the summer (NAJSU). Although the shipboard data are quantized I have assumed equal weighting between ranges. At least for visible wavelengths the calculations seem to be reasonable.

SYSTEM CONSIDERATIONS

So far the data has been presented as propagation parameters than can be used as inputs for system codes. If the maximum useable range for each optical system being incorporated into the Seafire fire control system can be related to some minimum transmission condition for a particular class of targets, the matrix of data presented can be used to indicate statistics of component effectiveness. Figure 10 is an example of this procedure where for convenience a 2% transmission is considered the cutoff for all systems. The calculations in this figure indicate that all systems are equally effective in the N.A. winter environment. Even though the aerosol extinction in the 8-12 region is generally smaller than in the visible the molecular absorption just makes up the difference. This procedure can be very effective for indicating for example how often a TV actually improves system effectiveness.

UNCLASSIFIED

CONCLUSION

The models used to convert weather reports to optics parameters are a mixture of partially verified and unverified relationships. The turbulence and molecular absorption models are a result of many years of experimental research which is ongoing and should improve. The least known factor is the aerosol modeling which relies on published aerosol distributions and almost negligible scattering data.

Even though this modeling and conversion of weather reports to optical parameters is a first step towards ultimate understanding of optical system limitations in the Marine environment, it is a very useful tool for systems designers presently working on such systems and should be expanded to cover other wavelengths and locations.

UNCLASSIFIED

References

1. D. Deirmendjian, Electromagnetic Scattering on Spherical Polydispersions, The Rand Corporation, R-456-PR, April 1969.
2. R. F. Lutomirski, W. L. Woodie, Maritime Aerosol Affects on High Energy Laser Propagation, Final Report Contract N60921-75-C-0181, NAVSURFWPNCEN/WOL.
3. Van de Hulst, Light Scattering by Small Particles, John Wiley and Sons, Inc., 1957, Chapter 14.
4. W. C. Wells, G. Gal and M. W. Munn, Aerosol Distributions in Marine Air, LMSC/D457849, November 1975.

CONVERSION OF METEOROLOGICAL OBSERVATIONS TO OPTICAL PARAMETERS

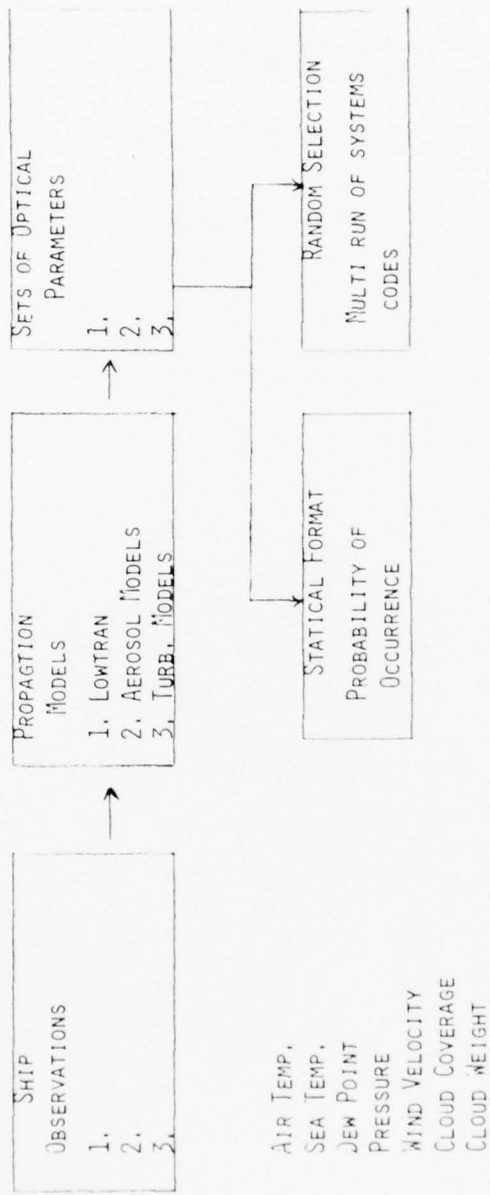


FIGURE 1. CONVERSION OF METEOROLOGICAL OBSERVABLES TO OPTICAL PARAMETERS

PROPAGATION MODELS

AEROSOL EXTINCTION

$$1. \text{ SIZE \# DIST.} \quad N(R) = \left\{ \begin{array}{l} 0.47 \left(\frac{R}{F} \right)^{-4} \exp(-H/HC) + \frac{\kappa}{2.3} (C_1 + C_2 V^{\delta}) \left(\frac{R}{F} \right) \\ \exp(-8.5 \left(\frac{R}{F} \right) \chi(v)) \exp(-H/HM) \end{array} \right\}$$

$$2. \text{ AEROSOL EXT.} = R_1 \int_{R_1}^{R_2} \pi R^2 N(R) Q(R) dR$$

R = RADIUS OF DRY AEROSOL

F = GROWTH FACTOR

V = WIND SPEED

AH = ABSOLUTE HUMIDITY

MOLECULAR ABSORPTION - LOWTRAN

$$n_{OL} = (A + B w^{1/2}) + (Cw + Dw^2) T_{Exp}^{-1800} T$$

LINE ABS.

w = GM/M² WATER CONTENT

T = TEMP. KELVIN

TURBULENCE - NAVAL POSTGRADUATE SCHOOL

$$C_N^2 = f(T_{AIR} - T_{SCA}, V, AH)$$

FIGURE 2. PROPAGATION MODELS.

Turbulence models came from Dr. Davidson NPGS, Monterey, California.

UNCLASSIFIED

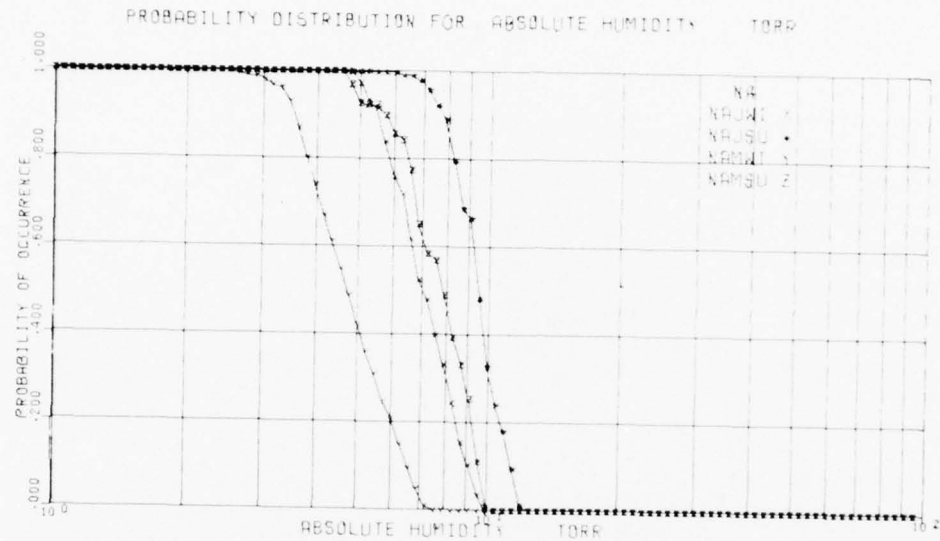


FIGURE 3A. PROBABILITY DISTRIBUTIONS FOR ABSOLUTE HUMIDITY GM/M³
Two North Atlantic Stations - J is near Ireland and M near Norway

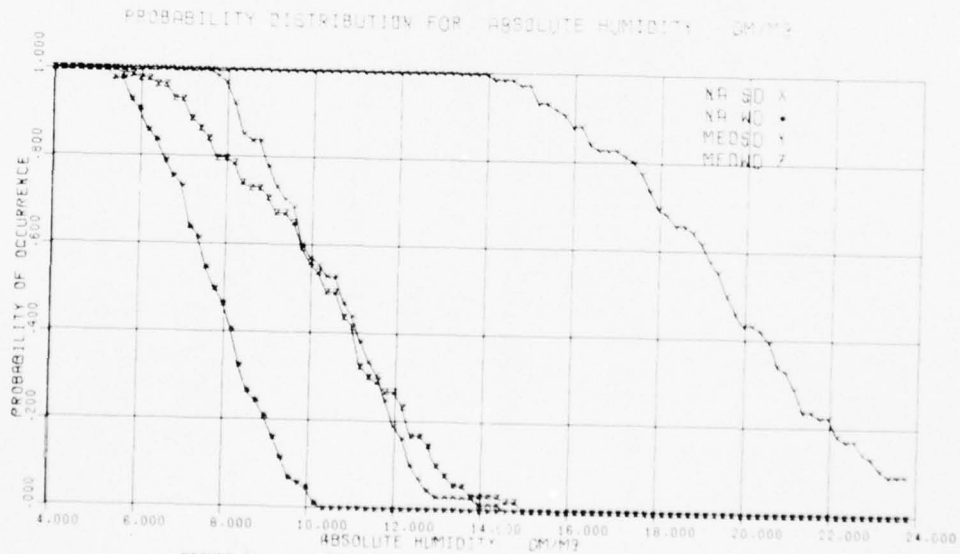


FIGURE 3B. PROBABILITY DISTRIBUTIONS FOR ABSOLUTE HUMIDITY GM/M³
Eastern Mediterranean and N. A. Station J.

UNCLASSIFIED

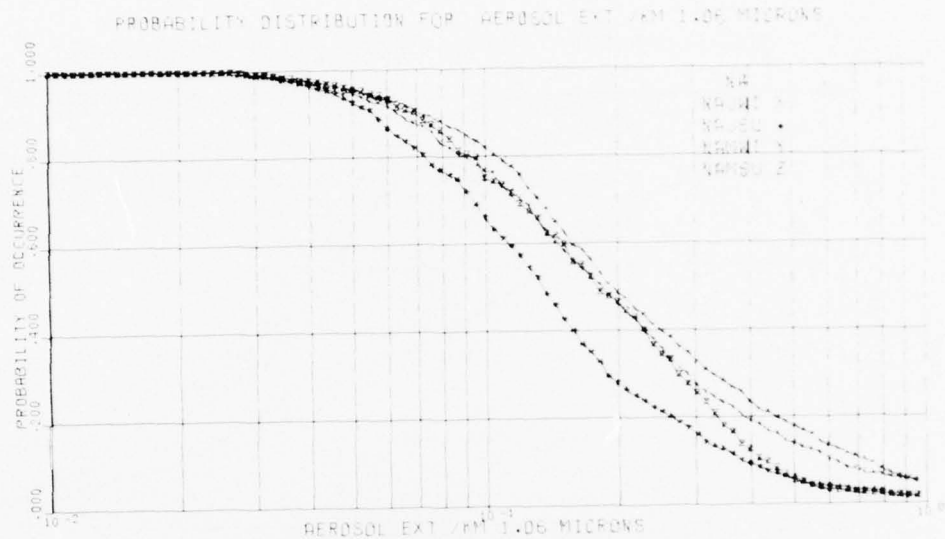


FIGURE 4A. PROBABILITY DISTRIBUTIONS FOR AEROSOL EXTINCTION
1.06 Microns

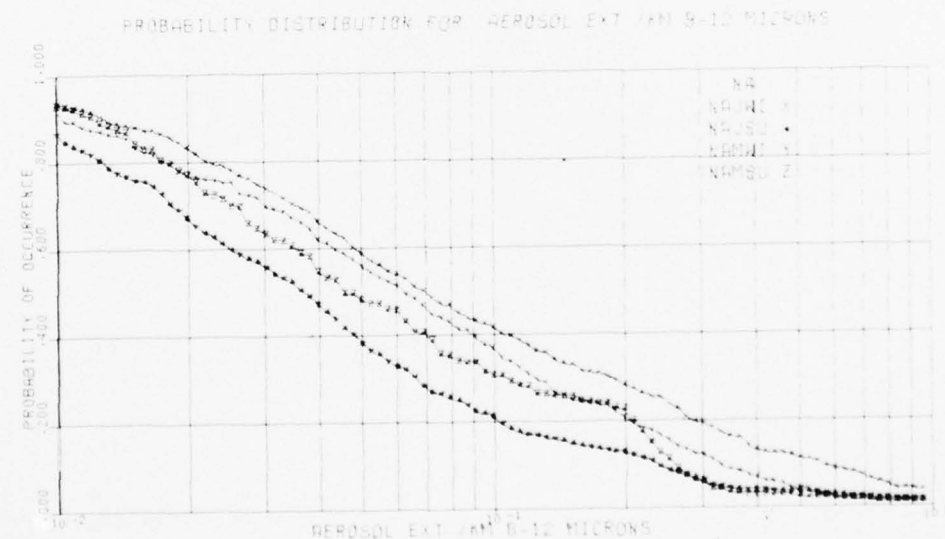


FIGURE 4B. PROBABILITY DISTRIBUTIONS FOR AEROSOL EXTINCTION
8-12 micron region weighted by thermal derivative of Planck is
Radiation equation assuming a 300°K temperature target.

UNCLASSIFIED

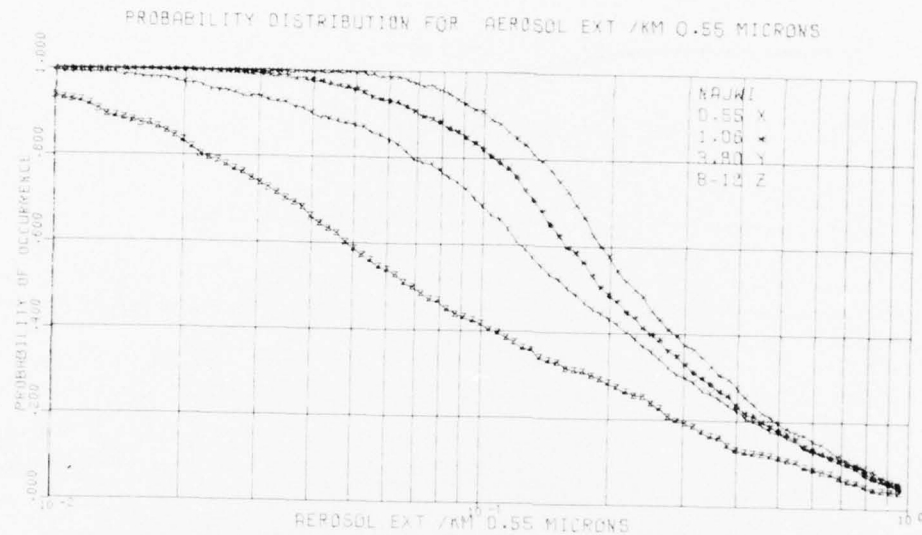


FIGURE 5. COMPARISON OF AEROSOL EXTINCTION IN VISIBLE AND IR WAVELENGTHS

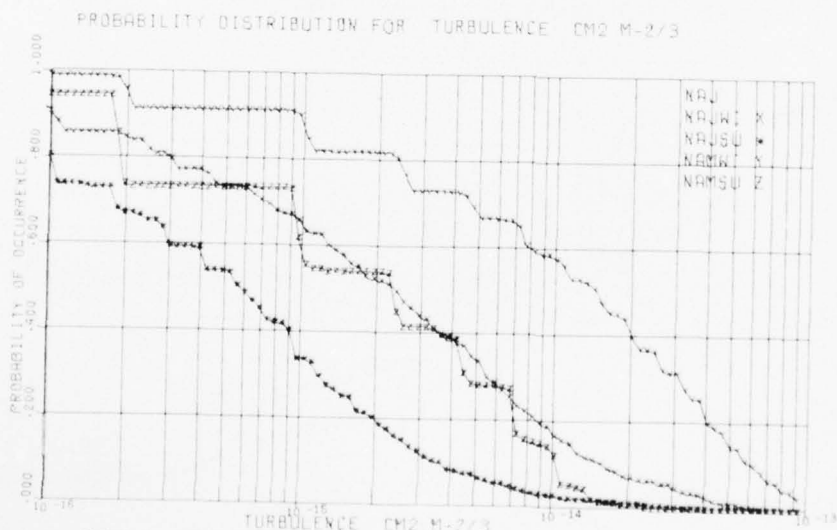


FIGURE 6. PROBABILITY DISTRIBUTION FOR ATMOSPHERIC TURBULENCE PARAMETER C_N^2
Calculations were done with NPGS code using air-sea temperature
difference, wind shear and absolute humidity assuming a height

UNCLASSIFIED

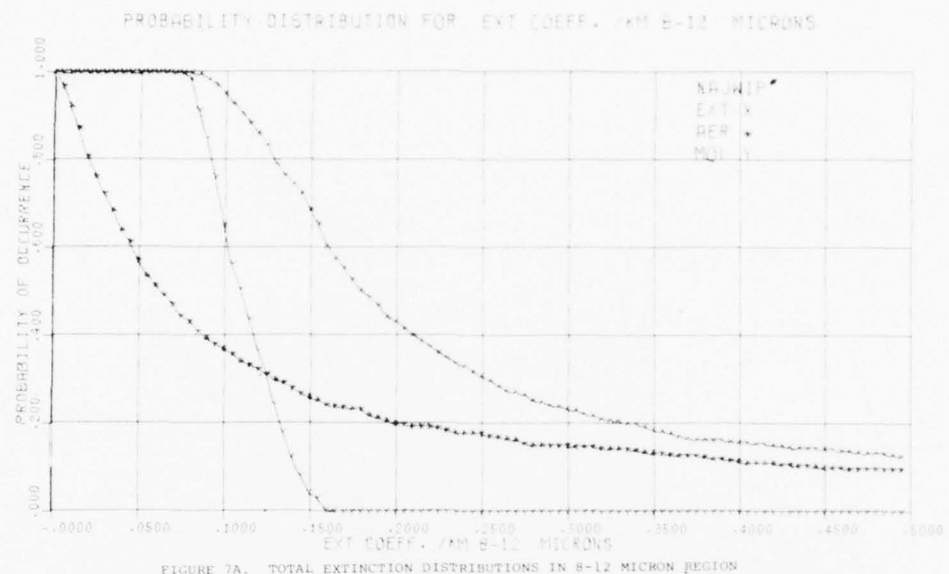


FIGURE 7A. TOTAL EXTINCTION DISTRIBUTIONS IN 8-12 MICRON REGION
North Atlantic ship J winter months (NAJWI)

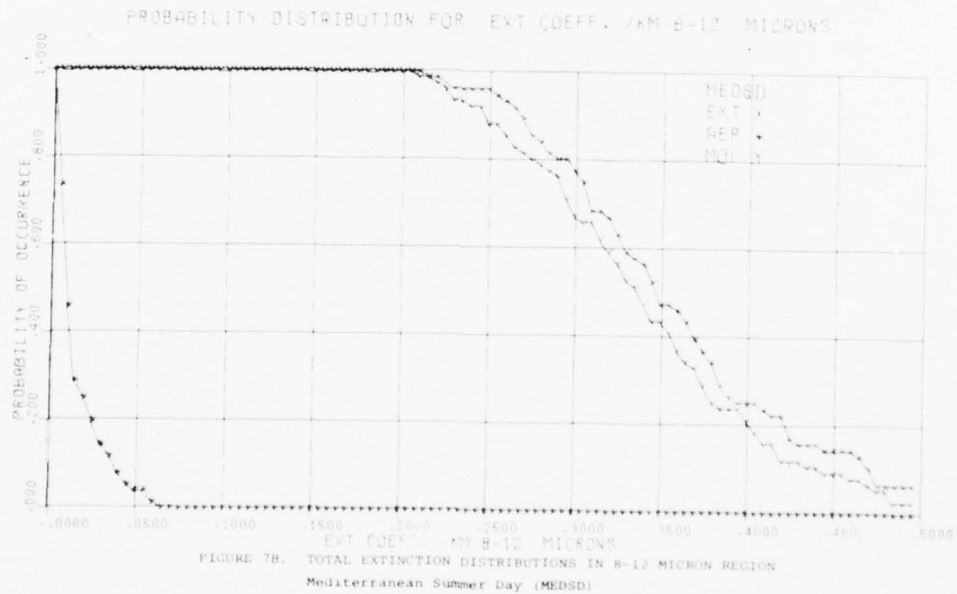


FIGURE 7B. TOTAL EXTINCTION DISTRIBUTIONS IN 8-12 MICRON REGION
Mediterranean Summer Day (MEDSD)

UNCLASSIFIED

UNCLASSIFIED

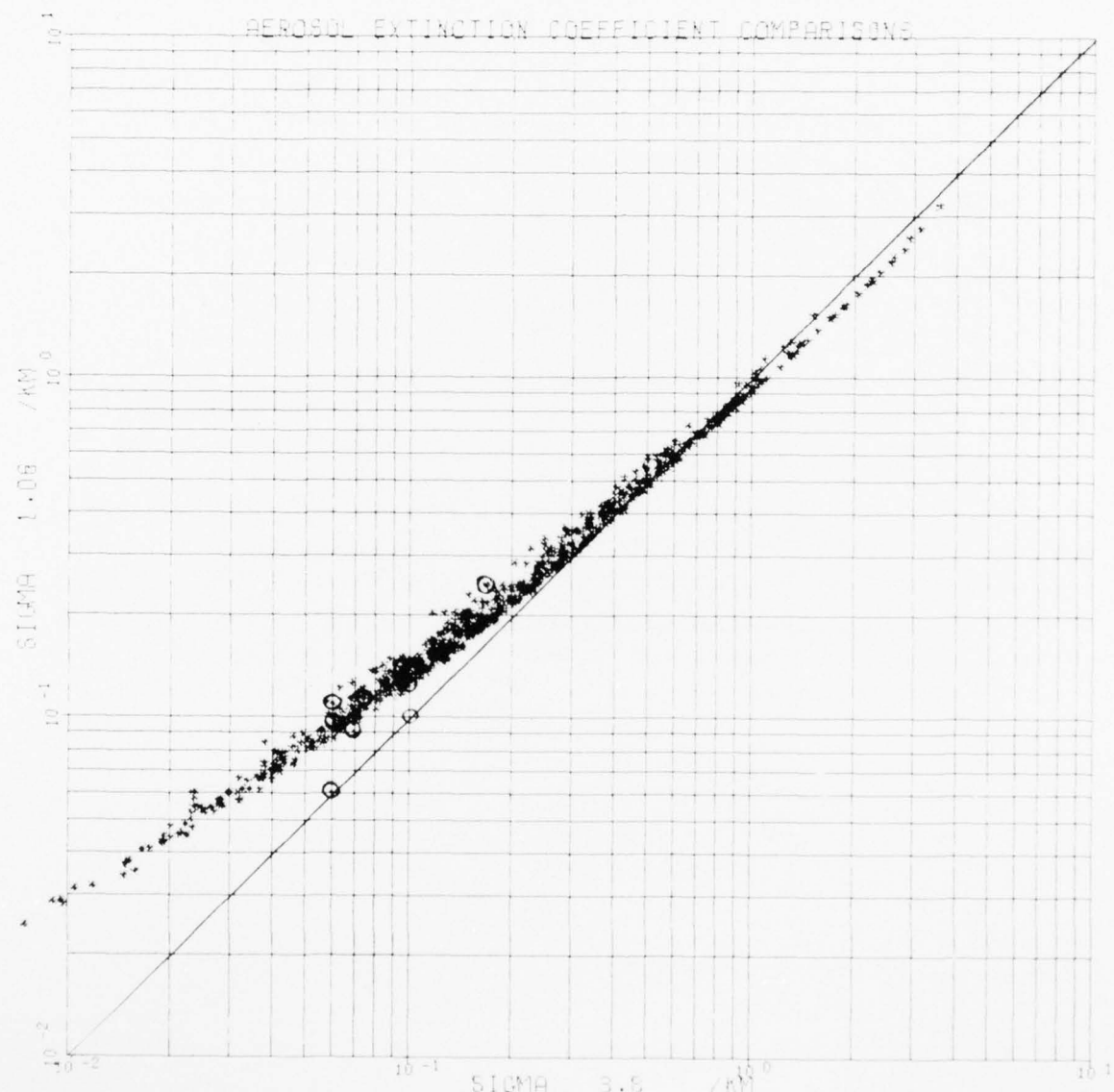


FIGURE 8A. WAVELENGTH COMPARISONS FOR AEROSOL EXTINCTION USING NAJWI DATA
1.06 vs. 3.8 with NRL Data plotted with large circles.

UNCLASSIFIED

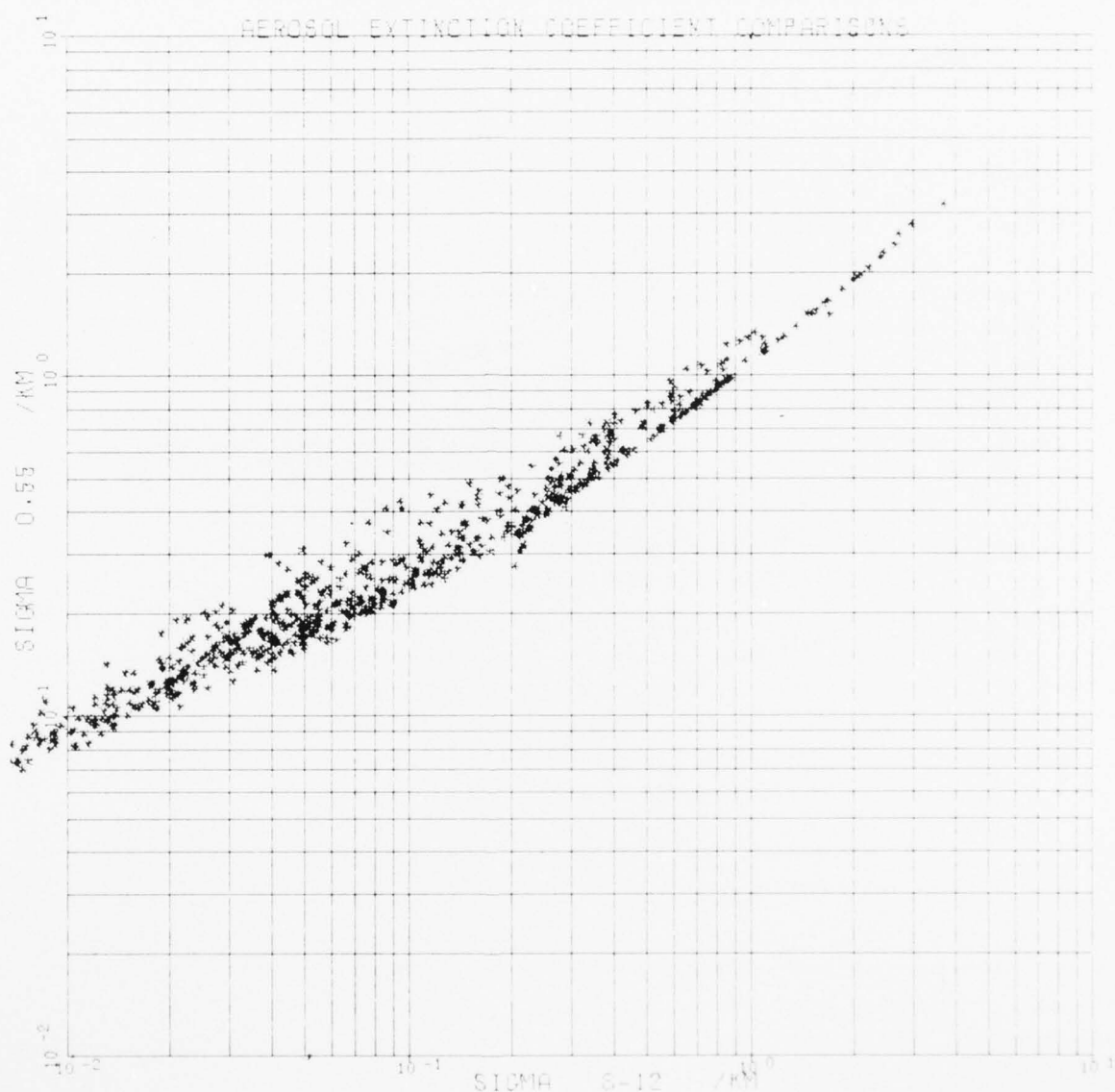


FIGURE 8B. WAVELENGTH COMPARISONS FOR AEROSOL EXTINCTION USING NAJWI DATA
.55 vs. 8-12 microns.

UNCLASSIFIED

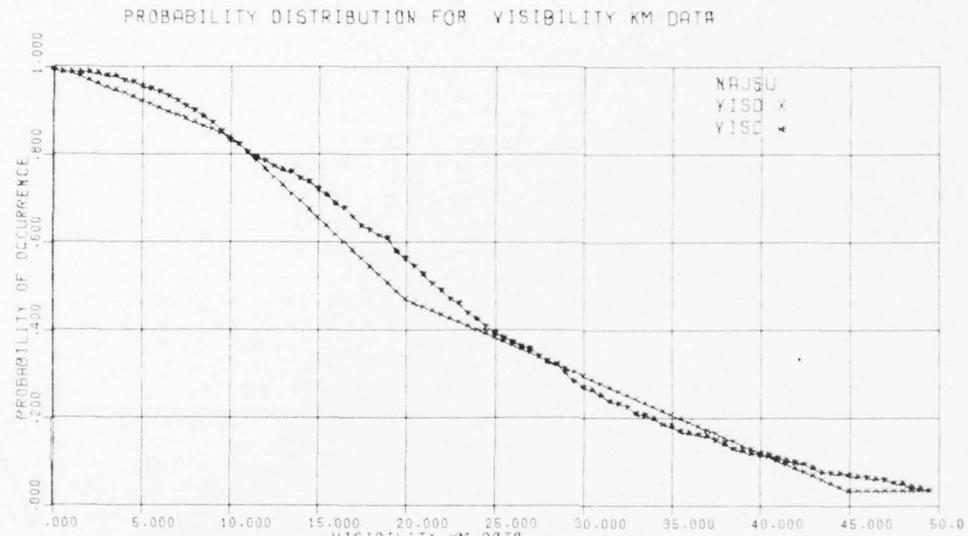


FIGURE 9. COMPARISON OF SUBJECTIVELY MEASURED AND CALCULATED VISIBILITIES
Visibility data is quantized from ship. We have assumed equal
weighting between quantized values.

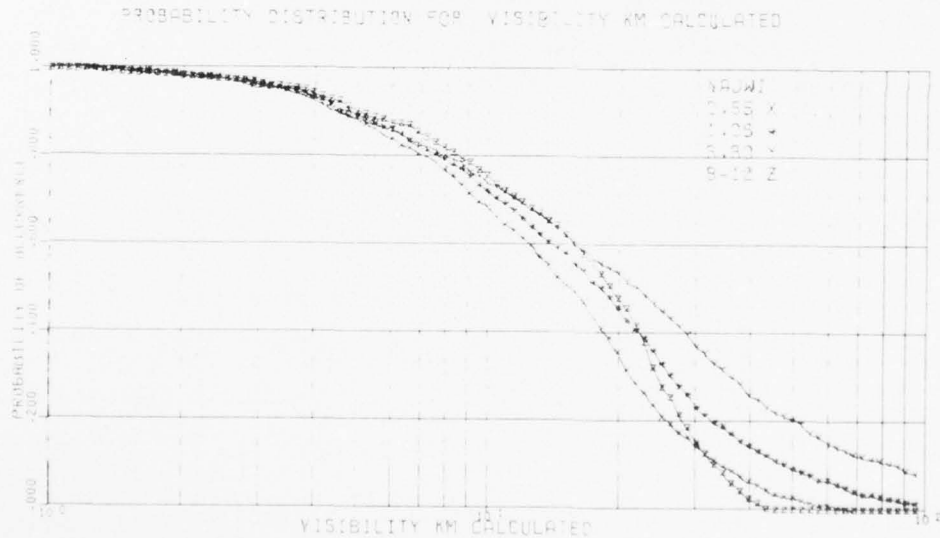


FIGURE 10. PROBABILITY DISTRIBUTIONS OF EFFECTIVE RANGES FOR DIFFERENT SYSTEMS
Assumed 2% transmission limits each system, (i.e., TV designator and FLIR).

AD-A037 812

OFFICE OF THE DIRECTOR OF DEFENSE RESEARCH AND ENGINE--ETC F/G 20/14
PROCEEDINGS OF THE OPTICAL-SUBMILLIMETER ATMOSPHERIC PROPAGATIO--ETC(U)
DEC 76

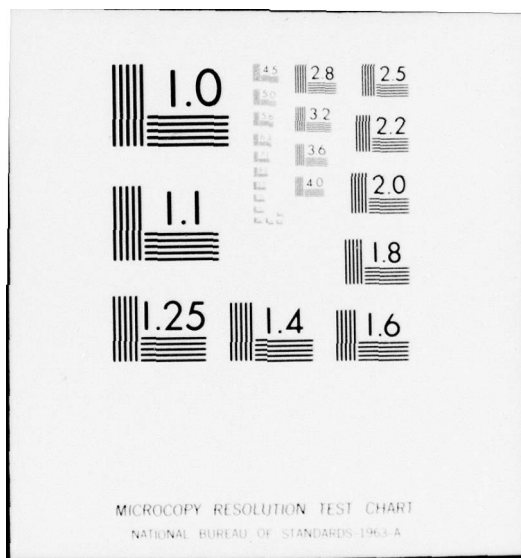
UNCLASSIFIED

NL

5 of 6
ADA037812

REF ID:
A6200





UNCLASSIFIED

A PRELIMINARY COMPARISON OF HIGH AND LOW RESOLUTION
ATMOSPHERIC TRANSMISSION MEASUREMENTS

R. Bergemann and M. Sola, U.S. Army Night Vision Laboratory;
J. A. Dowling, K. M. Haught, R. F. Horton, and J. L. Walsh,
Naval Research Laboratory; R. Roberts, Institute for Defense
Analyses

Atmospheric transmission measurements have been carried out simultaneously with low and high resolution instruments in the 3 to 5 micrometer window region of the atmosphere. The high resolution data have been averaged over the pass-band of the low resolution instrument and the results compared. For the high values of the atmospheric transmission ($T \sim 0.8$ to 0.9) which were found during this experiment in the region between 3.5 and 3.9 micrometers, the preliminary results of the two measurements agree to within 10 to 15 percent. Comparison at other wavelengths in this window has not yet been carried out because the interferometer calibration procedure is more complex in the presence of significant absorption line structure.

The measurements which are described were taken on two separate days in mid November 1976, over a 5.1 km path located near the Naval Air Test Center at Patuxent River, Maryland.

The low resolution measurement was made using the Barnes atmospheric transmissometer system as described by J. R. Moulton and F. M. Zweibaum (reference 1). This instrument transmits a 10 mr beam from a nominal 1273 Kelvin source through a nominal 10 cm aperture. The beam is square wave modulated at approximately 10^3 Hertz. The receiver collects and focusses this radiation on a cooled InSb detector. Calibration is based on the measurement of the received signal from a pinhole aperture of known size in the transmitter at zero range.

The high resolution results are obtained by combining the data from two separate measurements as described by Dowling (reference 2). In the first measurement, a scanning Michelson interferometer (SMI) system is used to obtain relative atmospheric transmission (with $\sim 0.1 \text{ cm}^{-1}$ resolution) over the complete range of interest. The source is a gray body operating in the vicinity of 1300 Kelvins. In a typical measurement, the average of approximately 100 scans is taken before the processing is started. In the second

UNCLASSIFIED

UNCLASSIFIED

measurement, we determine the absolute transmission at several DF laser wavelengths in the region between 3.6 and 4 micrometers. This measurement is absolute because the 1 meter transmitter optics projects a focussed laser beam which is completely captured by the 1.3 meter receiver optics at the operating range of 5.1 km. The laser transmission measurements provide an absolute calibration for the interferometer at selected wavelengths. Various interpolation procedures are applied to obtain calibration at other wavelengths.

For the relatively high values of atmospheric transmission encountered in this experiment ($T \approx 0.8$ to 0.9) there is agreement in the experimental results within 10% to 15% under conditions of low water vapor pressure (< 4 torr) and high visibility (> 40 km) in the 3.6 to 4.1 micrometer region. For these conditions, where the attenuation due to water vapor continuum and aerosols is small, the measurements are consistent with both Hitran and Lowtran predictions.

References:

1. J. R. Moulton and F. M. Zweibaum, "Atmospheric Transmissometer and Radiometer for EO Sensor Field Evaluation and Model Validation." Presented at the 20th Annual SPIE Technical Symposium, August 1976.
2. J. A. Dowling, "Atmospheric Transmission Measurements Using Infrared Lasers and Fourier Spectroscopy-- Techniques, Results, and Comparisons to Computer Models." Presented at the 20th Annual SPIE Technical Symposium, August 1976,

UNCLASSIFIED

....This paper is UNCLASSIFIED

ATMOSPHERIC TRANSMISSION FIELD
EXPERIMENTS USING IR LASERS,
FOURIER TRANSFORM SPECTROSCOPY AND
GAS FILTER CORRELATION TECHNIQUES⁺

J. A. Dowling, K. M. Haught, R. F. Horton,
S. T. Hanley, J. A. Curcio, D. H. Garcia,
and C. O. Gott

U. S. Naval Research Laboratory
Washington, D. C. 20375

ABSTRACT

An extensive measurement system for atmospheric transmission field experiments is described with emphasis placed on the recent additions of a high resolution scanning Fourier interferometer system and a gas filter correlation spectrometer. Examples are given of results obtained by means of three concurrent experiments used to generate a data base appropriate to high resolution transmission model validation. Laser extinction data, high resolution, long path atmospheric transmission spectra, and path integrated water vapor measurements are reported and discussed. Plans for future field experiments utilizing the three above measurement techniques plus broadband infrared transmissometer and infrared target signature measurement are discussed.

INTRODUCTION

The Naval Research Laboratory has been conducting field experiments concerned with studies of atmospheric propagation of infrared laser beams during the past several years. Earlier experiments were designed to study the effects of beam spreading and beam wander caused by atmospheric turbulence.¹⁻⁸ Recently primary emphasis has been placed upon measurements of atmospheric extinction at several laser wavelengths of interest to the Navy High Energy Laser Project, primarily those of the DF laser operating near 3.8 μ m.

⁺This work sponsored by the Naval Sea Systems Command PMS-405/PM-22.

UNCLASSIFIED

Two extensive experiments taking place during CY 1975 were conducted at coastal sites in Florida⁹ and later in California.¹⁰ The former experiment was a follow-on to initial DF laser transmission measurements performed at the Cape Canaveral Air Force Station (CCAFS) during February-March 1974.^{11, 12} The latter experiment was performed in conjunction with high power DF laser propagation tests conducted during the Joint Army-Navy Propagation Experiments at the TRW Capistrano Test Site during May-October 1975.

The results of several hundred measurements of DF and Nd-YAG laser transmission along with supporting meteorological data were used to test the validity of computer code transmission predictions based on a line-by-line atmospheric transmission calculation. The results of comparisons of the field measurements to predictions based on a HI-TRAN¹³ type calculation using the AFGL spectral line atlas¹⁴ as modified by Woods, et al^{15, 16} are presented in a forthcoming report.¹⁰ A summary of these results is presented in the next section of this paper.

Recent modifications to the trailer-based measurement system used during the earlier Florida and California experiments have included the addition of a high resolution atmospheric spectral measurement capability based on a Fourier transform spectrometer (FTS) system and the incorporation of a gas filter correlation spectrometer (GFCS). Details concerning the facilities used in and the operation of the laser extinction, FTS, and GFCS experiments are presented in a forthcoming report.¹⁷

The following sections of this paper will provide a brief description of the apparatus used in the three types of measurements, a statement of the philosophy underlying the experiments, and a presentation of some of the more important results obtained in recent studies. Experimental program plans for the near future will then be discussed.

LASER EXTINCTION MEASUREMENTS

a) Experimental Apparatus for Laser Extinction Measurements

The equipment used in these measurements is housed in the several van trailers shown in Figure 1. Several infrared lasers, transfer optics, and a large (90 cm aperture) collimating telescope are housed in an optical transmitter trailer second from the right in Figure 1. The 1600 CFM vacuum pump required to operate the CW DF laser used in these experiments is housed in a separate "pump" trailer and connected to the laser system in the transmitter trailer by a demountable, 20 cm diameter high vacuum line, installed once the trailers are properly positioned on site.

UNCLASSIFIED

UNCLASSIFIED

A third trailer containing a receiver optical system which is not shown in Figure 1 and which utilizes a 120 cm diameter collecting mirror completes the basic instrumentation suite used in the extinction experiments. Gas bottle storage and other supplies are carried in a fourth trailer, allowing the operation of the experiments to be predominately self-contained. This supply trailer is shown at the extreme right in Figure 1.

Meteorological conditions during these experiments are monitored using two nearly identical sensor systems used to measure wind velocity and direction, dew point, atmospheric pressure and temperature and insulation at each end of the propagation path. One system, in addition, incorporates an aerosol spectrometer used to obtain ambient aerosol distributions and is operated out of a meteorological/aerosol van not shown in Figure 1. The second meteorological system is operated out of a fifth trailer which also contains office space and is normally deployed at the opposite end of the measurement path from the van. The latter trailer is shown at extreme left of Figure 1.

A schematic of the optical system contained in the transmitter trailer is shown in Figure 2. The various components are identified in the Figure caption. By means of dichroic beam combining plates, the HeNe and Nd-YAG laser beams are coaxially combined and then in turn coaxially combined with the output beam from either the HF/DF, CO, or CO₂ lasers. Each of the latter three infrared lasers is operated single line, T_{em₀₀} mode, using intra-cavity grating reflectors.

The entire assembly of laser sources, transfer optics and large collimating telescope is mounted as a unit in a massive frame which can be steered over a range of a few degrees in azimuth and elevation with respect to a massive optical bench. This bench sits on piers extending through the trailer floor, resting on solid ground, thus decoupling the telescope from the trailer body. This massive assembly has proven to be quite stable during several years of use in the field; the output beam can be reproducibly pointed and maintained in alignment over angular changes as small as 10⁻⁵ rad. Details regarding the DF laser system, optics, and supporting equipment can be found in Reference 17.

The basic procedure used in the laser extinction measurements is outlined in Figure 3. The CW coaxial laser beam to be transmitted is brought to a focus by the off-axis parabolic mirror indicated and then diverges to fill the pupil of the 90 cm Cassegrain telescope as shown. The large aperture output beam is then focussed at the receiver site which is typically 5 km away. In practice, for moderate turbulence conditions, a 90 cm focused beam leaving the transmitter will have a 30 to 45 cm cross-sectional diameter at five km for $\lambda=3.8\mu\text{m}$. It has been established both theoretically^{18, 19} and experimentally⁶ that turbulence induced beam spreading is inversely proportional to some frac-

UNCLASSIFIED

UNCLASSIFIED

tional power of wavelength (0.2 to 0.33). Thus, visual observation that the beam is entirely collected by the 120 cm aperture receiver mirror shown in Figure 3 insures that the infrared laser beam distributions are also collected. Nearly perfect co-linearity of the visible and infrared beams is achieved by alignment techniques which require simultaneous superposition of the two beams at two locations in the transmitter Cassegrain telescope input optical train.

The laser beam collected by the receiver mirror is focused onto a spatially integrating detector assembly by a combination of a small (1 cm diameter) Newtonian diagonal mirror and ellipsoidal mirror shown in the Figure. The "mobile" detector position in the receiver optical system is indicated in Figure 3.

This detector can be located immediately behind the transmitter telescope primary mirror for calibration measurements as shown in Figure 3. Laser power is continuously monitored by a stationary or reference detector using that portion of the beam reflected by the 50% duty cycle, 37 Hz chopper as shown.

As shown in Figure 3 the transmitter and receiver trailers are periodically placed end to end in a "zero path" configuration for calibration of the optical system efficiency of the large transmitter telescope components as well as the receiver optics. This system efficiency factor is required in order to obtain actual atmospheric transmission.

The signal received by the mobile detector located in the receiver trailer is relayed by to a precision ratiometer located in the transmitter trailer by means of a GaAs data link as shown in Figure 3, so that atmospheric extinction can be obtained in real time, once the detector relative response and transmitter-receiver optical system efficiencies are known. Further details concerning the design and operation of this measurement system are contained in Reference 17.

b) Rationale For Laser Extinction Measurements

The laser extinction measurements performed in previous experiments^{9,10} have been used in comparisons to molecular absorption predictions based on a HI-TRAN calculation¹³ which makes use the AFGL spectral line atlas.¹⁴ The principal objective of this work has been to develop a reliable predictor for atmospheric transmission at DF laser frequencies. Certain improvements in HDO spectral line strengths have resulted in this process.^{15,16} via contractual support by Science Appl. Inc., Ann Arbor, Michigan.

Future laser extinction experiments will serve the twofold purpose of extending the results obtained in the DF region to the CO₂ and CO₂ laser regions respectively, and at the same time providing a basis for absolute transmission calibration of high resolution atmospheric absorp-

UNCLASSIFIED

UNCLASSIFIED

tion spectra taken with the FTS system to be described below.

c) Results of Laser Extinction Measurements

A comparison between observed extinction (which includes aerosol scattering effects) and calculated molecular absorption for 22 DF laser lines between 3.6 and 4.1 μm is shown in Figure 4. One would expect a constant offset between the two sets of points due to aerosol scattering. As seen in the figure, the agreement is quite good when the trends between the two sets of points are compared.

Data from both Florida⁹ and California¹⁰ experiments such as that shown in Figure 4, when corrected for aerosol effects²⁰ were compared to molecular absorption calculations. An example of such a comparison for the P1-8 DF laser line is shown in Figure 5. The open squares are Florida measurements and the crosses are data taken in California.

A summary of comparisons such as that shown in Figure 5 is presented in Table I for the mid-latitude summer water vapor partial pressure of 14.26 Torr. Column five of the table lists the differences between measured and calculated absorption coefficients for each of the DF laser lines listed in column one. The summary presented in Table I results from the use of new HDO line strengths and widths^{15,16} in the calculations. As can be seen from the table the agreements between theory and the field measurements are quite good with the worst case differences remaining about 20%.

2. Fourier Transform Spectroscopy Measurements

a) Experimental Apparatus Used in FTS Measurements

An FTS system based on a scanning Michelson interferometer (SMI) is now being used for high resolution atmospheric transmission studies. This instrument as well as the GFCS device mentioned earlier share the receiver optical system shown in Figure 6. The primary collector P1 is a 120 cm diameter, f/5 parabolic mirror which forms a Newtonian telescope with the small (1 cm minor diameter) diagonal mirror F1. The beam reflected from F1 passes through a focus f1 and then impinges on the elliptical mirror E, which refocuses the beam outside the entrance pupil of P1.

For extinction measurements, the mobile detector MD is placed near the secondary focus of the mirror E, namely f2. For SMI or GFCS experiments the mobile detector MD is removed and the beam passes through the focus f2 and is re-collimated with a 5 cm diameter cross section by the parabolic mirror P2 and then directed by flat transfer optics into either the SMI or GFCS instruments as shown in Figure 6. The optics and spectrometer instruments are housed in two separate rooms in the

UNCLASSIFIED

UNCLASSIFIED

receiver trailer. A third room houses the data processing system for the SMI device. A more detailed description of this instrumentation can be found in reference 11.

The SMI data system is used to control the SMI scan length and rate and to perform interrogram co-addition and fast Fourier transformation (FFT). In order to achieve a spectral resolution of 0.06 cm^{-1} over the interval from 1.3 to $6.0 \mu\text{m}$, a 256k point double precision (32bit) FFT must be processed. The present data system which utilizes a hardware FFT processor and 10^7 byte (8-bit) disc drive, can accomplish this procedure in ≤ 10 minutes. A digital tape drive is used with the system for recording observed spectra and an electrostatic plotter is used for graphical presentation. The SMI system was designed and built by the Carson Alexiou Corp., Newport Beach, California.

b) Rationale For Fourier Transform Spectroscopic Measurements

The fundamental objective underlying the FTS measurements is the generation of an extensive experimental data base for use in HI-TRAN code validations. The DF laser transmission measurement code comparisons described earlier have been most useful in identifying discrepancies between calculated and measured molecular line absorption features. The relatively wavelength independent and relatively weak absorption features due to molecular continua (N_2 and H_2O in the DF laser region) are not as readily identified by means of the laser line measurement-HI-TRAN code comparison procedure. The FTS data provide a one-to-one map of a spectral region for comparison to calculation as opposed to a comparison carried out only at several frequencies (22 laser line positions between 3.6 and $4.1 \mu\text{m}$ in the DF laser region for example).

Once the high resolution spectra are obtained and an absolute transmission calibration is obtained using laser extinction measurements throughout the observed region, the measured transmission spectra can be numerically degraded as required in order to make comparisons to infrared systems operating in finite spectral bands. Most E-0 devices now in use fall into this category, namely IR seekers, FLIRS, IR transmissometers, and the like. The truly correct starting point for modeling atmospheric transmission values for such comparisons is a properly calibrated HI-TRAN code. Low resolution calculations can diverge from banded sensor performance calculations because the details of actual atmospheric absorption structure, when convolved with the bandpass characteristics of a particular system, may not be adequately represented by the low resolution calculation. The narrower the operating band of the system, the greater the potential for such problems. Such ambiguities are resolved by the use of highly resolved spectral information for both the system bandpass and the atmosphere.

An example of the procedures outlined above is presented in

UNCLASSIFIED

UNCLASSIFIED

another paper at this conference.²¹ The preliminary results cited therein are representative of comparisons of high resolution data to the response of a banded system and should be repeated for a wide variety of transmission values to evaluate the response of the particular system under test to a variety of transmission conditions using structured as well as clear spectral regions.

c) Results of Fourier Transform Spectroscopic Measurements

The procedure used in calibrating the relative transmission spectra obtained with the FTS system by means of measured extinction of a laser line is illustrated graphically in Figure 7. The upper portion of the figure shows a transmission spectrum recorded at NATC, Patuxent River, Maryland for the conditions listed in the figure. The SMI response to the P1-8 DF laser line at 2717.538 cm^{-1} is shown in the lower portion of the figure. Using the procedures outlined above, the transmission measured at this line was 51% which value is used to calibrate the FTS spectra as shown. The traces shown in Figure 7 are copies of records produced by the FTS data system plotter and show actual signal to noise ratios observed in the 5 km transmission spectra.

An example of recent results obtained with the FTS system using several DF laser transmission calibration points is shown in Figures 8 and 9. The upper portion of each figure shows transmission spectra measured at NATC, Patuxent River, Maryland for the conditions indicated. The lower portion of each figure shows a calculation of molecular absorption for the conditions listed above the plot using the version of the HI-TRAN code which was used in the DF laser line calculations discussed earlier.^{15, 16} As evidenced in Figures 8 and 9 the overall agreement between calculation and measurement is remarkably good. The calculation indicates slightly larger line strengths than observed for some of the weaker absorption lines near 2500 cm^{-1} , but for the most part, is quite representative of observations in spectral regions shown in Figures 8 and 9.

Future laser-FTS measurements will include comparisons such as those shown above for a wide variety of atmospheric conditions and for other spectral regions, notably 4.8-5 μm and 9-11 μm using CO and CO₂ laser extinction measurements respectively for absolute transmission calibrations.

3. Gas Filter Correlation Spectrometer Experiments

a) Experimental Facilities Used in GFCS Measurements

As previously described, the receiver optical system shown in Figure 6 is used for both SMI and GFCS measurements. Referring

UNCLASSIFIED

UNCLASSIFIED

to Figure 6, the 5 cm diameter beam re-collimated by mirror P2 is directed into either instrument by means of a removable flat mirror. The basic operation of the GFCS device is shown in Figure 10. The average transmission of an atmospheric constituent in the spectral interval $\Delta\nu$ is given by the expression equated to T_a . The energy from a greybody source spectrally modulated by absorption due to one or more atmospheric constituents is collected by the receiver optical system as shown. This selectively transmitted energy is passed alternately through a spectrally non-selective attenuation arm with transmission T_R as shown in Figure 10, or through a cell containing a known amount of the absorber under study, whose transmission is $T_c(v)$. The non-selective transmission T_R is initially balanced against the average transmission of the cell during calibration. If the spectral character of the atmospherically transmitted energy resembles that of the cell absorber $T_c(v)$, then a difference in transmission and hence a modulation signal will result when the light from the distant source is passed alternately through the two arms of the GFCS instrument.

The particular version of the device used in these experiments contains a known amount of HDO in the reference cell and is based on correlating transmission through the local cell with the amount of HDO absorption in the atmosphere.

b) Rationale For Gas Filter Correlation Spectrometer Measurements

If the atmospheric abundance of HDO is measured along the 5 km path used for the laser extinction and SMI measurements by means of the GFCS then a path integral value for atmospheric water vapor¹⁴ may be obtained using the isotopic abundance of HDO/H₂O of 0.030%. Since water vapor is an important or dominant absorber in the infrared regions of interest for atmospheric transmission studies, a path integral measurement of water vapor concentration is very important for use in comparisons of transmission data to calculational models. Path integral measurements such as provided by the GFCS are particularly useful for overwater transmission experiments where mid-points along the path are not readily accessible to standard dew point observations.

The GFCS measurement cannot utilize normal water vapor as the filter gas because an amount of water equivalent to that present in a 5 km path at standard conditions cannot be maintained in the vapor state in the GFCS local reference cell. Due to the small amount of HDO normally present in the atmosphere, a greatly enhanced concentration relative to that in the atmosphere can be held in the vapor state in a multi-pass absorption cell. A 5 km path equivalent amount of HDO is contained in the GFCS multi-pass reference cell which affords a total path of 40 meters.

UNCLASSIFIED

UNCLASSIFIED

c) Gas Filter Correlation Spectrometer Measurement Results

Figure 11 is a plot of data taken during recent experiments at the Patuxent Naval Air Station showing a comparison of water vapor measurements obtained with the GFCS and with EG&G model 110 dew point hygrometers located on shore at each end of the 5.12 km overwater path. The GFCS data are consistently lower than the fixed point measurements by ~ 30% when a value for the HDO/H₂O ratio of 3x10⁻⁴ is used in reducing the GFCS data. Further analysis utilizing high resolution spectra such as that shown in Figures 8 and 9 is currently being pursued to resolve the apparent discrepancy between the two methods of water vapor measurement. Independent HDO/H₂O ratios will be derived from spectra taken during the GFCS measurement times shown in Figure 11 using measurements of individual H₂O and HDO spectral lines together with recent line strength data.^{15, 16} A good possibility exists that the 3x10⁻⁴ abundance ratio cannot be universally applied to all locations at sea level. Since the HDO/H₂O ratio is very important in determining DF laser propagation, it is quite important that this question be actively pursued.

Atmospheric Transmission Program Plans for the Near Future (FY77)

An in-depth atmospheric transmission measurement field experimental program is planned for execution during the period February-April 1977. Based on an evaluation of results obtained during earlier tests, a propagation range located at the Cape Canaveral Air Force Station (CCAFS), Cape Canaveral, Florida has been selected. Both 5.1 and 3.2 km overwater paths are available at this location. Large variations in absolute humidity (5-20 Torr H₂O partial pressure) were observed during a February-March 1975 measurements program at this site and, in addition, aerosol distributions typical of open ocean conditions were measured for easterly winds blowing across the measurement path from the Atlantic Ocean. A combination of factors including, good site access, relative proximity to NRL, and excellent range support provided by the Naval Ordnance Test Unit (NOTU) and the Air Force Eastern Test Range (AFETR), as well as anticipation of very desirable meteorological conditions make this location a compelling choice.

Laser extinction measurements using Nd-YAG, DF, short wavelength (4.8-5.1 μ m) CO, and CO₂ laser sources will be performed for the twofold purpose of a) laser line propagation algorithm development and b) high resolution transmission spectrum calibration. Gas filter correlation spectrometer data will be taken simultaneously as well as extensive meteorological data using fixed measurement stations at each end of the transmission path as well as a movable,

UNCLASSIFIED

UNCLASSIFIED

intermediate station. A current measurement objective calls for simultaneous dew point and aerosol distribution characterizations at two locations in an attempt to better define the homogeneity of conditions along the propagation path. Additional information concerning details of the NRL aerosol measurement system and capabilities are presented in a comparison paper at this conference.²²

In addition to addressing the principal objective of HI-TRAN code validation, the forthcoming CCAFS experiments will provide an ideal theater for extension of the transmissometer system evaluation begun during the Patuxent tests. A transmissometer system similar to the one described at this conference²¹ is scheduled for delivery to the Naval Weapons Center (NWC), China Lake, for use by the Optical Signatures Program (OSP). Simultaneous experiments with the NRL laser calibrated high resolution transmission measurements and the OSP transmissometer system for a wide variety of measurement conditions will significantly improve the understanding of the transmissometer's operating characteristics and should result in enhanced reliability. These joint experiments are now being planned.

A high resolution infrared target signatures measurement program utilizing the NRL-FTS capability will be evaluated for execution sometime after the CCAFS experiments. Several high resolution ($< 0.1 \text{ cm}^{-1}$) emission spectra from Navy jet aircraft operating at NATC, Patuxent River were obtained during the course of the transmission tests described above. High signal/noise, high quality emission spectra were obtained over a 5 km path using the system described earlier and demonstrate the feasibility of using the NRL system for a long path target signature measurement program.

Acknowledgements

The authors wish to acknowledge the continued encouragement, and programmatical/administrative support provided by Dr. D. Finkleman, Naval Sea Systems Command, PM-22/PMS-405 and Dr. P. B. Ulrich, Naval Research Laboratory throughout the course of this work. Excellent shop support was provided in the preparation of the receiver optical system by NRL-CBD machine shop personnel including M. Dement, J. Cox, and S. King.

Science Applications, Inc., Ann Arbor, Michigan has played a key role in the work described herein. Specifically, design and construction of the GFCS device by D. R. Woods and R. E. Meredith is gratefully acknowledged. Additionally, generation of calculated atmospheric transmission spectra by D. R. Woods, R. E. Meredith, F. G. Smith, and J. P. Walker is greatly appreciated as being of fundamental importance in the utilization of the NRL atmospheric measurements.

UNCLASSIFIED

UNCLASSIFIED

References

1. Progress in the NRL experiments carried out at NESTEF, Webster Field, St. Inigoes, Md. was reported in unclassified appendices appearing in several NRL High Energy Laser Program Progress Reports during the period 1970 to 1972. The information is contained in the following reports consistently titled "The Propagation of Focused Laser Beam Through Near Earth Atmospheric Turbulence":

<u>Reporting Period</u>	<u>NRL Memorandum Report Number (SECRET)</u>	<u>Report Publication Date</u>
1 July 1970-15 October 1970	2197	December 1970
15 October 1970-15 January 1971	2222	29 March 1971
15 January 1971-15 April 1971	2274	11 June 1971
15 April 1971-15 July 1971	2349	22 October 1971
15 July 1971-15 October 1971	2382	17 January 1972
15 October 1971-15 January 1972	2421	18 April 1972
15 January 1972-15 April 1972	2453	30 June 1972

2. J. A. Dowling, J. A. Curcio, and H. Shenker, "Experimental Studies of Focused Laser Beams Propagating Through Near Earth Atmospheric Turbulence," presented at the National OSA meeting Tucson, Arizona, 5-8 April 1971.

3. H. Shenker, J. A. Dowling, and J. A. Curcio, "Propagation of Focused Laser Beams," Proc. Electro-Optical Systems Design Conference-West, May 18-20, 1971, Anaheim, Calif., pp. 67-75.

4. J. A. Dowling, J. A. Curcio, and H. Shenker, "The Propagation of Focused Laser Beams Through Atmospheric Turbulence," paper 2.7, 1971 Conference on Laser Engineering and Applications, Wash., D. C., June 2-4, 1971.

5. J. A. Dowling, R. W. Harris, M. R. Kruer, and T. V. Blanc, "Measurement of Wavelength Effects in the Propagation of Focused Laser Beams Through Atmospheric Turbulence," paper WE13, National OSA Meeting, New York, N. Y., April 11-13, 1972.

6. J. A. Dowling and P. M. Livingston, "Behavior of focused beams in atmospheric turbulence: "Measurements and Comments on the Theory," J. Opt. Soc. Am. 63, 846, (1973).

7. J. A. Dowling, "Naval Research Laboratory Experimental Laser

UNCLASSIFIED

UNCLASSIFIED

Propagation Research , paper WB1, OSA Topical Meeting on Optical Propagation Through Turbulence, 9-11 July 1974, University of Colorado, Boulder, Colorado.

8. J. A. Dowling, "The Effects of Atmosphere Turbulence on High Power Laser Propagation , "unclassified article Journal of Defense Research, Volume 7B, Number 1, Spring 1975 (SECRET).

9. "Atmospheric Laser Propagation Measurements for 0.63, 1.06, 3.8 and 10.6 μm Wavelengths , "J. A. Dowling et al NRL Report in preparation, Jan 1977.

10. J. A. Dowling, K. M. Haught, R. F. Horton, F. L. Trusty, and J. A. Curcio, "Atmospheric Extinction Measurements at Nd-YAG DF Laser Wavelengths Performed in Conjunction With the JAN Propagation Tests: June-September 1975, " NRL Report 8058 to be published February 1977.

11. J. A. Dowling and P. M. Livingston, "Atmospheric Extinction Measurements for Several DF Laser Lines Near 3.8 μm , "paper IV-3, VI International Laser Radar Conference, 3-6 September 1974, Sendai, Japan.

12. Previously unpublished results of DF laser transmission measurements taken by NRL using a 5 km overwater path at Cape Canaveral Air Force Station appeared in "Molecular Absorption of Infrared Laser Radiation in the Natural Atmosphere , "by P. L. Kelley et al, Optical and Quantum Electronics 8, 117-144 (1976).

13. A HI-TRAN calculation uses a computer code to compute the spectral absorption coefficient (alternately the transmission over a specified path) point by point by first evaluating the combined contributions of several individual atmospheric absorption lines at a particular frequency and then incrementing the frequency by some small interval ($< .01 \text{ cm}^{-1}$) and repeating the process. The resultant is spectrum of absorption coefficient or transmission which exactly represents the detailed absorption structure of the atmosphere.

14. R. A. McClatchey, W. S. Benedict, S. A. Clough, D. E. Burch, R. F. Calfee, K. Fox, L. S. Rothman, and J. S. Garing, "AFCRL Atmospheric Absorption Line Parameters Compilation" AFCRL-TR-73-0096 (1973).

15. D. R. Woods, T. W. Tuer, and R. E. Meredith, "DF Laser Propagation Analysis-1st Informal Report," SAI-76-002-AA, April 1976.

16. D. R. Woods, T. W. Tuer, J. P. Walker, and R. E. Meredith "DF Laser Propagation Analysis-2nd Informal Report , "SAI-76-006-AA, August 1976.

UNCLASSIFIED

UNCLASSIFIED

17. J. A. Dowling, R. F. Horton, G. L. Trusty, T. H. Cosden, K. M. Haught, J. A. Curcio, C. O. Gott, S. T. Hanley, and P. B. Ulrich, "Atmospheric Transmission Measurement and Field Test Plan," to be published as an NRL Report (March 1977).
18. W. P. Brown, J. Opt. Soc. Am. 61, 1051 (1971).
19. H. T. Yura, J. Opt. Soc. Am. 62, 889 (1972).
20. K. M. Haught and J. A. Dowling, "Analysis of Long Path DF Laser Atmospheric Transmission Measurements," Paper TU013 presented at the 1976 Annual OSA Meeting, Tucson, Arizona, 18-22 October 1976.
21. R. Bergemann, M. Sola, R. Roberts, J. Walsh, J. Dowling, K. Haught and R. Horton "Preliminary Comparison Between Low Resolution and High Resolution Transmissometers," paper presented at the ODDR&E Optical/ Submillimeter Atmospheric Propagation Workshop, Colorado Springs, Colo., 6-10 December 1976.
22. G. L. Trusty and T. H. Cosden "An Aerosol Measurements System For Laser/Aerosol Interaction Studies," Ref. 21 op. cit.

UNCLASSIFIED

TABLE I

**COMPARISON OF MEASURED AND
CALCULATED MOLECULAR ABSORPTION FOR
MID LATITUDE SUMMER CONDITIONS
(14.26 TORR PARTIAL PRESSURE H₂O)**

LINE	POSITION (cm ⁻¹)	α (km ⁻¹)		(EXP-CAL)/CAL % DIFF	σ EXP/CAL %
		EXP	CAL		
P3(10)	2496.721	.0516	.0514	.4	4.7
P3(9)	2521.769	.0364	.0366	— .5	12.5
P2(12)	2527.391	.0340	.0346	— 1.7	4.0
P3(8)	2546.375	.0561	.0511	9.9	9.3
P2(11)	2553.952	.0360	.0365	— 1.3	16.0
P3(7)	2570.522	.0701	.0648	8.2	5.7
P2(10)	2580.096	.0736	.0678	8.7	17.7
P3(6)	2594.197	.0364	.0308	18.1	8.8
P2(9)	2605.806	.0554	.0513	8.0	16.2
P3(5)	2617.386	.0221	.0229	— 3.5	10.7
P2(8)	2631.067	.0302	.0360	— 16.0	13.3
P2(7)	2655.863	.1023	.1004	1.8	4.4
P1(10)	2665.219	.0460	.0381	20.5	16.7
P2(6)	2680.179	.0639	.0600	6.6	7.2
P1(9)	2691.606	.0435	.0463	— 6.1	6.9
P2(5)	2703.999	.0284	.0300	— 5.3	12.0
P1(8)	2717.538	.1456	.1437	1.3	2.5
P2(4)	2727.309	.0437	.0574	— 23.8	4.5
P1(7)	2742.997	.0311	.0350	— 11.1	12.3
P2(3)	2750.094	.0457	.0425	7.6	11.9
P1(6)	2767.968	.0764	.0876	— 12.3	8.1
P1(5)	2792.434	.0661	.0705	— 6.3	9.6

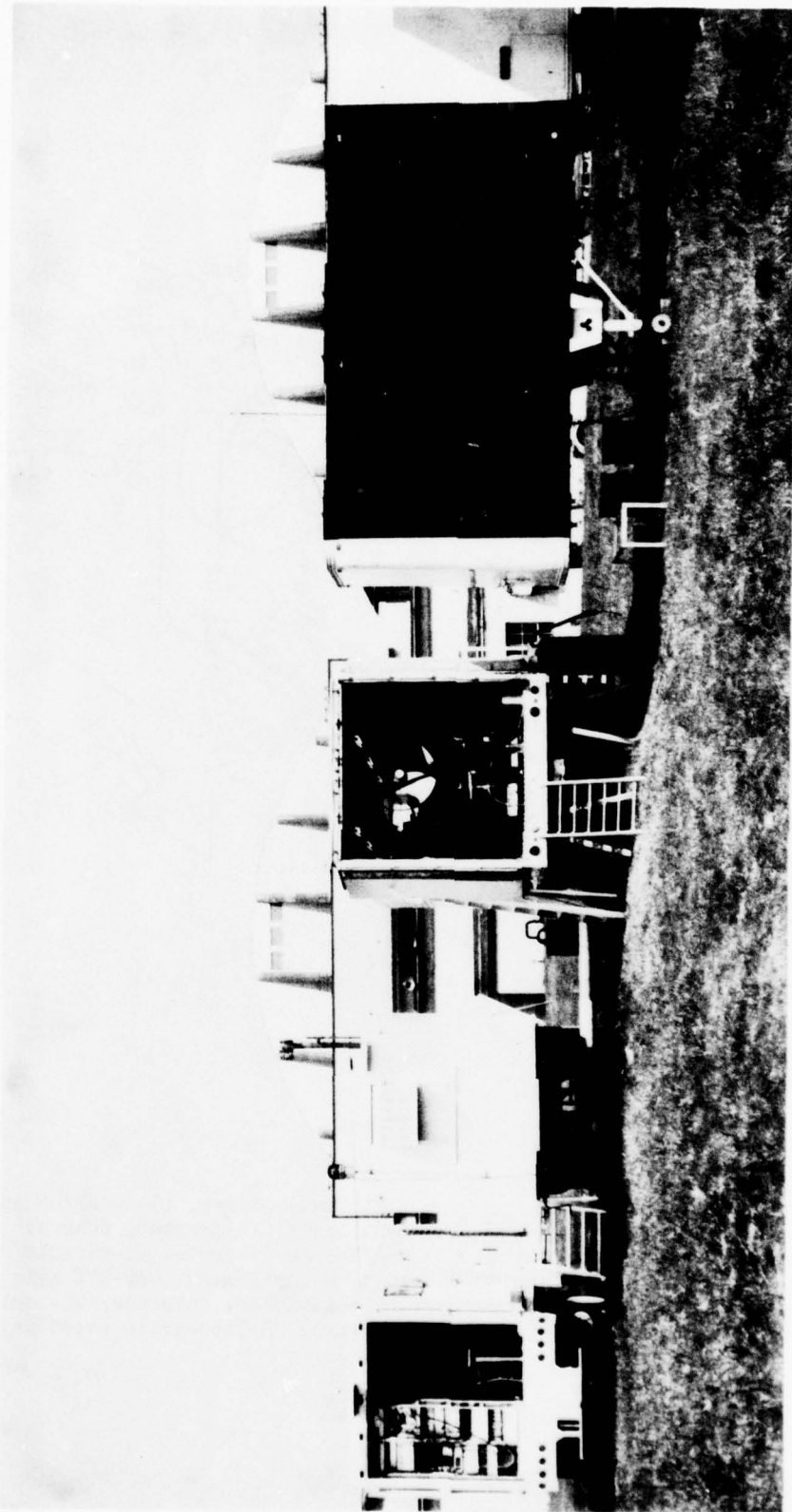


FIGURE 1. Transmitter Station for Patuxent MAS Experiments. From left to right: office trailer, pump trailer, transmitter trailer, supply trailer.

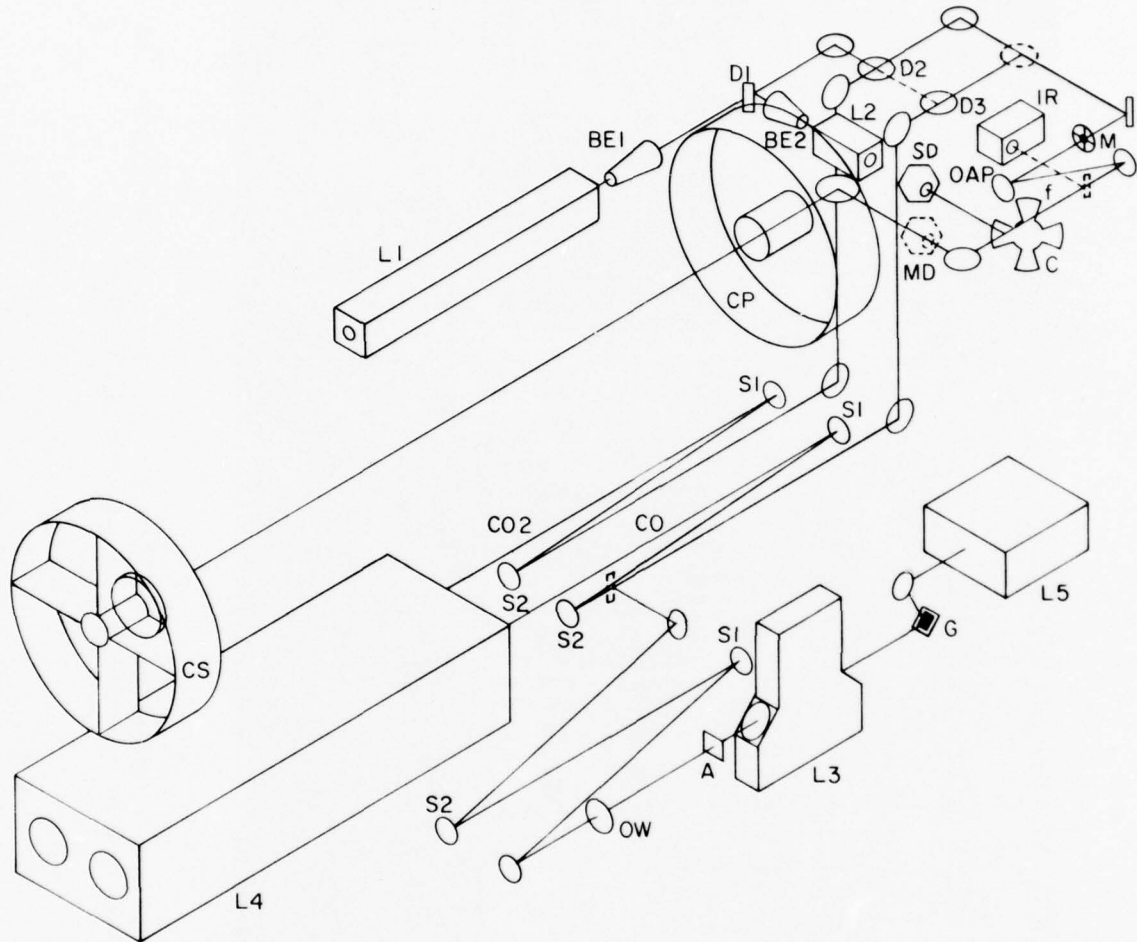


FIGURE 2. Transmitter Optical Schematic

Legend: L1-50mw HeNe laser, L2-0.25 watt Nd-YAG laser, L3-1w HF/DF laser, L4-20w CO₂/1w CO laser, L5-HeNe alignment laser, IR-greybody source, BE1-2-refracting beam expanders, D1-HeNe/Nd-YAG dichroic, D2-visible/CO₂ dichroic, D3-visible/HF/DF or CO dichroic, M-pupil mask, OAP-off axis parabolic mirror, C-37Hz, 50% chopper, SD-stationary detector, MD-mobile detector (calibration), CP-Cassegrain primary, CS-Cassegrain secondary.

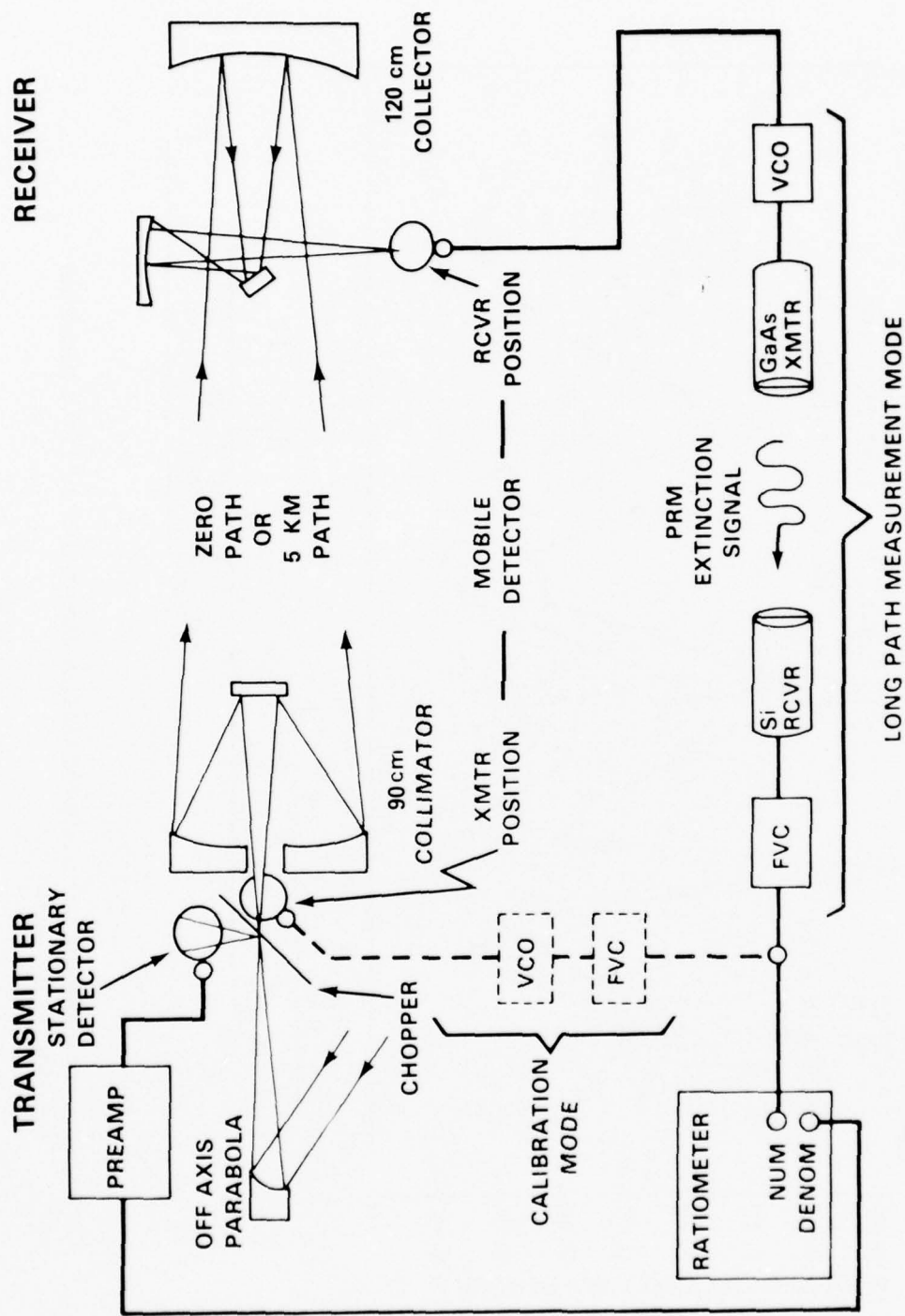


FIGURE 3. Laser Extinction Measurement Schematic
 Legend: VCO—voltage controlled oscillator, FVC—frequency to voltage converter, PRM—pulse rate modulated (extinction signal).

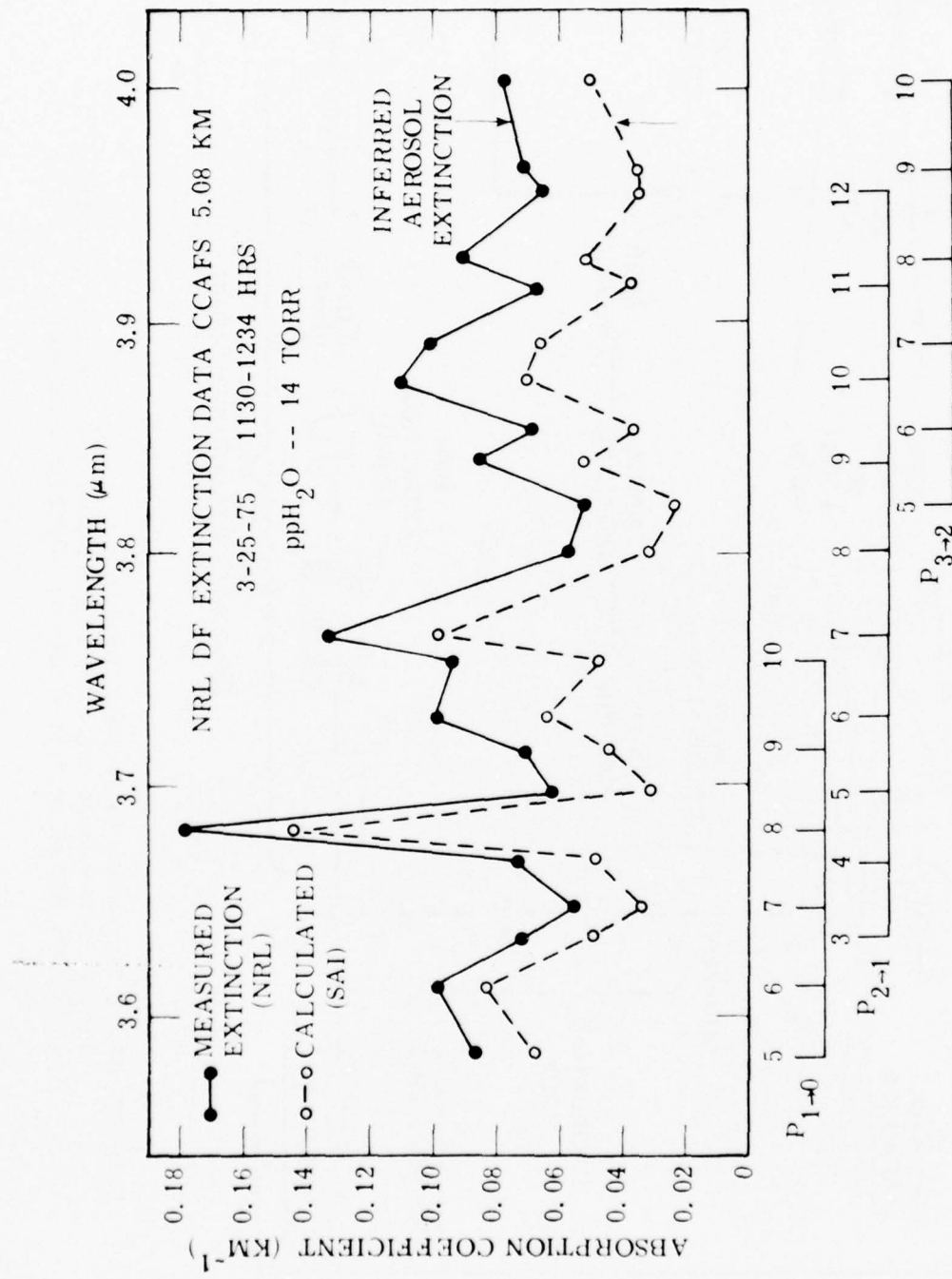


FIGURE 4. Comparison of Calculated Molecular Absorption to Field Measurements of DF Laser Extinction.

ABSORPTION VS WATER VAPOR PRESSURE

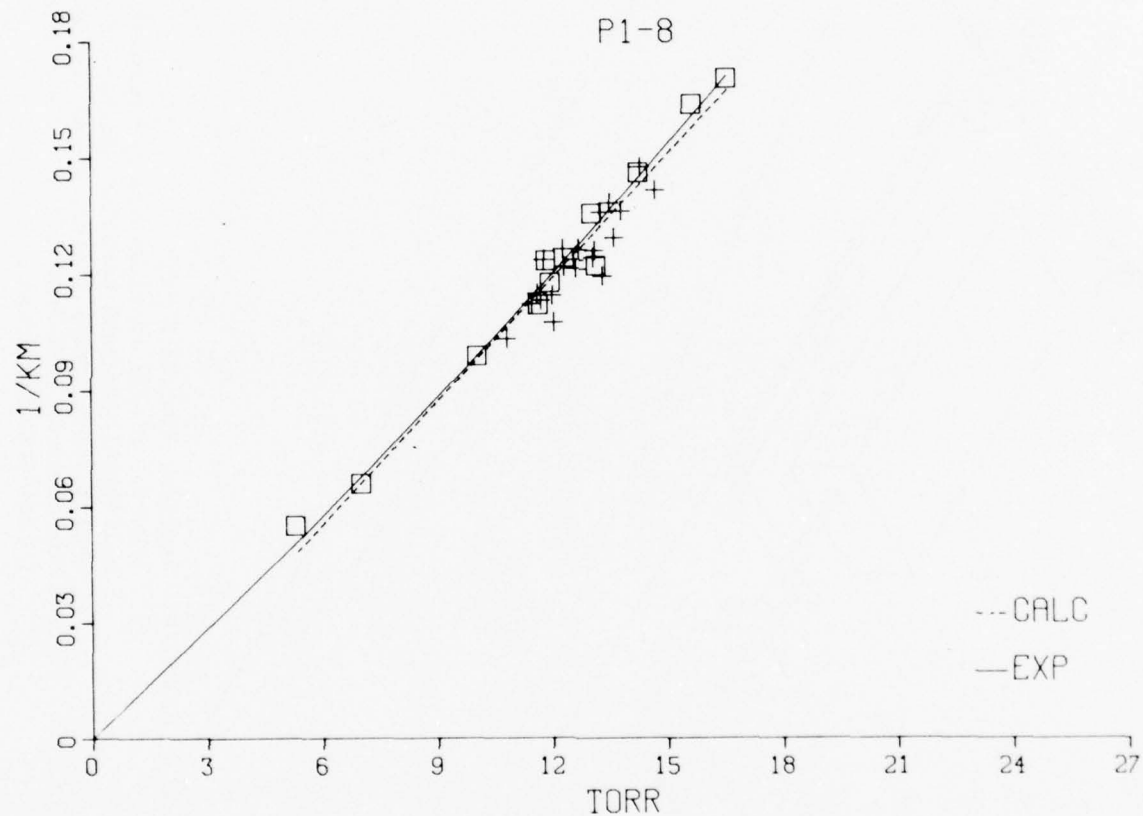


FIGURE 5. Comparison of Measured and Calculated Molecular Absorption for the P1-8 DF Laser Line vs. Water Vapor Partial Pressure.
 Legend: \square -measurements taken at Cape Canaveral Air Force Station, Florida, March 1975, $+$ -measurements taken at the TRW Capistrano Test Site, September 1975, — curve fit to experimental data, - - - curve fit to HI-TRAN calculations.

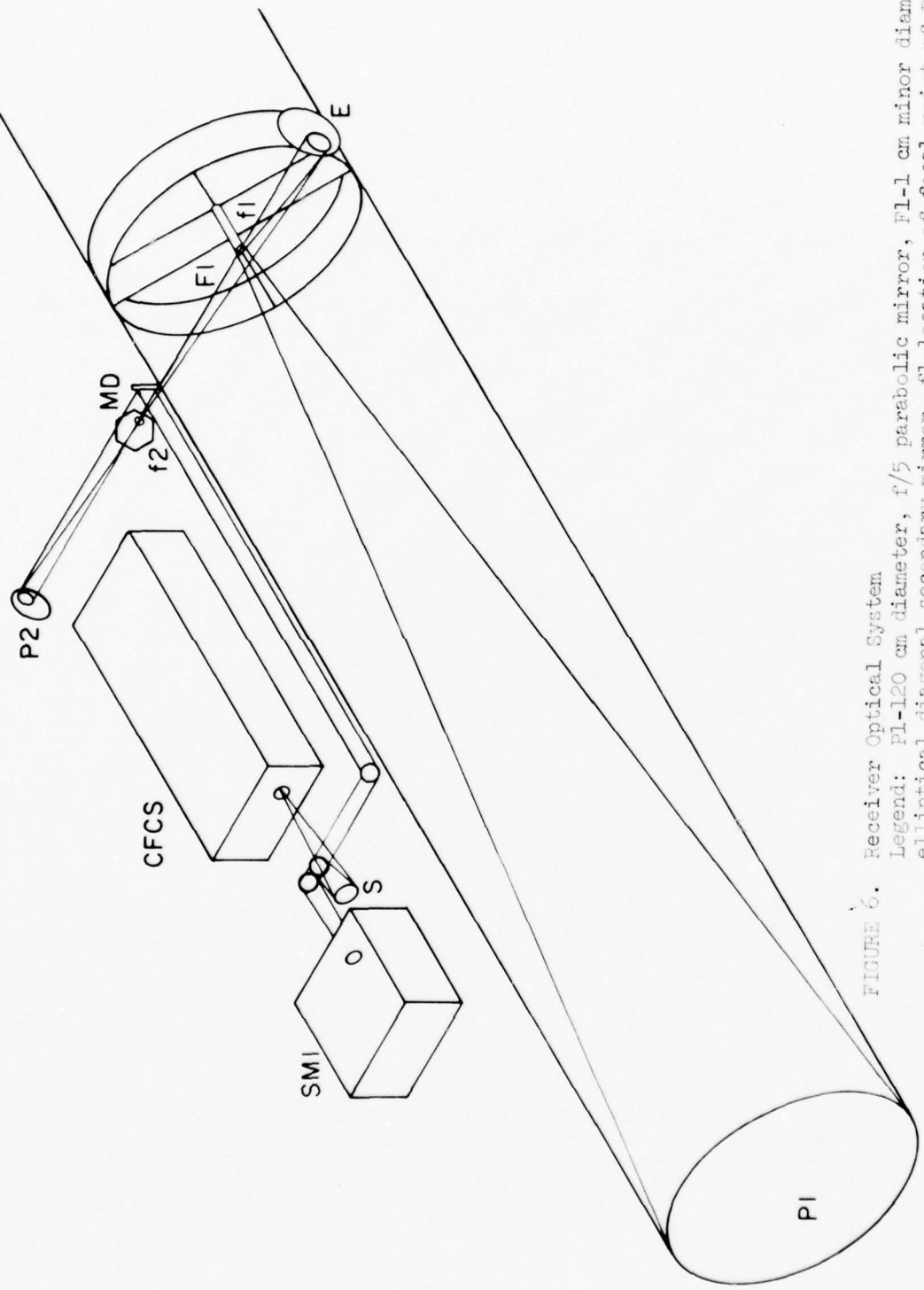


FIGURE 6. Receiver Optical System
 Legend: P1-120 cm diameter, f/5 parabolic mirror, f1-1 cm minor diameter
 elliptical diagonal secondary mirror, f2-location of focal point of P1,
 E-ellipsoidal relay mirror, MD-mobile detector, P2-re-collimating para-
 bolic mirror, SMI-Scanning Michelson Interferometer, CFCS-gas filter
 correlation spectrometer.

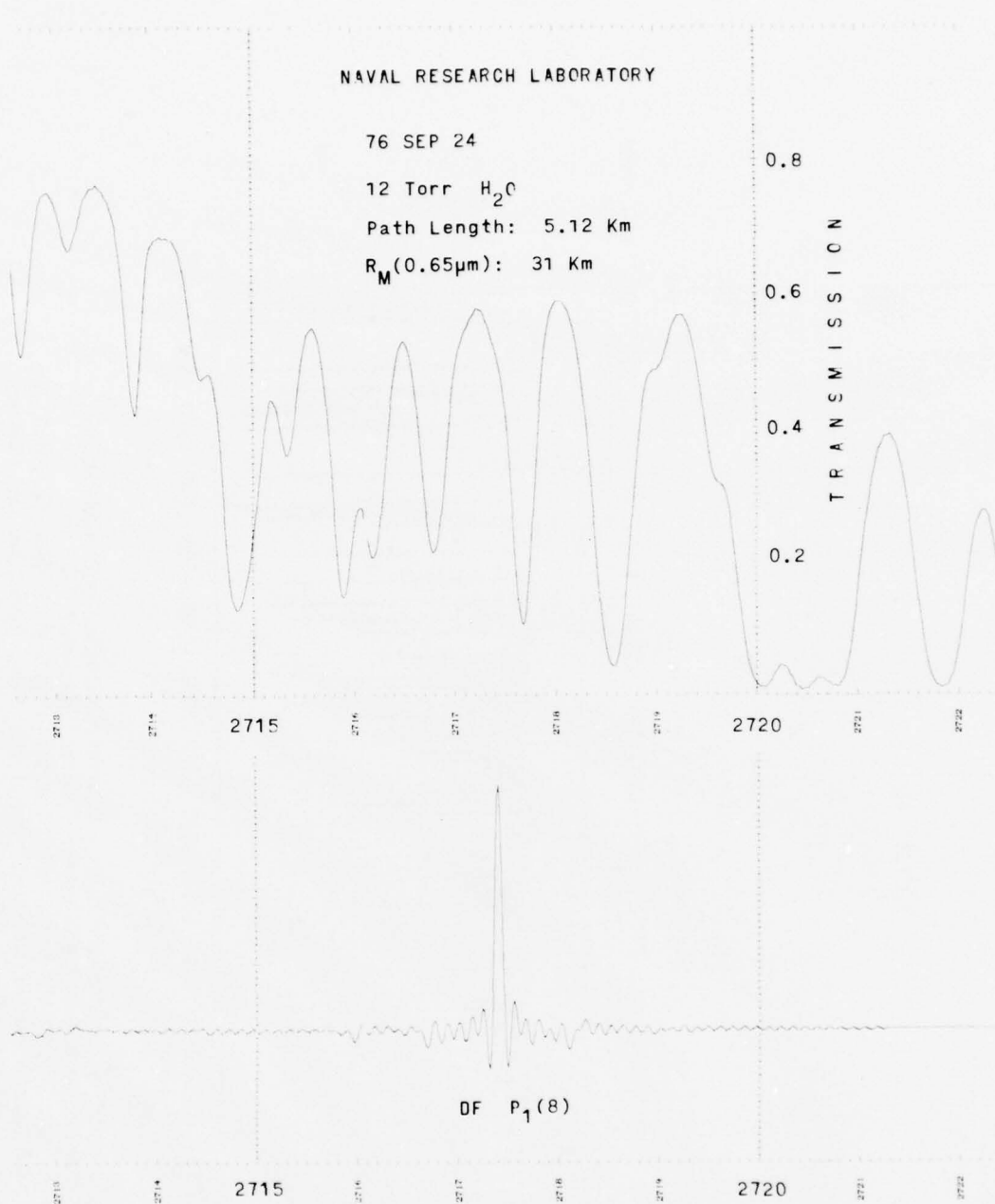


FIGURE 7. Scanning Michelson Interferometer Spectra Near 2720 cm^{-1} .
 Legend: upper trace-experimental measured transmission of a 5.12 km path for 12 Torr H_2O and a visual range at $0.65\mu\text{m}$ of 31 km. (Actual data trace); lower trace-SMI response to the P_1-8 DF laser line at 2717.538 cm^{-1} . The measured laser transmission was .51 under the above conditions and the upper trace was normalized to this value at the laser frequency.

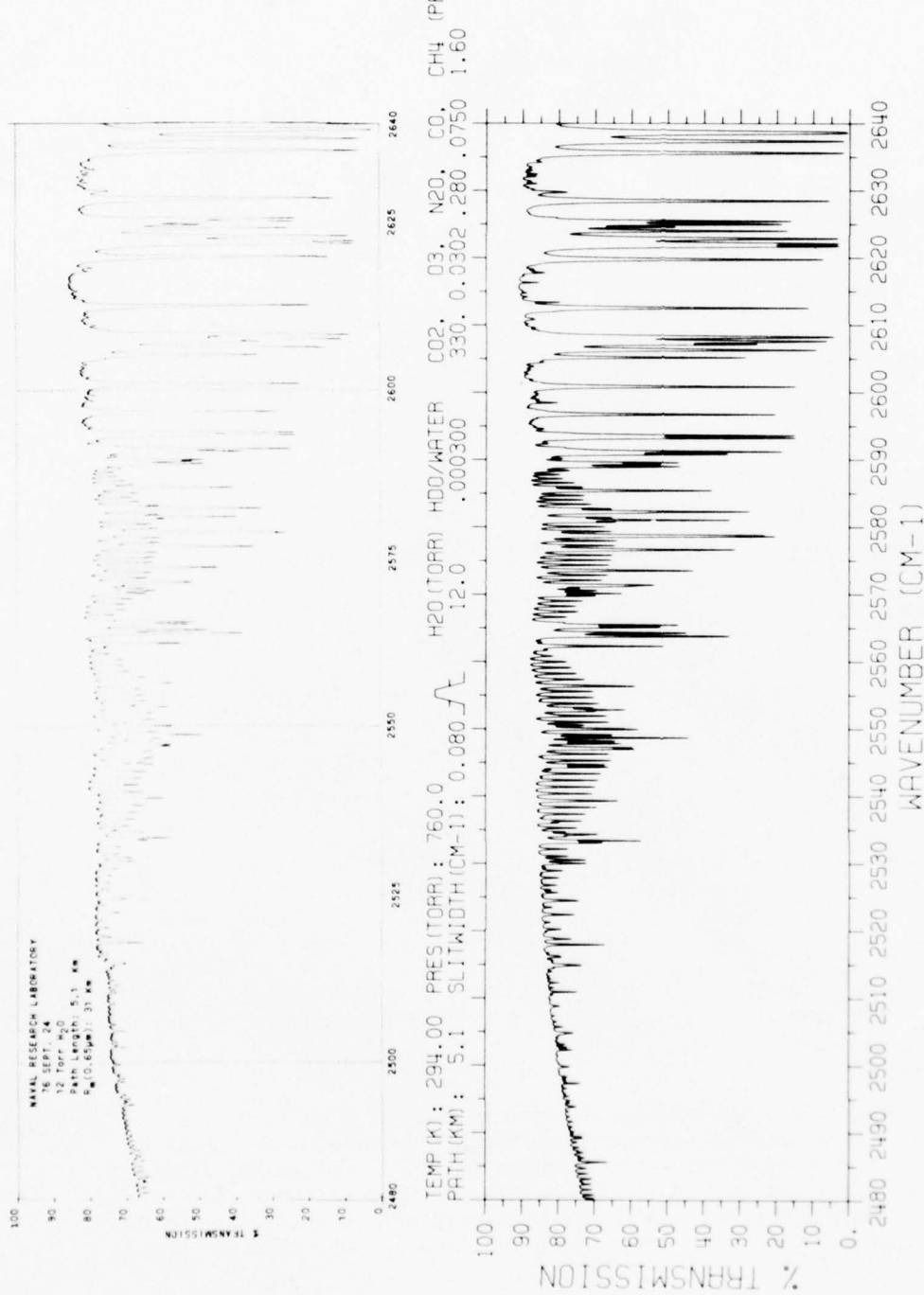


FIGURE 8. Comparison of Measured and Calculated Atmospheric Transmission Spectra in the 2480-2640 cm⁻¹ Spectral Region.
 Legend: upper trace-measured transmission for 12 Torr H₂O, 5.1 km path length and 31 km visual range (2% contrast at 0.65μm); lower trace-calculated molecular absorption¹⁰ for conditions indicated above the trace.

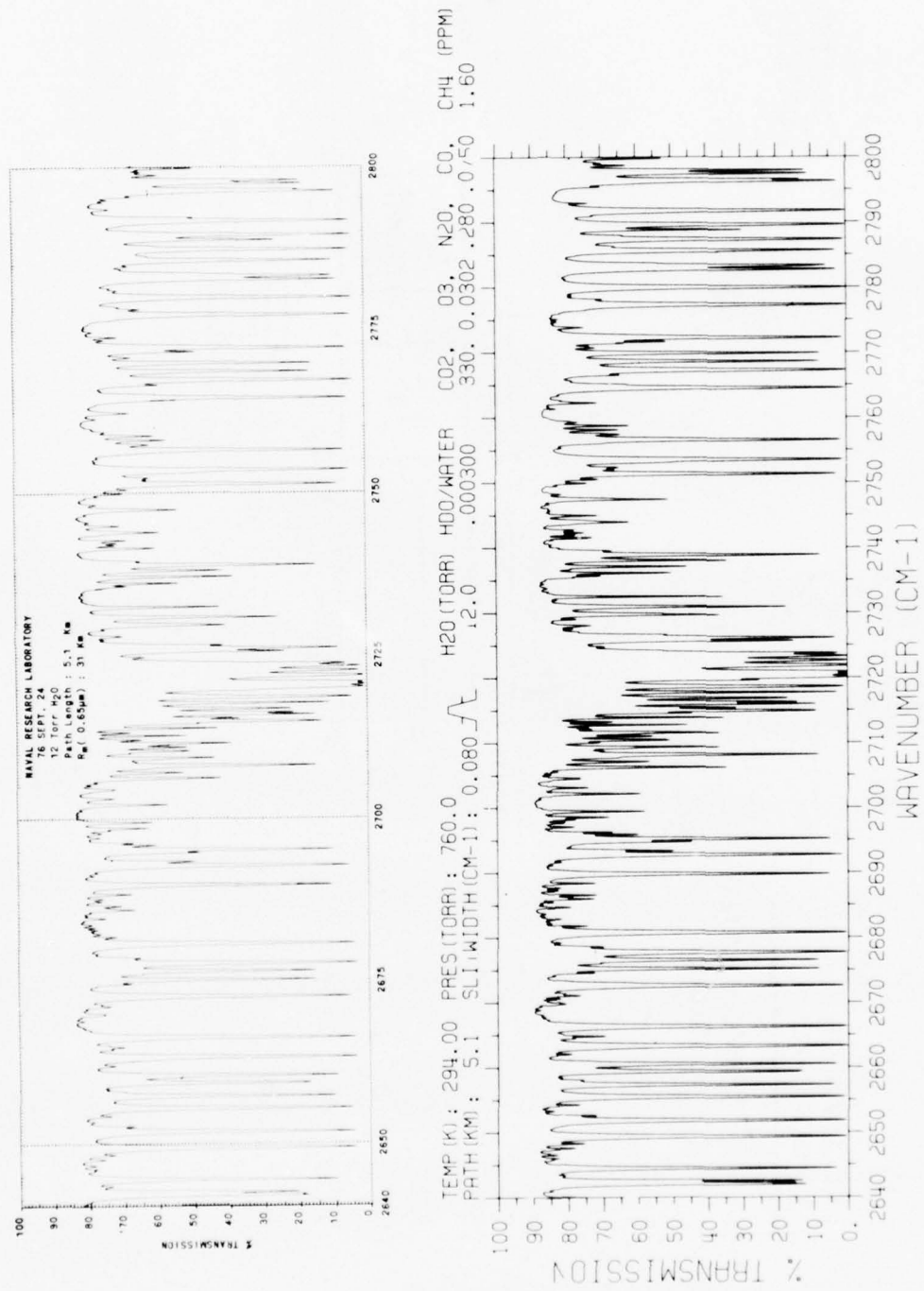


FIGURE 9. Comparison of Measured and Calculated Atmospheric Transmission Spectra in the 2640-2800 cm⁻¹ Spectral Region.
Legend: upper trace—measured transmission for 12 Torr H₂O, 5.1 km path length and 31 km visual range (2% contrast at 0.65 μm); lower trace—calculated molecular absorption₁₀ for conditions indicated above the trace.

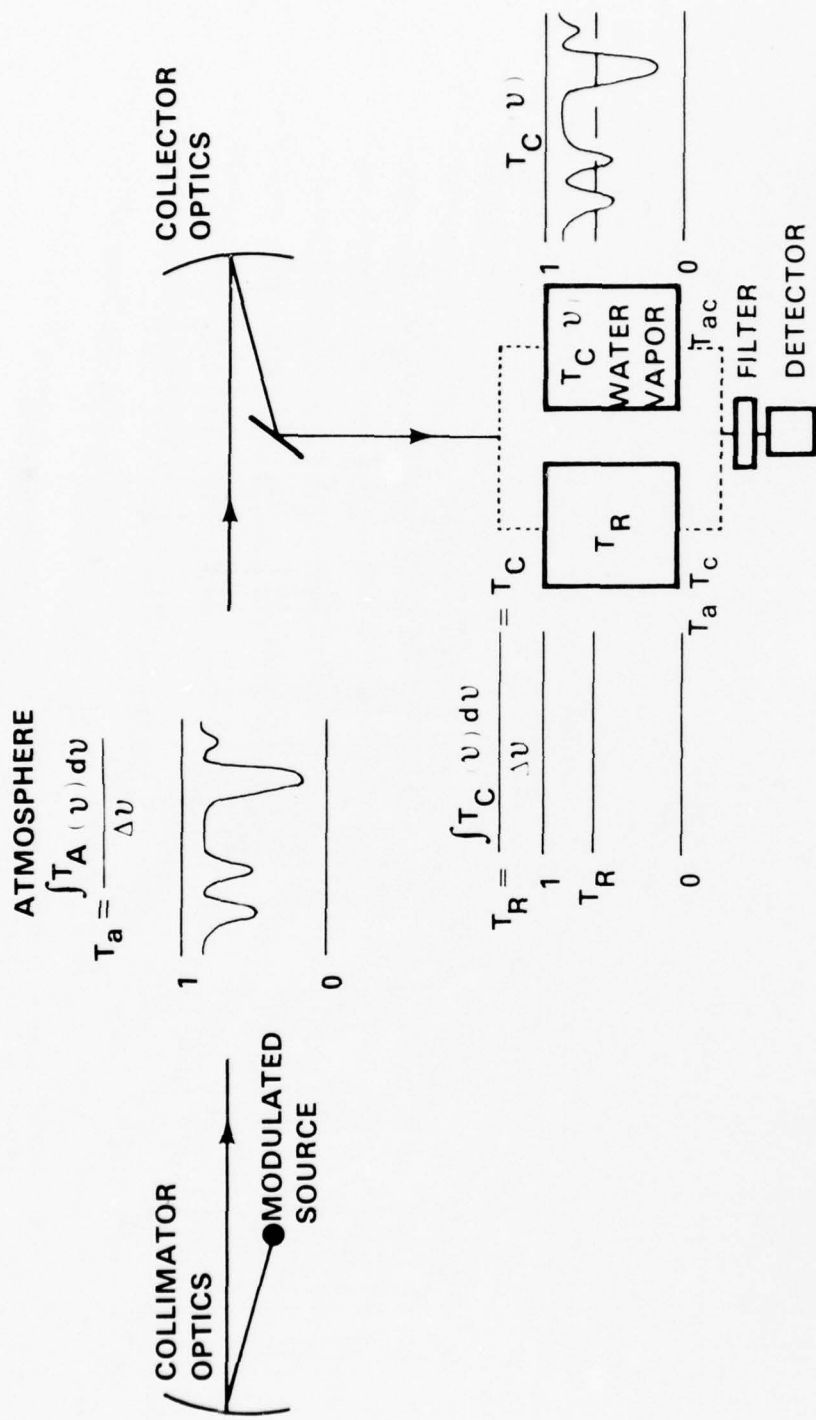


FIGURE 10. Gas Filter Correlation Spectrometer Measurement Schematic.

INTEGRAL PATH VS. FIXED POINT WATER VAPOR MEASUREMENTS

5.12 km PATH

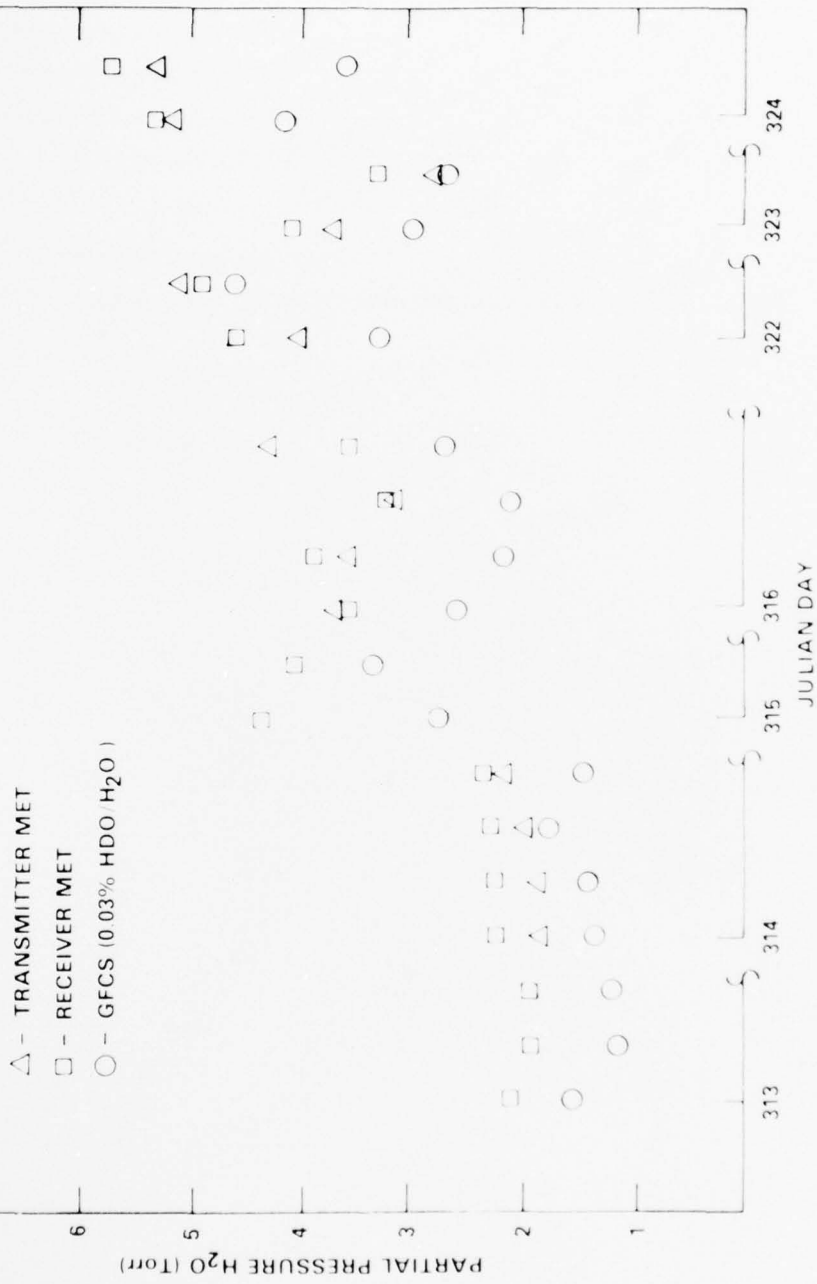


FIGURE 11. Comparison of Gas Filter Correlation Spectrometer and Fixed Point Water Vapor Measurements.

(This page intentionally left blank.)

This paper is UNCLASSIFIED

AN AEROSOL MEASUREMENT SYSTEM FOR
LASER/AEROSOL INTERACTION STUDIES

Gary L. Trusty and Thomas H. Cosden

U. S. Naval Research Laboratory
Washington, D. C. 20375

ABSTRACT

To complement a series of atmospheric laser transmission measurements, a system was designed and implemented which would allow site measurements of aerosol size distributions and other related meteorological parameters. The self-powered mobile laboratory and the equipment contained within it are described.

Two towers for mounting sensors can be located up to 40 meters from the van. Meteorological sensors are included for the measurement of air temperature, dew point, wind vector, solar radiation and barometric pressure. Two Particle Measuring Systems spectrometer probes are used for obtaining a particle size distribution from $0.1 \mu\text{m}$ to $15 \mu\text{m}$ radius. For bulk scattering measuring measurements, a 3-color nephelometer by HSS, Inc. is also included in some of the measurements. Data from all systems are recorded on a single 9-track computer tape for ease of reduction.

Representative data showing particle distributions from several locations are presented. A brief discussion of machine dependent curve modifications will be included.

A sample of the results of a comparison of the PMS probes with six other optical particle counters will be given.

Examples of the forms of output available from the data reduction programs will be presented. Included are parameters plotted vs. time of day and cross correlations between aerosol counts and several meteorological variables.

A description of the process of the calculation of an extinction coefficient from the resultant particle size distributions is given.

UNCLASSIFIED

Some problems associated with this process will be discussed.

A short description of future expansion of the system for studying spatial distributions of the aerosol field will also be presented.

SYSTEM DESCRIPTION

As stated in the title this paper describes an aerosol measurement capability used for the study of laser/aerosol interactions. The system itself will first be briefly described. This will be followed by samples of measurement results obtained over the last 2 years. Included there will be a discussion of the approach to data reduction. Finally, a presentation of the current state of this evolving system is given.

Initially, the aerosol monitoring system was put together as a support for optical transmission measurements in the field. The mobile laboratory shown schematically in Fig. 1 is the result of an effort to satisfy the requirements of that type of operation.

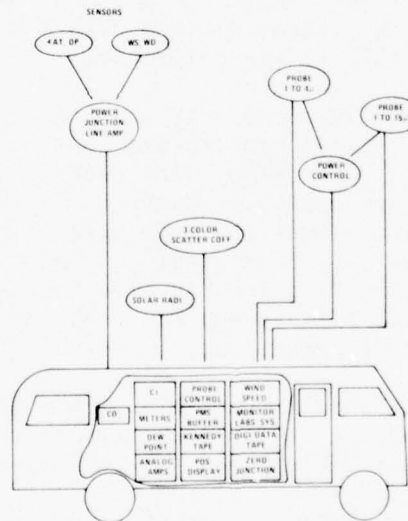


FIGURE 1. MOBILE LABORATORY

The system is composed of a vehicle for the electronic gear and two towers on which are mounted the meteorological sensors and the particle counters. The "met tower" holds sensors for monitoring air

UNCLASSIFIED

UNCLASSIFIED

temperature, dewpoint, wind speed and wind direction. The "aerosol tower" has mounted on it Particle Measuring System spectrometer probes. The PMS active probe counts and sizes particles from 0.1μ to about 4μ radius. The high volume PMS classical probe monitor particles from 1.0μ to 15μ . The two towers can be located up to 40 meters from the vehicle. Also routinely monitored are solar radiation (using an Eppley black and white pyrheliometer) and barometric pressure.

The van is a converted 25 ft. motor home, which can be driven nearly anywhere that doesn't require specialized vehicles. Inside it is the equipment which processes all the information from the two towers. The PMS Data Buffer contains 12 A/D channels for the met information and can handle up to 3 of the PMS aerosol probes. This device formats all the data and puts it on an IBM-compatible 9-track computer tape along with the year, day and time of day. Over 24 continuous hours of data can be written on one tape.

Also shown in Fig. 1 are a CO_2 monitor in the van which is available if needed and a 3-color scattering coefficient monitor. The latter instrument is a recent acquisition from HSS, Inc. It is a volume scattering nephelometer which measures light scattered forward between the cones of 45° and 55° . Three filters allow the measurement at 3 wavelengths, viz $.55 \mu$, $.7 \mu$ and 1.05μ . Further discussion of this instrument will be given in another report.

The outputs of both of the last two instruments are also placed into the A/D inputs in the PMS data buffer. In the past, spare channels have been used by other experimenters for ease of comparison with the aerosol and met data, e.g. for fog visiometer and MRI nephelometer outputs.

Data reduction is currently done by taking the magnetic tape back to the computer center. As well as printed data, graphical output is also available in 2 primarily forms. The first, shown in Fig. 2 is a plot of a 6 minute average aerosol distribution. Also on this dV/dr vs. r plot is given the total number of particles for the size range covered, and the cross sectional area and the volume of the particles in that size range. The squares and circles on the plot indicate 2 ranges of the active probe, the triangles denote data from the classical probe. For a typical data run, one of the plots is produced for each hour, although any time and time average is available upon request.

The second format output of the data reduction gives any of the met variables and some particle information plotted versus time of day. An example is shown in Fig. 3. In the upper graph is plotted the number of particles of certain size ranges as indicated by the

UNCLASSIFIED

UNCLASSIFIED

legend. These values are obtained by integrating curves of the form shown in Fig. 2. The lower shows the solar radiometer readings for the same times. Cross correlations between data sets for the same day are routinely made.

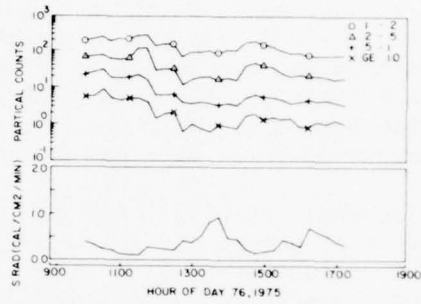
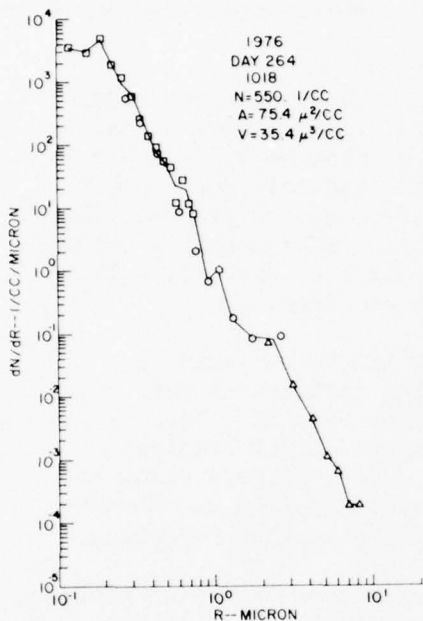


FIGURE 3. SAMPLE TIME-OF-DAY PLOTS

FIGURE 2. SAMPLE 6 MINUTE AVERAGE DISTRIBUTION

The example of Fig. 3 is given to point out a particular phenomenon. With respect to correlations, this day shows a particularly strong negative correlation between particle count and solar radiation for this day of broken clouds. For the appropriate humidity conditions, the following occurs. When the sun comes out from behind a cloud the particle count decreases as the individual particles are "boiled" down to a smaller size, this shifting the dN/dr curve to the left. When the sun goes back behind the cloud the opposite occurs. The importance of this is that it is important if an attempt is made to compare the point location aerosol measurement with a long path transmission experiment. It could easily be the case that the aerosol counter could be reading something that is not at all representative of the entire path under these and other conditions. More will be said about the spatial distribution of aerosols problem at a later point in this paper.

UNCLASSIFIED

UNCLASSIFIED

Some typical aerosol distributions made with the system before the addition of the high-volume Classical probe are shown in Figs. 4, 5 and 6. Three representative samples from a beach at Cape Canaveral are shown in Fig. 4. Note, there, that in general the slope of the curve is approximately the same ($\approx r^{-4}$) for those times; only the number has changed. There were days, however, when this was not the case.

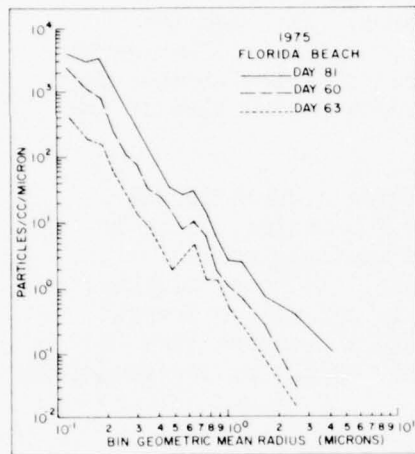


FIGURE 4. FLORIDA BEACH DISTRIBUTIONS

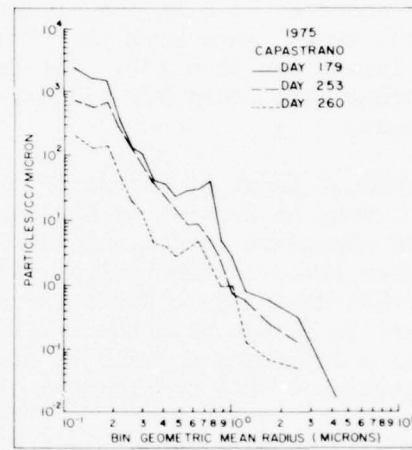


FIGURE 5. CAPISTRANO TEST SITE DISTRIBUTIONS

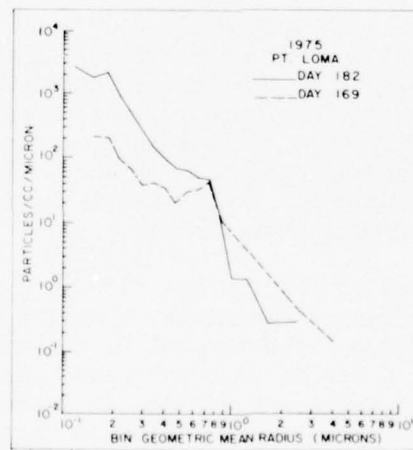


FIGURE 6. PT. LOMA DISTRIBUTIONS

UNCLASSIFIED

UNCLASSIFIED

In Fig. 5 is shown measurements made at the TRW Capistrano Test Site on the west coast. The sampling location was about 3 miles inland. Note, again, that the three curves could be roughly approximated by an r^{-4} slope with a varying total count.

Before becoming too complacent about the r^{-4} usage, however, consider in Fig. 6 the two samples taken on Point Loma in San Diego, CA. There the sampling was done at a point several hundred meters from the shore at an altitude of about 120 meters. Although the solid line shows, once more the r^{-4} dependence, the dashed line gives a slope less steep than r^{-3} . The latter was due to a low stratus fog which became more dense but was not at all evident at the time of the measurement.

An obvious point of interest in the last three figures is the prominent bump on several of the curves near 0.7μ radius. This is a machine dependent result and occurs due to a multiply valued sensitivity curve in the active scattering probe. It does, however, seem to also depend on other factors since it is not always present. It appears to change with the relative humidity, indicating that the different curve forms are due to either an index change or the sphericity of the particles or a combination of the two.

It should be pointed out that Fig. 2 is yet another sample distribution; one that includes the high-volume Classical scattering probe. The addition of this probe gives an obvious increase in knowledge of the distribution. The location for this sample is near the Chesapeake Bay about 40 miles southeast of Washington, D.C.

In the summer of 1976 we joined several other experimenters on an expedition to Trinidad, CA to make measurements on the recurring fog at that location. Many optical particle counters were available at the site. On several occasions of clear conditions, the optical counters were gathered to monitor a similar natural air sample in order to make comparisons between counters. Figure 7 is one result of that comparison. A more detailed evaluation involving about 14 such comparisons is being prepared for another report.

Since one of the purposes of the van and its equipment is the support of optical transmission measurements, a method for calculating the predicted extinction from a given aerosol distribution must be available. This is done in a second pass software operation on the data, i.e., files containing the averaged size distributions for the time desired are used with Mie scattering theory to calculate the desired scattering properties.

UNCLASSIFIED

UNCLASSIFIED

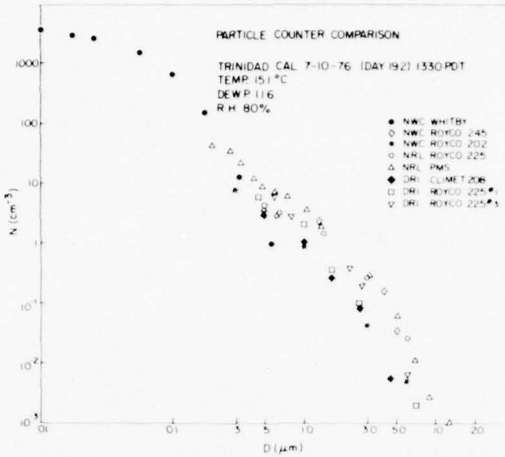


FIGURE 7. PARTICLE COUNTER COMPARISON

The extinction coefficient is calculated from the size distribution as shown in Eq. 1,

$$\sigma_{\lambda,n} = \int_0^{\infty} Q(\lambda,n) \frac{dN(r)}{dr} \pi r^2 dr \quad (1)$$

where σ is the extinction coefficient, dN/dr is the size distribution, r is the radius of the particle and Q is the Mie efficiency function for extinction, which is dependent both on λ , the wavelength and n , the complex index of refraction.

In doing this calculation, several assumptions are made. The first is that the particles are spherical. The second is that the index is not only known, but is taken to be constant over the distribution. Under many conditions, these assumption may be quite acceptable, e.g., under conditions of high relative humidity. When the assumption are not good the resultant error in the calculation may still be small. The particular situation must be evaluated.

To give an understanding of the process of the calculation, Eq. 1 is regrouped into the form

$$\sigma = \int r Q dS \quad (2)$$

UNCLASSIFIED

UNCLASSIFIED

where dS is referred to as the differential cross sectional area. Taking Fig. 8 as a sample distribution, the pieces of the integrand of Eq. 2 are plotted in the upper half of Fig. 9. The dS for that distribution is plotted there as well as the Mie scattering function for two different indices of refraction. The Q shown is for 3.8μ radiation. To do the integral of Eq. 2 one starts at the left of the plot, forming a product of the first QdS pair, which is added to the product of the next, etc., until the integral is finished. The resultant "running integral" obtained in this manner is shown in the lower half of Fig. 9. Four of them are shown for different values of the index of refraction.

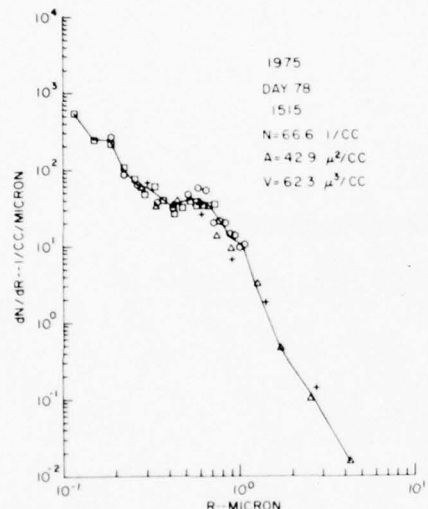


FIGURE 8. DISTRIBUTION FOR
CALCULATION DISCUSSION

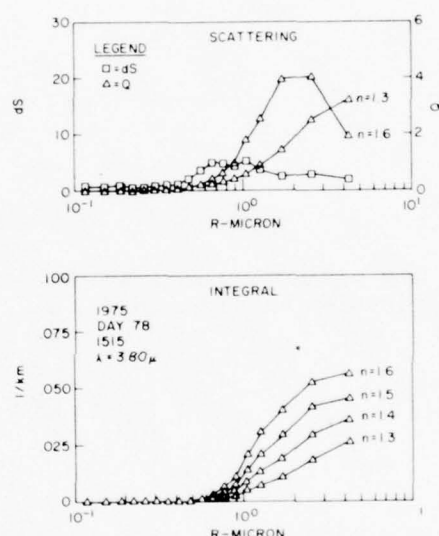


FIGURE 9. EXTINCTION CALCULATION

Equation 1 showed the integral to be over all particle sizes. Equation 2 shows only an integral over r , indicating that the integration is to be done only over the known range of the distribution. The importance of the form of the running integral is that it shows whether the integration is "finished". That is, in order for the integration to be complete, the curves of the running integral must be reaching a horizontal asymptote. Thus for this example, if the particles had an index of 1.6 the integral is nearly complete; if the index was 1.3 then more information is obviously needed about larger particles than is shown by the distribution. This sample distribution was obtained with only the active PMS probe

UNCLASSIFIED

UNCLASSIFIED

which was unable to count particles beyond about 5μ . Although it was sufficient for some distributions, it was not usually the case. The addition of the high-volume Classical probe to extend the range of the measurement alleviated this problem as will be shown below in another example.

Recently, during a field trip an unexpected occurrence produced some results which are thought to be quite interesting. While making aerosol distribution measurements under conditions of very clear air, a large cloud of smoke passed through and around the particle counting equipment. It happened that a machine gun was being tested about 150 meters directly upwind. A full 2 minutes of smoke from a 30 caliber machine gun was thus made available to us. This occurred twice during the day.

The particle size distributions during one of those periods is shown in Fig. 10. The distributions shown there are 1 minute averages. The 1514 time is before the smoke reached the counters. The unusual structure at the center of that curve is due to low counting statistics of the Active probe and the way the curve was chosen from the original data. The curve at 1515 is fully into the smoke as was 1516 which was nearly identical. At 1518 only a slight hint of the smoke shows in the large particle portion of the spectrum.

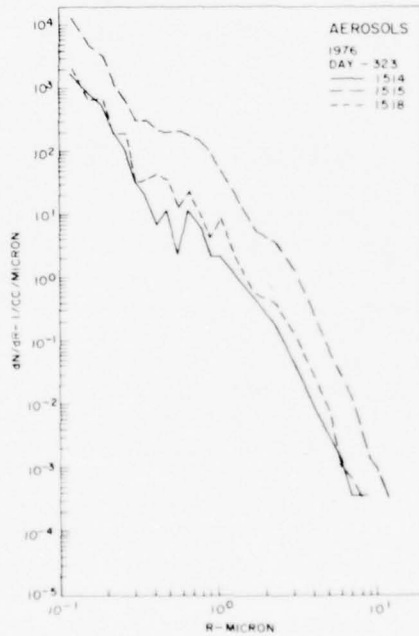


FIGURE 10. SMOKE DISTRIBUTIONS
UNCLASSIFIED

UNCLASSIFIED

A question was raised as to what extinction this smoke might present to 3.8μ radiation. Assuming the particles to be spherical and made primarily of water, a calculation was done to address this question. The results of the calculation are shown in Fig. 11.

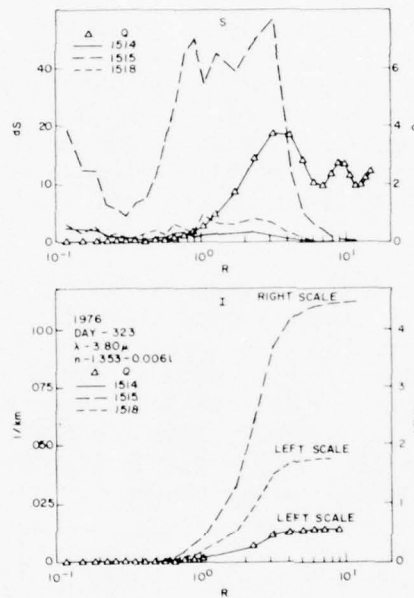


FIGURE 11. EXTINCTION CALCULATION IN SMOKE

In the upper portion it can be seen that most of the cross section presented to the beam is of a fairly limited size, a point that is not surprising, but one that shows up very well in this type of presentation. The lower half of the figure shows two things of interest. First, there is enough knowledge about the distribution shape in the large size end of the particle spectrum to "finish" the integral. Secondly, the seemingly small difference in the distributions at 1514 and 1518 results in nearly a factor of 4 difference when the extinction calculation is done.

It was stated earlier that one of the major problems presented in the optical propagation field involves the comparison of long path transmission measurements with point measurements of the extinction media. The cloud modulation of solar radiation produced a subtle but important example. More blatant is the effect of smoke.

UNCLASSIFIED

UNCLASSIFIED

Equipment is currently being assembled to begin a detailed study of this spatial distribution of aerosols. A small trailer which will be used as a remote station is being outfitted with a PMS classical probe and the required meteorological gear. The trailer configuration is shown in Fig. 12. Also seen in that figure is the microwave dish associated with the data link which will be capable of sending the information back to the main station (the van) at distances up to 10 km.

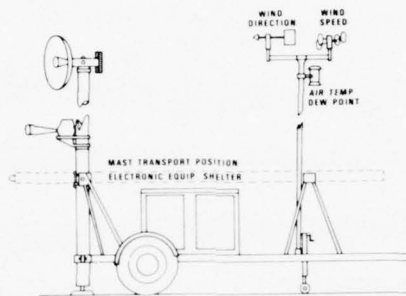
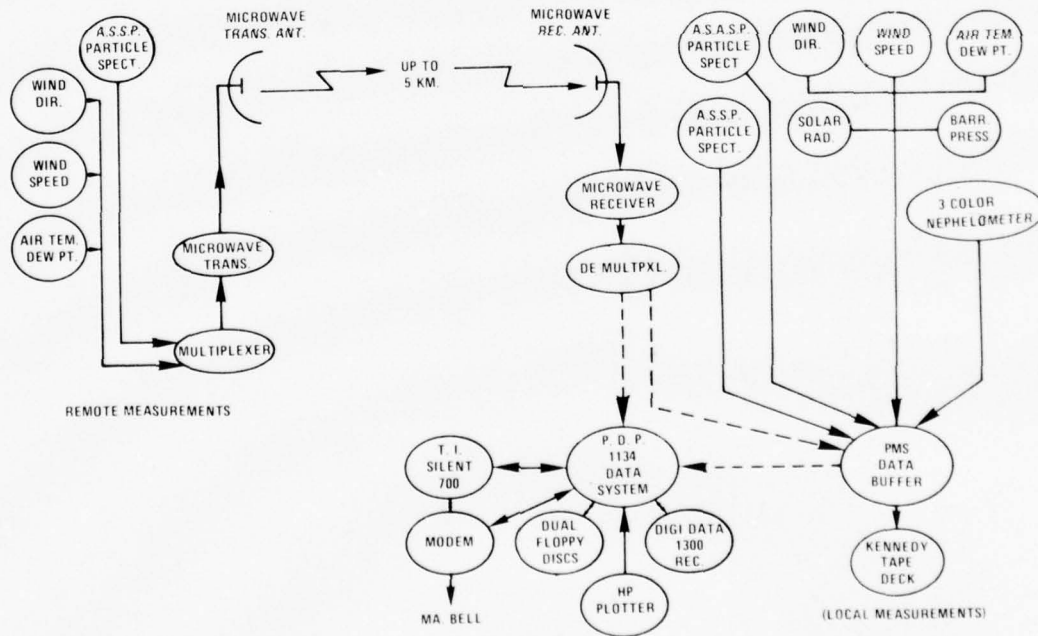


FIGURE 12. REMOTE AEROSOL STATION

FIGURE 13. AEROSOL MEASUREMENT SYSTEM
UNCLASSIFIED

UNCLASSIFIED

The entire proposed system is shown in Fig. 13. The PDP 11/34 Data System will be used for on-line examination of results; a capability sorely needed when operating in the field. With this system an important piece of information can be obtained concerning the spatial distribution of both aerosols and water vapor. By making measurements with different separations of the stations, and under various meteorological conditions the error budget associated with extrapolating point measurements to an extended path can be properly assessed.

This work sponsored in part by the Naval Sea Systems Command PMS-405/ PM-22.

UNCLASSIFIED

....This paper is UNCLASSIFIED

TESTING THE STANDARD MARINE ATMOSPHERE CONCEPT

Stuart Gathman
Naval Research Laboratory
Washington, D.C.

ABSTRACT

The vast marine meteorological data base amassed by the mariners of the world over the last century unfortunately does not provide information on certain parameters essential for the evaluation of electro-optical propagation through the atmosphere. An effort of similar magnitude in order to obtain these desired parameters in statistically significant quantity is out of the question. Although there exist several models which relate the desired parameters to shipboard observables, no statistical assessment of these parameters is directly possible because of the well known inequality that even the time average of a function of several variables is not equal to the functional value obtained by substituting into the functional formula the mean values of the variables. Therefore this paper describes a Monte-Carlo technique which computes from the existing marine meteorological data base, the desired statistics of any meteorological parameter significant in electro-optical propagation for which a model exists. In order to test this concept, a standard atmosphere consisting of a set of ogives of the shipboard observables of wind speed, air temperature, relative humidity, air-water temperature difference, and atmospheric pressure was assembled from the 1975 Fog cruise of the USNS Hayes in the area of Nova Scotia and Newfoundland. Ogives of turbulence and aerosol parameters were computed using this technique and the statistical results are then compared with the results of direct measurements made on the same cruise. This comparison shows that given an appropriate model, reasonable statistics of any parameter can be obtained from the existing data bases.

UNCLASSIFIED

INTRODUCTION

It is desirable to know the probability of occurrence of certain meteorological parameters which are believed to be important in the propagation of electro-optical energy through the marine atmosphere.

The historical climatologies represent a concept which could be useful in this respect. All of the available data can be presorted and expectation values of the key parameters are presented as functions of time of year and position. A naval officer who wishes to know how an electro-optical weapon system might perform the next day at a certain geographical location could use such an historical climatology. The precision of such a prediction could be improved however if he knows something else about the situation other than the date and position. If his shipboard measurements indicate an unusually cold air temperature for this time of year for instance, this type of information should be able to be used to increase the precision of the prognosis.

Unfortunately many of these specific parameters (for example the refractive index structure parameter) have not been measured enough to even provide the most rudimentary kind of historical data bank on the statistics of these parameters. At best representative values and/or empirical relationships between these desired parameters and the historically accumulated shipboard observations are all that can be provided in many cases. When such models are used they must be functions of observable parameters which are included in the historical data bank.

The most direct approach which utilizes these models is that of calculating the desired output function value from several simultaneously measured input parameters. Therefore in order to obtain statistics of the output function value, large groups of simultaneously measured input parameters are required. Using this technique then it would never do to use the wind speed data measured at dawn with the air temperature data measured at sundown nor the humidity data from ship "i" with the pressure data of ship "j". In order to design experiments with this technique one first must sort out the desired data group from the entire data bank and then from each complete simultaneously measured data group the desired manipulations can be done. Computed statistics from a large number of such operations comprise the statistics of the measurement.

UNCLASSIFIED

UNCLASSIFIED

An alternate approach (which does not require such an extensive data base to operate successfully) is to employ a Monte Carlo technique to generate the required input parameters. A Monte Carlo method solves the problem by means of a series of statistical experiments which are performed by applying mathematical operations to random numbers. This approach substitutes the requirement of having simultaneous measurements to that of requiring that each of the input parameters must be statistically independent of each other.

It is suggested that such directly measured parameters as: wind speed, air temperature, relative humidity, air - water temperature difference, and atmospheric pressure are sufficiently independent so as to be useful in such a Monte Carlo problem as of finding the true cumulative distributions of C_N^2 and aerosol size distribution.

If such a conclusion can be justified, then the required data bank for the prediction of parameters such as the refractive index structure parameter can be considerably reduced over that required in the direct approach. Using the Monte Carlo method, if certain parameters are known apriori to be within certain limits, it is quite a simple task to upgrade the data input in order to improve the "custom" calculation of the probability characteristics of key electro-optical parameters.

THE MONTE CARLO TECHNIQUE

The elementary technique used to generate the data in this paper is sketched briefly below. Prerequisites to using the technique are: first to have an appropriate model which defines the desired output function value in terms of measurables. There are at least two models at the present time which give either the refractive index structure parameter or the temperature structure parameter in terms of shipboard observables. One model is given by Friehe (1976) and is sometimes known as the bulk aerodynamic model, and the other is the work of Davidson of the NPGS and is also known as the Richardson's number model. Other models such as one by Fitzgerald and Ruskin (1976) are available to calculate aerosol size distributions in terms of shipboard observables. The second prerequisite is to have frequency distributions of all of the input parameters.

The procedure is to calculate random numbers between the maximum and minimum found in the input frequency distributions for each particular parameter. The next step is to

UNCLASSIFIED

UNCLASSIFIED

keep a frequency distribution of the random parameters used for the experiment. If at any point the frequency distribution of the random parameters exceeds the input parameter frequency distribution, the computer is to try another random number and to keep trying new random numbers until this condition is met. This process keeps going until a full set of semi-random input parameters is available. This set is then used to calculate the model value for the individual experiment. After N experiments, the frequency distributions of each of the random parameters which were finally kept for use in the experiment very closely resembles the input frequency distributions. In addition, the statistics of the results of the experiments may be kept and displayed at the conclusion of the random number experiments. This technique has a small flaw in that the standard deviation of the chosen random numbers tends to decrease as the numerical experiments continue. This problem could probably be overcome by a complete mixing of the random parameters prior to the actual calculation of the model values.

The data obtained from this technique is of course subject to several assumptions. It was mentioned earlier that a prime requirement is that the variables are truly independent of each other. Secondly the data from using this technique can only be as accurate as the model being used to describe the phenomena. Finally we assume that the input data used in the input frequency distributions is exactly what the designers of the model had in mind when the model calls for certain input parameters. To illustrate this last point, consider the so called sea surface temperature. Some sea surface temperature data is obtained from infrared thermometers aimed at the sea surface and these instruments provide true measurements of the temperature at the air-water interface. Other sea surface temperature data are obtained from "towed fish" or from bucket measurements. These devices measure water temperature below the air-sea interface. These simultaneously obtained temperatures can differ from each other by significant amounts but this difference is the result of real air-sea interface processes causing large temperature gradients near the surface and thus causing the apparent discrepancy between the two types of instruments. Because of these assumptions direct testing of the technique is necessary before it is credible.

INITIAL TESTS

An excellent opportunity to test this and other concepts is now available from the large broadly based data archive

UNCLASSIFIED

UNCLASSIFIED

which resulted from the recent marine fog cruise of the USNS Hayes, 29 July- 27 August 1975. This archive contains measurements of the temperature structure parameters which were obtained by Russell and Schacher (1976) at two levels by spectral analysis of temperature fluctuation data from 2.5 micron diameter platinum wires. The data from their report consists of 235 individual temperature structure parameter determinations taken throughout the portion of the cruise represented by the track shown in figure 1.

Throughout the same period of time many different meteorological measurements were taken on board the ship by many different investigators. Cumulative distributions of hourly observations of some of these key measurements are shown in figures 2 thru 4. The choice of why a particular instrument out of several available was chosen to represent a certain parameter was arbitrarily made. These distributions were then used as the input to a Monte Carlo program with the results shown in figure 5. This figure also shows two cumulative distributions obtained directly from Russell and Schachers data, one for the mast measurements and one for the bow tower measurements. Another scale is shown on the top of the figure which translates the temperature structure parameter into the refractive index structure parameter for ease in comparison with optical propagation problems.

The measurements show that a standard atmosphere of C_N^2 values for this region and time (ie the most probable 50% of the observations) were within the range

$$3 \times 10^{-15} > C_N^2 > 5 \times 10^{-16} \quad (m^{-2/3})$$

whereas the Monte Carlo method predicted the standard atmosphere to have values within the range

$$5 \times 10^{-15} > C_N^2 > 1 \times 10^{-15} \quad (m^{-2/3})$$

Similar methods using the data from cumulative distributions of windspeed and relative humidity can be used to predict a standard atmospheric aerosol distribution. Such a distribution is shown in figure 6 where the hatched area represents the standard atmosphere distribution (50% of the aerosol size distributions should fall inside of this area). A small randomly chosen set of measured size distributions from the USNS Hayes 1975 fog cruise is superimposed on this data. Here again predictive theory and experiment show a degree of agreement which I consider optimistic for an experiment

UNCLASSIFIED

UNCLASSIFIED

of this nature. I believe that refinements in both theory and instrumentation would reduce the offsets shown in figures 5 and 6.

CONCLUSION

In conclusion it should be noted that the above experiments were carried out in a very small portion of the ocean. NRL is planning a similar cruise for May and June 1977 which among other things will provide a broad data base for parts of the open North Atlantic and the Mediterranean Sea. If the standard atmosphere concept holds as well for this experiment as it did for the Nova Scotian data, I believe that the Monte Carlo computer method operating under the constraints of the "custom updated" historical data bank could be a valuable tool in the hands of an officer attempting to predict the quality of the operation of his electro-optical systems at some future date and place. Model development as well as the obtaining of good data on which the models can be tested are important areas for the establishment of an electro-optical climatology which can be improved as the data base is improved.

REFERENCES

- 1) Davidson, K. (1976) private comm.
- 2) Fitzgerald, J.W. and Ruskin, R.E. (1976)
"A model of the marine aerosol size distribution as a function of windspeed and relative humidity", proceedings of: Workshop on Remote Sensing of the Marine Boundary Layer 9 - 11 August 1976, Vail, CO. NRL mem rpt#.....
- 3) Friehe, C.A. (1976), "Estimation of the refractive-index temperature structure parameter in the atmospheric boundary layer over the ocean", Applied Optics (in press)
- 4) Russell, J.B. and Schacher, G. (1976) "Preliminary data analysis of turbulent wind and temperature measurements" Marine Fog Cruise - USNS Hayes, 29 July - 27 August 1975 NRL Report #8

UNCLASSIFIED

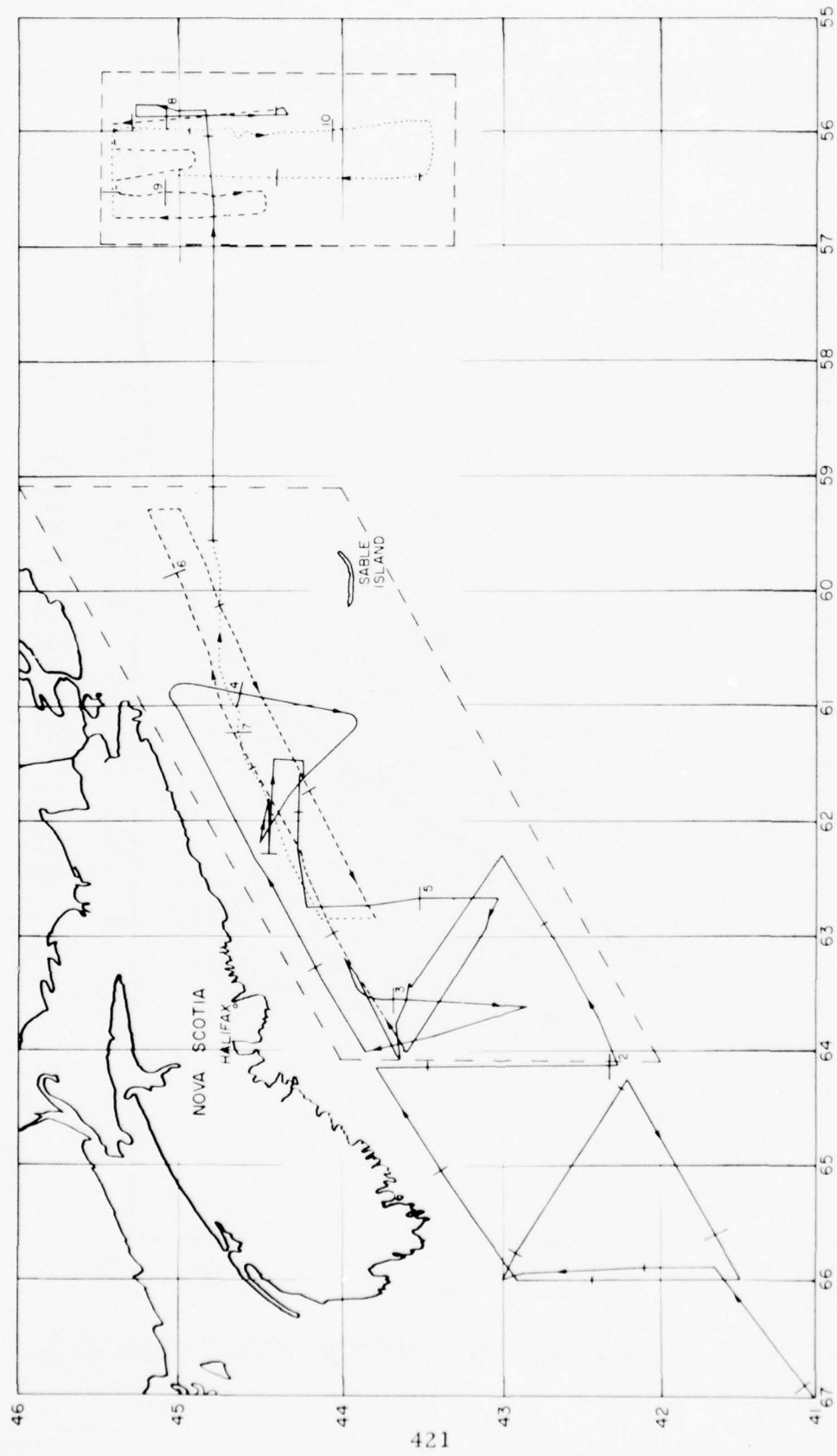


Fig. 1 Cruise track of USNS Hayes - 1975 (figure and caption unclassified)

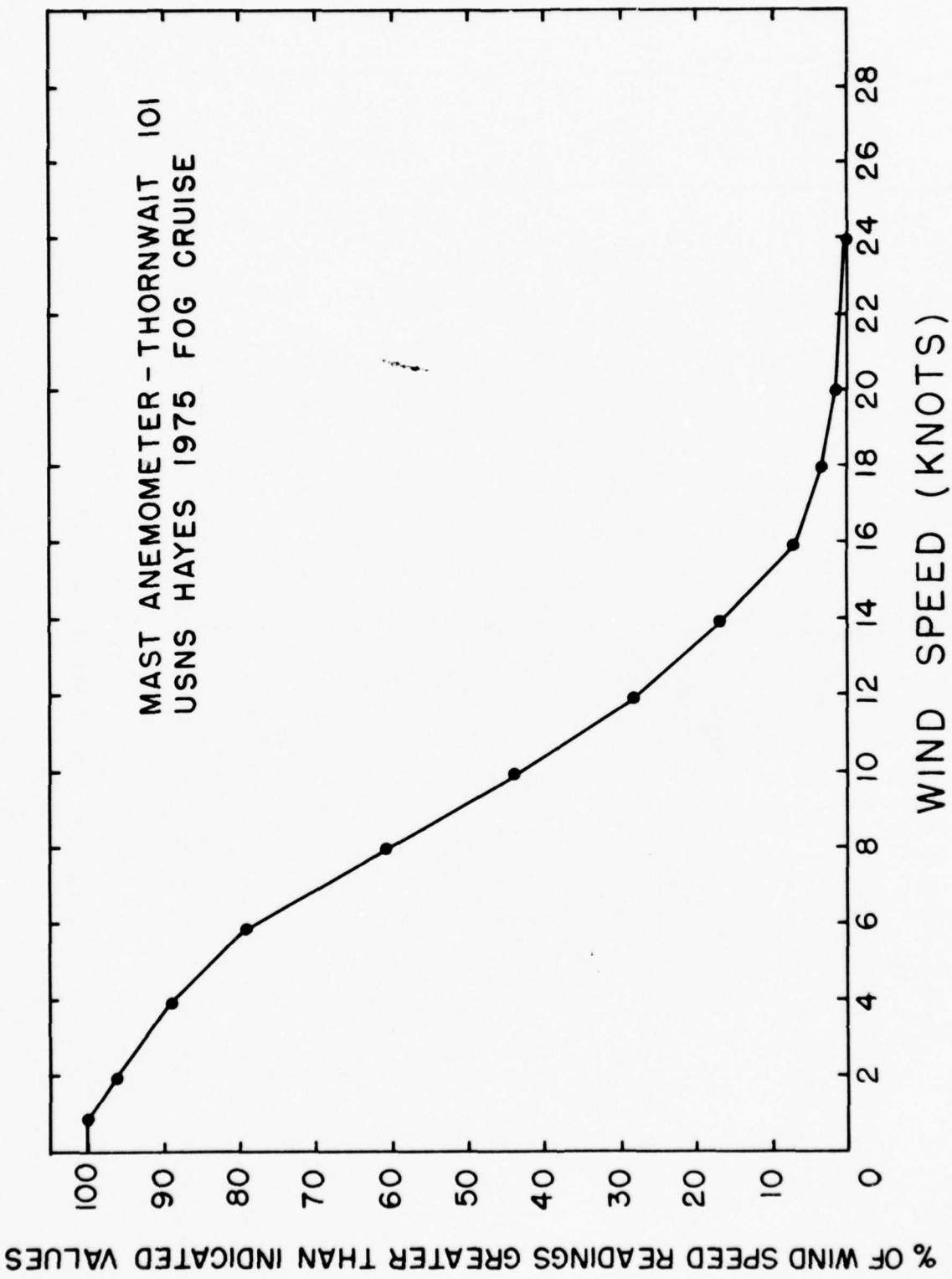


Fig. 2 Wind speed data (figure and caption unclassified)

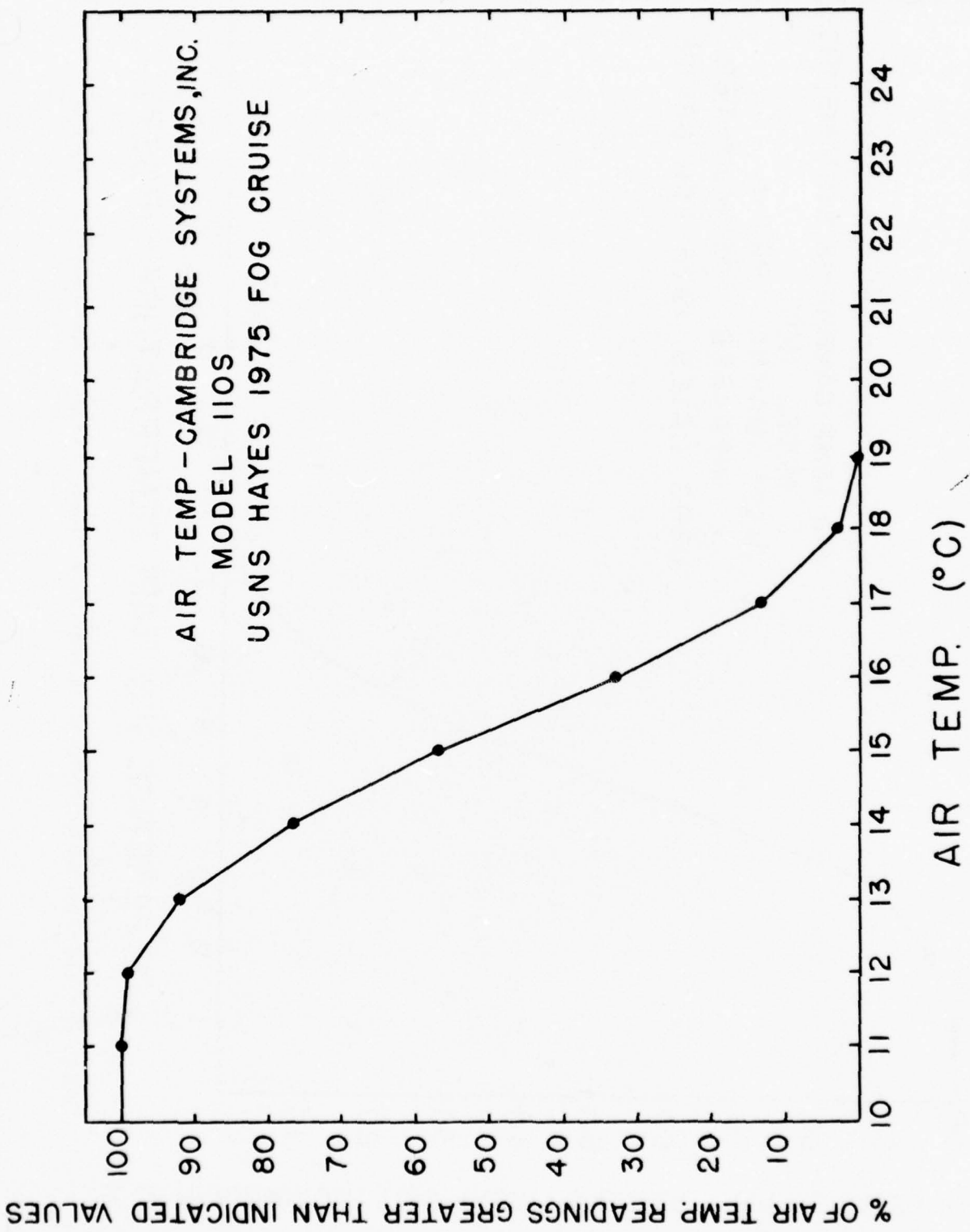


Fig. 3 Air temperature data (figure and caption unclassified)

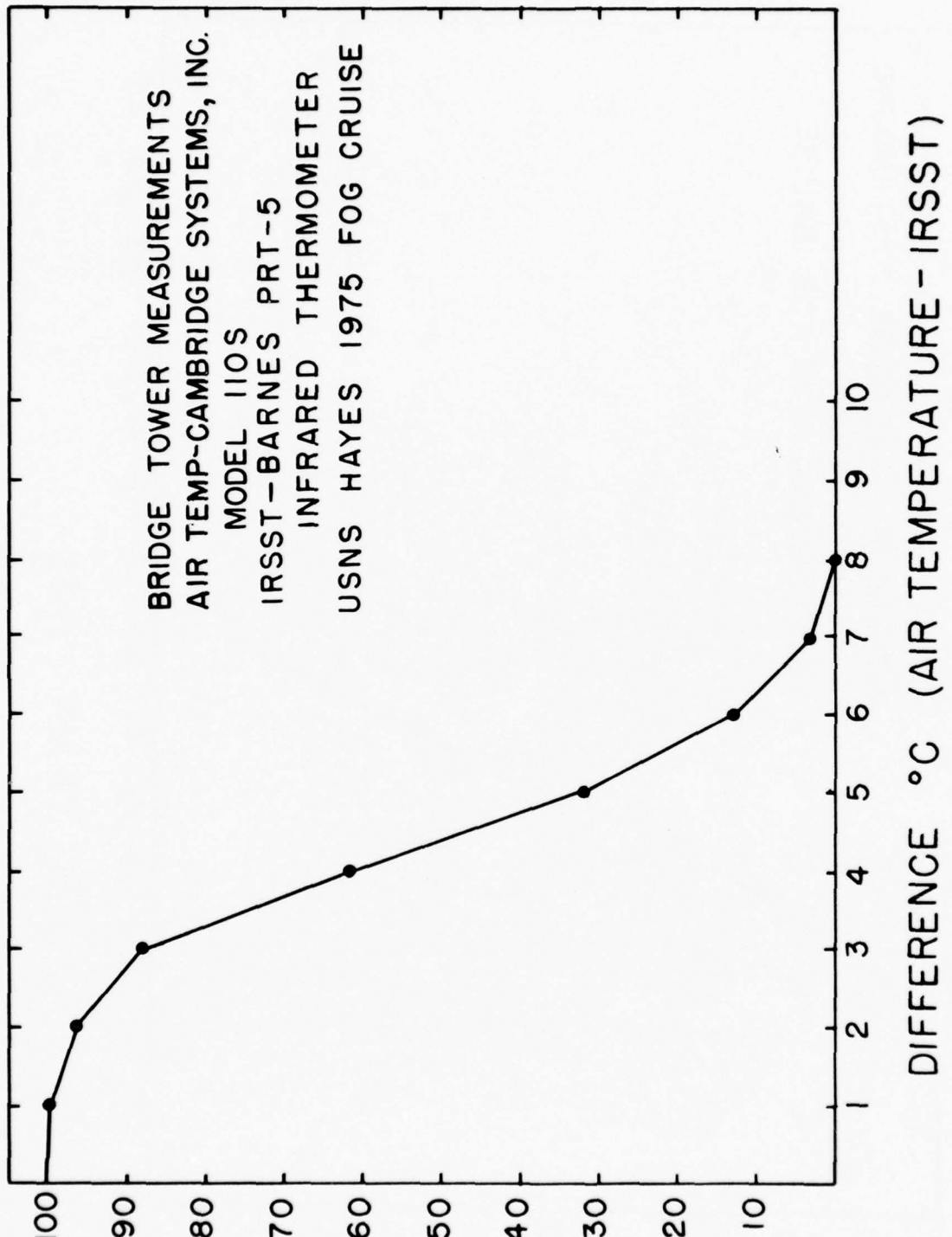


Fig. 4 Air-sea temperature difference data (figure and caption unclassified)

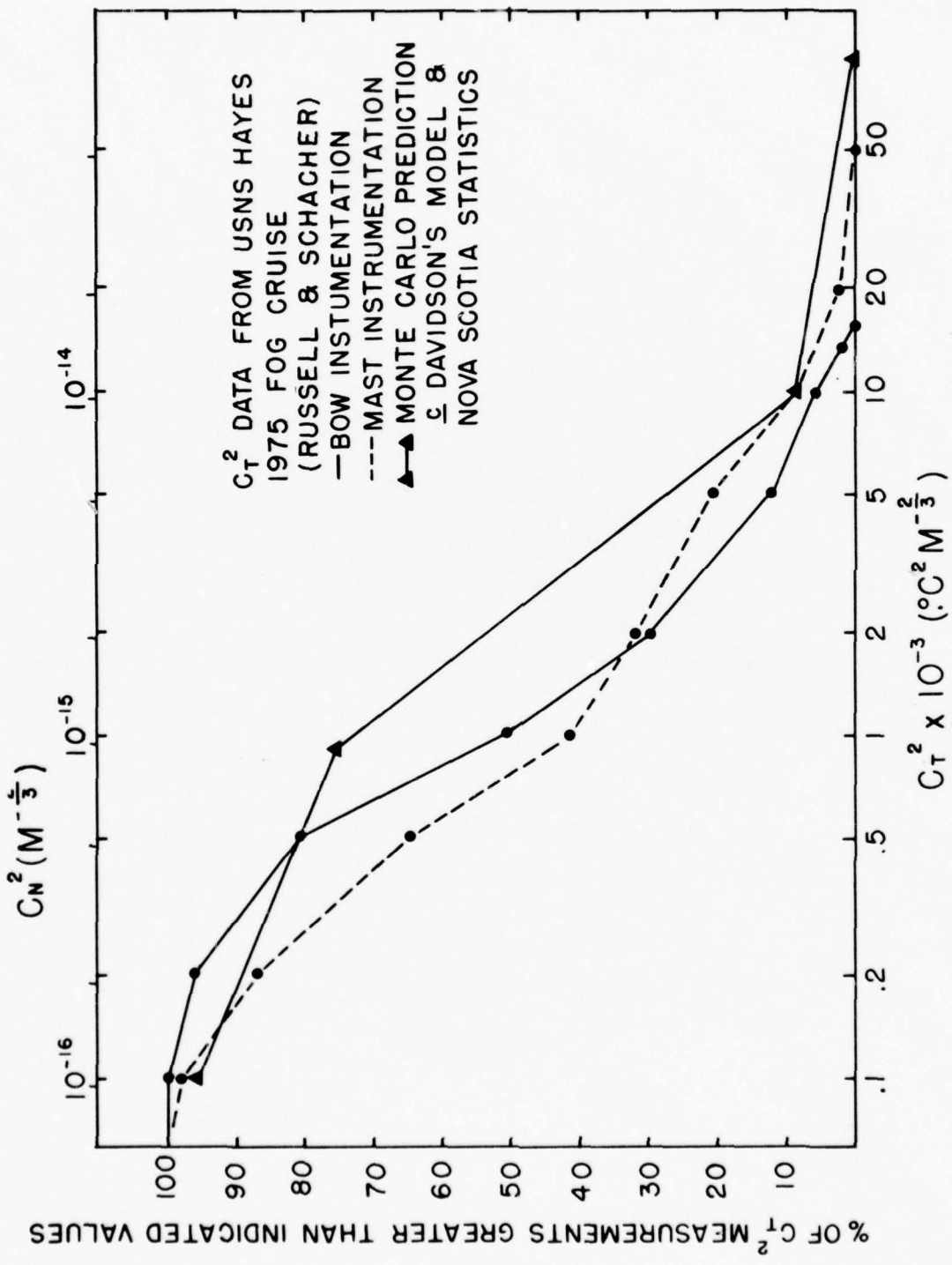


Fig. 5 C_T^2 and C_N^2 data and prediction (figure & caption unclassified)

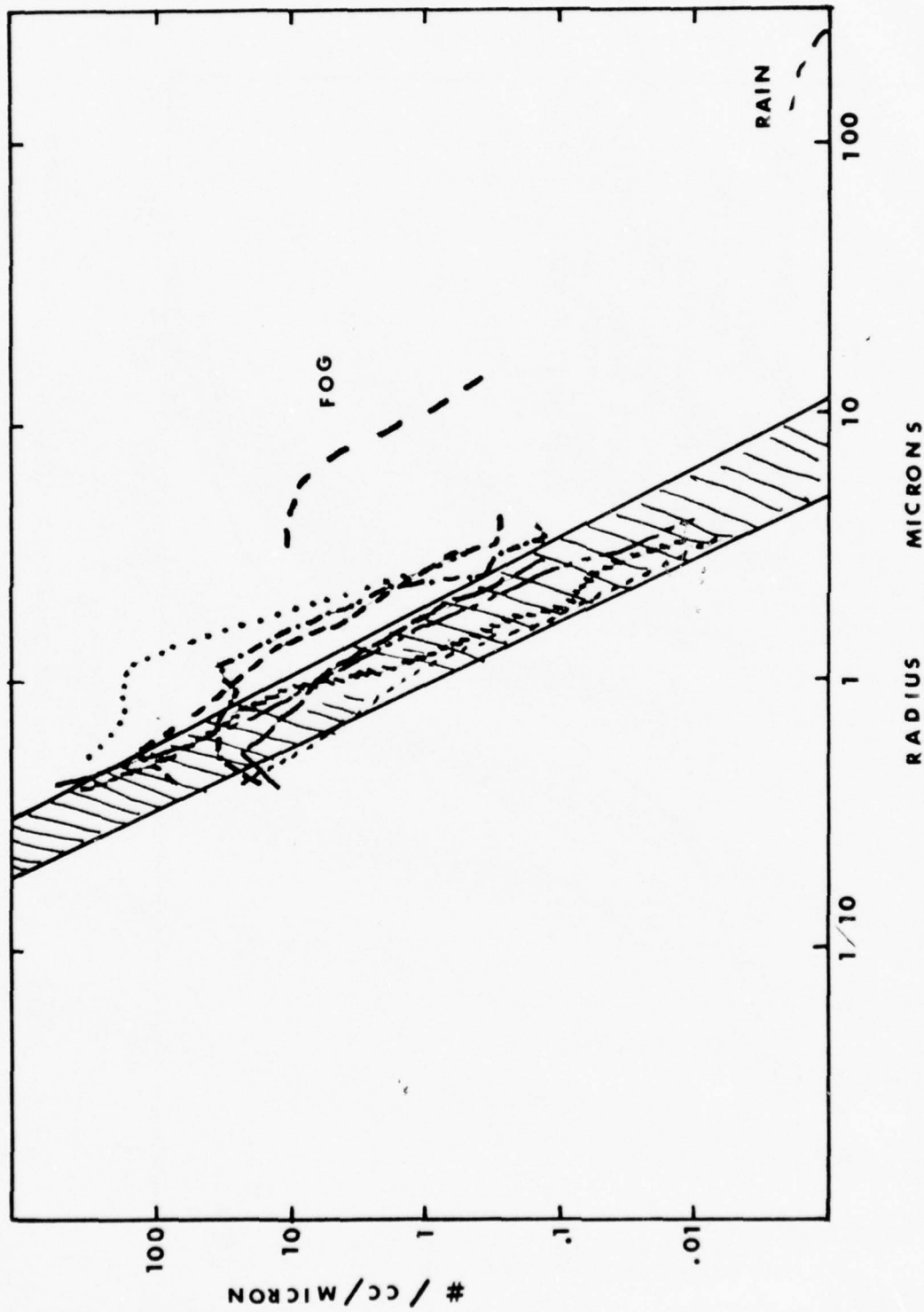


Fig. 6. Aerosol size distribution, date, and prediction (figure and caption unclassified)

UNCLASSIFIED

.... This paper is UNCLASSIFIED

A FACILITY FOR
CHARACTERIZATION
OF TARGETING SYSTEMS

CAPTAIN JAMES D. PRYCE
CAPTAIN EDWARD H. KELLY
AIR FORCE AVIONICS LABORATORY
WRIGHT-PATTERSON AIR FORCE BASE, OHIO

ABSTRACT

AFAL is responsible for developing techniques, hardware, specifications, and reliable predictive ability for Air Force targeting systems. Classical laboratory and flight experimental techniques fail to measure the real world utility of such systems. Characterization of targeting systems requires they be exercised in a calibrated real world. Air Force targeting sensors comprise human vision, photography, television, thermal imaging, radar and radiometry covering the spectrum from 0.4 to 1000 micrometers. This facility furnishes a 8 kilometer path calibrated for insolation, aerosols and transmission, as well as standard meteorological observables. In the center of the path is a large reservation for location of synthetic patterned targets (reflective and thermal) as well as operation of tactical targets such as trucks, guns and tanks. This facility will furnish the Air Force and AFAL necessary new ability to exploit technology options through all-weather test, evaluation and validation of breadboard, brassboard, prototype and production subsystems; through feedback to designer, developer and user, resulting in better sensors and smarter users; and through model validation permitting better prediction of real world utility.

The Air Force Avionics Laboratory, and specifically the Reconnaissance and Weapon Delivery Division, is responsible for developing techniques, hardware, specifications, and a reliable predictive ability for Air Force targeting systems. These targeting

UNCLASSIFIED

UNCLASSIFIED

sensors comprise human vision, photography, television, thermal imaging radar and radiometry covering the spectrum from 0.4 to 1,000 micrometers.

In developing the technology to support new and improved sensors, we are continually faced with the task of evaluating the merit of competing technological options. In the past, the state of technology itself often made that evaluation for us. For example, until just recently, the choice between 3-5 μm and 8-14 μm as a spectral region for thermal imaging was influenced heavily by the state of detector technology. Today, considering only the merit of available hardware, the choice between 3-5 μm and 8-14 μm is less obvious. We must look to other criteria on which to make this choice. The most important criterion we can look to is the eventual utility of a sensor in the real world. How does that sensor perform in the natural environment in which it must operate? Obviously, the scenario in which the sensor will be used exerts the major influence on the technological approach taken, especially when one considers the recent and rapid advancement in sensor technology at most wavelength regions. To aid in this evaluation, the Avionics Laboratory has taken the step to extend laboratory development of sensor systems out into the real world by establishing the Targeting Systems Characterization Facility.

The purpose of the Targeting Systems Characterization Facility is to quantitatively relate the performance of targeting systems with the natural environment in which they will be required to operate. The need to know this relationship stems from our basic mission and the fact that the development of technology must precede, by several years, the design of systems in which that technology is used. In the past, the evaluation of sensor performance was guessed at by the developer and discovered only the end user. Traditional ways of doing this performance evaluation are not satisfactory or complete. Classical laboratory measurements establish only baseline performance in a benign environment. Flight testing, while realistic, is time-consuming, difficult to instrument, beset by problems unrelated to the sensor, and extremely expensive. Computer modeling is an attractive alternative, but its reliability is often unknown. We still lack an understanding of many processes in the atmosphere and how they affect sensor performance and target/background signatures. There is almost a complete lack of high quality sensor performance data collected under known atmospheric conditions on which sensor performance models can be developed and their predictive ability verified.

The Targeting Systems Characterization Facility provides a complement to laboratory testing, which, although precise, accurate and cheap, is not a complete measure of real-world utility; and flight testing, which, although necessary and useful, is neither precise

UNCLASSIFIED

UNCLASSIFIED

nor accurate, yet is very costly. Due to the high cost and long lead time involved, a better and cheaper way to include a measure of real world utility must be inserted into the sensor development process. It cannot wait for the existence of prototype flight hardware. The Targeting Systems Characterization Facility gets us out into the real world to find out if the technology we are developing gives the performance we need and to optimize our approach at the least costly stage of development.

The physical description of the Targeting Systems Characterization Facility is relatively simple, consisting of three major components: the sensor platform, the target complex, and the array of instruments along the optical path from the platform to the target area. The sensor platform, in the upper floors of the Avionics Laboratory twin towers building, houses sensor bays, equipment racks, and sensor output display and recording equipment. A sensor in any stage of development can be placed on a dollied table, elevated to the platform, and easily rolled into place for operation. Space exists for pilot positions complete with sensor displays and controls for human factors evaluation. Side-by-side sensor bays permit comparative and/or competitive sensor evaluation.

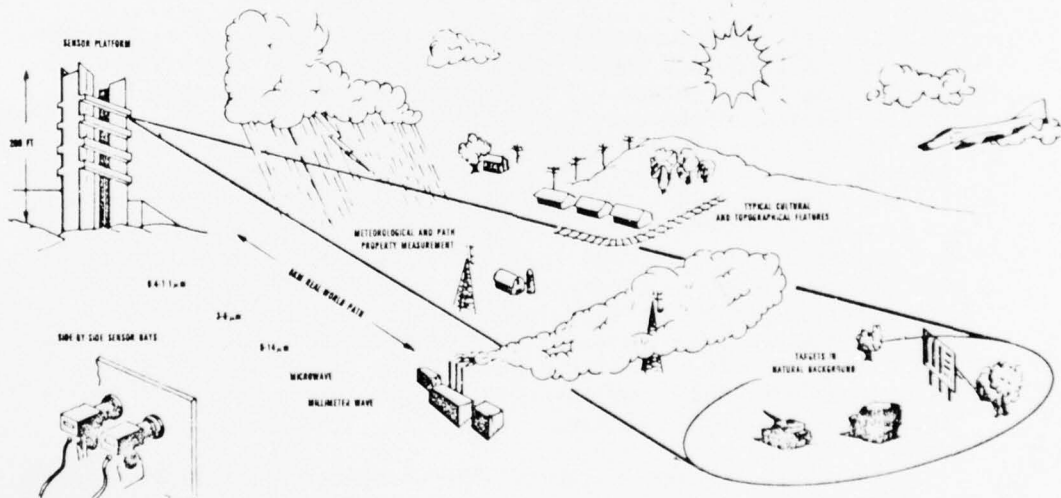


Figure 1. Targeting Systems Characterization Facility

UNCLASSIFIED

Located 8 kilometers east and at an elevation 200 feet lower than the sensor platform is Trebein Reservation. Positioned at Trebein are platform visual and infrared targets. Real military targets include buildings, radar antennas, trucks, and an antiaircraft gun. Synthetic targets such as impulse functions, both visual and infrared, and bar targets are also positioned at Trebein. The reservation is surrounded by grass/farm land, small wooded areas, and country highways. Between the target area and the sensor platform the gently rolling terrain is mostly grass/farm land dotted with wooded areas, barns, and clusters of houses and crisscrossed by power lines, country roads, several busy streets, and an interstate highway.

At the sensor platform, at the target complex, and along the path between, instrument packages collect data on both the more familiar meteorological parameters such as temperature and dew point, wind speed and direction, pressure, and rainfall; as well as those path parameters needed for a more complete evaluation of sensor performance such as aerosol size distribution, rain rate and drop size distribution, forward and integrated scatter, and the turbulent structure of the atmosphere. Atmospheric transmission in both the visible and infrared, in both narrow and broad wavelength bands, is measured over the entire 8-kilometer path.

Current and future efforts in the area of hardware evaluation include the PAVE TACK Thermal Imaging System (TIS) competitive prototypes, Next Generation TIS using focal plane array technology, the Common Aperture Techniques for Imaging Electro-optical Systems (CATIES) program, the Long Range Electro-optical Reconnaissance System (LOREOR) program, and the Electro-optical Fire Control System program, among others. Investigations planned to look at generic sensor problems, as opposed to specific pieces of hardware, include a comparison of 3-5 μm and 8-14 μm spectral regions for bandwidth optimization and comparative atmospheric/target/background effects, millimeter-wave transmission and target/background effects in both clear and adverse weather conditions, laser designator performance under low visibility conditions, scene dynamic range compression as a function of scene energy and cloud cover in both the visual and infrared regions, and a host of others.

An example of what a typical hardware evaluation might involve includes the standard performance parameters of signal-to-noise ratio, contrast, system MTF and MRT/MRC, and additionally, the detection range and recognition performance (including display and human factors) of the system over a wide range of environmental conditions. This characterization answers both the requirement of the system developer to know how close he is to his performance goals and provides the much-needed quantitative feedback to technology community indicating where future emphasis should be placed.

UNCLASSIFIED

UNCLASSIFIED

In summary, the complete characterization of sensor systems requires that they be exercised in a known real world environment. The Targeting Systems Characterization Facility brings together at the same time and place the three major factors which influence sensor performance: the sensor, the atmospheric path, and the target and its background. All three of these factors will be present in the operational users' world; all three should be included in the system developers' world at the earliest possible time. The Targeting Systems Characterization Facility will furnish the Air Force and the sensor community a new ability to exploit technology much more cost-effectively through real-world test, evaluation, and performance assessment of sensor systems at every stage of the development cycle. The resulting feedback to the designer, developer, and user will produce both improved sensors in less time and at less cost, and better understanding of the true operational capability that technology can offer to our customers.

UNCLASSIFIED

(This page intentionally left blank.)

....This paper is UNCLASSIFIED

DEFINITION OF THE PROPAGATION ENVIRONMENT WITH A
PORTABLE LONG-BASELINE TRANSMISSOMETER

GERBER, H.E. and STILLING, R.K.
Naval Research Laboratory, Washington, D.C. 20375

BUSER, R.G. and ROHDE, R.S.
U.S. Army Electronics Command, Ft. Monmouth, NJ 07703

ABSTRACT

A portable transmissometer was developed for assessing the influence of aerosols on atmospheric laser propagation. Atmospheric baselines on the order of 1 km were simulated over a folded path of 20 m in a cell by introducing aerosol in which the dispersed phase was concentrated up to two orders of magnitude. The designs of the concentrator and the transmission cell are described and results are given of some initial laser transmission measurements through concentrates.

1. INTRODUCTION - Rapid changes in the concentration, chemistry, and sizes of airborne particles may well be the norm in many battlefield situations. Under those conditions the rapid assessment of the influence of the aerosols on the propagation environment becomes essential. The combination of the new aerosol concentrator and a portable transmission cell has the potential of giving near real-time values of the aerosol scattering and absorption coefficients for radiation wavelengths extending into the infrared. The greatly increased particle concentration in the cell provides a favorable signal-to-noise ratio to make those measurements possible. This paper describes the current status of the concentrator and cell, the results of some transmission measurements with the system, and future plans.

2. INSTRUMENTATION - A device for concentrating aerosol particles in the suspended state must meet one major requirement in order that meaningful extinction measurements can be made through those particles: The physical nature of the particles in the concentrate must remain unchanged from its ambient state. Thus the device cannot expose the particles to significant temperature or pressure changes, since otherwise changes in the particles' relative size distribution would occur, and the concentrator must have small losses for

UNCLASSIFIED

particles whose sizes are important optically. Aerosol concentration is not a new idea, see for example Schutte (1966), Alt and Schmidt (1969), Budinsky (1970), and a description of cyclones by Green and Lane (1964). However, those instruments, which all concentrate particles by centrifugal means, are used primarily for pollution control or particle sampling and do not meet the requirement for an optically consistent concentrate.

The schematic of the new centrifugal aerosol concentrator designed specifically to preserve the physical nature of the suspended particles is shown in Fig. 1.

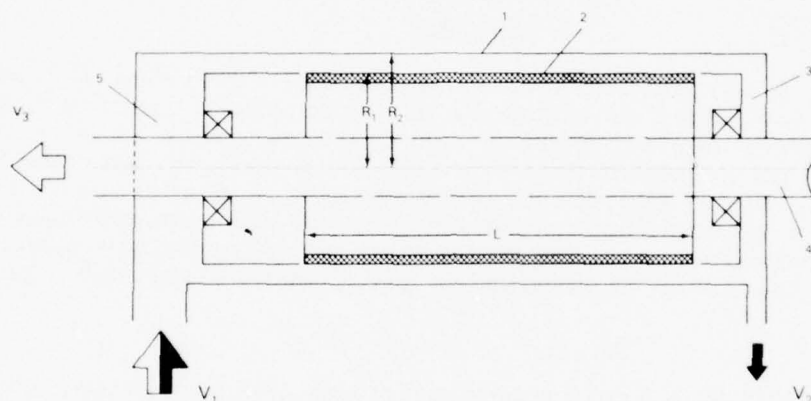


FIGURE 1. SCHEMATIC OF AEROSOL CONCENTRATOR.
(explanation in text)

Ambient aerosol flows at V_1 (liters/min) into the inlet manifold 5 and along a concentric annulus formed by a solid outer cylinder 1 at rest and a porous inner cylinder 2 rotating at high speed. Suction (V_3) applied to the hollow shaft 4 causes the dispersion medium to pass through the porous cylinder and into the shaft. Since the radial velocity of the aerosol particles is comparable to that of the inner cylinder near its surface, the particles move radially outward due to the centrifugal force in addition to their motion along the annulus. The particles reach their highest concentration at the end of the annulus near the outlet manifold 3 where they are drawn off at V_2 which is typically set equal to $0.02 V_1$. With no particle losses in the annulus the concentration increase of the aerosol particles is simply V_1/V_2 .

The inner cylinder consists of seamless sintered stainless steel which has uniform porosity and a tensile

UNCLASSIFIED

UNCLASSIFIED

strength which is sufficient to withstand the centrifugal force of 25,000 rpm ($L=30\text{cm}$, $R_1=4.4\text{cm}$). Pores cover 1/5 of the cylinder's surface and average $25\text{ }\mu\text{m}$ in diameter.

Particles smaller than a given size D are lost into the filter. This cutoff size is found by equating the Stokes' sedimentation velocity of the particles in the centrifugal field to the mean suction velocity into the filter:

$$D^2 \left\{ 1 + \frac{2\lambda}{D} \left[A + B \exp \left(- \frac{CD}{2\lambda} \right) \right] \right\} = \frac{9\eta(V_1 - V_2)}{\pi \rho \omega^2 R_1^2 L} , \quad (1)$$

where λ is the mean free path and η is the viscosity of the air, A , B , and C are slip corrections usually assigned the values 1.246, 0.42, and 0.87 respectively, ρ is the particles' density, and ω is the angular velocity of the rotor. Figure 2 gives D as a function of V_1 , V_2 , and rotor rpm under the conditions that $V_2 = 0.02V_1$ and $\rho = 1.0 \text{ gm/cm}^3$.

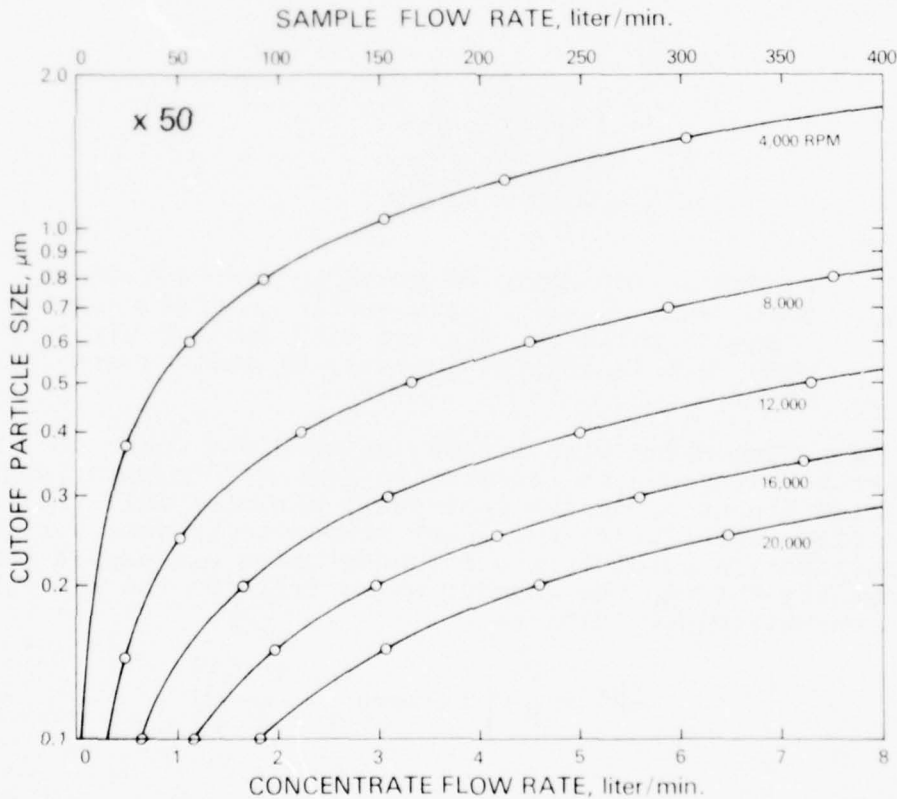


FIGURE 2. MINIMUM PARTICLE SIZE CONCENTRATED FOR RPM AND FLOWS OF CONCENTRATOR. See Eq. (1).

UNCLASSIFIED

The particles passing through the annulus are isolated from the large pressure drop existing across the filter, they only experience a pressure drop of a few hundreds psi between inlet and outlet manifolds. The effects of aerodynamic heating are minimized, since in the region of greatest shear near the filter surface the slightly warmed air is removed by suction into the filter.

A cell, Fig. 3, was constructed to measure the attenuation of laser radiation passed through the output of the concentrator. It consists of a slab-like vertical chamber

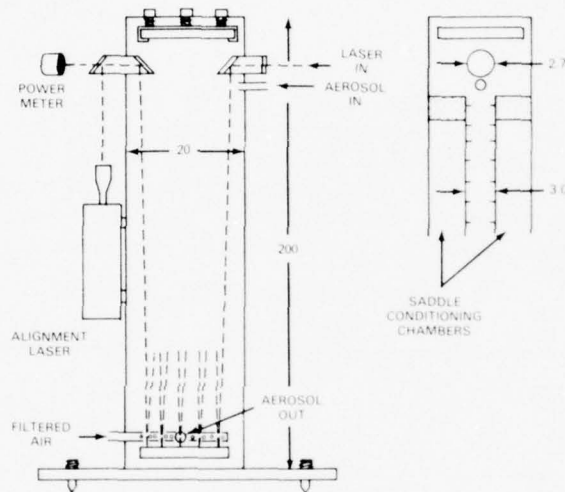


FIGURE 3. SCHEMATIC OF AEROSOL TRANSMISSION CELL. Head-on view shows saddle conditioning chambers which are flushed with ambient air when cell is located indoors. Dimensions are in cm.

200cm x 20cm x 3cm with mirrors at each end which step the laser beam through the chamber to give a 20 m path length. Baffles placed along the inner wall minimize wall reflections, and clean air flushes the lower mirror to prevent particle deposition. Aerosol from the concentrator are passed continuously through the chamber which fills to the equilibrium concentration according to

$$\frac{C(t)}{C} = \frac{V_1}{V_2} \left[1 - \exp \left(- \frac{t V_2}{V} \right) \right], \quad (2)$$

where $C(t)$ is the particle concentration in the cell as a function of time t , C is their concentration in the concentrator output, and V is the cell volume.

Given a concentration enhancement of 50, the transmission path in the cell simulates an atmospheric baseline of 1 km. Much greater baselines could be obtained with a more sophisticated cell. Attenuation in the present cell can be measured for optical thicknesses greater than 0.1, and Zuev et al. (1967) showed that the Bouguer law describes the attenuation for thicknesses up to 25 for a similar transmissometer.

3. EXPERIMENTAL RESULTS - The proper simulation of the 1 km atmospheric transmission path in the cell requires that the aerosol particles which significantly affect attenuation pass through the concentrator without losses. Figure 4 shows the results of measurements made to test that requirement for

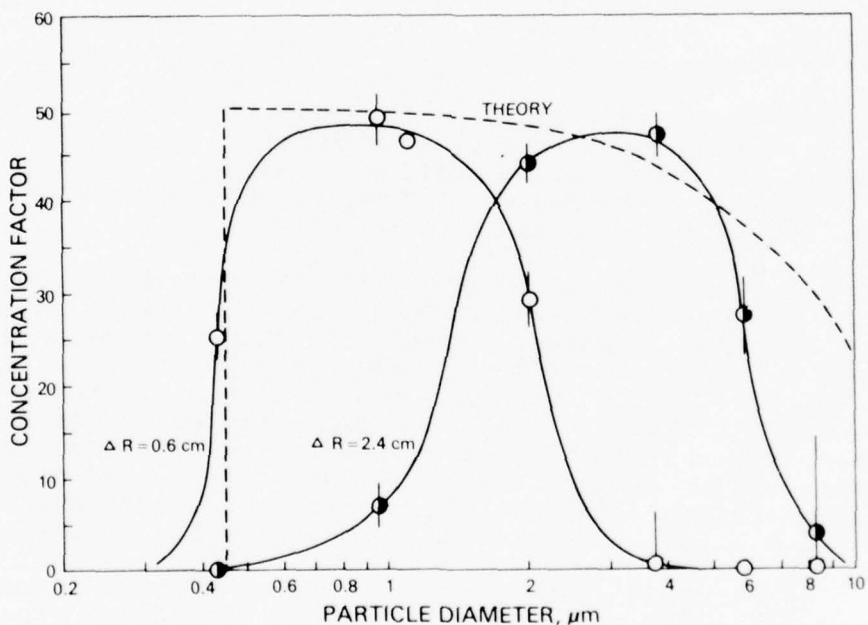


FIGURE 4. CONCENTRATION ENHANCEMENT AS A FUNCTION OF PARTICLE SIZE.

a rpm of 8000. Atmospheric particles were used in all the tests except for one where $1.090 \mu\text{m}$ latex particles were used. The concentration was measured with a Royco particle counter in the flow entering 5 and leaving 3, membrane filters were used to collect the latex particles. The concentration factor

UNCLASSIFIED

was expected to be 50 with flow rates of $V_1 = 200$ liters/min and $V_2 = 4$ liters/min.

In Fig. 4 the cutoff in the concentration factor for small particles for the case $\Delta R = R_2 - R_1 = 0.6$ cm is in the position predicted by Eq. (1). The decrease for large particles is at a smaller particle size than expected. This cutoff is a result of inertial impaction losses on the outer cylinder due to turbulence in the annulus as verified by hot-wire anemometry. The turbulence, found at all rpm values even though the uniform suction on the porous cylinder should have stabilized the flow much above the rpm corresponding to the critical Taylor's number for no suction (see Schlichting, 1968), was probably due to the surface of the cylinder rotating slightly off-axis at one end.

The inner cylinder was placed in a larger container with an effective ΔR of 2.4 cm and was again tested at 8000 rpm. The decrease of losses for larger particles shows that fewer impacted on the walls, and the shift of the lower cutoff to larger particle sizes suggests that the boundary layer moving with the cylinder was much thinner than in the previous case. The loss at the lower cutoff was now more consistent with the suction rate into individual pores than with the mean suction rate. The theoretical curve, from Davies (1966) for "stirred settling" losses in a chamber of size R_1 and L , gives the upper limit of the concentration factor for $\Delta R = 2.4$ cm and $V_2 = 0.02 V_1$.

The transmission of $0.6328 \mu\text{m}$ laser radiation through the cell is shown in Fig. 5 as the cell is filled with concentrated ambient aerosol and then is flushed with ambient aerosol ($\Delta R = 2.4$ cm, 8000 rpm). This particular case is given, since it shows the system's performance near its lower sensitivity limit. The estimated curve was calculated from the attenuation coefficient α obtained from the estimated 40 km visual range. The cell was flushed soon after the transmission value stabilized, to demonstrate the ease with which a 100% transmission calibration can be performed.

Figure 6 shows the transmission through an oil aerosol for which α was measured in the laboratory. The dashed curve was calculated from this α and from the concentration of oil aerosol in the cell, and the curves for other values of λ were calculated using the size distribution of the oil droplets and their scattering efficiency factors for the refractive index of 1.50. Those calculations suggest a measurable extinction at those wavelengths.

UNCLASSIFIED

UNCLASSIFIED

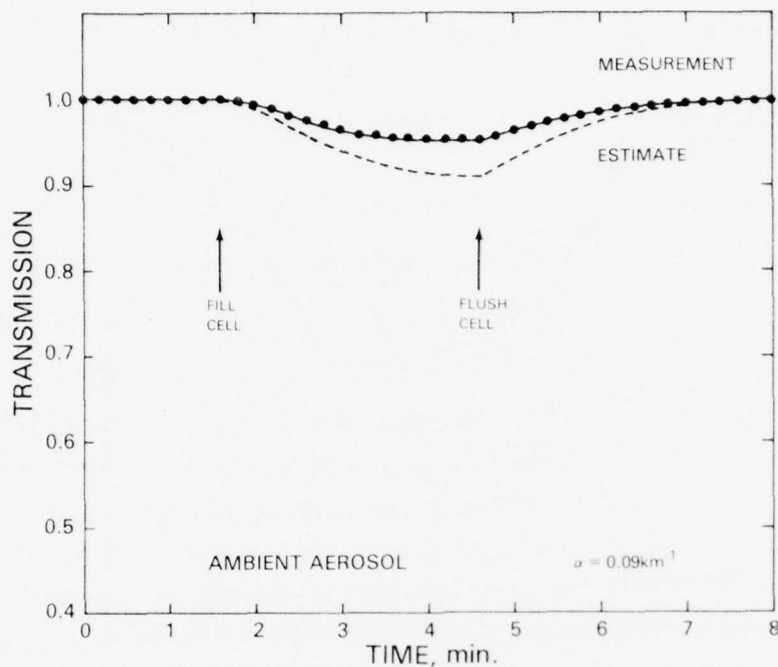


FIGURE 5. TRANSMISSION THROUGH CONCENTRATED ATMOSPHERIC AEROSOL. The simulated transmission path in the cell is 1 km long.

In both preceding examples the transmission cell gave about 1/2 the attenuation at $0.6328 \mu\text{m}$ which was expected for the concentration factor of 50. This occurred, since the particle size distributions in both cases exceeded the particle size bandpass shown in Fig. 4.

4. CONCLUDING REMARKS - The concentrator in its present configuration gives a 50-fold increase in the ambient particle concentration over a particle-size bandpass of about one decade. This capability greatly relaxes the requirements for measurements in aerosol extinction cells. For instance, it is possible to use a cell with simple optics, non-critical alignment, and with a small size that makes a portable system a possibility. Also, the small size permits the vertical operation of the cell which is essential when determining the interaction of aerosols with infrared radiation. Horizontal cells would show large sedimentation losses for the larger particles which are important in the infrared.

The concentrator and the cell give essentially a point measurement in space of the aerosol extinction. The system's time response depends on the size of the cell and

UNCLASSIFIED

UNCLASSIFIED

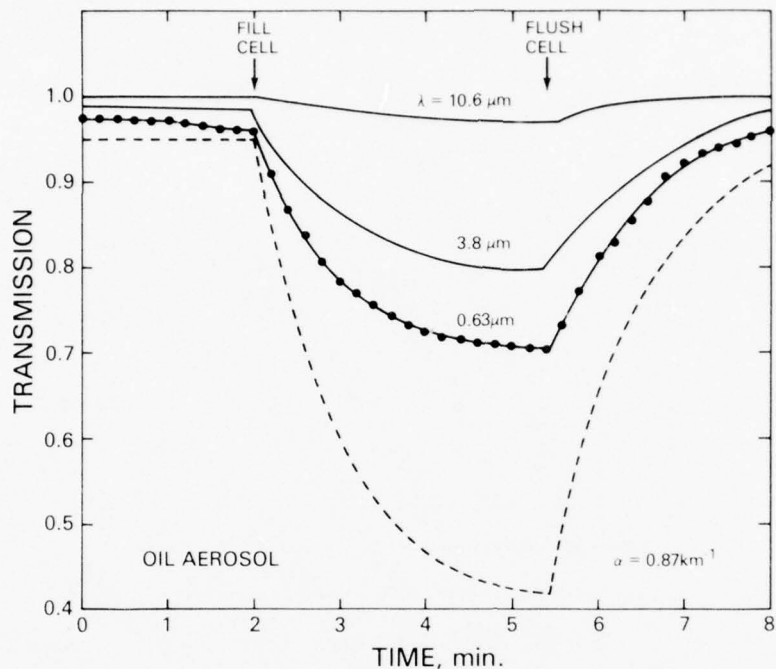


FIGURE 6. TRANSMISSION THROUGH CONCENTRATED OIL AEROSOL FROM A SMOKE-SCREEN GENERATOR. Dashed curve and curves labeled $3.8 \mu\text{m}$ and $10.6 \mu\text{m}$ were calculated, see text.

concentrator and on the amount of concentration enhancement. The present configuration responds to rapid aerosol changes in the environment in less than a minute for an enhancement of $\times 50$. The system is referenced to the 100% transmission calibration point by flushing with filtered air.

Measurements of the light scattered by the aerosol in the cell have not been made but are planned for the future. The configuration of the folded laser beam in the cell is ideal for scattering measurements using a 2π sensor as is done in nephelometers. Judging from estimates of the aerosol absorption coefficient (e.g., McClatchey et al., 1972; Waggoner and Charlson, 1976), the enhanced particle concentration in the cell should give enough of a difference between the scattered and transmitted light so that measurable values of the aerosol absorption coefficient are obtained under many atmospheric conditions for laser wavelengths extending into the infrared.

UNCLASSIFIED

The present emphasis is on optimizing the performance of the concentrator. In this regard a new sintered metal rotor with increased coverage of smaller pores and improved rotor concentricity promises to significantly increase the particle size range for which particles are concentrated with only small losses.

5. REFERENCES -

Alt,C. and P. Schmidt, 1969: Comparative studies of the separation efficiencies of various centrifugal dust collecting systems. Staub, 29, 1-4.

Budinsky,K., 1970: Rotating centrifugal separator with continuous dust removal. Staub, 30, 7-13.

Davies,C.N., 1966: Deposition from moving aerosols. Aerosol Science, Ed. C.N.Davies, Academic Press, NY, 393-446.

Green,H.L., and W.R.Lane, 1964: Particulate Clouds, D. Van Nostrand Co., NY, 318-323.

McClatchey,R.A., R.W.Fenn, J.E.A.Selby, F.E.Volz, and J.S. Garing, 1972: Optical properties of the atmosphere. AFCRL Report 72-0497. AFGL, Bedford, Mass.

Schlichting,H., 1968: Boundary-Layer Theory, McGraw Hill, NY, pp 748.

Schutte,A.H., 1966: Filter Apparatus. U.S. Patent 3,262,573.

Waggoner,A.P., and R.J.Charlson, 1976: Measurement of aerosol optical parameters. Fine Particles, B.Y.H.Liu, Editor, Academic Press, NY, 511-533.

Zuev,V.E., M.V.Kabanov and B.A.Sabel'ev, 1967: The limits of applicability of the Bouguer law in scattering media for collimated light beams. (English Trans.). Izv. Atm. and Oceanic Phys., 3, 724-732.

UNCLASSIFIED

(This page intentionally left blank.)

....This paper is UNCLASSIFIED

UNCLASSIFIED

THE ADVANCED OPTICAL TEST FACILITY

James L. Spencer, 1Lt
Rome Air Development Center
Griffiss AFB, New York 13441

Abstract

The Environmental Studies Section of Rome Air Development Center has been engaged in atmospheric propagation research for several years. Research efforts have included contractual work and in-house studies. The evolution of the Advanced Optical Test Facility into a fully instrumented optical propagation range for in-house experiments has been accompanied by significant contributions in atmospheric turbulence studies and instrument development. Micrometeorological studies which began only as support to optical propagation experiments have yielded important microtemperature turbulence data as well as better instruments to measure turbulence.

Introduction

The need to quantitatively describe the atmosphere is common to several scientific disciplines. Experimenters in optical propagation, whether they are interested in processing optical signals received from outside the earth's atmosphere or interested in establishing an optical data link between ground based terminals, are necessarily concerned about atmospheric effects. The Environmental Studies Section of Rome Air Development Center (RADC) has been engaged in atmospheric propagation research for several years, and they found the need to quantitatively characterize the atmosphere to be critical. In particular, much of their work required knowledge about phase distortion, which is predominantly caused by temperature turbulence (at least over land). As a result of these needs, RADC has developed the Advanced Optical Test Facility (AOTF) into a laboratory especially instrumented to measure temperature turbulence and important optical propagation parameters.

Many individuals have developed theoretical models of atmospheric temperature turbulence and relationships among different propagation parameters. It is critical that these theories be tested because they can have serious implications for programs in the Department of Defense and other agencies. In recognition of this, the AOTF has the following objectives: to test the validity of analytical models which describe temperature turbulence and optical propagation parameters; to test the relationships between these quantities; and to provide improved models where required.

The approach to these objectives has been to equip the AOTF with advanced "state-of-the-art" sensors which measure the pertinent parameters. The AOTF has several instruments which monitor temperature turbulence and provide measurements of the temperature structure constant, C_2 . Other sensors have been developed for measuring optical parameters such as angle of arrival, intensity fluctuations, and the modulation transfer function (MTF). In addition, the AOTF has an operational breadboard model of a predetection compensation system for telescopes.

UNCLASSIFIED

UNCLASSIFIED

Facility Description

The Advanced Optical Test Facility is located near Verona, New York, in the center of the Mohawk Valley. The terrain is essentially flat, with prevailing winds from the northwest. Figure 1 shows the physical layout of the range. The terrain is predominantly grass 0.1m to 1.5m tall (this is mowed annually to maintain a roughly uniform height). One laser shed is 305m northeast of the laboratory, and four other laser stations are to the southeast between 610m and 1525m (at 305m increments). The southeast range is instrumented with 3m towers also at 305m increments (the towers are now being replaced by 18m "tilt over-crank up" towers). The towers have wind speed and wind direction sensors, and they can each handle up to three microtemperature probes for monitoring turbulence. A high quality dew point-ambient temperature system is at each end of the southeast range.

The laboratory building itself is three stories tall with an observatory dome on top. Inside the building, but independent of its structure, is a three story, ultra stable, hollow concrete pier with walls 60-100cm thick. The floor of the pier provides an excellent base for the facility's one meter diameter, f/18, cassegrain telescope, which receives its incoming light by means of a precision, one meter diameter optical beam director mounted on top of the pier. This configuration is important because the instruments used in conjunction with the telescope are experimental and often being modified. Instruments are quickly interchanged without affecting telescope performance. The only restriction on the instrument size is the working area inside the pier (the walls are about 7m apart at the pier's base).

Optical instrumentation includes the Optical Measurement System (OMS) and the Real Time Atmospheric Correction System (RTAC). The OMS can make measurements at both visible and infrared wavelengths. The instrument provides the following optical propagation parameters: phase differences, angle of arrival, differential angle of arrival, modulation transfer function, and intensity fluctuations. The RTAC system is a feasibility model of a predetection compensation system. Its active element is a piezoelectric mirror which has 21 elements. It is used to measure optical propagation parameters which directly affect the Advanced Research Projects Agency (ARPA) Compensated Imaging Program.

The AOTF has several instruments for measuring temperature turbulence. The microtemperature probe (a cold wire device) directly measures fluctuations in temperature, from which the temperature structure constant, C_T^2 , can be easily calculated.¹ The acoustic sounder indirectly measures turbulence in a vertical profile from 30m to 300m above ground level. Direct output includes a facsimile trace and analog voltages (which can be processed to obtain C_T^2 values).

The microtemperature probe is an especially versatile sensor, now used routinely in support of all optical propagation experiments. The sensor is essentially a Wheatstone bridge which uses a thin diameter platinum wire (2.5 μ m) as one leg of the circuit. Temperature fluctuations change the resistance of this wire, and the resulting voltage changes are amplified. The overall sensor response has changed since the original design,² such that nominal values are now 0.5v/ $^{\circ}$ K with resolution of 0.02 $^{\circ}$ K. The probe's frequency

UNCLASSIFIED

UNCLASSIFIED

range is better than 0.01 to 100 Hz. From two probes placed a distance r apart, the temperature structure function and constant are easily calculated from the following relationships:

$$\begin{aligned} D_T(r) &= \langle (T_1 - T_2)^2 \rangle & (1) \\ &= C_T^2 \cdot r^{2/3} & l_0 \ll r \ll L_0 \end{aligned}$$

and

$$C_T^2 = [\sigma_1^2 + \sigma_2^2 - 2C_{12} + (\mu_1 - \mu_2)^2] r^{-2/3} \quad (2)$$

where l_0 and L_0 are the inner and outer scales for the microtemperature inertial subrange; σ_i^2 is the temperature variance measured by a probe; C_{ij} is the temperature covariance between the two probes; and $\mu_i = \langle T_i \rangle$. As long as the probes are at the same height, the means will be the same (for adequate sampling times), so that equation (2) becomes

$$C_T^2 = (\sigma_1^2 + \sigma_2^2 - 2C_{12}) r^{-2/3} \quad (3)$$

A minicomputer provides the variances and covariances.

Another common requirement for probe measurements is to provide temperature temporal power spectra, from which the Kolmogorov behavior of the turbulence can be determined. Very accurate results are obtained with special computer processing, but quicker results can be obtained by using the probe in conjunction with a commercially-available spectrum analyzer. Figure 2 shows the power spectrum for a probe under normal operation on a sunny afternoon, compared to the noise spectra for a capped sensor and a sensor with its wire element submerged in oil.¹

Another version of the probe uses a "fat" platinum wire (12.7 μ m diameter) strung in a spiral on insulative posts. It has the distinct advantage of being able to withstand higher winds, light rain, and moderate snow showers. Because this version's frequency response is altered, as shown in Figure 3³, it cannot be used to obtain temporal power spectra. Compensating for this different frequency response leads to a modified equation for C_T^2 . The correct value for C_T^2 from two fat-wire probes is now found from

$$C_T^2 = 1.2 (v/r)^{0.182} (C_T^2)' \quad (4)$$

where v is the wind velocity, r is the separation between the probes, and $(C_T^2)'$ is the uncorrected value obtained from equation (3).

In contrast to microtemperature probes, the acoustic sounder makes indirect measurements of thermal turbulence. The instrument, by means of a facsimile trace, displays in real time the structure of turbulence with respect to strength and height (temperature inversions and convective plumes are clearly seen). A detailed description of the sounder's operation is well documented,^{4,5} but the instrument can be described in simple terms as an acoustic backscatter radar. A pulse of sound, emitted vertically into the

UNCLASSIFIED

CLASSIFIED

air, is reflected by temperature gradients. The time of the return pulse is easily related to height, while the strength of the return is directly proportional to the strength of turbulence. These measurements provide knowledge about turbulence at heights which are difficult to sample - heights above most instrument towers and below the operation of airborne instruments. Sounder data can be used to supplement other experiments⁶ or independently.⁷ The importance of sounder data will continue to increase as the software for data reduction on minicomputers becomes available, allowing immediate quantitative results. Such programs will probably be based on published works which explain the quantitative evaluation of acoustic echoes.^{8,9}

The data processing capabilities of the AOTF consist of two Optical Data Processors (ODP), a PDP-8 computer, a data logger, and a NOVA 800 computer. The ODP's reduce data from optical experiments, with one ODP designed for visible wavelengths and the other dedicated to infrared wavelengths. They provide measurements of various optical propagation parameters. The PDP-8 is used extensively, but especially for measuring means, variances, and covariances. Its capabilities are enhanced by an analog-to-digital converter, a magnetic tape drive, and connections to two multi-channel analog tape recorders. The data logger is an analog-to-digital tape recording system. It has three selectable sampling rates, and it can handle up to 30 channels of data. The NOVA 800 computer including its tape drive, line printer, card reader, and teletype peripherals, is used primarily for driving the optical mount. It will be used in the future for both off-line and on-line data processing.

Previous Experiments

Much more work has taken place at the AOTF than can be presented in this short paper, but two important previous experiments are turbulence modeling and structurally - induced turbulence studies. The turbulence modeling examined how actual data differed from theory. The studies of structurally - induced turbulence investigated the turbulence occurring within the pier and dome areas of the AOTF.

The turbulence modeling work was done under the direction of Dr. Darryl P. Greenwood (now at Lincoln Laboratory). Since nearly all of propagation theory is based on an assumed refractive index spatial spectrum, it is vital that the theoretical spectrum be checked against actual data and be correct, or else theories would require modification. Early work at the AOTF had demonstrated that more power existed in the lower temporal frequencies than predicted by theory.¹⁰ The available data suggested that the discrepancy resulted from the von Karman spatial spectrum, which dominates the theoretical refractive index spectrum, or from the frozen-flow hypothesis. These two factors were carefully investigated in a series of experiments at the AOTF and the laser test range of Air Force Weapons Laboratory, Kirtland AFB, New Mexico.¹⁰

The validity of von Karman's spectrum was checked against the temperature structure function, since that relation does not depend on the frozen-flow hypothesis. Von Karman's spectrum,

$$\kappa_T(\kappa) = 0.0330 C_T^2 [\kappa^2 + (1/L_0)^2]^{-1/6} \quad (5)$$

CLASSIFIED

UNCLASSIFIED

when substituted into the structure function, $D_T(r)$, leads to the following limits:

$$D_T(r \ll L_0) = C_T^2 \cdot r^{2/3} \quad (6a)$$

$$D_T(L_0 \ll r) = 1.0468 C_T^2 \cdot L_0^{2/3} \quad (6b)$$

Empirical modeling led Greenwood to propose a new form for the temperature spectrum,

$$\phi_T(k) = 0.0330 C_T^2 [k^2 + (k/L_0)^2]^{-1/6} \quad (7)$$

Using this spectrum, the structure function limits now become

$$D_T(r \ll L_0) = C_T^2 \cdot r^{2/3} \quad (8a)$$

$$D_T(L_0 \ll r) = 1.1078 C_T^2 \cdot L_0^{2/3} \quad (8b)$$

This model leads to much better agreement with actual data, as evident in Figure 4a. The agreement of the theoretical temporal power spectrum with data is also improved by Greenwood's proposal. This is shown in Figure 4b. The remaining discrepancies between data and theoretical low-frequency values are attributed to weaknesses in the frozen-flow hypothesis.

Turbulence generated by buildings can be a phantom problem for many observatories, especially in winter at heated or semi-heated facilities. This structurally-induced thermal turbulence has been studied at the AOTF, where it has been observed in the pier and dome areas.¹¹ In the Phase I experiments the macrothermal characteristics of the building were determined for changing internal and external conditions. Phase II experiments were designed to precisely characterize the location and severity of the turbulence. Finally, Phase III experiments evaluated different attempts to minimize the turbulence. The experiments were extremely valuable in identifying areas of turbulence and gaining an understanding of turbulence causes. Some corrective fixes were implemented, and more will be tried after additional studies this winter. Any facility can make similar measurements with minimum instrumentation - only thermometers, thermographs, and microtemperature probes (for C_T^2 values) are needed.

Current Experiments

The most important experiment currently in progress at the AOTF is a long-term study of microtemperature turbulence near the ground. Turbulence (C_T^2) has been measured continuously under all conditions of weather. Complete data is available for the January - May 1975 time period. A detailed analysis of available data is now in progress.

The instruments used in the experiment are wind speed, wind direction, and three micro-temperature sensors on a tower 150m south of the building, plus an ambient temperature system 25m south of the building. The temperature system is 1.5m above ground level; the wind sensors are 2.5m high; the micro-temperature probes are 3m high. Microtemperature probes are checked at least

UNCLASSIFIED

UNCLASSIFIED

once a day (except weekends) for proper operation. The six raw signals are continuously recorded by the data logger, stopped only when all three probes require replacements. The data channels are sequentially sampled at a nominal rate of one cycle (six channels) per second. The magnetic tape holds over a week of data, which is then processed on RADC's Honeywell 6180 computer. The data on the tapes are reduced to 30 minute averages for wind speed and direction, temperature, and the "best" value of C_T^2 (or C_N^2 , the refractive index structure constant) from the three probe pairings. The averages are later combined in various ways for monthly figures.

The results at this time suggest that turbulence does behave in a characteristic diurnal cycle. Three types of behavior have been observed, which are somewhat related to cloud cover, as expected. Type I turbulence, as defined here, exhibits a "clean" diurnal cycle (or profile) with peak values at mid-day and a definite dip around sunset. Following this dip, the turbulence quickly regains much of its strength, but subsequently decreases during the night. This type of profile is generally associated with sunny days or only a light overcast. Type II turbulence is similar except that more bumps and glitches are present. The peaks and dips are not as prominent, either. The weather conditions are usually cloudy or overcast. The Type III turbulence profiles have little regular shape - the characteristic peaks and dips are often indiscernible. This behavior is consistently associated with heavy cloud cover or rapidly changing weather conditions. Figure 5 shows Type I profiles for the months of February and May 1975. The interesting features include nearly identical values for mid-day peaks and for sunset dips.

Future Work

Besides the possible continuation of the long-term turbulence study, future experiments at the AOTF will be centered around two instruments - the RTAC system and the Stellar Profilometer. The RTAC system, briefly described earlier, will be used to study the improvement it makes in various optical propagation parameters (including the Strehl ratio, the point spread function, and the modulation transfer function) over reference values from an "uncorrected" beam. The Stellar Profilometer is an improved version of an instrument already in operation at the ARPA Maui Optical Station.¹² The instrument uses a spatial filtering technique in conjunction with a stellar image to determine a profile of the temperature turbulence (C_N^2) for altitudes of 1.0 to 25km.

Although some of the planned work is quite ambitious, it is within the facility's capabilities. The AOTF can be expected to continue contributing in the area of optical propagation.

UNCLASSIFIED

UNCLASSIFIED

References

1. Darryl P. Greenwood and David B. Youmans, A Fine-Wire Microtemperature Probe for Atmospheric Measurements, RADC Technical Report RADC-TR-75-240, Griffiss AFB, NY (1975).
2. G.R. Ochs, A Resistance Thermometer for Measurement of Rapid Air Temperature Fluctuations, ESSA Technical Report IER47-ITSA46, Boulder CO (1967).
3. Darryl P. Greenwood and James L. Spencer, Frequency Response of Fat-Wire Probes, unpublished technical memorandum, RADC/OCSE, Griffiss AFB, NY (1975).
4. Edward J. Owens, Development of a Portable Acoustic Echo Sounder, NOAA Technical Report ERL 298-WPL 31, Boulder CO (1974).
5. Edward J. Owens, NOAA Mark VII Acoustic Echo Sounder, NOAA Technical Memorandum ERL WPL-12, Boulder CO (1975).
6. Darryl P. Greenwood, et al., AMOS Seeing Quality Measurements, RADC Technical Report RADC-TR-75-295, Griffiss AFB NY (1976).
7. N.A. Shaw, Observations of Atmospheric Structure Using an Acoustic Sounder, Argonne National Laboratory Report ANL/RER/75-2, Argonne IL (1974).
8. William D. Neff, Quantitative Evaluation of Acoustic Echoes from the Planetary Boundary Layer, NOAA Technical Report ERL 322-WPL 38, Boulder, CO (1975).
9. Duane A. Haugen, et al., The Use of an Acoustic Echo Sounder for Optical Tracking Applications, AFCRL Technical Report AFCRL-TR-75-0454, Hanscom AFB MA (1975).
10. Darryl P. Greenwood and Donald O. Tarazano, A Proposed Form for the Atmospheric Microtemperature Spatial Spectrum in the Input Range, RADC Technical Report RADC-TR-74-19, Griffiss AFB NY (1974).
11. James L. Spencer, Structurally - Induced Turbulence, unpublished technical memorandum, RADC/OCSE, Griffiss AFB NY (1975).
12. G.R. Ochs, et al., "Refractive - Turbulence Profiles Measured by One-Dimensional Spatial Filtering of Scintillations," Applied Optics 13 (1976).

UNCLASSIFIED

UNCLASSIFIED

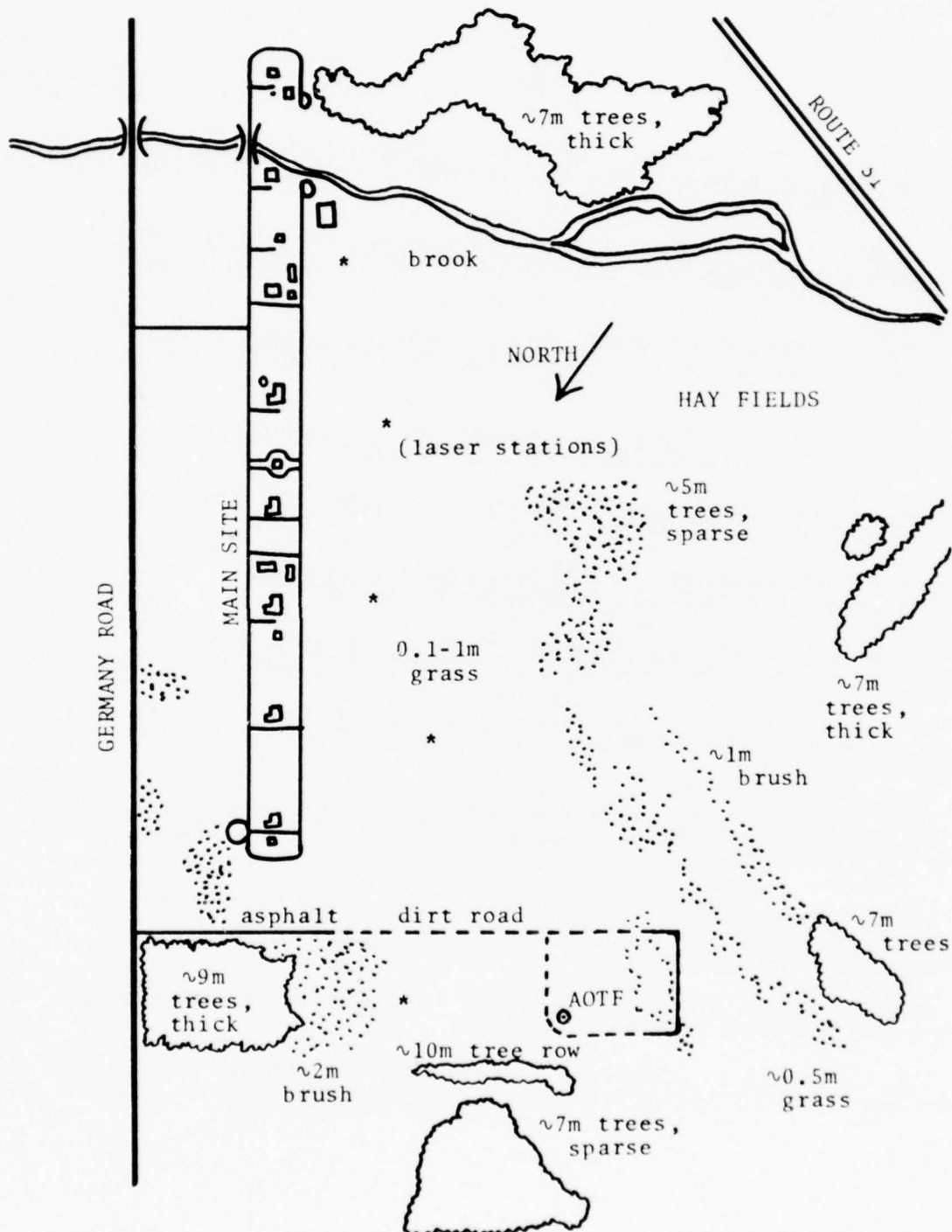


FIGURE 1. ADVANCED OPTICAL TEST FACILITY (Verona Test Site, NY)

UNCLASSIFIED

UNCLASSIFIED

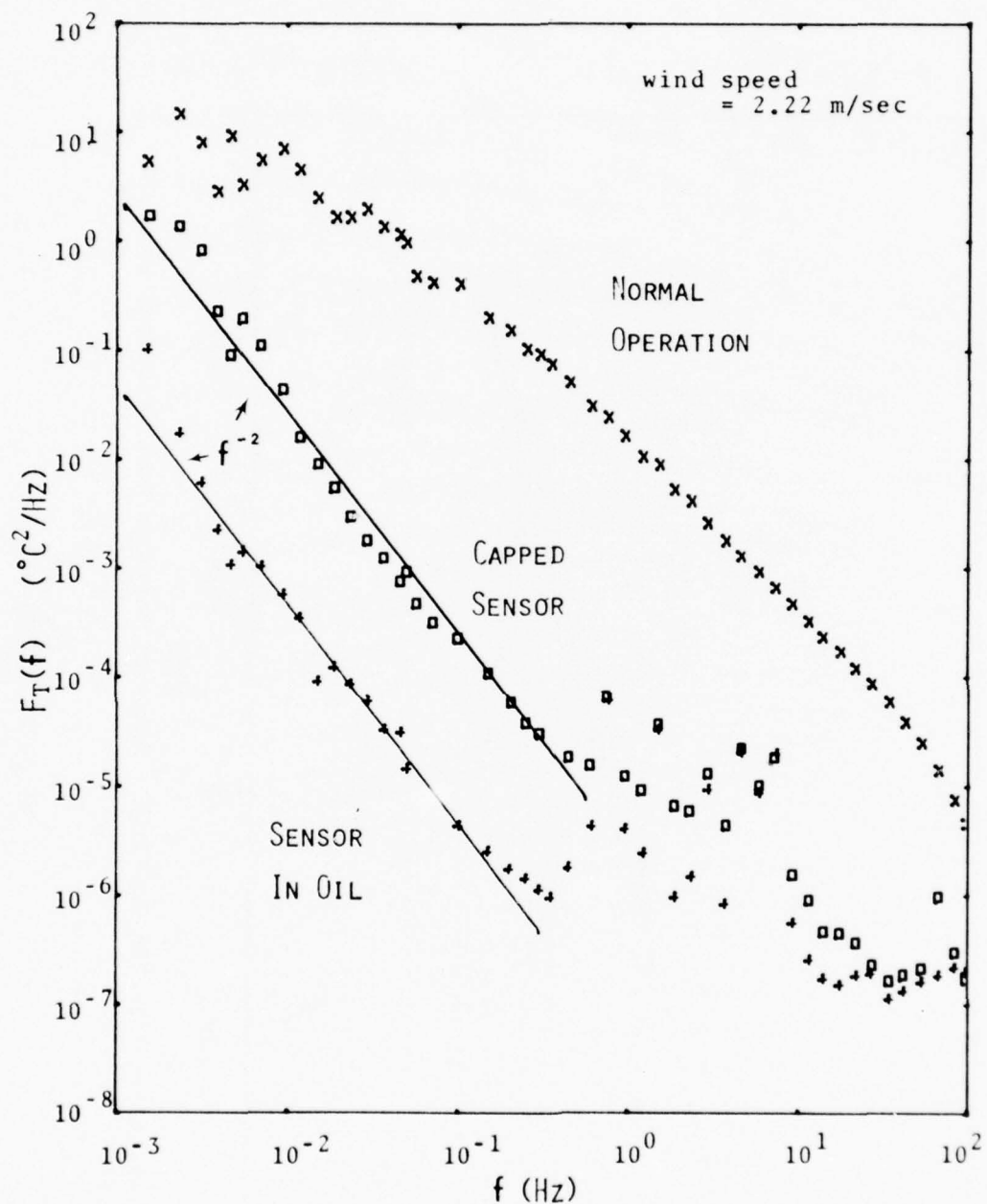


FIGURE 2. FINE-WIRE TEMPERATURE POWER SPECTRA. Temperature power spectra for a sensor in oil, a sensor in air and a sensor with its teflon cap in place.

UNCLASSIFIED

UNCLASSIFIED

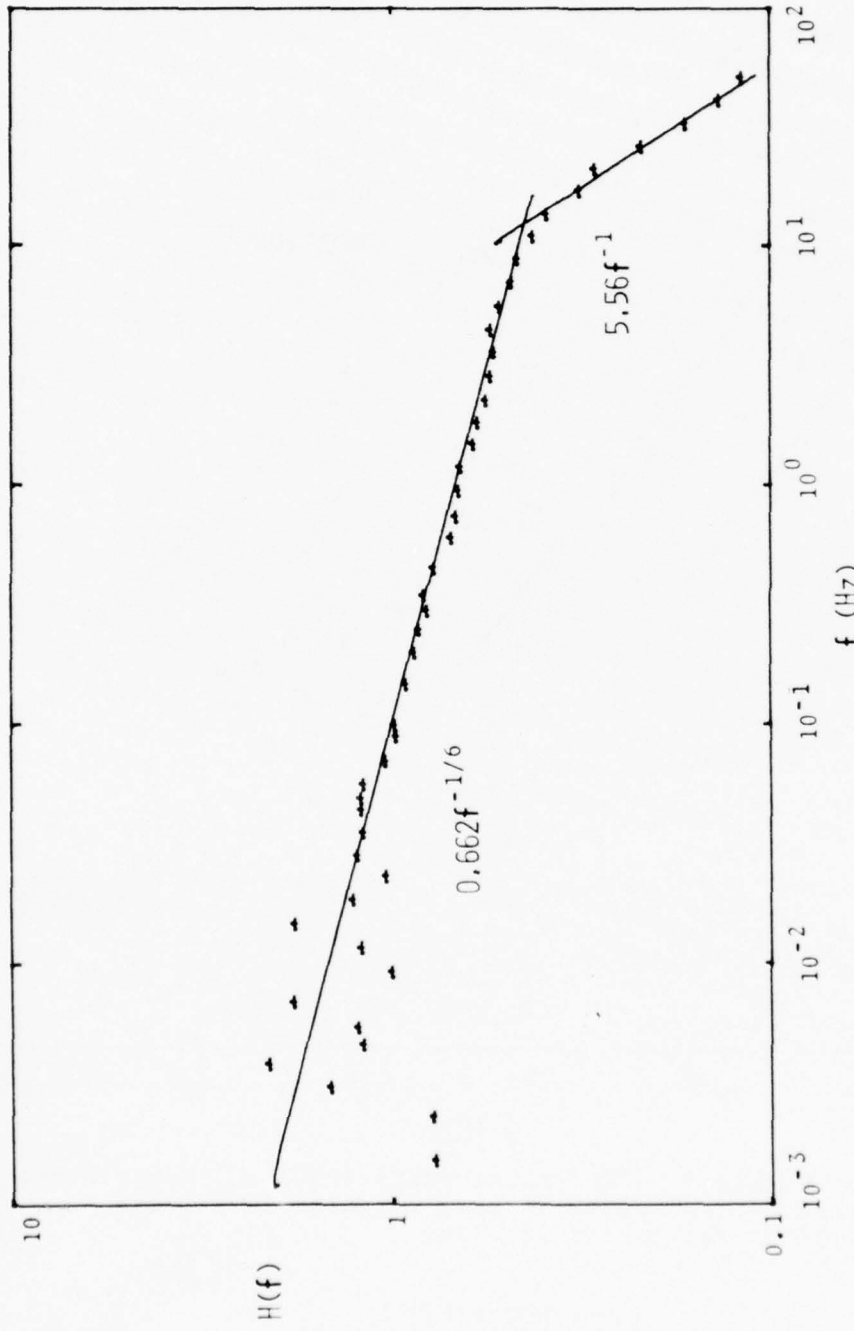


FIGURE 3. RELATIVE FAT-WIRE RESPONSE. Ratio of fat-wire power spectrum to fine-wire power spectrum.

UNCLASSIFIED

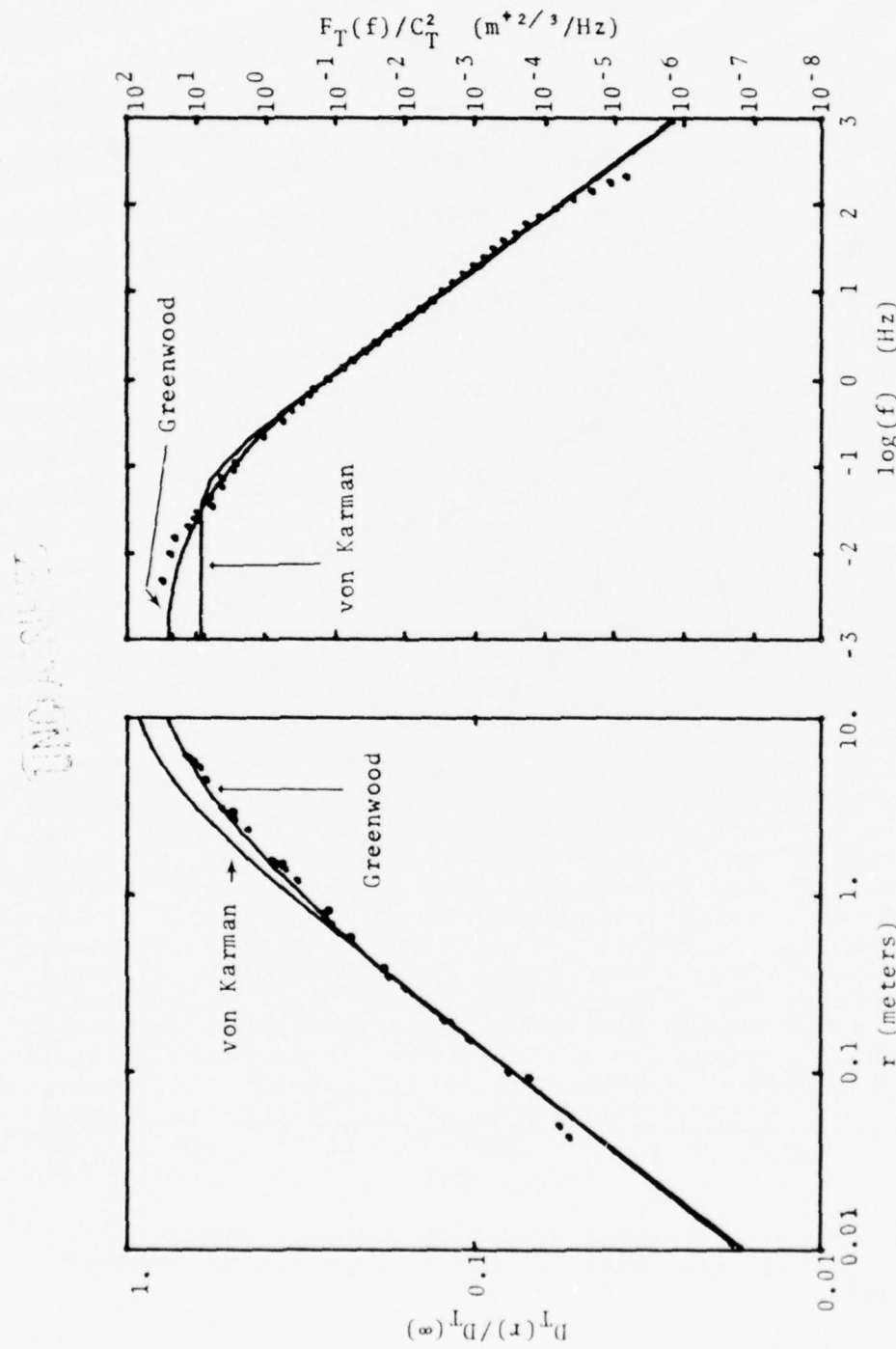


FIGURE 4a. TEMPERATURE STRUCTURE FUNCTION.
Normalized structure function data and
theoretical curves.

FIGURE 4b. TEMPERATURE POWER SPECTRUM.
Normalized power spectrum data and
theoretical curves.

UNCLASSIFIED

UNCLASSIFIED

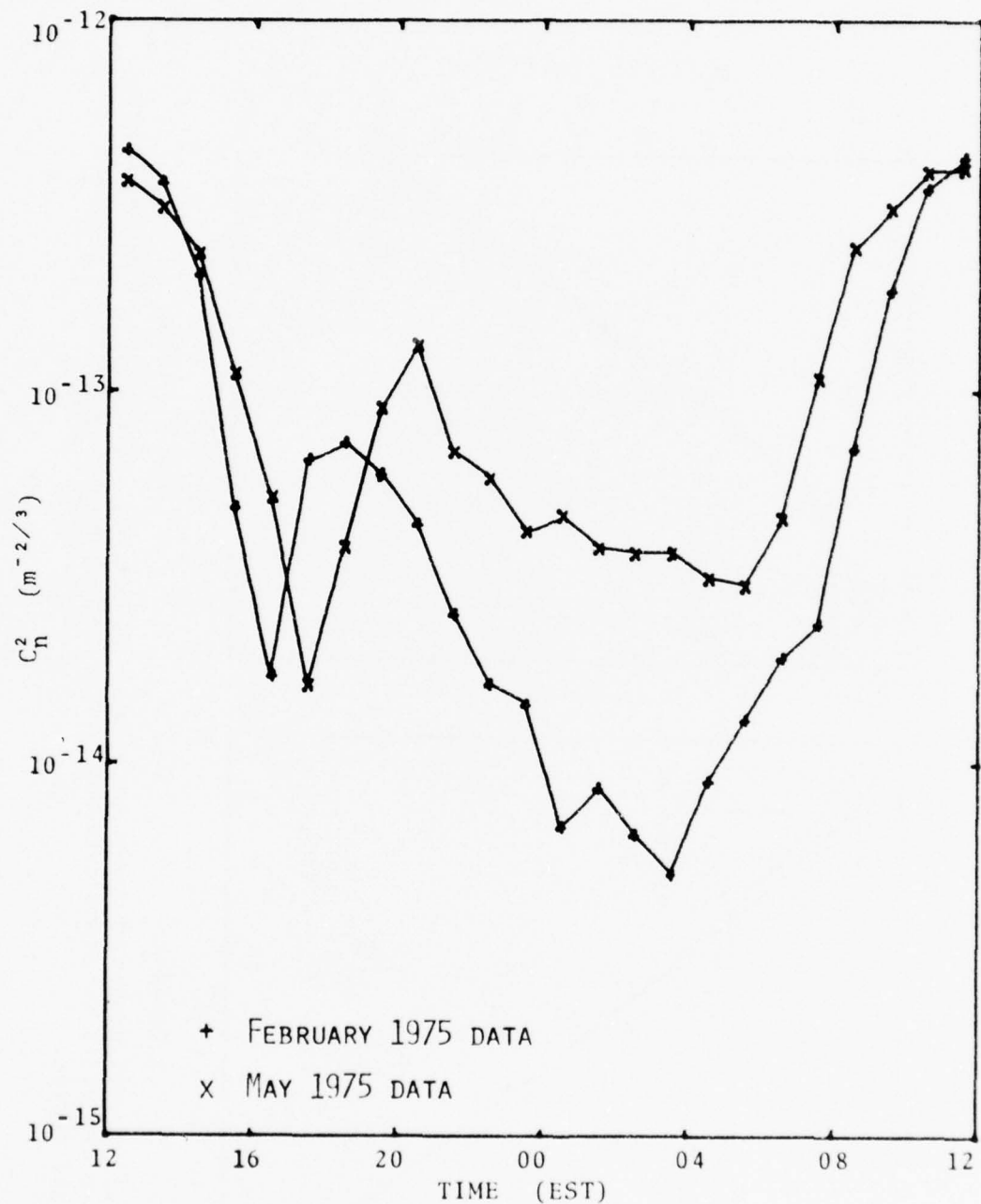


FIGURE 5. REFRACTIVE INDEX STRUCTURE CONSTANT VERSUS TIME OF DAY. One-hour time averages of C_n^2 (Type I) for February and May 1975.

.... This paper is UNCLASSIFIED

MARITIME ATMOSPHERIC CHARACTERIZATION AT
THE SAN NICOLAS ISLAND FACILITY

Lowell Wilkins

Alexis Shlanta

Naval Weapons Center

ABSTRACT

A maritime atmospheric observation station will be established at San Nicolas Island off the coast of Southern California. The purpose of the station is to collect atmospheric transmission data in selected spectral bands together with supporting meteorological data. The data will be analyzed to assess the utility of electro-optical instrumentation in a maritime environment. Specific objectives of the program include (1) statistically describing the atmospheric conditions on a day-to-day basis over a long period of time and (2) relating the atmospheric transmission to measurable meteorological parameters. During several scheduled periods of concentrated measurements, vertical profiling of selected meteorological parameters will be accomplished.

INTRODUCTION

Although the U.S. Navy has a recognized need for effective utilization of electro-optical (EO) weaponry in the maritime environment, major questions remain unanswered concerning EO system deployment. The availability of EO sensors (i.e., the percentage of time they are able to perform designated tasks), operating in selected spectral bands, is unknown for any oceanic location. Predictive computer codes, to estimate atmospheric effects on the propagation of optical energy, based on easily measurable meteorological quantities, are unproven in a maritime environment. In order to address these, and similar questions, the Navy will establish an atmospheric observation station on San Nicolas Island (SNI), off the coast of Southern California.

Under sponsorship of the Optical Signatures Program (OSP) the measurements will employ personnel from several Navy laboratories. Assistance in the initial set up will be provided by the Night Vision Laboratory (NVL).

The atmospheric transmission measurements are expected to commence in March, 1977. Participation in and sponsorship by OSP is scheduled through October, 1978. Meteorological measurements, in support of the transmission observations, will be recorded at selected land locations as well as on board a jack-up barge, permanently anchored off shore. The required personnel for manning the SNI station will be provided by Pacific Missile Test Center (PMTC), whereas the meteorological instrumentation on board the jack-up barge will be operated by Naval Research Laboratory (NRL) atmospheric physicists.

SAN NICOLAS ISLAND FACILITIES

The selection of the SNI location was made after a detailed study of several candidate sites on the East and West Coasts. The primary disadvantage of East Coast sites was the predominance of off-shore winds which impose continental aerosol conditions upon the measurement scene.

The SNI is characterized by a double-bay geographical shape at the northwest end. The bays provide natural over-the-water paths of 2.5 and 4.0 kilometers (Figure 1). Prevailing winds at the island are from the northwest (approximately 315 degrees true), providing extremely long fetches the great majority of the time. The atmospheric

UNCLASSIFIED

conditions are, therefore, highly indicative of an open-sea environment. The shortest distance to the mainland is approximately 100 kilometers, down wind.

The island is part of this country's National Test Range complex. It is Navy owned, controlled, and operated. The island is the hub of much test and evaluation (T&E) activity carried out by PMTC. Tight security conditions prevail.

Daily commercial airline travel to and from the island is available. Dining and berthing facilities exist to accommodate large numbers of visitors in addition to the permanently assigned PMTC work crews. It is not expected that additional housing will be required to support the transmissometer experiment.

SPECIFIC TASKS

During the 1½ years of data acquisition, a relatively long-term data base will be established. Analysis of the data will be performed to answer specific questions regarding deployment of EO equipment on Naval ships/boats and sea-deployed aircraft. Analytical topics include the following:

- (1) Statistical evaluation of atmospheric transmission in selected spectral bands;
- (2) Relationship of transmission to easily measurable meteorological parameters;
- (3) Relative effects of aerosol and molecular attenuation;
- (4) Vertical profile of atmospheric attenuators; and
- (5) Degraded-weather effects.

The above tasks address the questions "How much?" and "How often?". They implicitly recognize that generalized weather descriptions are not adequate for U.S. Navy's needs.

MEASUREMENT INSTRUMENTATION

A Model 14-712 Barnes Atmospheric Transmissometer System will be utilized to conduct atmospheric transmission measurements in selected spectral bands throughout the visible and infrared regions. The 14-712 system consists of two complete visible/infrared radiation source assemblies, which serve as transmitters, and three complete receiver assemblies, each of which has a different spectral sensitivity.

The radiation sources consist of one 3000° K special tungsten filament source of visible radiation, and one

UNCLASSIFIED

1200° K black-body source of infrared radiation. The radiation from both sources is, by means of a special beamsplitter, combined and transmitted through a common collimator. The radiation is full-field chopped with a 39-blade reticle to reduce background effect.

Three receiver heads collect the transmitted optical energy, one each to cover the visible and near infrared, near- and mid-infrared, and far-infrared regions. The first sensor is equipped with a silicon detector, operating at ambient temperature, to sense visible radiation flux. The second sensor employs a cooled indium antimonide detector and operates in the near and mid-infrared regions. Far infrared energy is sensed by the third sensor which utilizes a cooled mercury cadmium telluride detector. Detector cooling, as required, is provided by demandflow cryostats. All sensing heads have motordriven filter wheels; boresight telescopes are mounted on each receiver optical barrel.

Phase-lock circuitry in each receiver head permits precise phase-locking to the modulated source energy. Phase information is carried by land lines from the sources to the receivers. As a result, accurate transmission readings will be possible at low S/N values.

Supporting meteorological data will be recorded at land sites as well as on board the jack-up barge, anchored offshore. The meteorologically instrumented jackup barge can be permanently stationed in water as deep as forty feet. The barge instrumentation provides the capability to assess local wind speed/direction, air temperature, pressure, humidity, turbulence, solar radiation, water temperature, temporal wave-height statistics, and aerosol number and size distributions (Knollenberg counters).

A forty-foot tower, rising from the barge deck, is instrumented to permit vertical profiling of parameters of interest. Much of the data taken from the barge can be reduced in near real time. Computer programs exist to analyze the data and exhibit results in a variety of formats.

TEST SET-UP

The three receivers will be co-located at Site A (Figure 1). Radiation sources will be situated at the Calibration Site and Site C. Site B will be a back-up source site in the event the 4.0 kilometer path, between Sites A and C, is too long.

UNCLASSIFIED

The receiver spectral bands will be chosen in several categories; operational bands of military sensors; bands employed in other ongoing programs (such as OPAQUE); and bands which aid atmospheric investigations at selected spectral locations. (e.g., atmospheric windows and laser regions).

Low Mode and High Mode measurements will be performed. The Low Mode measurements will be conducted daily on a routine basis. Transmission readings will be performed hourly over an 8 to 12 hour period. Supporting meteorological data, taken at both ends of the transmission path, will include visibility (nephelometer), temperature, pressure, humidity, and wind speed/direction. All meteorological measurements during Low Mode will be performed from on-shore installations. Water temperature and wave-height statistics will be available from other ongoing programs.

High Mode operations will be conducted at intervals of approximately five weeks. Each High Mode period will last one week, during which time intensive meteorological data, both on-shore and off-shore, will be recorded together with atmospheric transmission data. During this time the jack-up barge will be continuously manned. Some measurements will be conducted after daylight hours. Vertical profiling of meteorological conditions will be done at four levels, using the forty-foot tower on the jack-up barge. All meteorological instrumentation previously described will be operated. Following High Mode operations data reduction will be performed by NRL (meteorology from jack-up barge) and PMTC. A cohesive report, detailing measurement results will be issued semi-annually by PMTC. More frequent distribution of raw data will be performed by PMTC. It is anticipated that much analysis of the raw data will be done by other programs.

In preparation for High Mode operations, extensive calibrations of all equipment will be conducted. The primary mode of calibration for the double-ended transmissometer system is the "head-to-head" technique in which the source is brought to very close proximity of the receiver. Calibrations performed in this manner, have been shown to be very accurate. During very clear weather, it may be possible to perform calibrations by direct measurements, at Site A, of the sources located at the "Calibration Site" (Figure 1).

UNCLASSIFIED

DATA ANALYSIS

Detailed analysis of the SNI data will commence early in FY-78. Atmospheric transmission values, and supporting meteorological data, will be stored in computer compatible format on magnetic tape. Analog or digital tapes will be used as appropriate. At intervals of approximately six months, the data will be recalled to investigate specific characteristics of the maritime environment.

Statistical Analysis of Temporal Variations in Atmospheric Transmission. Temporal variations in atmospheric transmission, in selected spectral bands, will be computed. Extrema and mean values will be catalogued. Diurnal, weekly, and monthly variations will be compiled and presented in histogram graphs. Variances about the mean values will be computed. Probability distribution plots will be generated.

Correlation of Atmospheric Transmission with Meteorological Parameters. A study of the relationship between easily measured meteorological variables and atmospheric transmission will be performed. Cross correlation analyses will be employed to identify high correlation parameters. Meteorological parameters will be considered both singly and in combination. Weighting functions, showing the relative importance of distinct meteorological parameters in the prediction of EO transmission, will be generated. The results will be applied to varied weather scenarios for validation purposes.

Relative Importance of Aerosol and Molecular Attenuation. Analyses will be performed to determine the relative contributions of aerosols and molecular attenuators in the extinction process. The total extinction due to molecular absorption and aerosol scattering will be measured by the transmissometer system in several spectral bands. The extinction due to molecular absorption, alone, will be computed with LOWTRAN. Inputting the measured atmospheric water vapor content and estimates for amounts of other absorbers, a simple subtraction, then, provides the extinction due to aerosol scattering. These results will be compared with aerosol size/number distributions obtained during High Mode operations.

Vertical Profiling of Atmospheric Aerosols. Analyses of the variations in size/number distributions of marine aerosols will be based on direct measurements performed during High Mode operations. Limited data will be available for heights from 10 to 50 feet MSL.

UNCLASSIFIED

These data will be taken on board the jack-up barge. If OSP funding permits utilization of an aircraft measurement platform, more complete aerosol data at heights above 100 feet MSL will be available. The aerosol data will be presented in graphical and tabular form. Probability distribution plots and other representations of the data will be reported.

Throughout the data analysis defined above, examinations of the effects of degraded weather will have a high priority. Frequency of occurrence, persistence of conditions, and effects on transmission will be quantified and reported.

The magnetic tapes generated during the SNI experiment will be made available to other programs upon request and receipts of need-to-know verification.

UNCLASSIFIED

SCHEDULE

Preparations for the transmissometer experiment have commenced. Actual measurements are scheduled to start in March, 1977

January, 1976	Transmissometer System Ordered
July, 1976	SNI selected as measurement site
November, 1976	Concrete Pads and Hard Power installed at SNI stations
November, 1976	Jack-up barge shipped to PMTC
March, 1977	Jack-up barge anchored off SNI
February, 1977	Delivery of transmissometer system
April, 1977	Meteorlogical and transmission measurements begin
October, 1977	First semi-annual report issued
April, 1978	Second semi-annual report issued
October, 1978	Third semi-annual report issued

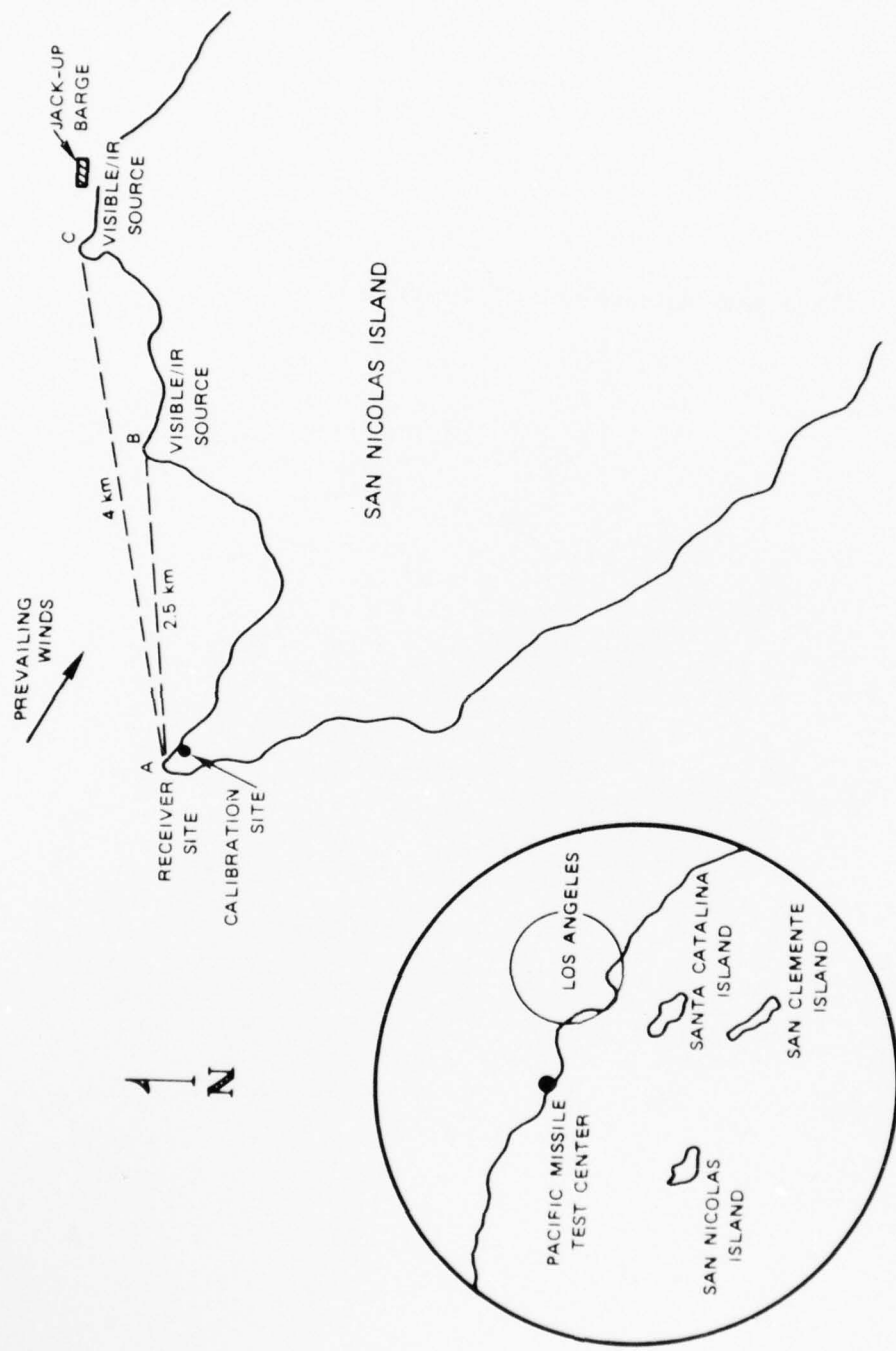


FIGURE 1. SAN NICOLAS ISLAND TEST FACILITY.

(This page intentionally left blank.)

. . . . This paper is UNCLASSIFIED

MICRO-METEOROLOGICAL MEASUREMENTS FOR ELECTRO-OPTICAL
PROPAGATION TESTS AT WHITE SANDS MISSILE RANGE

Glenn B. Hoidal
Donald L. Walters
Colburn L. Norton
and
Thomas H. Pries

Atmospheric Sciences Laboratory
US Army Electronics Command
White Sands Missile Range, New Mexico 88002

ABSTRACT

Electro-optical propagation through the atmosphere involves both linear and non-linear effects. The linear aspects include atmospheric thermal turbulence which modulates and redistributes the energy, and gaseous and aerosol extinction. When the electro-optical energy is sufficiently high, the atmospheric absorption will produce non-linear effects which result from the dissipated heat.

An extensive measurement program is currently underway at the Atmospheric Sciences Laboratory, White Sands Missile Range, to obtain climatological characterization of those specific atmospheric parameters which degrade electro-optical propagation. This field effort includes multi-level tower measurements of thermal turbulence, and pertinent meteorological quantities augmented by gaseous constituent concentrations and aerosol particulate size and number distributions. This paper includes a synopsis of preliminary data results and a discussion of their influence on electro-optical propagation.

INTRODUCTION

The emergence of military electrical-optical (EO) systems has re-kindled interest in atmospheric optics. The theoretical interpretation of EO propagation is very important; however, the physical interpretation of the results of actual field propagation tests is heavily dependent upon atmospheric measurements.

At the Tri-Service High Energy Laser (HEL) Systems Test Facility at White Sands Missile Range (WSMR), New Mexico, the Atmospheric Sciences Laboratory bears responsibility for the atmospheric characterization measurements. It is the purpose of this paper to discuss two of these measurements in detail - thermal turbulence and crosswind - and to present some general conclusions applicable to HEL propagation at WSMR.

ATMOSPHERIC EFFECTS

There are both linear and non-linear atmospheric effects on HEL beam propagation, effects which serve to degrade the overall beam quality. The main linear effects are due to thermal turbulence and molecular and aerosol extinction. Thermal turbulence results in scintillation, spot dancing, beam bending and therefore beam spread. It is a random process whereby small scale fluctuations of density change the index of refraction, thus rendering the atmosphere non-homogeneous and non-isotropic. Another linear effect is attributable to absorption and scattering of photons by gases, and by liquid and solid particles. Dr. Pinnick will address certain aspects of the latter in another paper presented at this conference¹.

Among the non-linear effects is thermal blooming. Thermal blooming results from absorption of energy in the laser beam by the medium (gas, liquid, solid). The absorption raises the temperature of the absorbing medium and hence lowers its density. Part of the energy is refracted out of the original beam path, thus reducing the beam quality. Since thermal blooming depends on the heat absorbed in the atmosphere, the magnitude of the effect is a function of the hydrodynamic motion of the medium across the beam, i.e. the so-called crosswind.

TOWER MEASUREMENTS

Current measurements are being taken at a 32 m meteorological tower which is located at the Tri-Service High Energy Laser Systems Test Facility (HELSTF), approximately 29 km north-northeast of the main post area at White Sands Missile Range. The tower is located on a flat-unobstructed surface between the San Andres and Sacramento Mountains. The instrument package on the tower consists of five pair of fast response temperature probes, located at 2, 5, 9, 16 and 32 m, four thermocouple probes located at the surface, 5, 9, and 32 m, three UVW Gill anemometers located at 9, 16, 32 m, and a net radiometer at 1 m.

THERMAL TURBULENCE

In the study of propagation of laser beams through the atmosphere, information about the refractive-index fluctuations is essential for meaningful comparison with theoretical predictions. The single most important parameter is the refractive-index-structure parameter (C_n^2). To obtain C_n^2 , it is assumed that at optical wavelengths and over small scale sizes, C_n^2 is a function of pressure, temperature and C_T^2 , the temperature-structure parameter. Thus²,

$$C_n^2 = \left(\frac{79P}{T^2} \times 10^{-6} \right)^2 C_T^2; [m^{-2/3}], \quad (1)$$

where P is in millibars, T is the Kelvin temperature. The temperature

structure parameter is measured by a pair of tungsten filament temperature probes which are separated in the vertical by 0.2 m. The purpose of these probes is to measure the instantaneous temperature differences ($T_2 - T_1$) which determines the temperature structure parameter,²

$$C_T^2 = \frac{(T_2 - T_1)^2}{r^{2/3}} ; [\text{DEGM}^{-2/3}], \quad (2)$$

where r is the separation of the two probes in meters.

Data for C_T^2 (from which C_n^2 can be derived) has been taken aperiodically at the HELSTF since April of 1976. The diurnal variation of C_T^2 (C_n^2) is shown in Fig. 1 for a typical clear day in June. The following formula,

$$C_n^2 = 6.0 \times 10^{-13} C_T^2, \quad (3)$$

converts C_T^2 to C_n^2 using equation (1) for typical values of 300.0°K and 890.0 mb for T and P , respectively. The three curves in Fig. 1 represent measurements of C_T^2 taken at the 5 m (---), 9 m (-) and the 32 m (- -) levels. These curves show thermal turbulence is strongest around noon and falls to a minimum near sunset and rises again to moderate levels at night. A minimum usually occurs near sunrise, the occurrence being strongly influenced by the structure of temperature inversions.

On a partly cloudy day C_T^2 (C_n^2) does not follow the consistent pattern as exhibited by Fig. 1 but is much more sporadic in nature and hard to predict. Figure 2 shows a partly cloudy day in August. Notice that the basic features are present but, C_T^2 (C_n^2) can be about a factor of four lower with clouds present.

In addition to "point" measurements of turbulence, indirect optical integrated path measurements of C_n^2 are being made. The Atmospheric Sciences Laboratory is currently utilizing a Campbell Model CA-9 Space Averaging Anemometer and a Saturation Resistant Crosswind Sensor both developed by Ochs et al. at the National Oceanic and Atmospheric Administration^{3,4}. The expression for indirectly computing C_n^2 for a spherical wave propagating in a random but statistically stationary turbulent medium is⁵

$$C_n^2 = 8.06 k^{-7/6} z^{-11/6} C_L(0) \quad (4)$$

where k is the wavenumber, z is the distance to the target in meters and $C_L(0)$ is the variance of the log-amplitude irradiance which is measured at the receiver. Various studies have been made to correlate optically measured C_n^2 with temperature probe measurements of C_n^2 ^{6,7}.

If slant path measurements of C_n^2 are needed, the measurement becomes more difficult. Tower measurement of C_T^2 (C_n^2) may be applicable up to the tower height which is typically 32 m. Optically measured C_n^2 have a very limited use due to the weighting of C_n^2 along the slant path which will bias the data toward the lower heights. For heights from 32 m to 500 m an acoustic sounder, for example, developed by Freeman Hall⁸ at the National Oceanic and Atmospheric Administration (NOAA) can provide C_n^2 as a function of altitude. For heights above 500 m, the Air Force Weapons Laboratory is working on a program of indirectly computing C_n^2 from normal Rawinsonde or Thermosonde measurements⁹.

CROSSWIND

The understanding of the meteorological effects on continuous wave thermal blooming is needed to describe HEL propagation. The meteorological parameters needed to understand these effects are: crosswind speeds, thermal turbulence, and total absorption which includes both molecular and aerosol absorption. Only the crosswind aspects will be discussed in this section.

Thermal blooming is inversely proportional to the crosswind speed¹⁰. The beam quality is influenced by the crosswind speed in that an increase of wind speed reduces the time in which heated constituents of the atmosphere are in the laser path.

There are two crosswind considerations which apply to high energy laser firing: 1) the climatology of wind speed and 2) the intermittency, which is defined as the process by which the crosswind speed is high enough at each point along the path so as not to decrease the beam quality to an unacceptable level.

The climatology of crosswind speed is needed to determine the extent to which a potential site may be used for HEL testing and to determine the optimum orientation for the range once the site has been selected. Once that the site and range orientation have been determined, and a HEL firing is to take place, the wind speed at various points along the path have now become of special interest.

At the HELSTF, there is no actual climatology of wind speed and direction. However, an extensive set of climatological wind data does exist for "similar" locations in the area. Thirty-year and 9-year statistics of wind speed and direction are available from Holloman Air Force Base¹¹ (located 32 km to the northeast of HELSTF) and Rat Scat Site¹² (located 18 km to the north) respectively. The extent to which the Holloman Air Force Base (AFB) data may be applicable to the HELSTF was examined by detailed comparison of the original wind records for various months in 1976. Figure 3 shows the comparison of Holloman AFB and HELSTF wind speed and direction for July 1976. As seen in this figure, the comparison shows that the data from each site is

similar. If this comparison holds for the remaining 11 months, the Holloman AFB data will be used to compile probabilities of wind speed for particular wind directions. Analysis of the climatological data wind speed at Holloman AFB shows the wind speed is the highest during the hours of 1500-1800 MST. Using this time interval, Fig. 4 shows the monthly variation of the probability of a crosswind speed greater than 5 m sec^{-1} for three laser propagation orientations. The highest crosswind speed occurs during the spring months and the NW-SE orientation maximizes the crosswind at least for the spring.

Realtime displays of the variation of wind speed along the laser path is important. These displays will delineate the critical stagnation zones for thermal blooming. Figure 5 shows a typical horizontal realtime plot of 20 UVW Gill anemometers (crosswind component) spaced by 25 m apart for 500 m as a function of time. This plot shows that if a HEL beam propagates through this wind pattern, there are places along the path where the windspeed is probably low enough to cause significant thermal blooming whereas an arithmetic average of 20 wind speeds would probably have been high enough for HEL propagation.

If winds along slant paths are needed, the measurement problem increases. Candidate systems for integrated path measurements are the aforementioned Campbell and Saturation resistant units. Path profiling systems such as laser doppler velocimeter¹³, Freeman Hall acoustic sounder and the NOAA¹⁴ are being investigated for application to the slant path problem.

SUMMARY

Climatologies of C_n^2 and wind velocity are being developed for the tentative site location of the HELSTF. Atmospheric Sciences Laboratory will continue to gather data on these parameters, determine how these parameters effect HEL propagation, and develop a capability to predict these parameters for realtime use. The prediction will not only focus on a week or hour in advance, but along a path when measurements are not made directly along the path.

From the climatological approach the best time to fire HEL with respect to C_n^2 and crosswind at the HELSTF is during the spring months between 1500-1800 hrs.

Basically this paper has dealt with some of the meteorological parameters needed for fixed path HEL firing. However a capability to make moving measurements of C_n^2 and crosswind speed needs to be developed.

REFERENCES

1. R. G. Pinnick, "Aerosol Size Distributions Measurements for Radiation Transfer Modeling", ODDRE Electro-Optical/Submillimeter Propagation Workshop, Air Force Academy, Colorado Springs, Colorado, 1976.
2. R. S. Lawerence, G. R. Ochs, and S. F. Clifford, J. Opt. Soc. AM. 60, 826 (1970).
3. R. S. Lawerence, G. R. Ochs, and S. F. Clifford, Appl. Opt. 11, 239 (1972).
4. G. R. Ochs, S. F. Clifford, and Ting-I Wangi, Appl. Opt. 15, 403 (1976).
5. V. I. Tatarski, Wave Propagation in A Turbulent Medium (McGraw-Hill, New York, 1961).
6. J. E. Pearson, J. Opt. Soc. AM 65, 938 (1975).
7. P. H. Deitz and N. J. Wright, J. Opt. Soc. AM 59, 527 (1969).
8. F. F. Hall, Jr., Remote Sensing of the Troposphere, US Dept. of Commerce, National Oceanic and Atmospheric Administration, 18 (1972).
9. Private communication with R. Nelson at Air Force Weapon Laboratory, Kirtland Air Force Base, New Mexico.
10. F. G. Gebhardt, Appl. Opt. 15, 1479 (1976).
11. "Percentage Frequency of Surface Winds - Holloman", WBAN #23002, (United States Air Force Environmental Technical Applications Center, Air Weather Service, Ashville, N. C., 1975).
12. "Percentage Frequency of Surface Winds - Rat Scat Site", WBAN #93066, (USAFETAC, Air Weather Service, Ashville, N. C., 1976).
13. L. Lading, Appl. Opt. 10, 1943 (1971).
14. Under Contract to NOAA by ASL

AD-A037 812

OFFICE OF THE DIRECTOR OF DEFENSE RESEARCH AND ENGINE--ETC F/G 20/14
PROCEEDINGS OF THE OPTICAL-SUBMILLIMETER ATMOSPHERIC PROPAGATIO--ETC(U)
DEC 76

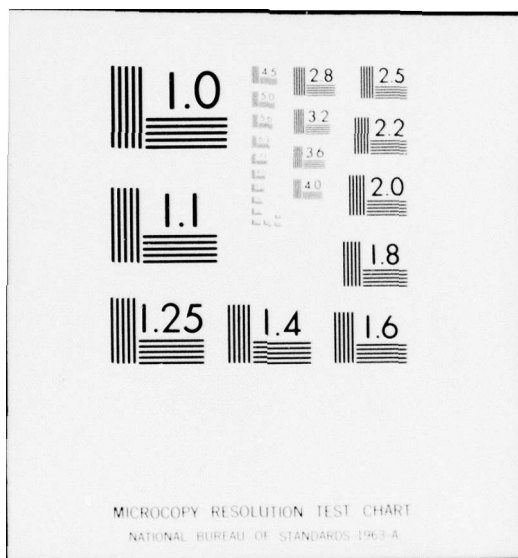
UNCLASSIFIED

NL

6 of 6
ADA037812

END

DATE
FILMED
4-77



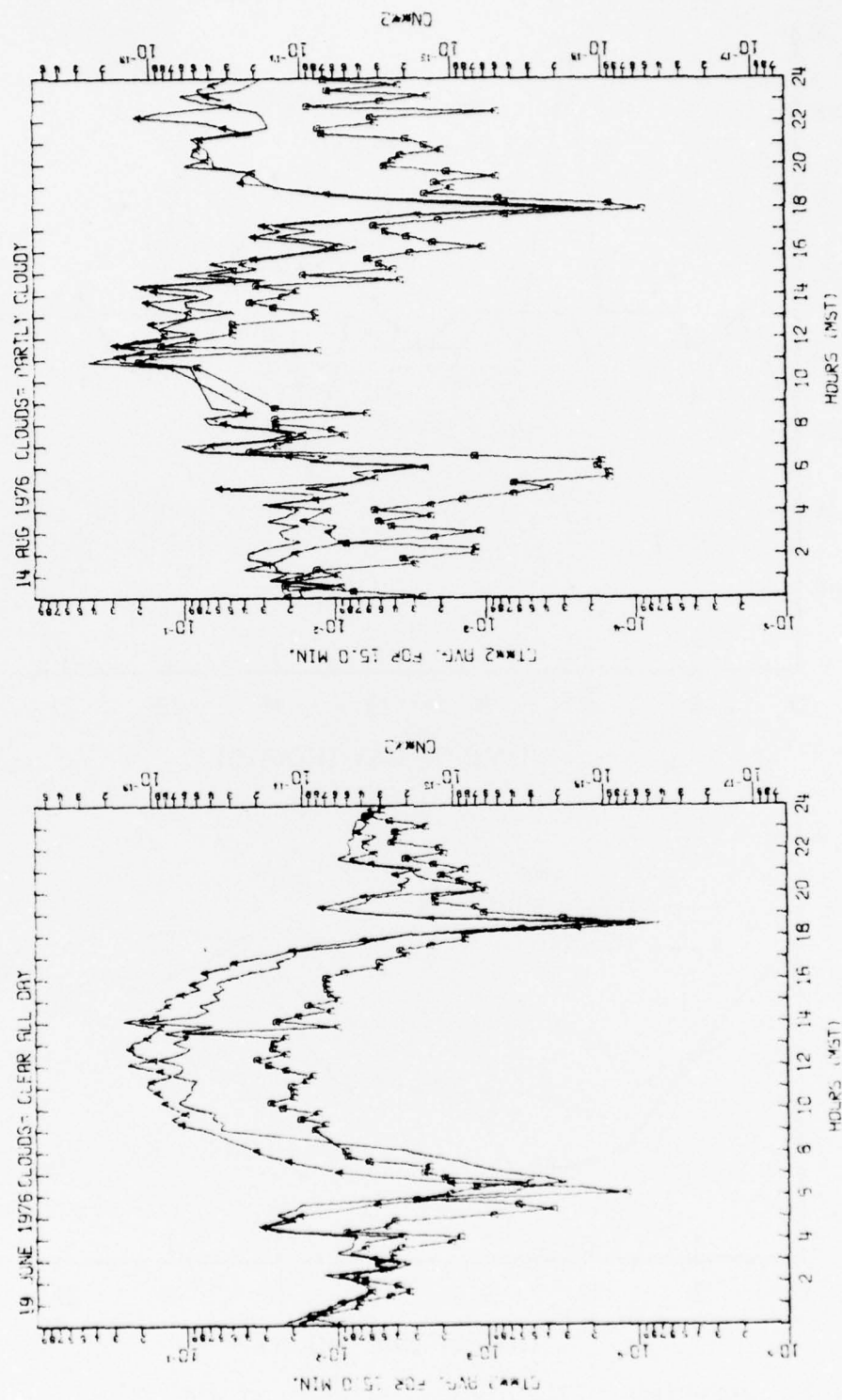


FIGURE 1. Diurnal Variation of $C_T^2 (C_n^2)$

FIGURE 2. Diurnal variation of $C_T^2 (C_\eta^2)$

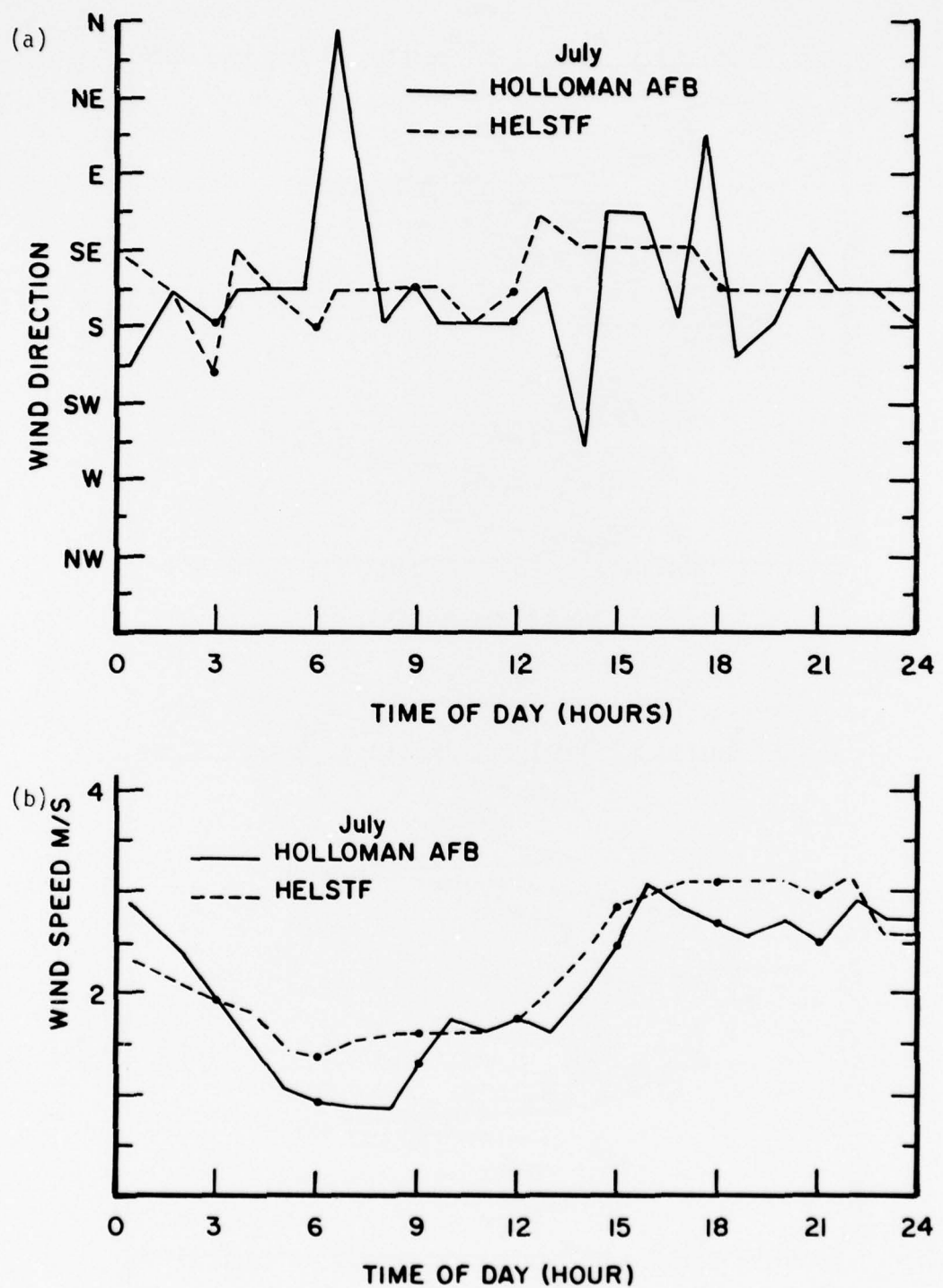


FIGURE 3. Comparison of the diurnal variation of wind velocity, (a) wind direction, (b) wind speed, for July.

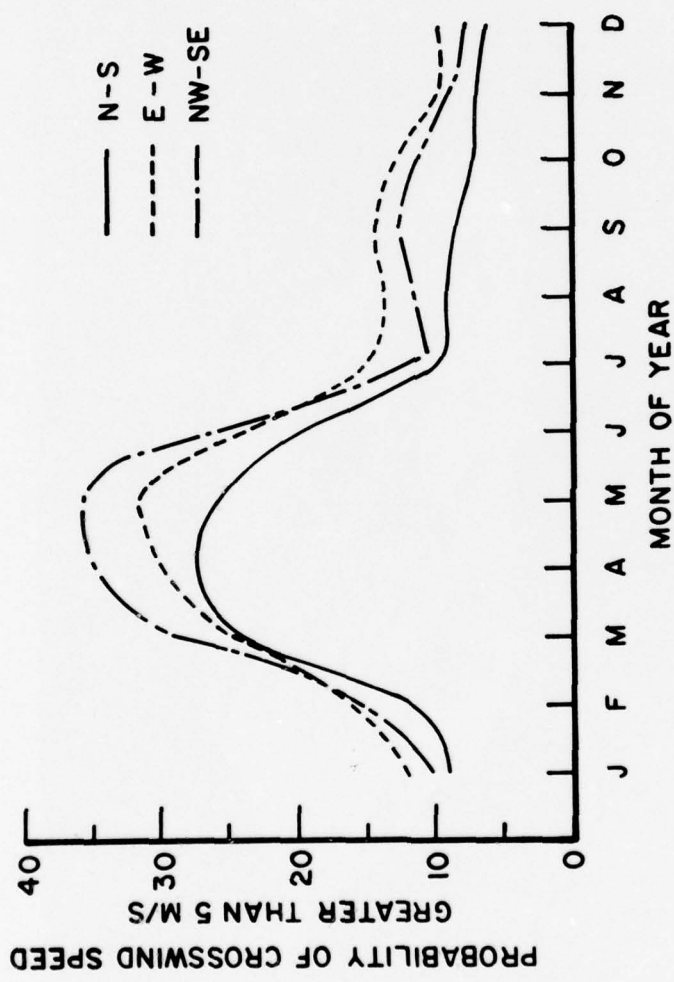


FIGURE 4. Probability of crosswind speed greater than 5 m/s at the HELSTF between 1500 and 1800 hrs MST as a function of month and orientation of the laser beam (based on Holloman data).

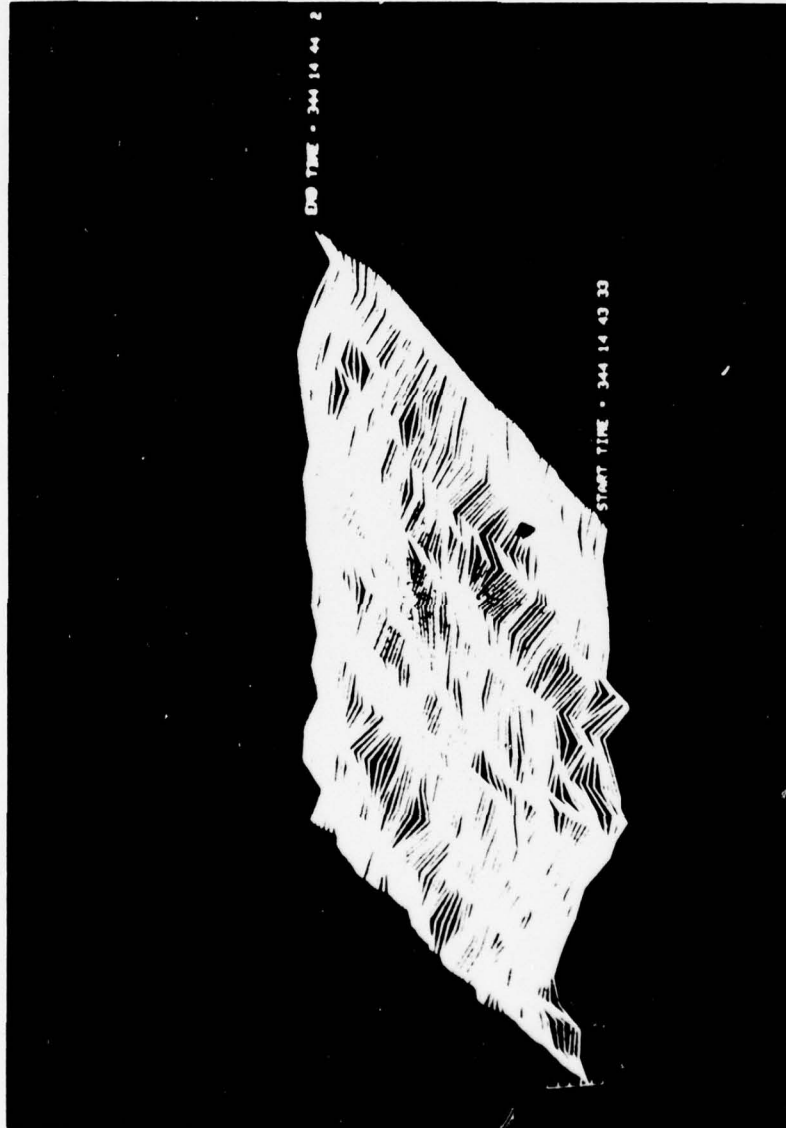


FIGURE 5. Plot of 20 UVW Gill anemometer (normal component) spaced 25 m apart for 500 m on the abscissa versus time. The time interval between each consecutive line is 0.5 s. One m/s tick marks with the origin being the first tick mark is in the bottom left corner.

UNCLASSIFIED

.... This paper is UNCLASSIFIED

EVALUATION OF THE PROPAGATION ENVIRONMENT USING LASER RADAR TECHNIQUES*

By

Edward E. Uthe
Stanford Research Institute
Menlo Park, California 94025

ABSTRACT

The atmosphere is a highly variable medium that can have limiting effects on the performance of many DoD communication and weapon systems. Atmospheric effects on these systems are typically poorly understood because of the difficulty in measuring critical atmospheric parameters with adequate spatial and temporal resolution over appropriate extended atmospheric regions--especially when the regions are made hazardous by use of the communication and weapon systems.

Lidar (laser radar) is one class of remote sensing instrumentation that provides a means to derive quantitative information on aerosol, cloud, and precipitation density distributions and optical properties over extended areas with extremely high spatial and temporal resolution, using instrumentation located at a single convenient site. SRI has developed a mobile lidar system, complete with its own power supplies, for immediate operation at any location. The system incorporates independent analog and digital data recording, processing, and display systems for providing reliable real-time analysis on operational programs, and for effective data collection on research programs. Both display systems can process a series of backscatter signatures in terms of intensity-modulated pictorial displays that depict time and space variations of atmospheric structure. In addition, the digital system can apply appropriate computational schemes to evaluate backscatter signatures in terms of physical and optical densities and relate this information to picture brightness.

This paper briefly describes the SRI Mark IX mobile lidar system and presents examples of data that demonstrate its capabilities for real-time observation of atmospheric aerosol, cloud, and precipitation elements over remote atmospheric volumes. Also presented are preliminary measurements of atmospheric attenuation at high energy laser (HEL) wavelengths made with an infrared (CO_2) lidar system.

*Preparation and presentation of this paper was supported by U.S. Army Research Office (Contract DAAG29-77-C-0001) and Stanford Research Institute.

UNCLASSIFIED

UNCLASSIFIED

I INTRODUCTION

Electromagnetic energy sources are available that can generate well-collimated beams or pulses for achieving very effective propagation of energy densities over long distances. However, military communication and weapon systems based on these sources can be adversely affected by atmospheric constituents that scatter and absorb energy of the wavelength being propagated. It is essential, therefore, to evaluate atmospheric effects on system performance. Experimental evaluation of the propagation environment for realistic atmospheres is difficult because of the large variations in atmospheric density and composition that can occur in very small increments of space and time. Analytical evaluation is also difficult, because particle single-scattering phase functions can vary in a complex manner with particle size, shape, and composition, and because multiple scattering cannot be accounted for accurately except in the case of very simple geometries of atmospheric density and propagation path. In addition, high-resolution absorption spectra for nonhomogeneous atmospheres require extensive computational efforts and are usually based on empirical data collected for homogeneous paths. Even if appropriate analytical techniques were readily available, measurement programs would be required to validate predicted effects for specific systems used during various meteorological conditions.

The propagation environment can be characterized in terms of the distribution of atmospheric constituents that can affect the propagation energy. If an important constituent is homogeneous in space and time, a single measurement at any location is all that is normally required to specify its effect on the propagation environment. However, if a constituent is extremely heterogeneous in space and time, measurements at many locations at the exact time of the propagation event may be required to define its effect. In addition, the propagation environment may be wavelength-dependent in such a manner that identification of the meteorological situation can provide a means to minimize atmospheric affects by proper choice of wavelength. Therefore, for experimental evaluation of the propagation environment, it is important to define, even on a relative density basis, time and space density variations of important atmospheric constituents.

Lasers provide a source of light energy with the characteristics necessary for strong interaction with atmospherically suspended particulate matter at remote distances. Recognizing this soon after the development of the first laser, scientists at SRI began a series of experiments in 1963 to develop and apply single-ended, range-resolved lidar (laser-radar) techniques. Most of the experiments were directed to the study of aerosol and cloud structure over extended atmospheric areas with spatial resolution and temporal coverage not possible with other techniques. Recent lidar developments can provide real-time pictorial displays of the relative densities of the distribution of

UNCLASSIFIED

aerosol, cloud, and precipitation over extended areas. The displays can be interpreted quantitatively in terms of the presence and location of smoke plumes, haze layers, cloud layers, and similar features. Several quantitative lidar studies have produced remote density measurements that compare favorably with *in situ* measurements. However, to derive absolute physical and optical densities by means of techniques of approximate solution, additional information or assumptions about the propagating medium are required. Further studies are needed to explore and evaluate fully the limitations of lidar techniques in measuring the propagation environment quantitatively.

II MARK IX LIDAR: EXAMPLES OF DATA

The SRI Mark IX ruby lidar system is the product of many years of experience in developing laser radars for application to research programs that require input data on atmospheric aerosol, cloud, and precipitation elements with high spatial and temporal resolution over remote areas. Operated from a mobile platform (see Figure 1) provided with power-generating facilities, it can be transported to any location for immediate operation. The Mark IX specifications are listed in Figure 1, and a system diagram is presented in Figure 2. One of the Mark IX's principal features is the use of two independent data recording, processing, and display systems for real-time viewing of pictorial displays of atmospheric structure. The displays are generated from backscatter data obtained from multiple laser firings while the lidar is being scanned in elevation, or azimuth, or with time. The analog (video disc) system provides nearly instantaneous access to any of 80,000 signatures recorded on a disc side, and the computer-based digital system provides digital records for processing in terms of physical and/or optical densities, in addition to controlled gray-scale presentations (Uthe and Allen, 1975). Examples of data obtained with the Mark IX lidar are presented below.

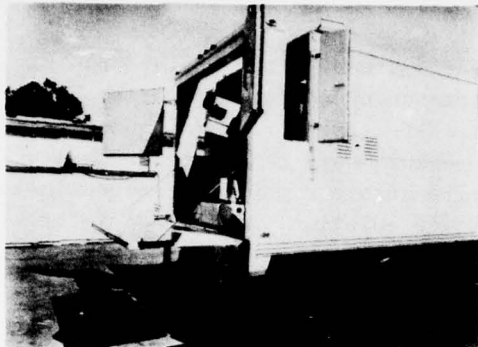
Figure 3 presents data collected during a weapon-firing exercise at an army base (Nanevicz et al., 1976). The Mark IX lidar was located approximately 4.2 km from background trees and 3.6 km from a firing mortar. The mortar shells impacted in an area 1 to 2 km from the lidar. Returns from the trees, mortar firing, and shell impact are visible on the data record. From the lidar observation of the mortar firing and impact particulates, the wind over the field is inferred to have a component in the direction of the mortar shell of approximately 1 km/min.

Figure 4 illustrates one application of the digital data system for observations of aerosol plume densities along possible propagation paths. The vertical plume cross section shown is plotted as an intensity-modulated array of points, each with brightness proportional to the logarithm of the backscatter signal (Uthe and Johnson, 1976). Since the backscatter signal array is also stored as an x-y array of digital numbers, a profile of plume density

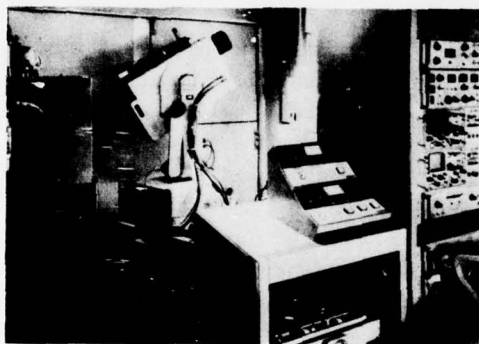
UNCLASSIFIED

UNCLASSIFIED

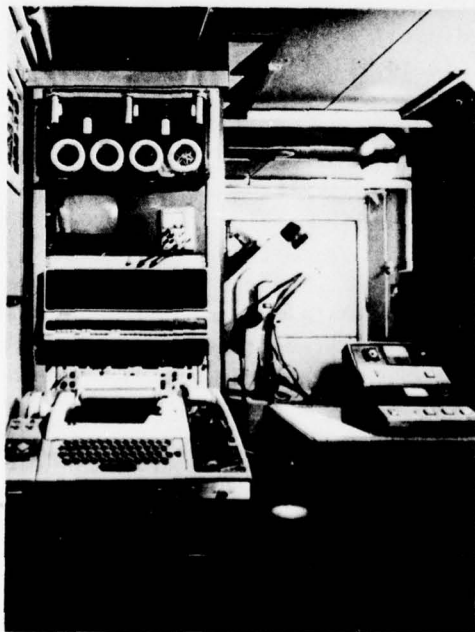
TA-653543-15



(a) MARK IX LIDAR VAN



(b) ANALOG DATA AND FIRE CONTROL ELECTRONICS



(c) DIGITAL DATA ELECTRONICS

MARK IX LIDAR SPECIFICATIONS

TRANSMITTER

6943 Å Wavelength
0.5 mrad Beamwidth
1.0 J Pulse Energy
30 ns Pulse Length
60 ppm Maximum PRF

RECEIVER

6 inch Newtonian
1 to 5 mrad Field of View
5 Å Prediction Filter
RCA 7265 PMT Detector
4 decade, 35 MHz Logarithmic Amplifier
Inverse range squared or step
function PMT modulation.

MOUNT

Automatic azimuth and elevation fire and scan with 0.1° minimum resolution. Automatic reset. Mechanical safety stops.

DATA SYSTEMS

Analog video disc recording (4.5 MHz) with A-scope and Z-scope real-time displays. Digital magnetic tape (data and programs) recording (25 MHz) with computer processing and real-time TV display (512 x 256 x 4 bit) of processed data.

FIGURE 1 THE SRI MARK IX LIDAR SYSTEM

UNCLASSIFIED

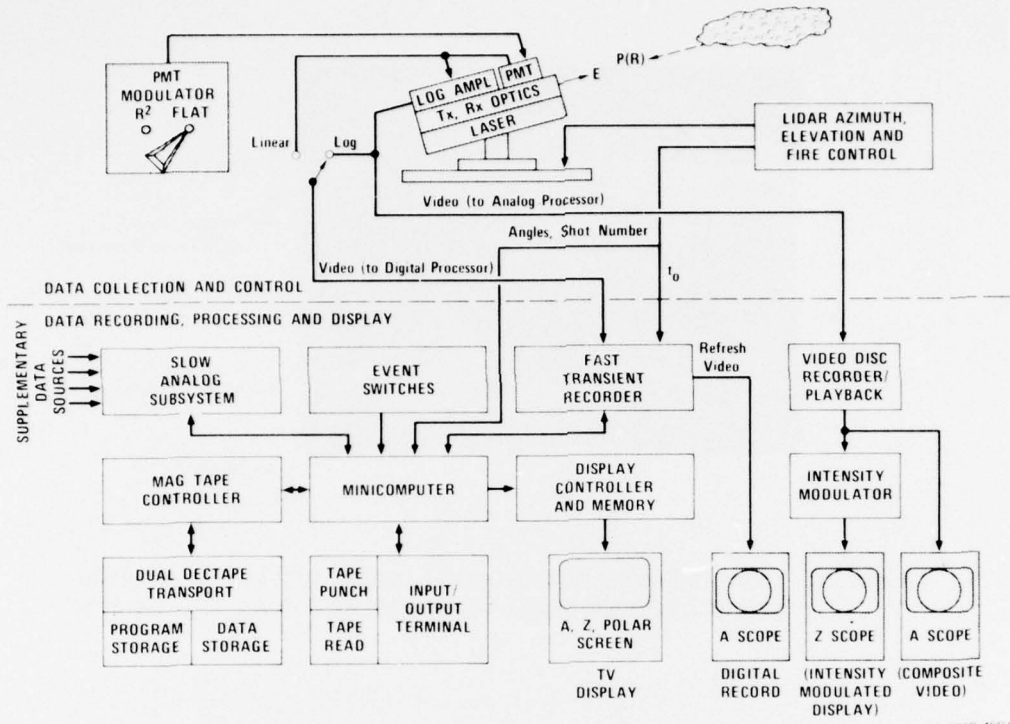


FIGURE 2 BLOCK DIAGRAM OF THE SRI MOBILE MARK IX LIDAR SYSTEM

can easily be determined for any geometric path. In this example, the lidar operator instructed the program to plot five vertical plume density profiles at the horizontal distances marked by a short vertical line segment above the plume cross section. The vertical relative-density profiles are plotted on the screen in terms of 10 dB/division (10 dB = one order of magnitude of variation in plume density), and each profile is offset 10 dB for clarity. Similar procedures could be used to derive relative-density profiles along propagation paths of any orientation.

Figure 5 illustrates the capabilities of the Mark IX digital display system and of the ability to incorporate supplementary data (see Figure 2) for effective analysis. The TV display has 256 vertical raster lines, each with 512-point resolution in the vertical; each point, in turn, is displayed as one of 16 brightness levels (the most significant 4-bits of each 8-bit data word stored on tape). In this figure, the top half of the TV screen is used for generating a height/time cross section of atmospheric structure as observed with the lidar. The bottom half of the screen is used to generate a corresponding height/time cross section of atmospheric structure observed with an acoustic radar (sodar). Each vertical raster line presents an intensity modulated display of the

UNCLASSIFIED

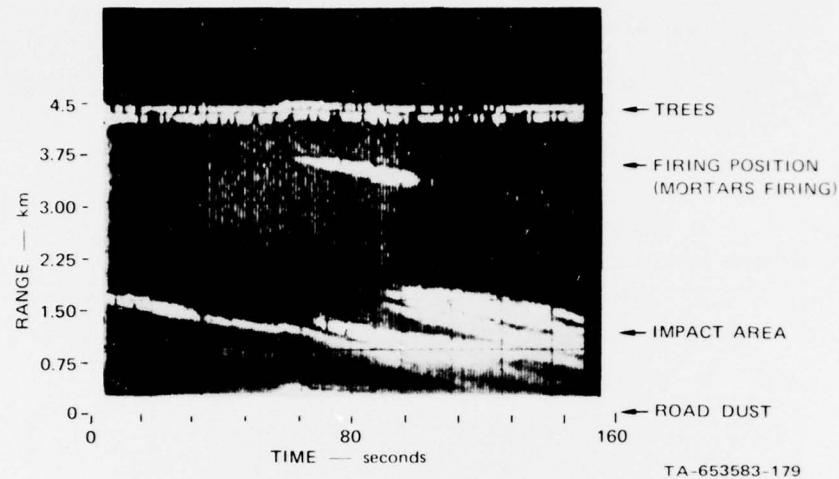


FIGURE 3 LIDAR-DERIVED DISTANCE/TIME CROSS SECTION OF AEROSOL STRUCTURE RESULTING FROM MORTAR FIRING AND IMPACT

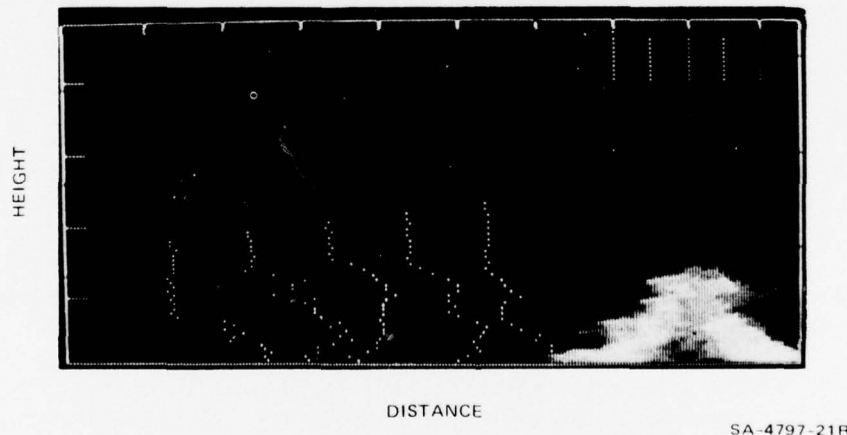


FIGURE 4 EXAMPLE OF COMPUTER-GENERATED VERTICAL PLUME DENSITY PROFILES

Lidar is located at lower left corner. The height and distance scale is 75 m/div. Plume vertical concentrations (relative to clear air with a scale of 10 dB/div) are plotted at the lower left and the horizontal position associated with each profile is plotted in the upper right.

UNCLASSIFIED

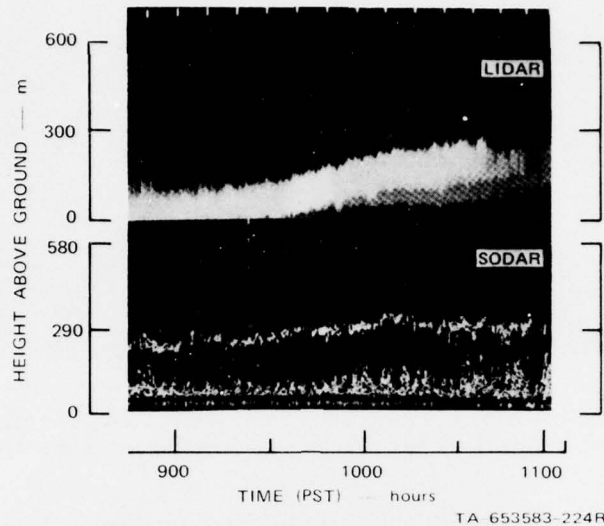


FIGURE 5 DUAL LIDAR/SODAR DISPLAY OF ATMOSPHERIC STRUCTURE MEASURED AT MENLO PARK, CALIFORNIA

The most intense lidar return shown is from fog and stratus cloud, which the lidar pulses did not completely penetrate before 1030 PST.

backscatter signature recorded from one sound pulse and one laser pulse that are emitted nearly simultaneously into the atmosphere.

The records presented in Figure 5 were collected at Menlo Park, California, beginning with the presence of a low-visibility, surface-based stratus cloud layer. The lidar pulses did not completely penetrate the stratus layer before 1030 PST, and hence the layer top is not defined by the early lidar data. However, the layer top is determined from the sodar data, because acoustic backscattering results from temperature (and, possibly, humidity) inhomogeneities occurring in the subsidence inversion that caps the stratus layer. The lidar data show that the stratus layer lifts from the surface with the beginning of the larger convective plumes shown on the sodar record (\sim 0950 PST). As the optical density of the layer decreases, as shown by the lidar, the layer top determined by the lidar and sodar records agree. Lidar and sodar data are complementary for the study of the propagation environment above the surface; the lidar detects the suspended particulate matter associated with the sodar-detected thermal structure, and the sodar can be used effectively to evaluate the penetration capabilities of various lidar systems.

The use of an overhead lidar scan to observe spatial variation of sub-visible cirrus is illustrated by the data presented in Figure 6 (data collected at White Sands Missile Range). Repetitive angular scans can be used to observe movement in cloud (and aerosol) patterns, thus, providing information

UNCLASSIFIED

UNCLASSIFIED

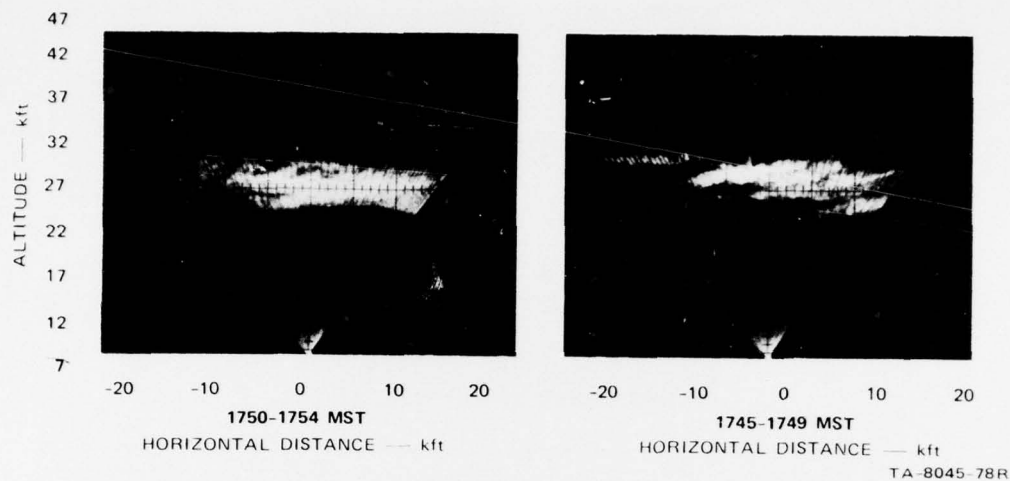


FIGURE 6 LIDAR ELEVATION ANGULAR SCAN OBSERVATIONS OF CIRRUS CLOUD STRUCTURE DURING THE PERIOD 1745-1755 MST ON 22 MARCH 1973

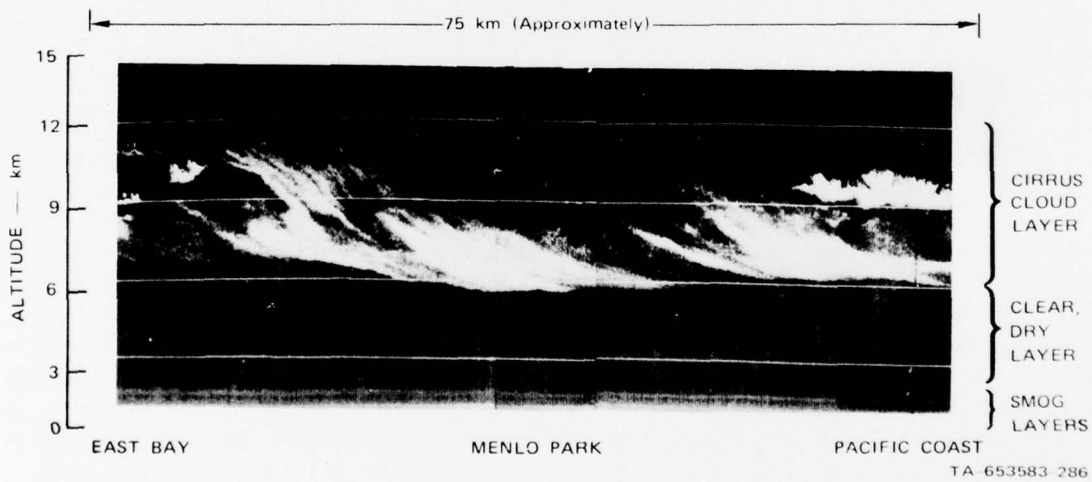


FIGURE 7 LIDAR OBSERVED CIRRUS CLOUD STRUCTURE OBSERVED OVER MENLO PARK, CALIFORNIA FROM 1000 TO 1200 LOCAL TIME (23 JANUARY 1976).

Time has been equated to horizontal distance by assuming wind information at cloud altitude and that cloud structure remains constant as the clouds are advected by the wind

UNCLASSIFIED

on wind direction and velocities. Figure 7 presents data that show the structure of cirrus clouds passing overhead at Menlo Park, California. Only the densest elements were visible to surface observers.

The lidar has been used at Kwajalein to document absolute cirrus cloud densities along reentry paths (Uthe et al., 1976; Uthe et al., 1974). Use of in situ sampling aircraft is limited, because of possible large time and space variations of cloud densities, and because of possible dangers. The lidar technique could be used equally well to define cloud densities along propagation paths. The data collected established a high frequency throughout the year of tropical high-altitude (12-18 km) subvisible cirrus clouds that typically persist for several days. Cloud thicknesses were frequently observed to be less than 1 km, and in many cases the clouds were relatively dense (high water content), though they were subvisible to surface and airborne observers and to visible and infrared satellite sensors. Applying computational algorithms written for operation on the Mark IX computer-based digital system, absolute cloud densities were evaluated in real-time for operational use (Uthe and Allen, 1975). By comparison with in situ measurements of cloud density, it was concluded that the lidar-derived values were not critically dependent on assumed factors of crystal size and shape.

Lidar can also provide high space and time resolution information on the density structure of falling precipitation. An example is shown in Figure 8. The excellent penetration of the lidar pulse (0.7 μ m wavelength) through the precipitation elements (up to the cloud base) is explained by the large forward scattering associated with scattering particles much larger than the illuminating wavelength. The forward scattered light is effectively added to the unscattered pulse, decreasing the effective attenuation of the laser energy. Therefore, in this case, useful information on the transmission properties of the propagation medium is obtained. Interesting features evident in Figure 8 include the obvious wind shear, the elevated precipitation not reaching ground level (virga), and a dark band near an altitude of 4 km, which has also been observed on other data.

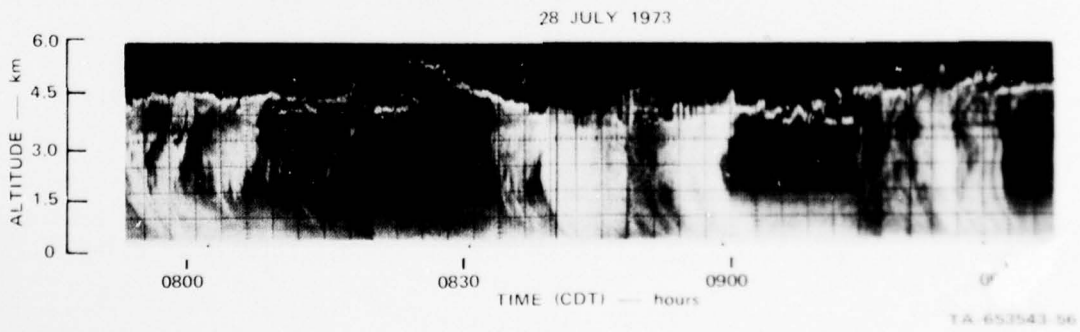


FIGURE 8 LIDAR OBSERVATIONS OF PRECIPITATION STRUCTURE OVER ST. LOUIS, MO

UNCLASSIFIED

III QUANTITATIVE EVALUATION OF OPTICAL AND PHYSICAL DENSITIES

The single-scattering lidar equation (Equation 1, Collis and Uthe, 1972) describes factors that determine the response of a lidar system for a given atmospheric condition. Included in the formulation are two optical parameters that relate characteristics of the atmospheric medium along the propagation path to the response (signature) function. The backscatter coefficient determines the amount of light backscattered at a given distance from the lidar, and the extinction coefficient determines the transmission properties along the path intervening between the backscattering volume and the lidar system. For relatively clear atmospheres, the attenuation term can normally be ignored or well approximated, using standard atmospheric models. Only a system calibration or reference to an atmospheric region of known backscatter is required to evaluate the lidar signature in terms of absolute volume backscatter coefficients. However, for atmospheric regions of large attenuation rates, information on the backscatter-to-extinction ratio must be independently measured or estimated, in order to remove the effect of attenuation. Derivation of optical or physical density terms requires information on backscatter-to-extinction or backscatter-to-density ratios representative of the atmospheric medium being observed. Collis and Russell (1976) and Collis and Uthe (1972) provide further discussion. Examples applied to the derivation of smoke plume densities are given by Johnson and Uthe (1971), and Viezee et al. (1969) discuss derivation of extinction coefficients for low visibility atmospheres. Lidar has also been used to measure transmission losses in dust clouds that are generated by near-surface high-explosive events (Viezee and Uthe, 1976).* Some additional results that demonstrate possible quantitative applications are given below.

In quantitatively evaluating the propagation environment from backscatter data, it is important to define possible variations in the backscatter-to-extinction or backscatter-to-density ratios resulting from uncertainties of particle size, shape, and composition distributions. For example, Figure 9 presents data derived from lidar observations of both black and white smoke plumes, generated by using the same instrumentation technique but different chemical composition (Uthe, 1975). As the density of the plume was increased, its opacity was measured by analyzing the clear air lidar returns observed before and after the plume return; these values are related to the plume return in Figure 9. These data show that approximately 5 dB (factor of 3) of signal variation can occur for extreme changes of composition.

A more controlled experiment has been reported by Uthe and Lapple (1972). A large-scale chamber was especially designed and constructed for making remote (≈ 500 ft) observations of generated aerosols of known particle size, shape,

* These results are classified and are not presented in this unclassified written paper. They will, however, be discussed in the oral presentation.

UNCLASSIFIED

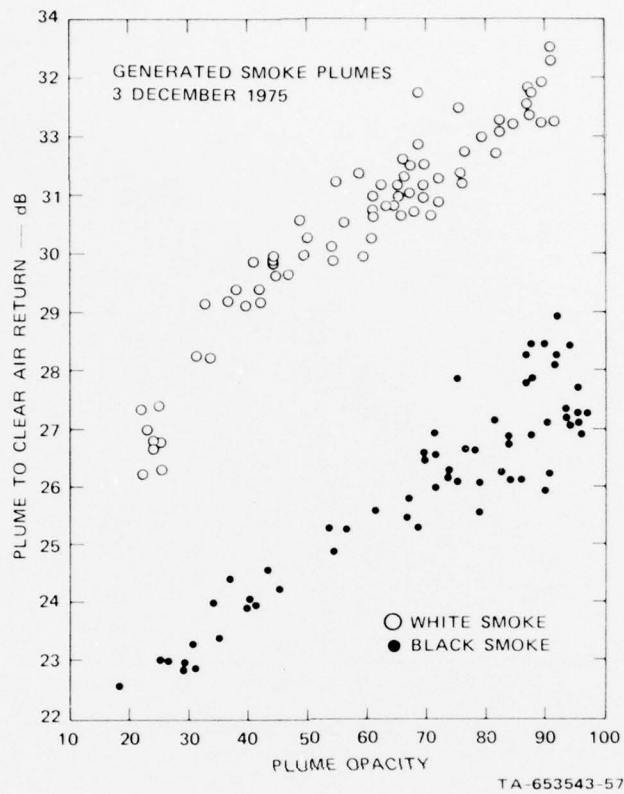


FIGURE 9 PLUME RETURNS PLOTTED AGAINST OPACITIES
DERIVED FROM NEAR- AND FAR-SIDE CLEAR
AIR RETURNS

composition, and concentration. Figure 10 presents the results of using actual fly ash from a coal-burning power plant, classified into four size categories. The results show that for a $0.7 \mu\text{m}$ wavelength lidar system, the backscatter-to-extinction ratio is nearly independent of the particle-size classification. It was also shown, however, that at this wavelength the backscatter-to-mass concentration ratio is greatly dependent on particle size. Results using a $1.06 \mu\text{m}$ wavelength lidar indicated that the backscatter-to-extinction ratio is more dependent on particle size, but the backscatter-to-mass ratio is less dependent on particle size than at the $0.7 \mu\text{m}$ wavelength.

Multiple wavelength lidar systems can be used to derive range-resolved gas attenuation coefficients. The differential absorption technique uses atmospheric aerosols as targets to backscatter energy to the lidar receiver. If one wavelength is within the center of an absorbing gas line, while the other wavelength is outside of the line, then the difference in receiver energy at the two wavelengths can be analyzed for gas attenuation rates. Range-resolved demonstrations of the technique have been made using visible (Schotland, 1966; Grant et

UNCLASSIFIED

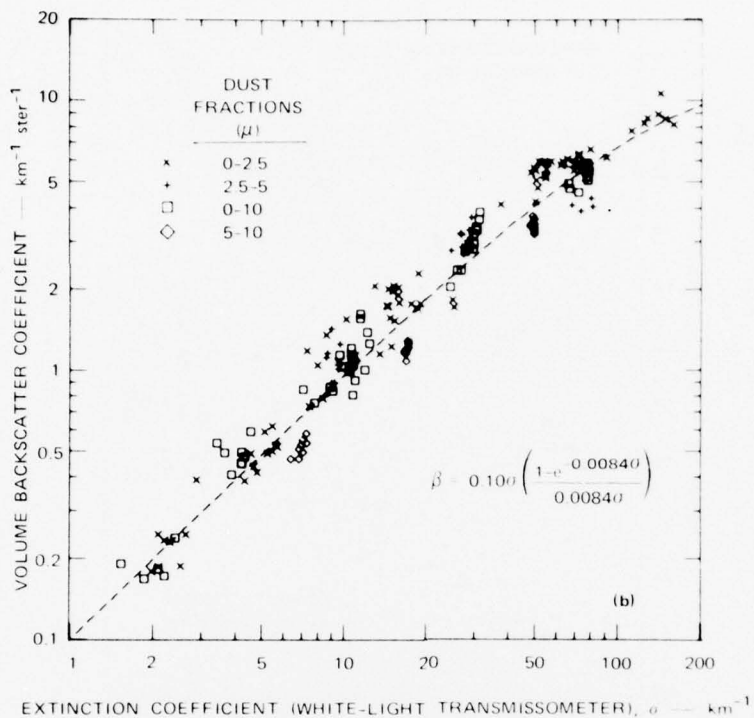


FIGURE 10 VOLUME BACKSCATTER COEFFICIENTS (β) OBSERVED AT A LIDAR WAVELENGTH OF 0.7μ RELATED TO WHITE-LIGHT VOLUME EXTINCTION COEFFICIENTS

The dashed line represents the best fit to the data of the nonlinear equation indicated.

al., 1974) and ultraviolet (Grant and Hake, 1975) lasers. Extending these capabilities to the infrared region of the spectrum permits access to the characteristic infrared absorption lines of hundreds of additional gaseous species. For example, Figure 11 presents data derived with a CO_2 lidar system (Murray et al., 1976). A parametric series of expected lidar signatures has been generated for homogeneous atmospheres with extinction coefficients varying between 0 and 0.8 km^{-1} . Superimposed on this plot are two observed signatures taken on the R(18) and R(20) lines (10.260 and $10.247 \mu\text{m}$ wavelengths). The total extinction coefficients appear to be approximately 0.1 and 0.8 km^{-1} for the R(18) and R(20) lines, respectively. As a check on these lidar-derived values, in situ humidity measurements and the water-vapor absorption coefficients measured by Shumate et al. (1975) were used to estimate the extinction coefficients as 0.093 and 0.83 km^{-1} . Thus the in situ estimates are in good agreement with the lidar-derived values.

UNCLASSIFIED

UNCLASSIFIED

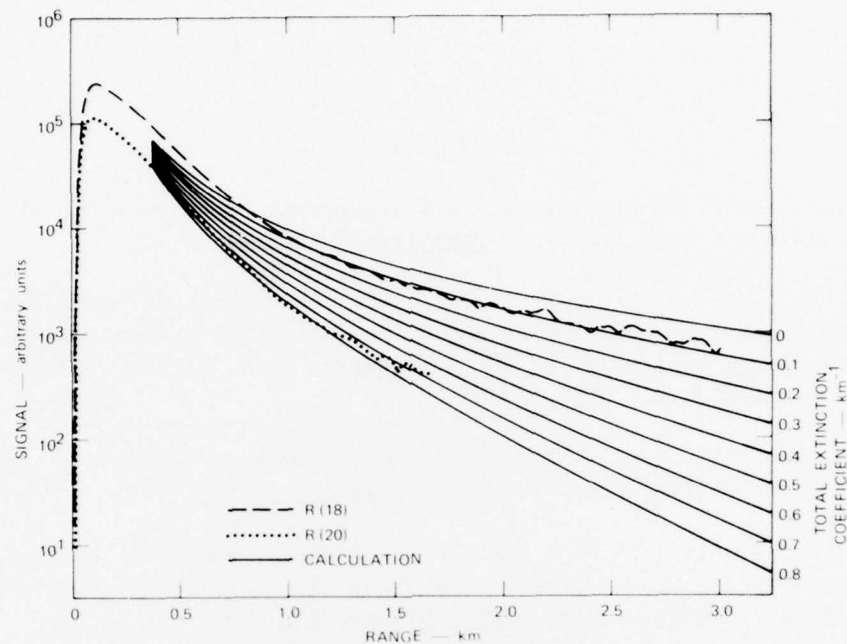


FIGURE 11 SINGLE-ENDED MEASUREMENT OF THE TOTAL EXTINCTION COEFFICIENT USING THE INFRARED LIDAR SYSTEM

This single-ended method to measure total extinction may be a valuable tool in assessing infrared, high-energy laser propagation characteristics of the atmosphere. By using the simultaneous information on particulate backscattering contained in the lidar data, a useful separation of particulate and gaseous attenuation could also be attempted. SRI is now actively pursuing research on both the particulate and gaseous aspects of the propagation medium.

IV CONCLUSIONS AND RECOMMENDATIONS

The experimental results presented in this paper illustrate the potential of the lidar technique for measuring the propagation environment, with the spatial and temporal resolution required for evaluating its effect on military communication and weapon systems.

Additional experimental programs are recommended to extend the data base for evaluating the capabilities and limitations of the lidar technique. Specific experiments should include various wavelength lidar systems, and they should also provide in situ observations of such quantities as aerosol characterization (particle size, shape, composition, and concentration), atmospheric transmission (using conventional two-ended transmissometers), and meteorological variables (temperature, humidity, pressure, winds). Measurements should be made for various natural atmospheric conditions and for controlled, man-made particulate and gas environments.

UNCLASSIFIED

UNCLASSIFIED

REFERENCES

Collis, R.T.H., and E. E. Uthe, 1972: Mie scattering techniques for air pollution measurement with lasers. Opto-Electronics, 4, 87-99.

Collis, R.T.H., and P. B. Russell, 1977: Lidar measurement of particles and gases by elastic backscattering and differential absorption. To be published in Laser Monitoring of the Atmosphere, E. D. Hinkley, Editor. Springer-Verlag, N.Y., N.Y.

Grant, W. B., and R. D. Hake, 1975: Calibrated remote measurement of SO_2 and O_3 using atmospheric backscatter. J. Appl. Phys., 46, 3019.

Grant, W. B., R. D. Hake, E. M. Liston, R. C. Robbins, and E. K. Proctor, 1974: Calibrated remote measurement of NO_2 using the differential-absorption backscatter technique. Appl. Phys. Letts., 24, 550.

Johnson, W. B., and E. E. Uthe, 1971: Lidar study of the Keystone stack plume. Atmos. Environment, 5, 703-724.

Murray, E. R., J. E. van der Laan, J. G. Hawley, R. D. Hake, and M. F. Williams, 1976: Remote sensing of gases using single-ended differential-absorption lidar systems. Paper presented at the Workshop on Remote Sensing of the Marine Boundary Layer, Vail, Colorado, 9-11 August.

Nanevicz, J. E., J. B. Chown, and R. J. Allen, 1976: Lidar surveillance, location and identification of weapon firings. Paper presented at Seventh Department of Defense Conference on Laser Technology, U.S. Military Academy, 10 June.

Schotland, R. M., 1966: Some observations of the vertical profile of water vapor by a laser optical radar. Proceedings of the Fourth Symposium on Remote Sensing of Environment, Ann Arbor, Michigan, 12-14 April.

Shumate, M. S., R. T. Menzies, J. S. Margolis, and L. G. Rosengran, 1975: Proceedings of the IEEE/OSA Conference on Laser Engineering and Applications, Washington, D.C.

Uthe, E. E., 1975: Lidar applications for smoke plume opacity measurements. Final Report, U.S. Environmental Protection Agency, P.R. No. TS-129. Stanford Research Institute, Menlo Park, California.

UNCLASSIFIED

UNCLASSIFIED

Uthe, E. E., and R. J. Allen, 1975: A digital real-time lidar data recording, processing, and display system. J. Optical and Quantum Electronics, 7, 121-129.

Uthe, E. E., R. J. Allen, and P. B. Russell, 1974: Light detection and ranging (LIDAR) support for STM-8W and PVM5 reentry operations. Final Report, Contract No. F04701-74-C-0016 (USAF/SAMSO), Stanford Research Institute, Menlo Park, California.

Uthe, E. E., and W. B. Johnson, 1976: Lidar observations of plume diffusion at Rancho Seco generating station. Final Report, study SOA75-316 (Electric Power Research Institute), Stanford Research Institute, Menlo Park, California.

Uthe, E. E., and C. E. Lapple, 1972: Study of laser backscatter by particulates in stack emissions. Final Report, Contract CPA70-173, Environmental Protection Agency. Stanford Research Institute, Menlo Park, California.

Uthe, E. E., W. Viezee, and R. J. Allen, 1976: A mobile laser radar system and results from its application to military programs (U). Paper presented at Seventh Department of Defense Conference on Laser Technology, U.S. Military Academy, 10 June.

Viezee, W., E. E. Uthe, and R.T.H. Collis, 1969: Lidar observations of airfield approach conditions: an exploratory study. JAM, 8, 274-283.

Viezee, W., and E. E. Uthe, 1976: Laser experiments during pre-dice throw II. Final Report, Defense Nuclear Agency, Contract DNA001-75-C-0264 (Report DNA POR 6911), Stanford Research Institute, Menlo Park, California.

UNCLASSIFIED

(This page intentionally left blank.)

UNCLASSIFIED

....This paper is UNCLASSIFIED

HIGH ENERGY LASER PROPAGATION METEOROLOGICAL SENSITIVITY ANALYSIS (U)

D. Cordray, J. Fitzgerald, S. Gathman,
J. Hayes, J. Kenney, G. Mueller, and R. Ruskin
U.S. Naval Research Laboratory
Washington, D.C. 20375

ABSTRACT (Unclassified)

(U) An analysis of the sensitivity of the propagation of high energy laser (HEL) beams to fluctuations in two of the most important meteorological variables is presented. A brief review of the features of HEL propagation is discussed in order to render the sensitivity study meaningful to those unfamiliar with HEL systems. The study is presented as a prototype "EO-MET" investigation. Definitive conclusions are drawn and recommendations are made for future research work in propagation and in meteorology.

1. INTRODUCTION

a. Definition of a Sensitivity Study

(U) A sensitivity study here shall mean the establishment of relationships between one set of important dependent variables and another set of important independent variables, followed by an analysis of what errors, and the distributions in the latter set, imply for the former set. Within the framework of an "EO-MET" study, the first, dependent, set of variables will be the principal optical quantities that are required to characterize a piece of electro-optic hardware, design or idea, while the second independent set of variables will be the meteorological parameters that affect the performance of that equipment. In an idealized EO-MET program, as indicated by Figure 1, a data bank would exist that would contain all the necessary optical and meteorological data; with a particular piece of equipment in mind, we define the important optical and meteorological parameters and return to the data bank for their relationship. If the data bank is not large enough, the study itself may need to establish the required relationships (and add the result to the data bank). These relationships then provide the basis for a "Performance" analysis where the concept of "performance" must be carefully understood. The ensuing study could then provide the operational limitations of the device or idea, feedback information to alter device design for improvement or rejection of it; assuming the latter does not instantly occur, the study should produce recommendations for new EO designs if necessary, and for further meteorological work.

(U) Figure 2 is an illustration of these ideas in a more specific case, namely applying the general ideas to the HEL weapons system (HELWS) concept. This figure will be discussed in more detail later.

(U) Just as it is very important to specify what a given sensitivity study is, it is equally important to emphasize what it is not. The presentation made here is not a systems analysis of an HELWS, nor is it an effectiveness study of the HELWS concept (wherein kill probabilities, etc. are defined). We shall be more precise after we have had a chance to discuss, briefly, the HELWS concept and the basic features of HEL propagation.

b. Structure of an HELWS

(U) A high energy laser weapon system (HELWS) is a complicated entity consisting of many components each of which must perform intrinsically difficult tasks under short notice and at high speed. Figure 3 is a schematic representation of what such a system might be like. Such a

UNCLASSIFIED

diagram is very useful, even if only tentative, because it provides a framework on which one may identify and discuss, among other things, potential component electro-optical systems, electro-optic and propagation research and development ideas, meteorological research areas and meteorological hardware needs, HEL laser design needs, engineering problems, command and control hardware and software requirements, problems of system integration, and many more items. While this diagram is only suggestive and applies just to HELWS, similar such analyses can and ought to be performed in detail for other electro-optic weapons and systems.

(U) The diagram indicates that the heart of an HELWS is the command control center, C³, (whatever that may consist of and however it may be physically configured). It will receive long range tracking data presumably from conventional radars, but possibly laser radars and, earlier, infrared search sets (IRSS). All this information would be gathered for each hostile aircraft approaching the mother vessel and the path of each would be determined; in the meantime C³ would return signals to the detectors instructing them on what to concentrate or scanning rates to use, ECM to employ, etc.

(U) Separate from the detection and long range tracking would be a meteorological suite. We shall see how wind, water vapor aerosols, wind and temperature turbulence and ship boundary layer effects can or might affect the instantaneous, real-time performance of the HEL beam itself, while optical clutter, water vapor, turbulence will affect IRSS's, FLIRS and other detection/imaging devices. Generally, there will be no feedback from C³ to the meteorological suite. It is most probable that remote sensing of all these variables, if all indeed are needed, will be necessary because point measurements onboard ship may prove to be totally misleading due to shipboard induced variations in all of the meteorological parameters. In addition, we must consider the possibility of "slaving" a meteorological suite to each HELWS aboard ship.

(U) C³ must receive information from each of the HEL devices onboard ship, noting their locations (which propagation has taught us to be vital)^{1),2)}, types (i.e., wavelengths, size, beam shape, cw, multiple pulse,....), fuel supply and a host of other data not of concern to us here.

(U) A very important component of the HELWS will be the Navy Pointer/Tracker (NPT) or some variation of it. C³ will select a target for each HELW aboard ship and command the corresponding NPT to "coarse track" it, ultimately handing over to "fine track," employing techniques such as suggested in several AUSAM (Automatic Aimpoint Selection and Guidance) proposals to identify the target at as far a range as possible, select a vulnerable spot or spots on the missile, fire the HEL beam and keep it on until the missile has been destroyed or deflected. The NPT will use a battery of E-O devices which may include FLIRS (near and far IR), LLTV, laser radar, possibly active FLIRS, and, of course, the HEL beam itself. The NPT will be mechanically constructed to cover as wide a view of the sky and horizon as possible, while also maintaining internal temperature, pressures and humidities as constant as possible. The exit port for the high energy laser beam will consist of a large hole with an "air curtain" (as we see in many modern office buildings) to maintain constant gradients in temperatures between the inside and out, and to prevent aerosols and other foreign objects from hitting or coming to rest on vital optical components. One of the final mirrors in the optical train that will carry the beam from the laser to the outside will be "flexible" so that deliberate distortions may be introduced into it, so that they will undo the deleterious effects of the atmosphere on the beam as much as possible^{3),4)}. The method is called adaptive optics and has already been successfully demonstrated in a large number of low power applications and in HEL simulations.

(U) Finally, the HELWS must have a method of damage assessment; a rough measure of time of exposure to the HEL should be predetermined for various vulnerable spots and how the missile will behave after lethal exposure has occurred must somehow be convolved into the system.

(U) All the information gathered by these components will be funneled to the C³ where there must exist, among other things, target identification algorithms, target selection algorithms (i.e., tactical strategy methods built into the system), laser monitoring algorithms which, besides keeping track of what condition each laser is in will assign one to each target, laser device control (e.g., setting power and focussing of the beam during the engagement, propagation information with which to do these laser settings, lethality data to help determine tactical strategies, estimate burn times, NPT control algorithms for handover times, for determining which portion of which missile should first be exposed, integration of HELWS with other onboard long range and close-in weapons systems, and many more such functions. It is important to recognize that an HELWS is a close-in weapons system for hard kills; if we put five kilometers as its extreme range, for purposes of illustration only, then, for a Mach 1 missile, the total engagement time must be of the order of 15 sec; for Mach 3 missiles, ~ 5 sec. In addition, exposure times must be as short as possible, 1 - 3 seconds, because the enemy is expected to try to saturate the defenses of the capital ships and therefore one laser will probably have to handle more than one target.

(U) Because the anti-ship cruise missile trajectories are expected to be flat, i.e., at or

UNCLASSIFIED

about deck level, and for reasons of propagation²⁾ (i.e., stagnation zones) that will not be discussed until later, it is felt that the closer the NPT's are to the stern of the ship, the better they can perform their job. The meteorological sensitivity study will raise questions about this choice of location as well.

c. Synopsis of High Energy Laser Propagation

(U) In order to understand the strategy used in the meteorological sensitivity study and the results obtained, a brief characterization of the results of HEL propagation for CW beams must be provided¹⁾. The meteorological phenomena which alter the structure of an HEL beam from what would have been its vacuum configuration are: 1) wind velocity; 2) absolute water vapor; 3) temperature turbulence; 4) aerosols; and 5) jitter. If we ignore temperature turbulence, jitter and aerosols, and do not admit adaptive optics, then the results, assuming uniform wind velocity and water vapor (beam attenuation), are easily described. The beam attenuation heats the air whose index of refraction is thereby decreased. Hence the beam deflects into the wind and increases in size (this phenomenon is called "thermal blooming"). Using the peak intensity in the focal plane as a measure of the performance of an HELWS plotted against the power emanating from the NPT, Figure 4 displays the main features that always appear for any beam; such curves are generally referred to as "power optimization curves." Without thermal blooming, the intensity on target increases in proportion to the power emanating from the NPT; because of thermal blooming, however, a power is ultimately achieved beyond which any further increase in aperture power causes more thermal blooming and less peak intensity on target. Two curves are shown here, one for zero slew rate and one for a positive slew rate. Formulae for these curves can be obtained by curve fits to the data provided by sufficiently many computer runs and are called "scaling laws;" a symbolic representation is shown with the figure and the function Γ depends upon four dimensionless parameters - the distortion number $N_p \sim \alpha P/V$, the absorption number $N_A = \alpha f$, the Fresnel number $N_F = ka^2/f$, and the slewing number $N_w = wf/V$. α and V are the meteorological variables; α is the absorption coefficient and V is the transverse component of wind flow across the beam (a combination of ship velocity, wind velocity and slewing or tracking speed). The values (P, I) at optimum are called optimum power P_{op} and optimum peak intensity I_{op} and depend critically upon the absorption and wind speed V . The present scaling laws placed the target at the focal plane; I_{op} , P_{op} are sensitive to this range also. Under a wide variety of expected tactical scenarios, P_{op} has been shown to vary dramatically²⁾ by several orders of magnitude. No laser can deliver a peak intensity better than I_{op} - hence the laser will do no better than predictions made with P_{op} . An important implication to laser designers is that P must be variable on an instantaneous basis; how variable it must be and over what range will depend upon a better understanding of the lethality values required by different targets, keep out ranges, last deposition ranges, and acceptable definitions and values for kill probabilities. This latter subject lies in the province of an effectiveness study which is not discussed here.

(U) The above propagation results are not qualitatively altered by the introduction of adaptive optics;⁵⁾ the optimization phenomenon still occurs, but a higher powers and yielding higher peak intensities. However, there are now two scaling laws - one that describes the power optimization curve and a second that prescribes the phase distortions that must be applied to the adjustable mirror. Second scaling law may be explicitly calculated in the "open-loop" version of adaptive optics, or it may become automatically developed in the "closed-loop" version, COATS, of adaptive procedures. Our discussion has been confined to CW high power lasers; the propagation of high power multiple pulse beams will not be treated here.

2. HEL PROPAGATION SENSITIVITY STUDY

(U) At the request of PM-22, the Navy High Energy Laser Program Office, a short sensitivity study covering the NPT and the HEL beam was to have been conducted over a period of three months⁶⁾. One-third of the time into the study, money and manpower changes reduced the study group by over one-third and therefore only the sensitivity of the HEL beam was continued. The results will be summarized here.

(U) As the previous discussion has shown, propagation seems still to be a necessary component of the information to be stored in C³; whole propagation codes could be stored there, but one computation of intensity on target at one range would take longer than the entire engagement time; in addition, the propagation programs cannot give, ab initio, the optimum laser power. In contrast the scaling laws can give optimum power and deliverable intensity and beam size at any range and under given meteorological conditions in micro-seconds. Therefore, it has been our hope and our strategy to determine whether or not the scaling laws could be preserved in spite of the meteorological fluctuations that occur in the real atmosphere which violate the assumptions upon which the scaling laws were based.

(U) To accomplish our task, we had to define: 1) the threats, 2) the scenarios, 3) the weapons system, 4) the prime electro-optic intitities under consideration, 5) the meaning of

UNCLASSIFIED

UNCLASSIFIED

"performance", and then perform the necessary calculations to prove or disprove our guess.

(U) The threat is taken to be an antiship cruise missile which flies "horizontally" (or almost so) at about deck height above the average ocean surface at speeds from Mach 1 to Mach 2.5; the lethality values for destruction of the missile are of no consequence here because of our definition of "performance". The scenarios, in general, will have the cruise missiles attacking the ship from any angle, but because this leads to a very wide variety of variables, the scenarios used here will tend to bracket the "best" and "worst" possible cases, as is illustrated in Figure 5. (There are, in fact, better cases, and there are in fact many worse cases than our "best" and "worst" cases, respectively, but our results will cover those.) The basic feature about our "worst" or most unfavorable case is that there is no slewing of the beam, and the wind and ship speed have the tendency to cancel each other.

(U) We shall choose as our tentative weapons system a chemical DF laser with the power output in lines clustered about $3.8 \mu\text{m}$ - the BDL and the NACL output. The weighted average absorption coefficient is about $.05 \text{ km}^{-1}$, but this will be doubled in some of our cases. The lasers will be placed, as shown in Figure 5, at the stern of the ship. Mirror diameters will range from $.75 \text{ m}$ to 1.25 m . Beam configuration will be that of an infinite Gaussian, a truncated Gaussian, or uniform circular beam, and the NACL and BDL outputs will be used as well. Target ranges, and therefore focal lengths, will range from $.5 \text{ km}$ to 5 km . The prime electro-optic parameters of the beam are: 1) its peak intensity I_{pk} on target, 2) its "area" on target (which is related to I_{pk}), 3) the power P emanating from the NPT, the optimum values of these quantities, and, if we were to do effectiveness studies the turn-on times, the burn times, and delivered fluence. The "performance" of the high energy laser beam will be the percentage errors in the critical optical quantities due to percentage errors in the measurement of, or due to fluctuations in, the absorption coefficient (dependent greatly on water vapor density), the large scale fluctuation in the transverse component of the wind, fluctuations in aerosols and in temperature turbulence. Thus, "performance" is the set of values that $\delta I/I$, $\delta P/P$, $\delta Q/Q$ (Q is defined as fluence), etc. can assume for given fluctuations. Meteorological data for mean values of many important meteorological variables were collected for the North Atlantic and the Eastern Mediterranean and cumulative probability distributions of some of these quantities will be discussed later in this session by B. Katz. Fluctuations about mean values were chosen in accordance with the measurements made by Kaimal, et al, and those assembled by them in their 1972 paper, which contained data taken over land and over water. Their data were used by us in a way so as to worsen our conclusions; for example, we always selected unstable conditions to reflect the case of highest wind turbulence. Temperature turbulence on the other hand can be incorporated into the scaling laws in the way suggested by L. C. Bradley and independently confirmed by W. P. Brown, Jr. In this study we had not the time to deal with fluctuations in the turbulence levels or the aerosols. (Indeed, the effect of aerosols on HEL beams is still being investigated by the propagation community.)

(U) First we note that different types of beams under what are otherwise identical conditions, will give different results. Therefore, the immediate question to answer is, does each require a separate sensitivity study. Figure 6 shows a nomogram which gives $\delta I/I$ for various combinations of $\delta a/a$ and $\delta v/v$ where δa and δv are taken to uniform errors in measurement; the effects of three different beams for which scaling laws were available are indicated by the three different kinds of lines and it is seen that no significant differences in $\delta I/I$ for a given value of $\delta a/a$, $\delta v/v$ appear. The propagation codes were used for NACL and BDL runs with the result that these beams were slightly less sensitive. For this figure, P was set at P_{op} , 1 meter optics, $v=10 \text{ m/sec}$, and $f = 1 \text{ KM}$; $a = .05 \text{ km}^{-1}$. Hence we immediately have the significant result that the sensitivity of the beam performance does not depend significantly on the beam shape. This result is a time and money saving result; we shall work, in the case of scaling laws, with Gaussian beams henceforth. Figure 7 shows the same kind of plot for Gaussian beams using, as in the previous figure, the worst case, but varying the mirror size from $.75 \text{ M}$, 1.00 M , to 1.25 M . Power here was again P_{op} and $R = 1 \text{ km}$. The significance of this result is that the sensitivity of the beam to mirror size for fixed beam shape is virtually nil.

(U) Figure 8 compares sensitivities at two extreme ranges; this shows that, although the intensity on target is highly attuned to range, its "performance" or "sensitivity" is not strongly range dependent.

(U) The results implied Figures 6,7,8 are slightly power dependent, but for the region where blooming is important, not strongly so.

(U) The same kinds of studies were done using the propagation codes but with velocity fluctuations included; i.e., if x were the direction down the beam, the transverse component of velocity was $u(x) = U + u'(x)$. Here U is time average and $u'(x)$ is a perturbation on it. $u'(x)$ was chosen in conformance with the results of Kaimal, et al, and those whose work they summarize; it was chosen to worsen the thermal blooming in most instances by picking the most unstable cases and by choosing realizations of the wind turbulence that would be most detrimental to the beam. These cases will occur in reality with very small probability. The results of these studies gave

UNCLASSIFIED

UNCLASSIFIED

results that never exceeded the results from the one-sided average errors depicted in Figure 6,7 and 8. Indeed, the sensitivity of the beam in these cases proved generally less than systematic measurements. (Details can be found in Cordray, et al⁶) Long-wave length fluctuations, as might be expected, tended to give results like the one-sided errors of a single sign; fluctuations whose linear dimensions were short compared to the focal length cause errors in target intensity to cancel one another to a great degree.

(U) The results could be summarized by a formula derivable from the Gaussian scaling law:

$$\frac{\delta I}{I} \approx \frac{\delta \alpha}{\alpha} + \frac{\delta v}{v} \quad (\text{at } P_{op})$$

with $\delta I/I$ showing a slight power dependence away from P_{op} . $\delta v/v$ here may be interpreted as $\sigma_u / [V + U + \alpha x]$ where σ_u is the variance in $u(x)$, or $\delta v/v$ is one-sided error discussed earlier. The value of $\delta U \approx .20$, perhaps up to 50% in extreme cases, but $\sigma_u / [V + U + \alpha x]$ will in general be much smaller since the ship speed will generally dominate the denominator. At close ranges, where α is a fast function of range, slewing will also dominate. Conditions will arise where $V + U + \alpha x = 0$, the so-called stagnation zone condition. Propagation in the presence of stagnation zones is very poor; the theoretical predictions and experimental results agree and have been reported elsewhere⁸). The important implication here is that the attack geometry and meteorological conditions cause a bow laser to be plagued by stagnation zones while stern lasers are not.

(U) The absorption coefficient, coming into $\delta I/I$ in much the same manner as $\delta v/v$, nevertheless does not have the same importance as $\delta v/v$ because $\delta \alpha/\alpha$ is down by an order of magnitude or more.

(U) In summary, the conclusion of the HEL beam propagation sensitivity study may be quite simply stated that fluctuations of the real wind across the beam path do not seriously affect the delivered intensity on target. Concomitantly, we may also conclude that systems analyses, effectiveness analyses, etc. whose results depend upon the using of scaling laws/propagation codes which do not include velocity turbulence will not have their results significantly altered by the presence of large scale velocity turbulence. Water vapor turbulence is wholly negligible. A third way of stating our results is that the beam will propagate well or badly as determined by the average wind and not affected greatly by wind fluctuations.

(U) It is important to note that we make no statement about the effects of fluctuations in temperature turbulence (see Gathman - these proceedings) or of aerosols. We also note that we have included homogeneous temperature turbulence into the scaling laws by root sum squaring the induced angular spread with that due to blooming⁷). We do not state here that temperature turbulence is or is not important; it will depend upon many factors and must simply be taken into account as a fact of propagation life, adaptive optics or not.

3. RECOMMENDATIONS

1. (U) NPT sensitivity studies must be performed. Design/performance studies on FLIRS have already been done (C. F. Moser, P.⁹) but the specific instruments used in the NPT must be analyzed. Also the AUASAM techniques of target identification, target orientation, aim point selection and maintenance will, like FLIRS, be dependent on transmittance and especially on turbulence and optical clutter. Selection of a contractor to perform these studies has been made.

2. (U) Development of Scaling Laws for:

- a) stagnation zone blooming
- b) high dive attack angles

should continue; this kind of work is presently going on in the propagation community of the HEL program and is very difficult (to say the least). However, the results may prove vital to the use of a potential bow laser may thus become a useful part of a total HELWS.

3. (U) Sensitivity Studies for Adaptive Optics Methods are recommended, both for the open and closed loop variety. At first glance, this may seem unnecessary because the results obtained here probably apply to the scaling laws obtained with adaptive techniques. However, there are other more compelling reasons for such a study. First, as has already been noted, there is a second "scaling law" when deformable mirrors are used that may be far more sensitive to errors and fluctuations in wind, attenuation aerosol and turbulence measurements. Second, the plungers which deform the mirror have a finite inertia or response time and finite deformation limit; there are only a finite number of them. In short, the real septum will fall short of the idealized one, so that sensitivity studies ought to be done on real systems. Our third reason has to do with aerosol backscatter. It has already been shown¹⁰ that, for the closed COATS system, the SNR

UNCLASSIFIED

may be rendered quite low because the backscatter signal from ocean ambient aerosols may be comparable to the diffuse signal returned from the target. Now what has been neglected heretofore in propagation of HEL beams from a naval vessel are the effects of the vessel itself on the environment. Two things occur which are important to adaptive optics and the NPT. The ship creates a wake as it plows through the water which increases the aerosol densities in the ship's environs by an amount which may be several orders of magnitude over ocean ambient densities¹¹). The magnitudes and size distributions are, at present, unknown, but the effect has been seen. Secondly, the ship creates turbulent atmospheric boundary layer about itself which grows in size with ship speed and as the stern is approached. For a 30 KT carrier it is estimated to be 150 m - 300 m in radius at the stern of the ship. This turbulent boundary layer will carry the aerosols upward into the high energy laser beam exacerbating any SNR problem the ambient aerosols alone would have produced. Indeed, the noise signal may be so strong as to render adaptive optics inoperative (in the closed loop method). A second effect also occurs. There are large temperature differences in the air between the bow and the stern of any ship $\gtrsim 50^{\circ}\text{C}$ ¹²); as the air flows past the ship, temperature eddies develop which cause refractive index fluctuation. As these pass the exit port in the NPT, they behave like lenses just as ordinary ambient turbulence would. However, their strength and sizes are probably large, but unknown. While adaptive optics are supposed to correct for temperature turbulent fluctuations, there are limits to a real system. Finally a third effect should be mentioned; the NPT will have an air curtain whose main functions are to keep foreign objects off of the optics and to maintain a constant temperature gradient across the aperture from inside to out. With ship induced large temperature small scale fluctuations, this may not be possible. Finally, we note that wind tunnel studies on the USNS HAYES, the NRL research vessel, as well as on other ships, has shown that wind reversals can take place about the ship because of its structure, leading possibly to permanent stagnation zones or wind reversals. Therefore, while all these effects lead us to suggest adaptive optics sensitivity studies, we also recommend :

4. (U) A Study of Ship Induced Meteorological Effects for the reasons cited above. The study should include velocity distribution, temperature distribution, aerosols densities and size distributions and water vapor and all their fluctuations in the areas of importance to any and all EO systems that might be placed onboard ship.

5. (U) Acquisition of an Accurate Larger Data Set of the Above Meteorological Quantities for the ocean ambient case (i.e., away from ship-induced effects). These quantities should also be obtained as a function of altitude and cumulative probabilities and joint probabilities for oceanic areas of particular interest could be developed from the data. The data can be used to check various models and theories that will help to condense our knowledge into more manageable form.

6. (U) Development, Acquisition and Use of Remote Sensing Meteorological Suite. The meteorological quantities that are desired have been mentioned above; the data would be of use to all types of EO systems that compose the HELWS, and other kinds as well. With the acquisition and use of such systems, meteorologists can calibrate them, use them to acquire new data, improve their design, and provide experience and guidance to the Navy user.

4. SUMMARY

(U) We have described some of the progress that has been made in the understanding of the propagation of HEL beams as an introduction of the HEL beam sensitivity study. We have shown that large scale wind fluctuation will not seriously affect the results already achieved by ignoring them. Finally, we have mentioned a few new areas that need investigation. We have seen that the HELWS program is broad enough to spawn a whole array of EO-MET programs that can occupy the attention of a large number of EO and meteorological investigators for some time to come.

REFERENCES

1. Brief survey papers on HEL propagation papers may be found in several papers. Hayes, J. N., "Propagation of High Power Laser Beams Through the Atmosphere; An Overview," AGARO Conference Proceedings No. 183, NATO, Oct. 1975; Edelberg, Seymour, "An Overview of the Limitations on the Transmission of (Multiple Pulse) High Energy Laser Beams Through the Atmosphere by Nonlinear Effects," same proceedings; Ulrich, P. B. in the Proceedings of Second DOD High Energy Laser Conference, Colorado Springs, 1976, to be published.
2. Hayes, J. N., Hancock, J. H., Ulrich, P. B., Takhan, E. K., Cordray, D. M., Proceedings of the First DOD High Energy Laser Conference, 1974.
3. Bradley, L. C., "Laser Propagation Through a Turbulent Medium," Optics Research (Lincoln Lab Report #1), 1972.

UNCLASSIFIED

4. Bridges, W. B., Brenner, P. T., Lazzara, S. P., Nussmeier T. A., O'Meara, T. R., Sangrienen, J. A., and Brown, W. P., Jr., "Coherent Optical Adaptive Techniques," *Applied Optics* 14, p. 50 (1974).
5. Bradley, L. C., and Herrmann, J., "Phase Compensation for Thermal Blooming," *Applied Optics* 13, p. 331, 1974.
6. D. Cordray, J. Fitzgerald, S. Gathman, J. Hayes, J. Kenney, G. Mueller and R. Ruskin, "Meteorological Sensitivity Study on High Energy Laser Propagation," NRL Report, to be published, 1976.
7. Bradley, L. C. (unpublished), Brown, W. P., Jr., (unpublished).
8. Berger, P., Ulrich, P., Ulrich, S., and Gebhardt, F., "Transient Thermal Blooming of a Slewed Laser Beam Containing a Region of Stagnant Absorber," to appear in *Applied Optics* (Feb).
9. Moser, P., "Flir Performance Modelling and its Dependence upon Climatology and Meteorology," *Proceedings of the Electro-Optical/Meteorology Meeting of 7 August 1975*, NRL Memo Rpt #3240.
10. Otto, R. G., et al, "Tracker Backscatter Study," Lockheed Palo Alto Research Laboratory, May 1976.
11. Ruskin, R. (private communication)
12. Ruhnke, L. (private communication)

UNCLASSIFIED

A GENERAL FORMAT FOR EO-MET SENSITIVITY STUDIES

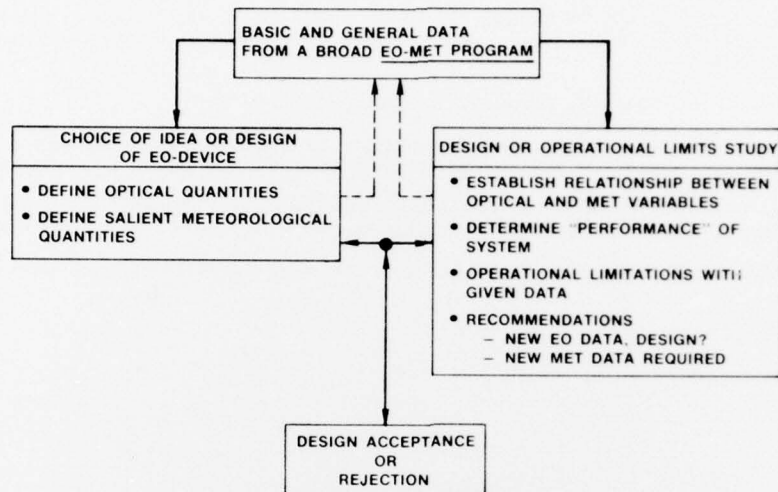


Figure 1. General Format for Electro Optical/Meteorology Sensitivity Study (U)

SPECIFIC FORMAT FOR HEL SENSITIVITY STUDY

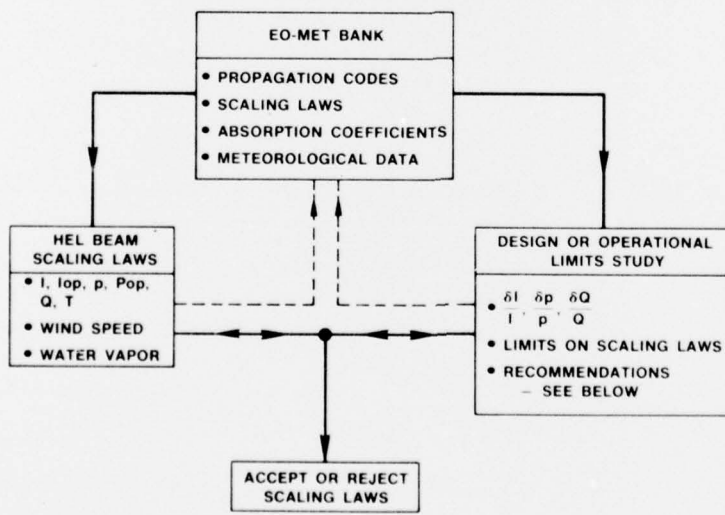


Figure 2. The Format of Figure 1 Applied Specifically to the HEL Beam Sensitivity Study. (U)

UNCLASSIFIED

UNCLASSIFIED

THE STRUCTURE OF THE HIGH ENERGY LASER WEAPON SYSTEM(S)

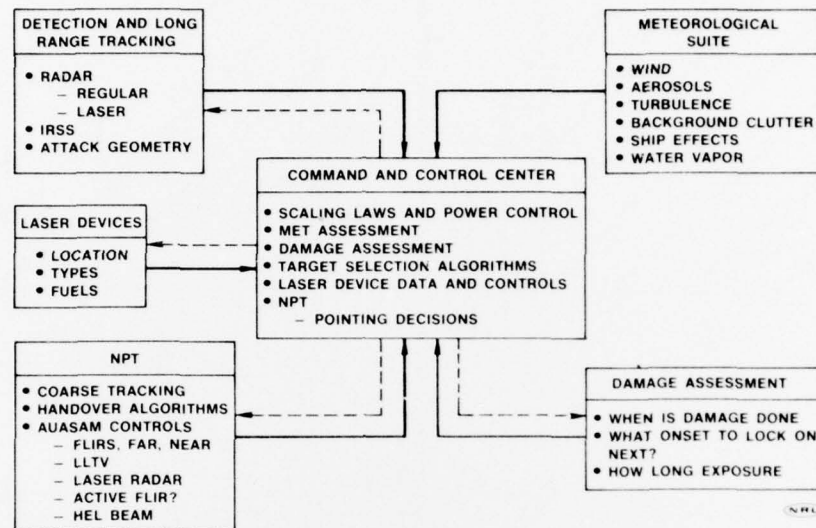


Figure 3. A Postulated Structure of an HELWS. (U)

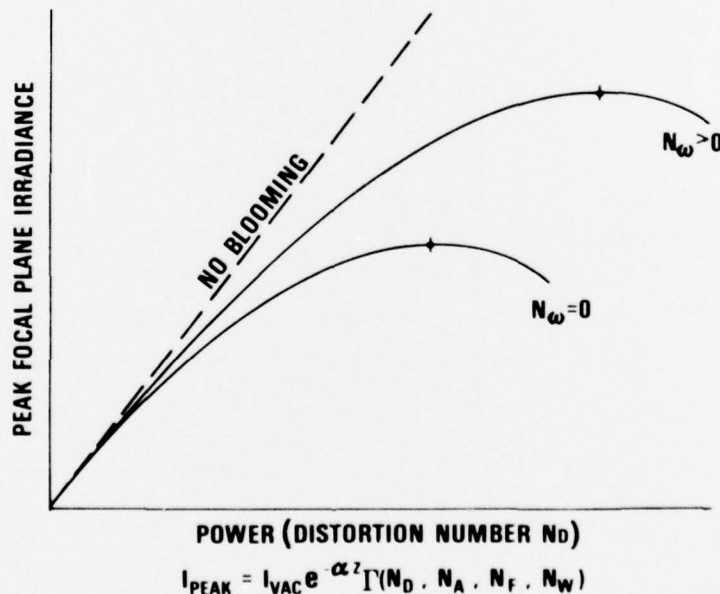


Figure 4. Power Optimization Curves Derived from the Theory of HEL Beam Propagation. Optimum Power and Intensity Prints are Indicated for both the Non-Slewing ($N_w = 0$) and Slewing Cases ($N_w > 0$). (U)

UNCLASSIFIED

UNCLASSIFIED

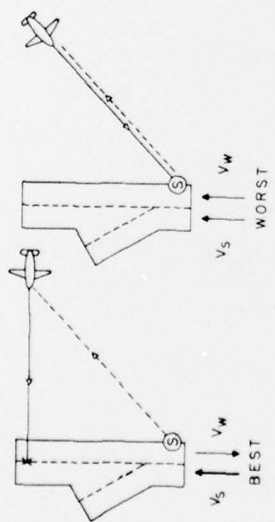


Figure 5. Schematic Representation of Favourable and Unfavourable Scenarios. (U)

500

UNCLASSIFIED

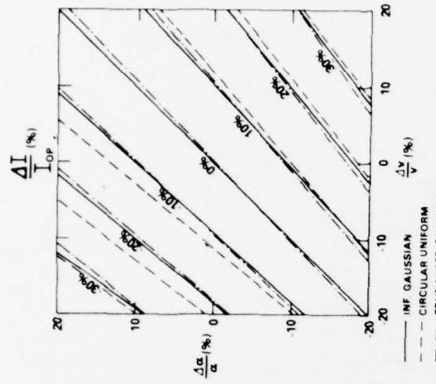


Figure 6. Nomogram Comparing Sensitivities of HEL Beams of Three Different Beam Shapes. (U)

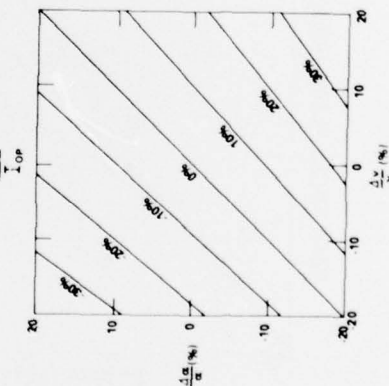


Figure 7. Nomogram Comparing Sensitivities of HEL Beams of Three Different Mirror Sizes (no discernable difference appears). (U)

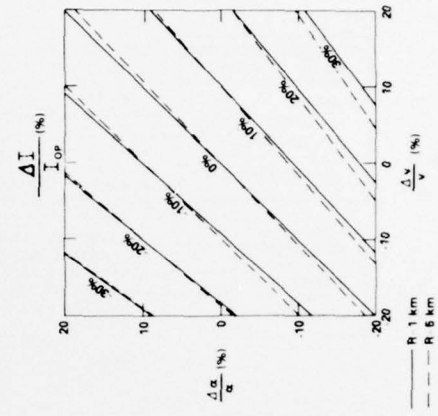


Figure 8. Nomogram Comparing Sensitivities of a Given HEL Beam at 1 km and 5 km. (U)

UNCLASSIFIED

UNCLASSIFIED